

---

**Functional Analysis  
of the Xin-Repeat Protein Family  
in Cross-striated Muscle**

---

D I S S E R T A T I O N

zur

Erlangung des Doktorgrades (Dr. rer. nat.)

der

Mathematisch-Naturwissenschaftlichen Fakultät

der

Rheinischen Friedrich-Wilhelms-Universität Bonn

von

Stefan Eulitz

aus

Berlin

Bonn, 2011



Angefertigt mit Genehmigung der Mathematisch-Naturwissenschaftlichen Fakultät der  
Rheinischen-Friedrich-Wilhelms-Universität Bonn

1. Gutachter: Herr Prof. Dr. Dieter O. Fürst

2. Gutachter: Herr PD Dr. Gregor Kirfel

Tag der Promotion: 09. September 2011

Erscheinungsjahr: 2011

Die vorliegende Arbeit wurde von November 2005 bis Februar 2011 in der Arbeitsgruppe molekulare Zellbiologie am Institut für Zellbiologie der Rheinischen Friedrich-Wilhelms-Universität Bonn unter Anleitung von Prof. Dr. Dieter O. Fürst erstellt.

Hiermit versichere ich, dass ich die vorliegende Dissertation, abgesehen von den ausdrücklich bezeichneten Hilfsmitteln, persönlich, selbständig und unter Offenlegung der erhaltenen Hilfen angefertigt habe.

Diese Arbeit hat bisher noch keiner anderen Prüfungskommission zur Begutachtung vorgelegen.

Stefan Eulitz

Parts of this work have been already published:

## **Publications**

Otten, J.; van der Ven, P.F.; Vakeel, P.; Eulitz, S.; Kirfel, G.; Brandau, O.; Boesl, M.; Schrickel, J.W.; Linhart, M.; Hayess, K.; Naya, F.J.; Milting, H.; Meyer, R.; Fürst, D.O. (2010). Complete loss of murine Xin results in a mild cardiac phenotype with altered distribution of intercalated discs.

*Cardiovascular Research* (2010), doi: 10.1093/cvr/cvp345

## **Poster and Presentations**

Stefan Eulitz, Elisabeth Ehler, Padmanabhan Vakeel, Jörg A. Schenk, Hendrik Milting, Burkhard Micheel, Dieter O. Fürst, Peter F. M. van der Ven (2006). Unusual splicing events result in distinct Xin isoforms that associate differentially with filamin c and Mena/VASP.

*Poster and presentation, European Muscle Conference, Heidelberg*

Stefan Eulitz, Alina Morsch, Prisca Boisguerin, Dirk Anhuf, Katrin Hayeß, Peter F. M. van der Ven, Dieter O. Fürst. (2010)

*Poster and presentation, Annual Meeting of Bonner Forum Biomedizin*

# Abstract

The assembly of the sarcomere of cross-striated muscle involves a plethora of transcription factors, signalling and structural proteins and requires their coordinate interplay in order to construct this uniquely regular structure. Its early upregulation in muscle precursor cells during embryonic development and in activated satellite cells upon skeletal muscle damage render the protein Xin an interesting candidate for being involved in orchestrating muscle morphogenesis. The establishment of the H-2K cell line as a new reliable model system for studying myofibrillogenesis *in vitro* using immunofluorescence microscopy and protein expression analysis of major structural components of the sarcomere in this work provided a new tool to investigate Xin function during myogenic differentiation. Examining the transcription level revealed that all three Xin isoforms A, B and C are being upregulated upon initiation of differentiation while downregulated as soon as H-2K cells gain their contractility. On the protein level, only the expression of isoforms A and B was doubtlessly identified exhibiting a course related to their transcriptional level. During differentiation, Xin was strongly associated with non-striated myofibrils (NSMF), where it colocalized with its binding partner filamin C, but not with Z-disc precursor structures. Consistently, in contractile myotubes Xin was absent from mature Z-discs but longitudinally connected to immature sarcomeres.

In this work, the SH3 domains of nebulin and nebulette were identified as novel ligands of Xin isoforms A and C and peptide scans elucidated for the first time the exact peptide motif and the residues essential for this interaction. Bimolecular fluorescence complementation (BiFC) assays of Xin C and nebulette in embryonic cardiomyocytes selectively demonstrated the potential cellular sites of this interaction since BiFC complexes were exclusively formed along NSMF's in early developmental stages but not at mature Z-discs. This finding was corroborated by localization studies of nebulin and Xin in H-2K cells as colocalization was only observed at specific sites of NSMF's substantiating the developmental regulation of this interaction.

Identification of the protein LIMCH1 as the first binding partner exclusively interacting with the largest Xin isoform A provided first insights into isoform-specific functions. Yeast two-hybrid and biochemical studies mapped the binding interface to the C-terminal LIM domain of LIMCH1 and impressively showed its specificity. Investigation on the mRNA and protein level during myofibrillogenesis of H-2K cells displayed that LIMCH1 is also upregulated at the onset of differentiation constantly increasing until the final stage pointing to an interaction during that process. In rat skeletal muscle tissue and H-2K cells an additional larger LIMCH1 isoform (LIMCH1 muscle) was detected which pre-

sumably contains the LIM domain and functional coiled-coil motifs like the other isoform LIMCH1 FL. BiFC experiments in A7r5 cells using fragments of LIMCH1 and Xin might imply that LIMCH1 is capable of restricting the site of their interaction.

The Xin-Repeat protein family in human comprises two members, Xin and the larger Xirp2. Since both share a similar domain layout and the ability to bind actin filaments and Ena/VASP proteins, dissection of complementary and exclusive binding properties suggests discrimination of their function. While Xirp2, similar to Xin, could be shown to be a filamin C-specific binding protein which can form multimers and also interacts with the SH3 domain of nebulin and nebullette via a consensus motif, the interaction with  $\alpha$ -actinin is an exclusive quality of the Xirp2 repeat region. Furthermore, this study clearly demonstrated that human Xirp2 is upregulated during myogenic differentiation and, in contrast to Xin, a constituent of the mature Z-disc. Immunofluorescence studies using antibodies raised against different epitopes of Xirp2 provided a first clue to the spatial orientation of Xirp2 within the Z-disc thereby determining the arrangement of its binding partners.

Investigating cryo-sections of human skeletal muscle with antibodies against Xin and Xirp2 directly showed for the first time their involvement in skeletal muscle remodelling. Skeletal muscle areas lacking a proper sarcomere arrangement exhibited Xin and Xirp2-containing longitudinal structures connecting adjacent sarcomeres. These strands were not prominently associated with major structural components of the Z-disc such as  $\alpha$ -actinin and nebulin while filamin C was newly identified to be associated with these structures.

In conclusion, this work provides a detailed view on differences and similarities of Xin-Repeat protein thereby offering further insights into their function. While both Xin and Xirp2 are involved in early events of myogenic differentiation, Xin takes over a rather transient role whereas Xirp2 presumably contributes to a permanent scaffold for Z-disc structure. Their participation in skeletal muscle remodelling render Xin-Repeat proteins important players of myogenic development and remodelling processes.

# Contents

List of Figures	ix
-----------------	----

List of Tables	xv
----------------	----

<b>1 Introduction</b>	<b>1</b>
1.1 The Musculature . . . . .	1
1.1.1 Vertebrate Skeletal Muscle . . . . .	1
1.2 Skeletal Muscle Development . . . . .	4
1.2.1 Embryonic development . . . . .	4
1.2.2 Myogenesis . . . . .	5
1.2.2.1 Embryonic Myogenesis . . . . .	5
1.2.2.2 Fetal Myogenesis . . . . .	5
1.2.2.3 Adult Myogenesis . . . . .	6
1.2.2.4 Sarcomerogenesis . . . . .	7
1.3 Skeletal Muscle Regeneration . . . . .	8
1.4 Skeletal Muscle remodelling . . . . .	10
1.5 Sarcomere Structure . . . . .	11
1.5.1 Thin Filaments . . . . .	11
1.5.2 Thick Filaments . . . . .	13
1.5.3 Nebulin . . . . .	14
1.5.4 Nebulette . . . . .	15
1.5.5 The Z-disc . . . . .	16
1.5.5.1 $\alpha$ -Actinin . . . . .	17
1.5.5.2 Filamin C . . . . .	18
1.5.6 The M-Band . . . . .	20
1.6 The Myotendinous Junction . . . . .	21
1.7 Costameres . . . . .	21

---

1.8	The Heart . . . . .	23
1.8.1	Heart Development . . . . .	23
1.8.2	Cardiomyocytes . . . . .	24
1.9	Cellular Junctions . . . . .	26
1.9.1	Cadherins . . . . .	26
1.9.1.1	$\beta$ -Catenin . . . . .	29
1.9.2	Integrins . . . . .	30
1.9.3	Vinculin . . . . .	32
1.9.4	Talin . . . . .	33
1.10	Xin-Repeat Proteins . . . . .	34
1.11	Aim of the Study . . . . .	37
<b>2</b>	<b>Material and Methods</b>	<b>39</b>
2.1	Chemicals . . . . .	39
2.2	Culture Media . . . . .	39
2.3	Antibiotics . . . . .	40
2.4	Bacterial and Yeast Strains . . . . .	40
2.4.1	Cloning . . . . .	40
2.4.2	Protein Expression . . . . .	40
2.4.3	Yeast Two-Hybrid System . . . . .	40
2.5	Vectors and cDNA Libraries . . . . .	40
2.5.1	Protein Expression Vectors . . . . .	41
2.5.1.1	pET23aEEF . . . . .	41
2.5.1.2	pET23aT7 . . . . .	41
2.5.1.3	pET23aMyc . . . . .	41
2.5.1.4	pET28a . . . . .	41
2.5.1.5	pGEX-6P-3 . . . . .	41
2.5.2	Vectors for Eukaryotic Protein Expression . . . . .	42
2.5.2.1	Venus NT . . . . .	42
2.5.2.2	Venus CT . . . . .	42
2.5.2.3	Venus1-C . . . . .	42
2.5.2.4	Venus2-C . . . . .	42
2.5.2.5	Venus1-N3 . . . . .	43
2.5.2.6	Venus2-N3 . . . . .	43
2.5.3	Vectors for Yeast Two-Hybrid Assays . . . . .	43

---

2.5.3.1	pLexPd . . . . .	43
2.5.3.2	pACT Pd . . . . .	43
2.5.4	cDNA Libraries . . . . .	44
2.6	Molecular Biology Techniques . . . . .	44
2.6.1	cDNA Synthesis . . . . .	44
2.6.2	Polymerase Chain Reaction . . . . .	44
2.6.3	Semiquantitative RT-PCR Analysis . . . . .	45
2.6.4	Agarose Gel Electrophoresis . . . . .	46
2.6.5	DNA Fragment Purification from Agarose Gels . . . . .	47
2.6.6	DNA Digestion . . . . .	47
2.6.6.1	Analytical Restriction Digest . . . . .	47
2.6.6.2	Preparative Restriction Digest . . . . .	47
2.6.7	Ligation . . . . .	48
2.6.8	Production of Competent Bacterial Cells . . . . .	48
2.6.9	Measurement of Transformation Competence . . . . .	48
2.6.10	Transformation of Competent Bacteria . . . . .	48
2.6.11	Small-Scale Plasmid Preparation . . . . .	49
2.6.12	Large-Scale Plasmid Preparation . . . . .	49
2.6.13	Spectrophotometric DNA and RNA Quantitation . . . . .	49
2.7	Protein Chemistry . . . . .	50
2.7.1	Expression of Recombinant Proteins in <i>E. coli</i> . . . . .	50
2.7.2	Protein Expression Analysis . . . . .	50
2.7.3	Preparative Protein Expression . . . . .	51
2.7.4	Purification of Recombinant Proteins . . . . .	51
2.7.4.1	Protein Purification under Native Conditions . . . . .	51
2.7.5	Cell and Tissue Extracts . . . . .	52
2.7.5.1	Protein Extracts for SDS-PAGE . . . . .	52
2.7.5.2	Isolation of RNA from Cells and Tissues . . . . .	52
2.7.6	Protein Quantitation . . . . .	53
2.7.6.1	Bradford Assay . . . . .	53
2.7.7	SDS Polyacrylamide Gel Electrophoresis (SDS-PAGE) . . . . .	53
2.7.8	Protein Transfer . . . . .	54
2.7.8.1	Semi-Dry Western Blot . . . . .	54
2.7.8.2	Tank-Blotting . . . . .	54
2.8	Immunological Methods . . . . .	55



---

2.8.1	Immunodetektion . . . . .	55
2.8.1.1	Quantitative Analysis . . . . .	55
2.8.1.2	Qualitative Analysis . . . . .	56
2.8.2	Antibodies . . . . .	56
2.8.2.1	Purification of Polyclonal Antibodies . . . . .	56
2.8.3	Frozen Tissue Sections . . . . .	59
2.8.4	Immunostaining of Cells and Tissues . . . . .	60
2.8.4.1	Paraformaldehyde Fixation . . . . .	60
2.8.4.2	Methanol-Acetone Fixation . . . . .	61
2.8.4.3	Staining . . . . .	61
2.9	Protein Interaction Assays . . . . .	62
2.9.1	Yeast Two-Hybrid System . . . . .	62
2.9.1.1	Sequential Transformation . . . . .	62
2.9.1.2	Test of Activation of the <i>HIS3</i> Reporter Gene . . . . .	63
2.9.1.3	Test of $\beta$ -Galactosidase Activity . . . . .	63
2.9.2	Co-Immunoprecipitation . . . . .	64
2.9.3	Chemical Cross-linking . . . . .	64
2.9.4	Peptide Scan . . . . .	65
2.9.5	Bimolecular Fluorescence Complementation (BiFC) Analysis . . . . .	65
2.10	Cell Culture . . . . .	67
2.10.1	Cell Lines . . . . .	68
2.10.1.1	H-2K <sup>b</sup> -tsA58 Cells . . . . .	68
2.10.1.2	A7r5 Cells . . . . .	68
2.10.2	Cell Thawing . . . . .	69
2.10.3	Cell Passaging . . . . .	69
2.10.4	Cell Freezing . . . . .	69
2.10.5	Isolation of Embryonic Mouse Cardiomyocytes . . . . .	70
2.10.6	Transient Transfections . . . . .	70
2.10.6.1	TurboFect Transfection . . . . .	70
2.10.6.2	Electroporation of Embryonic Mouse Cardiomyocytes . . . . .	71
2.11	Microscopy . . . . .	71
2.11.1	Transmitted Light Microscopy . . . . .	71
2.11.1.1	Epi-fluorescence Microscopy . . . . .	71
2.11.1.2	Confocal Laser Scanning Microscopy . . . . .	73
2.11.1.3	Fluorescence Recovery After Photobleaching (FRAP) . . . . .	73

---

2.11.2	Scanning Electron Microscopy . . . . .	74
2.11.2.1	Production of Locator Cover Slips . . . . .	74
2.11.2.2	Membrane Extraction and Fixation . . . . .	74
2.11.2.3	Critical Point Drying . . . . .	75
2.11.2.4	Sputter Coating . . . . .	75
2.11.3	Image Processing . . . . .	76
<b>3</b>	<b>Results</b>	<b>77</b>
3.1	<i>In vitro</i> Myofibrillogenesis of Murine H-2K <sup>b</sup> -tsA58 Cells . . . . .	77
3.1.1	Sarcomere Development . . . . .	79
3.1.1.1	Early Phase (Day 1–2) . . . . .	80
3.1.1.2	Intermediate Phase (Day 3–4) . . . . .	84
3.1.1.3	Late Phase (Day 5–8) . . . . .	87
3.1.2	Expression Profile of Sarcomeric Proteins . . . . .	91
3.2	Murine Xin in H-2K <sup>b</sup> -tsA58 Myoblasts During Myofibrillogenesis . . . . .	94
3.2.1	Transcription of Murine Xin During Myofibrillogenesis of H-2K <sup>b</sup> - tsA58 Cells . . . . .	94
3.2.2	Protein Expression of Murine Xin During Myofibrillogenesis of H- 2K <sup>b</sup> -tsA58 Cells . . . . .	97
3.2.3	Xin Localization During <i>In vitro</i> Myofibrillogenesis of Murine H- 2K <sup>b</sup> -tsA58 Cells . . . . .	100
3.2.3.1	Xin and $\alpha$ -Actinin . . . . .	100
3.2.3.2	Xin and Filamin C . . . . .	102
3.2.3.3	Xin and Nonmuscle Myosin IIA . . . . .	104
3.2.3.4	Xin and $\beta$ -Catenin . . . . .	107
3.2.3.5	Xin Isoforms . . . . .	107
3.3	Xin is a Novel Ligand of the SH3 Domain of Nebulin and Nebulette . . . . .	110
3.3.1	Xin A and C Interact with Nebulin . . . . .	111
3.3.2	Human Xin also Binds to Nebulette . . . . .	112
3.3.3	Biochemical Verification of the Nebulin/Nebulette-Xin Interaction . . . . .	114
3.3.4	Identification of the Nebulin/Nebulette SH3 Domain Binding Se- quence in Human Xin . . . . .	115
3.3.5	Xin and Nebulin Localization During Myofibrillogenesis of H-2K Cells	117
3.3.6	The Site of Xin and Nebulette Interaction Visualized by Bimolecular Fluorescence Complementation (BiFC) . . . . .	124

---

3.3.6.1	Analysis of the Dynamics of BiFC Complexes Using Fluorescence Recovery After Photobleaching (FRAP) . . . . .	124
3.3.6.2	BiFC Analysis of the Xin C and Nebulette Interaction in A7r5 Cells . . . . .	129
3.3.6.3	Localization of the Xin-Nebulette Interaction in Embryonic Mouse Cardiomyocytes . . . . .	136
3.4	Xin Contains Functional Heptad Repeats . . . . .	143
3.4.1	Localization of Xin C Dimerization . . . . .	146
3.4.2	Murine Xin Can Also Form Oligomers . . . . .	152
3.5	The Protein LIMCH1 is the First Xin A-Specific Binding Partner . . . . .	154
3.5.1	The LIM Domain of LIMCH1 Specifically Binds Xin A . . . . .	155
3.5.2	Biochemical Verification of the Xin-LIMCH1 interaction . . . . .	159
3.5.3	Targeting of LIMCH1 Fragments in A7r5 Cells . . . . .	160
3.5.4	Visualization of the Xin-LIMCH1 Interaction in A7r5 Cells Using BiFC . . . . .	162
3.5.5	Expression of LIMCH1 in Cells and Tissues . . . . .	166
3.5.6	Identification of a New Murine LIMCH1 Splice Variant . . . . .	169
3.5.7	Transcription of Murine LIMCH1 During Myofibrillogenesis of H-2K <sup>b</sup> -tsA58 Myoblasts . . . . .	172
3.5.8	LIMCH1 Contains Functional Heptad Repeats . . . . .	174
3.6	The C-terminus of Xin B Targets to Focal Adhesions . . . . .	176
3.7	Characterization of Human Xirp2 . . . . .	181
3.7.1	Human Xirp2 is a Filamin C-Specific Binding Partner . . . . .	181
3.7.2	Human Xirp2 Binds to the SH3 Domain of Nebulin and Nebulette . . . . .	184
3.7.3	The Human Xirp2-Repeat Region and not the Xin-Repeat Region Interacts With $\alpha$ -Actinin . . . . .	188
3.7.4	Human Xirp2 Forms Dimers <i>In Vitro</i> . . . . .	191
3.7.5	Transcription of Murine Xirp2 During Myofibrillogenesis of H-2K <sup>b</sup> -tsA58 Cells . . . . .	191
3.7.6	Protein Expression of Murine Xirp2 During Myofibrillogenesis of H-2K <sup>b</sup> -tsA58 Cells . . . . .	195
3.7.7	Human Xirp2 Localization in Adult Skeletal Muscle Tissue . . . . .	196
3.8	Xin-Repeat Proteins During Skeletal Muscle Remodelling . . . . .	202
3.8.1	Xin-Repeat Proteins and $\alpha$ -Actinin in Structures of Human Skeletal Muscle Remodelling . . . . .	203

---

3.8.2	Xin-Repeat Proteins and Nebulin in Structures of Human Skeletal Muscle Remodelling . . . . .	208
3.8.3	Xin-Repeat Proteins and Filamin C in Structures of Human Skeletal Muscle Remodelling . . . . .	214
<b>4</b>	<b>Discussion</b>	<b>218</b>
4.1	Myofibrillogenesis of Murine H-2K <sup>b</sup> -tsA58 Cells . . . . .	218
4.2	Xin-Repeat Proteins During <i>In Vitro</i> Myofibrillogenesis of Murine H-2K <sup>b</sup> -tsA58 Cells . . . . .	221
4.2.1	Transcription and Expression of Xin Isoforms . . . . .	221
4.2.2	Localization of Xin Isoforms . . . . .	223
4.3	Xin-Repeat Proteins Are Novel Ligands of the SH3 Domain of Nebulin and Nebulette . . . . .	225
4.3.1	The Site of Interaction of Xin-Repeat Proteins with Nebulin/Nebulette Interaction . . . . .	228
4.3.2	Evolutionary Conservation of the Nebulin/Nebulette Binding Motifs in Xin-Repeat Proteins . . . . .	231
4.4	Xin-Repeat Proteins and Skeletal Muscle Remodelling . . . . .	234
4.5	LIMCH1 – The First Xin A-Specific Binding Partner . . . . .	237
4.5.1	Expression of LIMCH1 Isoforms in Cells and Tissues . . . . .	238
4.5.2	Oligomer Formation of LIMCH1 . . . . .	240
4.5.3	Dissection of Functional Domains in LIMCH1 . . . . .	241
4.5.4	The Site of Xin–LIMCH1 Interaction . . . . .	241
4.5.5	The Potential Role of the Xin–LIMCH1 Interaction . . . . .	243
4.6	Xin and Xirp2 – Overlapping and Distinct Function . . . . .	243
4.7	Xirp2 Orientation and Interactions Within the Sarcomeric Z-disc - Implications for Z-disc Structure . . . . .	247
	<b>Bibliography</b>	<b>252</b>
	<b>A Abbreviations</b>	<b>I</b>
	<b>B Sequences of Primers</b>	<b>IV</b>
	<b>C Vector Maps</b>	<b>VII</b>
	<b>D Human Xin cDNA Sequence</b>	<b>XX</b>

---

E Murine Xin cDNA Sequence	XXVII
F Human Xirp2 cDNA Sequence	XXXII
G Murine Xirp2 cDNA Sequence	XL
H Human LIMCH1 cDNA Sequence	XLIX
I Murine LIMCH1 cDNA Sequence	LIII

# List of Figures

1.1	Schematic Overview of the Organization of Skeletal Muscle . . . . .	3
1.2	Sarcomere Structure . . . . .	11
1.3	Schematic Overview of the Filamin Protein Family . . . . .	18
1.4	Electron Micrograph of a Myotendinous Junction . . . . .	22
1.5	Cellular Location of Costameres in Striated Muscle . . . . .	22
1.6	Heart Development and Cardiac Looping Process . . . . .	25
1.7	Expression of Cellular Junction Proteins During Muscle Development . . . . .	27
1.8	Schematic Overview of Human Xin-Repeat Proteins . . . . .	34
2.1	Combinations of Fusion Proteins Tested in a BiFC Assay . . . . .	66
2.2	SEM Locator Cover Slips . . . . .	74
3.1	Morphological Changes of H-2K Cells During Myofibrillogenesis . . . . .	78
3.2	$\alpha$ -Actinin Precedes Myomesin Expression at the Initial Stage of H-2K Cell Differentiation . . . . .	80
3.3	$\alpha$ -Actinin and Myomesin Expression in an Early Phase of H-2K Cell Differentiation . . . . .	81
3.4	Titin and the Actin Cytoskeleton in an Early Phase of H-2K Cell Differentiation . . . . .	83
3.5	$\alpha$ -Actinin and Myomesin Exhibit First Regions of Early Sarcomeres . . . . .	85
3.6	The Assembly of Premature Z-discs Precedes the Reorganization of the Actin Cytoskeleton into I-Bands . . . . .	86
3.7	Late Contractile Myotube Without Laterally Aligned Myofibrils . . . . .	87
3.8	Latest Stage of Sarcomere Development in H-2K Cells . . . . .	88
3.9	Thin Filament Arrangement In Contractile H-2K Myotubes . . . . .	90
3.10	Quantitation of Protein Expression During Myofibrillogenesis of H-2K Cells . . . . .	92

---

3.11	Quantitation of the Transcription Level of Murine Xin Isoforms During Myofibrillogenesis of H-2K Cells . . . . .	96
3.12	Protein Expression of Murine Xin During Myofibrillogenesis of H-2K Cells . . . . .	98
3.13	Localization of Xin and Sarcomeric $\alpha$ -Actinin During Myofibrillogenesis of H-2K cells . . . . .	101
3.14	Localization of Xin and Filamin C During Myofibrillogenesis of H-2K cells . . . . .	103
3.15	Localization of Xin and Nonmuscle Myosin IIA During Myofibrillogenesis of H-2K cells . . . . .	105
3.16	Localization of Xin and $\beta$ -Catenin During Myofibrillogenesis of H-2K cells . . . . .	108
3.17	Localization of Xin Isoforms During Myofibrillogenesis of H-2K cells . . . . .	109
3.18	Nebulin Fragments Interacting With Xin PR3+4 Identified in a Yeast Two-Hybrid Screen . . . . .	110
3.19	Mapping of the Nebulin Interaction Site in Human Xin . . . . .	111
3.20	Yeast Two-Hybrid Experiment of Human Xin and Nebulette . . . . .	113
3.21	Co-Immunoprecipitation of Xin and Nebulin and Nebulette . . . . .	114
3.22	Identification of the Nebulin/Nebulette SH3 Domain Binding Sequence in Human Xin . . . . .	116
3.23	Localization of Xin and Nebulin in Early Phases of Myofibrillogenesis of H-2K Cells . . . . .	119
3.24	Localization of Xin and Nebulin in Myotubes of Intermediate Stage of Differentiation . . . . .	120
3.25	Localization of Xin and Nebulin in Contractile Myotubes . . . . .	123
3.26	FRAP of BiFC Complex of Homodimerized VASP in A7r5 Cells . . . . .	125
3.27	Mobile Fractions of VASP BiFC Complex and Intact Venus . . . . .	128
3.28	Nebulette Targeting in A7r5 Cells . . . . .	131
3.29	Xin C Targeting in A7r5 Cells . . . . .	134
3.30	Localization of the BiFC Complex of Nebulette and Xin C in A7r5 Cells . . . . .	135
3.31	Localization of Nebulette in Embryonic Mouse Cardiomyocytes . . . . .	137
3.32	Localization of Xin C in Embryonic Mouse Cardiomyocytes of Late Developmental Stage . . . . .	138
3.33	Localization of Xin C in Embryonic Mouse Cardiomyocytes of Early Developmental Stage . . . . .	139
3.34	Localization of the Xin C-Nebulette Complex in Embryonic Mouse Cardiomyocytes of Late Developmental Stage . . . . .	141

---

3.35	Localization of the Xin C-Nebulette Complex in Embryonic Mouse Cardiomyocytes . . . . .	142
3.36	Prediction of Functional Heptad Motifs in Human Xin . . . . .	144
3.37	Homodimerization of Human Xin . . . . .	148
3.38	Coiled-Coil Formation of Human VASP . . . . .	149
3.39	Chemical Cross-linking of Human Xin . . . . .	150
3.40	Localization of Xin C Dimers in A7r5 Cells . . . . .	151
3.41	Chemical Cross-linking of Murine Xin C . . . . .	153
3.42	LIMCH1 Clones Identified as Xin Interaction Partners in a Yeast Two-Hybrid Screen . . . . .	154
3.43	The LIM Domain of LIMCH1 Specifically Binds Xin A . . . . .	156
3.44	Co-Immunoprecipitation of Human Xin and LIMCH1 . . . . .	158
3.45	Overview of LIMCH1 Constructs Used for Transfection . . . . .	160
3.46	Targeting of LIMCH1 Fragments in A7r5 Cells . . . . .	161
3.47	BiFC Complex Formation of Xin PR3+4 and LIMCH1 Fragments in A7r5 Cells . . . . .	164
3.48	BiFC Complex Formation of Xin A and LIMCH1 Fragments in A7r5 Cells . . . . .	165
3.49	Expression of LIMCH1 in Cells and Tissues . . . . .	167
3.50	Identification of Novel Exons in the Murine LIMCH1 Gene . . . . .	170
3.51	Quantitation of the Transcription Level of Murine LIMCH1 During Myofibrillogenesis of H-2K Cells . . . . .	173
3.52	Chemical Cross-linking of Human LIMCH1 . . . . .	175
3.53	Localization of Xin A and Xin B in A7r5 Cells . . . . .	177
3.54	Localization of Xin A $\Delta$ rep in A7r5 Cells . . . . .	178
3.55	Localization of Xin PR3+4 in A7r5 Cells . . . . .	179
3.56	Co-Immunoprecipitation of Human Xirp2 and Filamin C . . . . .	182
3.57	Co-Immunoprecipitation of Human Xirp2 and Filamin A . . . . .	183
3.58	Co-Immunoprecipitation of Human Xirp2 and Filamin B . . . . .	185
3.59	Yeast Two-Hybrid Experiment of Human Xirp2 and Nebulin and Nebulette . . . . .	186
3.60	Co-Immunoprecipitation of Human Xirp2 and Nebulin and Nebulette . . . . .	186
3.61	Identification of the Nebulin/Nebulette SH3 Domain Binding Sequence in Human Xirp2 . . . . .	187
3.62	Yeast Two-Hybrid Experiment of Human Xirp2 and $\alpha$ -Actinin 2 . . . . .	189
3.63	Co-Immunoprecipitation of Human Xirp2 and $\alpha$ -Actinin 2 . . . . .	190
3.64	Dimerization of Human Xirp2 . . . . .	192



---

3.65	Quantitation of the Transcription Level of Murine Xirp2 During Myofibrillogenesis of H-2K Cells . . . . .	193
3.66	Protein Expression of Murine Xirp2 During Myofibrillogenesis of H-2K Cells	195
3.67	Epitopes of Human Xirp2 Antibodies . . . . .	197
3.68	Localization of Human Xirp2 N-terminus and Center in Skeletal Muscle . .	198
3.69	Localization of Human Xirp2 C-terminus and $\alpha$ -actinin in Human Skeletal Muscle . . . . .	199
3.70	Localization of Human Xirp2 C-terminus and Filamin N-terminus in Human Skeletal Muscle . . . . .	200
3.71	Localization of Human Xirp2 C-terminus and Nebulin in Human Skeletal Muscle . . . . .	201
3.72	Xin A/B and $\alpha$ -Actinin in Areas of Skeletal Muscle Remodelling . . . . .	204
3.73	Xin A/C and $\alpha$ -Actinin in Areas of Skeletal Muscle Remodelling . . . . .	205
3.74	Xirp2 and $\alpha$ -Actinin in Areas of Skeletal Muscle Remodelling . . . . .	207
3.75	Xin A/B and Nebulin in Areas of Skeletal Muscle Remodelling . . . . .	209
3.76	Xin A/C and Nebulin in Areas of Skeletal Muscle Remodelling . . . . .	210
3.77	Xirp2 (N-terminus) and Nebulin in Areas of Skeletal Muscle Remodelling .	212
3.78	Xirp2 (Central) and Nebulin in Areas of Skeletal Muscle Remodelling . . .	213
3.79	Xin A/B and Filamin C in Areas of Skeletal Muscle Remodelling . . . . .	215
3.80	Xin A/C and Filamin C in Areas of Skeletal Muscle Remodelling . . . . .	216
3.81	Xirp2 and Filamin in Areas of Skeletal Muscle Remodelling . . . . .	217
4.1	Alignment of the Nebulin/Nebulette Interaction Motif in Xin-Repeat Proteins of Different Species . . . . .	232
4.2	Proteins Interacting with Xin and Xirp2 . . . . .	244
4.3	Model of Z-disc Architecture . . . . .	249
C.1	Vector map pET23aEEF . . . . .	VIII
C.2	Vector map pET23aMyc . . . . .	IX
C.3	Vector map pET23aT7 . . . . .	X
C.4	Vector map pET28a . . . . .	XI
C.5	Vector map pLexPD . . . . .	XII
C.6	Vector map pACT2 . . . . .	XIII
C.7	Vector map Venus NT . . . . .	XIV
C.8	Vector map Venus CT . . . . .	XV
C.9	Vector map Venus1-C . . . . .	XVI

---

C.10	Vector map Venus2-C . . . . .	XVII
C.11	Vector map Venus1-N3 . . . . .	XVIII
C.12	Vector map Venus2-N3 . . . . .	XIX
D.1	Human Xin cDNA . . . . .	XXI
D.2	Human Xin cDNA - continuation . . . . .	XXII
D.3	Human Xin cDNA - continuation . . . . .	XXIII
D.4	Human Xin cDNA - continuation . . . . .	XXIV
D.5	Human Xin cDNA - continuation . . . . .	XXV
D.6	Human Xin cDNA - continuation . . . . .	XXVI
E.1	Murine Xin cDNA . . . . .	XXVIII
E.2	Murine Xin cDNA - continuation . . . . .	XXIX
E.3	Murine Xin cDNA - continuation . . . . .	XXX
E.4	Murine Xin cDNA - continuation . . . . .	XXXI
F.1	Human Xirp2 cDNA . . . . .	XXXIII
F.2	Human Xirp2 cDNA - continuation . . . . .	XXXIV
F.3	Human Xirp2 cDNA - continuation . . . . .	XXXV
F.4	Human Xirp2 cDNA - continuation . . . . .	XXXVI
F.5	Human Xirp2 cDNA - continuation . . . . .	XXXVII
F.6	Human Xirp2 cDNA - continuation . . . . .	XXXVIII
F.7	Human Xirp2 cDNA - continuation . . . . .	XXXIX
G.1	Murine Xirp2 cDNA . . . . .	XLI
G.2	Murine Xirp2 cDNA - continuation . . . . .	XLII
G.3	Murine Xirp2 cDNA - continuation . . . . .	XLIII
G.4	Murine Xirp2 cDNA - continuation . . . . .	XLIV
G.5	Murine Xirp2 cDNA - continuation . . . . .	XLV
G.6	Murine Xirp2 cDNA - continuation . . . . .	XLVI
G.7	Murine Xirp2 cDNA - continuation . . . . .	XLVII
G.8	Murine Xirp2 cDNA - continuation . . . . .	XLVIII
H.1	Human LIMCH1 cDNA . . . . .	L
H.2	Human LIMCH1 cDNA - continuation . . . . .	LI
H.3	Human LIMCH1 cDNA - continuation . . . . .	LII

---

I.1	Murine LIMCH1 cDNA . . . . .	LIV
I.2	Murine LIMCH1 cDNA - continuation . . . . .	LV
I.3	Murine LIMCH1 cDNA of the insertion identified in skeletal muscle . . . . .	LVI

# List of Tables

2.1	Composition of Culture Media . . . . .	39
2.2	Antibiotics in Molecular Biology . . . . .	40
2.3	PCR Program for Proofreading DNA Polymerases . . . . .	45
2.4	PCR Program for Conventional DNA Polymerases . . . . .	45
2.5	Composition of a PCR Reaction . . . . .	46
2.6	Primary Antibodies . . . . .	57
2.7	Secondary Antibodies . . . . .	58
2.8	Fluorescently-labeled Phalloidins . . . . .	58
2.9	Overview of Cell Culture Media . . . . .	67
2.10	Objectives for Microscopy . . . . .	72
2.11	Filter Sets . . . . .	72
2.12	Lasers Mounted in LSM 710 . . . . .	72
2.13	Progressive Ethanol Dehydration Schedule . . . . .	75
3.1	Overview of BiFC Vector Combinations Used for Analyzing the Xin–LIMCH1 Interaction . . . . .	163
B.1	Sequences of Primers used for Cloning of Xin Fragments . . . . .	IV
B.2	Sequences of Primers used for Cloning of Xirp2 Fragments . . . . .	V
B.3	Sequences of Primers used for Cloning of Nebulin and Nebulette Fragments	V
B.4	Sequences of Primers used for Cloning of LIMCH1 Fragments . . . . .	V
B.5	Sequences of Primers used for RT-PCR of Murine Xin . . . . .	VI
B.6	Sequences of Primers used for RT-PCR of Murine Xirp2 . . . . .	VI
B.7	Sequences of Primers used for RT-PCR of Murine LIMCH1 . . . . .	VI

# Chapter 1

## Introduction

### 1.1 The Musculature

The survival of higher animals depends on their ability of precise movement in order to acquire food or to find a partner for reproduction. This quality is provided by a special type of tissue, the musculature, which is essential for the voluntary control of force generation. It is achieved by the skeletal musculature, which is distributed throughout the body, thus enabling varying postures and locomotion. A prerequisite for life is the continuous supply of every organ with blood, which transports essential substances and therefore guarantees correct organ function and consequently life. The heart represents the specialized biological engine attributed to the maintenance of blood circulation. The force generation needed for keeping the blood flowing is produced by contraction of the cardiac musculature. Both types of muscle share a common appearance when visualized with microscopes using polarized light: alternating dark and bright bands, so that skeletal and cardiac muscle are designated as cross-striated muscle. Apart from these two types of muscle, a third one is essential for survival, which lacks a cross-striated pattern, the smooth muscle, which is responsible for the involuntarily contraction of hollow organs such as arteries or the gastrointestinal tract. In general it contracts slowly but in a sustained fashion.

#### 1.1.1 Vertebrate Skeletal Muscle

Skeletal muscle is internally organized into fascicles and fibres by intramuscular connective tissue (IMCT), which can be divided into three structures according to their composition and appearance, the epimysium, perimysium and endomysium (Purslow, 2002). The in-

dividual muscle is encased by the epimysium and the muscle fibre bundles are surrounded by the perimysium, the latter forming a physical continuity from myofibres to tendons and therefore being involved in lateral force transmission (fig. 1.1). The major components are intermediate filament proteins of the fibrillar collagens type I and III. The perimysium of bovine *Flexor radialis muscle* is further organized into four hierarchical levels comprising the nonfibrillar collagens VI and XII. The continuous connection of two tendons is achieved by collagen cables glued together to form walls of honeycomb tubes from tendon to tendon. Large, interwoven fibres generating a loose lattice are ramified in numerous collagen plexi attaching adjacent myofibres (Passerieux *et al.*, 2007). The perimysium is linked to myofibres by focal attachment points characterized by an accumulation of collagen III described as Perimysial Junctional Plates (PJP) (Passerieux *et al.*, 2006). Individual muscle fibres are enclosed by a continuous sheath covering the full length of myofibres as far as the myotendinous junction (MTJ), the endomysium, which merges with the perimysium at the PJP. It consists of a reticular layer of mainly fibrillar collagen IV constituting the regular mosaic basement membrane and attaching myofibres sarcolemma to transmembrane proteins, such as integrins (cf. section 1.9.2), providing a direct link from the extracellular matrix to the cytoskeleton and thus enabling the contractile force transmission between adjacent myofibres (Borg und Caulfield, 1980; Kovanen, 2002).

The multinucleated muscle fibres contain a highly regular arrangement of basic contractile units of cross-striated muscle, the sarcomere (cf. section 1.5), which is composed of highly ordered thin filaments (cf. section 1.5.1) and thick filaments (cf. section 1.5.2). This precise alignment of different filament systems can be observed in the microscope using polarized light revealing the light I-band (isotropic) corresponding to the thin filaments, mainly containing actin, and the dark A-band (anisotropic), which refers to the thick filaments comprising myosin (fig. 1.1). Both filament systems overlap in the A-band but display a zone lacking actin filaments, the H-zone. The Z-disc represents the lateral boundaries of the sarcomere and is made up of a dense protein network which anchors the actin-containing thin filaments in parallel arrays (cf. section 1.5.5). Two additional filament systems are required to form the ordered structure of the sarcomere. The largest vertebrate protein titin ( $M_r \approx 3\text{--}3,7$  MDa) spans half a sarcomere. The N-terminal parts of titin from adjacent sarcomeres overlap in the Z-disc and interact with Z-disc proteins like  $\alpha$ -actinin (cf. section 1.5.5.1). In the I-band region titin exhibits elastic properties and is designated to function as a molecular spring. Additionally, titin binds the myosin tail in the A-band region and ends within the M-band with a catalytically active serine/threonine kinase (cf. section 1.5.6). The fourth filament system in vertebrate skeletal

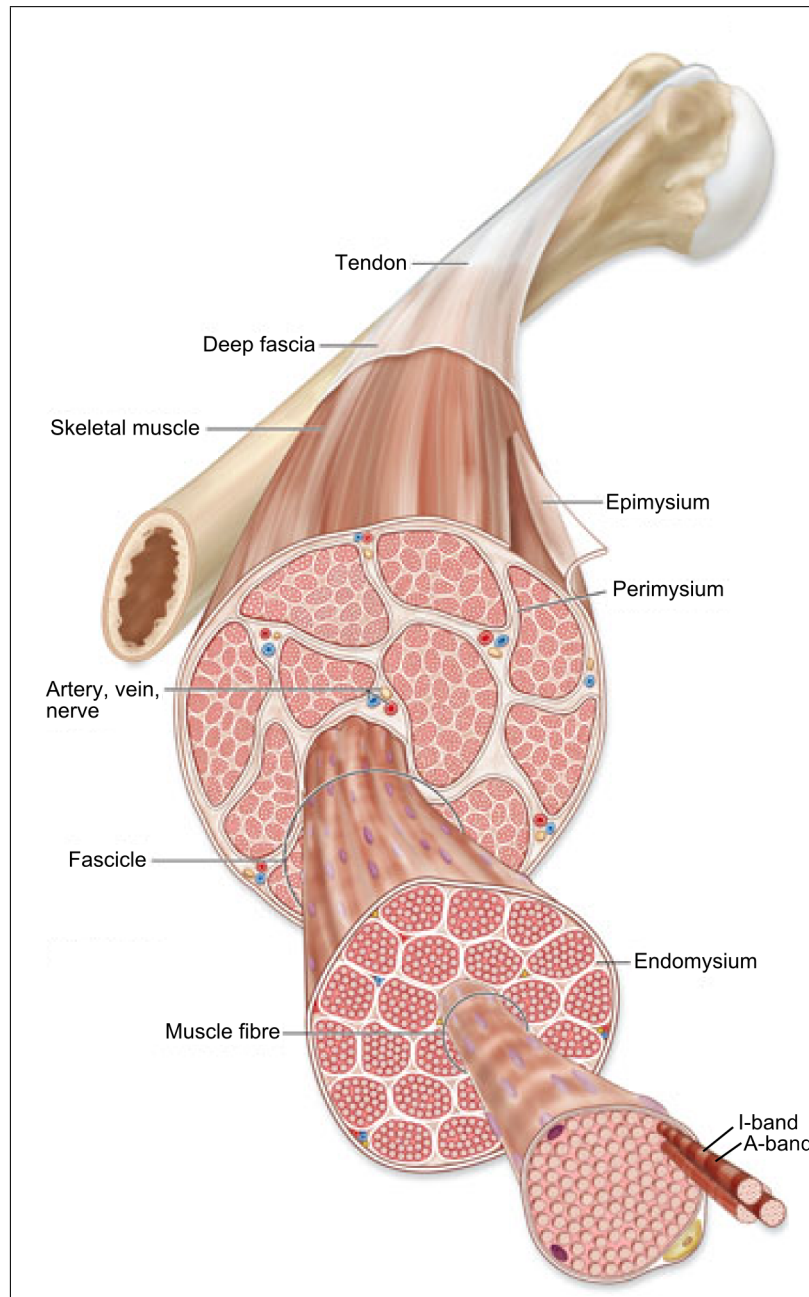


Figure 1.1: **Schematic overview of the organization of skeletal muscle.** The tendon connects the muscle to the bone. Skeletal muscle consists of multiple muscle fibre bundles (fascicles) which are surrounded by the collagen-containing perimysium. Individual muscle fibres are also encased by a layer of fibrillar collagen, the endomysium. The bundle of fascicles representing the individual muscle is enclosed by another ECM layer, the epimysium. Taken and modified from Michael McKinley (2009).

muscle is composed of the giant protein nebulin ( $M_r \approx 600\text{--}900$  kDa), which covers nearly the entire thin filament length from the Z-disc to the pointed ends of actin filaments and is involved in thin filament length regulation, Z-disc maintenance and myofibril alignment (cf. section 1.5.3).

## 1.2 Skeletal Muscle Development

### 1.2.1 Embryonic development

Except for the head muscles which derive from the unsegmented paraxial and prechordal mesoderm, all vertebrate skeletal muscles originate from the somites, an epithelial structure flanking the notochord and the neural tube (fig. 1.7). The ventral portion differentiates into the sclerotome and the dorsal epithelium, the dermomyotome, which gives rise to the derm and the entire muscle of the body and the limbs. At the onset of myogenesis, cells committed to the myogenic lineage delaminate from the edges of the dermomyotome forming the nascent primary myotome. These cells express the myogenic determination factors Myf5 (myogenic factor 5) and MRF4 (myogenic regulatory factor 4) promoting further determination and can be identified firstly at day 8.75 (E8.75) of the embryonic development of the mouse (Biressi *et al.*, 2007a). Among yet unidentified factors, one key regulator of early skeletal muscle development of the limb is the paired homeobox domain transcription factor Pax3, which is expressed in presomitic mesoderm and throughout the whole somite, before becoming restricted to the dermomyotome (Relaix *et al.*, 2004). This protein directly controls the expression of the c-met receptor (Epstein *et al.*, 1996), a receptor tyrosine kinase, which is indispensable for delamination and migration (Buckingham *et al.*, 2003), and regulates the early activation of Myf5 via modulating its target Dmrt2, a DM domain containing transcriptional regulator and direct activator of Myf5, thus essentially promoting the progression of cell migration and determination (Sato *et al.*, 2010). The correct migration upon delamination and final localisation of delaminating cells is dependent on the interaction of  $\alpha 6\beta 1$  integrin with laminin, which is further capable of repressing premature myogenesis in the dermomyotome (cf. section 1.9.2 and Bajanca *et al.* 2006). Maintenance of the epithelial structure of the dermomyotome is indispensable for the ordered progression of myogenesis and is regulated by Wnt signalling (Ikeya und Takada, 1998). This pathway acts on the transcription factor *paraxis* (Tcf15) to keep the integrity of the epithelial organisation and induces myogenic determinant genes (MyoD and Myf5) either directly via the canonical Wnt-mediator  $\beta$ -catenin (cf. section



1.9.1.1 and Linker *et al.* 2005) or PKA and its effector CREB (cAMP responsive element binding protein) (Chen *et al.*, 2005). Once the myotome has been created, the muscle precursor cells differentiate into the skeletal muscle of the myotome and migrate to their final destination where they develop into their cognate muscle. At this stage the cells are designated as myoblasts characterized by proliferation activity and expression of the muscle-specific transcription factors Myf5 and MyoD (myogenic determination factor).

## 1.2.2 Myogenesis

Vertebrate myogenesis passes through three successive waves, which are described in the following sections.

### 1.2.2.1 Embryonic Myogenesis

The initial formation of multinucleated myotubes is referred to as embryonic or primary myogenesis. At around E10.5 of mouse development, fusion of terminally differentiated myoblasts, which derived from a fraction of Pax3<sup>+</sup>-positive progenitor cells during primary myotome formation, gives rise to a small number of primary myofibres setting up the basic muscle pattern (Biressi *et al.*, 2007a; Hutcheson *et al.*, 2009). This embryonic differentiation into multinucleated muscle fibres seems to depend on the myogenic transcription factor MRF4, for a loss of MRF4 in MRF4-Myf5 double mutants disturbs primary myogenesis, whereas Myf5 null embryos are not affected (Kassar-Duchossoy *et al.*, 2004). Primary muscle fibres progressively grow in size by incorporating only Pax3<sup>+</sup> progenitor cells and are characterized by a typical round shape from a transverse view. Additionally, the period of emergence of a muscle fibre determines its phenotype, because nearly all fibres generated in mouse from E10.5-E14.5, i.e. during embryonic myogenesis, express a slow isoform of myosin heavy chain (MHC) (Charrasse *et al.*, 2003). Throughout primary myogenesis, the expression of Pax3<sup>+</sup> muscle precursor cells is downregulated starting at E13.5 but remains still persistent in a small number of cells, which are designated to be satellite cells (Hutcheson *et al.*, 2009; Relaix *et al.*, 2006).

### 1.2.2.2 Fetal Myogenesis

After the basic muscle pattern has been established, the number of muscle fibres increases in the second step of myogenesis upon fusion of fetal myoblasts either with each other or to form secondary fibres or with primary fibres to contribute to their growth (Biressi *et al.*, 2007a). Two different cell populations generate these secondary fibres, the previously

described Pax3<sup>+</sup> cells (cf. section 1.2.2.1) and a newly formed subset of Pax3<sup>+</sup> and Pax7<sup>+</sup> progenitor cells. All of the latter cells derive from Pax3<sup>+</sup> progenitors and can be identified by spatial restriction to the central portion of the dermomyotome in the somites at E9 after the beginning of Pax3 expression (cf. section 1.2.1). In the mouse limb Pax7 expression initiates at E11.5 and is maintained during secondary myogenesis by adult satellite cells. The number of Pax7<sup>+</sup> cells is positively regulated by activated  $\beta$ -catenin, but this protein is not required for preservation of Pax7 expression (Hutcheson *et al.*, 2009). Secondary myofibres initially form at the site of innervation of primary fibres, which are originally innervated by multiple axons, and remain attached to them for a short period before elongating and becoming independent. In comparison to embryonic myoblasts, fetal myoblasts reveal many differentially expressed genes among others resulting in an adoption of a fast phenotype (Biressi *et al.*, 2007b,a). The differences between primary and secondary myogenesis are additionally mirrored by their varying dependencies on myogenic transcription factors. While MRF4 alone can establish primary myogenesis (cf. section 1.2.2.1) in Myf5<sup>-/-</sup>:MyoD<sup>-/-</sup> mice, secondary myogenesis is completely disrupted (Kassar-Duchossoy *et al.*, 2004). Furthermore, mice lacking myogenin, another basic helix-loop-helix myogenic regulatory factor, exhibit a more severe effect on secondary myogenesis (Venuti *et al.*, 1995). At the end of this second phase around E17.5, muscle satellite cells can be morphologically identified for the first time as mononucleated cells located between the basal lamina and the fibre plasma.

### 1.2.2.3 Adult Myogenesis

Once fetal development is completed and the organism is born, the muscle fibres formed still need to grow in the course of postnatal development. Due to the inability of the muscle nuclei to divide, fusion of a surrounding cell population must contribute to muscle fibre expansion. These adult myoblasts originate in Pax3<sup>+</sup> and Pax7<sup>+</sup> cells, which kept their Pax7 expression during secondary myogenesis and did not account for fetal myofibre formation (Buckingham, 2006). Pax7 expression is essential for maintenance and renewal of these cells by virtue of its antiapoptotic effects, because loss of Pax7 severely disturbs adult myogenesis and makes adult myoblasts disappear (Relaix *et al.*, 2006; Oustanina *et al.*, 2004; Kuang *et al.*, 2006). The impact of this cell population on myofibre maturation is substantiated by the estimation that more than 90 % of the nuclei of a fully developed adult muscle fibre derive from this subset. During postnatal myofibre maturation embryonic and fetal MHC isoforms are progressively replaced (cf. section 1.5.2), but

how the fusing adult myoblasts and their internal gene expression program influence this process remains to be elucidated (Biressi *et al.*, 2007a,b).

#### 1.2.2.4 Sarcomerogenesis

The assembly of the contractile apparatus in cross-striated muscle is not completely understood but there is emerging evidence for a partly integrin-dependent process involving the formation of precursor structures, which appears to be conserved among different species for both types of striated muscle, heart and skeletal muscle (Sparrow und Schöck, 2009; Sanger *et al.*, 2005). At the beginning of myofibrillogenesis, F-actin filaments, the major constituent of thin filaments in muscle, originate in integrin adhesion sites crosslinked by  $\alpha$ -actinin and associated with muscle isoforms of tropomyosin and troponin. The early progenitors of the lateral boundary of the sarcomere, the Z-disc, can be identified as membrane-bound complexes containing F-actin, integrins and typical components of integrin adhesion sites like talin and vinculin. The latter proteins are the first arranged in a periodic pattern and their positioning as well as subsequent sarcomere formation are dependent on integrin function revealed by many genetic studies in different organisms (Tokuyasu, 1989; Fujita *et al.*, 2007). During progression of myofibril assembly, the Z-disc constituent ZASP (Z band alternatively spliced PDZ-motif protein, cypher, oracle) recruits sarcomeric  $\alpha$ -actinin, another prominent Z-disc element, to these sites (Jani und Schöck, 2007). This step is critical for myofibril assembly because ablation of ZASP in *Drosophila melanogaster* results in disruption of Z-disc assembly and muscle attachment at the myotendinous junction (Jani und Schöck, 2007). Subsequently, the giant protein titin accumulates in these complexes presumably engaged by  $\alpha$ -actinin, since it contains independent binding sites for ZASP and titin (Au *et al.*, 2004; Jani und Schöck, 2007). These structures are then designated as Z-bodies and mark the boundaries of minisarcomeres displaying a spacing different from mature sarcomeres (Sanger *et al.*, 1986). Actin filaments of opposing polarity arising from adjacent Z-bodies incorporate nonmuscle myosin II, thus displacing crosslinking  $\alpha$ -actinin (Sparrow und Schöck, 2009). While integrating nonmuscle myosin II, these structures represent premyofibrils, which then further mature through replacing nonmuscle myosin with the respective muscle isoform (Sanger *et al.*, 2005). At this stage of nascent myofibrils, bipolar muscle myosin II filaments exhibit a continuous decoration of actin filaments upon fluorescent labeling probably due to overlap of thick filaments. When Z-bodies are laterally aligned and coalesce to form Z-discs, myosin filaments display a banded pattern, which corresponds to the A-band. In order

to achieve and maintain mature spacing and the highly regular pattern of functioning sarcomeres, contractility is essential, for improper contractility leads to sarcomere disassembly (Sparrow und Schöck, 2009). Myofibrils need proper anchorage of the contractile apparatus to transmit the force generated, which is established by costameres (cf. sections 1.7), integrin-based adhesion structures on a level with the Z-disc linking the sarcomere to the extracellular matrix, and myotendinous junctions at the end of the myofibril (cf. section 1.6).

### 1.3 Skeletal Muscle Regeneration

Regeneration of damaged skeletal muscle fibres requires the coordination of multiple steps. At first, damaged tissue undergoes necrosis and is subsequently removed by phagocytic inflammatory cells which enter the damaged fibre in response to the trauma. These active immune cells and the myofibre itself secrete growth factors which predominantly control the activation, proliferation and fusion of muscle stem cells, the satellite cells, to the existing fibre or to each other in order form a new one (Broek *et al.*, 2010). Satellite cells reside between the sarcolemma and the basal membrane of skeletal muscle and this specific niche keeps them quiescent for most of the time. This is achieved by signalling mediated via the cell-cell contacts of M-cadherins (cf. section 1.9.1) to the adjacent myofibre and the attachment of  $\alpha7\beta1$  integrin (cf. section 1.9.2) to laminin of the ECM (Broek *et al.*, 2010). Damage of the myofibre causes the release of growth factors mainly by invading inflammatory cells. The vasculature, the satellite cell itself and motor neurons also contribute to the secretion of growth factors. Furthermore, growth factors and cytokines captured in the ECM by proteoglycans are liberated by matrix metalloproteinases produced by the satellite cell itself. Upon damage this cocktail controls the activation, proliferation and differentiation of satellite cells (Hawke und Garry, 2001; Chargé und Rudnicki, 2004; Broek *et al.*, 2010). In the initial phase, quiescent satellite cells migrate to the site of injury. These cells are characterized by the expression of the Pax7 transcription factor and they transform into myoblasts due to expression of the myogenic factors MyoD and Myf5 (Wagers und Conboy, 2005). They start to proliferate in order to provide enough cells for proper muscle repair and subsequently, they differentiate into muscle cells indicated by downregulation of Pax7 (Broek *et al.*, 2010). Growth factors can be divided into stimulatory and inhibitory factors whose highly coordinated temporal effects are essential for proper skeletal muscle regeneration. The main stimulatory growth factor is insulin-like growth factor 1 (IGF-1) which mainly acts via the phosphatidylinositol 3

(PI3)-kinase pathway and alters the expression of myogenic factors thereby influencing satellite cell behaviour. This pathway is also largely responsible for the development of hypertrophy. Hepatocyte growth factor (HGF) stimulates the proliferation rather than differentiation of satellite cells and its expression level seems to vary in proportion with the degree of injury. Angiogenesis is essential for the healing process in order to provide nutrient and oxygen supply and requires the action of vascular endothelial growth factor (VEGF) (Broek *et al.*, 2010). Inhibitory factors such as myostatin or transforming growth factor (TGF)- $\beta$ 1 and - $\alpha$ , are responsible for the homeostasis of muscle mass by maintaining satellite cell quiescence or inhibition of myoblast differentiation and recruitment which is demonstrated by extensive muscle hypertrophy in mice lacking myostatin (Broek *et al.*, 2010). All factors belong to the TGF- $\beta$  superfamily which cause receptor dimerization upon binding, activation of the receptor kinase and finally, phosphorylation of Smad transcription factors. Smad proteins then translocate to the nucleus and regulate transcription of target genes (Kollias und McDermott, 2008). Although these factors described represent key players of muscle regeneration, there is emerging evidence that there are additional factors involved which fine tune the process. As mentioned above, myoblast fusion to the damaged myofibre or each other is essential for proper muscle repair. This process is partly regulated by the serine/threonine phosphatase calcineurin (Olson und Williams, 2000). Depending on the elevation of the cellular calcium level, calcineurin dephosphorylates members of the NFAT (nuclear factor of activated T cells) transcription factor family in the cytoplasm and causes their translocation to the nucleus. These act on target genes such as the membrane-associated dysferlin and myoferlin which are essential for resealing the membrane since lack of dysferlin leads to a marked delay of muscle membrane resealing (Demonbreun *et al.*, 2010). Interestingly, calcineurin and NFATs can also mediate the effects of IGF-1 and are therefore involved in the hypertrophic response (Olson und Williams, 2000). In order to maintain a sufficient number of satellite cells being capable of contributing to further regeneration processes the satellite cell pool needs to be replenished. Recent findings point to a heterogenous satellite cell pool harbouring self-renewing stem cells and myogenic precursor cells with limited replicative capacity which both occupy identical positions around the myofibre. The exact control of self-renewal is not known but Pax7, Notch and Wnt signalling have been implied in these processes (Zammit, 2008).

## 1.4 Skeletal Muscle remodelling

Unaccustomed or high intensity exercise of skeletal muscle can lead to a feeling of pain and stiffness generally occurring 24-48 h after the exercise which is named delayed onset muscle soreness (DOMS) (Yu *et al.*, 2002). While older studies attribute this phenotype to myofibrillar damage characterized by invasion of inflammatory cells and disruption of membrane integrity causing an increase of muscle proteins in the blood (Jones *et al.*, 1986; Round *et al.*, 1987), there is emerging evidence that eccentric exercised muscle undergo adaptive remodelling rather than being damaged. This has been demonstrated using high resolution immunofluorescence microscopy of ultra thin sections originating from muscle biopsies taken from man which were exposed to eccentric contraction. While no invasion of inflammatory cells or prominent fibronectin staining within the myofibre could be observed (Yu *et al.*, 2002), the latter serving as a marker for sarcolemmal disruption (Thornell *et al.*, 1992), inflammation or damage of myofibres does not seem to reflect the ongoing processes. Instead, the regular striated pattern of desmin and actin is replaced by longitudinal strands which link adjacent sarcomeres (Yu und Thornell, 2002). Such a disruption of the cross-striation can cover multiple sarcomeres or only two connected by a single strand but it does not affect the general myofibrillar organization (Yu und Thornell, 2002; Yu *et al.*, 2003, 2004). In these areas, prominent Z-disc proteins like  $\alpha$ -actinin, titin and nebulin are absent and they are also not associated with such strands (Yu und Thornell, 2002; Yu *et al.*, 2003, 2004). Intriguingly, within these remodelling structures the formation of additional Z-discs is observed resulting in supernumerary sarcomeres reflected by a mismatch of the sarcomere number in longitudinal register (Yu *et al.*, 2003). It has been proposed that new sarcomere formation can be achieved either by a split of a single Z-disc or by an alteration of a single sarcomere (Carlsson *et al.*, 2007). Apart from desmin and actin, myotillin and obscurin are also involved in these processes (Carlsson *et al.*, 2007, 2008). However, the exact composition of these strands and the temporal course of adaptation to eccentric exercise awaits further results. Interestingly, such a mechanism has been also detected in cardiomyocytes which were exposed to uniaxial static strain, since they also showed addition of new sarcomeres at the ICD and throughout the cell length (Yu und Russell, 2005).

## 1.5 Sarcomere Structure

The sarcomere is the basic contractile unit and exhibits a highly ordered architecture (fig. 1.2), which is described in detail in the following sections.

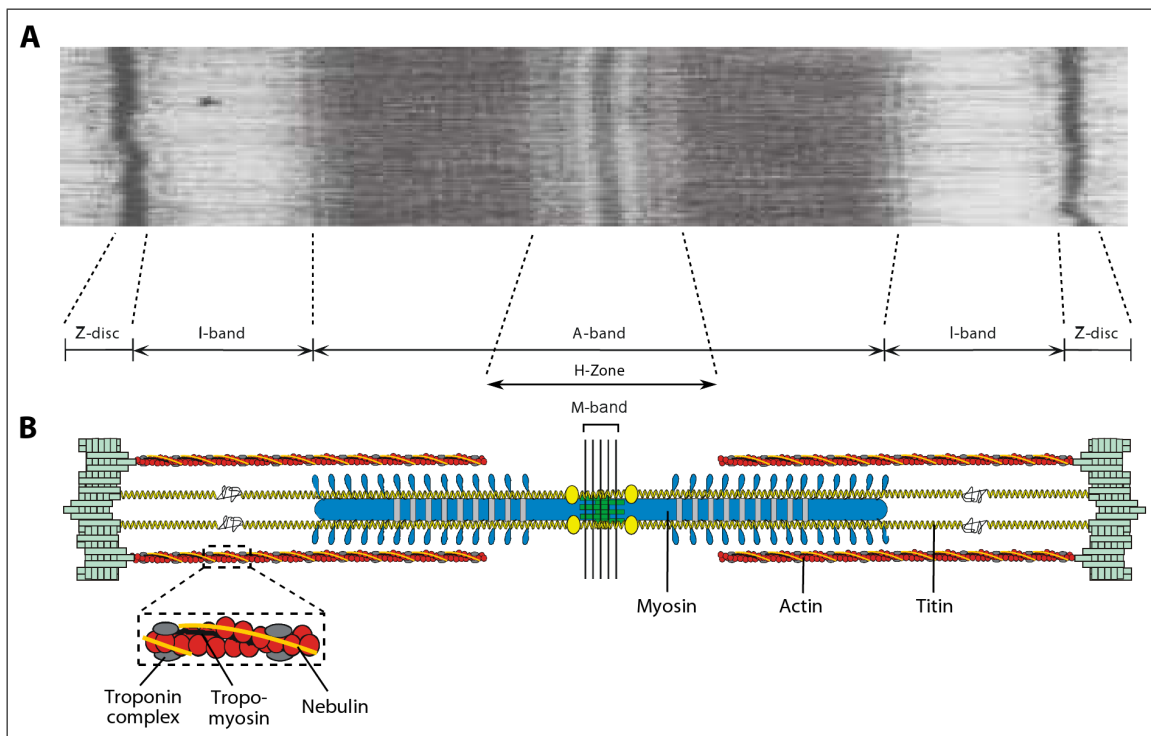


Figure 1.2: **Structure of the Sarcomere.** **A.** Electron micrograph of a longitudinal section of a skeletal muscle fibre (From Fürst *et al.* 1988). The bright I-band comprises the thin filaments whereas the dark A-band reflects the overlap of thin and thick filaments. The H-zone does not contain thin filaments. The Z-disc represents the sarcomeric boundary. **B.** Schematic overview of the composition of a sarcomere.

### 1.5.1 Thin Filaments

Thin filaments in cross-striated muscle provide the binding site for myosin heads (cf. section 1.5.2) activating its ATPase activity, which results in the conformational change generating the force for muscle contraction. They are anchored in the Z-disc and span half a sarcomere (approx. 1  $\mu\text{m}$ ) interdigitating with the thick filaments in the A-band. They consist of filamentous actin (F-actin) and associated proteins such as tropomyosin and the troponin complex (Clark *et al.*, 2002). Actin is the most abundant protein in cross-striated muscle and highly conserved among species, as the amino acid sequence of chicken skeletal muscle actin matches exactly the human isoform. Only four of the six actins known are expressed in striated muscle tissue, cardiac, skeletal, vascular and visceral actin. While vascular and visceral actins only transiently occur in muscle fibres during development,

cardiac and skeletal muscle actins are co-expressed and their proportion depends on muscle fibre and developmental stage. Actin filaments form upon polymerization of globular actin (G-actin) monomers, which results in a left-handed single-stranded helix, displaying a rotation per monomer between 166 ° and 167 °, depending on the muscle type. The thin filament adopts a flat conformation because of the relative rotation by 20 ° of the two major subdomains of the G-actin (Oda *et al.*, 2009). Due to a nucleotide-binding site located in a cleft between both subdomains, the filament gains polarity according to the orientation of the actin monomer in the filament relative to the ATP-binding site. The end opposite to the cleft is referred to as plus or barbed end and the minus or pointed end is located at the nucleotide's side. The nomenclature barbed and pointed end derives from myosin head fragments, which decorate the actin filament pointing to the plus end. The polymerization of G-actin to F-actin requires the initial formation of a G-actin trimer, the nucleus, which facilitates the addition of further subunits (Winder und Ayscough, 2005). Thin filament length in muscle is regulated by capping proteins at either end, CapZ in the Z-disc and tropomodulin at the barbed and pointed end, respectively. The proteins driving actin nucleation and polymerization during muscle development and maintaining thin filament integrity are still largely unknown. In nonmuscle cells, the Arp2/3-complex generates new filaments from the barbed ends of existing actin strands branched by an angle of around 70 ° (Pollard, 2007). Formins, another class of actin nucleators, elongate existing filaments from the barbed end therefore producing unbranched F-actin (Pollard, 2007). One formin, Fhod3, has already been identified as crucial for the maintenance of sarcomere organization in cardiomyocytes corroborating the dynamic character of the thin filaments albeit precisely regulating size and localization (Taniguchi *et al.*, 2009). Fhod3 accumulates in the center of the sarcomere a feature shared with leiomodin, another candidate for thin filament nucleation. This protein can interact with actin as well as tropomyosin, the latter potentiating its nucleation activity, a unique feature among the actin nucleators already known (Chereau *et al.*, 2008). Tropomyosin forms a functional dimer and is associated with each of the two grooves of the thin filament thus stabilizing F-actin and increasing its stiffness. In humans, four tropomyosin genes exist but only three encode striated muscle isoforms, which can generate homodimers or heterodimers. A dimer spans seven actin monomers and overlaps with its neighbouring molecule in a head-to-tail manner but the exact position on the actin filament depends on its isoform composition. Tropomyosin masks the myosin head-binding site, but Ca<sup>2+</sup>-binding to the troponin complex (see below) shifts tropomyosin localization and uncovers the interaction site, hence enabling contraction. The troponin complex, consisting of troponin C, I and T



(TnC, I, T) in conjunction with tropomyosin, forms the regulatory switch for modulation of actomyosin interaction during force generation (fig. 1.2 B). The calcium sensitivity of contraction is mediated by TnC because it changes the binding to TnI, a complete inhibitor of the actomyosin interaction, upon chelating  $\text{Ca}^{2+}$  with its EF-hand motifs. This reduces the affinity of TnI to actin and increases its binding strength to TnC and TnT. In addition to TnI and TnC, TnT binds to tropomyosin and this interaction is likely weakened, when the  $\text{Ca}^{2+}$ -binding to TnC is transmitted, and allows tropomyosin for relocating its position on the thin filament (Clark *et al.*, 2002).

## 1.5.2 Thick Filaments

The force generated in cross-striated muscle requires an actin-based motor protein since actin is the major component of the thin filaments (cf. section 1.5.1). The diverse superfamily of myosins encompasses a multitude of different variants of this actin motor protein. Class II of conventional myosins comprises among others the genes of the eight yet identified myosin heavy chains (MHC) expressed in cross-striated muscle, which can form filaments due to multimerization of their C-terminal coiled-coil region and the expression of which depends on the muscle type (Sellers, 2000; Clark *et al.*, 2002). In striated muscle these filaments are associated with regulatory proteins and referred to as thick filaments representing the A-band (fig. 1.2). A muscle myosin dimer consists of 2 MHC's and 4 myosin light chains (MLC). The N-terminus of each MHC and 2 of the MLC'S is designated as the head domain, including the ATPase-domain and the actin-binding site responsible for cross-bridge formation. The C-terminal rod domain mediates the polymerization. The force is generated by the power stroke of myosin, a positional change of the myosin head relative to the thick filament while bound to actin. The resulting contraction is a cyclic process denoted by cross-bridge cycling. Upon  $\text{Ca}^{2+}$  binding to the troponin complex (cf. section 1.5.1), tropomyosin shifts its position on the actin filament and exposes a weak binding site for myosin on the filament. Myosin binds to actin, increasing myosin's binding strength, followed by the release of phosphate which results in the power stroke. The release of ADP completes the tail swing of the molecule, which stays in this state until it is set free by ATP-binding. This reconstitutes the initial conformation and the nucleotide is hydrolysed (Geeves *et al.*, 2005). Different contractile properties are attained by muscle fibres composed of varying MHC isoforms and MLC's as well as associated proteins such as myosin binding protein C, which is also implicated in the regulation of contraction (Clark *et al.*, 2002).

### 1.5.3 Nebulin

The giant protein nebulin (500-900 kDa) is considered the fourth filament system in skeletal muscle as it spans nearly the entire length of the actin-containing thin filaments (Clark *et al.*, 2002). The most prominent structural features in nebulin are 185 35-amino acid modules (M1-185) comprising a conserved SXXXY sequence motif exhibiting high affinity to F-actin (Jin und Wang, 1991; Labeit und Kolmerer, 1995; Kazmierski *et al.*, 2003). The central modules M9-162 are arranged into 7-module super-repeats, each super-repeat potentially binding to the troponin-tropomyosin regulatory complex (Ogut *et al.*, 2003). Nebulin is anchored in the Z-disc with its C-terminus, where it is associated with the barbed end capping protein CapZ (Witt *et al.*, 2006; Pappas *et al.*, 2008), and its N-terminus extends almost to the pointed end of actin filaments, there interacting with the capping protein tropomodulin (McElhinny *et al.*, 2001). Therefore, it was regarded as a molecular ruler regulating thin filament length, but recent results challenge this idea and expand the view of nebulin function. Although nebulin is capable of interacting with tropomodulin, the pointed end capper, it was clearly demonstrated that tropomodulin localization does not always overlap with nebulin's N-terminus, thus indicating the existence of thin filaments exceeding nebulin length (Castillo *et al.*, 2009). Furthermore, thin filament length varies among different muscle types with alternative splicing within the nebulin gene not accounting for the variability discovered (Castillo *et al.*, 2009), but giving rise to different isoforms throughout muscle development (Buck *et al.*, 2010). Nevertheless, ablation of nebulin in mice reduces thin filament length and disposes of the H-zone, the area without actin/myosin overlap, due to variable actin filament length (Bang *et al.*, 2006; Tonino *et al.*, 2010). Instead of length regulation, nebulin can stabilize actin filaments equal to or longer than itself and reduces the dynamics of thin filament components (Pappas *et al.*, 2010). Very recently, nebulin has been identified to form unbranched actin filaments from the Z-disc in cooperation with N-WASP independent of the Arp2/3 complex. This process seems to be involved in muscle maturation and hypertrophy and is induced by IGF-1 which activates the PI3-kinase–Akt signalling pathway (Takano *et al.*, 2010). The association of nebulin with thin filaments also positively affects cross-bridge cycling kinetics, which is displayed by optimization of actomyosin interaction providing reduced tension cost and improved cooperativity during contraction (Bang *et al.*, 2009; Chandra *et al.*, 2009). Additionally, nebulin keeps Z-discs of adjacent myofibrils in register possibly by recruiting desmin, an intermediate filament protein linking neighbouring myofibrils at the Z-disc level (Bang *et al.*, 2002; Tonino *et al.*, 2010). Additionally, nebu-

lin can attach the myofibril to the sarcolemma via direct interaction with archvillin (Lee *et al.*, 2008). Apart from longitudinal alignment, nebulin seems to be a pivotal candidate to control Z-disc structure, since its absence causes abnormally shaped and wider Z-discs (Tonino *et al.*, 2010). This effect could be mediated by interactions of the terminal SH3 domain situated within the Z-disc, which interacts among others with major structural components of the sarcomere boundary such as  $\alpha$ -actinin (Nave *et al.*, 1990; Moncman und Wang, 1999), titin (Witt *et al.*, 2006) or myopalladin (Bang *et al.*, 2001; Ma und Wang, 2002). The newly identified interaction with N-WASP has been proposed to be also mediated by the SH3 domain albeit direct evidence is missing (Takano *et al.*, 2010). The impact on Z-disc architecture is further corroborated by the correlation of the expression pattern of different-sized nebulin splice variants and changes in Z-disc width in different skeletal muscle types throughout development (Buck *et al.*, 2010). Latest findings suggest that nebulin expression is not restricted to skeletal muscle because transcripts were also detected in heart, liver and neuronal cells even if to a minor extent (Kazmierski *et al.*, 2003; McElhinny *et al.*, 2003). In heart muscle, a smaller nebulin repeat-containing protein is predominantly expressed, which is named nebulette and described below.

#### 1.5.4 Nebulette

One major difference between heart and skeletal muscle is the low abundance or even absence of nebulin in cardiomyocytes. However, in cardiac muscle the nebulin-related protein nebulette displaying an overall similar domain layout represents the predominant protein of this family. Nebulette contains an acidic N-terminal region followed by only 22 copies of nebulin-like repeats, which are not organized as super repeats (cf. section 1.5.3) and therefore represents the main divergence between both family members, which is manifested in the small size of 110 kDa of nebulette. The highly homologous SH3 domain at the C-terminus of nebulette exhibits an overlapping set of binding partners compared to nebulin and is connected to the repeats by a linker domain (Millevoi *et al.*, 1998). In cardiomyocytes, the nebulette SH3 domain integrates into the Z-disc and its actin-binding repetitive motifs presumably extend 150 nm along the thin filaments, there stabilizing the association of tropomyosin (Bonzo *et al.*, 2008). Overexpression of truncated protein fragments results in complete disruption of the contractile apparatus pointing to an involvement in the formation or stabilization of cardiac myofibrillar architecture (Moncman und Wang, 2002). During development, nebulette localizes to early dense bodies at pre-myofibril stage and displays Z-disc decoration in mature myofibrils (Esham *et al.*, 2007).

Despite sharing most of the binding partners designated for nebulin, nebulette repeat modules are considered to interact with the very C-terminus of filamin C even though the significance of this possible interaction remains to be elucidated (Holmes und Moncman, 2008).

### 1.5.5 The Z-disc

The Z-disc demarcates the sarcomere boundaries and represents a protein framework providing mechanical stability by anchoring the thin filaments, but also a nodal point of signalling between the intracellular contractile machinery and adjacent myofibrils as well as the ECM. Actin filaments of opposing polarity from neighbouring sarcomeres are cross-linked by a varying, muscle type-dependent number of layers consisting of  $\alpha$ -actinin. These layers account for the ultrastructural zigzag-like appearance and their number delineates the Z-disc width ranging from 30 to 50 nm in fast fibres to 100 nm in slow or cardiac fibres (Luther, 2009). Differentially expressed splice variants of the giant proteins titin and nebulin (cf. sections 1.1.1 and 1.5.3) presumably form a template to define Z-disc width (Castillo *et al.*, 2009; Buck *et al.*, 2010). The N-termini of titin, consisting of two Ig-domains, Z1 and Z2, followed by a varying number of repetitive motifs denoted by Z-repeats, overlap in the Z-disc and the number of Z-repeats expressed correlates with Z-disc length. The length of the actin filaments is controlled by the capping protein CapZ, which interacts with nebulin and is therefore connected to the Z-disc-width controlling protein network (Luther, 2009).  $\alpha$ -actinin, whose arrangement depends on Z-disc width, as depicted above, turns up to be a universal adaptor tethering scaffolding and signalling proteins (cf. section 1.5.5.1). The protein networks of adjacent Z-discs are connected by the intermediate filament protein desmin, which provides a link to the sarcolemma as a component of costameres (cf. section 1.7). Desmin is part of the mechanical sensor receiving signals from the surroundings and transforms these into transcriptional events. Furthermore, the Z-disc directly harbours signalling proteins such as PKC and a multitude of anchoring proteins for signalling components like the calsarcin family (FATZ, calsarcin, myozenin) as adaptors for the phosphatase calcineurin and myospryn as an PKA-anchoring protein (Pyle und Solaro (2004); Reynolds *et al.* (2007)). The plethora of proteins localized at the Z-disc and the fact that mutations in Z-disc proteins cause multiple diseases make this structure a key player in maintaining sarcomere integrity. The important Z-disc constituents  $\alpha$ -actinin and filamin C are described in further detail below.

### 1.5.5.1 $\alpha$ -Actinin

The actin-binding protein  $\alpha$ -actinin is a major component of the Z-disc of cross-striated muscle and belongs to the spectrin superfamily of proteins comprising spectrins and dystrophin. In mammalian cells four different genes encode for at least six different  $\alpha$ -actinin isoforms each displaying a specific tissue distribution and expression profile. All proteins are composed of a similar domain layout starting with an N-terminal actin-binding domain (ABD) followed by four consecutive spectrin repeats and a C-terminal calmodulin (CaM)-like domain.  $\alpha$ -actinin forms a functional anti-parallel dimer with high affinity ( $K_d = 100$  nM), which permits the cross-linking of actin filaments to the ABD, consisting of a tandem pair of type 1 and type 2 calponin homology (CH) domains at either end of the rod-shaped molecule. Apart from the cross-linking function,  $\alpha$ -actinin has been recently shown to bind along a single actin filament. Only in muscle tissue are  $\alpha$ -actinin 2 and 3 expressed, where they cross-link the thin filaments of adjacent sarcomeres. While  $\alpha$ -actinin 2 is expressed in all skeletal muscle fibres,  $\alpha$ -actinin 3 is restricted to fast glycolytic fibres. A common null polymorphism causes the deficiency of  $\alpha$ -actinin 3 in more than one billion humans worldwide. Its lack is compensated by  $\alpha$ -actinin 2, therefore, its presence is not crucial to survival, although it has beneficial effects on sports. The general importance of the existence of  $\alpha$ -actinin in muscle is emphasized by the lethality of  $\alpha$ -actinin mutants in the fruit fly *Drosophila melanogaster*. Both muscle proteins further diverge from the nonmuscle isoforms concerning the calcium-chelating capacity of the EF-hand motifs within the CaM-like domain. In contrast to  $\alpha$ -actinin 1 and 4, calcium cannot exert its regulatory control over the interaction with actin or other binding partners in muscle  $\alpha$ -actinins due to the loss of the calcium-binding ability of the CaM-like domain. In fact,  $\alpha$ -actinin 2 and 3 are regulated by binding of phospholipids as phosphatidylinositol 4,5-biphosphate (PIP<sub>2</sub>) and phosphatidylinositol 3,4,5-triphosphate (PIP<sub>3</sub>) without the exact mechanism being clear yet. The plethora of binding partners of  $\alpha$ -actinin yet identified including different classes of proteins, e.g. transmembrane, adaptor and signalling proteins as well as metabolic enzymes, represents a peculiar quality of  $\alpha$ -actinin. During muscle development  $\alpha$ -actinin is a part of integrin-based adhesion structures, which are recognized as costamere precursors and starting points of myofibril assembly. There it interacts with the cytoplasmic tail of  $\beta$ -integrins, with vinculin and ZASP, the latter recruiting  $\alpha$ -actinin to these adhesion sites. Along the actin filaments,  $\alpha$ -actinin associates in a periodic pattern as a component of dense bodies, where it binds to zyxin and muscle LIM protein. Disruption of the interaction of  $\alpha$ -actinin and MLP can

cause dilated cardiomyopathy (DCM). In adult cross-striated muscle  $\alpha$ -actinin resides in the sarcomeric boundaries and forms complexes with components of the contractile apparatus such as titin and nebulin as well as with scaffolding proteins of the paladin protein family (paladin, myotilin, myopaladin), the calsarcin family (FATZ, calsarcin, myozenin) and the multiadaptor protein myopodin. Upon their association with metabolic enzymes of the glyconeogenesis like fructose 1,6-bisphosphatase and aldolase, which are localized at the Z-disc, the muscle isoforms of  $\alpha$ -actinin can alter the physiological characteristics of muscle fibres. Furthermore,  $\alpha$ -actinin has been identified to be a constituent of the dystrophin glycoprotein complex, which provides a link between the subsarcolemmal cytoskeleton and the ECM. These multiple interactions render  $\alpha$ -actinin a key player of maintaining muscle architecture, mechanosensing and metabolic control.

### 1.5.5.2 Filamin C

Filamin C is the predominant isoform of the filamin family of proteins in cross-striated muscle where it localizes to the Z-disc, myotendinous junction, sarcolemma and intercalated disc (van der Ven *et al.*, 2000a). All three isoforms A, B and C share a high sequence homology of about 70 % and a similar domain layout. However, filamin C contains a unique insertion of 81 amino acids in the immunoglobulin (Ig)-like domain 20.

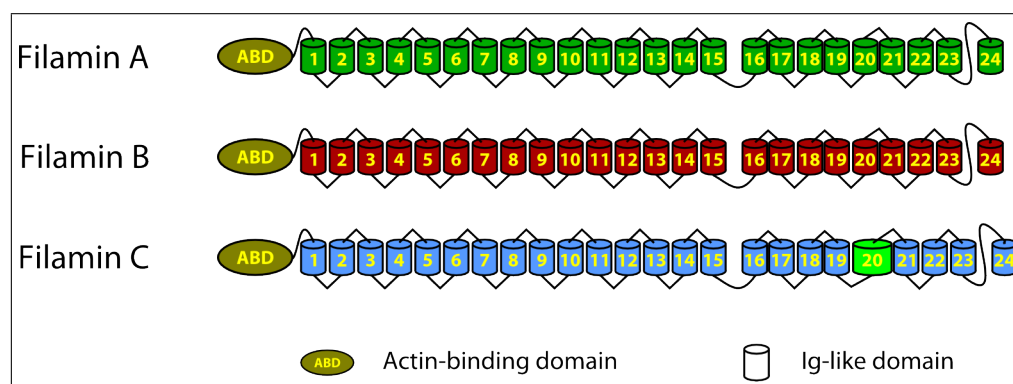


Figure 1.3: **Schematic overview of the filamin protein family.** The filamin protein family in vertebrates consists of three proteins, filamin A, B and C. All three members display a similar domain layout starting with a tandem actin-binding CH domain followed by 24 Ig-like domains. Only filamin C has an unique insertion of 81 amino acids in Ig-like domain 20. The Ig-like domain 24 functions as a dimerization interface enabling the homodimerization of filamin A, B and C as well as heterodimerization between filamin B and C (Himmel *et al.*, 2003).

Filamins are characterized by an N-terminal actin-binding domain consisting of a tandem pair of CH domains (cf. section 1.5.5.1), followed by a long rod-shaped domain of 24 homologous Ig-like domains. This region is separated into two domains by two hinge

regions between Ig-like domain 15 and 16, 23 and 24, respectively, which provide flexibility to allow its V-shaped dimeric form (Zhou *et al.*, 2010). The dimerization interface is located in Ig-like domain 24 and exhibits a limited capacity of heterodimerization with other isoforms, because only filamin C and B can form heterodimers *in vitro*, whereas filamin A only exists as a homodimer (Himmel *et al.*, 2003). Due to its dimeric state, filamin C and filamins in general can cross-link actin filaments at perpendicular angles, which is assisted by a second actin-binding site on the Ig-like domains 9 to 15. A plethora of more than 70 binding partners has already been identified for all filamin isoforms together and their binding sites are mainly located in the second part of the rod domain presumably due to this region not being associated with actin and therefore being free to interact. Furthermore, in filamin A this domain reveals a pairwise domain arrangement, where the even domains 16, 18 and 20 are partly unfolded and tightly associated with the following (Lad *et al.*, 2007). Upon application of mechanical force, a binding site for the cytoplasmic tail of  $\beta$  integrins is exposed, thus enabling the interaction (Heikkinen *et al.*, 2009; Pentikäinen und Yläne, 2009). Filamin competes with talin for integrin binding, which is presumably regulated by mechanical stress or migfilin, another binding partner, which interacts with this integrin-binding region in filamin (Ithychanda *et al.*, 2009). The  $\beta$ 1A integrin binding site has been also identified within filamin C (Gontier *et al.*, 2005) and it is likely that the mechanism resembles the one described by Pentikäinen und Yläne (2009). Apart from integrin-binding, filamin C targets to the sarcolemma due to its association with sarcoglycans, components of the dystrophin glycoprotein complex (Thompson *et al.*, 2000). In the Z-disc, filamin C is tethered by interactions to FATZ (Gontier *et al.*, 2005), myotilin (van der Ven *et al.*, 2000b) and myopodin (Linnemann *et al.*, 2010). During mouse muscle development, filamin C is up-regulated at E8.5 in the myotome of the somite and the developing heart and remains restricted to striated muscle upon developmental progression (Goetsch *et al.*, 2005). The loss of filamin C causes a severe muscle phenotype revealing defects in embryonic myogenesis (cf. section 1.2.2.1) resulting in a decreased number of primary fibres and excessive fibre size variations as well as disturbance of sarcomere architecture (Dalkilic *et al.*, 2006). In cultured cells, filamin C transcription is immediately up-regulated after inducing myogenic differentiation (Goetsch *et al.*, 2005) and it can interact with Xin (cf. section 1.10 and van der Ven *et al.* (2006)), a muscle-specific protein also involved in myofibrillogenesis and the first binding partner of the unique insertion. Except for its numerous interactions with adaptor and transmembrane proteins, filamin coordinates signalling pathways of small GTPases, which differentially affect actin dynamics and structure (Zhou *et al.*, 2010).

These multiple structural and signalling functions identify filamin C as a global player in maintaining sarcomeric integrity, which is further sustained by the fact that mutations in filamin C lead to impaired muscle function (Vorgerd *et al.*, 2005; Löwe *et al.*, 2007; Shatunov *et al.*, 2009) and its localization is severely altered in many different types of myofibrillar myopathies (Claeys *et al.*, 2009).

### 1.5.6 The M-Band

Whereas the Z-disc demarcates the lateral boundaries of the sarcomere and anchor the thin filaments, the antiparallel bundles of myosin-containing thick filaments are aligned into a regular hexagonal lattice and stabilized in the middle of the sarcomere at the level of the M-band. This attachment complex reveals a fibre type-dependent ultrastructure in electron micrographs highlighted by the appearance of a varying number of M-lines which reflects differences in protein composition and arrangement. The giant ruler protein titin originating from opposing Z-discs overlaps with its C-terminus within the M-band and interacts with major M-band components, providing a mechanical and signalling link of thick filament contraction events to the entire sarcomere. All types of vertebrate striated muscle comprise the myosin-binding protein myomesin, which forms antiparallel dimers with its C-terminus and interacts with titin. The myomesin fibronectin type III (Fn) and immunoglobulin type II (Ig) domains as well as a splice variant-specific, intrinsically disordered insertion (EH-myomesin) show elastic properties comparable to titin, pointing to a function as tension absorber and or sensor (Agarkova und Perriard, 2005). The presence of myomesin splice variants and their relatives, M-protein and the newly identified myomesin 3, seem to define the muscle fibre type, because M-protein and EH-myomesin are mutually exclusively expressed in fast and slow muscle fibres, respectively (Agarkova *et al.*, 2004; Agarkova und Perriard, 2005), and myomesin 3 is absent from the heart at any stage during development (Schoenauer *et al.*, 2008). Moreover, the M-band composition correlates with the incorporation of titin isoforms of different sizes corroborating the interdependence of fibre type and M-band layout (Agarkova und Perriard, 2005). Moreover, myomesin could provide a connection to the sarcolemma due to its ability of binding certain integrins (Deshmukh *et al.*, 2007), thus further enhancing sarcomere stability. Lateral anchorage of the M-band to the sarcoplasmic reticulum (SR) is mediated by the huge protein obscurin ( $\approx 800$  kDa), for deletion of obscurin in mice results in changes in longitudinal SR architecture (Lange *et al.*, 2009). Obscurin mainly localizes to the M-band periphery (Carlsson *et al.*, 2008), where it can interact with myomesin and



titin establishing a signalling connection from the thick filaments to the surroundings of the contractile apparatus (Pernigo *et al.*, 2010; Ford-Speelman *et al.*, 2009). This ternary complex can also be formed by its small homologue obscurin-like-1, which is another integral component of the M-band (Fukuzawa *et al.*, 2008; Pernigo *et al.*, 2010).

## 1.6 The Myotendinous Junction

Vertebrate motility is achieved by the transduction of force generated by the contractile apparatus of skeletal muscle. The myotendinous junction (MTJ) is the specialized structure at the end of myofibrils, where the sarcolemma interdigitates with the tendon and the force transmission takes place (fig. 1.4). It is characterized by large invaginations, which increase the surface and therefore reduce the force applied to any one area of the membrane. The tendons mainly consist of collagen fibres, which are anchored to a thin muscle basement membrane predominantly comprised of laminin 2 (Trotter, 2002). The linkage of the myofibril to this underlying extracellular matrix is mediated by  $\alpha7\beta1$  integrin, the dystrophin glycoprotein complex (DGC) and the related utrophin glycoprotein complex (Trotter (2002); Ervasti (2007)). At the cytoplasmic side of the MTJ, actin filaments extend from the last A-band (cf. section 1.5) and are connected to the transmembrane complexes via adaptor proteins. Integrin-based adhesions are linked to actin by talin and vinculin in conjunction with N-RAP (nebulin-related-anchoring protein), a nebulin-related protein exclusively localized at the MTJ in skeletal muscle, which is also able to bind F-actin (Luo *et al.*, 1999). The dystrophin and the utrophin complex share an analog composition but they differ in their modes of contact with actin and  $\beta$ -dystroglycan (Ervasti, 2007). All of these adhesion complexes mentioned contribute to the proper architecture and mechanical stability of the MTJ as the loss of  $\alpha7$  integrin (cf. section 1.9.2), talin (cf. section 1.9.4), dystrophin and utrophin results in altered MTJ structure and impaired muscle function (Welser *et al.* (2009); Conti *et al.* (2008); Conti *et al.* (2009); Nawrotzki *et al.* (2003)).

## 1.7 Costameres

Costameres were originally identified as a vinculin-containing cortical lattice in skeletal muscle, which was assumed to laterally transmit the force from sarcomeres across the sarcolemma to the ECM (Pardo *et al.*, 1983). This structure circumferentially aligns

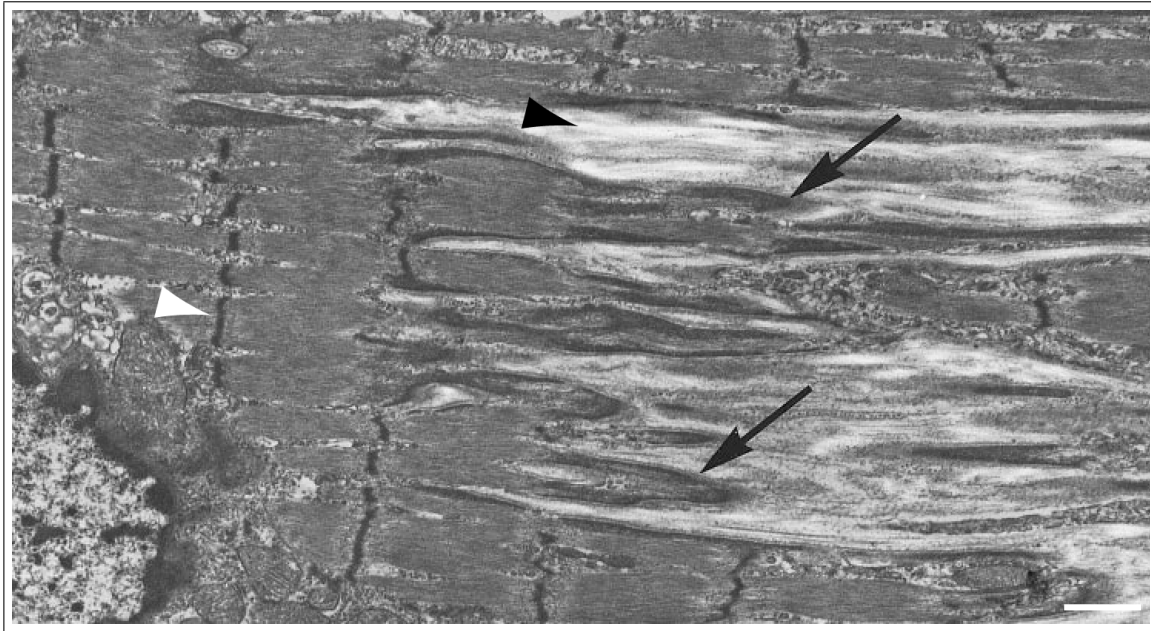


Figure 1.4: **Electron micrograph of a longitudinally sectioned myotendinous junction in murine soleus muscle.** Myotendinous junctions reveal a characteristic electron dense band at the end of myofibrils (arrow). The connective tissue of the underlying extracellular matrix is indicated by the brighter area adjacent to the dense band (black arrowhead). The myofibrils contain the typical striated pattern (Z-disc, white arrowhead). Bar, 1  $\mu$ m. Modified from Carlsson *et al.* (1999).

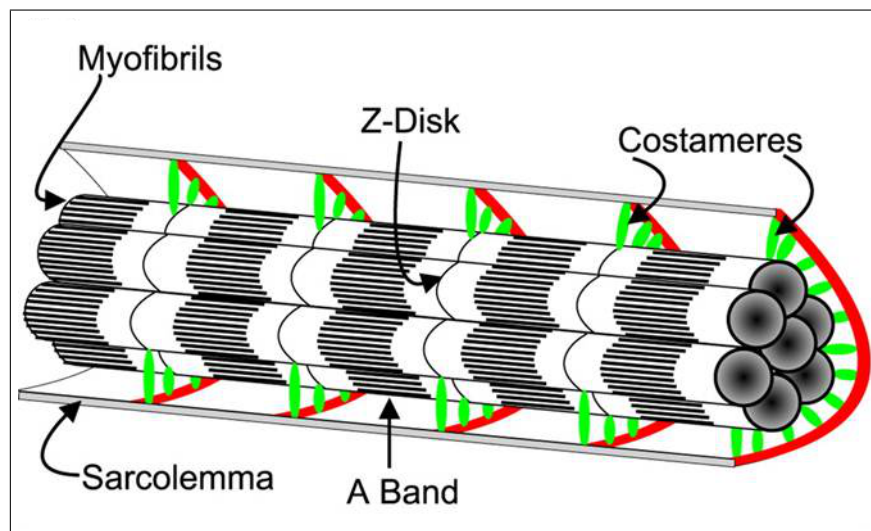


Figure 1.5: **Schematic illustration of the cellular location of costameres in striated muscle.** Costameres (green) represent attachment structures of lateral force transmission circumferentially positioned at the level of Z-discs of peripheral myofibrils. These adhesion sites are tethered within the sarcolemma (red) and connect the contractile apparatus to the extracellular matrix. Taken from Ervasti (2003).

with the Z-disc of peripheral myofibrils and contains a multitude of different proteins (fig. 1.5). The fact that apart from vinculin other typical constituents of focal contacts such as talin,  $\alpha$ -actinin, paxillin and ponsin are components of this complex, which is linked to the ECM by integrins, suggests that costameres are muscle-specific elaborations of focal adhesions sites (Ervasti, 2003; Gehmlich *et al.*, 2007, 2010; Sparrow und Schöck, 2009). Additionally, the linkage to the basement membrane is also mediated by the dystrophin-glycoprotein complex (DGC) and associated proteins such as filamin C (cf. section 1.5.5.2). Recent reports also implicate the giant protein nebulin in the direct attachment of the contractile apparatus to the sarcolemma, since archvillin, an actin-bundling protein and component of early costameres, has been shown to interact with the nebulin repeat modules M184-M185 (Oh *et al.* (2003); Lee *et al.* (2008)). The costameres do not only establish a mechanical link of force transmission but also function as sensors inducing signalling events leading to altered protein expression. Upon denervation or mechanical unloading of muscle cells, costameres change their composition or disintegrate because vinculin and  $\beta$ 1 integrin lose their costameric localization and dystrophin as well as other components of the DGC reorientate longitudinally along the muscle fibre. Electric stimulation can rescue this phenotype because contraction up-regulates vinculin and talin expression. Furthermore, passive stretch activates signalling of the transcription factor NFATc (nuclear factor of activated T-cells) and MEF2 (myocyte enhancer-binding factor 2), which corroborates costameres as mechanical sensors. Costameres also provide a link to the cortical cytoskeleton containing  $\gamma$ -actin and intermediate filament proteins, e.g. desmin (Craig und Pardo (1983); Ervasti (2003)). Although there are also connective structures to the M-band (cf. 1.5.6), the term costamere usually indicates the peripheral Z-disc structure. Costameres are also present in cardiomyocytes with some differences between human and rodent heart (Anastasi *et al.*, 2009).

## 1.8 The Heart

### 1.8.1 Heart Development

A requirement for life is to establish circulation in order to supply the whole organism with essential nutrients. Accordingly, the heart is the first organ to function during embryonic development at about E8.5-E9 in mice, although its formation is completed only postnatally. Cardiac precursor cells are arranged in the heart-forming fields, bilaterally paired areas of lateral mesoderm, which merge in the midline starting at their anterior

edges to form the cardiac crescents and subsequently creating a linear heart tube (fig. 1.6 A). This heart tube represents a tubular pump consisting of an undivided endocardial lumen confined by an endocardial cell layer, which is separated from the myocardium by ECM components, the cardiac jelly. The heart tube elongates by the constant addition of new cardiac segments and gains contractility immediately prior to the onset of cardiac looping. This process essentially approximates heart tube segments and developing great vessels, allowing for the development of a four-chambered heart (fig. 1.6 B). During looping, the heart tube changes its appearance into a C-shaped loop pointing towards the right side of the embryo, which establishes the left/right asymmetry of the ventricular components. The loop further winds counterclockwise resulting in a more S-like structure and develops a chambered appearance by ballooning of atrial and ventricular segments and the formation of the cardiac septum (Männer, 2009; Zaffran und Frasch, 2002; Hirschy *et al.*, 2006). A key regulator of vertebrate cardiac development is the NK-class homeodomain transcription factor Nkx2.5 acting cooperatively with various other factors including e.g. GATA4 or Tbx5 (Bruneau, 2002; Riazi *et al.*, 2009), which is likely to be controlled by JAK-Stat (Janus kinase, signal transducer and activator of transcription) signalling pathways (Snyder *et al.*, 2010).

### 1.8.2 Cardiomyocytes

The myocard differs from the likewise cross-striated skeletal musculature as it is only a functional syncytium consisting of electrochemically coupled mono- or binucleated cells interconnected by a specialized junctional structure, the intercalated disc (ICD). At early stages of embryogenesis, cardiomyocytes display a polygonal or round shape comprising irregularly arranged myofibrils and adhere to each other via cadherin-based cell-cell contact sites distributed throughout the whole membrane. During developmental progression in mammalia, cardiac muscle cells grow in length accompanied by a parallel orientation of myofibrils as well as addition of sarcomeres and reveal exceptional bipolar cell-cell contacts, early ICD's (Hirschy *et al.*, 2006). In these immature ICD's, the localization of desmosomes and adherens junctions is spatially distinct, shown by mutually exclusive staining patterns of desmosomal and classical cadherins at the timepoint of first contraction (Pieperhoff und Franke, 2007). While maturation proceeds, these adhesion sites constantly coalesce, thus creating an unique junctional structure designated as area composita (Franke *et al.*, 2006; Borrmann *et al.*, 2006; Pieperhoff und Franke, 2007). The formation of areae compositae requires plakophilin-2, a cytoplasmic adaptor pro-

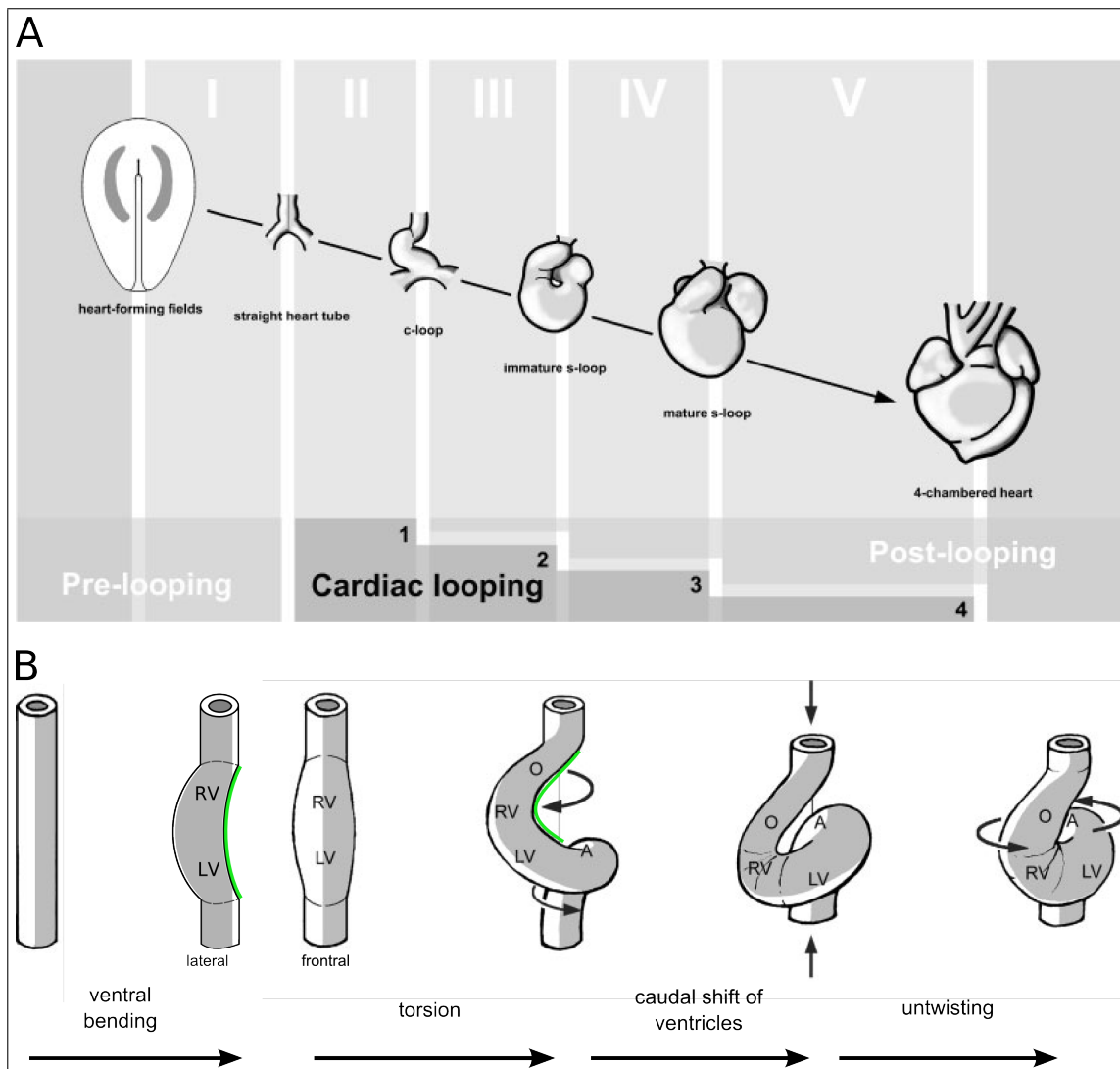


Figure 1.6: **Development of the four-chambered heart and the cardiac looping process.** **A.** Cardiac precursor cells are arranged in the heart-forming fields, which fuse to form the cardiac crescent and later the linear heart tube. This tube undergoes the looping process finally resulting in a four-chambered heart. **B.** The looping process starts with ventral bending of the linear heart tube. At this stage, *Xin* expression starts in chicken embryos as indicated in green (Wang *et al.*, 1999). Rotation of the tube leads to a C-shaped heart and the distance decreases between both ends of the heart tube. Untwisting of the ventricles and the outflow tract finalizes the looping process. A, common atrium; LV, embryonic left ventricle; O, outflow tract; RV, embryonic right ventricle. Modified from Männer (2009).

tein associated with desmosomal junctions, since reduction of plakophilin-2 protein levels abolishes the construction of the composite junction (Pieperhoff *et al.*, 2008). Besides the mechanical connection of cardiomyocytes, alterations of plakophilin-2 influence the electrochemical coupling of adjacent cells, for the total expression level of connexin 43 is reduced (Oxford *et al.*, 2007). Connexins are the building units of connexons, which form a conductive channel through the ICD of adult heart and associate with opposing connexons of neighbouring cells thus constructing gap junctions and generating a functional syncytium (Severs *et al.*, 2008). Apart from specialized cell architecture, myofibrils in cardiomyocytes exhibit additional differences in the composition of the contractile apparatus. In contrast to skeletal muscle, the thin filaments display greater length variations (Burgoyne *et al.*, 2008; Robinson und Winegrad, 1977) and are associated with heart-specific proteins like nebulin (cf. section 1.5.4). Furthermore, cardiac muscle contains aberrant isoforms or altered expression levels of sarcomeric proteins in comparison to skeletal muscle (Clark *et al.*, 2002).

## 1.9 Cellular Junctions

The important role of junctional structures to adjacent cells and the ECM during muscle development and formation of the contractile apparatus is depicted in sections 1.2, 1.8 and 1.5. In order to further explain the molecular architecture, a selection of the major constituents of cell-cell and cell-matrix contact sites is described in further detail.

### 1.9.1 Cadherins

The construction and maintenance of tissues depends on the stable connections of participating cells established by many different transmembrane proteins. Cadherins define a class of calcium-dependent mainly single-pass transmembrane proteins whose members are detectable in all tissues (Nollet *et al.*, 2000). In this part classical and desmosomal cadherins are introduced, which can be distinguished within the cadherin superfamily according to the number of extracellular cadherin (EC) domains. Their extracellular region consists of 5 EC domains, whose fold is rigidified by binding of three calcium ions between successive domains. The first EC domain mediates homo- and heterophilic interactions with ectodomains of opposing cadherins of the neighbouring cell. At the cytoplasmic level they associate with various adaptor proteins transmitting signals to the cellular interior.

Classical cadherins comprise E-, N-, P-, M-, R- and VE-cadherins, but only N-, M-



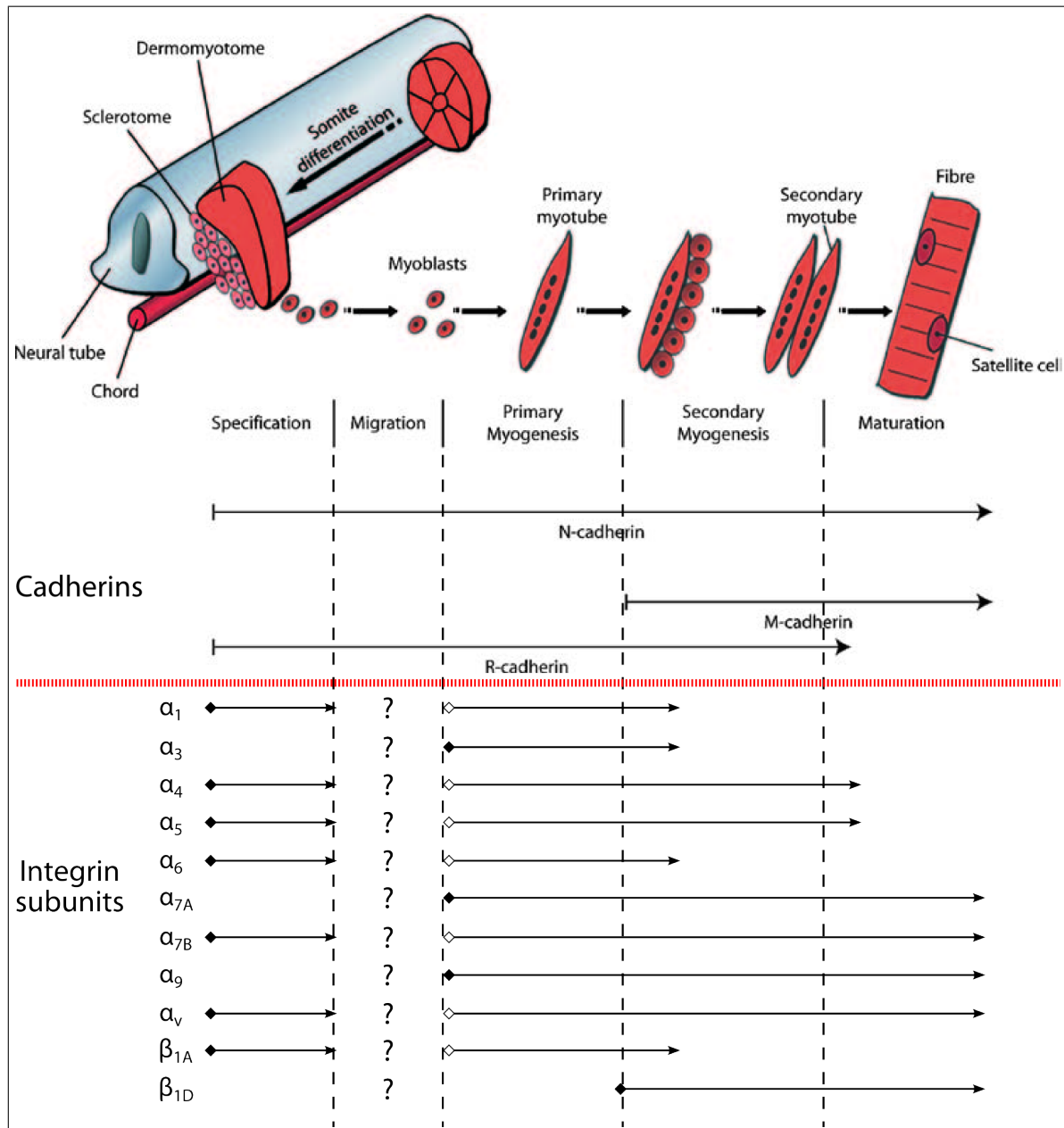


Figure 1.7: **Expression of cellular junction proteins during muscle development.** Schematic overview of embryonic development and the cadherins and integrins expressed in the different phases of myogenesis. Taken and modified from Charrasse *et al.* (2003); Gullberg *et al.* (1998).

and R-cadherin are expressed during skeletal muscle development (cf. section 1.2, fig. 1.7). While N-cadherin is expressed during the complete process, R-cadherin is detected in somites and limbs as well as cell-cell contacts of myoblasts (Charrasse *et al.*, 2003). It is downregulated in adult muscle and it has been shown to inhibit myogenesis via increase of Rac1 activity and downregulation of N- and M-cadherin expression (Kucharczak *et al.*, 2008). However, R-cadherin is capable of inducing striated muscle in embryonic stem cells lacking E-cadherin. This quality is exclusive to R-cadherin since neither N- nor E-cadherin display the same capability (Krauss *et al.*, 2005). Although the exact function is still elusive, this points to a non-redundant function of R-cadherin. M-cadherin occurs at the onset of secondary myogenesis and is involved in fusion and terminal differentiation (Charrasse *et al.*, 2003). Loss of M-cadherin does not result in a severe muscle phenotype but triggers upregulation of N- and E-cadherin which implies compensation of M-cadherin function by other classical cadherins (Hollnagel *et al.*, 2002). In adult muscle M-cadherin attaches satellite cells with the adjacent myofibre and potentially regulates satellite cell quiescence (Broek *et al.*, 2010). The most prominent cadherin in muscle is N-cadherin and its signalling is essential for myogenesis. N-cadherin is early expressed in somites, the myotome and the limb buds and its expression is also maintained in adult muscle (Charrasse *et al.*, 2003). Induction of RhoA signalling and suppression of Rac1 activity promotes myogenic differentiation via muscle-specific gene transcription by serum response factor (Charrasse *et al.*, 2003). Furthermore, it induces p38 MAPK signalling which leads to MyoD-dependent, muscle-specific gene expression substantiating N-cadherin's myogenic role (Lu und Krauss, 2010). At the cytoplasmic side classical cadherins are connected to the actin cytoskeleton by  $\beta$ -catenin and  $\alpha$ -catenin, although this does not seem to be a stable link (cf. section 1.9.1.1). On the contrary, desmosomal cadherins provide a connection to the intermediate filament system via plakoglobin and desmoplakin. Strikingly, plakoglobin and  $\beta$ -catenin are structurally related and indeed, plakoglobin can also bind to  $\alpha$ -catenin and is present in adherens junctions which is presumably required to initiate the assembly of desmosomes which appear to form after adherens junctions (Choi *et al.*, 2009). Desmosomal cadherins comprise four desmogleins and three desmocollin isoforms. Desmosomes as well as adherens junctions are the major structural links in ICDs of cardiomyocytes (cf. section 1.8).



### 1.9.1.1 $\beta$ -Catenin

The cytoplasmic form of the protein  $\beta$ -catenin is a key regulator of canonical Wnt signalling and belongs to a family of armadillo repeat proteins comprising p120 catenin, plakoglobin (or  $\gamma$ -catenin), importin- $\alpha$  or APC (MacDonald *et al.*, 2009; Choi *et al.*, 2009; Coates, 2003). Wnt proteins are secreted ligands for receptor-mediated signalling and cause the stabilization of dephosphorylated  $\beta$ -catenin upon receptor binding in the canonical Wnt signalling pathway. This protects cytoplasmic  $\beta$ -catenin from constant degradation by the ubiquitin-proteasome system due to N-terminal phosphorylation by the glycogen synthase kinase 3- $\beta$  (GSK-3 $\beta$ ) and simultaneously enables its translocation to the nucleus. There, it binds to transcription factors of the Lef/Tcf family (lymphoid enhancer binding factor/T cell-specific transcription factor) via its armadillo repeats, each repeat formed by three spatially distinct  $\alpha$ -helices, and therefore activating various target genes (MacDonald *et al.* (2009) and Behrens *et al.* (1996)). In embryonic development, Wnt6/ $\beta$ -catenin signalling essentially controls the maintenance of the dermomyotome through activation of the transcription factor *paraxis* (Linker *et al.*, 2005). At the onset of myogenesis and cell determination,  $\beta$ -catenin directly induces the transcription of the muscle determination factor Myf5 using two Lef/Tcf binding sites present in the Myf5 enhancer (Borello *et al.*, 2006). Even though the signalling pathway remains active during the course of muscle development, its effects are only critical for secondary myogenesis, because it positively regulates the number of Pax7<sup>+</sup> progenitor cells (cf. 1.2.2.1 and 1.2.2.2) and affects the overall number of myofibres (Hutcheson *et al.*, 2009). Besides its regulatory function concerning the transcription of target genes in the canonical Wnt signalling pathway,  $\beta$ -catenin is also a cytoplasmic component of cadherin-mediated adhesion complexes (cf. section 1.9.1), providing a link to the actin cytoskeleton. Not so long ago, this connection was regarded as a stable mechanical link, because  $\beta$ -catenin can interact with  $\alpha$ -catenin, which is in turn an F-actin binding protein (Koslov *et al.*, 1997; Rimm *et al.*, 1995). However, recent studies revealed that  $\alpha$ -catenin cannot bind  $\beta$ -catenin and F-actin simultaneously thus challenging this model (Yamada *et al.*, 2005) and favouring different linker proteins and cell-cell adhesion-independent functions of  $\alpha$ -catenin (Benjamin *et al.*, 2010). During skeletal muscle development, cadherin-based junctional complexes are involved in the regulation of muscle regulatory proteins and myoblast fusion processes (cf. section 1.9.1). Directly after the onset of muscle differentiation,  $\beta$ -catenin is recruited to newly formed adherens junctions and induces the expression of myogenin, another myogenic regulatory factor (MRF) of the basic helix-loop-helix family of skeletal muscle

transcription factors regulating progression towards the terminal stages of myofibrillogenesis (cf. section 1.2 and Goichberg *et al.* 2001). At these adhesion sites,  $\beta$ -catenin can be cleaved by the  $\text{Ca}^{2+}$ -dependent, nonlysosomal, cysteine protease calpain 3, which is considered an important organizer of proper sarcomere development (Kramerova *et al.*, 2006; Beckmann und Spencer, 2008). Accordingly,  $\beta$ -catenin plays a major role in myogenesis because deregulation of its multiple functions in the transcription of target genes and mediating adhesion leads to severe defects in muscle development.

### 1.9.2 Integrins

Integrins are heterodimeric transmembrane proteins consisting of an  $\alpha$  and  $\beta$  subunit each spanning the membrane once. Most of the two polypeptide chains is exposed to the extracellular space leaving only short cytoplasmic tails of 20-50 amino acids for interactions with intracellular proteins or modifications except the  $\beta 4$  subunit, which comprises an approx. 1000 aa cytosolic domain. Integrins are only found in metazoa, but the set of subunits has dramatically increased from the sponge possessing only one  $\alpha\beta$  heterodimer to human having 18  $\alpha$  subunits and 8  $\beta$  subunits generating 24 distinct integrin dimers (Hynes, 2002; Hughes, 2001). Their extracellular domains adhere either to ECM components (including fibronectin, laminin and collagen), or to counterreceptors of the Ig-superfamily cell surface receptors to mediate heterotypic cell-cell adhesion dependent on the composition of the integrin heterodimer (Humphries *et al.*, 2006). The short cytoplasmic tail provides a link mainly to the F-actin cytoskeleton via adaptor proteins such as talin, kindlin,  $\alpha$ -actinin or filamin. Integrins can adopt three different conformations: a bent closed, an intermediate extended and an extended open one, which represent discrete states of activation. Integrin activation or inactivation is the critical event for the regulation of signalling function. Inactivated integrins presumably exhibit the bent closed conformation, which can be altered by extracellular ligand binding, leading to an extended open conformational state and causing an “outside-in” signalling cascade. The ability of cytoplasmic activation or inactivation by adaptor proteins like talin or filamin (i.e. ‘inside-out’) resulting in an intermediate extended conformation enables the bidirectional transmission of biochemical signals and mechanical force, which is important for cell migration and development as well as for the maintenance of the contractile apparatus in cross-striated muscle (Shattil *et al.*, 2010). During vertebrate skeletal muscle development (cf. section 1.2) many different integrin subunits are expressed in a tightly regulated pattern (fig. 1.7). The major  $\beta$  chain detectable in developing muscle belongs to the  $\beta 1$  class, which occurs in four differ-

ent splice variants (A–D) affecting the cytoplasmic tail (Gullberg *et al.*, 1998; Belkin *et al.*, 1996). While the  $\beta 1A$  isoform predominates in proliferating and fusing myoblasts, the expression of the  $\beta 1D$  subunit is initiated immediately after forming the first myotubes and increases during myotube growth and maturation accompanied by a simultaneous downregulation of the  $\beta 1A$  subunit. In adult skeletal muscle,  $\beta 1D$  integrin localizes to costameres, the myotendinous and neuromuscular junction (Belkin *et al.*, 1996). Loss of  $\beta 1$  integrin in mice results in defective costameres (cf. section 1.7) lacking talin and vinculin and impaired fusion probably due to a spoilt fusion complex missing the tetraspanin CD9. Furthermore, the absence of the  $\beta 1$  subunit damages sarcomere assembly because the myotubes does not develop a mature striated pattern (Schwander *et al.*, 2003). During early heart development,  $\beta 1A$  integrin is the major subunit but this switches perinatally due to an upregulation of the  $\beta 1D$  chain (de Melker und Sonnenberg, 1999). Targeted reduction of  $\beta 1D$  integrin in cardiomyocytes results in cardiac failure which demonstrates its essential role in heart function (Shai *et al.*, 2002). Although the number of  $\beta$  subunits expressed throughout muscle development is limited as mentioned above, many different  $\alpha$  integrins, i.e.  $\alpha 1$ ,  $\alpha 3$ ,  $\alpha 4$ ,  $\alpha 5$ ,  $\alpha 6$ ,  $\alpha 7$ ,  $\alpha 9$  and  $\alpha v$ , appear transiently or persistently during myofibrillogenesis, but only the loss of  $\alpha 7$  integrin causes a prominent muscle phenotype suggesting redundant functions. In early muscle development of mice at 24 somite stage, delamination of muscle precursor cells starts to form the myotome. The first  $\alpha$  integrin subunits detected in these cells are the laminin and collagen receptor  $\alpha 1$  and the exclusive laminin receptor  $\alpha 5$ . The latter integrin is present in all Pax3<sup>+</sup> and later Myf5<sup>+</sup> cells and remains expressed throughout primary myogenesis. At E10.5 in mice,  $\alpha 4$  expression occurs in already formed muscle masses comparable to Pax3 and Myf5 distribution, which is not lost until the end of embryonic myogenesis. The onset of MHC expression in the cells of the myotome coincides with a positive signal of  $\alpha 6$  integrin in these cells, which is persistent on primary myotubes (Bajanca und Thorsteinsdóttir, 2002; Cachaço *et al.*, 2005). Early myotubes display  $\alpha 3$  integrin transiently localized to nascent MTJ prior to  $\alpha 7$  integrin and excluded from areas containing striations. In contrast, the  $\alpha v$  isoform, whose expression is initiated at E10.5 in muscle masses and differentiating muscle cells, is associated with the Z-disc, after titin and  $\alpha$ -actinin show a striated pattern but prior to desmin, and can also be attached to the sarcomeric M-band to a lower extent (McDonald *et al.* (1995) and Cachaço *et al.* (2005)). Adult skeletal muscle fibres are predominantly linked to the tendons by  $\alpha 7$  integrin and its loss causes disruption of the myotendinous junction and sarcomere structure (Mayer *et al.* (1997), Rooney *et al.* (2006) and Welser *et al.* (2009)). This isoform also resides in the NJ and in the myofibre membrane and

appears first in elongated myotomal cells at E11.5 during primary myogenesis (Burkin und Kaufman, 1999; Cachaco *et al.*, 2005). The set of  $\alpha$  integrin chains expressed on cardiac myocytes comprises  $\alpha1$ ,  $\alpha3$ ,  $\alpha5$ ,  $\alpha6$ ,  $\alpha7$ ,  $\alpha10$  and  $\alpha11$ . In adult heart muscle,  $\alpha3$  and  $\alpha7$  are the predominant isoforms, whereas  $\alpha1$  and  $\alpha5$  are present during embryonic heart development but are downregulated postnatally. Their expression can be re-induced by mechanical loading or aortic constriction thus proposing a role in tissue regeneration (Ross, 2002).

### 1.9.3 Vinculin

Vinculin is the key regulator of focal adhesion formation and links the actin cytoskeleton to the ECM via integrins and to cadherin-based cell-cell contacts (Humphries *et al.*, 2007). It is ubiquitously expressed and resides in the cytoplasm in an inactive state characterized by intramolecular association of the globular head with the tail domain. Upon increased mechanical load, vinculin is recruited to focal adhesion sites where it is activated by the release of the head-to-tail interaction (Ziegler *et al.*, 2006). This requires binding of multiple proteins such as talin,  $\alpha$ -actinin, ponsin, VASP, Arp2/3, actin, paxillin and phosphatidylinositol (4,5)-bisphosphate (Geiger *et al.*, 2001; Hüttelmaier *et al.*, 1998; Ziegler *et al.*, 2006). Vinculin recruitment stabilizes the active conformation of integrins and leads to their clustering (Askari *et al.*, 2010). Vinculin possesses two actin binding sites at its tail enabling actin bundling activity (Jockusch und Isenberg, 1981). Recently, it has been demonstrated that vinculin is capable of nucleating actin polymerization at adhesion sites (Wen *et al.*, 2009). Apart from linking to the ECM, vinculin is associated with adherens junctions (cf. section 1.9.1) and interacts with  $\alpha$ -catenin therefore potentially providing a stable link of cadherin-based junction to F-actin (Weiss *et al.*, 1998). During development of skeletal muscle, vinculin is among the first proteins arranged in a periodic pattern (Tokuyasu, 1989; Fujita *et al.*, 2007). In adult skeletal muscle vinculin is a major component of the costameres sensing the lateral force transmission and stabilizing these adhesion sites since contractile arrest of cardiomyocytes depletes vinculin from there (Pardo *et al.*, 1983; Samarel, 2005; Sharp *et al.*, 1997). Cardiomyocyte-specific inactivation of vinculin results in sudden death caused by tachycardia, abnormal adherens junctions with a reduced level of cadherins and integrins as well as dilated cardiomyopathy (DCM) which demonstrates its important function in the ICD (Zemljic-Harpf *et al.*, 2007). In muscle tissue as well as in platelets, a splice variant, termed metavinculin, containing an insertion of 68 amino acids at the C-terminus is co-expressed. While it

is low abundant in skeletal muscle, in cardiac muscle it can be expressed at levels equal to vinculin (Witt *et al.*, 2004). The insertion appears to take over a regulatory function since metavinculin is impaired binding to phospholipids and it requires activated vinculin to form heterodimers with it (Witt *et al.*, 2004). Furthermore, both proteins have a different impact on F-actin structure since vinculin mainly forms bundles while metavinculin generates highly viscous webs (Rüdiger *et al.*, 1998). The existence of these isoforms in muscle and their cooperation render them a versatile tool for sensing mechanical strength and adaptation to it. During muscle development, their nucleation activity could be important for the formation of thin filament precursors arising from integrin-based adhesive structures (cf. section 1.2.2.4).

#### 1.9.4 Talin

Talin proteins are encoded by two different genes, which are presumed to be created by gene duplication prior to emergence of vertebrates (Senetar und McCann, 2005). Both genes share conserved intron-exon boundaries and 74 % identity in amino acid sequence. Whereas talin 1 is ubiquitously expressed, talin 2 was identified to be most abundant in brain, heart and skeletal muscle. Recent studies revealed that talin 2 is also present in a wide variety of tissues and isoforms performing functions distinct from talin 1 (Debrand *et al.*, 2009; Senetar *et al.*, 2007). A complete loss of talin 1 in mice causes embryonic lethality at E8.5–E9.5 emphasizing its essential role in development and confirming the non-redundant function of both proteins. Talin proteins link the actin cytoskeleton to the ECM and cell-cell adhesion sites with their ability to bind the cytoplasmic tail of  $\beta$  integrins. Furthermore, this interaction activates integrins thus regulating the affinity for their ligands (cf. section 1.9.2). The largest talin isoforms have an approximate molecular weight of 270 kDa and exhibit a similar domain structure. The N-terminal globular head domain, which contains among others a binding site for  $\beta$  integrins and F-actin, is followed by a flexible rod domain displaying multiple binding interfaces to vinculin, a second integrin and two additional F-actin binding sites. At the C-terminus,  $\alpha$ -helices are able to form antiparallel dimers (Critchley und Gingras, 2008). The different functions of talin 1 and talin 2 were explored by tissue-specific gene inactivation and expression and localization studies with isoform-specific reagents. These analyses revealed that talin 2 is upregulated during myofibrillogenesis and resides in costameres and ICDs in adult striated muscle, from which talin 1 is absent (Senetar *et al.*, 2007). Both isoforms seem to be involved in the maintenance of MTJs, because ablation of either talin 1 or

talin 2 results in severe defects in their structure (Conti *et al.*, 2008, 2009). Throughout muscle development they are also indispensable for proper myoblast fusion and sarcomere assembly (Conti *et al.*, 2009).

## 1.10 Xin-Repeat Proteins

Differential mRNA display revealed a transcript markedly upregulated during embryonic heart development of chicken, which corresponded to an as yet unidentified protein comprising a new repetitive sequence motif (Wang *et al.*, 1996, 1999). Because of its involvement in the cardiac looping process of chicken heart (cf. section 1.8), the protein was named Xin, the Chinese character for heart in pronunciation. Xin-Repeat proteins are present in all vertebrates with the number of genes encoding Xin-Repeat-containing proteins varying among species. While the lamprey contains only one Xin gene, analysis of the mammalian genome discovered two genes and zebrafish even express a third one. The differences originate from gene and genome duplication events as well as persistent loss of anciently duplicated genes (Grosskurth *et al.*, 2008).

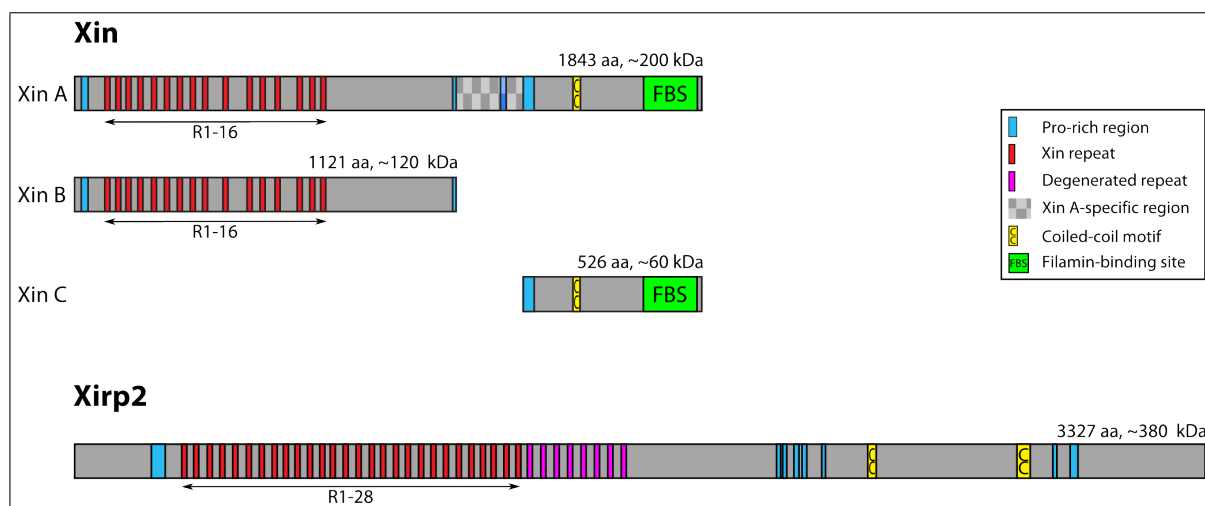


Figure 1.8: **Schematic overview of human Xin-Repeat proteins.** In human, two genes encode Xin-Repeat proteins, CMYA1 and CMYA3, which give rise to two proteins denoted by Xin and Xirp2, respectively. Intraexonic splicing events generate three isoforms of human Xin marked as A, B and C. Until now, no other isoforms of human Xirp2 have been described.

In human, a gene on chromosome 3, entitled CMYA1 (cardiomyopathy-associated 1), comprising only one large coding exon encodes human Xin and gives rise to three different isoforms, A, B, C, due to intraexonic splicing events (fig. 1.8). The largest isoform Xin A (1843 aa,  $\approx$  200 kDa) harbours an N-terminal proline-rich region including an EVH1

domain-binding consensus motif, which is shown to be functional in binding type I EVH1 domains of the members of the Ena/VASP protein family, vasodilator-stimulated phosphoprotein (VASP), mammalian enabled (Mena) and Ena/VASP-like protein (EVL) (van der Ven *et al.*, 2006). This region is followed by the most prominent and eponymous feature, the Xin repeats. Human Xin encompasses 16 copies of this 16 aa-comprising consensus sequence, which defines a novel F-actin-binding motif and therefore identifies Xin-repeat proteins as members of the plethora of actin-binding proteins (Pacholsky *et al.*, 2004). But these repetitive motifs seem to display additional binding capacities, since a direct interaction of the terminally located repeat region to  $\beta$ -catenin was recently demonstrated (Choi *et al.*, 2007). The succeeding sequence also reveals different putative binding sites and some of them were already proven to have the predicted binding potential, at least *in vitro*. The proline-rich region situated on the C-terminal side of the repeats contains putative SH3 domain interaction motifs including a prognosticated binding site of the SH3 domain of the actin-binding protein cortactin exhibiting the binding properties attributed to it (Sparks *et al.*, 1996; Eulitz, 2005). In the C-terminal part of Xin A, the existence of several consecutive heptad motifs raises the possibility of the formation of Xin dimers or oligomers. The most striking feature of Xin A, apart from the repeats, is the filamin C-specific binding site (FBS) mapped to the C-terminus, because Xin represents the first protein identified exclusively binding to this muscle-specific filamin isoform (van der Ven *et al.*, 2006). The other human Xin variants differ from the largest isoform insofar as they are lacking the C-terminal proline-rich region and the filamin binding site or the complete N-terminus with the repeats in Xin B (1121 aa,  $\approx$  120 kDa) or Xin C (526 aa,  $\approx$  60 kDa), respectively (fig. 1.8). The human gene CMYA3 on chromosome 2 encodes a  $\approx$  380 kDa second Xin-Repeats-containing protein, Xirp2 (Xin-Repeat Protein 2), which deviates from Xin in the number of repetitive motifs displaying 28 repeats and 8 degenerated sequences (fig. 1.8). On the contrary, its sequence motif organization shares high homology to Xin, because the repeats are also enclosed by proline-rich regions and there are several heptade motifs at the C-terminus. In addition to the N-terminal proline-rich region, which was also shown to interact with the EVH1 domain of Ena/VASP proteins, Xirp2 includes a second cluster of functional EVH1 domain binding sites located C-terminally to the repeats (Eulitz, 2005). While no splicing events of the human Xirp2 have been detected, recently three different mRNAs of mouse Xirp2, also called mXin $\beta$  or myomaxin, were identified, which only affect the C-terminus (Wang *et al.*, 2010). The expression of both Xin-Repeat proteins, Xin and Xirp2, appears to be restricted to cross-striated muscle and its precursors (Wang *et al.* 1999 and personal ob-



servation). During murine embryonic development, Xin can be detected as early as E8.0 in cardiogenic cells of the heart tube and is present in the first rostral somites at E10, which points to an involvement in the formation of heart and skeletal muscle (Sinn *et al.*, 2002). This notion is substantiated by the observation that blocking the expression of the unique Xin-Repeat protein in chicken interferes with the cardiac looping process (cf. section 1.8.1) and ablation of the murine Xirp2 results in misorganized myocardium and diastolic dysfunction accompanied by postnatal growth defects leading to death before weaning (Wang *et al.*, 1999, 2010). Interestingly, total loss of all Xin isoforms in mice generates only a mild cardiac phenotype with an altered distribution of intercalated discs and little aberrations in conduction, which is not the consequence of compensation by upregulation of Xirp2 (Otten *et al.*, 2010). In adult muscle tissue, Xin is localized at the MTJ of skeletal muscle and the specialized cell-cell contacts of cardiomyocytes, the ICDs (cf. section 1.8), where it is supposed to function as a multiadaptor protein interacting with F-actin, filamin C, Ena/VASP proteins and  $\beta$ -catenin (Beatham *et al.*, 2006; Pacholsky *et al.*, 2004; van der Ven *et al.*, 2006; Choi *et al.*, 2007). Xirp2 shows a similar yet distinct distribution pattern in adult striated muscle, for it also resides in the intercalated discs but additionally is a component of the sarcomeric Z-disc (Wang *et al.*, 2010; Claeys *et al.*, 2009). The set of binding partners of the Xin-Repeat proteins reveals only a partial overlap, for the interactions to F-actin and Ena/VASP proteins are verified for Xirp2, however, the interaction described of murine Xirp2 to  $\alpha$ -actinin is neither predicted nor shown with Xin (Pacholsky *et al.*, 2004; van der Ven *et al.*, 2006; Huang *et al.*, 2006). Both Xin family proteins are concerned with the direct, immediate response to stress applied to muscle tissue although from different kinds of stress. Upon eccentric contraction or cardiotoxin-mediated skeletal muscle injury, Xin expression increases directly and is detected in muscle satellite cells, hence suggesting an implication in muscle regeneration (Barash *et al.* (2004); Hawke *et al.* (2007), cf. sections 1.2.2.2 and 1.4). This view is supported by the conspicuous behaviour in human myofibrillar myopathies and the muscle dystrophic kyphoscoliotic-ky mouse, where Xin expression dramatically rises coinciding with mislocalization and formation of aggregates (Beatham *et al.*, 2006; Claeys *et al.*, 2009). Skeletal muscle fibres affected by myofibrillar myopathies also exhibit an altered distribution of Xirp2 (Claeys *et al.*, 2009) referring to the stress responsiveness mentioned above. In cardiac muscle, angiotensin II-induced hypertension and myocardial damage increases transcription of Xirp2 mediated by the myogenic enhancer factor (MEF) 2A, which binds to its consensus site in the Xirp2 promoter (McCalmon *et al.*, 2010; Huang *et al.*, 2006). The regulation of Xin transcriptional activity is also controlled by myogenic



transcription factors, but the set of functional proteins has already expanded to MEF2, MyoD and Myf5 (Hawke *et al.*, 2007). All these results point to a role for Xin-Repeat proteins in cross-striated muscle development and repair (cf. muscle+heart), but the interplay of different isoforms already identified is still not completely understood. The accidental generation of a transgenic mouse lacking Xin A and Xin B but still retaining the shortest isoform Xin C, provides a first insight. In contrast to a complete loss of Xin, these mice develop cardiac hypertrophy and suffer from disrupted ICD structure and myofilament disarray. Furthermore, Xirp2 expression is upregulated and some Xin A and Xin B binding partners change their localization, which cannot be observed during total Xin absence (Gustafson-Wagner *et al.*, 2007; Otten *et al.*, 2010). These results are consistent with the findings that Xin C protein cannot be found in normal human heart tissue but is elevated in hypertrophic organs (Otten *et al.*, 2010). Localization studies of the three human Xin isoforms in neonatal rat cardiomyocytes demonstrated that all Xin proteins target to nonstriated myofibrils, while only Xin A and C are incorporated into the ICD and only Xin C can colocalize with  $\alpha$ -actinin at the Z-disc (van der Ven *et al.*, 2006) underlining the importance of investigating the different isoforms in order to shed more light on Xin-Repeat protein function.

## 1.11 Aim of the Study

In mammals, the expression of Xin-Repeat proteins seems to be restricted to skeletal muscle and starts very early during myogenic development. Although disruption of Xin and Xirp2 function in mice results in disturbed of muscle integrity and function, their exact role during myofibrillogenesis remains still elusive. In order to address this lack of knowledge, a new *in vitro* cell model based on conditionally immortalized myoblasts originating from the genetically modified H-2K<sup>b</sup>-tsA58 mouse was to be established and characterized. Using isoform-specific antibodies, to be partly characterized in this work, the localization of Xin during different stages of myofibrillogenesis should be studied. The Xin gene gives rise to three different isoforms which share overlapping sequences. However, the relevance of each isoforms is still unknown. Hence, analyses of the transcription and protein expression in the course of myogenic differentiation of H-2K cells should be performed in order to evaluate the respective impact. Both Xin-Repeat proteins in human have an overlapping set of binding partners while showing different localization in the mature muscle. Therefore, detailed investigation of the binding capacities of known and newly identified binding partners concerning Xin-Repeat proteins should be done to clarify redundant or

distinct qualities of Xin-Repeat proteins. Examination of the exact site of interactions in cells were to be carried out with the bimolecular fluorescence complementation assay. In concert with the biochemical characterization of such an interaction this should give a detailed view on the behavior of Xin-Repeat proteins during myofibrillogenesis. Xirp2 is a large, intrinsically unfolded protein which permanently resides in the mature Z-disc but nothing is known about its orientation. Thus, the localization of Xirp2 was to be investigated in mature skeletal muscle using antibodies directed against specific epitopes.

# Chapter 2

## Material and Methods

### 2.1 Chemicals

The exact description of all chemicals used can be found in the corresponding sections. Chemicals were supplied by Roth, Sigma, Merck, Fluka, Serva or Biorad in analytical standard grade.

### 2.2 Culture Media

Medium	Composition
LB-medium	10 g trypton, 5g Hefeextrakt, 10 g NaCl, pH 7,5
YPD-medium	20 g trypton, 10 g yeast extract, 20 g glucose, pH 6,5
DOB-medium	1,7 g yeast nitrogen base, 20 g glucose, 5 g (NH <sub>4</sub> ) <sub>2</sub> SO <sub>4</sub> , pH 5,8 amino acid dropout supplements (Clontech)

Table 2.1: **Table of the composition of culture media.** The utilized masses refer to a final volume of 1 l unless otherwise noted.

Table 2.1 depicts the composition of culture media used for molecular biology techniques. All media were prepared with ddH<sub>2</sub>O and the solutions were sterilized at 125 °C and 1,4 bar in an autoclave (Systec) for 20 min. The time was reduced to 15 min for media including glucose.

## 2.3 Antibiotics

Antibiotics were added to the autoclaved culture medium immediately before use.

Antibiotic	Final Concentration
Carbenicillin	100 µg/ml
Chloramphenicol	34 µg/ml
Kanamycin	50 µg/ml

Table 2.2: **Final concentrations of antibiotics used in culture media** (see tab. 2.1). Antibiotics were generally available in a 1000-fold higher concentrated stock solution.

## 2.4 Bacterial and Yeast Strains

### 2.4.1 Cloning

*E. coli* **JM109**, Stratagene Co., genotype: e14<sup>-</sup>(McrA<sup>-</sup>) recA1 endA1 gyrA96 thi-1 hsdR17(r<sub>k</sub><sup>-</sup> m<sub>k</sub><sup>+</sup>) supE44 relA1 Δ(lacproAB) [F' traD36 proAB lacI<sup>q</sup>ZΔM15]

### 2.4.2 Protein Expression

*E. coli* **BL21(DE3)CodonPlus(DE3)-RP**, Stratagene Co., genotype: B F<sup>-</sup> ompT hsdS(r<sub>B</sub><sup>-</sup> m<sub>B</sub><sup>-</sup>) dcm<sup>+</sup> Tet<sup>r</sup> gal λ(DE3) endA Hte [argU proL Cam<sup>r</sup>]

*E. coli* **BL21(DE3) C43**, described in Miroux und Walker (1996).

### 2.4.3 Yeast Two-Hybrid System

*Saccharomyces cerevisiae* **L40**, Invitrogen Co., genotype: MATα his3D200 trp1-901 leu2-3112 ade2 LYS2::(4lexAop-HIS3) URA3::(8lexAop-lacZ) GAL4.

## 2.5 Vectors and cDNA Libraries

All plasmids are derivatives of commercially available vectors with modified multiple cloning sites, promoters or fusion proteins. Origins and changes are depicted below. The corresponding vector maps are included in the appendix (cf. section C).

## 2.5.1 Protein Expression Vectors

### 2.5.1.1 pET23aEEF

For recombinant protein expression in *E. coli* a vector with a modified multiple cloning site was used which derived from Novagen's pET23a plasmid, named pET23aEEF. DNA fragments were cloned between the recognition sites of the restriction enzymes MluI (5'-end) and Sall (3'-end). The resulting recombinant protein contains a C-terminal hexahistidine sequence for purification (cf. section 2.7.4.1) and in addition an immunotag comprising the last three amino acids glutamate, glutamate and phenylalanine (EEF).

### 2.5.1.2 pET23aT7

This vector is a derivative of Novagen's pET23a plasmid. The multiple cloning site was modified to clone DNA fragments using a MluI restriction site (5'-end) and a Sall site (3'-end). In contrast to the pET23aEEF plasmid, the target protein encoded by the pET23aT7 vector has a T7 immunotag with the amino acid sequence MASMTG-GQQMGR fused to the N-terminus which derived from the capsid protein of the bacteriophage T7. The hexa-histidine tag used for purification is located at the C-terminus.

### 2.5.1.3 pET23aMyc

The pET23aMyc vector backbone is similar to Novagen's pET23a. The altered multiple cloning site includes EcoRI and MluI restriction sites applicable for cloning at the 5'-end and a Sall site at 3'-end. Identical with all pET23a vectors, the hexa-histidine tag is placed at the C-terminus of the expressed protein which can be detected with antibodies against the N-terminal c-myc immunotag (EQKLISEEDL), an epitope which stems from a human oncoprotein.

### 2.5.1.4 pET28a

The pET28a vector was purchased from Novagen and contains an N-terminal hexahistidine tag for purification and a T7 immunotag for detection of the expressed protein. All inserts were cloned between the EcoRI and Sall restriction sites.

### 2.5.1.5 pGEX-6P-3

The pGEX-6P-3 vector encodes a fusion protein with a N-terminal glutathione-S-transferase (GST) which can be cleaved by PreScission™ Protease (GE Healthcare). Cloning frag-

ment were inserted either using the SalI site (5'-end) and the NotI site (3'-end) or the BamHI site (5'-end) and the SalI (3'-end). GST-tagged proteins were used for purification of polyclonal antibodies (cf. section 2.8.2.1) or peptide scans (cf. section 2.9.4) and purified according to manufacturer's recommendations.

## 2.5.2 Vectors for Eukaryotic Protein Expression

### 2.5.2.1 Venus NT

This plasmid expresses a fusion protein of a N-terminally located derivative of the yellow fluorescent protein EYFP (Enhanced Yellow Fluorescent Protein), called Venus (Nagai *et al.*, 2002), and the inserted DNA fragment. The expression is controlled by the human cytomegalievirus (CMV) immediate early promoter. The promoter and the rest of the vector backbone derived from the pECFP-C1 plasmid commercially available from Clontech. The multiple cloning site was modified in order to introduce in-frame restriction sites of BamHI, MluI and SalI which were used for cloning.

### 2.5.2.2 Venus CT

The Venus CT plasmid includes the same multiple cloning site as in Venus NT but upstream from the sequence encoding the fluorescent protein Venus (Nagai *et al.*, 2002). The backbone originates from Clontech's pECFP-N1.

### 2.5.2.3 Venus1-C

The vector backbone of Venus1-C is identical with Venus NT (cf. section 2.5.2.1) but the plasmid encodes only the first 154 amino acids of the yellow fluorescent protein Venus (Nagai *et al.*, 2002) fused with the C-terminus to a FLAG-tag, an immunotag comprising the eight amino acids DYKDDDDK, and the inserted protein fragment. DNA fragments were mainly cloned into the EcoRI/SalI site. The expressed fusion protein is non-fluorescent and was used for bimolecular fluorescence complementation (BiFC) assays combined with proteins encoded by the vectors Venus2-C and Venus2-N3.

### 2.5.2.4 Venus2-C

In the Venus2-C plasmid the inserted protein is fused with its N-terminus to a non-fluorescent fragment of the yellow fluorescent protein Venus (Nagai *et al.*, 2002) comprising the amino acids 155–238. The resulting fusion protein can be detected using

antibodies raised against the amino acids 98-106 of the human influenza hemagglutinin (HA-immunotag YPYDVPDYA) because its coding sequence is located between the non-fluorescent fragment and the multiple cloning site. The vector backbone emanates from Clontech's pECFP-N1.

#### 2.5.2.5 Venus1-N3

The Venus1-N3 plasmid contains the multiple cloning site of the vector pEGFP-N3 (Clontech) and expresses the same nonfluorescent fragment of the yellow fluorescent protein Venus (Nagai *et al.*, 2002) as in the Venus1-C plasmid (cf. section 2.5.2.3) but located at the C-terminus of the encoded fusion protein. For immunodetection a FLAG-tag is integrated at the N-terminus of the cloned insert. The backbone is similar to the plasmid pECFP-N1 (Clontech).

#### 2.5.2.6 Venus2-N3

The vector Venus2-N3 is identical to the Venus1-N3 (cf. section 2.5.2.5) apart from the included nonfluorescent fragment which comprises the amino acids 155–238 of the yellow fluorescent protein Venus (Nagai *et al.*, 2002) and the FLAG-immunotag which is replaced by the HA-immunotag (cf. section 2.5.2.4).

### 2.5.3 Vectors for Yeast Two-Hybrid Assays

#### 2.5.3.1 pLexPd

The yeast two-hybrid interaction analysis is based on the completion of a heterologous transcription factor consisting of a DNA binding domain and an activation domain when they are brought in close proximity to each other by interaction of proteins fused to the domains (cf. section 2.9.1). The bait protein is fused to the C-terminus of the LexA DNA binding domain encoded by the pLexPd vector, a derivative of Clontech's pLexA plasmid. The cDNA was cloned into the MluI/SalI or EcoRI/SalI site of the modified multiple cloning site. The fusion protein was constitutively expressed under the control of the alcohol dehydrogenase (ADH) promoter.

#### 2.5.3.2 pACT Pd

The completion of a heterologous transcription factor needs the close proximity of the DNA binding domain and the activation domain (cf. section 2.9.1). The Gal4 activation

domain is expressed by the prey vector pACT Pd which stems from the pACT2 plasmid (Clontech/BD Bioscience). The multiple cloning site was modified so that a DNA fragment can be cloned into the MluI/XhoI site. The activation domain is fused to the N-terminus of the cloning fragment and the expression of the resulting protein is controlled by the ADH promoter.

#### 2.5.4 cDNA Libraries

For yeast two-hybrid assays and cloning experiments two MATCHMAKER cDNA libraries from Clontech were used which contain cDNA from human heart or skeletal muscle cloned into the pACT2 vector.

## 2.6 Molecular Biology Techniques

Chemicals and enzymes were obtained from Fermentas unless otherwise noted.

#### 2.6.1 cDNA Synthesis

Isolated RNA from cells or tissues (cf. section 2.7.5.2) served as a template for cDNA synthesis which was necessary for cloning purposes and mRNA expression analysis. RNA was transcribed into cDNA with the reverse transcriptase Omniscript (Qiagen). For that purpose 4 U of Omniscript were mixed on ice with the adequate buffer supplied with the polymerase, dNTP's (0,5 mM each, Qiagen), 10  $\mu$ M random nonamers (TIBmolbiol, Invitrogen), 10 U of the RNase inhibitor RNasin (Promega) and 1  $\mu$ g of RNA in a final volume of 20  $\mu$ l RNase-free water. The RNA was transcribed in a thermocycler (Biometra) for 60 min at 37 °C and finally stored at -20 °C until further use.

#### 2.6.2 Polymerase Chain Reaction

The polymerase chain reaction (PCR) (Saiki *et al.*, 1988) was used to amplify DNA fragments out of cDNA generated from RNA of cultured cells, cDNA libraries or existing plasmid DNA. Cloning fragments were produced with PHUSION High-Fidelity DNA Polymerase (Finnzymes) or KAPA HiFi DNA Polymerase (Peqlab) in order to minimize errors during amplification. Mouse typing or RT-PCR's were performed with FIREPol DNA Polymerase (Solis Biodyne) or recombinant Taq DNA polymerase. All enzymes were used in PCR reactions optimized in cycling conditions and composition according



Polymerase	PHUSION		KAPA HiFi		No. of cycles
	Temp.	Time	Temp.	Time	
Initial denaturation	98 °C	30 s	98 °C	2 min	1
Denaturation	98 °C	10 s	98 °C	30 s	35
Annealing	68 °C	30 s	65 °C	30 s	
Extension	72 °C	15 – 30 s/1 kb	68 °C	15 – 30 s/1 kb	
Final extension	72 °C	5 – 10 min	68 °C	5 min	1
	4 °C	hold	4 °C	hold	

Table 2.3: **PCR program for proofreading DNA polymerases.** Amplification of DNA for cloning purposes was performed with the depicted proofreading DNA polymerases. PCR reactions which did not yield the desired results were optimized using touchdown PCR cycling conditions. Such a program employed an initial annealing temperature 10 °C above the projected melting temperature of the primers being used. This temperature is decreased 1 °C every cycle to the estimated melting point. This procedure was repeated four times.

to the manufacturer’s instructions (see tab. 2.3 and 2.4). A list of components and their corresponding concentration range used in a standard analysis can be seen in table 2.5. The reaction was performed in a thermocycler (Biometra).

Polymerase	FIREPol		No. of cycles
	Temp.	Time	
Initial denaturation	95 °C	5 min	1
Denaturation	95 °C	30 s	35
Annealing	58–65 °C	30 s	
Extension	72 °C	30 s/1 kb	
Final extension	72 °C	5 min	1
	4 °C	hold	

Table 2.4: **PCR program for conventional polymerases.** Conventional DNA polymerases were employed in mRNA expression analysis. In some cases the PCR reaction was also optimized with touchdown conditions described in table 2.3.

The result was analysed with agarose gel electrophoresis (cf. section 2.6.4). The size of the obtained DNA fragment was evaluated in comparison to a DNA molecular weight marker (Fermentas, Solis Biodyne).

### 2.6.3 Semiquantitative RT-PCR Analysis

Transcription levels of proteins were analyzed with semiquantitative RT-PCR using DNA-free cDNA (cf. section 2.6.1) obtained from RNA of cells or tissues (cf. section 2.7.5.2). The PCR reaction was performed with FIREPol DNA Polymerase (Solis Biodyne) generally according to the cycling instructions depicted in table 2.4. In order to eliminate variations in the amount of PCR product obtained due to cycling conditions, the optimal

Component	Concentration Range	
template DNA	10-200 ng	provided with with the polymerase TIB Molbiol, Invitrogen TIB Molbiol, Invitrogen
dNTP's	200 $\mu$ M each	
sense primer	0,16-0,5 $\mu$ M	
antisense primer	0,16-0,5 $\mu$ M	
MgCl <sub>2</sub>	1,5-6 mM	
DMSO (optional)	$\leq$ 5 %	
Buffer	1x	
DNA Polymerase	0,02-0,05 U/ $\mu$ l	
ddH <sub>2</sub> O	added to 20-25 $\mu$ l	

Table 2.5: **Composition of a PCR reaction.** The performed PCR reactions comprised the depicted components in the concentration range mentioned.

cycling parameters were figured out adjusting primer concentration, MgCl<sub>2</sub> concentration and annealing temperature (Marone *et al.* (2001)). Quantitation will only be possible, if the PCR reaction does not reach a plateau, i.e. additional cycles do not proportionally change the amount of product. Therefore, the number of cycles was determined before reaching a plateau. The amount of product amplified at optimal conditions was compared to results obtained with a reference gene. In order to have an internal control, duplex PCR's were performed using primer pairs of the target and the reference gene in one reaction which did not reveal any competition, i.e. the product yield had to be the same in the duplex reaction compared to amplification at optimal conditions alone. All results were analyzed with agarose gel electrophoresis (cf. section 2.6.4). The amount of PCR product was determined measuring the band intensities with a Gel Doc XR system (BioRad) and the software program QUANTITY ONE (version 4.6).

## 2.6.4 Agarose Gel Electrophoresis

The size and percentage of the agarose gels were adapted to the requirements. The appropriate mass of agarose was dissolved in TAE buffer (40 mM Tris-acetate, pH 8,3, 1 mM EDTA) during heating in a microwave. After the temperature had been shortly cooled, down the 3x GelRed solution (Biotium, final dilution 1:20000) or ethidium bromide (AppliChem, 1  $\mu$ g/ml) were dissolved in the agarose solution upon stirring. This mixture was poured into a gel tray placed in a casting stand (Peqlab) and a comb formed the wells needed. While cooling down the agarose became solid and the gel tray was put into an electrophoresis chamber filled with TAE buffer. Then the comb was carefully removed so that the samples could be loaded. Before injection the samples were mixed

with Loading Dye (final concentration 10 mM EDTA, 10 % glycerol, 1,7 mM Tris-HCl, 0,005 % bromphenol blue, 0,005 % xylene cyanol FF). The gel was run at 80-180 V and the result was documented with a Gel Doc XR System (BioRad) using transmitted UV light. Images were exported using the software QUANTITY ONE (version 4.6.).

### **2.6.5 DNA Fragment Purification from Agarose Gels**

PCR reactions or restriction digests were separated using agarose gel electrophoresis (cf. section 2.6.4). Afterwards the gel was put on a glass plate in order to reduce damages of the sample caused by the subsequent illumination with transmitted UV light. The designated DNA band was visualised with reduced light intensity from a transilluminator (Schütt Labortechnik) and excised with a scalpel. DNA fragments larger than 200 bp were isolated with the column-based Wizard Gel and PCR Clean-Up System (Promega) and fragments of smaller size using SureClean (Bioline).

### **2.6.6 DNA Digestion**

Plasmid DNA or PCR fragments were predominantly digested with MluI or EcoRI and SalI due to the cloning strategies (cf. section 2.5). Double digestions were performed using buffer conditions recommended by Fermentas.

#### **2.6.6.1 Analytical Restriction Digest**

In order to control the result of cloning experiments, approx. 200 ng DNA from a DNA mini-preparation were digested with 2 U of each of the adequate restriction enzymes in a total volume of 20 µl. After at least 1 hour at 37 °C in an incubator the digestion was stopped with the addition of loading dye (Fermentas) and the complete sample was loaded on an agarose gel (cf. section 2.6.4).

#### **2.6.6.2 Preparative Restriction Digest**

DNA fragments for cloning purposes were obtained by preparative digestion of existing plasmid DNA or PCR results over night. PCR reactions were purified prior to use as described in section 2.6.5. The required mass of DNA was digested with at least 10 U/1 µg DNA in a total volume comprising no more than 10 % of enzyme. The reaction was scaled up according to the requirements and the sample was loaded completely on an agarose gel after the addition of loading dye.

### 2.6.7 Ligation

Plasmids containing cDNA fragments were constructed ligating cohesive ends. The designated plasmids and DNA fragments with compatible ends were obtained by restriction digest (cf. section 2.6.6). Both parts were ligated with T4 ligase at least 1h at room temperature or at 16 °C in a thermocycler over night. The reaction includes the reaction buffer provided by the manufacturer in 1x concentration and plasmid DNA and cDNA fragment at the ratio of at least 1 to 3. Subsequently, the complete mixture was transformed into the desired competent bacterial strain (cf. section 2.4).

### 2.6.8 Production of Competent Bacterial Cells

Competent bacterial cells for transformation of plasmid DNA into the bacterial strains mentioned above (cf. section 2.4) were created from glycerol stocks stored at -80 °C as described in Inoue *et al.* (1990).

### 2.6.9 Measurement of Transformation Competence

The transformation efficiency was tested transforming three different amounts of plasmid DNA (cf. section 2.6.10) and the number of colonies grown were counted. A number of 100 colonies per 10 pg of plasmid DNA corresponds to  $1 \cdot 10^7$  cfu/ $\mu$ g plasmid DNA.

### 2.6.10 Transformation of Competent Bacteria

A total volume of 100  $\mu$ l competent bacterial cells were transformed with 50–500 ng of plasmid DNA. The bacteria were thawed 15 min on ice and then gently mixed with the DNA. After 30 min on ice the mixture was exposed to a heat shock for 80 s at 42 °C and again incubated 5 min on ice. Subsequently, 500  $\mu$ l of LB-medium containing 20 mM glucose was added and the bacteria were incubated 1 h at 37 °C upon permanent shaking. Finally, the cells were spun down 5 min at 6000 rpm. 400  $\mu$ l of the supernatant were discarded and the pellet was dissolved in the remaining growth medium. This bacteria suspension was plated on a prewarmed agar plate selecting for the corresponding antibiotic resistance encoded on the vector. The plates were exposed to 37 °C overnight in an incubator.

### 2.6.11 Small-Scale Plasmid Preparation

Plasmids containing freshly cloned DNA fragments were isolated with the alkaline lysis method in a small scale. In order to check the cloning results, 4 ml of an overnight culture comprising LB-medium and adequate antibiotics and inoculated with one transformed bacterial clone (cf. section 2.6.10) were centrifuged 5 min at 6000 rpm in a microcentrifuge (Heraeus). The pellet was resuspended with 100  $\mu$ l cold resuspension buffer (50 mM Tris-HCl, pH 8,0, 10 mM EDTA, 100  $\mu$ g/ml RNase A) and the cells were lysed because of the addition of 200  $\mu$ l lysis buffer (200 mM NaOH, 1 % (w/v) SDS). After 5 minutes of incubation at room temperature, 150  $\mu$ l of the neutralizing buffer (3 M K-Acetate, pH 5,5) were added followed by a further incubation step of 5 min at RT. Cell debris was pelleted by centrifugation at maximum speed for 30 min in a microcentrifuge. The supernatant containing the plasmid DNA was immediately collected in a new microcentrifuge tube and the addition of 900  $\mu$ l of 100 % ethanol precipitated the DNA. Afterwards the plasmid DNA was spun down at maximum speed for 20 min and the supernatant was discarded. The pellet was washed with 1 ml of 70% ethanol and again followed by centrifugation at maximum speed for 5 min. The isolated plasmid DNA was shortly dried and finally dissolved in 50  $\mu$ l of 1x TE-buffer (10 mM Tris-HCl, pH 8,0, 1 mM EDTA). The DNA was further analyzed with restriction digest (cf. section 2.6.6) and correctly constructed plasmids were stored as a glycerol stock, i.e. 1 ml of the overnight culture was mixed with glycerol (final concentration 30 %) and frozen in liquid nitrogen in order to keep it at -80 °C.

### 2.6.12 Large-Scale Plasmid Preparation

Large amounts of clean plasmid DNA were purified for transfection studies with a *Plasmid Midi Kit* (Qiagen). The volume of the bacterial culture was increased to 50 ml or 100 ml for high- or low-copy plasmids, respectively. The isolation was carried out according to the manufacturer's instructions. The yield was determined (cf. section 2.6.13) and the concentration adjusted to 1  $\mu$ g/ $\mu$ l.

### 2.6.13 Spectrophotometric DNA and RNA Quantitation

The concentration of isolated DNA and RNA was determined spectrophotometrically using the Cary 50 photometer (Varian) or Eppendorf's *Biophotometer Plus*. The nucleic acid was dissolved in either nuclease-free water or TE-buffer (10 mM Tris-HCl, pH 8,0,

1 mM EDTA) and the corresponding buffer served as a blank value. The measurement was performed in a quartz glass cell (Hellma, thickness 1 cm) or a tray cell (Hellma, thickness 0,2 mm or 1 mm) at 260 nm. An extinction of 1,0 was defined as a concentration of 50 µg/ml double-stranded DNA or 40 µg/ml single-stranded RNA. Additional parameters, the ratio of the absorbance readings at 260 nm and 280 nm and the extinction at 230 nm, displayed the contamination with proteins or organic solvents.

## 2.7 Protein Chemistry

### 2.7.1 Expression of Recombinant Proteins in *E. coli*

Recombinant proteins were expressed in *E. coli* using the pET-Expression System (Novagen). The proteins were cloned into pET-vectors (cf. section 2.5.1) which encode proteins with an either N- or C-terminal hexa-histidine tag. The expression is driven by the T7-promotor and can be induced with isopropyl- $\beta$ -D-thiogalactoside (IPTG).

### 2.7.2 Protein Expression Analysis

A volume of 3 ml LB-medium containing adequate antibiotics was inoculated with one clone of transformed *E. coli* belonging to a BL21 bacterial strain (cf. section 2.4.2) and this culture grew at 37 °C over night constantly shaking in an incubator (Sartorius). 1 ml of the overnight culture was added to freshly prepared and prewarmed 4 ml LB-Medium supplemented with antibiotics appropriate for the final volume. The bacteria grew for 1 hour at 37 °C in a shaker incubator. Afterwards, a noninduced control sample of 500 µl was taken and the protein expression was induced by adding isopropyl- $\beta$ -D-thiogalactoside (IPTG) to a final concentration of 0,1–1 mM. After 3 hours of expression at 37 °C in the shaker incubator, an induced control sample of 1 ml was drawn and centrifuged at 6000 rpm for 5 min in a microcentrifuge. The supernatant was discarded and the pellet resuspended in 100 µl 2-fold concentrated SDS sample buffer (30 mM Tris-HCl, pH 6,8, 1,5 % (v/v)  $\beta$ -mercaptoethanol, 3 % (w/v) SDS, 6 % (v/v) glycerol, 1 mM EDTA, 0,02 % (w/v) bromphenol blue). The non-induced control sample was treated equally, but the pellet was dissolved only in 50 µl 2-fold concentrated SDS sample buffer. The protein expression was analyzed on a polyacrylamide gel either stained with Coomassie Blue (cf. section 2.7.7) or transferred to a nitrocellulose membrane for immunodetection (cf. section 2.7.8).

### 2.7.3 Preparative Protein Expression

In order to express enough protein for purification, 1-2 ml of an overnight culture were applied to 100-200 ml of fresh LB-medium supplemented with antibiotics and further incubated at 37 °C in a shaking incubator until an absorbance of 0,4–0,8 at 600 nm measured with the Cary 50 photometer (Varian). The expression was induced by adding IPTG to a final concentration of 0,1–1 mM and the protein was expressed at 30 °C for 3h. Subsequently, the cells were harvested by centrifugation at 4500 rpm for 10 min in a benchtop centrifuge (Heraeus) at 4 °C and the pellet was stored at -20 °C. A noninduced and a positive control sample were taken as described above (cf. section 2.7.2).

### 2.7.4 Purification of Recombinant Proteins

Proteins encoded by pET-vectors contain a hexa-histidine tag either fused to the N- or C-terminus, which enables the purification using immobilized-metal affinity chromatography. Nitrilotriacetid acid (NTA) chelates nickel ions occupying four of the six ligand binding sites of the coordination sphere and provides a high affinity binding system of hexa-histidine-tagged proteins either under native or denaturing conditions.

#### 2.7.4.1 Protein Purification under Native Conditions

Frozen bacterial pellets of preparative protein expressions (cf. section 2.7.3) were thawed 15 min on ice and resuspended in 5 ml lysis buffer (50 mM NaHPO<sub>4</sub>, 300 mM NaCl, 10 mM imidazole, pH 8,0). The lysis was supported by the addition of 1 mg/ml lysozyme and incubation for 30 min on ice followed by sonication (sonicator UP 50H, Hielscher). The lysate was spun down at 4500 rpm for 30 min at 4 °C in a tabletop cooling centrifuge (Heraeus) to separate cell debris and the soluble protein. During the first purification of a recombinantly expressed protein control samples of the supernatant and the pellet were taken and mixed with 2-fold concentrated SDS sample buffer to analyse the solubility of the protein in order to adjust the culturing conditions. The supernatant was mixed with 1 ml of a the 50 % Ni-NTA slurry (Qiagen) and gently shaken at 4 °C for 60 min or overnight. The mixture was centrifuged for less than 3 min at 1500 rpm and 4 °C. Again a sample of the supernatant was taken and mixed with 2-fold concentrated SDS sample buffer to verify binding to the Ni-NTA beads. The remaining supernatant was discarded and the beads were washed with 5 ml cold wash buffer (50 mM NaHPO<sub>4</sub>, 300 mM NaCl, 20 mM imidazole, pH 8,0). Simultaneously, a gravity-flow column (Evergreen Scientific)



was equilibrated with wash buffer. The washing procedure of the beads was repeated twice and finally they were dissolved in wash buffer and applied to the equilibrated column to let the buffer flow through. Then the protein was eluted with elution buffer (50 mM NaHPO<sub>4</sub>, 300 mM NaCl, 250 mM imidazole, pH 8,0) and collected in four fractions of 500 µl in microcentrifuge tubes. The purification was analyzed on a polyacrylamide gel and the samples were kept at 4 °C. Protein expression clones providing a suitable expression level and a soluble recombinant protein were stored as a glycerol stock at -80 °C (cf. section 2.6.11).

## 2.7.5 Cell and Tissue Extracts

### 2.7.5.1 Protein Extracts for SDS-PAGE

Petri dishes of cultured cells designated to cell extracts were put on ice, the medium was removed and the cells were washed twice with ice-cold PBS. 2-fold concentrated SDS sample buffer was added and the cells were carefully scraped from the surface with a cell scraper. The mixture was filled into a microcentrifuge tube and heated for 30 min at 55 °C followed by sonication. This procedure was repeated and after centrifugation for 30 min at maximum speed in a microcentrifuge (Heraeus), the supernatant was saved and stored at -20 °C. Tissue specimens were disrupted in liquid nitrogen with mortar and pestle and transferred to a microcentrifuge tube where 2-fold SDS sample buffer was included. Subsequently, the sample was processed similar to the cell extracts described above.

### 2.7.5.2 Isolation of RNA from Cells and Tissues

Transcription analysis and cloning experiments were made with RNA obtained from cultured cells or tissue specimens. RNA from cultured cells was isolated using the *Quick-RNA Mini Kit* (Zymo Research) or the *RNeasy Mini Kit* (Qiagen) according to the manufacturer's instructions. To increase the amount of RNA purified from frozen tissues the isolation was made with the *RNeasy Fibrous Tissue Mini Kit* (Qiagen) as described in the manual. The isolated RNA was checked for DNA contamination applying the PCR technique (cf. section 2.6.2) using the RNA as a template. Potential trace DNA was eliminated with DNase digestion followed by an additional column-based purification step and a control PCR. This procedure was repeated until no DNA contamination had been detected. The enzyme was provided by Zymo Research or Qiagen and used according to the instructions.



## 2.7.6 Protein Quantitation

### 2.7.6.1 Bradford Assay

The concentration of purified protein (cf. section 2.7.4.1) was determined using the Bradford method (Bradford, 1976). This colorimetric assay bases on the absorbance shift of the dye Coomassie Blue G-250 (Fisher Scientific) after complex formation with basic and aromatic amino acid residues. The concentration of purified proteins was estimated with a Ponceau red (3 % (w/v) trichloroacetic acid, 0,2 % (w/v) Ponceau S Red) staining of a 1  $\mu$ l spot of the protein solution on nitrocellulose membrane (Whatman). According to the intensity the proteins were diluted in PBS (137 mM NaCl, 3 mM KCl, 8 mM Na<sub>2</sub>HPO<sub>4</sub>, 1,5 mM KH<sub>2</sub>PO<sub>4</sub>, pH 7,3) to match the appropriate concentration range of the assay. Three wells of a 96-well microtiter plate (Greiner, TPP) were filled with 50  $\mu$ l of the dilution which enables to calculate the standard deviation in order to evaluate the measurements. To start the colorimetric reaction 200  $\mu$ l of a 1:5 dilution of BioRad Protein Assay Dye Reagent Kit were added and incubated for 5 min. Then the absorbance at 595 nm was measured in a microtiter plate reader (Elx800, BioTek). The protein concentration was determined with the help of a dilution series of bovine  $\gamma$ -globulin which was used to plot a regression line in the spreadsheet EXCEL (Microsoft) or CALC (OpenOffice, Oracle). The concentration was calculated substituting the variable for absorbance with the measured value of the protein dilution in the resulting linear equation.

### 2.7.7 SDS Polyacrylamide Gel Electrophoresis (SDS-PAGE)

This technique was used to separate proteins according to their molecular weight as it is described in Laemmli (1970). Gels for protein expression analysis (cf. section 2.7.2) were cast in the Miniprotean II apparatus (Biorad) whereas gels loaded with cell or tissue extracts were run in Hoefer vertical units with larger gel size in order to improve the resolution. The polyacrylamide gels depicted by U. K. Laemmli consist of a separation gel with smaller pore size and a stacking gel. First, stacking gels of different pore sizes due to varying acrylamide concentrations (6–14 %) were poured (acrylamide/bisacrylamide (37,5:1) 6–14 % (v/v), 1,5 M Tris-HCl, pH 8,8, 0,8 % (w/v) sodium dodecyl sulfate (SDS), 0,083 % (v/v) ammonium persulfate (APS), 0,1 % (v/v) tetramethylethylenediamine (TEMED)) according to the requirements. Then a stacking gel of 3 % acrylamide (3 % (v/v) acrylamide/bisacrylamide (19:1), 0,5 M Tris-HCl, pH 6,8, 0,8 % (w/v) SDS, 0,45 % (v/v) APS, 0,3 % TEMED) was poured and a comb created the wells needed. All

samples loaded were mingled with SDS sample buffer and heated for 5 min on a thermoblock (Lab4You, HLC) at 95 °C. To avoid precipitation of large proteins cell or tissue extracts were only exposed to 55 °C (cf. section 2.7.5). The proteins ran through the stacking gel at a constant voltage of 100 V in electrophoresis buffer (25 mM Tris-Base, 192 mM Glycin, 0,1 % (w/v) SDS). After passing the stacking gel, the voltage of gels for protein expression analysis was increased to 200 V. After finishing the run, the gels were either stained with Coomassie Blue G250 Solution (Fisher Scientific) or further processed for immunodetection (cf. section 2.7.8). Stained gels were documented with a Scanner (AGFA) with a built-in transparency unit or with the *Odyssey Infrared Imaging System* (LiCOR).

## 2.7.8 Protein Transfer

After separation of proteins using SDS-PAGE (cf. section 2.7.7), the samples were transferred to nitrocellulose membrane (Protran, 0,2 µm pore size, Whatman) for antibody-based detection methods. The transfer method were chosen according to considerations below.

### 2.7.8.1 Semi-Dry Western Blot

The semi-dry western blot method can be used to quickly transfer proteins with a molecular weight up to 100 kDa. In comparison to the tank blot method (cf. section 2.7.8.2), the transfer efficiency is reduced in general and especially in the molecular weight range above 100 kDa, so that it was only used for transferring protein expression and purification samples in a semi-dry transfer cell (Biorad). A run polyacrylamide gel was equilibrated in the transfer buffer (20 % (v/v) methanol in electrophoresis buffer (cf. section 2.7.7)) and placed on a nitrocellulose membrane (Whatman). This array was encompassed with filter papers saturated with the transfer buffer and put on the electrode. Potential air bubbles were removed rolling a pipet over the surface. The proteins were transferred for 75-90 min at constant current  $I$  (in mA) which depended on the gel area  $A$  (in cm<sup>2</sup>).

$$I = A \cdot 0,8 \text{ mA} \quad (2.1)$$

### 2.7.8.2 Tank-Blotting

Proteins with a higher molecular weight than 100 kDa were transferred using the Tank-Blotting technique. The polyacrylamide gel was equilibrated in the transfer buffer (25 mM

Tris-Base, 192 mM glycine, 20 % (v/v) methanol, 0,01 % (w/v) SDS) and put on a saturated nitrocellulose membrane (Whatman) arranged in a sandwich of soaked filter papers. This array was surrounded by a blotting cassette lined with fibre mats and put into the blotting apparatus (BioRad) which was filled with transfer buffer. The transfer was performed at a constant current of 250 mA overnight at 4 °C upon permanent agitating of the buffer by a magnetic stirrer.

## 2.8 Immunological Methods

### 2.8.1 Immunodetektion

Immobilised proteins (cf. section 2.7.8) were detected probing the nitrocellulose membrane with protein specific or tag antibodies (see tab. 2.8.2). According to the requirements, different detection systems were used which are described in section 2.8.1.1 and 2.8.1.2. In order to prevent non-specific binding of the antibody, unreacted sites on the membrane are blocked incubating 30–60 min with blocking buffer (4 % (w/v) nonfat dry milk dissolved in TBST: 50 mM Tris-HCl, pH 7,9, 150 mM NaCl, 0,05 % (w/v) Tween-20). Afterwards, the blocking solution was removed and excessive reagent was washed away three times for 5 min with TBST. The membrane was immersed for 1 h at RT or overnight at 4 °C with agitation in a solution containing the antibody diluted in TBST detecting the antigen of interest. To decrease the background some primary antibodies were diluted in blocking buffer. The incubation was followed by a washing step as described before. Depending on the analysis appropriately labeled secondary antibodies recognizing the primary antibody used were incubated for 45–60 min and subsequently removed by washing three times with TBST for 5 min. Then the binding of the secondary antibody to the complex of antigen and primary antibody was detected as described in the following sections.

#### 2.8.1.1 Quantitative Analysis

Quantitation of protein expression levels was performed using infrared fluorescent labeled antibodies detected on the Odyssey Infrared Imaging System (LI-COR). This method provides a broad, linear dynamic range to accurately detect strong and weak bands on the same western blot. After removing the primary antibody by washing with TBST (cf. section 2.8.1) an appropriate secondary antibody labeled with IRDye 800 (LI-COR) was incubated for 45–60 min in a box avoiding any light exposure to preserve the infrared fluorescent dye. Then the membrane was washed in TBST as mentioned above still

preventing light exposure. The emission of infrared fluorescent light was detected on the Odyssey System after excitation with different intensities of a solid-state 785 nm laser. The blue-coloured-bands of a prestained protein marker (Fermentas) could be visualized by the 685 nm laser. The quantitative analysis was performed using the software supplied by LI-COR.

### 2.8.1.2 Qualitative Analysis

For qualitative analysis proteins decorated by primary antibodies were detected by horseradish peroxidase (HRP) labeled secondary antibodies and visualized with enhanced chemiluminescence. After incubation and removal of the secondary antibody (cf. section 2.8.1), the membrane was completely covered with the working solution of the *SuperSignal West Pico Chemiluminescent Substrate* (Thermo) and incubated for 5 min. Then excess reagent was drained and the membrane was covered with a plastic wrap and placed in a film cassette (Sigma). The emitted light caused by the enzymatic conversion of the substrate was exposed to a X-ray films (Fujifilm) which were developed in a machine (Curix 60, AGFA). The exposure time was adapted to the signal intensities. Films were documented with a transparency unit of a scanner (AGFA).

## 2.8.2 Antibodies

Table 2.8.2 delineates antibodies used for detection of endogenous proteins in cells and tissues and bacterially expressed recombinant proteins. The antibodies are arranged in alphabetical order according to their epitope and their type and origin are mentioned.

Secondary antibodies coupled to horseradish peroxidase (HRP) were utilized in qualitative immunodetection with ECL (cf. section 2.8.1.2). Quantitative analysis of protein expression levels was performed using the Odyssey infrared laser scanning system which needs infrared fluorescence dyes like IRDye800CW. Proteins in cells and tissues were visualized with secondary antibodies labeled with fluorescent dyes. All secondary antibodies are depicted in table 2.7.

Filamentous actin was labeled using the toxin phalloidin from the death cap (*Amanita phalloides*) coupled to fluorescent dyes summarized in table 2.8.

### 2.8.2.1 Purification of Polyclonal Antibodies

In order to improve the specificity of polyclonal antibodies raised in rabbits, the antibodies were purified using bacterially expressed protein (cf. section 2.7.3). Non-specific

Epitope	Name	Type	Origin
$\alpha$ -actinin	a653	rabbit	van der Ven <i>et al.</i> (2000a)
$\alpha$ -actinin	BM75.2	mouse IgM	Sigma
$\beta$ -catenin	AB19022	rabbit	Chemicon
c-myc	$\alpha$ -c-myc (9E10)	mouse IgG1	ICI Chemikalien
EEF-tag	$\alpha$ -EEF (YL1/2)	rat IgG2a	Wehland <i>et al.</i> (1983)
filamin A,C	RR90	mouse IgA	van der Ven <i>et al.</i> (2000a)
filamin C	Anti-FLNC	rabbit	Sigma-Aldrich
GAPDH (rabbit)	Anti-GAPDH	mouse IgG1	Calbiochem
LIMCH1 (C-term)	DKFZ	rabbit	GeneTex, Inc.
mena	$\alpha$ -Mena	rabbit	Gareus (2001)
myomesin	BB78	mouse IgG2a	Vinkemeier <i>et al.</i> (1993)
nebulin	Nb2	mouse IgG1	Fürst <i>et al.</i> (1988)
nebulin	Nbm176-181	rabbit	Pappas <i>et al.</i> (2008)
nonmuscle MHCIIA	Anti-Myosin IIA (nonmuscle)	rabbit	Sigma
T7-tag	$\alpha$ -T7	mouse IgG2b	Merck
titin	T12	mouse IgG1	Fürst <i>et al.</i> (1988)
Xin (C-term)	XC1	mouse IgG1	Eulitz (2005)
Xin (repeats)	XR1B	mouse IgG1	Eulitz (2005)
mouse Xin C	$\alpha$ -mXin C	rabbit	sections 3.2.2, 3.2.3.5
Xirp2 (aa 1-311)	Xirp2 N-terminus	rabbit	section 3.7.7
Xirp2 (aa 2045-2226)	Xirp2 central	rabbit	section 3.7.7
Xirp2 (aa 2768-3327)	Xirp2 C-terminus	mouse IgG1	section 3.7.7

Table 2.6: **Table of primary antibodies used for endogenous proteins in cells and tissues.** The epitopes mentioned reflect the origin of the protein or the size of protein fragments which were used for immunization. The raise of polyclonal antibodies in rabbits firstly described in this work was performed by Biogenes (Berlin).

Name	Donor	Epitope	Conjugate	Origin
GAM-PO	goat	mouse IgG	HRP	Dianova
GAM-PO	goat	mouse IgG Fc gamma1	HRP	Dianova
GARat-PO	goat	rat IgG	HRP	Dianova
GAM IRDye800CW	goat	mouse IgG	IRDye800	LI-COR
GAR IRDye800CW	goat	rabbit IgG	IRDye800	LI-COR
GARat IRDye800CW	goat	rabbit IgG	IRDye800	LI-COR
GAR alexa405	goat	rabbit IgG	alexa405	Molecular Probes
GAM IgG1 alexa488	goat	mouse IgG1	alexa488	Molecular Probes
GAR Cy2	goat	rabbit IgG	Cy2	Dianova
GAM IgM alexa546	goat	mouse IgM	alexa546	Molecular Probes
GAM IgA TXR	goat	mouse IgA	Texas red	Southern Biotech
GAM IgG1 alexa594	goat	mouse IgG1	alexa594	Molecular Probes
GAM Cy5	goat	mouse IgG	Cy5	Dianova
GAR Cy5	goat	rabbit IgG	Cy5	Dianova

Table 2.7: **Summary of secondary antibodies.** Antibodies coupled to horseradish peroxidase (HRP) were used for ECL. Quantitative analysis of protein expression levels on blot were performed using IRDye-labeled secondary antibodies. Fluorescently-labeled secondary antibodies utilized for immunofluorescence microscopy are arranged according to the emission spectrum of the respective fluorescent dye.

Conjugate	Wavelength (max. emission)	Origin
alexa405	405 nm	Molecular Probes
PromoFluor-405	405 nm	PromoKine
TRITC	572 nm	Sigma
alexa633	633 nm	Molecular Probes
PromoFluor-633	633 nm	PromoKine

Table 2.8: **Summary of fluorescently-labeled phalloidins.** F-actin in cells and tissues was visualized using fluorescently-labeled phalloidin toxins. TRITC, Tetramethylrhodamine-5-(and 6)-isothiocyanate

antibodies were eliminated expressing a protein fragment fused to the same immuno-tags as the antigen used for immunization of the respective rabbit. The expression was performed in the same bacterial strain as the antigen (cf. sections 2.7.3 and 2.4.2). The protein was processed like during protein purification (cf. section 2.7.4.1) until loading on Ni-NTA agarose beads and subsequent washing. Afterwards 1 ml of the polyclonal serum were added to 250  $\mu$ l of the Ni-NTA beads loaded with the recombinant protein and shaken at 4°C for 6 h. Then the slurry was centrifuged for 3 min at 1500 rpm. The supernatant was collected in a microcentrifuge tube. Apart from removing unspecific antibodies, the concentration of specific antibodies was enriched using a GST-tagged epitope coupled to GSH-coated beads (GE Healthcare, BD Bioscience, Macherey & Nagel, Miltenyi Biotech). The epitope was expressed in *E. coli* as a fusion protein with GST by the pGEX-6P-3 plasmid (cf. sections 2.7.3 and 2.5.1.5). The bacterial pellet was resuspended in ice-cold PBS supplied with 1-fold concentrated protease inhibitors (Roche) and the cells were lysed with 1 mg/ml lysozyme for 30 min on ice. After sonication, Triton X-100 was added (final concentration 0,5 %) and the mixture was centrifuged for 30 min at 4500 rpm in a tabletop cooling centrifuge. The supernatant was collected and added with GSH-coated beads suspension followed by 30 min incubation at 4 °C upon shaking. Afterwards, the antibody serum was added and again shaken at 4 °C for additional 2-3 h. Then the slurry was applied to an equilibrated gravity-flow column (Evergreen Scientific) and the flow-through was collected in a microcentrifuge tube to analyze on unbound antibody. The bound antibodies were eluted in several 100  $\mu$ l fractions using an antibody elution buffer (0.1 M citrate buffer, pH 4.0, 150 mM NaCl). The fractions were collected in microcentrifuge tubes already containing 20  $\mu$ l of 1 M Tris-HCl pH 8.5 in order to neutralize the elution. In addition to that the concentration of the antibody solution could be increased using Centricon centrifugal filter units (Millipore). Antibodies were enriched with Centricons with a cut-off molecular weight of 30 kDa or 50 kDa. The filter units were spun at 5000xg for 30 min. Afterwards, the flow-through was removed and the antibody solution refilled and again centrifuged. This procedure was repeated several times until the antibody solution had reached the concentration desired.

### 2.8.3 Frozen Tissue Sections

To investigate the localization of proteins *in vivo* with immunostaining (cf. section 2.8.4), frozen tissue sections from rat and mouse organs were produced. After cervical dislocation of the animal, the tissues desired were dissected and immediately frozen in liquid

nitrogen pre-cooled isopentane and stored at  $-80\text{ }^{\circ}\text{C}$ . Prior to sectioning the specimen was embedded in an optimal cutting temperature compound (Tissue Teck, Lab-Tek Products) and then cut into the thickness desired (4–10  $\mu\text{m}$ ) using a cryostat microtome (Leica). The tissue sections were mounted on superfrost glass slides and stored at  $-80\text{ }^{\circ}\text{C}$  for later use. Human muscle biopsies were obtained from Universitätsklinikum Bonn and Berufsgenossenschaftliches Universitätsklinikum Bergmannsheil Bochum and processed as described above.

## 2.8.4 Immunostaining of Cells and Tissues

To study the *in vivo* localization of proteins, cells and tissue sections were stained using protein-specific antibodies and fluorescently labeled secondary antibodies as listed in tables 2.8.2 and 2.7. In general, fixed cells or tissue specimen were processed in a two-step method including the consecutive incubation with the primary and secondary antibody and final mounting with mowiol. The differences in processing cells and tissue sections are described in the corresponding sections.

### 2.8.4.1 Paraformaldehyde Fixation

Paraformaldehyde is a cross-linking reagent which forms intermolecular bridges through cross-linking free amino groups thus better preserving cell structure, but needs an additional permeabilization step. This fixation method is necessary to decorate F-actin with phalloidin (see tab. 2.8), a toxin from the death cap (*Amanita phalloides*). Transfected cells were mainly fixed with paraformaldehyde in order to preserve the localization of the overexpressed protein.

Cells were seeded on glass cover slips, transfected and cultured until detectable expression of the transfected protein. Then the culture media was removed and the cells were washed twice with PBS. The cells were fixed with 4 % paraformaldehyde in PBS for 10 min. Afterwards, the paraformaldehyde was aspirated and the fixed cells were rinsed again twice with PBS. Prior to immunostaining the cells were permeabilized for 10 min with 0,5 % Triton X-100 in PBS. Then the cells were washed again with PBS and stained as delineated in 2.8.4.3. Tissue sections were fixed with 4 % paraformaldehyde in PBS for 20 min and washed three times for 5 min with 0,05 % Triton X-100 in PBS. To make the epitopes accessible for antibodies, the specimen was permeabilized for 1 h with 1 % Triton X-100 in PBS at RT followed by rinsing three times for 5 min in PBS and surrounded with a water repellent film before stained as depicted in 2.8.4.3.



#### 2.8.4.2 Methanol-Acetone Fixation

The methanol-acetone fixation method does not require a permeabilization step because incubation with these organic solvents remove lipids, dehydrate the cells and precipitate the proteins on the cellular architecture. Therefore, this technique cannot be applied to visualize cytosolic proteins which are not anchored at cellular structures, since they would be lost in the fixation procedure.

The medium of cells grown on sterile glass cover slips was aspirated and the cells were washed twice with PBS. The PBS was carefully removed and the cells were fixed for 5-10 min at -20 °C in a 1:1 mixture of methanol and acetone pre-cooled to -20 °C. The fixative was aspirated and the fixed cells were washed twice with PBS and stored in PBS at 4 °C until staining. Slides with frozen tissue sections were warmed at RT and fixed for 2 min at -20 °C in pre-cooled methanol followed by permeabilizing for 20 s at -20 °C in pre-cooled acetone. Then the acetone evaporated at RT and the specimen was encircled with a PAP pen (Science Services) which provided a water repellent barrier in order to keep the staining reagents on the tissue section. Afterwards the slides were processed immediately as described in section 2.8.4.3.

#### 2.8.4.3 Staining

Unreacted binding sites of fixed cells grown on glass cover slips were blocked for 30 min at 37 °C with 10 % Normal Goat Serum (NGS) and 1 % BSA in PBS. The blocking solution was removed and the cells were incubated with primary antibodies dissolved in 1 % BSA in PBS for at least 1 h in a wet chamber. Before adding the secondary antibodies also dissolved in 1 % BSA in PBS, the cover slips were washed three times with PBS. After 45 min of incubation, the antibody solution was removed washing three times with PBS and once in ddH<sub>2</sub>O to eliminated potential salt precipitates. The cover slips were mounted on glass slides (Menzel) with 10 % N-propyl gallate (NPG) in Mowiol or analyzed without mounting in a micro-aquarium filled with ddH<sub>2</sub>O if further processed for the scanning electron microscope. Fixed tissue sections were blocked with 10 % Normal Goat Serum (NGS) and 1 % BSA in PBS for 60 min at 37 °C. After removal of the blocking reagent the binding of the primary antibodies dissolved in 1 % BSA in PBS was performed at 4 °C overnight in a wet chamber. The section was washed twice with 0,05 % Triton X-100 in PBS and then once with PBS. The secondary antibodies were dissolved in 1 % BSA and then incubated at 37 °C for 2 h. The reaction was stopped by washing three times with PBS for 5 min and finally the section was mounted in Mowiol containing 10 % NPG.

## 2.9 Protein Interaction Assays

### 2.9.1 Yeast Two-Hybrid System

A first proof of a protein interaction was provided by a yeast two-hybrid experiment. This assay is based on the completion of a heterologous transcription factor consisting of a LexA DNA binding domain and a Gal4 activation domain. Both domains are expressed as a C-terminal fusion to one of the potential interaction partners, so that binding of the investigated proteins brings the domains in close proximity and results in a functional transcription factor activating the reporter genes *HIS3* and *lacZ*. The transcription of the the *HIS3* and *lacZ* gene can be displayed by growth on medium lacking the essential amino acid histidine and the activity of the enzyme  $\beta$ -galactosidase, respectively. The assay was performed in the L40 yeast strain (cf. section 2.4.3) which contains inactivated genes indispensable for the synthesis of the essential amino acids leucine and tryptophane. The pLexPd plasmid (cf. section 2.5.3.1) encoding the LexA DNA binding domain fusion protein, in the following denoted by bait plasmid, includes the gene information for synthesizing tryptophane and the pACTPd vector (cf. section 2.5.3.2) expressing the transactivation domain fusion protein, below referred to as prey plasmid, provide the ability to grow on medium lacking leucine. Thus both vectors allow for the selection of positive transformants.

#### 2.9.1.1 Sequential Transformation

At the beginning the L40 yeast strain was transformed separately with the bait and prey plasmid in order to check for autoactivation of the reporter genes (cf. section 2.9.1) and toxic effects of the vectors. For this purpose nontransformed yeasts were cultured for 36-48h in YPD-medium (see tab. 2.1) at 30 °C and 1,5 ml were pelleted for 5 min at 5000 rpm in a microcentrifuge. These cells were resuspended in a transformation solution (10 mM Tris-HCl, pH 7,5, 1 mM EDTA, 100 mM lithium acetate, 0,1 mg herring sperm DNA, 16 % polyethylene glycol 4000) for lithium acetate-mediated transformation. After incubation for 15 min at RT, 0,1 volume of dimethyl sulfoxide (DMSO) was added and the cells were heat shocked by heating to 42 °C for 12 min in a water bath followed by chilling on ice for 1-2 min. Then the mixture was centrifuged for 5 min at 6000 rpm and washed with sterile ddH<sub>2</sub>O. The addition of 1 ml YPD-medium permits the transformants to proliferate for 1 h at 30 °C in a shaking incubator. Afterwards the cells were spun down and washed as described above and plated on the appropriately selecting agar plate to let

them grow at 30 °C for 5 days.

If no toxic effect and no autoactivation of the *lacZ* gene was detected (cf. section 2.9.1.3) and the yeasts had not grown on agar lacking the amino acid histidine, they would be transformed with the bait or prey plasmid, respectively. For co-transformation the cells proliferated for 36-48 h in the adequate dropout base medium (DOB-medium, see tab. 2.1) at 30 °C in a shaker incubator (Sartorius) until the absorbance at 600 nm reached 1,5. The required cell number was diluted to an extinction of 0,2–0,3 in a final volume of 300 ml YPD-medium after sedimentation and washing of the cells. This culture grew to an optical density of 0,4–0,6 at 30 °C followed by centrifugation and washing with sterile ddH<sub>2</sub>O. To prepare the cells for co-transformation, they were resuspended in TE-buffer (10 mM Tris-HCl, pH 8,0, 1 mM EDTA) containing 100 mM LiAc. A transformation solution (600 µl, 40 % (w/v) polyethylene glycol 4000, 10 mM Tris-HCl pH 7,5 1 mM EDTA) was supplemented with 0,1-1 µg plasmid DNA and 0,1 mg herring sperm DNA which was then added to 100 µl of the yeast cell suspension. Before the heat shock was performed as mentioned above, the cells were thoroughly mixed, cultured at 30 °C for 30 min and 70 µl DMSO was carefully added. The heat shocked cells were washed with sterile ddH<sub>2</sub>O and resuspended in 1 ml YPD-medium to let them proliferate for 1 h at 30 °C. These cells were washed again with sterile ddH<sub>2</sub>O and resuspended in TE-buffer in order to plate them on double dropout agar plates (-leucine, -tryptophane) selecting for co-transformants. The interaction was examined after 5 days of growth at 30 °C.

### 2.9.1.2 Test of Activation of the *HIS3* Reporter Gene

The yeast strain L40 is not capable of synthesizing the amino acid histidine, but they contain a Gal4-responsive *HIS3* gene enabling their growth in -histidine minimal medium upon activation. Therefore transformed yeasts were spread on agar plates lacking the corresponding amino acids to test for autoactivation of the *HIS3* gene or interaction of the investigated proteins (cf. section 2.9.1.1). The plates were incubated 2-5 days at 30 °C in comparison to a positive control.

### 2.9.1.3 Test of $\beta$ -Galactosidase Activity

The activation of the *lacZ* reporter gene indicating autoactivation in singly transformed cells and interaction of two proteins in co-transformed yeasts were analysed by visualizing the enzymatic activity of the  $\beta$ -galactosidase. This enzyme is able to convert the substrate X-Gal (5-bromo-4-chloro-3-indolyl- $\beta$ -D-galactopyranoside) to the insoluble blue product

5,5'-dibromo-4,4'-dichloro-indigo. Yeast colonies were transferred to a nitrocellulose membrane (Whatman) and grew for 2-5 days at 30 °C on dropout medium agar plates. Then the membrane was frozen in liquid nitrogen and thawed six times in order to destroy the cell membrane. The nitrocellulose membrane was placed on a filter paper saturated with a staining solution (60 mM Na<sub>2</sub>HPO<sub>4</sub>, 40 mM NaH<sub>2</sub>PO<sub>4</sub>, 10 mM KCl, 1 mM MgSO<sub>4</sub>, 0,3 % (v/v) β-mercaptoethanol, 0,85 mg/ml X-Gal) and incubated at 37 °C. The reaction was documented with a digital camera (Nikon) and compared to a positive control.

## 2.9.2 Co-Immunoprecipitation

Novel protein interactions identified in yeast two-hybrid assays were verified using the co-immunoprecipitation method. In such an approach, the designated binding partners were recombinantly expressed (cf. section 2.7.3) as fusion proteins with different tags and purified (cf. section 2.7.4.1). Both proteins were incubated with each other allowing for complex formation in solution. An antibody recognizing one binding partner was added so that the interaction partners could be immobilized on magnetic protein G beads. An interaction was proved if the designated binding partner could be co-precipitated. In order to prove a newly found interaction, 1–10 µg of each binding partner estimated according to results obtained in a Bradford assay (cf. section 2.7.6.1) were diluted in immunoprecipitation buffer (0,05 % Triton X-100, 1 % BSA in PBS) to a final volume of 100 µl and incubated for 1 h at RT. For complex recognition 0,5–1 µg of a tag antibody were added and further incubated for 30 min. The formed antibody:protein:protein complex was immobilized for 1 h at RT or at 4 °C overnight by adding 20 µl of the protein G coupled magnetic dynabeads suspension (Invitrogen). The beads were washed three times with 200 µl PBS containing 0,05 % Triton X-100 in a magnetic rack to extract the protein bound beads. To avoid unspecific binding the washing buffer was sometimes supplemented with 0,5 M NaCl or 0,5 % Triton X-100. The interaction complex was eluted with 20 µl 2x SDS sample buffer (cf. section 2.7.2), briefly heated to 55 °C and then loaded on a polyacrylamide gel (cf. section 2.7.7) and further processed for immunodetection (cf. section 2.8.1).

## 2.9.3 Chemical Cross-linking

Chemical cross-linking provides another opportunity to investigate protein interactions because the binding partners are covalently linked by the cross-linker therefore preserving the bound state. This is done by the homobifunctional N-hydroxysuccinimide ester (NHS

ester) ethylene glycol bis[sulfosuccinimidylsuccinate] (EGS; spacer arm 1,6 nm, Pierce) which reacts with accessible  $\alpha$ -amine groups present in N-termini of proteins and peptides and in the amino acid lysine. Purified proteins were dialysed overnight at 4 °C against the cross-linking buffer ( $\text{Na}_2\text{HPO}_4/\text{NaH}_2\text{PO}_4$  [77,4:22,6], pH 7,4, 600 mM NaCl, 1 mM  $\text{MgCl}_2$ , 1 mM DTT [freshly added]) in order to remove any interfering substances. The proteins were diluted with the cross-linking buffer to a concentration of 2-10  $\mu\text{M}$  according to the measured protein concentration (cf. section 2.7.6.1) in a total volume of 50–120  $\mu\text{l}$  and incubated for 5 min at 37 °C. Afterwards, 1  $\mu\text{l}$  of a freshly prepared 65 mM solution of EGS dissolved in DMSO was added to start the cross-linking. The reaction was stopped after incubation at 37 °C for at most 15 min by adding 5x SDS sample buffer and further incubation at 37 °C for 10 min. The samples were separated on a polyacrylamide gel (cf. section 2.7.7) and transferred to a nitrocellulose membrane (cf. section 2.7.8.2) for immunodetection (cf. section 2.8.1).

## 2.9.4 Peptide Scan

Peptide interaction motifs were identified using 15-mer peptides spotted on cellulose membranes. Experiments were performed by Prisca Boisguerin of the Department of Medical Immunology at the Charité in Berlin, Germany. Membranes were produced using a modified SPOT synthesis technique and processed as described in (Frank, 1992; Licha *et al.*, 2000; Boisguerin *et al.*, 2004). Recombinant protein fragments used for overlaying were expressed as fusion proteins with GST (cf. section 2.5.1.5).

## 2.9.5 Bimolecular Fluorescence Complementation (BiFC) Analysis

The bimolecular fluorescence complementation assay was used to visualize protein interactions in living cells and is based on the association between two nonfluorescent fragments of a fluorescent protein when they are brought in close proximity to each other by an interaction between proteins fused to the fragments (Kerppola, 2006). Here, two fragments of the yellow fluorescent protein Venus (Nagai *et al.* (2002)) were used which offers an improved speed and efficiency in maturation and increased resistance to environment. The N-terminal fragment (1) comprises the amino acids 1-154 and is expressed by the vectors Venus1-C and Venus1-N3 (cf. sections 2.5.2.3 and 2.5.2.5, respectively). The C-terminal fragment (2) starts at amino acid 155 and encompasses the remaining residues of the

full-length Venus. This nonfluorescent part is fused to proteins cloned into the Venus2-C and Venus2-N3 vectors (cf. sections 2.5.2.4 and 2.5.2.6).

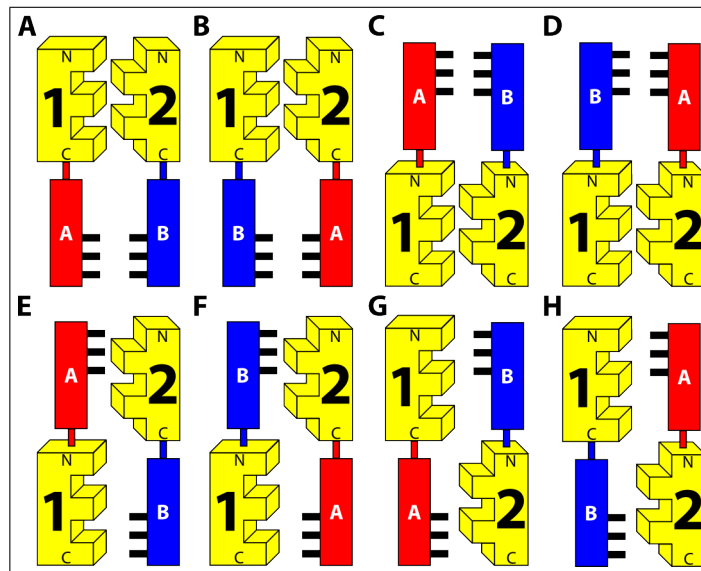


Figure 2.1: **Combinations of fusion proteins tested in a BiFC assay.** Interacting proteins A and B can be expressed as fusion proteins with the N-terminal (1) or C-terminal (2) nonfluorescent fragment of the yellow fluorescent protein Venus which is reflected by the vector name encoding these proteins, Venus1 and Venus2, respectively. Fusion to the N- or C-terminus of the Venus fragment is indicated by N or C, respectively. The respective vectors are named correspondingly, Venus1C, Venus2C, Venus1N3 and Venus2N3. **A-H.** All potential combinations of fusion proteins enabling BiFC complex formation. Figure adapted from Kerppola (2008).

The only protein interactions studied were already verified by yeast two-hybrid assays (cf. section 2.9.1) and co-immunoprecipitations (cf. section 2.9.2) or chemical cross-linking (cf. section 2.9.3). Then both binding partners were cloned into all Venus vectors so that they were expressed as N- or C-terminal fusion proteins of both nonfluorescent fragments in order to accommodate all possible spatial constraints of the interaction. Firstly, compatible fusion proteins were co-transfected (cf. section 2.10.6) into A7r5 cells (cf. section 2.10.1.2) to investigate functional combinations (Kerppola, 2008). The maximum number of combinations of fusion proteins is depicted in figure 2.1. According to the results, combinations were used for the analysis in embryonic mouse cardiomyocytes (cf. section 2.10.5). The cells were fixed and counterstained with applicable antibodies (cf. section 2.8.4). The samples were analysed with microscopy (cf. section 2.11). As negative controls, all fusion proteins were co-transfected with the compatible nonfluorescent Venus fragments in order to evaluate unspecific BiFC complex formation.

## 2.10 Cell Culture

The cultured eucaryotic cells and their handling are depicted in detail in the following section. All cells proliferated in CO<sub>2</sub> incubators (Thermo) with a constant CO<sub>2</sub> concentration of 5 % and saturating humidity. The temperature is mentioned in the paragraph describing the cell line. Cell culture dishes were obtained from TPP and general cell culture reagents from Invitrogen/Gibco unless otherwise noted. PBS was prepared according to sambrook and sterilized in an autoclave (cf. section 2.2). Handling and processing of cells was done inside a laminar flow hood (Thermo) using sterile equipment.

Medium	Composition
A7r5 proliferation medium	10 % FCS (PAA, Sigma) 4 mM L-glutamine 100 U/ml penicillin, 100 µg/ml streptomycin DMEM low glucose, - phenol red (Gibco)
A7r5 freezing medium	complete growth medium supplemented with 5 % (v/v) DMSO
H-2K <sup>B</sup> -tsA58 proliferation medium	20 % FCS (PAA) 2 % chicken embryo extract (SLI) 100 U/ml penicillin 100 µg/ml streptomycin 20 U/ml interferon-γ (IFN-γ) (Millipore) DMEM GlutaMAX (Gibco)
H-2K <sup>B</sup> -tsA58 differentiation medium	5 % horse serum (Sigma) DMEM GlutaMAX (Gibco)
Embryonic mouse cardiomyocyte proliferation medium	20 % FCS (Gibco) 2 mM L-glutamine 2 mM NEAA 100 U/ml penicillin 100 µg/ml streptomycin 50 pM β-mercaptoethanol IMDM (Invitrogen)

Table 2.9: **Overview of cell culture media.** The culture media were prepared inside a laminar flow box. (DMEM = Dulbecco's modified Eagle medium; FCS = fetal calf serum; IMDM = Iscove's modified Dulbecco's medium; NEAA = nonessential amino acids)



## 2.10.1 Cell Lines

### 2.10.1.1 H-2K<sup>b</sup>-tsA58 Cells

These cells derive from leg muscles of H-2K<sup>b</sup>-tsA58 transgenic mice. These mice express a thermolabile tsA58 mutant of the simian virus 40 (SV40) large tumor antigen (TA<sub>g</sub>) under the control of the major histocompatibility complex H-2K<sup>b</sup> class I promotor (Jat *et al.*, 1991). The promotor activity varies among different tissues but can be increased by supplementing interferon- $\gamma$  (IFN- $\gamma$ ), which transforms the cells into conditional immortal cells. This enables them to proliferate under permissive conditions, i.e. culturing at 33 °C in proliferation medium (see tab. 2.9) containing IFN- $\gamma$ . A switch to 37 °C and the replacement of the proliferation medium with IFN- $\gamma$ -free differentiation medium (non-permissive conditions) eliminates large TA<sub>g</sub> expression and induces myogenic differentiation (Morgan *et al.*, 1994). Cells passaged for differentiation were transferred to cell culture dishes coated with BD Matrigel™ Basement Membrane Mix (BD Biosciences) in order to obtain basement stiffness suitable for contraction. Matrigel was diluted to a final concentration of 0,1 mg/ml in cold serum-free DMEM GlutaMAX and incubated at 37 °C for 30 min. Afterwards, the dishes were washed with sterile PBS or DMEM GlutaMAX and the cells were plated directly after. Differentiation medium was exchanged completely every two days and the cells could be maintained in culture for about twelve days. After 5-6 days, some of the myotubes formed exhibit spontaneous contractions (cf. section 3.1), which persist about 2-3 days. For microscopic analysis, cells were seeded on Matrigel™-coated locator cover slips (cf. section 2.11.2).

### 2.10.1.2 A7r5 Cells

A7r5 cells derive from the thoracic aorta of embryonic BDIX rats and possess many characteristics of smooth muscle cells (Kimes und Brandt, 1976). Since the CMV promotor exhibits a modest activity in A7r5 cells they are a suitable cell system to analyze functional vector combinations for BiFC complex formation (cf. section 2.9.5) because the higher the level of overexpression the more increases the probability of unspecific aggregates. Furthermore, these cells contain prominent actin stress fibres facilitating the investigation of actin-associated proteins. Chemical transfection efficiency using TurboFect *in vitro* Transfection Reagent (Fermentas) never fall below 50 % (cf. section 2.10.6) and growth on glass cover slips was slightly reduced but not significantly impaired.



### 2.10.2 Cell Thawing

A vial of frozen cells was removed from liquid nitrogen and thawed in a water bath heated to 37 °C. The cells were pipetted into a centrifugation tube containing prewarmed growth medium immediately after thawing not allowing them to warm up. In order to remove the DMSO included in the freezing medium (see tab. 2.9), the cells were centrifuged at 800 rpm for 3 min in a benchtop centrifuge (Heraeus), the supernatant was aspirated and the cells were resuspended in fresh growth medium. The suspension was transferred to a cell culture dish and thoroughly mixed to ensure even distribution throughout the vessel. The cells were incubated overnight under their usual growth conditions and the next day the medium was replaced.

### 2.10.3 Cell Passaging

Adherent cell cultures can cease proliferating or finally die if they are left in a confluent state for too long. Therefore, they need to be routinely passaged, i.e. a fraction of cells grown to an appropriate cell density is transferred to a new cell culture dish. For that, cells were detached from the surface using the proteolytic enzyme trypsin. At first, the medium of a dense cell culture was aspirated and the layer washed with PBS containing 0,5 mM EDTA in order to loosen cell-cell contacts. The cells were trypsinized at 37 °C with 1 ml 0,1 % trypsin in PBS per 60 cm<sup>2</sup>-dish. The detachment was assisted by tapping the side of the dish with palm of hand. The cells were resuspended in growth medium and gently pipetted up and down to avoid creating foam and to disrupt cell clumps. The adequate cell number was transferred to a new culture dish with prewarmed growth medium and incubated at their usual growth condition.

### 2.10.4 Cell Freezing

For long-term storage cells dissolved in freezing medium were kept in the vapor phase of liquid nitrogen. Trypsinized cells were collected in a centrifuge tube and spun down for 3 min at 800 rpm. The supernatant was aspirated and the cells resuspended in freezing medium. The composition varies among the different cell types and is described in table 2.9. A cryo vial containing the cell suspension was placed in an isopropanol freezing box and put into a -80 °C freezer overnight to control temperature drop ensuring maximal cellular viability before storing in liquid nitrogen.

### 2.10.5 Isolation of Embryonic Mouse Cardiomyocytes

Pregnant female mice were sacrificed at day 16,5–18,5 post coitum by cervical dislocation assuming that day one is the first day the plug was observed. The uterine horns with the embryos were dissected out using sterilized instruments and placed into a petri dish containing cold PBS. Each embryo was separated from its placenta and surrounding membranes and sacrificed by cutting the head. Then the thorax was opened to extract the heart which was put into cold PBS. In order to facilitate the the heart was minced with sterilized tweezers and the incubated in dissociating enzyme solution (1 mg/ml collagenase B (Sigma), 10 mM CaCl<sub>2</sub>) for 30 min at 37 °C. The collagenase was carefully aspirated and the sedimented cells were resuspended in PBS. The cells were sieved through a 100 µm nylon mesh pore of a cell strainer (Gibco/Invitrogen) and collected in 50 ml conical falcon tubes. The cell strainer was washed twice with PBS and the cells collected were centrifuged for 5 min at 1200 rpm. The supernatant was removed and the cells resuspended in PBS. This procedure was repeated and the cells were dissolved in an adequate volume of PBS for electroporation (cf. section 2.10.6.2).

### 2.10.6 Transient Transfections

Transient transgene expression in eukaryotic cells was achieved by either chemical-based (cf. section 2.10.6.1) or non-chemical (cf. section 2.10.6.2) introduction of cDNA inserted in eukaryotic expression vectors (cf. section 2.5.2) in order to investigate the localization and interactions of certain proteins in cells. The adequate number of cells were transferred to a cell culture dish of the favoured size. For protein extracts (cf. section 2.7.5) the cells were not seeded on glass cover slips, which were only used for subsequent immunostaining (cf. section 2.8.4).

#### 2.10.6.1 TurboFect Transfection

The transfection of cells with TurboFect *in vitro* Transfection Reagent (Fermentas) is based on the complex formation of a cationic polymer and DNA, which is delivered into eukaryotic cells. Cells were transfected at a confluency of  $\approx 70\%$  in order to prevent a completely overgrown culture. The appropriate number of cells was plated 4 h or the evening before transfection and then transfected with plasmid DNA according to the manufacturer's instructions. After 48 h post-transfection the cells were fixed and stained as described in section 2.8.4.

### 2.10.6.2 Electroporation of Embryonic Mouse Cardiomyocytes

After the final centrifugation step of the isolation procedure of embryonic mouse cardiomyocytes (cf. section 1.8.2) the cells of 6–8 embryonic hearts were resuspended in 600  $\mu$ l cold PBS and then filled in a pre-cooled electroporation cuvette (0,4 cm gap width, BioRad). The mass of 20  $\mu$ g plasmid DNA was added which was designated to be delivered into the cells. The cells were permeabilized with an exponential decay pulse from a capacitor charged to a voltage of 240 V ( $R = \infty$  ,  $C = 500 \mu$ F). Afterwards PBS was added to a final volume of 1,5 ml and the cells were distributed in three wells of a 24-well plate filled with embryonic mouse cardiomyocyte proliferation medium (see tab. 2.9). For fluorescence microscopy analysis (cf. section 2.11.1) the cells were plated on glass cover slips coated with 0,1 % gelatine (Sigma) and cultured at 37 °C. The medium was replaced the next morning and after two days the cells were processed for immunofluorescence microscopy (cf. section 2.8.4).

## 2.11 Microscopy

Cell morphology or protein localizations were analyzed with microscopic techniques. The equipment and the corresponding applications are explained in the following sections.

### 2.11.1 Transmitted Light Microscopy

Growth of cultured cells was controlled using a Nikon Eclipse TS 100 light microscope. The microscope was equipped with objectives depicted in table 2.10. Images were acquired with an Axiocam ICm (Carl Zeiss MicroImaging GmbH) CCD camera and the software AXIOVISION (version 4.8).

#### 2.11.1.1 Epi-fluorescence Microscopy

Fixed transfected cells were analyzed using the epi-fluorescence microscope AxioImager (Carl Zeiss MicroImaging GmbH). Objectives and filter sets are depicted in table 2.10 and 2.11. Images were acquired with an Axiocam MRm (Carl Zeiss MicroImaging GmbH) CCD camera and the software Axiovision (version 4.8).

Manufacturer	Objective	Magnification	Numerical Aperture	Microscope
Nikon	Plan Fluor	4x	0,13	Eclipse TS 100
Nikon	Achromat ADL	10x	0,25	Eclipse TS 100
Zeiss	EC Plan-Neofluar Ph1	10x	0,3	AxioImager
Zeiss	EC Plan-Neofluar	10x	0,3	LSM 710
Nikon	Achromat LWD ADL	20x	0,4	Eclipse TS 100
Zeiss	Plan-Neofluar Ph2	20x	0,5	AxioImager
Zeiss	Plan-Apochromat	20x	0,8	AxioImager
Zeiss	LCI Plan-Neofluar	25x	0,8	LSM 710
Nikon	Achromat LWD ADL	40x	0,55	Eclipse TS 100
Zeiss	EC Plan-Neofluar	40x	1,3	LSM 710
Zeiss	Plan-Neofluar Ph3	63x	1,25	AxioImager
Zeiss	Plan-Apochromat	63x	1,4	LSM 710
Zeiss	Plan-Neofluar Ph3	100x	1,3	AxioImager
Zeiss	$\alpha$ Plan-Apochromat	100x	1,46	LSM 710

Table 2.10: **Objectives for microscopy.** The objectives are ordered by magnification. More detailed informations about optical corrections and specialized optical properties can be obtained from the manufacturer's website. (Zeiss: <http://www.zeiss.de>, Nikon: <http://www.nikoninstruments.com>)

Filter Set	Filter Characteristics			Fluorochrom
	Excitation	Beam Splitter	Emission	
49	G 365	FT 395	BP 445/50	Alexa 405
38 HE	BP 470/40	FT 495	BP 525/50	Alexa 488, Cy2, EGFP
46 HE	BP 500/25	FT 515 HE	BP 535/30	Venus
43 HE	BP 550/25 HE	FT 570 HE	BP 605/70	Alexa 546, Cy3
45	BP 560/40	FT 585	BP 630/75	Alexa 594
50	BP 640/30	FT 660	BP 690/50	Alexa 633, Cy5

Table 2.11: **Summary of filter sets in fluorescence microscopes of Carl Zeiss MicroImaging GmbH.** The filter sets are ordered by increasing wavelength of excitation. A selection of fluorescent dyes or fluorescent proteins detectable with the respective filter set is delineated in the last column. HE = high efficiency. BP = bandpass. FT = beam splitter filter transmission from ... nm.

Wavelength	Laser	Max. Power
405 nm	UV-Laser diode	30 mW
458 nm	Argon	25 mW
488 nm	Argon	25 mW
514 nm	Argon	25 mW
561 nm	DPSS	15 mW
594 nm	Helium-Neon	2.0 mW
633 nm	Helium-Neon	5 mW

Table 2.12: **Summary of lasers mounted in LSM 710.** Lasers were selected according to excitation maximum of the fluorescent dye utilized. The power of the laser beam did not exceed 12 % of the maximum. DPSS = diode pumped solid state.

### 2.11.1.2 Confocal Laser Scanning Microscopy

Optical sections of cells and tissues were obtained using a LSM 710 of Carl Zeiss MicroImaging GmbH. Fluorescent dyes used for indirect immunofluorescence microscopy (see tab. 2.7 and 2.8) were excited with a laser beam corresponding to wavelengths around the excitation maximum of the dye (see tab. 2.12). In general, the intensity of the beam was never raised over 12 % of the maximum power. The master gain of the photon detector was always used below 800 and the digital gain below 2.0. Images of mounted cells and tissue sections were acquired using a mode providing maximal elimination of cross-talk between simultaneously used fluorescent dyes. Unmounted cells were analyzed in chambered slides containing ddH<sub>2</sub>O and were labeled with combinations of secondary antibodies enabling single track image acquisition without cross-talk. Objectives are listed in table 2.10. Images were exported using the software ZEN (version 2008, 2009).

### 2.11.1.3 Fluorescence Recovery After Photobleaching (FRAP)

In order to determine protein dynamics within transfected cells, fluorescence was bleached and the recovery rate was detected. Such a FRAP analysis was performed in A7r5 cells (cf. section 2.10.1.2) transfected as described in section 2.10.6.1. Fluorescence recovery was measured 24 h after transfection using the LSM 710 confocal microscope (cf. section 2.11.1.2). Regions of interest (ROI) were determined and bleached with 100 % power of a 405 nm laser beam until less than 10 % of the original fluorescence intensity was left. Lower power did not bleach to sufficient low levels in an appropriate time which was due to a malfunction of the laser. After bleaching, a picture was taken every second in a time series of 100 s. Generally, the fluorescence was recovered to a constant level after 60 s. Images were analyzed in a four-step process described in (G. Rabut, 2005) using the software program IMAGEJ (version 1.44). After background subtraction, correction and normalization, mobile fractions  $M_f$  were calculated according to the following equation:

$$M_f = \frac{F_{end} - F_{post}}{F_{pre} - F_{post}}. \quad (2.2)$$

$F_{end}$  refers to the maximal fluorescence intensity after recovery,  $F_{post}$  is the value of the fluorescence intensity directly after bleaching and  $F_{pre}$  states the initial fluorescence intensity. The half time of exchange  $t_{\frac{1}{2}}$  was not calculated because the laser beam did not always bleach below 10 % of the initial level and  $t_{\frac{1}{2}}$  is strongly dependent on sufficient bleaching whereas determination of mobile fractions still remained possible. The dynamics

of each transfected construct were analyzed in at least three different cells.

### 2.11.2 Scanning Electron Microscopy

Scanning electron microscopy was used to reveal changes in the morphology of cytoskeletal structures in differentiating H-2K<sup>B</sup>-tsA58 cells (cf. section 2.10.1.1). The microscope was a XL 30S manufactured by Philips Company.

#### 2.11.2.1 Production of Locator Cover Slips

In order to locate the position of cells, circular glass cover slips (Menzel) with an alpha numerical pattern were produced. Therefore a finder grid (Plano, see fig. 2.2 A) was put on a cover slip with a diameter of 15 mm and then coated with a 4 nm layer of platinum-palladium in a Sputter Coater (Cressington). The resulting pattern on the glass cover slip is depicted in figure 2.2B. The cover slips were heated for 4 h at 180 °C to avoid the dislocation of the metal layer and to sterilize them, enabling the use in cell culture. Then, cells could be seeded on the surface and located in light microscopes and a scanning electron microscope (SEM).

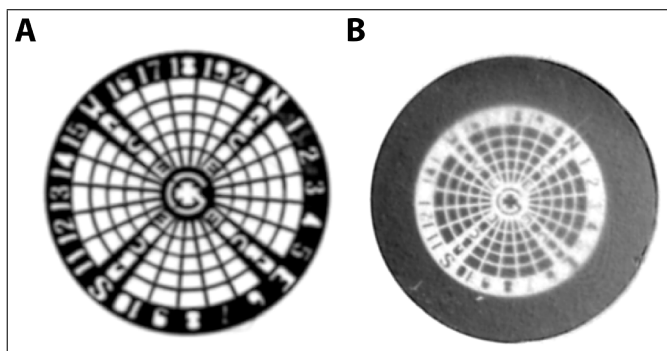


Figure 2.2: **Production of SEM locator cover slips.** **A.** Finder grid which served as a template for producing the alpha numerical pattern on glass cover slips. **B.** Complete glass cover slip with locator pattern.

#### 2.11.2.2 Membrane Extraction and Fixation

Cells cultured on locator cover slips (see fig. 2.2) were processed as described in section 2.8.4 prior to SEM preparation. In this way, the membrane of already fixed and immunostained cells were extracted through treatment with PEG-GTX buffer (10 mM PIPES, 50 mM EDTA, 27 mM KOH, 1 % Triton X-100, 4 % PEG 6000, 10 % glycerol) three times for 20 min with agitation. The cytoskeletal architecture was preserved due to fixation with 4 % glutaraldehyde in CB-buffer (10 mM MES, pH 6,1, 150 mM NaCl, 4 mM MgCl<sub>2</sub>, 5 mM glucose, 5 mM EGTA, 25 mg/l streptomycin) for 20 min followed by

washing with ddH<sub>2</sub>O. Any liquid was removed by critical point drying, which is described in the next section.

### 2.11.2.3 Critical Point Drying

Every sample analyzed by a scanning electron microscope must be completely dried before mounting while conserving cellular structures. Locator cover slips were placed in a holder and in a first step the specimen was progressively dehydrated with ethanol according to the following schedule:

<b>% Ethanol</b>	30	50	70	90	99,8	99,8	100 MS	100 MS
<b>Time [min]</b>	10	10	10	10	10	10	10	10

Table 2.13: **Progressive ethanol dehydration schedule.** The cover slips placed in a holder were constantly covered with ethanol during the dehydration process in order to avoid them running dry. The final steps were performed with absolute ethanol on a molecular sieve (MS) which selectively absorbed the residual water from the solution.

Then ethanol was exchanged for liquid CO<sub>2</sub> in eight steps in a critical point dryer (BAL-TEC) because CO<sub>2</sub>'s critical conditions (31,1 °C, 7,38 MPa) are well-suited for drying without damaging the specimen. The drying run was completed by slowly heating to 40 °C, allowing for CO<sub>2</sub> being brought to the gas phase without crossing the liquid-gas boundary, thus preventing the sample from damage due to surface tension. The carbon dioxide was carefully vented to avoid condensation effects and the hygroscopic specimen was stored in an exsiccator until analysing with the SEM.

### 2.11.2.4 Sputter Coating

Samples designated to be analysed in the SEM need to emit secondary or backscattered electrons in order to be visualized. However, biological samples mainly consisting of carbon compounds usually do not possess the necessary conductivity. Therefore, they are mounted onto a stub and held to it by a conductive paste immediately before use. Then, the specimen is covered with a 2 nm layer of platinum-palladium in a sputter coater (Cressington) and analysed in the SEM (Philips).

### **2.11.3 Image Processing**

Greyscale images obtained from microscopic samples (cf. section 2.11), polyacrylamide gels (cf. section 2.7.7), agarose gels (cf. section 2.6.4) and western-blot (cf. section 2.8.1) were acquired as described in the respective section. All images were exported as RGB .tif files with software utilized for acquisition and a minimum resolution of 150 dpi. In the case of multi-channel microscopic images RGB channels were allocated according to the colour of the emitted light of the respective fluorescent dye. Modest adjustments of contrast and brightness as well as cropping of picture details were made with the image processing software GNU IMAGE MANIPULATION PROGRAM (GIMP) version 2.6.10. Processed images were exported as non-compressed .png files for further use. Figures were composed using the vector-based graphics software INKSCAPE (version 0.48) and exported as .png files with a minimum resolution of 300 dpi.

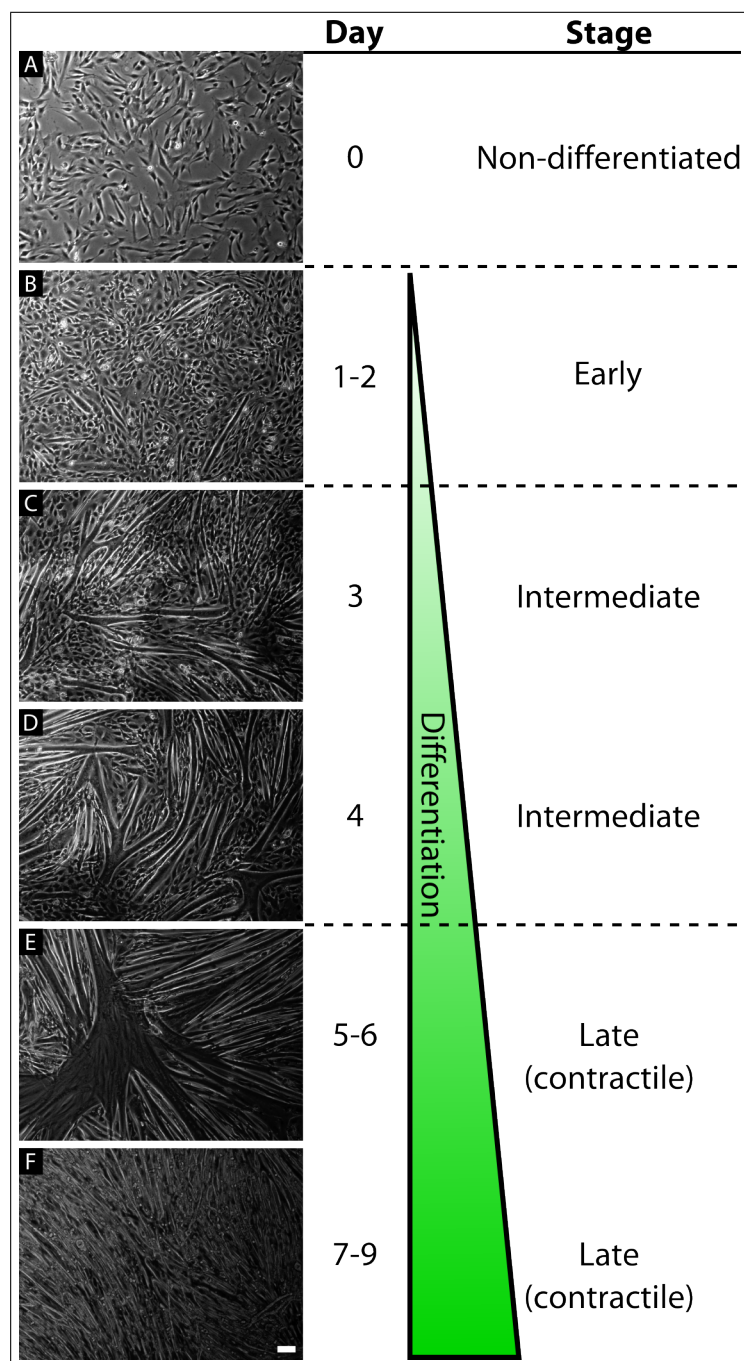


# Chapter 3

## Results

### 3.1 *In vitro* Myofibrillogenesis of Murine H-2K<sup>b</sup>-tsA58 Cells

Myogenic differentiation of cultured cells offers a valuable tool for analyzing myofibrillogenesis *in vitro*. Standard model systems like murine C2C12 cells (Blau *et al.*, 1983) or human skeletal muscle cells (van der Ven *et al.*, 1992) have already been widely used. However, these cells reveal certain limitations concerning the final stage of differentiation and contractility as well as the control of the onset of myofibrillogenesis and retention of their differentiation capacity. In this regard, myoblasts obtained from leg muscles of H-2K<sup>b</sup>-tsA58 transgenic mice, in the following designated as H-2K cells, offer multiple advantages since they allow for conditional immortalization and concomitant retention of their differentiation capacity due to their constitutive expression of a thermolabile large tumor antigen (Jat *et al.*, 1991; Morgan *et al.*, 1994). Its transcription is controlled by the major histocompatibility complex H-2K<sup>b</sup> class I promotor, which is active at various levels in different tissues and inducible to higher levels by interferons. Therefore, these cells proliferate at permissive conditions including exposure to interferon and keeping at 33 °C and differentiate into contractile myotubes upon culturing at non-permissive conditions at 37 °C without interferon (cf. section 2.10.1.1). The progression of differentiation was tracked for 8-9 days and the changes in cell morphology are depicted in figure 3.1. The myogenic program was started at high cell density before they reach a confluent state (fig. 3.1 A). According to their morphological changes and the stage of maturation of the contractile apparatus (cf. section 3.1.1) the myofibrillogenesis of H-2K cells will be divided into an early, intermediate and late phase. The following paragraph describes



**Figure 3.1: Morphological changes of H-2K cells during myofibrillogenesis.**

Upon myogenic differentiation H-2K cells dramatically change their morphology from mononucleated, mostly elongated cells to a branched network of multinucleated contracting myotubes depicted in images from transmitted light microscope (A-F). **A.** Non-differentiated mononucleated myoblasts immediately before switching to non-permissive conditions (day 0). **B.** Early phase of differentiation (day 1-2). First multinucleated myotubes can be detected and adjacent cells adopt the myotube's orientation. **C.** In the intermediate phase starting at day three of differentiation branched myotubes occur and their number and size has increased. **D.** The branched myotubes reveal an interconnected meshwork at day four of myogenic differentiation. **E.** The onset of contraction marks the entrance into the late phase of differentiation which starts not before day five after the induction of differentiation. The myotubes are interconnected to large meshworks at this stage. **F.** Due to contraction many cells loose their attachment and alter their shape into slender myotubes because of the lack of complete three-dimensional anchorage. Scale bar 20  $\mu\text{m}$ .

the morphological changes and analysis of the expression level and localization of key components of the myofibrillar apparatus which is delineated in sections 3.1.2 and 3.1.1.

During the first 2 days of differentiation (early phase), the cells fused and formed small myotubes, which had a larger diameter than single cells (fig. 3.1 B). Adjacent to these early myotubes, mononucleated cells elongated and adopted the myotube's orientation. In the course of development, the number of cells beginning differentiation increased and by fusing with existing myotubes contributed to their growth. In the intermediate phase, these myotubes expanded and came into contact with other syncytial cells, which led to the formation of branched networks of myotubes first detected around day 3 of differentiation (fig. 3.1 C). These networks enlarged and the number of mononucleated cells constantly decreased (fig. 3.1 D). When the myotubes gained their contractile property at day 5-7, they entered the late phase of differentiation and were arranged in an extended interconnected meshwork (fig. 3.1 E). Contraction promoted further maturation of the contractile apparatus and is indispensable to reach an adult muscle phenotype (cf. section 1.2.2.4). Contracting cultured cells, however, often detached from the surface, if the force generated exceeded the strength of their adhesion to the ground of the culture dish. This may result from the myotubes lacking a proper three-dimensional anchorage, which is established by costameres and myotendinous junctions *in situ* (cf. section 1.7 and 1.6, respectively). Consequently, the morphology of non-detached cells changed into slender myotubes (fig. 3.1 F). The myotubes could keep their contractility and morphology until day 10-12 of differentiation accompanied by a progressive loss of cells.

### 3.1.1 Sarcomere Development

H-2K muscle cells developed a functional contractile apparatus around day 5-7 after changing the culture conditions to non-permissive parameters (cf. sections 3.1 and 2.10.1.1 as well as fig. 3.1). The developmental steps of the assembly of a contractile sarcomere (cf. section 1.2.2.4) were depicted by visualization of components of the major structural elements of the sarcomere, the Z-disc and the M-band. Furthermore, F-actin staining showed the remodelling of the thin filament system. All cells were fixed and immunostained using specific primary antibodies and fluorescently-labeled secondary antibodies or phalloidin in the case of F-actin (cf. section 2.8.4, tab. 2.8.2 and 2.7). The specimens were analyzed using a confocal laser scanning microscope (LSM) (cf. section 2.11.1.2).

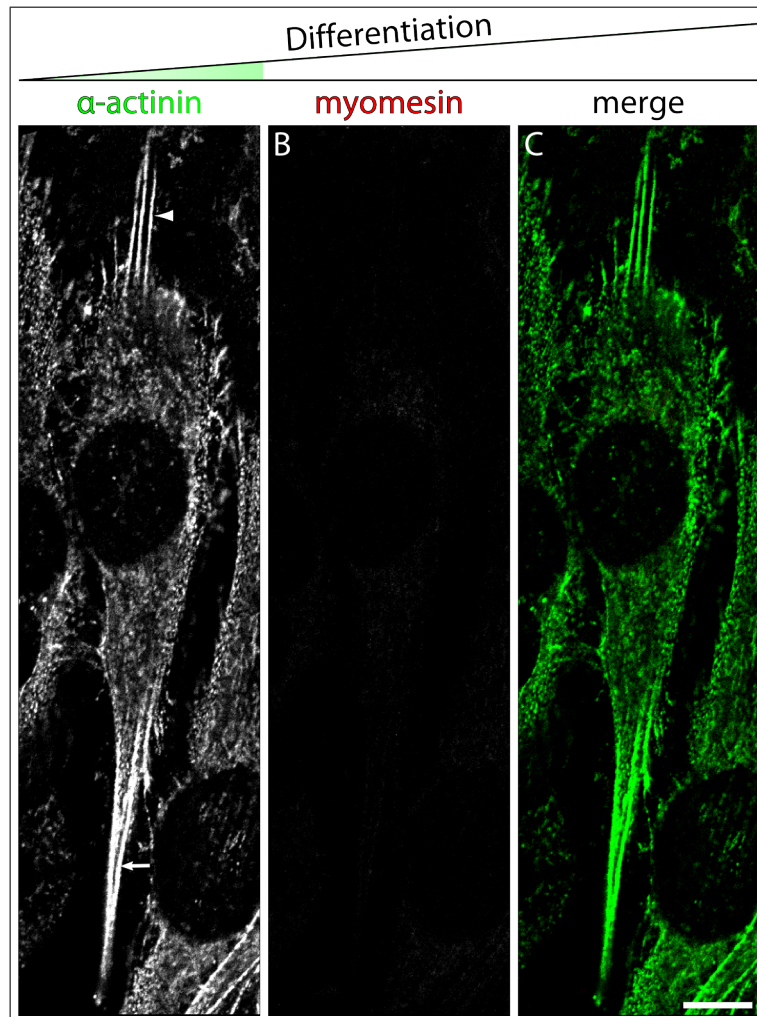


Figure 3.2:  **$\alpha$ -Actinin precedes myomesin expression at the initial stage of H-2K cell differentiation.** Confocal LSM images of differentiating H-2K cells of early stage labeled with antibodies against sarcomeric  $\alpha$ -actinin and myomesin (see tab. 2.8.2). **A.** After the induction of myogenic differentiation,  $\alpha$ -actinin strongly labels peripheral cellular extensions (arrowhead), which are indicators of elongating cells. In the cell periphery,  $\alpha$ -actinin continuously decorates actin filaments, whereas it exhibits an unordered punctate expression throughout the rest of the cell. **B.** Myomesin cannot be detected at this early stage thus  $\alpha$ -actinin precedes the expression of myomesin. **C.** Combined image of the  $\alpha$ -actinin (green) and myomesin (red) signal. Scale bar 10  $\mu$ m.

### 3.1.1.1 Early Phase (Day 1–2)

Myogenic differentiation coincides with the expression of muscle-specific isoforms of proteins building the sarcomere. A prominent constituent of the Z-disc is sarcomeric  $\alpha$ -actinin (cf. section 1.5.5.1), which can be detected at very early stages of myofibrillogenesis in Z-disc precursor structures (cf. section 1.2.2.4). It precedes the expression of the M-band myosin-binding protein myomesin (cf. section 1.5.6) and strongly decorated peripheral cellular extensions (fig. 3.2 A, arrowhead) and actin filaments (fig. 3.2 A, arrow), whereas myomesin was hardly detectable at this stage.

The cellular localization of sarcomeric proteins depended on the z-level of the optical sections analyzed. Therefore, the localization of  $\alpha$ -actinin and myomesin was analyzed at extracellular matrix (ECM) contact sites and in the center of the cell body. The first molecules of muscle-specific proteins could be initially seen around the nucleus. At the level of ECM contact sites, these proteins revealed altered targeting compared to the cy-



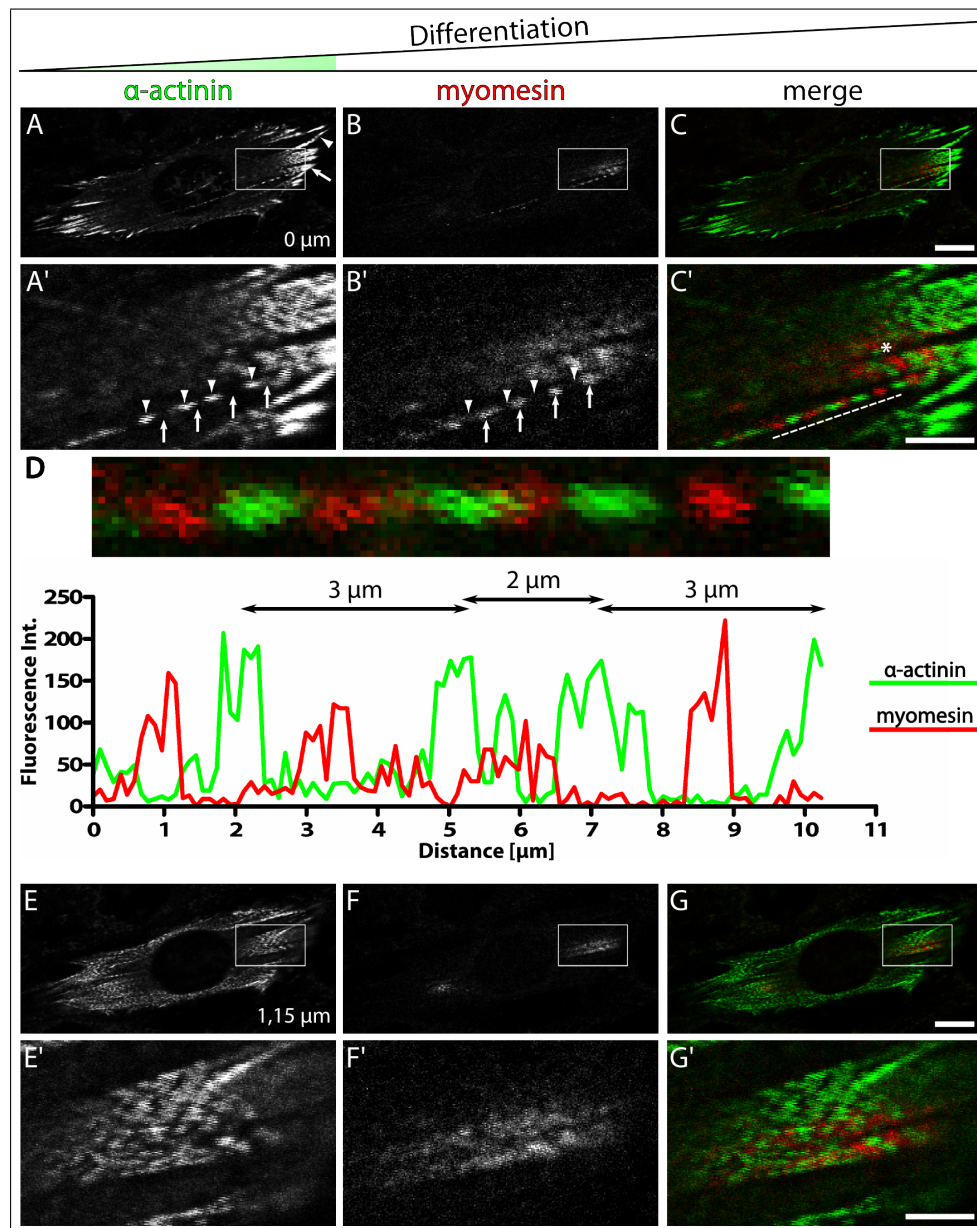


Figure 3.3:  $\alpha$ -Actinin and myomesin expression in an early phase of H-2K cell differentiation.

Different optical sections of confocal LSM images of differentiating H-2K cells of early stage labeled with antibodies against sarcomeric  $\alpha$ -actinin and myomesin. The level of the section is marked in images **A** and **E**. 0  $\mu\text{m}$  stands for ECM attachment level. In the merge images (**C**, **C'**, **D**, **G**, **G'**)  $\alpha$ -actinin and myomesin are tinted green and red, respectively. **A**. At ECM attachment level  $\alpha$ -actinin is mainly located at peripheral cellular extensions (arrowhead) and focal contacts in the periphery (arrow). **B**. Myomesin, if already expressed, is absent from focal contacts or cellular extensions. **A'**.  $\alpha$ -Actinin exhibits a regular spacing on actin filaments (arrowheads). **B'**. Myomesin alternates with  $\alpha$ -actinin on actin filaments (arrows). **C'**. Distribution of  $\alpha$ -actinin and myomesin is reminiscent of early sarcomere-like arrangement (asterisk). The dotted line indicates the length magnified in **D**. **D**.  $\alpha$ -Actinin and myomesin reveal already spacings of mature sarcomeres ( $\approx 2 \mu\text{m}$ ). **E**. At upper sections,  $\alpha$ -actinin is not restricted to the periphery and displays an unordered punctate pattern throughout the whole cell. **F**. Expression level and frequency of myomesin does not change at elevated z-levels. Scale bar 10  $\mu\text{m}$  (A-C, E-G) and 5  $\mu\text{m}$  (A'-C', E'-G').

toplasmic region near the nucleus, if the proteins were involved in cell adhesion structures, such as  $\alpha$ -actinin. Thus,  $\alpha$ -actinin revealed differences in the cellular distribution regarding the cellular regions mentioned above (fig. 3.3 A, D). Near the membrane (marked as 0  $\mu\text{m}$  in fig. 3.3 A),  $\alpha$ -actinin prominently labeled peripheral cellular extensions (fig. 3.3 A, arrowhead) and focal contact sites (fig. 3.3 A, arrow). Additionally, it was associated with actin filaments in a typical punctate pattern but lacking a regular spacing (fig. 3.3 D). The distance amounted to either about 3  $\mu\text{m}$  or 2  $\mu\text{m}$ , the latter resembling the spacing of a mature sarcomere (fig. 3.3 A'-C' and D). In contrast to the distances described in chicken cardiomyocytes (Sanger *et al.*, 1986), the gaps between the  $\alpha$ -actinin signals did not clearly fall below 2  $\mu\text{m}$  on actin filaments, if a basic ordered association could be observed. In cells still lacking myomesin expression (fig. 3.2)  $\alpha$ -actinin seemed to be more closely positioned but its localization was not comparably ordered along the actin filaments. After induction of myomesin expression (fig. 3.3 B, E), myomesin decorated the same actin filament alternating with  $\alpha$ -actinin in equivalent distances (fig. 3.3 D). In contrast to  $\alpha$ -actinin, myomesin was completely absent from focal contacts or peripheral cellular extensions. Even in this early phase,  $\alpha$ -actinin and myomesin exhibited an alternating distribution pattern reminiscent of early sarcomere arrangement (fig. 3.3 C', asterisk), although myomesin appeared to be less ordered in comparison to  $\alpha$ -actinin's more punctate distribution along actin filaments. Apart from the localization near the membrane described above, in optical sections of an upper position depicting the cell body,  $\alpha$ -actinin was distributed throughout the whole cell in a still unordered punctate pattern and not restricted to the periphery (fig. 3.3 E). The intensity and frequency of myomesin did not change at this position (fig. 3.3 F).

Myogenic differentiation alters the structure of the actin cytoskeleton, which qualifies F-actin as a good marker visualizing the progression of myofibrillogenesis. At the onset of the myogenic program, H-2K cells elongated and their extensions at the cell periphery contained F-actin (fig. 3.4 B, arrow). These extensions were strongly decorated by an antibody recognizing an epitope of the giant protein titin positioned 100 nm away from the Z-disc (Fürst *et al.* (1988), cf. section 1.5.5, fig. 3.4 A, arrow). Titin is an important ruler of sarcomere assembly and is included in Z-disc precursor structures (cf. section 1.5.5). The strongest expression of titin was obtained near the nucleus (fig. 3.4, asterisk), which is a common feature of the early muscle-specific protein expression (see above). Even in this early stage, actin filaments existed displaying a Z-body-like association of titin with a spacing of about 2  $\mu\text{m}$ , which approximates the distance in mature sarcomeres (fig. 3.4 A, arrowheads). This association pattern could only rarely be detected at

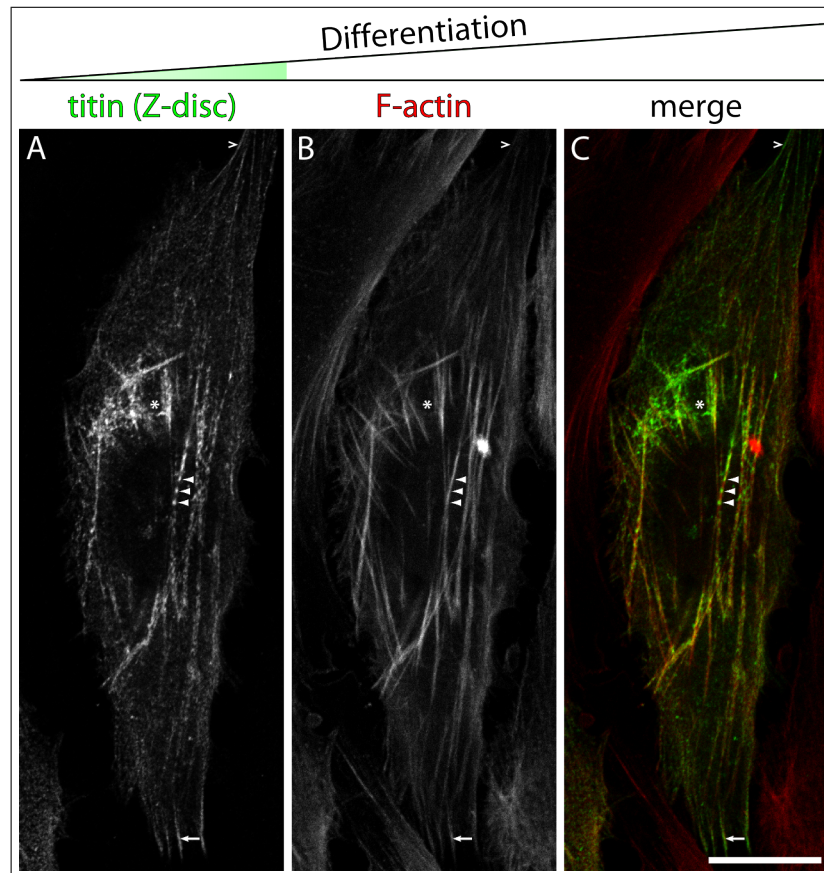


Figure 3.4: **Titin and the actin cytoskeleton in an early phase of H-2K cell differentiation.** Confocal LSM images of a differentiating H-2K cell of early stage labeled with a titin-specific antibody recognizing a Z-disc epitope and phalloidin to visualize actin filaments. **A.** The strongest titin expression can be detected near the nucleus (asterisk). Titin decorates cellular extensions at the periphery (arrow) and reveals a Z-body-like association of actin filaments with a mature spacing of  $\approx 2 \mu\text{m}$  (arrowheads). Apart from this, titin also exhibits a continuous labeling of actin filaments (open arrowhead). **B.** Cellular extensions in the periphery contain F-actin (arrow). Although titin occasionally associates with actin filaments in a punctuate pattern (arrowheads), the phalloidin signal is still continuous. **C.** Merge image of titin (green) and F-actin (red). Scale bar  $10 \mu\text{m}$ .

this early developmental phase, since titin predominantly decorated actin filaments in an apparently unordered discontinuous fashion. At the cell periphery and, to a lesser extend, at strongly labeled actin filaments, titin revealed a continuous decoration (fig. 3.4 A, open arrowhead).

In summary, after the initiation of myofibrillogenesis in murine H-2K cells, components of Z-disc precursor structures, like  $\alpha$ -actinin and titin, exhibit a related targeting. Cellular extensions of the elongating cell are continuously labeled by  $\alpha$ -actinin and titin (fig. 3.2 A arrowhead and fig. 3.4 A arrow, respectively). Both proteins predominantly show a punctate, unordered pattern occasionally being replaced by an arrangement, which displays spacings resembling the distance of mature sarcomeres (fig. 3.3 and 3.4). The expression of muscle-specific proteins can be firstly detected around the nucleus apparently unordered and intensifies there upon progression of differentiation. The important M-band constituent myomesin does not belong to the class of early myogenic marker because it is still undetectable, when  $\alpha$ -actinin already noticeably decorates actin filaments in a

punctate pattern (fig. 3.2 and 3.3). In conclusion, the morphological changes of the H-2K cells are accompanied by the expression of early sarcomeric proteins, which rapidly show localization at precursor structures of the sarcomeric Z-disc and M-band.

### 3.1.1.2 Intermediate Phase (Day 3–4)

Continuous fusion of adjacent myoblasts let the early myotubes grow in length and width due to fusion of adjacent cells and myotubes resulting in a developing branched meshwork (fig. 3.1 C). Simultaneously, the maturation of the myofibrillar apparatus proceeds, which includes changes in expression level and localization of myofibrillar markers. 3 to 4 days after the onset of myogenic differentiation, myotubes already contained regions with laterally fused Z-bodies (Z-disc precursor structures) and properly spaced M-bands forming early sarcomeres delineated by the signals of  $\alpha$ -actinin and myomesin staining (fig. 3.5 asterisk). These structures were still restricted to a minor area of the cell, whereas the rest displayed  $\alpha$ -actinin associated with actin filaments either continuously or punctatedly as shown for the early stages (cf. section 3.1.1.1). Myomesin was restricted to regions of a punctate  $\alpha$ -actinin pattern in the center of the myotube near nuclei (3.5 B, n) and did not decorate actin filaments continuously in the periphery as observed for  $\alpha$ -actinin.

A comparison of the localization of both Z-disc markers,  $\alpha$ -actinin and titin, revealed an analogous distribution throughout the cell. As stated for  $\alpha$ -actinin, titin also showed small areas of early Z-discs correctly spaced (fig. 3.6 A, asterisk). These regions could preferentially be detected in the direct vicinity of nuclei (n), which had been expected from the double staining of  $\alpha$ -actinin and myomesin. Although Z-disc markers displayed a regular pattern resembling mature sarcomeres, the assembly of the different filament systems was not yet completed because F-actin staining was still continuous and did not reveal discontinuous labeling which would have indicated the incorporation of myosin filaments (fig. 3.6 B, asterisk). Thus, the assembly of premature Z-discs preceded the reorganization of the actin cytoskeleton into I-bands during myofibrillogenesis. On actin filaments not presenting an advanced myogenic phenotype, titin localization remained punctate and apparently unordered but intensified at the peripheral ends (fig. 3.6 A, arrow). At these sites the phalloidin signal clearly decreased pointing to an impeded accessibility of its binding sites (fig. 3.6 B, arrow).

To sum up, in this intermediate phase, constituents of Z-disc and M-band have adopted a mature spacing pattern near nuclei in the center of the myotube, which, however, represents only a minor portion of the cell. The majority still exhibits the early phenotype



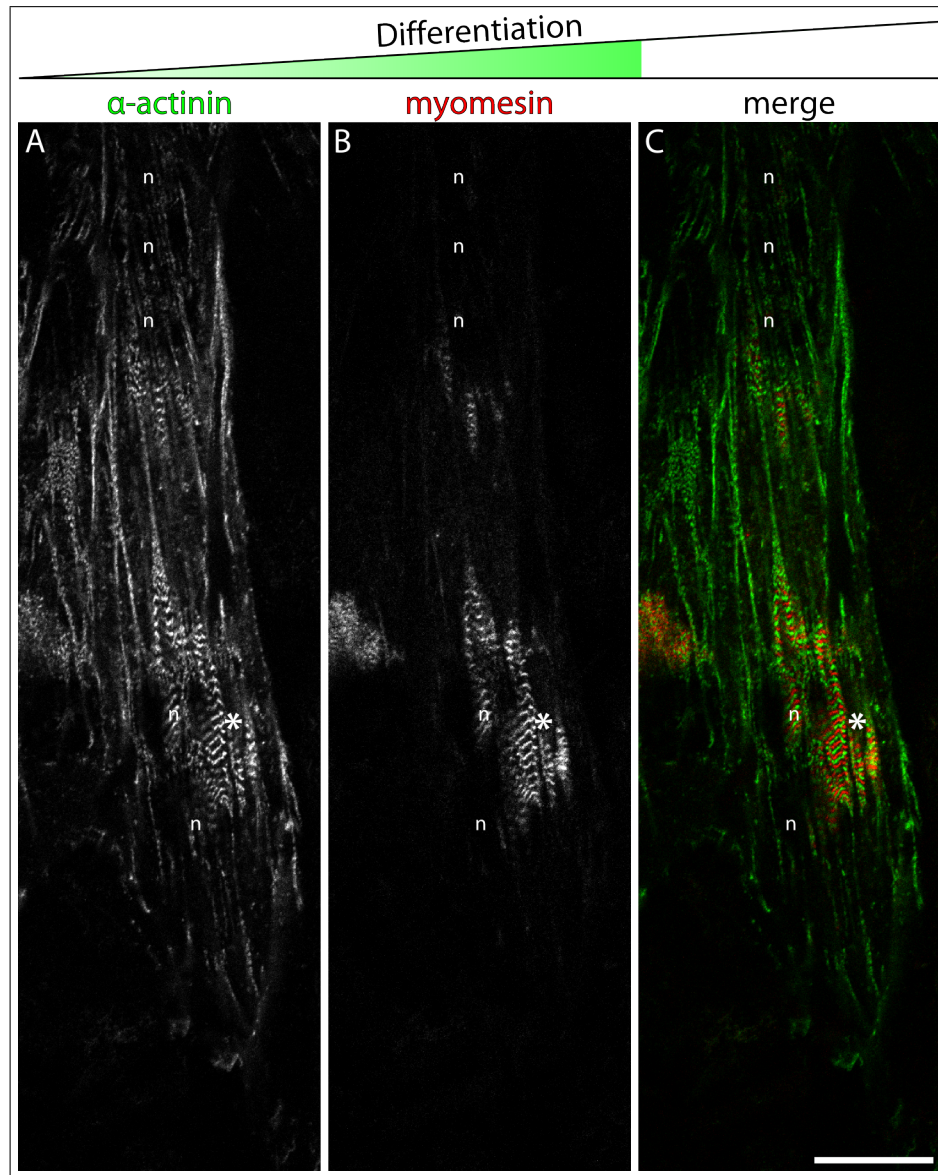
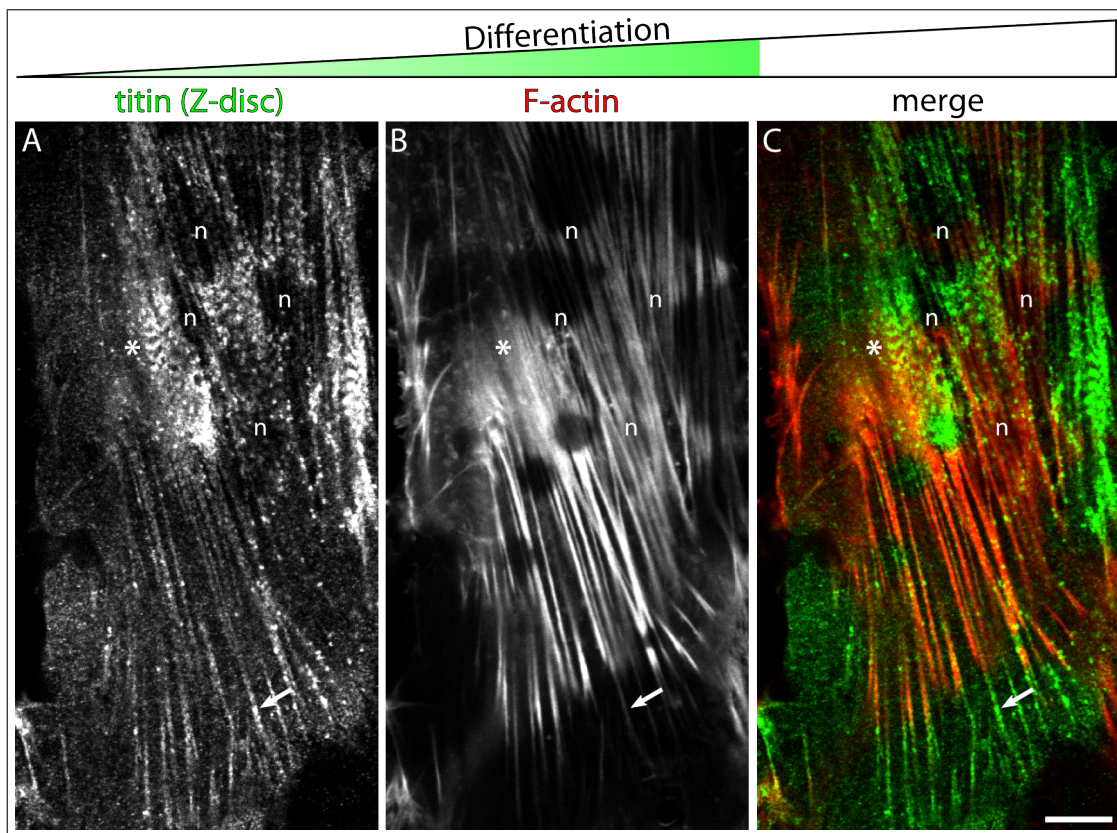


Figure 3.5:  $\alpha$ -Actinin and myomesin exhibit first regions of early sarcomeres. Confocal LSM images of differentiating H-2K cells of intermediate stage labeled with antibodies against sarcomeric  $\alpha$ -actinin and myomesin. **A.**  $\alpha$ -Actinin is still mainly associated with actin filaments either continuously or punctated. The myotube already contains an area of laterally fused Z-bodies (asterisk). **B.** Myomesin shows regions of early M-bands (asterisk). **C.** Merge image of  $\alpha$ -actinin (green) and myomesin (red). Early sarcomeres are indicated by the alternating pattern of  $\alpha$ -actinin and myomesin. Myomesin is restricted to areas of  $\alpha$ -actinin discontinuously associated with actin filaments. Nuclei are denoted by 'n'. Scale bar 10  $\mu$ m.

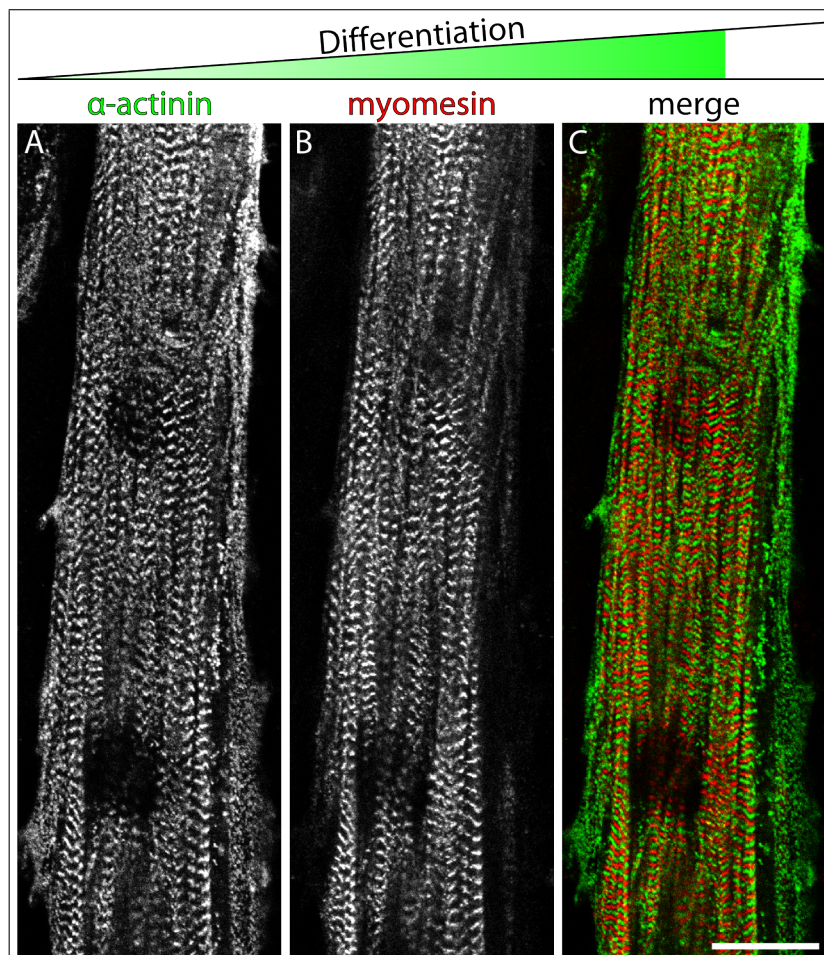


**Figure 3.6: The assembly of premature Z-discs precedes the reorganization of the actin cytoskeleton into I-bands.** Confocal LSM images of a differentiating H-2K cell of intermediate stage labeled with a titin-specific antibody recognizing a Z-disc epitope and phalloidin to visualize actin filaments. **A.** Titin displays areas of laterally fused Z-bodies near nuclei (asterisk). Nevertheless it is mainly associated with actin filaments enriched at their peripheral ends. **B.** Actin filaments are not organised as I-bands in areas of premature Z-discs (asterisk). Phalloidin labeling of actin filaments is decreased at the peripheral ends (arrow). **C.** Merge image of titin (green) and F-actin (red). Nuclei are denoted by 'n'. Scale bar 10  $\mu\text{m}$ .



described in section 3.1.1.1. The premature status of these myotubes is underlined by the lack of actin filaments assembled as I-bands clearly demonstrating the immature sarcomere status. Therefore, the appearance of early sarcomeres indicated by premature Z- and M-bands precedes the reorganization of actin filaments into I-bands.

### 3.1.1.3 Late Phase (Day 5–8)



**Figure 3.7: Late contractile myotube without laterally aligned myofibrils.** Confocal LSM images of a differentiating H-2K cell at late stage labeled with antibodies against sarcomeric  $\alpha$ -actinin and myomesin. **A.** Myofibrils pervade the myotube showing mature spacing of Z-discs containing  $\alpha$ -actinin, which are still not aligned laterally. **B.** The localization of myomesin also exhibits the correct distance along the myofibrils but lacks proper alignment laterally. **C.** Merge image of  $\alpha$ -actinin (green) and myomesin (red). The myotube contains the typical alternating pattern of  $\alpha$ -actinin and myomesin representing the array of Z-discs and M-bands, respectively. Scale bar 10  $\mu\text{m}$ .

H-2K myotubes gain their contractility, when they have formed a dense branched network (fig. 3.1 E). At this stage, multiple myofibrils pervaded the cell, which were not properly aligned laterally but exhibited mature spacing of Z- and M-band components (fig. 3.7).

The maturation of the myofibrillar apparatus proceeded upon constant contraction, which allowed for a precise adjustment of neighbouring myofibrils (fig. 3.8 A–C). Although the alternating pattern of  $\alpha$ -actinin and myomesin, representing the Z-disc and the M-band, respectively, had been improved, these myotubes still contained regions of

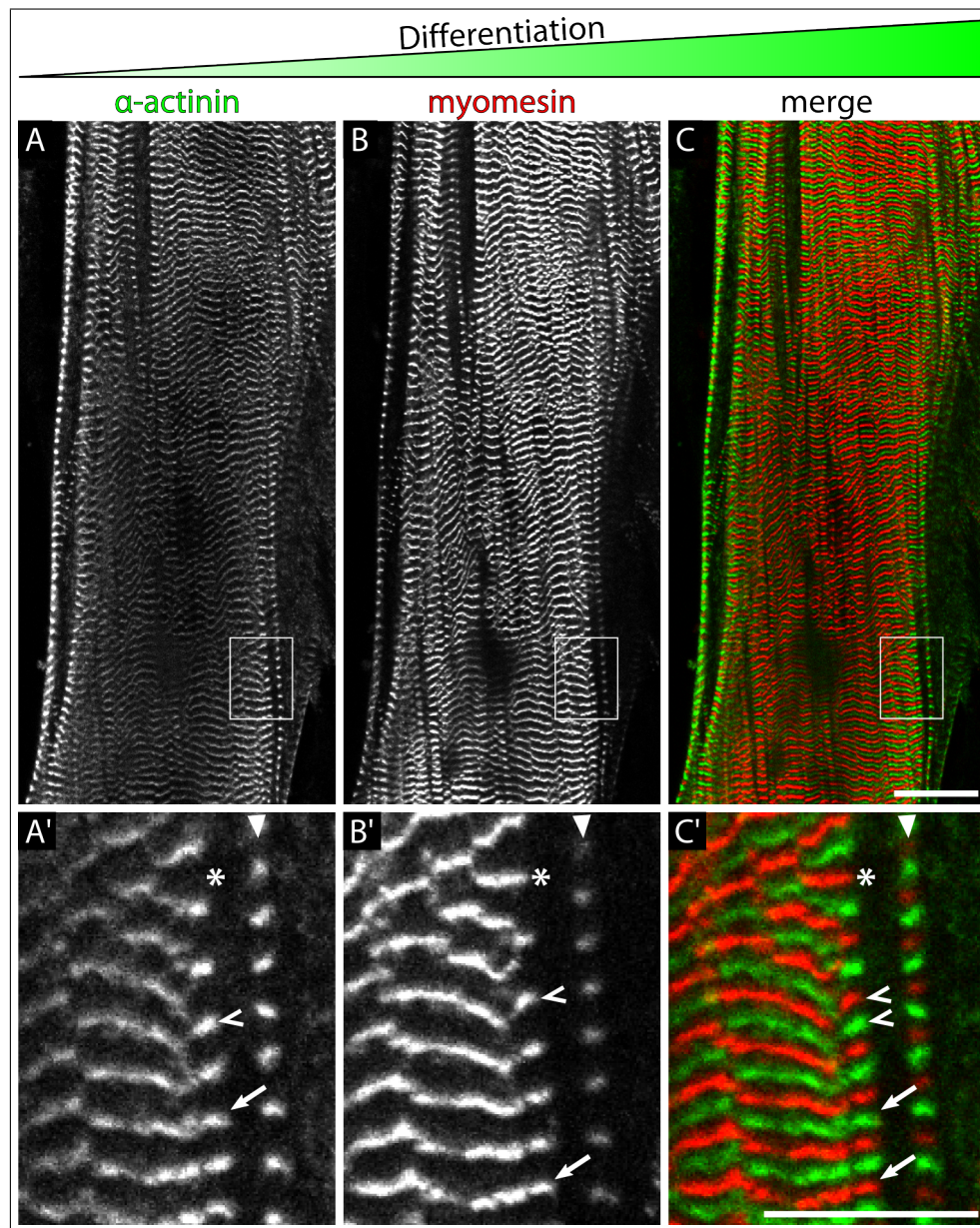


Figure 3.8: **Latest stage of sarcomere development in H-2K cells.** Confocal LSM images of a finally differentiated H-2K myotube labeled with antibodies against sarcomeric  $\alpha$ -actinin and myomesin. In the merge images **C** and **C'**  $\alpha$ -actinin and myomesin are tinted green and red, respectively. **A.**  $\alpha$ -Actinin shows a well-aligned cross-striated pattern only with some irregularities. **B.** The M-band protein myomesin also reveals cross-striation including only some deviation. **A'–C'.** Magnification of the box in A-C. There are still myofibrils which have not fused yet but seem to be perfectly aligned laterally (arrowhead). Other myofibrils are about to coalesce with the mature contractile apparatus revealing sites of completed incorporation (arrow) and close approximation (open arrowheads). Delta-shaped structures represent areas where the number of adjacent sarcomeres does not match (asterisk). Scale bar 10  $\mu\text{m}$ .

irregularities in the sarcomere architecture (fig. 3.8 A'–C'). There were small myofibrils, which were perfectly aligned laterally with the adjacent sarcomeres, but had not yet fused with them to form a continuous array of Z-discs and M-bands (fig. 3.8 A'–C', arrowhead). Another myofibril was about to coalesce with the myofibrillar apparatus revealing sites of completed incorporation (fig. 3.8 A'–C', arrows) and close approximation (fig. 3.8 A'–C', open arrowheads). Furthermore,  $\alpha$ -actinin and myomesin staining exhibited delta-shaped areas, which includes supernumerary sarcomeres, i.e. the number of sarcomeres on one myofibril does not match the number of the adjacent one (fig. 3.8 A'–C', asterisk). Analogous structures can be found in eccentric exercised muscle, where new sarcomeres are inserted to adapt the sarcomeric organization to increased strain (Yu *et al.*, 2003). The addition of new sarcomeres is a stepwise process, which is characterized by an altered localization of myofibrillar components compared to normal adult muscle. Actin filaments lose their I-band organization and span these areas continuously and Z-disc components like  $\alpha$ -actinin and titin are incorporated by and by in a dotted fashion displaying the new number of sarcomeres and the final layout of the myofibril (Yu und Thornell, 2002; Yu *et al.*, 2003). In H-2K myotubes of the late phase, Z-disc epitopes of titin were perfectly aligned all over the cell (fig. 3.9 A, arrow) underlining the strong myogenic potential of this cell line. As observed with the  $\alpha$ -actinin stain, the regular striation was interrupted by areas displaying delta-shaped structures representing sites of a mismatch of sarcomere number (fig. 3.9 A, asterisk). These irregularities were also reflected by the actin filament organization. Although the myotube showed a clear I-band array throughout the whole cell (fig. 3.9 B, arrow), regions of supernumerary sarcomeres could be identified as delta-shaped structures (fig. 3.9 B, asterisk).

In summary, H-2K cells develop contractile myotubes after 5 days of differentiation, which are able to contract for 3 to 4 days, whereby the myotubes change their morphology. At the onset of contraction, the myofibrils already show mature cross-striation but they are not well-aligned laterally. As contraction is indispensable for proper muscle development, the order of the sarcomere arrangement improves and the myotubes contain larger regions of perfectly aligned myofibrils. Nevertheless, these cells still possess areas, where the number of Z-discs and M-bands to be fused does not match therefore demanding further adjustment. This level of sarcomere assembly defines the final stage of H-2K differentiation capability because upon constant contraction the cells will lose their attachment thus impeding further maturation. Furthermore, in adult skeletal muscle the nuclei are located directly underneath the plasma membrane. All H-2K myotubes harbouring a well-developed striated pattern of Z-disc components reveal centrally located



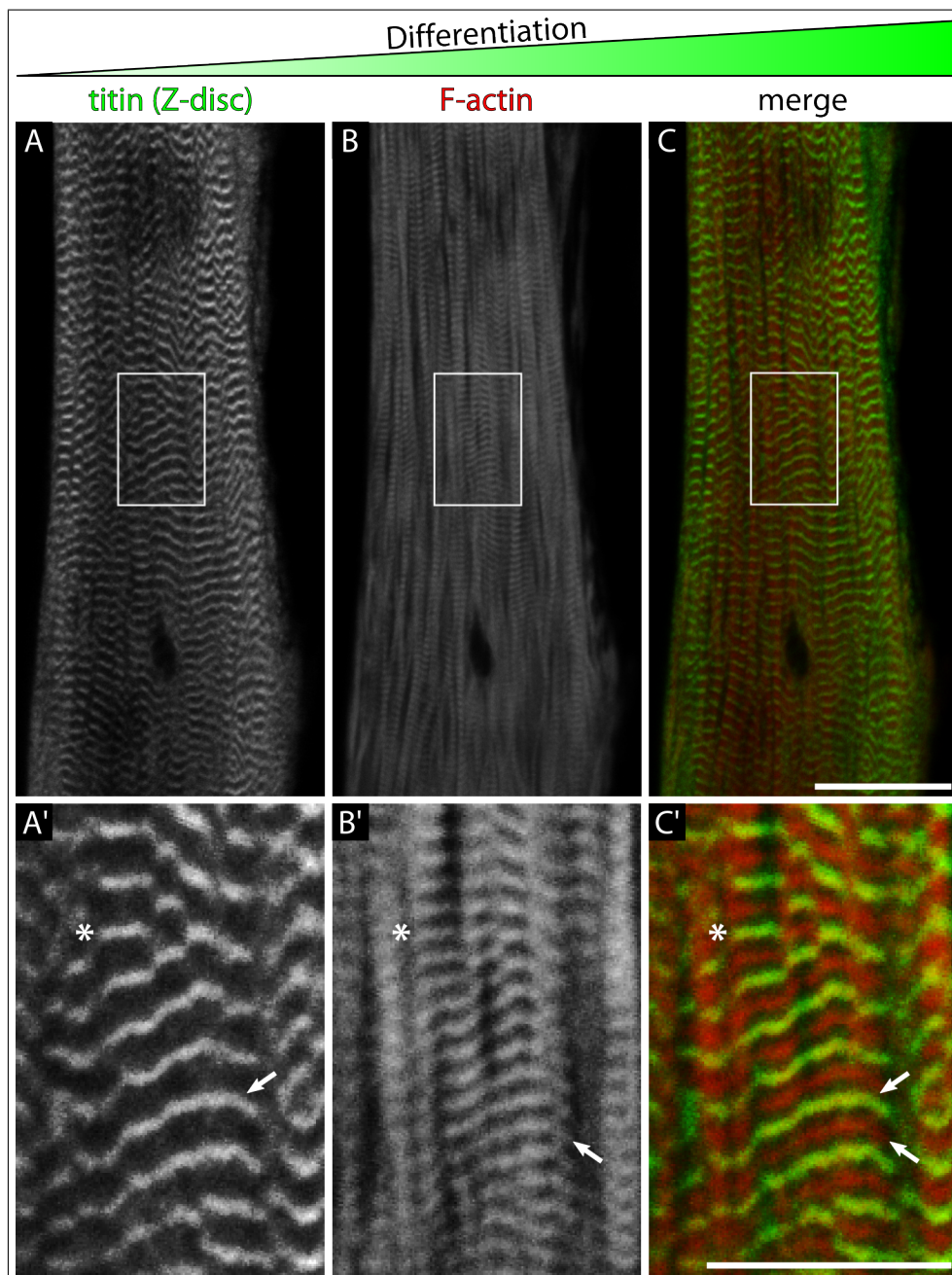


Figure 3.9: **Thin filament arrangement in contractile H-2K myotubes.** Confocal LSM images of a contractile H-2K cell labeled with a titin-specific antibody recognizing a Z-disc epitope and phalloidin to visualize actin filaments. In the merge images titin and F-actin are tinted in green and red, respectively. **A.** At the latest stage of H-2K differentiation, titin reveals an overall cross-striated pattern. **B.** Actin filaments are arranged in I-bands indicated by gaps in the phalloidin stain. **A'.** A detailed view on the striated pattern provides areas of supernumerary sarcomeres marked by delta-shaped arrangement of titin signals (asterisk), which can be differentiated well from sites of perfect sarcomere alignment (arrow). **B'.** The regular organization of the thin filaments (arrow) is also occasionally interrupted by regions of a mismatch of sarcomere number (asterisk). Scale bar 10  $\mu\text{m}$ .

nuclei demonstrating additional deviations from the adult muscle. Thus, although H-2K cells gain contractility and exhibit correctly spaced sarcomeres, there are some significant differences compared to adult muscle *in situ*. Nevertheless, H-2K cells represent a reliable tool for investigating muscle differentiation until the appearance of the first contraction events.

### 3.1.2 Expression Profile of Sarcomeric Proteins

In the previous section localization studies of sarcomeric proteins demonstrated the suitability of H-2K cells to investigate sarcomere development until first contraction events. Although contraction can be observed after 5 days of differentiation (cf. section 3.1), detailed immunofluorescence analysis revealed that contracting myotubes do not reach a phenotype comparable to adult muscle (fig. 3.8 and 3.9). In order to further delineate the course of myofibrillogenesis in H-2K cells, the expression level of sarcomeric proteins was determined. Muscle myosin heavy chain II (MHC II) and myomesin were analysed as representators of the thick filament system and its associated proteins (cf. sections 1.5.2 and 1.5.6). The Z-disc components  $\alpha$ -actinin and filamin C were chosen to outline the development of sarcomeric boundaries (cf. sections 1.5.5.1 and 1.5.5.2). In non-differentiated H-2K myoblasts, non-muscle MHC IIA is the predominant myosin isoform. During myofibrillogenesis the non-muscle myosin isoform is replaced by the respective muscle variant (cf. section 1.2.2.4), so that the expression level of non-muscle MHC IIA can also shed light on the differentiation status. The protein  $\beta$ -catenin is no constituent of the contractile apparatus but, among others, a regulator of muscle development (cf. section 1.9.1.1) and a binding partner of Xin (cf. section 1.10). Thus, its expression level was also measured to reveal putative changes during myofibrillogenesis. The protein content was analyzed in SDS total extracts (cf. section 2.7.5) of H-2K cells of developmental stages starting with non-differentiated cells and finishing with contracting cells at day 8 of differentiation and quantitation performed using the Odyssey infrared laser scanner (cf. section 2.8.1.1). The antibodies used for the detection of the respective proteins are depicted in table 2.8.2. Changes in protein expression level were obtained in relation to tyrosinated  $\alpha$ -tubulin which was identified to show lesser variations during differentiation of H-2K cells than glyceraldehyde-3-phosphate dehydrogenase (GAPDH) (data not shown). The highest ratio of the respective protein and  $\alpha$ -tubulin was set to 100 % or 1.0, respectively.

Nonmuscle MHC IIA was mostly expressed before induction of differentiation (fig.

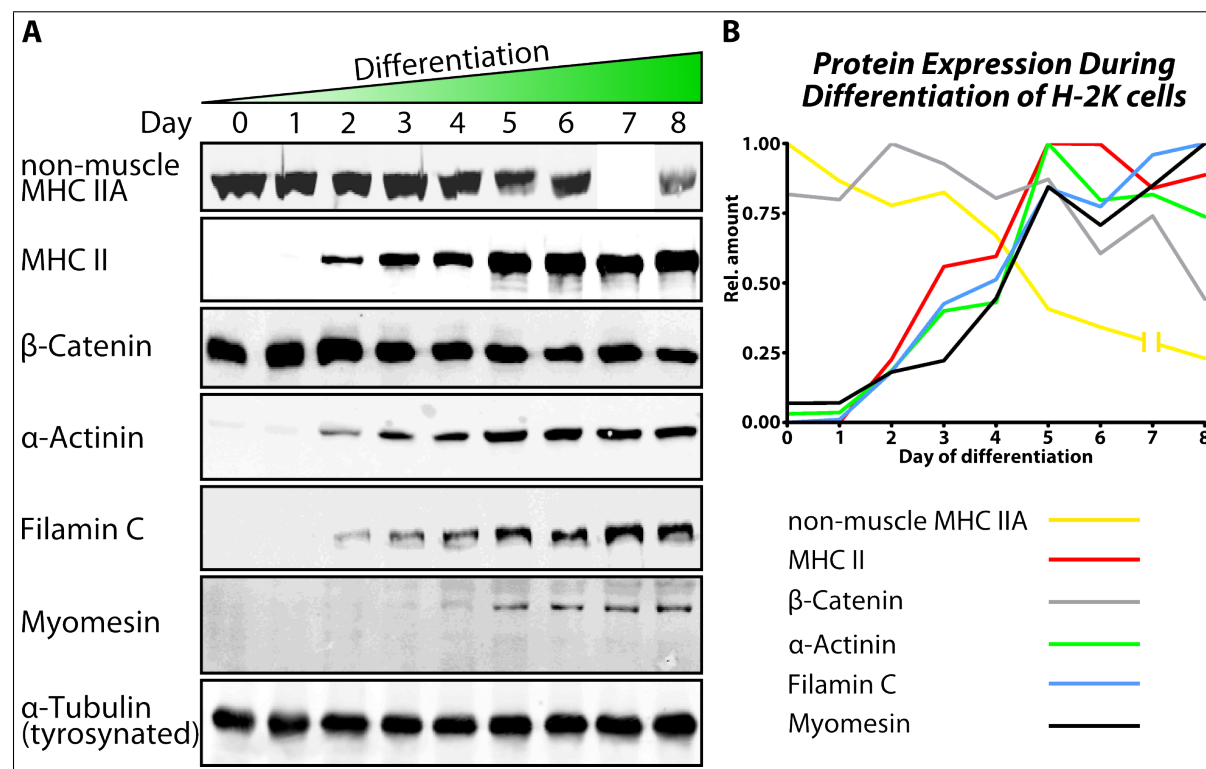


Figure 3.10: **Quantitation of protein expression during myofibrillogenesis of H-2K cells.** Total protein extracts of differentiating H-2K cells were separated with SDS-PAGE and blotted. The respective protein investigated was decorated with a specific antibody and quantified using secondary antibodies coupled with infrared fluorescent dyes and the Odyssey laser scanner. **A.** Non-muscle MHC IIA expression constantly decreases during differentiation but does not disappear completely. The protein amount of day seven could not be analyzed due to a blotting problem. MHC II is firstly detected at day two and the expression level clearly increases throughout myogenic development. Sarcomeric  $\alpha$ -actinin and filamin C exhibit a similar course of protein expression. Very low amounts of  $\alpha$ -actinin can already be seen before induction of differentiation and directly after probably due to spontaneously differentiating cells. Myomesin is expressed at lower levels and considerable amounts can be detected at day five.  $\beta$ -catenin does not show dramatic alterations on protein expression level. Tyrosynated  $\alpha$ -tubulin serves as a loading control. **B.** The course of protein expression is depicted as changes in the ratio of the respective protein and tyrosylated  $\alpha$ -tubulin. The highest ratio was set to 1.0. All myofibrillar proteins display the steepest increase from the beginning of differentiation until day five, the phase of first contraction events. Whereas  $\alpha$ -actinin and MHC II reach their maximum expression at day five, filamin C and myomesin expression increase until day eight. Non-muscle MHC IIA expression decreases by 75%.  $\beta$ -Catenin does not reveal prominent changes in expression level but a moderate decrease can be detected.



3.10). After the beginning of myofibrillogenesis the expression level constantly decreased until day 8 by 75 %. This clearly indicates the progression of myofibrillogenesis and sarcomere maturation but also shows that there still exists a considerable amount of cells containing the non-muscle isoform. On the one hand this is due to cells which did not start differentiation but on the other hand the existing myotubes are still not fully differentiated which fits the observations obtained with fluorescent labeling of sarcomere proteins (cf. section 3.1.1). The more non-muscle MHC IIA expression decreased the more muscle MHC II increased (fig. 3.10) which could be firstly detected at day 2 of differentiation reaching the highest level at day 5, the phase of first contraction events. Upon progression of differentiation a slight reduction of expression was observed. This decrease can be explained by the loss of cells due to contraction thus the number of differentiated cells reduces relative to non-contracting cells. Sarcomeric  $\alpha$ -actinin also showed a comparable phenomenon. Before induction of differentiation the cells expressed very little amounts and the first considerable increase was detected at day 2 similar to MHC II (fig. 3.10). The expression reached maximum level at day 5 and afterwards the protein level decreased a little which was also shown by MHC II. The low but detectable expression level in non-differentiating cells presumably reflects the amount of cells spontaneously starting to enter the myogenic program. Therefore, early markers of differentiation could occasionally be detected although at very low levels. Myofibrillogenesis is characterized by switching to muscle-specific isoforms of certain proteins. The filamin family of proteins comprises the muscle-specific isoform filamin C which was expressed at detectable levels at day 2 (fig. 3.10). In contrast to sarcomeric  $\alpha$ -actinin and MHC II, filamin C reached maximum expression at day 8. However, the increase was strongest between the beginning and day 5 of differentiation. The M-band component myomesin was identified to be expressed later than  $\alpha$ -actinin (cf. section 3.1.1.1) which was confirmed by the protein expression data. Although myomesin could be detected at day 2, the expression level was still very low (fig. 3.10 A). Only at day 4 myomesin was expressed at considerable amounts and reached its maximum expression at day 8. In general, the amount of myomesin was lower than all other proteins of the contractile apparatus tested. While all proteins described before showed dramatic changes in their expression level, the expression of  $\beta$ -catenin displayed only a mild decrease during differentiation (fig. 3.10). Whether this reflected a general tendency of downregulation during myofibrillogenesis is not clear since H-2K cells do not develop proper three-dimensional anchoring structures like costameres (cf. section 1.7) or MTJ's (cf. section 1.6) and  $\beta$ -catenin is preferentially localized to sites of cellular adhesion.

In summary, all myofibrillar components display a strong increase in expression upon induction of myogenic differentiation. Apart from myomesin, which is only detected at significant amounts at day 4, all other sarcomeric proteins reach a considerable expression level at day 2. Some of the myofibrillar components have their highest expression as soon as day 5 ( $\alpha$ -actinin, MHC II), the day of first contraction events, whereas filamin C and myomesin expression raises until day 8. The non-muscle MHC IIA decreases constantly from the beginning of differentiation but does not disappear completely. This underlines the previous observation that H-2K cells gain contractility but still need further maturation to reach an adult phenotype.

## 3.2 Murine Xin in H-2K<sup>b</sup>-tsA58 Myoblasts During Myofibrillogenesis

The Xin-Repeat protein family in mammals comprises cross-striated muscle-specific proteins which can be identified at very early stages of development (cf. section 1.10). In mice, Xin is detected as early as embryonic day 8 in cardiogenic cells and at day 10 in the first rostral somites. Loss of Xin results in muscle defects and therefore it is most likely involved in myofibrillogenesis. In order to gain further insight into the function of Xin and its isoforms, transcription (cf. section 3.2.1), protein expression (cf. section 3.2.2) and its localization were studied during *in vitro* myofibrillogenesis of H-2K cells.

### 3.2.1 Transcription of Murine Xin During Myofibrillogenesis of H-2K<sup>b</sup>-tsA58 Cells

The genomic organization of the murine Xin (mXin) gene is highly homologous to the human orthologue. The gene comprises two exons but the complete coding sequence is only encoded by the second, large exon. Intraexonic splicing events result in 3 different isoforms in human, A, B and C (fig. 3.11 A). This splicing pattern has also been proven for murine Xin (Otten *et al.*, 2010). In order to analyze the transcription level of all isoforms, semiquantitative RT-PCR was performed on RNA of differentiating H-2K cells (cf. section 2.6.3). Three independent differentiation series were analyzed and yielded similar results. As it was only a semiquantitative assay the results of only one series are depicted as a representative. Results were obtained with two different approaches, simplex and duplex PCR's, i.e., separate reaction of the control primer pair and control

primer pair included, respectively.

Transcripts of all Xin isoforms were already present before induction of myogenic differentiation (fig. 3.11 B). To some extent this is presumably due to cells spontaneously differentiating despite of culturing at non-permissive conditions (cf. section 2.10.1.1). These were however only very few cells and cannot account for the relatively high amount of PCR product. Thus, the mRNA of all Xin isoforms is already transcribed before the initiation of differentiation. Primer pairs I–II, amplifying transcripts of the isoforms A and B, generally provided a significantly higher yield than primer pair IV which detected mXin C mRNA (fig. 3.11 B). The PCR reactions with primer pair I and II were performed with only 30 cycles whereas the PCR program of primer pair IV contained 36 cycles (fig. 3.11 C). Accordingly, PCR reactions of the control primer pair HPRT were performed with the respective cycle number enabling quantitation. Therefore, it can be concluded that mXin A and mXin B transcription levels are significantly higher than that of mXin C. The course of transcription levels depended on the primer pair used and the PCR method chosen. In simplex PCR reactions using primer pair I which amplified mRNA's of mXin A and B, the highest ratio between Xin and HPRT could be detected at day 2 of differentiation, afterwards dropping down to about 25 % of the peak value at day 9 (fig. 3.11 D) indicating that the amount of both mRNA species is reduced after the early phase of differentiation (cf. section 3.1). The duplex PCR reaction of primer pair I displayed some differences compared to the simplex PCR. After the induction of differentiation, the transcription level strongly increased at day 1 and remained on high level reaching the peak value at day 5. In the late phase of differentiation, the mRNA amount immediately decreased by about 50 % and did not alter until day 9 (fig. 3.11 E). The mRNA quantitation of mXin A alone using primer pair II revealed a constant decrease from the beginning of differentiation in the simplex assay (fig. 3.11 D). This is completely different from duplex PCR's which showed an increase of mXin A transcription level at day one without prominent changes until day 7. Only in the late phase of differentiation the transcription was reduced below the initial level (fig. 3.11 E). mXin A mRNA was also detected with primer pair III but this reaction was only performed as a simplex assay since the PCR product of HPRT is of similar size as the mXin B product. There, mXin A transcription exhibited the peak value at day 2 followed by a nearly constant reduction until day 9 (fig. 3.11 D). This PCR provided the only opportunity to detect mXin B mRNA alone which showed a different course than mXin A. The highest mXin B transcription level was obtained at day 5 which was about twice as high as the initial level. Afterwards, it decreased again in the late phase of differentiation (fig. 3.11 D). Except

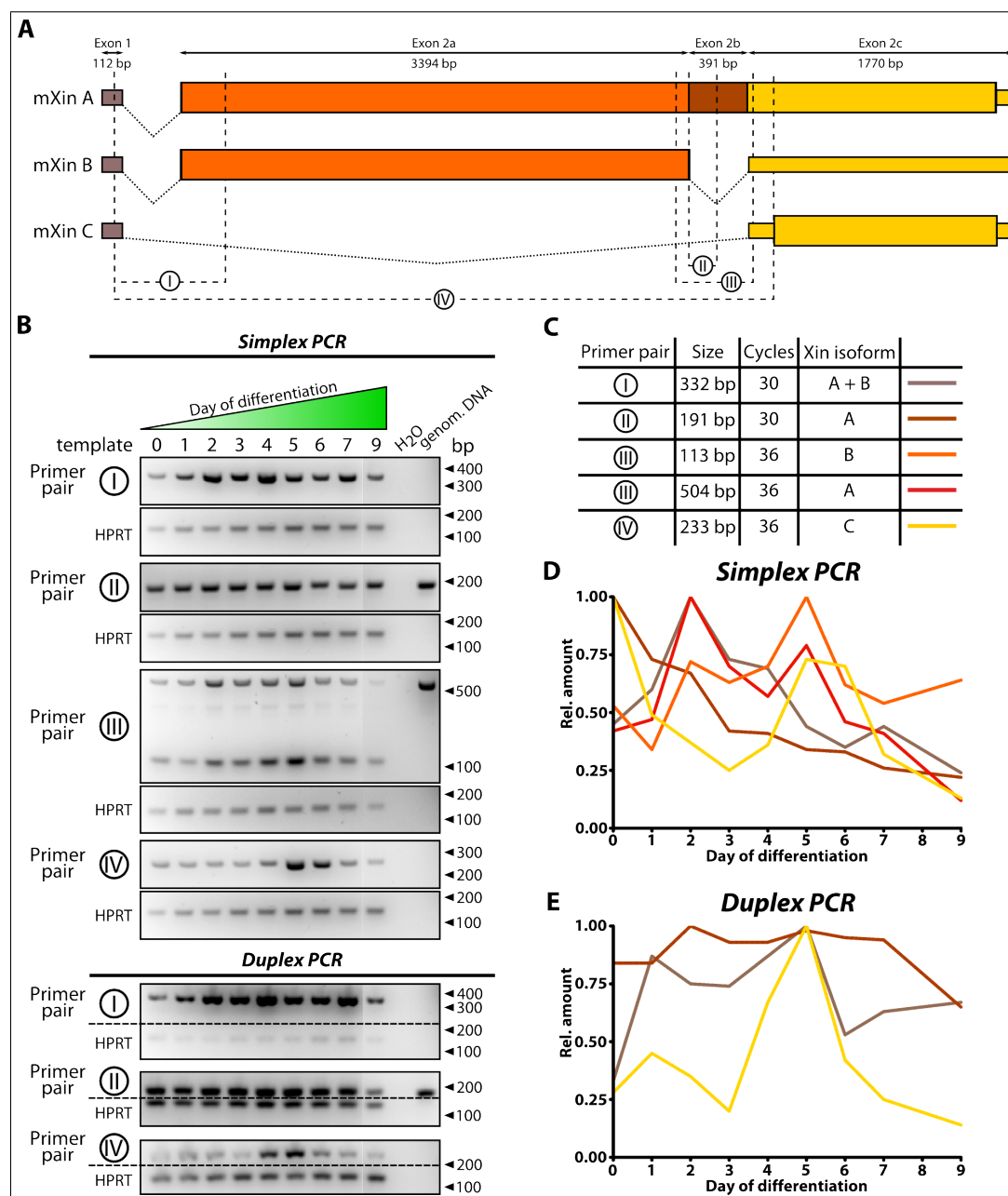


Figure 3.11: **Quantitation of the transcription level of murine Xin isoforms during myofibrillogenesis of H-2K cells.** Quantitation was performed with three independent differentiation series showing essentially the same results. Therefore, only one experiment is depicted. **A.** Schematic overview of the three Xin isoforms and the primer pairs used for semiquantitative RT-PCR. The UTR's are indicated by narrow bars and the coding regions are depicted by a broad bar. **B.** Results of the simplex and duplex RT-PCR's. Lane numbering corresponds to the day of differentiation at which the template RNA for cDNA synthesis was isolated. The mRNA of hypoxanthine phosphoribosyltransferase 1 (HPRT) serves as a reference. Migration distances of PCR products are shown in base pairs (bp). **C.** Tabular overview of the PCR primer pairs, expected product size, number of PCR cycles, detected isoform and the respective colours used in D and E. **D+E.** Changes in the transcription level of murine Xin isoforms in relation to HPRT obtained with either simplex (D) or duplex (E) PCR reactions. The highest ratio between the Xin product and HPRT of each primer pair was set to 1.0.

from the initial transcription level, simplex and duplex PCR reactions of primer pair IV detecting mRNA of mXin C revealed a related development. Both approaches showed a very high or even highest transcription level at day 5 and subsequently a prominent reduction until day 9. The only difference lay in the high initial ratio between mXin C and HPRT in simplex PCR reaction (fig. 3.11 D and E).

In summary, the results vary between the two PCR methods used. However, there are some consistencies enabling some general statements. Murine Xin is transcribed very early in or even before myogenic differentiation. All mXin isoforms seem to reach their maximum transcription level in the early phase around day 2 or at the beginning of their late phase at day 5. In addition, the mRNA level of all isoforms decreases until day 9 leading to the conclusion that transcription is downregulated upon progression of differentiation perhaps after the first contraction events which occur around day 5. A comparison of mXin A and B indicates that there are presumably only slight variations between both isoforms. In general, these isoforms exhibit a higher transcription level than mXin C, as an increased number of cycles in the PCR program of primer pair IV was necessary to detect suitable amounts for quantitation.

### 3.2.2 Protein Expression of Murine Xin During Myofibrillogenesis of H-2K<sup>b</sup>-tsA58 Cells

The analysis of the transcription level of murine Xin isoforms during myofibrillogenesis of H-2K cells revealed that mXin mRNA of all isoforms can be detected very early but transcription is probably downregulated in the late stages of differentiation (cf. section 3.2.1). In order to find out how the course of transcription affects protein expression, total protein extracts of H-2K cells of different developmental stages were quantitatively analyzed for mXin protein expression using the infrared laser scanner Odyssey (cf. section 2.8.1.1). mXin was detected with the  $\alpha$ -XR1B antibody which was raised against the repeat region of human Xin and exhibits cross-reactivity with murine Xin A and Xin B (Eulitz, 2005). The protein expression was quantified in relation to tyrosinated  $\alpha$ -tubulin and the highest ratio was set to 1.0 (cf. section 3.1.2). I produced a new polyclonal antibody against mXin C ( $\alpha$ -mXin C) recognizing the isoforms A and C which was also tested on H-2K cell extracts after purification of the antibody (cf. section 2.8.2.1). The protein amount of these samples was also standardized in relation to tyrosinated  $\alpha$ -tubulin.

Directly before induction of myogenic differentiation, the expression level of mXin A

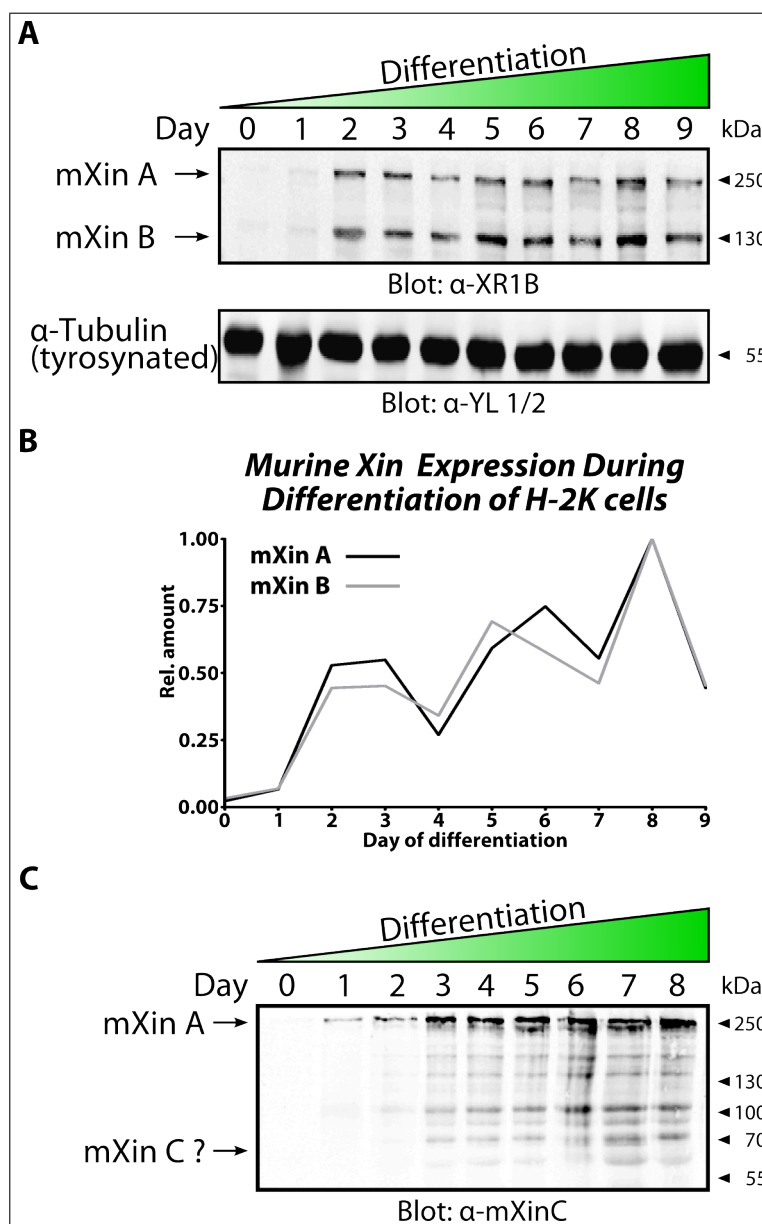


Figure 3.12: **Protein expression of murine Xin during myofibrillogenesis of H-2K cells.** **A.** Blot of protein extracts of a differentiation series of H-2K cells. mXin A and mXin B are decorated by the  $\alpha$ -XR1B antibody and visualized using the Odyssey laser scanner system. Tyrosynated  $\alpha$ -tubulin serves as a loading control. **B.** Quantitation of mXin A and mXin B expression. The highest ratio of mXin and  $\alpha$ -tubulin expression is set to 1.0. Both isoforms display the highest expression at day eight. **C.** Test of the purified polyclonal  $\alpha$ -mXin C antibody on protein extracts of a differentiation series of H-2K cells. The antibody clearly detects mXin A at  $\approx$  250 kDa but mXin C cannot be assigned to a protein band beyond doubt. Migration distances are shown in kDa.

and B was nearly below the detection limit (fig. 3.12 A). Two faint bands could be detected which migrated at 250 kDa and 130 kDa corresponding to mXin A and B, respectively. The intensity of both bands increased slightly at day 1 so that mXin A and B were still weakly expressed but clearly detectable. Between day 1 and day 2, the protein expression of both isoforms raised most prominently (fig. 3.12 B). The highest expression level was reached in the late phase at day 8 showing a general trend to increase during differentiation. Afterwards, the expression dropped down again to half of the highest ratio. In comparison to the course of transcription level of mXin A and B mRNA, the changes in protein amount differed a little. While the amount of mXin A and B transcripts showed already quite a high level before starting the differentiation process (cf. section 3.2.1), the protein remained nearly undetectable (fig. 3.12 A). These low protein levels derived from spontaneously differentiating cells which could be occasionally identified directly before induction of differentiation. During the early phase of differentiation, both the mRNA and the protein level increased (fig. 3.12 B). However, upon further progression, only the protein level showed a constant increase, whereas mXin A and B transcription exhibited no homogenous trend because of deviating results from simplex and duplex PCR's. Nevertheless, the protein expression also exhibited a decrease in the late phase of differentiation similar to the reduction of mXin transcription although reduction in transcription started earlier at day 5. This reduction could not be attributed to the loss of contracting cells for the expression level of Xin was very low at this stage (cf. section 3.2.3) thus more likely indicating downregulation. The faint bands between 130 kDa and 250 kDa were most prominently seen at day 9 of differentiation and most probably reflected proteolysis. Finally, it must be stated that the protein expression level rapidly increased directly after induction of differentiation presumably due to the high level of mRNA already present at this stage. The decrease in protein amount at the end of differentiation was preceded by a reduction of transcription as early as day 5.

The new polyclonal antibody raised against murine Xin C detected a prominent band migrating around 250 kDa at day 1 which represented mXin A (fig. 3.12 C). Below this signal, there were up to seven distinct bands which could not be identified with the antibody  $\alpha$ -XR1B directed against the Xin repeats. The calculated molecular weight of mXin C approximates 54 kDa but no protein bands could be observed in the molecular weight range below 55 kDa (data not shown). The recombinant protein expressed in *E. coli* migrated between 55 kDa and 70 kDa which is presumably due to the high proline content of 10 % (fig. 3.39 and 3.41). The smallest polypeptide identified by the  $\alpha$ -mXin C antibody was located in this molecular weight range and occurred at day 3.



The intensity increased until day 7 and is again reduced at day 8. This applied to all other polypeptides bound by the antibody thus no band revealed a distinctive regulation during myofibrillogenesis of H-2K cells. Therefore, mXin C cannot be clearly assigned to a protein band. In human heart, Xin C is upregulated in samples of patients suffering from hypertrophic cardiomyopathy but absent in normal adult heart (Otten *et al.*, 2010). Consequently, it needs to be considered that the expression level of mXin C might be very low and is presumably lower than that of mXin A and mXin B as supported by the measurement of the mRNA level (cf. section 3.2.1) which could impair its detection. Furthermore, the signals below mXin A resemble proteolytic fragments because such proteolytic cleavage can be prominently seen upon recombinant expression of Xin isoforms in *E. coli* (data not shown). However, extensive proteolysis cannot be detected with the  $\alpha$ -XR1B antibody thus the exact character of the numerous bands remains to be determined.

### 3.2.3 Xin Localization During *In vitro* Myofibrillogenesis of Murine H-2K<sup>b</sup>-tsA58 Cells

The expression level of murine Xin isoforms A and B is upregulated during myofibrillogenesis but seems to decrease when reaching late phases (cf. section 3.2.2). Although Xin is an early marker of muscle development and exhibits dramatic dislocalization in different types of myofibrillar myopathies (cf. section 1.10), the function remains to be elusive. Therefore, the exact localization of Xin during myofibrillogenesis of H-2K cells was defined in relation to the key components of myofibril formation  $\alpha$ -actinin, filamin C and nonmuscle MHC IIA.

#### 3.2.3.1 Xin and $\alpha$ -Actinin

Sarcomeric  $\alpha$ -actinin is one of the first structural components of the myofibrillar apparatus identified at the onset of myofibrillogenesis of H-2K cells. As co-stainings of  $\alpha$ -actinin and Xin repeats reveal, some cells already expressed  $\alpha$ -actinin but no Xin immediately after the initiation of myogenic differentiation (fig. 3.13 A-C). At this early stage,  $\alpha$ -actinin was continuously associated with actin filaments especially in the cell periphery. When Xin expression started,  $\alpha$ -actinin was already decorating some actin filaments in a dotted pattern displaying spacings of around 2  $\mu\text{m}$  (fig. 3.13 E, arrowheads). These filaments were only weakly associated with Xin in contrast to peripheral cellular extensions where the Xin signal was more intense and colocalized with  $\alpha$ -actinin (fig. 3.13 D-E, arrows). Xin showed only continuous decoration of actin filaments similar to  $\alpha$ -actinin at these sites.



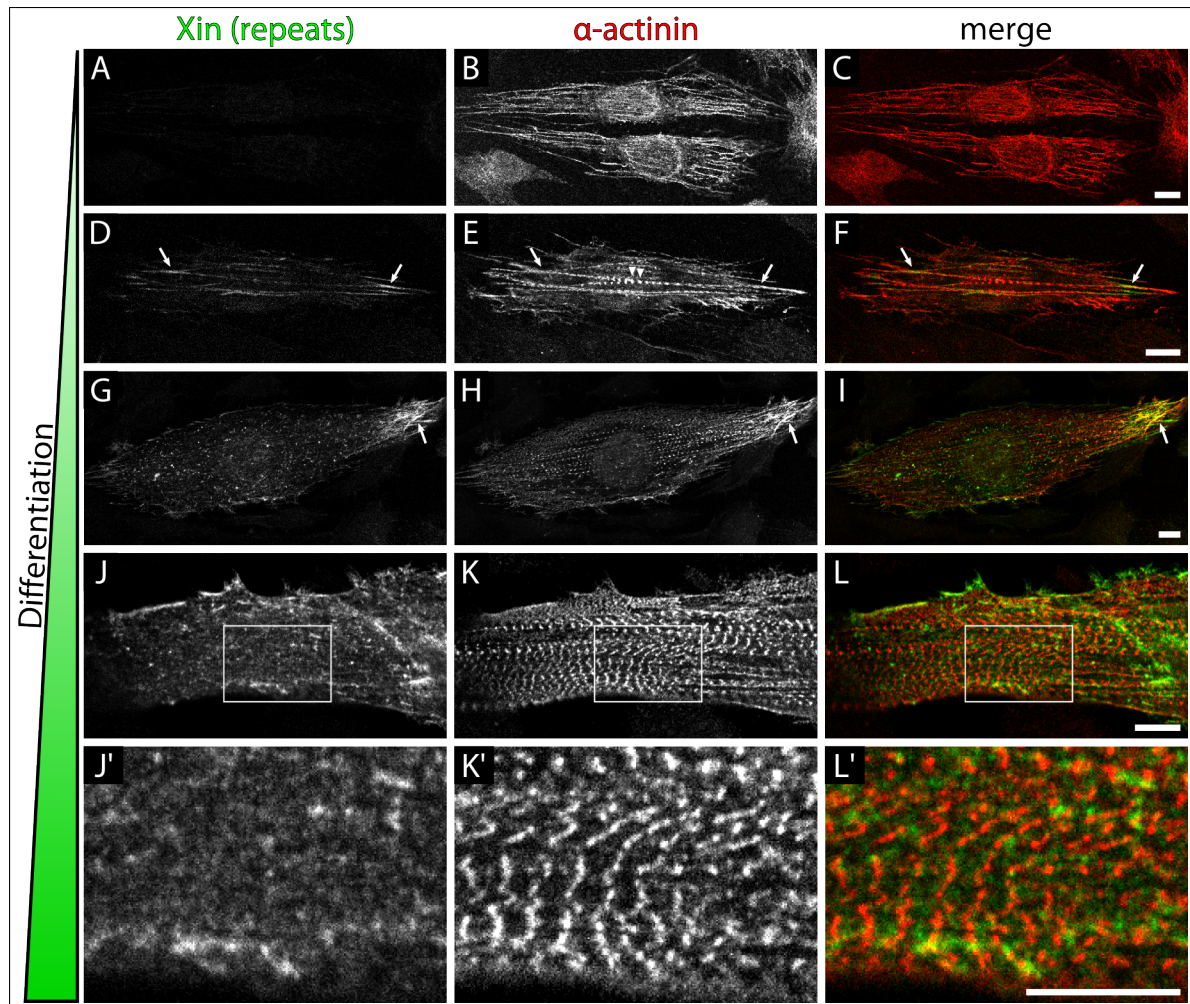


Figure 3.13: **Localization of Xin and  $\alpha$ -actinin during myofibrillogenesis of H-2K cells.** Confocal LSM images of a differentiation series of H-2K cells labeled with antibodies against Xin-Repeats and sarcomeric  $\alpha$ -actinin. In merge images (C, F, I, L, L') Xin and  $\alpha$ -actinin are tinted green and red, respectively. **A.** Already differentiating cells do not necessarily express Xin, even if  $\alpha$ -actinin can be already detected **B.** **D.** When Xin is expressed, it targets to actin filaments in the periphery in a continuous pattern (arrows) but not directly to the tip. **E.** Some actin filaments already show a dense-body-like association of  $\alpha$ -actinin (arrowheads) and no prominent Xin localization can be detected there. **G.** Xin distribution changes into a punctate pattern in the cell body and a submembranous targeting. At peripheral cellular extensions, actin filaments displaying an intense and continuous decoration with Xin exist (arrow). **H.** These actin filaments are also continuously associated with  $\alpha$ -actinin although most actin filaments have transformed into early myofibrils indicated by the dense-body-like association of  $\alpha$ -actinin. **J.** In late stages of differentiation, Xin-containing dots and submembranous targeting are still observed. **K.** The cell body contains a quite regular array of premature Z-discs. **J'-L'.** Magnification revealed that the myofibrils are still not perfectly aligned and Xin shows no prominent colocalization with  $\alpha$ -actinin. Scale bar 10  $\mu$ m.

However, Xin was not localized to the tips of these filaments in contrast to  $\alpha$ -actinin which showed strong targeting there. In the course of differentiation, Xin localization changed into an apparently randomly distributed punctual pattern in the cell body and a weak presumably submembranous targeting at the cell periphery (fig. 3.13 G). Nevertheless, some cellular extension sites existed where Xin strongly decorated actin filaments which were also regularly associated with  $\alpha$ -actinin (fig. 3.13 G-I, arrow). At this stage,  $\alpha$ -actinin staining mainly revealed a dense-body-like distribution along early myofibrils. Upon further differentiation, these precursor structures of Z-discs aligned longitudinally and fused laterally to form a regular array of sarcomere boundaries. Xin remained mainly localized near the plasma membrane and only few Xin-containing dots were detected in the cell body (fig. 3.13 J-L). Although Z-discs were still not perfectly aligned, Xin exhibited no clear targeting in these regions (fig. 3.13 J'-K').

In conclusion, it is clearly demonstrated that Xin is expressed later than sarcomeric  $\alpha$ -actinin but still at very early stages. Then Xin partially decorates actin filaments predominantly in the cell periphery. This continuous association changes into a punctate distribution in the cell body and submembranous targeting which does not alter in the late stages of differentiation.

### 3.2.3.2 Xin and Filamin C

Filamin C is the first muscle-specific binding partner of Xin A and a prominent constituent of the sarcomeric Z-disc (van der Ven *et al.*, 2006, 2000a). While resting myoblasts only express filamin A, the nearly ubiquitously expressed family member, an isoform switch to filamin C expression is induced at the onset of the myogenic program. Simultaneous tracking of filamin C and Xin expression during myofibrillogenesis of H-2K cells can therefore provide new insights into the function of Xin and the Xin-filamin interaction. Filamin C was identified using a polyclonal anti-filamin C antibody (tab. 2.8.2) raised against the linker region between Ig-like domains 23 and 24 and the Ig-like domain 24 itself. However, blot analysis of recombinant fragments of all filamin family members comprising the respective region revealed that there is a modest cross-reactivity with isoforms A and B but with lower affinity (P. van der Ven, personal communication). Nevertheless, during myofibrillogenesis filamin C is the predominant isoform expressed so that the signal provided by this antibody basically reflects filamin C.

In early differentiating H-2K cells, both Xin and filamin decorated actin filaments (fig. 3.14 A-C), especially at peripheral cellular extensions (arrow) and underneath the

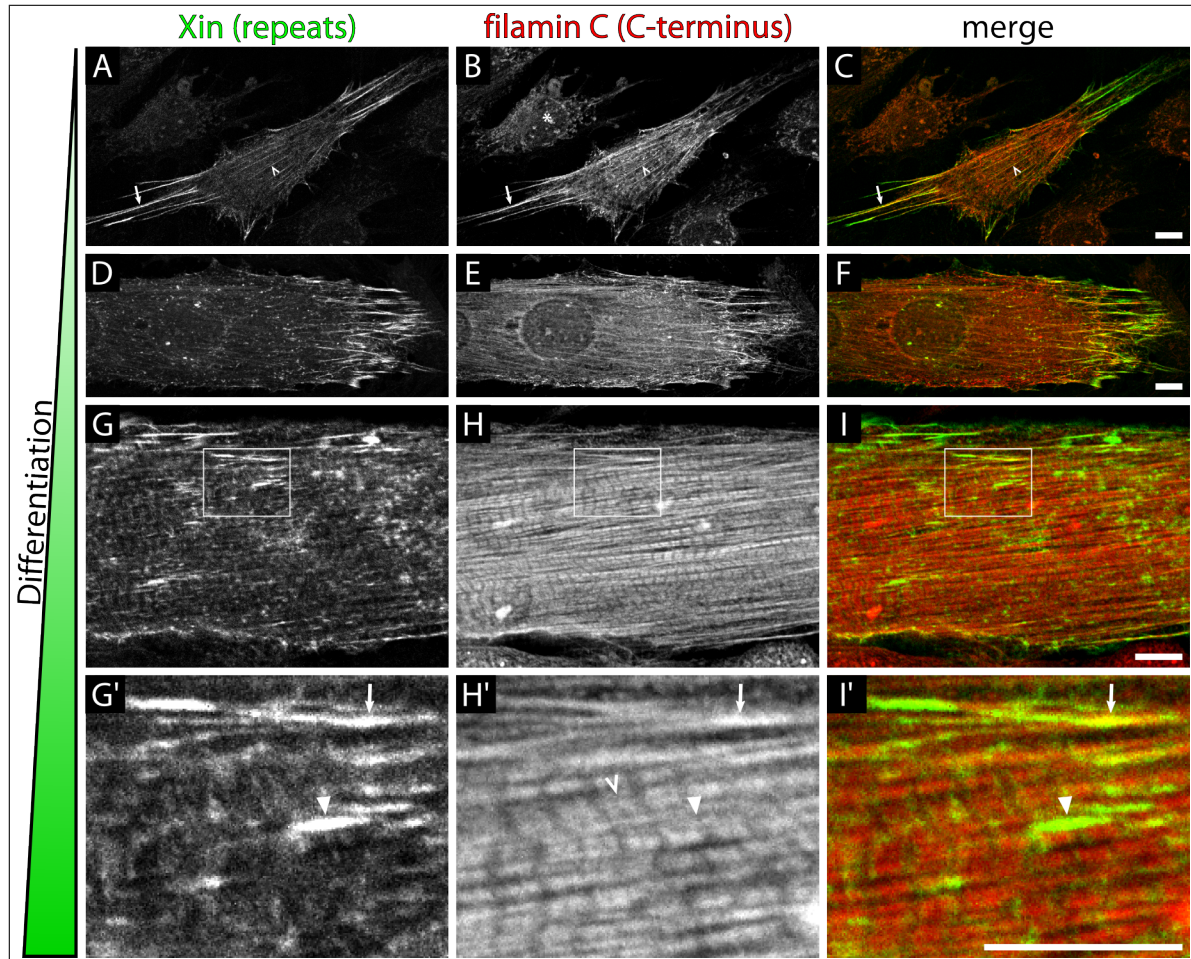


Figure 3.14: **Localization of Xin and filamin C during myofibrillogenesis of H-2K cells.** Confocal LSM images of a differentiation series of H-2K cells labeled with antibodies against Xin-Repeats and the C-terminus of filamin C. In merge images (C, F, I, I') Xin and filamin C are tinted green and red, respectively. **A.** At the beginning of differentiation Xin decorates actin filaments at peripheral cellular extensions (arrow) and below the nucleus (open arrowhead). **B.** There, filamin C colocalizes with Xin and continuously decorates actin filaments at cellular extensions and below the nucleus. **D.** Xin expression remains restricted to peripheral cellular extensions upon further differentiation and displays a punctate pattern in the cell body. **E.** Filamin C is associated with actin filaments or early myofibrils throughout the whole cell. **G.** In late myotubes, Xin is still associated with actin filaments which have not developed into myofibrils yet and displays a punctate distribution in regions of sarcomeric arrangement. Additionally, a very weak decoration of Z-discs can be detected. **H.** Filamin C exhibits Z-disc-like array albeit occasionally disrupted by immature myofibrils. **G'.** Xin longitudinally connects immature Z-discs (arrowhead) and continuously decorates actin filaments in the periphery (arrow). **H'.** Filamin C colocalizes with Xin at these actin filaments (arrow). The Z-disc signal obtained with this antibody provides a broader band than with an antibody detecting the N-terminus. Occasionally, a gap can be detected in between (open arrowhead) then appearing as a band doublet. Scale bar 10  $\mu\text{m}$ .



nucleus (open arrowhead) and exhibited a wide colocalization. Due to the cross-reactivity of the filamin antibody with other filamin isoforms, the chronology of the emergence of Xin and filamin C could not be determined, which was indicated by the staining of resting myoblast (asterisk). Multinucleated myotubes at the intermediate stage again displayed the apparently randomly distributed punctate pattern of Xin and a weak membranous targeting (fig. 3.14 D). However, at the periphery of the myotube Xin was still strongly enriched at cellular extensions. Filamin C could be also detected there but additionally it bound continuously to actin filaments or early myofibrils throughout the whole myotube (fig. 3.14 E). In late stages of H-2K differentiation, filamin C localization revealed Z-disc organization although sarcomere arrangement was still not perfect (fig. 3.14 H). Interestingly, the antibody directed against the C-terminus provided a broader band than those obtained with an antibody against the N-terminus (fig. 3.70 and 3.81). The band width was about 1,3  $\mu\text{m}$  and occasionally a small gap could be detected in between (open arrowhead). Given that this gap is the center of the Z-disc, these stainings showed that the C-terminus of filamin C is not located in the Z-disc center but distributed up to 650 nm away. Xin is not a constituent of the sarcomeric Z-disc in adult muscle although a weak Z-disc staining could be detected (fig. 3.14 G). Probably this targeting disappears upon further differentiation. The major localization of Xin in this phase was a continuous decoration of actin filaments and an even association with filamin C but no Z-disc precursor structures (arrows). Within the developing contractile apparatus, Xin longitudinally connected Z-discs of premature sarcomeres (arrowhead).

These stainings reveal that Xin and filamin C colocalize on actin filaments especially at peripheral cellular extensions at early stages of differentiation. While filamin C keeps to be associated with actin filaments throughout the whole myotube, Xin expression remains mainly restricted to the periphery. In later phases of differentiation, Xin longitudinally connects Z-discs of immature sarcomeres and filamin C exhibits Z-disc arrangement. Since the signals obtained with the antibody directed against the C-terminus of filamin C provide broader Z-discs, it is tempting to assume that the C-terminus of filamin C is pointing away from the Z-disc center.

### 3.2.3.3 Xin and Nonmuscle Myosin IIA

The shift from nonmuscle myosin to muscle myosin II during sarcomere development represents the key event of the transition from premyofibrils to nascent myofibrils (cf. section 1.2.2.4). Changes in the localization and the disappearance of nonmuscle myosin II there-

fore clearly indicate the developmental phase of differentiating cells. The predominant nonmuscle myosin II variant in H-2K cells is isoform IIA. Nonmuscle myosin IIB, characteristic for embryonic cardiomyocytes, could not be detected in H-2K cells neither in protein extracts on blots nor in fixed cells using immunofluorescent labeling. Due to a lack of a suitable antibody, the third nonmuscle isoform IIC was not investigated. Protein expression analysis in total extracts of a differentiation series of H-2K cells has confirmed downregulation of nonmuscle myosin IIA especially during the intermediate phase (cf. section 3.1.2). In order to reveal a potential function of Xin during the muscle myosin II incorporation, differentiating H-2K cells were stained with antibodies detecting Xin A and B and nonmuscle myosin heavy chain (MHC) IIA (tab. 2.8.2).

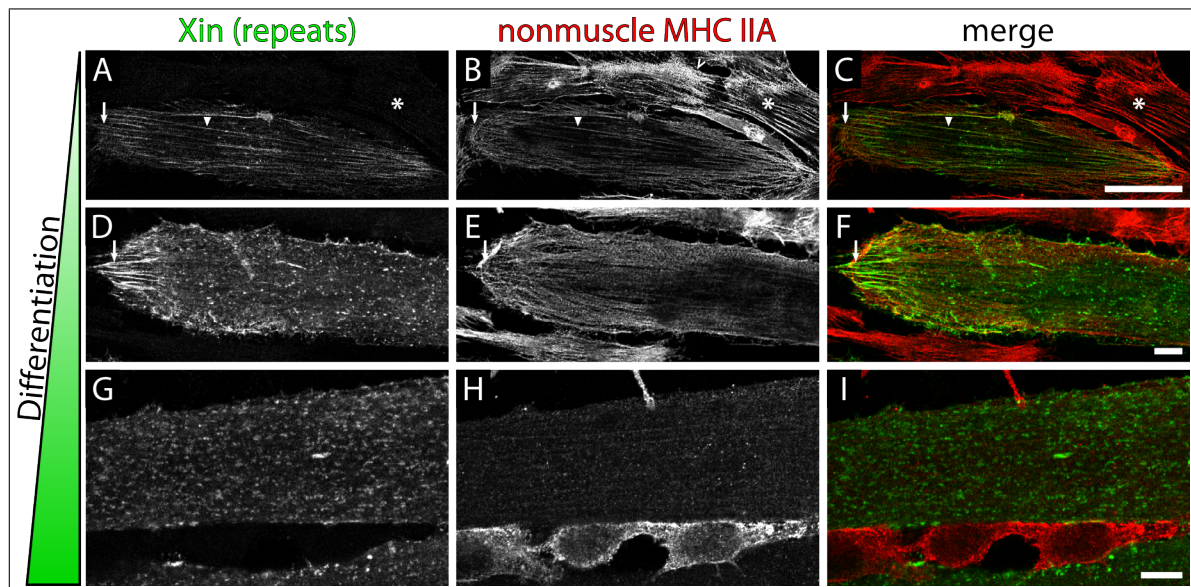


Figure 3.15: **Localization of Xin and nonmuscle myosin IIA during myofibrillogenesis of H-2K cells.** Confocal LSM images of a differentiation series of H-2K cells labeled with antibodies against Xin-Repeats and the heavy chain of nonmuscle myosin IIA. In merge images (C, F, I) Xin and nonmuscle myosin IIA are tinted green and red, respectively. **A.** Xin cannot be detected in non-differentiating myoblasts (asterisk) but decorates actin filaments spanning the whole cell (arrowhead) and peripheral cellular extensions (arrow). **B.** Nonmuscle myosin IIA is expressed in non-differentiating myoblasts (asterisk) and occasionally exhibits a banded pattern (open arrowhead). It can also be identified along the actin filaments decorated by Xin (arrowhead) and filopodia-like extensions (arrow). **D.** In early myotubes, Xin-containing extensions still exist (arrow) but the localization has changed into an apparently random punctate distribution. **E.** Nonmuscle myosin is still associated with cellular extensions albeit weakly (arrow). Early myotubes contain premyofibrils throughout the whole cell indicated by the periodical pattern of nonmuscle myosin IIA. **G.** In contractile myotubes, Xin still appears to be randomly distributed as dots or short filamentous structures. **H.** Nonmuscle myosin IIA expression is dramatically reduced and it has nearly disappeared from the emerging sarcomeres indicating the incorporation of muscle myosin II. Cells still expressing nonmuscle MHC IIA represent non-differentiated cells. MHC, myosin heavy chain. Scale bar 10  $\mu$ m.

Proliferating H-2K myoblasts contained significant amounts of nonmuscle myosin IIA

which displayed prominent association with stress fibres (fig. 3.15 B, asterisk). The periodic incorporation resulted in a banded pattern (fig. 3.15 B, open arrowhead). After induction of myogenic differentiation, Xin expression rised and bound predominantly to actin filaments in the periphery which appeared to form peripheral cellular protrusions (fig. 3.15 A, arrow). These filaments were also labeled with nonmuscle myosin IIA (fig. 3.15 B, arrow) but in contrast to Xin its localization was not restricted to these filaments as cortical actin also contained nonmuscle myosin IIA. Some of the actin bundles spanned the whole cell and exhibited association with both Xin and nonmuscle myosin IIA (fig. 3.15 A+B, arrowhead). Upon further differentiation, Xin localization changed and Xin-decorated actin filaments spanning the entire early myotube could no longer be detected (fig 3.15 D). On the contrary, except from peripheral cellular extensions (arrow), Xin exhibited an apparently random punctate distribution. At this stage, nonmuscle myosin IIA was still prominently expressed and revealed a more or less ordered periodical pattern in regions of the myotube where Xin showed its punctate pattern (fig. 3.15 E). Xin-containing cellular extensions still contained low amounts of nonmuscle myosin IIA (arrow). In contractile myotubes, nonmuscle myosin IIA expression was dramatically reduced indicating the incorporation of muscle myosin II (fig. 3.15 H). The distribution of Xin had not changed apparently at this stage since there were still Xin-containing dots and short filamentous structures (fig. 3.15 G). However, the number of these structures seemed to be increased.

Labeling of nonmuscle myosin IIA in differentiating H-2K cells clearly demonstrates changes in the cytoskeleton during sarcomere development. While stress fibres are also prominently associated with nonmuscle myosin IIA in non-differentiating myoblasts, upon further progression of myofibrillogenesis its localization changes into a periodical pattern in multinucleated myotubes of intermediate stage until its expression is downregulated when muscle myosin II is incorporated into premyofibrils and the myotube gain its contractility. Nonmuscle myosin IIA and Xin colocalize on actin filaments in the early phase of differentiation. Xin localization is altered into an apparently random punctate pattern when nonmuscle myosin IIA-containing premyofibrils have formed throughout the early myotube. After the incorporation of muscle myosin II, Xin is still detectable whereas nonmuscle myosin IIA has nearly disappeared. Thus, Xin function is still needed when nascent myofibrils have formed and nonmuscle myosin IIA is no longer expressed.

### 3.2.3.4 Xin and $\beta$ -Catenin

The armadillo repeat protein  $\beta$ -catenin is an important regulator of embryogenesis including muscle development and a component of cadherin-based cellular junctions (cf. sections 1.2.1 and 1.9.1.1). Additionally, it has been shown to be a novel interaction partner of Xin-Repeat-containing Xin isoforms A and B (cf. section 1.10). The function of this novel interaction still remains to be determined but it has been speculated that Xin links the adherens junction complex in ICD's of the heart to the actin cytoskeleton (Choi *et al.*, 2007). In order to unravel a potential function of this interaction during myofibrillogenesis of H-2K cells, differentiating cells were stained with antibodies against Xin and  $\beta$ -catenin (see tab. 2.8.2).

In non-differentiating H-2K cells,  $\beta$ -catenin was expressed and mainly localized in the cytoplasm (fig. 3.16 B). A weak accumulation could be detected at cell-cell contacts (arrowhead) and occasionally at the membrane (open arrowhead). The cellular distribution did not change upon induction of differentiation since membranous staining and cytoplasmic localization remained unaffected (fig. 3.16 E). Typical sites of Xin targeting, as peripheral cellular extensions, were not prominently labeled with  $\beta$ -catenin (fig. 3.16 D-F, arrow). While  $\beta$ -catenin was highly enriched at cellular junctions (arrowhead and open arrowhead), Xin did not clearly colocalize there (arrowhead) or exhibited a submembranous localization with only a narrow overlap (open arrowhead), if at all. Elongating multinucleated myotubes of intermediate stage did not show any alterations in  $\beta$ -catenin distribution compared to the non-differentiated stage although these myotubes contained regions of different developmental stages (fig. 3.16 G-I). Neither in regions presumably harbouring pre- and nascent myofibrils indicated by the punctate localization of Xin nor in earlier stages marked by strong Xin decoration of actin filaments (arrow)  $\beta$ -catenin revealed any deviation of its cytoplasmic and junctional distribution (arrowhead) and no colocalization with Xin (arrow). Contractile myotubes yielded the same results (data not shown). Thus,  $\beta$ -catenin localization remains mainly unaffected by myogenic differentiation of H-2K cells and displays no prominent colocalization with Xin. Therefore, the function of this interaction during myofibrillogenesis is still elusive.

### 3.2.3.5 Xin Isoforms

Antibodies raised against Xin repeats can only detect the isoforms A and B. A new polyclonal antibody directed against murine Xin C ( $\alpha$ -mXin C) offers the opportunity to discover similarities and differences between Xin isoforms during differentiation of H-2K



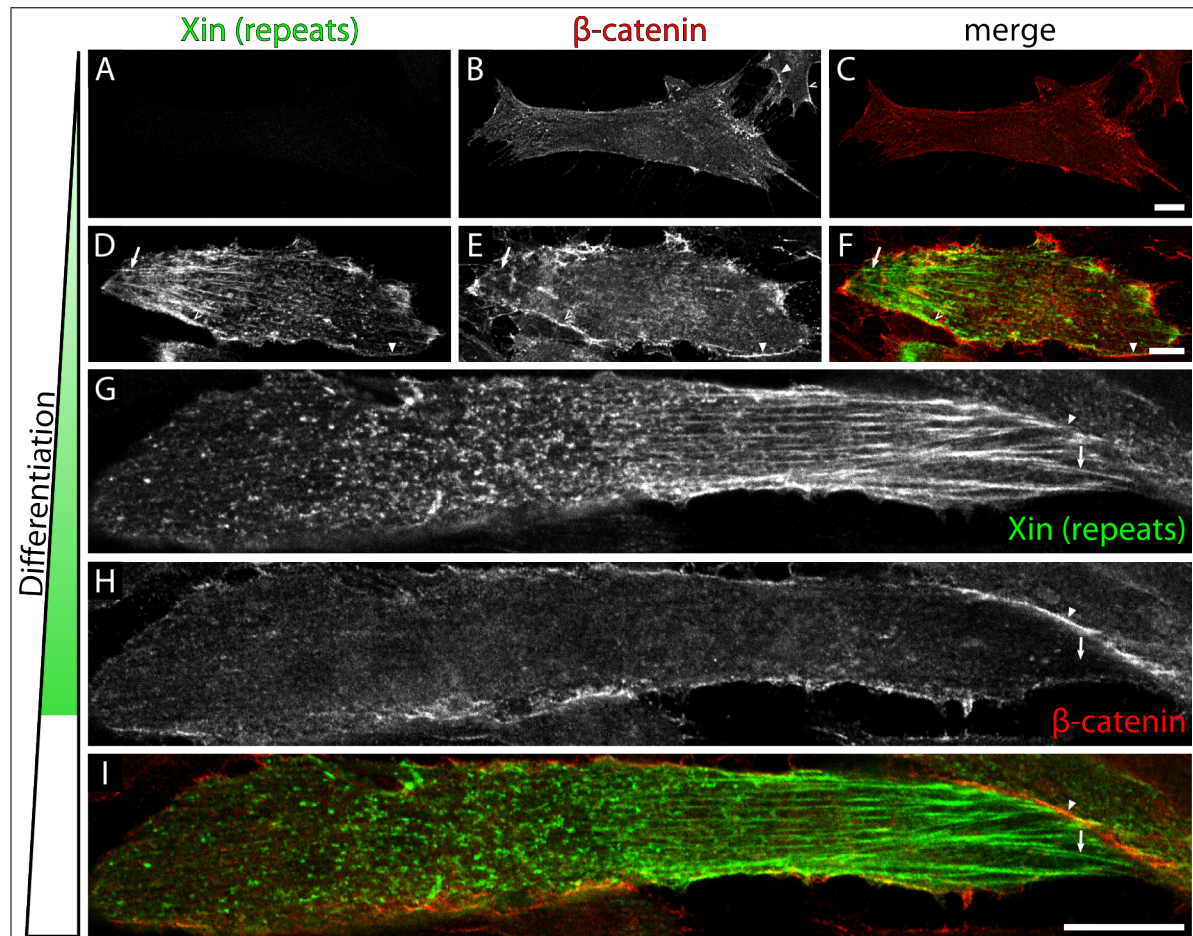


Figure 3.16: **Localization of Xin and  $\beta$ -catenin during myofibrillogenesis of H-2K cells.** Confocal LSM images of a differentiation series of H-2K cells labeled with antibodies against Xin-Repeats and  $\beta$ -catenin. In merge images (C, F, I) Xin and  $\beta$ -catenin are tinted green and red, respectively. **A.** Xin cannot be detected in non-differentiating myoblasts. **B.**  $\beta$ -Catenin is mainly localized in the cytoplasm and occasionally shows enrichment at cell-cell contacts (arrowhead) or at the membrane (open arrowhead). **D.** Upon induction of differentiation Xin expression is upregulated and targets to peripheral cellular extensions (arrow). At cellular junctions, Xin does not exhibit strong targeting (arrowhead) or only submembranous localization (open arrowhead). **E.** Differentiation does not alter  $\beta$ -catenin localization, i.e. it is still enriched at cell-cell contacts (arrowhead). Peripheral cellular extensions are not prominently decorated (arrow). Direct colocalization with Xin cannot be observed at sites of submembranous Xin targeting (open arrowhead). **G.** Elongating multinucleated myotubes of intermediate stage comprise areas of premyofibril or nascent myofibril state indicated by punctate distribution of Xin and regions of earlier differentiation state since Xin continuously decorates actin filaments (arrow). There is no prominent labeling of cell-cell contacts (arrowhead). **H.** Prominent targeting of  $\beta$ -catenin to cell-cell contacts (arrowhead) but no association with actin filaments (arrow). Scale bar 10  $\mu$ m.



cells. In total protein extracts of H-2K cells, this antibody reliably decorates Xin A but a clear detection of Xin C failed (cf. section 3.2.2). In order to reduce background signals and increase the concentration, the  $\alpha$ -mXin C antibody was purified prior to utilization in immunofluorescent labeling (cf. section 2.8.2.1).

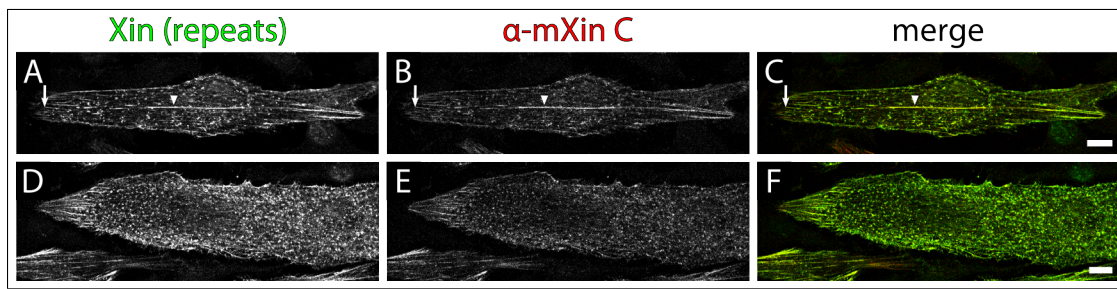


Figure 3.17: **Localization of Xin isoforms during myofibrillogenesis of H-2K cells.** Confocal LSM images of a differentiation series of H-2K cells labeled with antibodies against Xin-Repeats and Xin C-terminus ( $\alpha$ -mXin C). In merge images (C, F) Xin-Repeats and the C-terminus of Xin are tinted green and red, respectively. **A-C.** Both antibodies provide the localization known for Xin in early differentiating myoblast. Xin decorates peripheral cellular extensions (arrow) and is associated with actin filaments in the cell body (arrowhead). In this cell, a dotted-like distribution of Xin is already quite prominent. **D-F.** At the intermediate stage, punctate distribution of Xin dominates throughout the whole myotube. In the periphery there are still filopodia-like extensions labeled with Xin. Scale bar 10  $\mu$ m.

In early differentiating H-2K cells, both antibodies could not detect any difference between the onset of expression of Xin isoforms (fig. 3.17 A-C). On the contrary, there was an almost complete overlap of both signals because peripheral cellular extensions (arrow) and actin filaments in the cell body (arrowhead) were decorated by both antibodies. In addition to that localization known, the punctate distribution, typical of later stages of differentiation, was quite pronounced. Myotubes of intermediate stage exhibited the localization pattern characteristic for Xin (fig. 3.17 D-F). Both the antibody against the repeats and  $\alpha$ -mXin C provided an identical signal revealing the apparently random punctate distribution and the association with cellular extensions in the periphery. When the myotubes acquired their contractility, deviations in the structures labeled with both antibodies could not be revealed (data not shown). Thus, all isoforms expressed, i.e. predominantly Xin A and Xin B (cf. sections 3.2.1 and 3.2.2), display an identical localization pattern.

### 3.3 Xin is a Novel Ligand of the SH3 Domain of Nebulin and Nebulette

All three human Xin isoforms contain a high frequency of the amino acid proline, which is highest in Xin C (11,22 %) and only slightly less in Xin A (10,36 %) and Xin B (9,03 %). Hence, proline is among the most abundant amino acids building these proteins and Xin is referred to as proline-rich. The prolines are arranged into clusters including putative binding motifs of ena/VASP homology 1 (EVH1) or src homology 3 (SH3) domains (fig. 3.18 A). Some of these putative binding interfaces have already been shown to be functional *in vitro*, such as the N-terminal EVH1 domain-binding sequence (van der Ven *et al.*, 2006) and the cortactin SH3 interaction motif predicted (Sparks *et al.*, 1996; Eulitz, 2005).

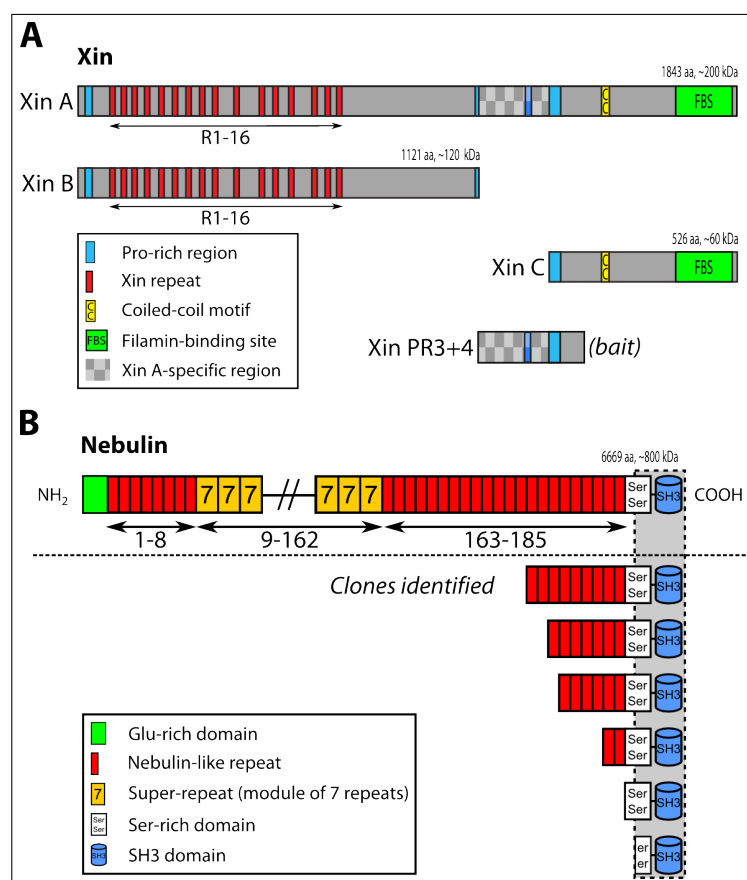


Figure 3.18: **Nebulin fragments interacting with Xin PR3+4 identified in a yeast two-hybrid screen.** **A.** Schematic overview of the isoforms of human Xin and the bait (Xin PR3+4) used in a yeast two-hybrid screen. **B.** Structural motifs of nebulin are depicted in the sketch at the top. Positive clones obtained in the screen comprise different portions of the C-terminus of nebulin. The minimal consensus is indicated by a grey background encased by a broken line.

In order to unveil new interacting proteins, a yeast two-hybrid screen (cf. section 2.9.1) was performed using a human Xin fragment as a bait comprising the centrally located proline-rich regions 3 and 4 (denoted by Xin PR3+4, see fig. 3.18 A) and a skeletal muscle cDNA library (cf. section 2.6.1) as a prey. This assay resulted in ten clones positive for activating the *HIS3* and *lacZ* reporter gene (cf. sections 2.9.1.2 and

2.9.1.3) containing a C-terminal portion of the huge cross-striated muscle-specific protein nebulin (cf. section 1.5.3). All sequences obtained include the C-terminal SH3 domain and at least a small part of the serine-rich domain (fig. 3.18). These findings were verified in independent forced yeast two-hybrid studies where no construct exhibited any autoactivation of reporter genes (cf. sections 2.9.1.2 and 2.9.1.3). Thus, these results confirm the interaction of Xin with the C-terminus of nebulin comprising the SH3 domain and a part of the serine-rich linker sequence.

### 3.3.1 Xin A and C Interact with Nebulin

The bait fragment Xin PR3+4 used in the yeast two-hybrid experiment, which identified nebulin as a novel ligand of Xin, contains sequences specific for the largest human Xin isoform Xin A and the first N-terminal 99 amino acids of Xin C. In order to locate the responsible binding region, a further yeast two-hybrid study (cf. section 2.9.1) was performed using Xin C as an additional bait.

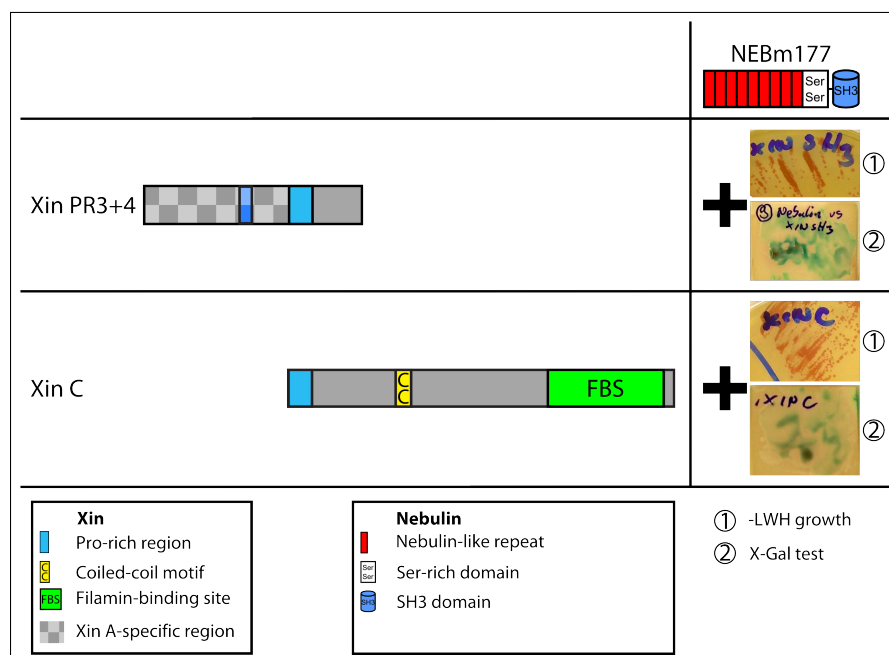


Figure 3.19: **Mapping of the nebulin interaction motif in human Xin.** Results obtained in a yeast-two hybrid assay testing Xin PR3+4 and Xin C for binding to nebulin. Images marked as 1 depict growth on -LWH selective medium. Positive growth is indicated by newly formed deep red colonies. Activity of the  $\beta$ -galactosidase is displayed by blue-coloured colonies in images marked as 2. Both bait fragments clearly interact with nebulin identifying the N-terminus of Xin C as interaction site.

This assay showed that Xin C can also interact with nebulin thus pointing to the N-terminus of Xin C as the binding interface. The amino acid sequence of Xin C starts with 33 residues containing many putative SH3 domain binding consensus motifs encompassing a PXXP sequence, where X denotes any amino acid. A motif consisting of the amino acids 6 to 16 of murine Xin C (KPPVPPKPAHL; cf. section 3.2.1) has been predicted

to bind the SH3 domain of the actin associated protein cortactin according to the results of a comparative analysis of the ligand preferences of different SH3 domains (Sparks *et al.*, 1996). Yeast two-hybrid and biochemical experiments could confirm the binding properties of this region in the human protein *in vitro* (Eulitz, 2005). The fact that on the one hand the minimal Xin-binding sequence in nebulin, apart from a fragment of the serine-rich linker domain, comprises the complete SH3 domain (fig. 3.18 B) and on the other hand the binding region in Xin includes many potential and already proven polyproline interaction motifs allowed the conclusion that the interaction of nebulin to the N-terminal portion of Xin C is very likely mediated by the SH3 domain.

### 3.3.2 Human Xin also Binds to Nebulette

The members of the nebulin-repeat protein family, nebulin and nebulette (cf. sections 1.5.3 and 1.5.4), share a highly conserved C-terminal SH3 domain possessing nearly 90 % homology of the amino acid sequence. This domain inserts into the Z-disc and has been already described as a binding partner of prominent components of the sarcomeric Z-disc such as  $\alpha$ -actinin, titin or CapZ (Nave *et al.*, 1990; Moncman und Wang, 1999; Witt *et al.*, 2006). In this work, the human protein Xin has been identified as a novel ligand of the C-terminus of nebulin (cf. section 3.3.1). Nebulin is predominantly expressed in skeletal muscle, whereas in cardiac muscle nebulette is the predominant member of the nebulin-repeat protein family (fig. 3.20 A). Xin can also be identified in both muscle types, which raises the possibility that Xin also interacts with nebulette, because the SH3 domain very likely mediates the association (cf. section 3.3.1). This assumption is further supported by the low degree of homology of the serine-rich linker, which amounts to only 36 %.

Therefore, a yeast two-hybrid study was carried out using Xin PR3+4 and Xin C as a bait and a nebulette fragment containing the SH3 domain and a number of residues of the serine-rich domain comparable to the clone comprising the minimal Xin-binding sequence (denoted by NET SH3+L). All fragments were tested negatively for autoactivation of both reporter systems (cf. section 2.9.1). This assay clearly demonstrates that Xin additionally interacts with the heart muscle-specific nebulin-related protein nebulette because the *HIS3* as well as the *lacZ* reporter gene are activated (fig. 3.20 B), which is depicted by the growth on  $-LWH$  medium and the blue-coloured colonies in the  $\beta$ -galactosidase activation assay, respectively. This result further substantiates the notion that the SH3 domain is the binding interface due to the higher degree of conservation among the nebulin-repeat

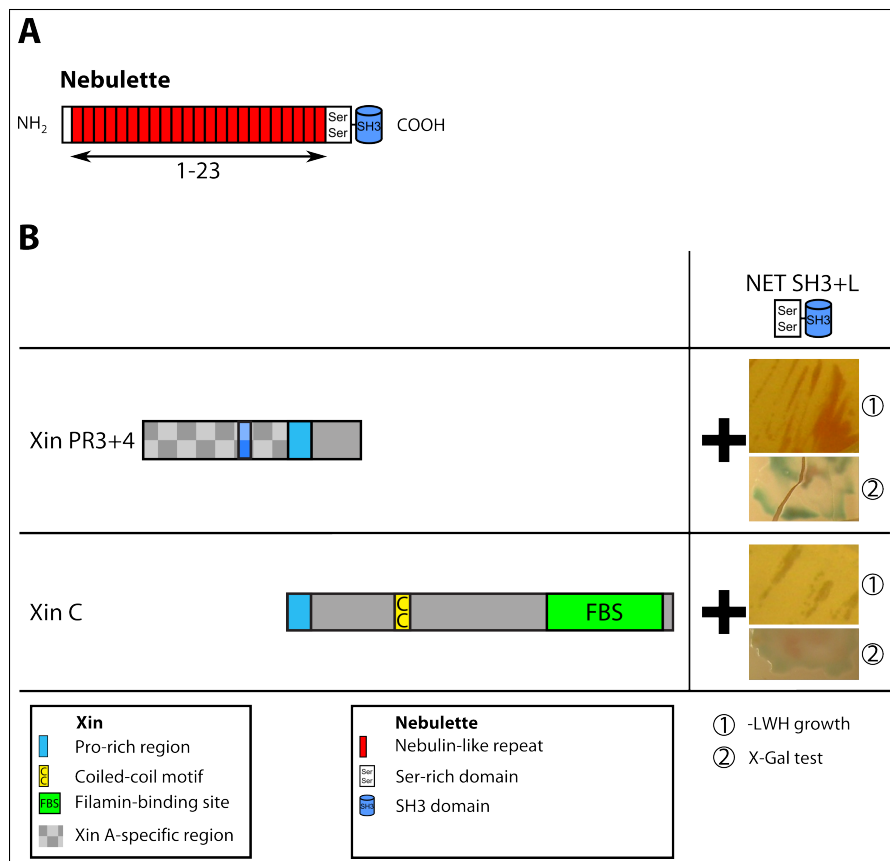
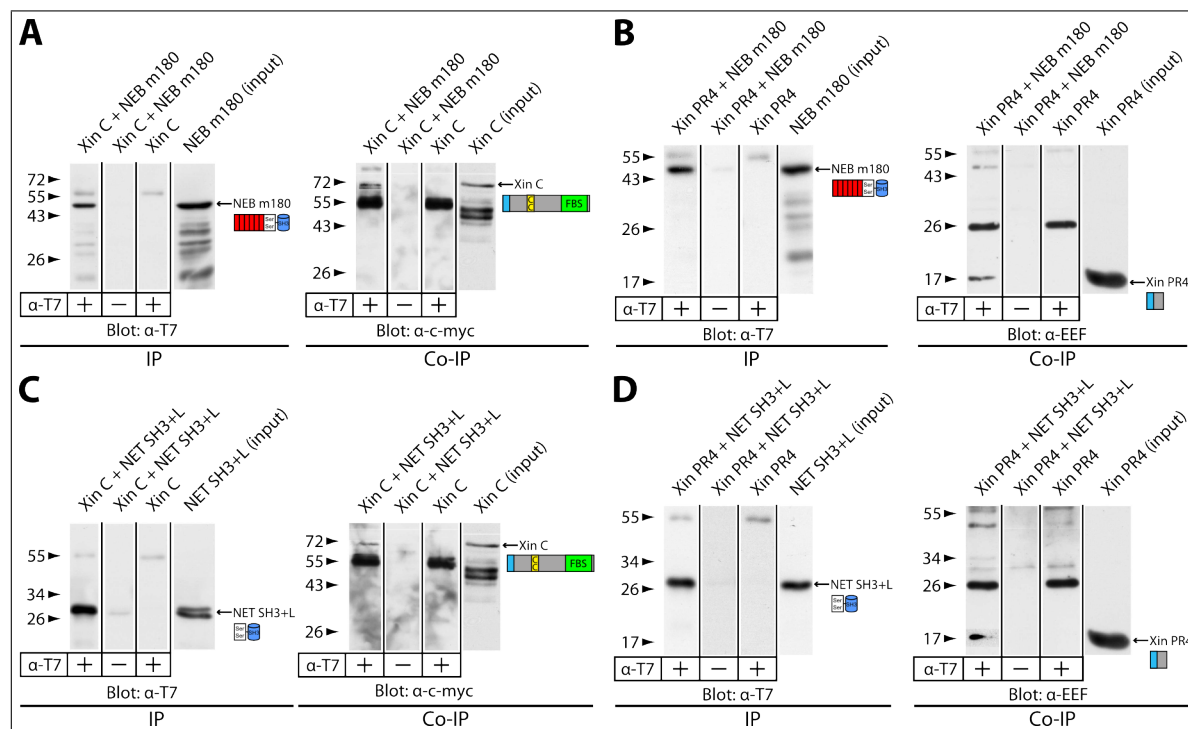


Figure 3.20: **Human Xin binds to nebulette.** **A.** Schematic overview of the domain organization of nebulette. **B.** Result of a yeast two-hybrid experiment using fragments of human Xin (PR3+4, C) as a bait and the nebulette SH3 domain with a linker sequence (NET SH3+L) as a prey. The activation of the *HIS3* reporter gene is depicted in the pictures denoted by 1. Additional activation of the *lacZ* reporter gene is delineated in the images numbered 2. Both bait fragments can interact with nebulette. Therefore, nebulin and nebulette share the same interaction site on Xin, the N-terminus of Xin C.

protein family members compared to the linker sequence.

### 3.3.3 Biochemical Verification of the Nebulin/Nebulette-Xin Interaction



**Figure 3.21: Co-Immunoprecipitation of Xin and Nebulin and Nebulette.** The protein composition of an assay is depicted above the particular lane. Fragments of nebulin (A, B) or nebulette (C, D) were precipitated with a monoclonal T7-tag antibody (see tab. 2.8.2). Addition of antibody is indicated by a + below each lane. The antibody used for probing the membrane is noted at the bottom of the respective blot. The protein detected is marked by an arrow and a sketch below delineates the fragment. Blots probed with  $\alpha$ -T7 antibody show the successful immunoprecipitation of the respective nebulin and nebulette fragment whereas the other blots display the co-precipitated Xin. Migration distances are shown in kDa. **A.** Co-immunoprecipitation of nebulin and Xin C. **B.** Co-immunoprecipitation of nebulin and Xin PR4. **C.** Co-immunoprecipitation of nebulette and Xin C. **D.** Co-immunoprecipitation of nebulette and Xin PR4. Xin C as well as Xin PR4 are always co-precipitated with all nebulin and nebulette fragments used.

Yeast two-hybrid experiments identified nebulin and nebulette as interaction partners of human Xin (fig. 3.18 B and cf. section 3.3.2). The responsible binding region of Xin was mapped to the N-terminus of Xin C, which comprises a cluster of putative SH3 domain interaction motifs. In order to confirm this interaction with biochemical methods, recombinantly expressed fragments of nebulin and nebulette as well as Xin were purified and tested for binding in a co-immunoprecipitation assay (cf. sections 2.7.4.1 and 2.9.2). The nebulin and nebulette fragments were cloned into a pET28a plasmid to express them

as fusion proteins with a N-terminal hexa-histidine tag for purification and a proximate T7-tag for immunodetection and precipitation. Both recombinant proteins do not have any amino acid added to the C-terminus due to a stop codon directly behind the SH3 domain, since any C-terminal addition disrupts interactions (personal observation). Two Xin fragments were investigated on binding, the complete isoform Xin C and the first N-terminal 99 amino acids of Xin C, designated as Xin PR4. Xin C could be detected using an anti-c-myc antibody, because it is encoded by the pET23aMyc vector, which provides a fusion protein containing a N-terminal c-myc-tag and a C-terminal hexa-histidine tag. Xin PR4 does not comprise any N-terminal tag, since it is expressed in the vector pET23aEEF conferring a C-terminal hexa-histidine and EEF-tag.

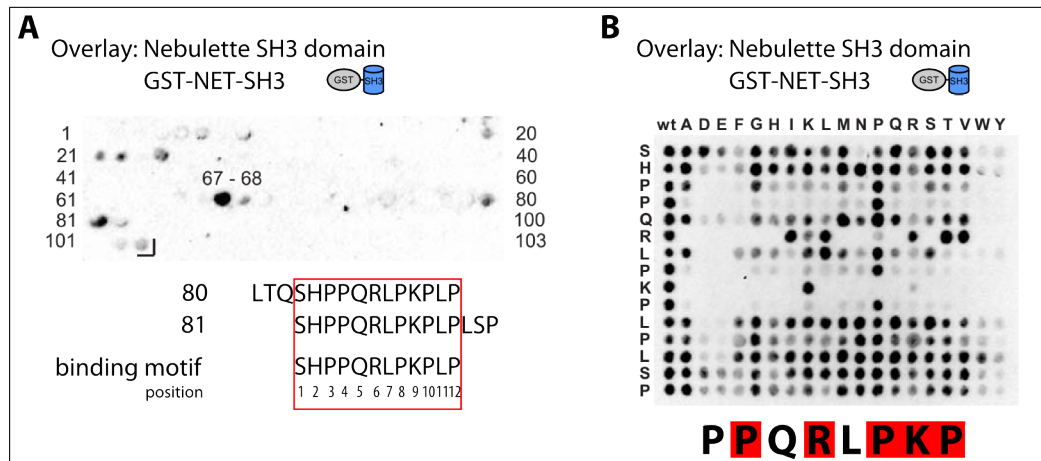
All proteins were tested for unspecific precipitation but none of them revealed any stickiness to the protein G-coated magnetic beads or cross-reactivity with the tag-antibodies used (fig. 3.21, every blot lanes 2 and 3). The precipitation of the nebulin and nebulette fragments was successful, delineated by the prominent band in lane 1 of the blots probed with the anti-T7 antibody (see fig. 3.21, right panel). In every case, the corresponding lane of the CoIP blot shows a clear band at the molecular weight of the Xin protein (fig. 3.21, left panel) indicating the interaction of both proteins. Thus, these assays point to the SH3 domain of nebulin and nebulette as a direct binding partner of human Xin.

### 3.3.4 Identification of the Nebulin/Nebulette SH3 Domain Binding Sequence in Human Xin

The interaction of nebulin and nebulette to Xin is very likely mediated by their C-terminal SH3 domain (fig. 3.18 and section 3.3.2). SH3 domains represent a common module of protein interactions generally recognizing polyproline ligands. The interaction is mediated by a large hydrophobic patch flanked by the so-called RT and n-Src loops of the SH3 domain. This interface binds ligands, which adopt a polyproline II helical conformation comprising the minimal consensus motif *PXXP*. In principle, ligands can bind the hydrophobic pocket in either orientation but directionality is conferred by the interaction of positively charged amino acids with the RT-loop of the SH3 domain. Therefore, ligands binding with their N-terminus to the RT-loop contain the peptide motif *+XXPXXP* (+ denotes a positively charged amino acid) and are classified as type I. Class II peptides have the consensus sequence *PXXPX+* and are bound with their C-terminus to the RT-loop. The three-dimensional structure of the nebulin SH3 domain has already been resolved and the analysis of its ligand preferences revealed selective interactions of class II



peptides (Politou *et al.*, 1998, 2002). The designated binding region in human Xin comprises many potential interaction motifs among others the functional cortactin binding motif.



**Figure 3.22: Peptide scan for identification of the nebulin/nebulette SH3 domain binding sequence.** **A.** 15-mer peptides covering the complete sequence of the Xin fragment PR3+4 added N-terminally with 24 residues were coupled with a  $\beta$ -alanine spacer to a membrane. The sequence of consecutive peptides was shifted with three amino acids C-terminally. The membrane was probed with the nebulette SH3 domain N-terminally tagged with GST (GST-NET-SH3). The antibody against GST detected specific binding at spots 80 and 81, which determines the binding motif (red frame). **B.** In order to elucidate the essential residues and thus the binding mode the peptide sequence identified was mutated and the binding properties analyzed by overlaying GST-NET-SH3. All residues whose mutation severely affects the binding capacity are delineated at the bottom. Essential amino acids are highlighted by a red background. The motif comprises an essential lysine (*K*) residue at the C-terminus pointing out Xin as a class II ligand (Politou *et al.*, 2002).

In order to identify the relevant residues in human Xin, Prisca Boisguerin of the Department of Medical Immunology at the Charité in Berlin, Germany, performed peptide scans using a nebulette SH3 domain-GST fusion protein (GST-NET-SH3) as interaction partner of the peptides spotted (cf. section 2.9.4). The scan covered the complete amino acid sequence of the bait fragment Xin PR3+4 used in the initial yeast two-hybrid screen (cf. section 3.3) plus 24 amino acids at the N-terminus. The peptides were spotted as 15-mer and the consecutive peptide sequence was shifted with three amino acids C-terminally. All peptides were coupled with a  $\beta$ -alanine spacer to the membrane. The antibody against the GST-tag prominently detected two spots 67 and 81. The former one represents unspecific binding in the control experiment of the GST alone, i.e. without fusion to the nebulette SH3 domain (data not shown). Spot number 81 and to a lower extend spot 80 displayed the signal the most intense obtained with GST-NET-SH3 as overlaid protein. Both peptides share the sequence *SHPPQRLPKPLP* thus this 12-mer delineates the minimal binding motif in human Xin of the nebulette–Xin interaction. As



depicted above, SH3 domains interact with ligands containing a minimal consensus motif *PXXP*, but surprisingly the peptide sequence obtained does not follow this rule because the prolines included are separated by one or three residues. Hence, it is difficult to discern the essential amino acids, which is necessary to identify the binding mode. This question was addressed by synthesizing peptides mutated at one position and analyzing the binding properties of the resulting peptide. This assay reveals that essential residues are located at positions four (*P*), six (*R*), eight (*P*), nine (*K*) and ten (*P*) (see fig. 3.22 A). The fact that mutation of the lysine at position ten completely abolishes the interaction strongly supports the conclusion that the Xin peptide belongs to class II, because it is located C-terminally from most of the other indispensable residues confirming the prediction of the binding preferences. Accordingly, the prolines defining the SH3 domain binding motif are separated by three amino acids, *QRL*, demonstrating that slight changes from the overall consensus motif are tolerable provided that certain essential positions remain completely preserved. Due to the high homology of the SH3 domains of nebulin and nebulette, one can conclude that the results obtained with the nebulette SH3 domain can be applied to nebulin as well. Consequently, Xin A and C bind to the SH3 domain of nebulin and nebulette in a class II-specific manner.

### 3.3.5 Xin and Nebulin Localization During Myofibrillogenesis of H-2K Cells

The giant protein nebulin represents one of the four filament systems in adult skeletal muscle (cf. section 1.5.3). In this work, human Xin is established as a novel ligand of the nebulin SH3 domain (cf. previous sections). The expression of both proteins is restricted to cross-striated musculature, which suggests an important role of this interaction predominantly in skeletal muscle because the expression of nebulin in cardiac muscle is apparently very low (Kazmierski *et al.*, 2003; McElhinny *et al.*, 2003). While nebulin is an indispensable ruler of sarcomere architecture during development and in adulthood, Xin is highly expressed during myogenesis. However, it is not a constituent of the adult contractile apparatus but resides in the MTJ. Therefore, it seems to be likely that the interaction of both proteins takes place during development rather than in the adult state. To study developmental processes during myofibrillogenesis, the differentiation of H-2K cells offers a reliable tool (cf. section 3.1). Thus, cells were differentiated until they had shown contraction and then fixed and stained at different stages. Nebulin was detected with a polyclonal antibody recognizing the nebulin modules M176-M181 located in the

Z-disc region. Two isoforms of human Xin, A and C, are binding partners of nebulin and both exist also in mice (cf. section 3.2.1), but only Xin A can be detected doubtlessly on protein level during differentiation of H-2K cells (cf. section 3.2.2), whereas Xin C only seems to be upregulated at pathogenic states in the heart (Otten *et al.*, 2010). At this time, no Xin A-specific antibody was available, so an antibody was used raised against the repeat region therefore detecting Xin A as well as Xin B. All cells were analyzed with a confocal LSM and subsequently processed for scanning electron microscopy.

Directly after the onset of myogenic differentiation Xin as well as nebulin Z-disc epitopes were expressed (fig. 3.23 A-C). Even in this early phase Xin was more widely distributed throughout the cell and nebulin has only started to appear in the perinuclear region. Xin apparently preceded nebulin occurrence and both showed a similar non-regular punctate placement. In the course of early development Xin accumulated in cellular extensions in the periphery, which emerged upon stretching of the mononucleated cell, and at submembranous sites (fig 3.23 D). Nebulin was completely absent from these structures and its signal intensified in the perinuclear space displaying a continuous decoration of presumably actin stress fibres due to the ability of nebulin repeats to bind F-actin (fig. 3.23 E). Xin also continuously associated with actin filaments but it only partly colocalized with nebulin (fig. 3.23 D-F, arrowhead). Some actin filaments exhibited an association mainly with Xin (open arrowhead), whereas others revealed a partially overlapping Xin and nebulin signal (arrowhead). At the filament portion directed to the cell periphery only Xin could be detected (arrow) but around the nucleus nebulin was predominantly associated with these filaments. Furthermore, Xin appeared to decorate the actin filaments in advance of nebulin and nebulin spread out from the perinuclear space. The peripheral cellular extensions contained notable amounts of Xin (fig. 3.23 G, G') and nebulin was only weakly expressed and diffusely located, if present at all (fig. 3.23 H, H'). The cytoskeleton of this cell displayed two different appearances in the scanning electron micrograph (fig. 3.23 J). In the cell periphery, where Xin was enriched, the cytoskeleton was organized as a branched network (fig. 3.23 K). The cellular interior harboured thick fibres arranged in parallel spanning the cell (fig. 3.23 L). Some of these fibres probably represented actin stress fibre bundles, which explains their larger diameter. Since they were only detected in a large area around the nucleus, the site of the first expression of nebulin, these are presumably those actin filaments, which were firstly associated with nebulin.

Upon progression of myogenic differentiation, nebulin expression increased and revealed binding to actin filaments spanning the entire cell (fig. 3.24 A). Within the my-

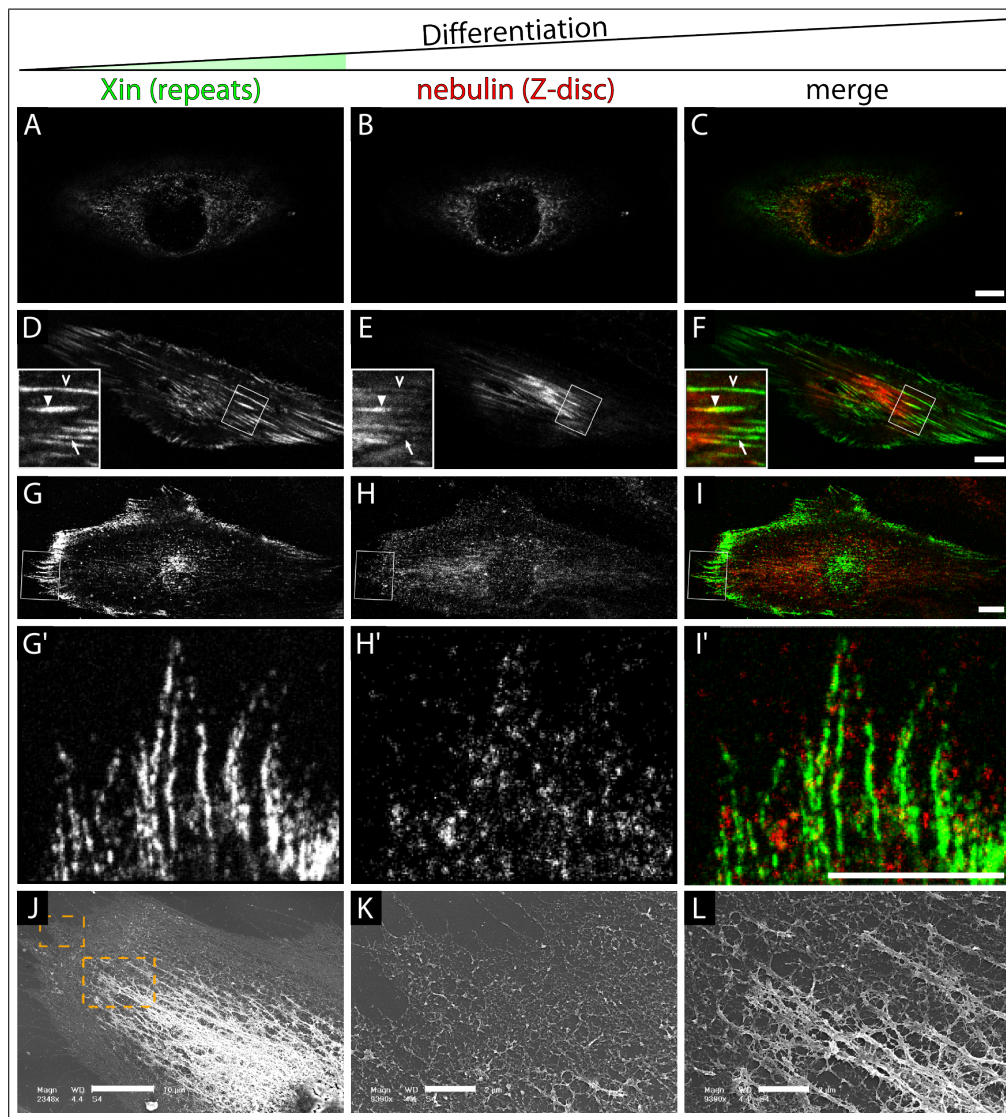


Figure 3.23: **Localization of Xin and nebulin in early phases of myofibrillogenesis of H-2K cells.** **A-I'**. Confocal LSM images of H-2K cells at early stage of myofibrillogenesis labeled with antibodies against Xin-Repeats and nebulin repeat modules M176-M181 located near the Z-disc. In merge images (C, F, I, I') Xin and nebulin are tinted green and red, respectively. **A.** Xin is more widely distributed in an unordered punctate pattern. **B.** Nebulin localization is restricted to the perinuclear region. **D.** Xin accumulates in peripheral cellular extensions and submembranous sites. Inset: Xin is associated with actin filaments. **E.** Nebulin enriches at actin filaments in the perinuclear region. **F.** No colocalization of Xin and nebulin at peripheral cellular extensions and submembranous sites. Inset: Xin and nebulin only partially colocalize at actin filaments (arrowhead). Xin always associates with the filament portion directed to the periphery (arrow) whereas nebulin labeling dominates around the nucleus. At some filaments nebulin is nearly absent (open arrowhead). **G+G'.** Strong Xin decoration of filopodia-like extensions. **H+H'.** Nebulin exhibits a weak and diffuse distribution at peripheral cellular extensions. **J-L.** Scanning electron micrographs of the cell depicted in G-I. **J.** The cell contains two different cytoskeletal manifestations. **K.** The peripheral cytoskeleton appears as a branched network. **L.** Around the nucleus and in the cell body, the cytoskeleton contains thick bundles. Scale bar 10  $\mu\text{m}$  (**A-I'**), 5  $\mu\text{m}$  (**J**) and 2  $\mu\text{m}$  (**K,L**).



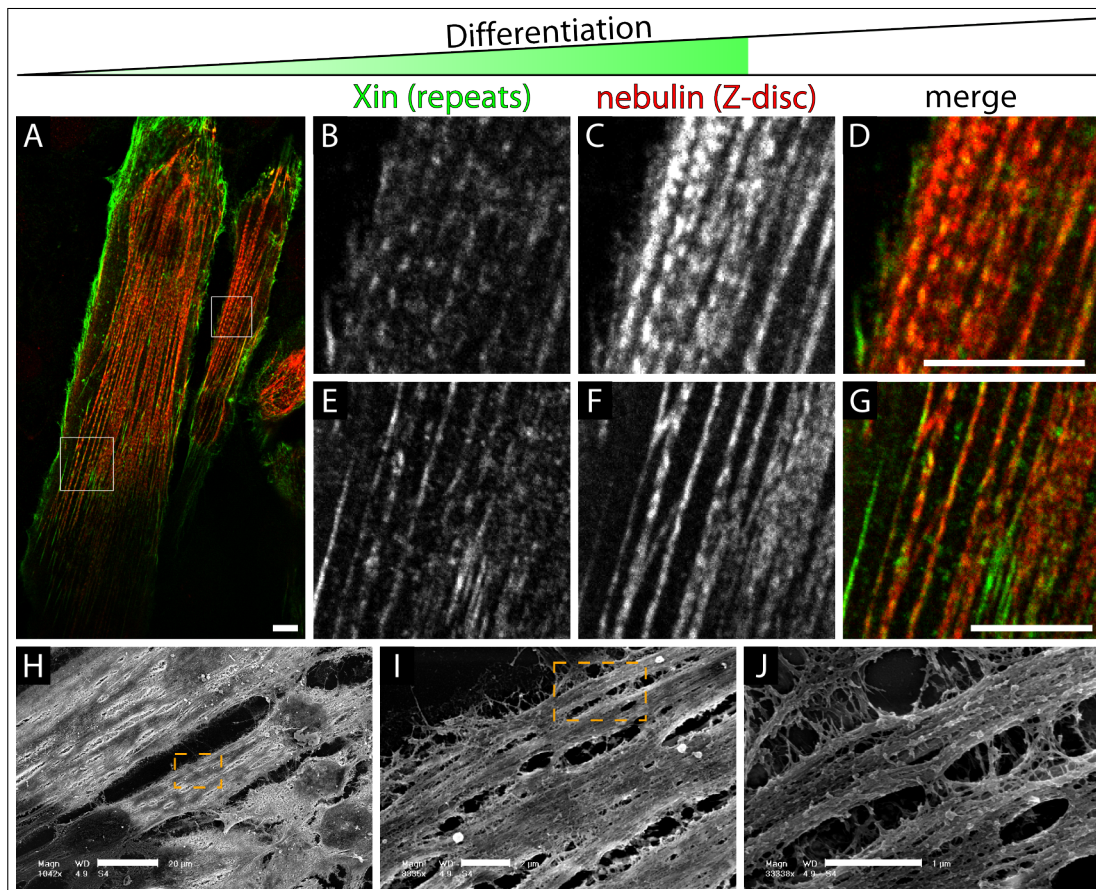


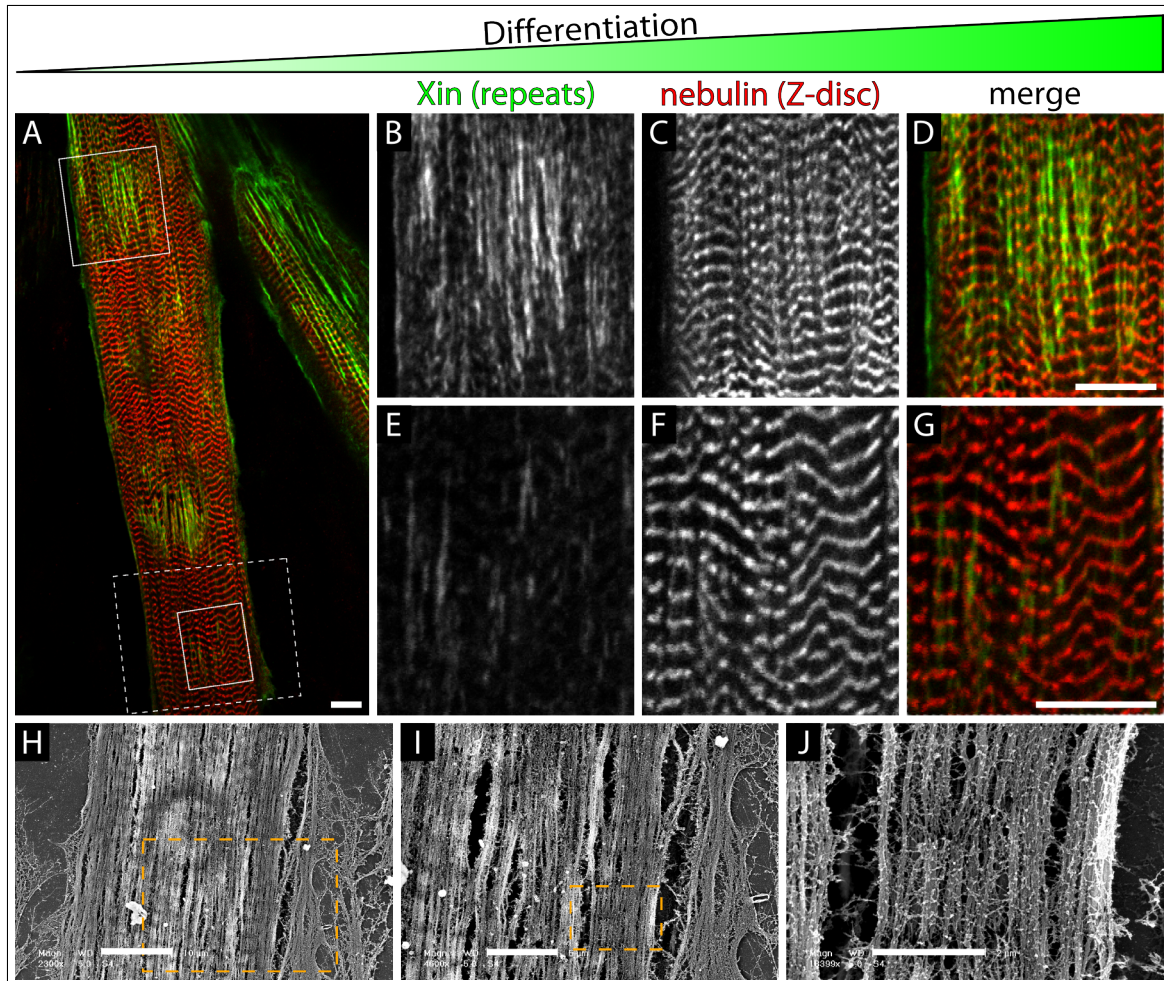
Figure 3.24: **Localization of Xin and nebulin in myotubes of intermediate stage of differentiation.** **A-G.** Confocal LSM images of H-2K cells at intermediate stage of myofibrillogenesis labeled with antibodies against Xin-Repeats and nebulin repeat modules M176-M181 located near the Z-disc. In merge images (A, D, G) Xin and nebulin are tinted green and red, respectively. **A.** Multinucleated myotubes contain nebulin-associated early myofibrils pervading the entire cell. Xin is enriched in the membranous region. **B-D.** Xin weakly labels early myofibrils already decorated with nebulin in a punctate pattern. **E-G.** Myotubes of intermediate stage still contain actin filaments with a continuous Xin association accompanied by weak decoration of nebulin. Further differentiation of future myofibrils leads to a decrease of Xin association. **H-J.** Scanning electron micrographs of the cells depicted in A. The cytoskeleton mainly comprises large fibre bundles and branched networks are hard to detect. Scale bar 10  $\mu\text{m}$  (**A-G**), 20  $\mu\text{m}$  (**H**), 2  $\mu\text{m}$  (**I**) and 1  $\mu\text{m}$  (**J**).

otube only low amounts of nebulin targeted to submembranous sites, whereas Xin enriched there. In contrast, myofibrils already displaying a high level of nebulin expression and a rudimentary punctate pattern exhibited only a minor Xin association (fig. 3.24 B-D). At these sites, Xin was no longer continuously decorating actin filaments but revealed a dot-like arrangement. These structures presumably represent Z-bodies because Z-disc epitopes of nebulin were strongly expressed. Multinucleated myotubes of this degree of differentiation still included actin filaments with low nebulin association and a continuous Xin signal, the latter constantly decreasing upon nebulin targeting (fig. 3.24 E-G). The cytoskeleton at nebulin-rich sites already revealed large fibre bundles in the periphery of the cell illustrating the changes during myofibrillogenesis (fig. 3.24 H-J). These multinucleated myotubes nearly exclusively contained large fibre bundles spanning the whole cell but missed a branched network characteristic for migrating cells which was still present at the onset of myofibrillogenesis. While Xin could locate to this cytoskeletal subpopulation, nebulin targeting was limited to actin filaments already designated to evolve into myofibrils. When the differentiation of H-2K cells reached the final state, i.e. cross-striated contractile myotubes still containing areas of Z-discs to be laterally aligned, the filamentous targeting of nebulin Z-disc epitopes had been clearly reduced in favour of a Z-disc arrangement of mature spacing (fig. 3.25 A). Areas showing a prominent Xin signal indicated Z-discs, which still needed to be properly aligned (fig. 3.25 B-D). Xin connected Z-bodies and the emerging Z-discs longitudinally, where lateral fusion of Z-bodies took place and the number of neighbouring Z-discs needed to be adjusted in order to establish a regular array of sarcomeres. These areas could also be identified by the nebulin localization because it was as well a component of these longitudinally connecting structures although to a minor extent. Furthermore, nebulin revealed irregularities in the sarcomere arrangement and these matched the sites of Xin expression. As the sarcomere maturation proceeded, Xin expression dramatically decreased (fig. 3.25 E-G). It was still associated with submembraneous compartments but nearly absent from the contractile apparatus, although a very small amount remained to be localized at the Z-disc. Consequently, this stage identifies Xin as a marker of fully developed sarcomeres since it is missing in adult sarcomeres but connects adjacent Z-discs although they exhibit a mature spacing and seemingly a mature appearance. Therefore, even in this late stages it is very difficult to obtain a striated pattern with the scanning electron microscopy (fig. 3.25 H-J). This requires a very high degree of differentiation throughout the whole cell body, which is not always achieved in H-2K cell culture. Striated areas showed a succession of thick fibre bundles and a narrow zone containing small connective structures and lacking these

prominent bundles. The character of these structures could not be determined without specific antibody detection therefore a further description can only be speculative.

In summary, Xin emerges directly after the onset of the myogenic program and precedes the expression of nebulin in the early phase of H-2K cell myogenic differentiation. Xin is predominantly localized in cellular extensions at the periphery and some actin filaments in the cell body, whereas nebulin is restricted to actin filaments in the perinuclear region. Both proteins colocalize only at distinct sites on a subset of actin filaments. Xin was shown to associate with non-striated myofibrils (NSMF) in neonatal rat cardiomyocytes, precursor structures of mature myofibrils. The colocalization of nebulin and Xin on these filaments very likely marks them as analogous structures in H-2K cells. After further differentiation, nebulin expression increases and its association with actin filaments changes into a punctate pattern. Xin localization reduces at these sites and appears to be dotted-like. At submembraneous regions Xin expression predominates, which does not change during the entire differentiation process. By contrast, Xin constantly disappears from the myofibrils the more the Z-discs gain mature spacing and a regular arrangement. Irregularities in the sarcomere array are indicated by longitudinal Xin-containing connective structures comprising very low amounts of nebulin. Further maturation of the contractile apparatus continuously let these structures disappear and Xin remains to be positioned at the Z-disc, however, very weakly. The fact that Xin is absent from adult Z-discs supports the observation that H-2K cells do not reach an adult stage albeit contractile (cf. section 3.1.1) and Xin is a suitable marker in order to distinguish adult and immature state of the sarcomere. Furthermore, Xin and nebulin obviously interact only transiently during sarcomere development at actin filaments designated to become myofibrils and later at sites of Z-disc arrangement but not in the adult stage.





**Figure 3.25: Localization of Xin and nebulin in contractile myotubes.** **A-G.** Confocal LSM images of contractile H-2K myotubes labeled with antibodies against Xin-Repeats and nebulin repeat modules M176-M181 located near the Z-disc. In merge images (A, D, G) Xin and nebulin are tinted green and red, respectively. **A.** In contractile myotubes, nebulin exhibits an overall regular Z-disc organization and Xin is located near the membrane and at sites of still immature myofibrils. **B-D.** Xin longitudinally connects immature myofibrils, where nebulin reveals Z-discs not properly aligned. To a minor extend, nebulin also decorates these structures. **E-G.** This longitudinal connection is constantly reduced upon further maturation so that Xin can only weakly be detected at sites of irregular Z-disc arrangement. **H-J.** Scanning electron micrographs of the cell area encased by a dotted line in A. Cross-striation appears as thick fibre bundles interrupted by a narrow zone containing connective structures. Scale bar 10  $\mu\text{m}$  (**A-H**), 5  $\mu\text{m}$  (**I**) and 2  $\mu\text{m}$  (**J**).



### **3.3.6 The Site of Xin and Nebulette Interaction Visualized by Bimolecular Fluorescence Complementation (BiFC)**

Comparing Xin and nebulin localization during myogenic differentiation of H-2K cells has revealed that their interaction seems to be important during sarcomere development. Therefore it is crucial to define precisely the site of this interaction in the cell in order to elucidate its function. Biochemical methods can only provide this information if both proteins interact. Furthermore, Xin and especially nebulin elude this approach due to their high insolubility and the necessity of very strong detergents to extract them. To study the localization of proteins in living cells proteins can be expressed as fusion proteins with fluorescent proteins (FP) transfected into the cell type desired. The fluorescent signal emitted then marks the position of the protein of interest therefore providing data about localization. Some non-fluorescent fragments of FP's retrieve their capability of emitting fluorescent light, if they contact their missing part (Hu und Kerppola, 2003). Both fragments reconstitute the original three-dimensional structure of the complete FP therefore allowing for complementation of the fluorescence. This quality can be utilized to visualize protein interactions in living cells by fusing the non-fluorescent fragments to the respective binding partner, which results in a fluorescent signal upon interaction if the fragments are close enough to associate and the construct provides enough flexibility (cf. section 2.9.5). This technique is called bimolecular fluorescence complementation (BiFC) and its applicability has been widely tested for transcription factors and transmembrane proteins. Very rare data is available about actin cytoskeleton-associated proteins, so the applicability to that protein subset has to be investigated in advance.

#### **3.3.6.1 Analysis of the Dynamics of BiFC Complexes Using Fluorescence Recovery After Photobleaching (FRAP)**

The BiFC approach enables the visualization even of transient interactions because they are trapped by the association of the fluorescent fragments which can form an irreversible complex (Kerppola, 2008). In order to evaluate the results obtained in BiFC assays and facilitate subsequent interpretation, it was analyzed how BiFC complex formation affects the dynamics of the proteins in the cell.

The fluophore formation in a BiFC assay follows sigmoidal kinetics in contrast to the exponential curve observed with intact FPs (Kerppola, 2008). This difference mirrors the formation of the fluorescent complex, which the non-fluorescent fragments start to form after having been brought in close proximity due to binding of their respective fused

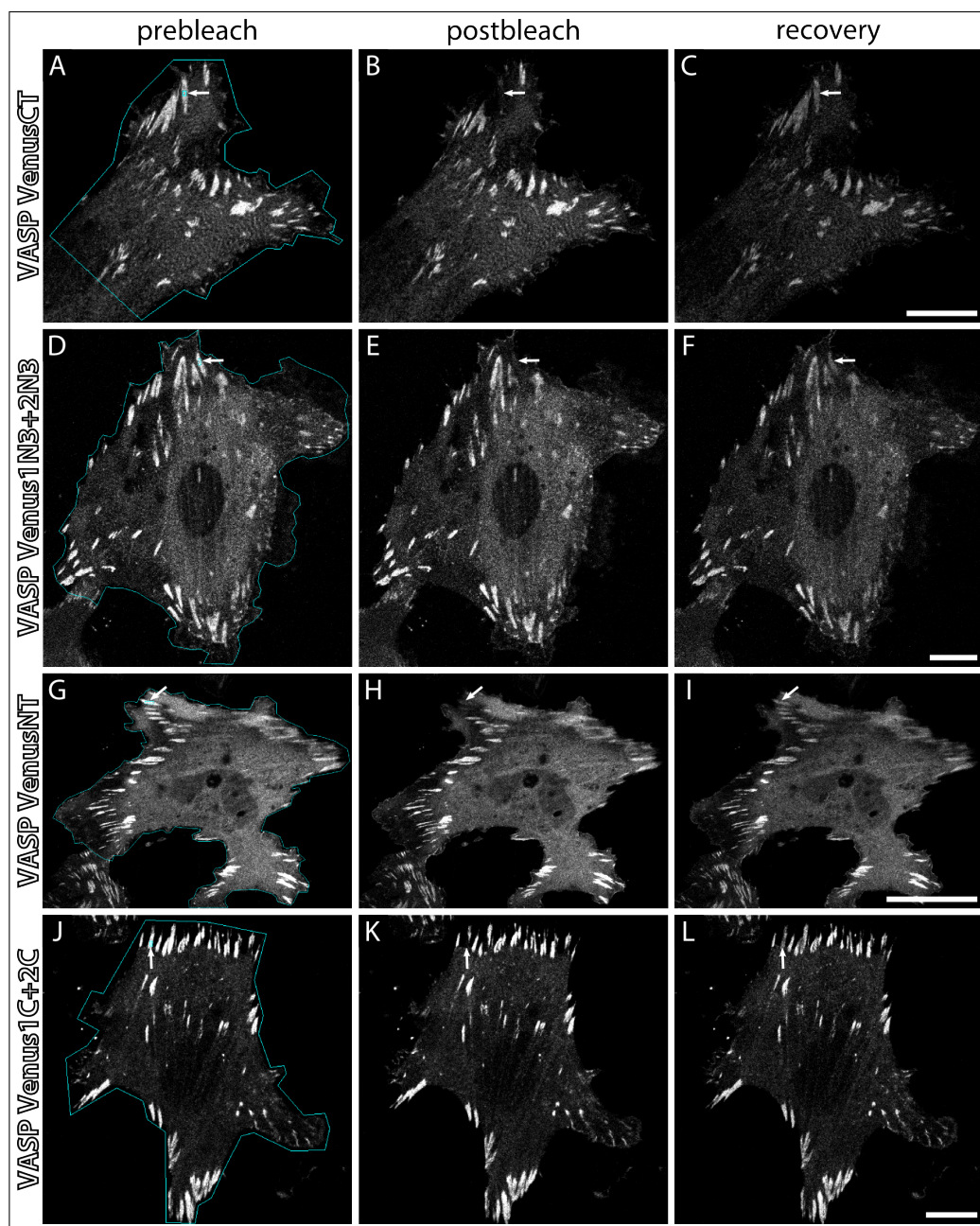


Figure 3.26: **FRAP of BiFC complex of homodimerized VASP in A7r5 cells.** Confocal LSM images of A7r5 cells either transfected with VASP fused to a complete Venus FP (**A-C**, **G-H**) or co-transfected with VASP fused to fragments of Venus enabling BiFC complex formation (**D-F**, **I-K**). The blue line enclosing the cell indicates the area, where total fluorescence intensity is measured. Arrows point to the bleaching region. Pictures are shown taken before bleaching (prebleach), directly after (postbleach) and after 60 s of recovery (recovery). **A-C**. Transfection of VASP fused to the N-terminus of the complete Venus FP. **D-F**. Co-transfection of VASP fused to the N-terminus of non-fluorescent fragments of the Venus FP. **G-I**. Transfection of VASP fused to the C-terminus of the complete Venus FP. **J-L**. Co-transfection of VASP fused to the C-terminus of non-fluorescent fragments of the Venus FP. Scale bar 10  $\mu\text{m}$ .

proteins. During this initial phase, the complex formation is still reversible so that other ligands can compete for binding partners. The complex undergoes changes resulting in an apparently irreversible association with a half-time of 1 min. After this lag-phase, the fluorescent complex matures at a rate comparable to a complete FP (Kerppola, 2008). Therefore, this assay can visualize transient interactions because of the complex stabilization by the association of the non-fluorescent fragments. However, this does not allow real-time analysis of complex formation and separation due to the apparent irreversibility. The exchange dynamics of such a complex are still not known thus fluorescence recovery after photobleaching (FRAP) experiments were performed to analyse the impact of BiFC complex formation on protein dynamics. This assay can identify alterations in rate and amount of replacement of the FP-labeled protein as the recovery of the fluorescent signal is measured after irreversible bleaching by an intense laser beam (cf. section 2.11.1.3). As an example of a prominent regulator of the actin cytoskeleton and a binding partner of Xin-Repeat proteins (van der Ven *et al.*, 2006), the dimerization in the potential tetrameric complex of vasodilator-stimulated phosphoprotein (VASP) was investigated (Zimmermann *et al.*, 2002). VASP belongs to the Ena/VASP family of proteins consisting of VASP, mammalian Ena (Mena) and Ena-VASP-like protein (EVL), which share a similar domain layout. Their N-terminal EVH1 (Ena/VASP homology 1) domain binds ligands including a FP<sub>4</sub> consensus motif, which targets Ena/VASP proteins to focal adhesions, filopodia and lamellipodia via vinculin, lamellipodin and zyxin. The central proline-rich region is most divergent among the members but conveys binding to SH3 or WW domains as well as profilin (Krause *et al.*, 2003). At the C-terminus, the EVH2 domain interacts with G- and F-actin and harbours the heptade motifs responsible for tetramerization (see fig. 3.38). The tetramers are arranged in parallel, i.e. all monomers have the same orientation (Zimmermann *et al.*, 2002; Kühnel *et al.*, 2004). Because the structural constraints of the tetramer are known and the protein is easy to transfect, this interaction was chosen to verify the functionality of the plasmids used and to analyze the dynamics of BiFC complex assembly and replacement. The full-length VASP protein was fused to each non-fluorescent fragment of the yellow fluorescent protein Venus, a derivative of YFP, at the N-terminus as well as the C-terminus designated as Venus1C, Venus2C and Venus1N3, Venus2N3, respectively (fig. 2.1). Plasmids containing the intact Venus protein fused to the N-terminus of VASP (VenusNT) and the C-terminus (VenusCT) served as a control without additional stabilization because of the BiFC complex (cf. section 2.5.2). The assay was carried out in the cell line A7r5, which stems from aortic smooth muscle of the rat (cf. section 2.10.1.2), since other easily transfectable cell lines as HEK293

were too prone to non-specific aggregate formation due to dramatic overexpression if the transcription of the fusion protein was controlled by the CMV promotor like in the Venus vectors. In A7r5 cells, the CMV promotor did not show such a high activity so that no fluorescent aggregates were detected when expressing two corresponding non-fluorescent fragments simultaneously independent of the combination. All non-fluorescent VASP fusion proteins were also tested on BiFC complex formation with the corresponding Venus fragment not fused to VASP. None of these experiments resulted in detectable fluorescence demonstrating the specificity of this approach (data not shown).

One of the advantages of a BiFC assay is that no steric information is required to perform such an experiment for the maximum of eight combinations of N- and C-terminal fusions covers a lot of potential conformations albeit without any guarantee of success (cf. section 2.9.5). Data about the three-dimensional arrangement of the VASP tetramer is available (see above). Therefore only those combinations were tested, where the Venus fragments were fused either to the N- (Venus1C + Venus2C) or the C-terminus (Venus1N3 + Venus2N3) (fig. 3.27 E). Both combinations displayed a BiFC signal comparable to those obtained with the intact FP (fig. 3.26). VASP was targeted strongly to focal adhesions and associated with actin filaments in a dotted pattern. The BiFC complex was formed at analogous structures with the cells not showing any abnormalities. Due to the higher fluorescence intensity, a subset of focal adhesion sites was selected for bleaching (fig. 3.26, arrows). These regions were exposed to a 405 nm laser beam until the fluorescent signal intensity was reduced to 10 % or less (fig. 3.26 B, E, H, K). The recovery of the fluorescence was tracked until no further increase could be detected (fig. 3.26 C, F, I, L). The region analyzed was set to the central core of the focal adhesion and after data analysis the results were plotted in a diagram in order to extract parameters (fig. 3.27 A-D). Unfortunately, the UV laser diode was not able to accomplish bleaching in each experiment and broke down before enough cells were measured in order to quantitate the different fractions and the time of exchange of half of the mobile fraction ( $t_{\frac{1}{2}}$ ). Thus, the values of  $t_{\frac{1}{2}}$  were not determined although the data was fitted because  $t_{\frac{1}{2}}$  strongly depends on the bleaching efficiency (cf. section 2.11.1.3). The mobile fractions depicted only served to compare the experiments qualitatively and did not represent real absolute values (fig. 3.27 E). In general, the mobile fractions of VASP fused to the intact Venus protein was larger compared to the BiFC complexes. The mobile fraction of VASP tagged at the C-terminus with complete Venus (VASP VenusCT) was  $0,63 \pm 0,13$  and of the corresponding N-terminally-tagged construct VASP VenusNT  $0,52 \pm 0,09$ . Although the value of VASP VenusNT is less than VASP VenusCT, without any further measurements

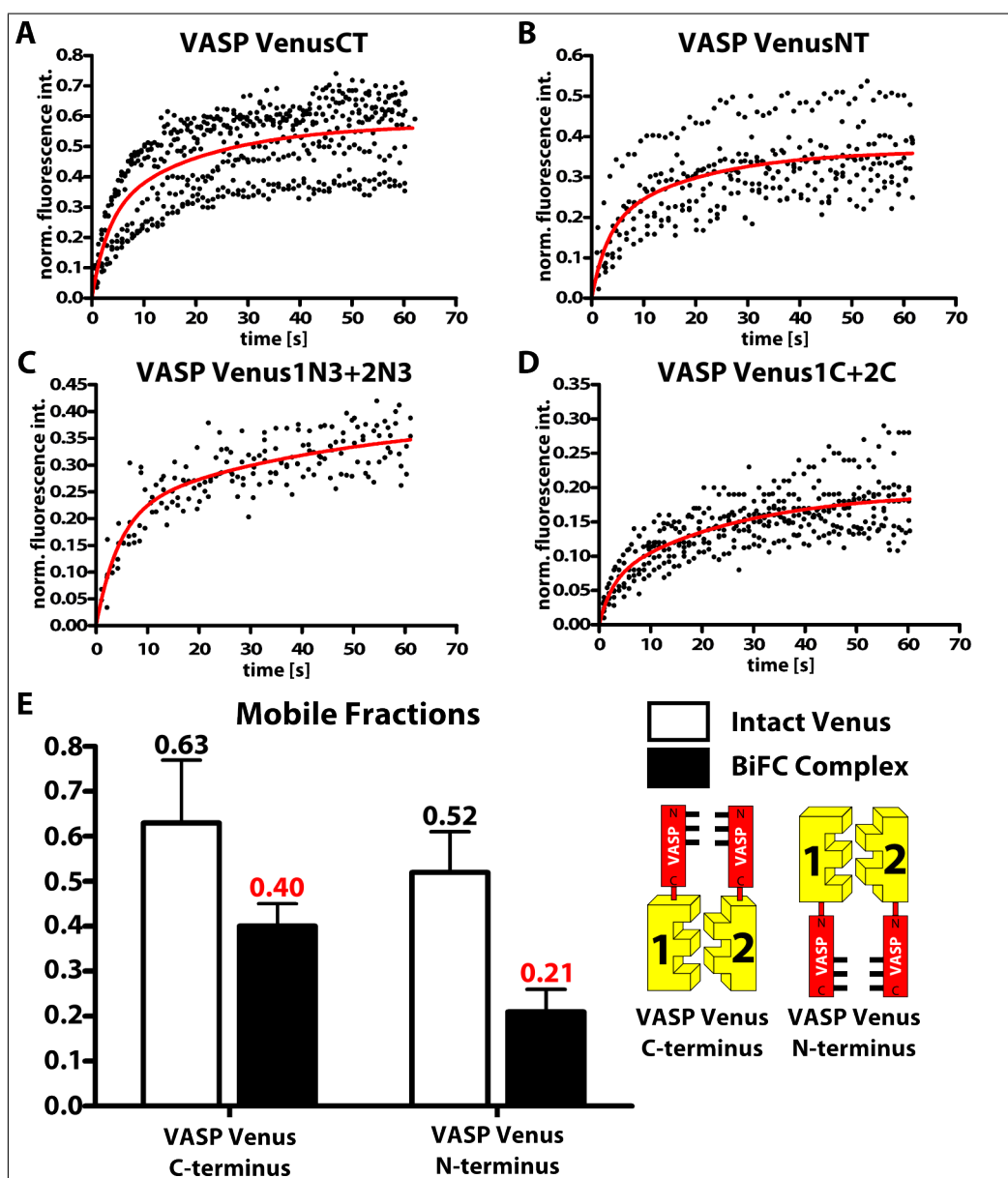


Figure 3.27: Mobile Fractions of VASP BiFC Complex and Intact Venus. Data analysis of FRAP assays depicted in fig. 3.26. Plotted data starts after finishing bleaching ( $t=0$  s). The fitted curve is coloured in red. **A.** Fluorescence recovery of VASP C-terminally tagged with intact Venus FP. **B.** Fluorescence recovery of VASP N-terminally tagged with intact Venus FP. **C.** Fluorescence recovery of the BiFC complex of C-terminally tagged VASP. **D.** Fluorescence recovery of the BiFC complex of N-terminally tagged VASP. **E.** Calculation of the mobile fractions. Mobile fractions of VASP coupled to the respective intact Venus FP are clearly larger than those of the BiFC complexes. A schematic overview of the combinations used is depicted on the right side.



it cannot be excluded that this is not significant. Nevertheless, this trend was confirmed when analyzing the mobile fractions of the BiFC complexes, since the difference between the N-terminal BiFC complex VASP Venus1C+2C ( $0,40 \pm 0,05$ ) and the C-terminal one VASP Venus1N3+2N3 ( $0,21 \pm 0,05$ ) was more obvious. Thus, albeit carefully, it can be concluded that the BiFC complex of a VASP dimer presumably embedded in a homo- or heterotetramer reduces the mobile fraction and an N-terminally-located FP or complex formation amplifies this effect. This result allows the assumption that complex formation in general can impair exchange dynamics, which is coherent with the potential irreversibility of the complementation and this effect is increased if the non-fluorescent fragment is fused to the protein region responsible for targeting, in this case the N-terminal EVH1 domain of VASP. Despite these alterations and limitations the BiFC assay and the components used are suitable for analyzing actin cytoskeleton-related proteins and structures.

### 3.3.6.2 BiFC Analysis of the Xin C and Nebulette Interaction in A7r5 Cells

The interaction between Xin and the SH3 domain of nebulin and nebulette is mediated by a proline-rich motif included in the isoforms Xin A and Xin C. While Xin A can be detected on protein level directly after the onset of myogenic differentiation of H-2K cells, only the existence of Xin C mRNA can be doubtlessly proved (cf. sections 3.2.2 and 3.2.1). However, Xin C seems to be upregulated in pathogenic conditions of the heart (Otten *et al.*, 2010), which makes it perhaps suited as a protein marker for certain cardiomyopathies. Furthermore, this isoform lacks the eponymous repetitive motifs and hence investigating this isoform can shed more light also on the function of the other two isoforms. Due to the first identification of Xin C in the heart, the interaction of human Xin C and human nebulette, the most abundant nebulin-repeat-containing protein in the heart, was analyzed in embryonic mouse cardiomyocytes using the BiFC method (cf. section 3.3.6.3). In order to identify suitable combinations of the fusion proteins and to prove the functionality of the constructs used, first complementation experiments were performed in A7r5 cells (cf. section 2.10.1.2). To study the localization of this interaction only full-length proteins or isoforms were transfected to avoid artifacts caused by the use of protein fragments and to simulate *in vivo* situations. Xin C derived from cDNA of human skeletal muscle cells and nebulette was amplified from the cDNA clone IRAMp995M168Q bought from imaGenes, Berlin. Both were subsequently cloned into mammalian expression vectors to obtain a fusion protein with the intact yellow fluorescent

protein (VenusNT, VenusCT, cf. sections 2.5.2.1 and 2.5.2.2) and fragments for fluorescent complementation (Venus1C, Venus2C, Venus1N3, Venus2N3, cf. section 2.9.5 and fig. 2.1). Adding a C-terminal tag to nebulette completely abolishes the interaction to Xin (cf. section 3.3.3), therefore the Venus protein or fragment was only fused to nebulette's N-terminus (VenusNT, Venus1C, Venus2C). Single transfections of Xin C and nebulette coupled to intact Venus served as a control to identify positive combinations of BiFC plasmids. All four potential combinations of fusion proteins were tested but only the mixture of nebulette in Venus1C and Xin C in Venus2C revealed a complementation signal.

Nebulette contains 22 copies of nebulin-like repeats and a C-terminal SH3 domain (cf. section 1.5.4). In cardiomyocytes, nebulette targets to the Z-disc and a fragment comprising only the repeats associates with actin filaments proving their F-actin binding capacity. Transfection in nonmuscle cells results in dense body-like decoration of actin filaments and incorporation into focal contacts (Moncman und Wang, 1999). Expression of nebulette in A7r5 cells basically confirmed these results but extended the view. In general, the transfection of nebulette did not show any toxic effect or abnormally altered the cell shape or size. Nebulette mainly exhibited a punctate association with stress fibres, sometimes interrupted by a more continuous signal (fig. 3.28 A, D, G and D' arrowhead and A' open arrowhead, respectively). Stress fibres can be subdivided into dorsal and ventral stress fibres as well as transverse arcs, which are probably generated by different mechanisms (Hotulainen und Lappalainen, 2006). A closer look at these structures revealed striking differences in the decoration pattern of nebulette. While transverse arcs of the cortical stress fibres displayed the dense body-like targeting known (fig. 3.28 D'-F' arrowhead), dorsal stress fibres were continuously decorated (fig. 3.28 D'-F' arrow). The latter probably arises from formin-dependent polymerization from focal adhesions resulting in unipolar filaments presumably cross-linked by  $\alpha$ -actinin but lacking myosin II. In contrast to that, transverse arcs form upon endwise association of small actin bundles with myosin II bundles in the cell periphery (Hotulainen und Lappalainen, 2006). Therefore, a punctate localization of nebulette possibly indicates incorporation of myosin II and contractile stress fibres. Although the dorsal stress fibres did not terminate in very prominent v-shaped focal adhesions in this cell, the ends of these dorsal stress fibres broadened (fig. 3.28 D'-F', arrow), which could mark small focal contacts. Nevertheless, nebulette was also present in focal adhesions, identified by their shape and accumulation of F-actin (fig. 3.28 G-I, arrow). In conclusion, these results conform to others previously obtained (Moncman und Wang, 1999) and show that transfection of nebulette does not



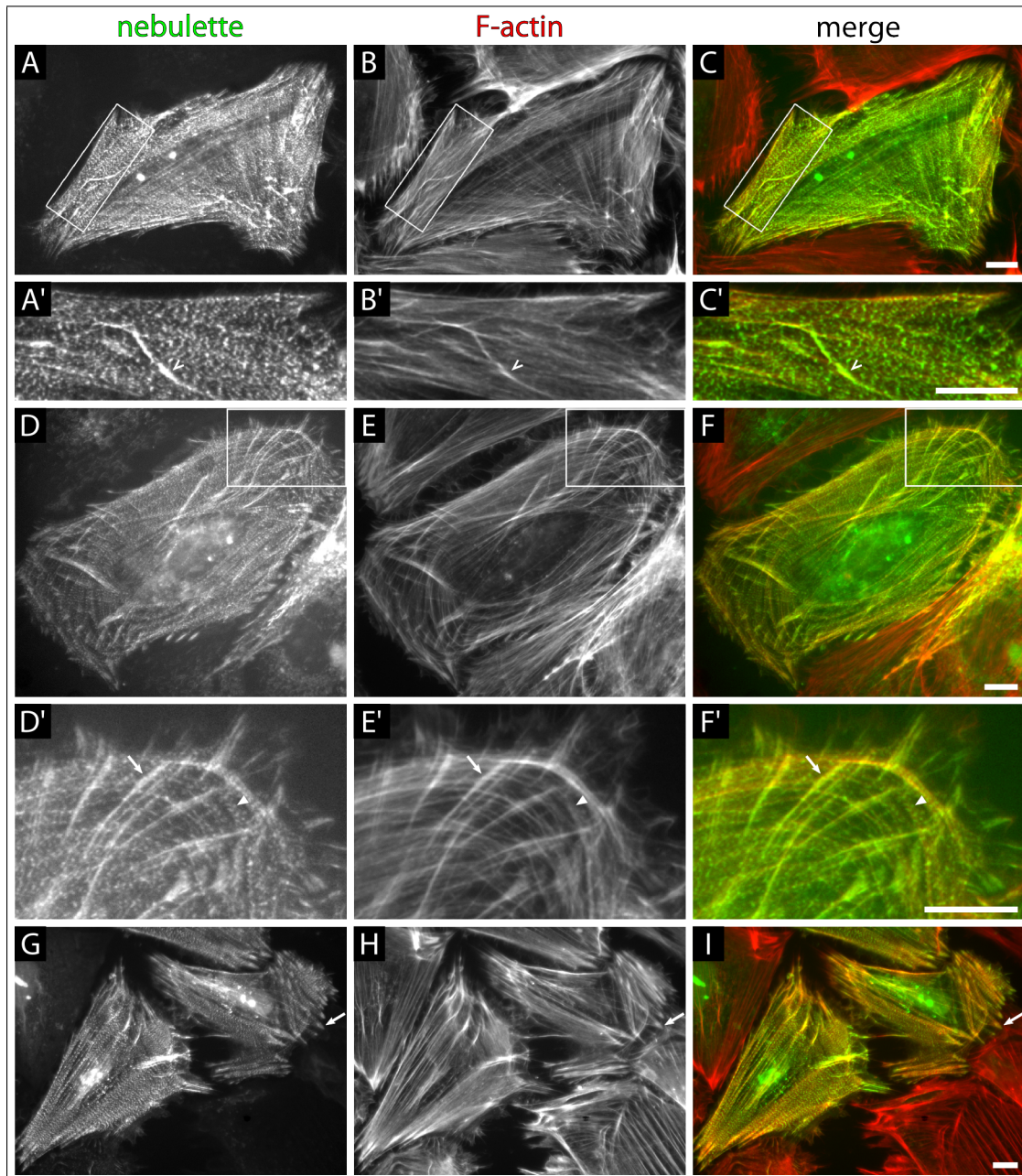


Figure 3.28: **Nebulette targeting in A7r5 cells.** Epi-fluorescence images of A7r5 cells transfected with nebulette N-terminally tagged with the yellow FP Venus and labeled with phalloidin. In merge images (C, C', F, F', I) nebulette and F-actin are tinted green and red, respectively. **A-C.** Nebulette predominantly associates with actin filaments in a punctate pattern. **A'-C'.** Some actin filaments exhibit a continuous nebulette decoration (open arrowhead). **D-F.** Cell with prominent cortical and dorsal stress fibres and nebulette targets to both actin filament populations. **D'-F'.** Transverse arcs show a periodic association with nebulette (arrowhead) whereas dorsal stress fibres are continuously labeled (arrow). **G-I.** Nebulette targets to focal adhesions (arrow). Scale bar 10  $\mu\text{m}$ .

negatively alter the actin cytoskeleton of A7r5 cells, as different subpopulations of stress fibres can still be identified. Furthermore, it very likely indicates incorporation of myosin II in contractile stress fibres by a punctate decoration of actin filaments.

Xin-Repeats have been shown to bind actin filaments in A7r5 cells and stabilize them against depolymerization caused by Latrunculin A (Pacholsky *et al.*, 2004). The smallest Xin isoform Xin C lacks the repeats but harbours the binding site for filamin C (cf. section 1.10). Transfection of Xin C had a dramatic effect on the architecture of the actin cytoskeleton of A7r5 cells, which was independent of the fusion protein used. Xin C accumulated in aggregates at perinuclear sites (fig. 3.29 A and D, open arrowhead) and these aggregates occasionally contained actin (fig. 3.29 D, open arrowhead). At these sites the otherwise prominent stress fibres (fig. 3.29 A and D, asterisks) were clearly reduced in number and size. In the cell periphery, remnants of the typical stress fibre arrangement of transverse arcs and dorsal stress fibres could be detected (fig. 3.29 B'), and some of the dorsal stress fibres were continuously decorated by Xin C (fig. 3.29 A' and B', arrow). A strong labeling of Xin C was always accompanied by accumulation of F-actin, whereas most of the cell exhibited Xin C-containing dots not clearly associated with actin and less ordered than nebullette. Additionally, Xin C targeted to the leading edge of the lamellipodium (fig. 3.29 A'–C', arrowhead) and other submembranous regions (fig. 3.29 A–C and D–F, arrowheads) as well as to small filopodia-like structures (fig. 3.29 D'–F'). Some of these structures showed a continuous Xin C decoration, which was most intense at sites of actin accumulation (fig. 3.29 D'–F', arrow). The submembranous actin cytoskeleton displayed less linear and stronger branched filaments, which were mainly free from Xin C but decorated by Xin C at sites of a strong phalloidin signal in an irregular, continuous pattern (fig. 3.29 D''–F''). In comparison to nebullette, a prominent targeting to focal adhesions was missing, however, it was occasionally found in terminal regions of stress fibres (fig. 3.29 D–F, arrow). In summary, although Xin C does not have any direct interaction site to actin filaments, it dramatically alters its organization. The characteristically prominent stress fibres of A7r5 cells are clearly reduced in the cell body, where Xin C is mainly detected in dots and larger aggregates, and thereby seemingly antagonizing the protective effect of the Xin-Repeats-containing isoforms described earlier (Pacholsky *et al.*, 2004). In the cell periphery, the stress fibres appear in a branched network and distinct dorsal stress fibres and transverse arcs are missing. Actin filaments providing a very intense phalloidin signal are mostly continuously decorated with Xin C, a targeting pattern of Xin C completely restricted to these type of actin filaments.

The single transfection of Xin C and nebullette revealed different localization patterns

and effects on A7r5 cells, which raises the question if and where both proteins interact, which can be indicated by a fluorescence complementation signal upon cotransfection of both interaction partners fused to FP fragments. As depicted above, only one combination of fusion proteins (nebulette Venus1C and Xin C Venus2C) provided BiFC complex formation. Analogue to Xin C alone, a BiFC signal was obtained in aggregates in the center of the cell, most of which did not contain actin (fig. 3.30 A–C). Although the actin cytoskeleton was altered in all cells providing a BiFC signal, the effect was not as pronounced as in Xin C transfected cells. While the actin cytoskeleton had disappeared at sites of Xin C–nebulette aggregates, the cortical actin was still detectable (fig. 3.30 A–C and G–I). There, the complex continuously decorated stress fibres strongly labeled with phalloidin. At the cell membrane, the complex was associated with the termini of actin filaments and microspikes (fig. 3.30 A–I, arrow). Apart from that, a punctate localization obtained with both interaction partners alone could also be detected, however to a lower degree. These results show that the BiFC assay can be applied to study the localization of the Xin–nebulette interaction at least in A7r5 cells and qualifies one combination of fusion proteins for testing in embryonic mouse cardiomyocytes. This combination demonstrates that nebulette cannot completely compensate for the effect of Xin C on the actin cytoskeleton. Furthermore, the localization of the complex stronger resembles the Xin C pattern (fig. 3.29) probably due to perturbations of the actin cytoskeleton.



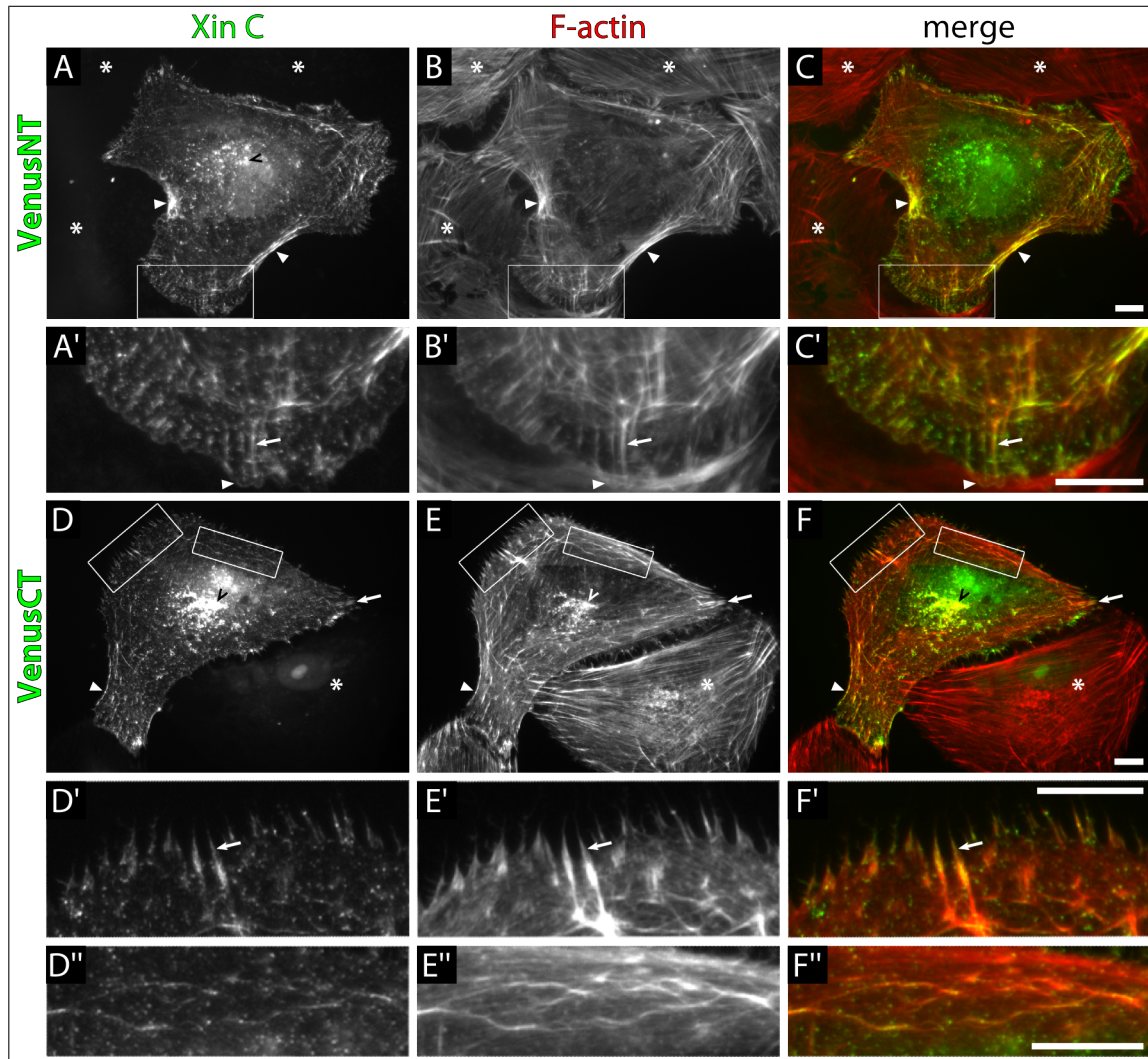


Figure 3.29: **Xin C targeting in A7r5 cells.** Epi-fluorescence images of A7r5 cells transfected with Xin C N- or C-terminally tagged with the yellow FP Venus and labeled with phalloidin. In merge images Xin C (C, C', F, F', F'') and F-actin are tinted green and red, respectively. Targeting of Xin C is not dependent on the site of FP-tag. **A-C.** Upon transfection of Xin C the typical prominent actin cytoskeleton of A7r5 cells (asterisks) is reduced and its architecture is dramatically altered. Xin C accumulates in perinuclear aggregates (open arrowhead) and in peripheral regions of actin enrichment (arrowhead). **A'-C'.** Remnants of typical cortical actin and dorsal stress fibres. Xin C localizes to the leading edge of the lamellipodium (arrowhead) and is continuously associated with dorsal stress fibres (arrow). **D-F.** Xin C aggregates occasionally contain actin (open arrowhead). Although no prominent focal adhesion targeting can be detected, Xin C is identified at terminal ends of actin filaments (arrow). Xin C continuously decorates submembranous actin filaments (arrowhead). **D'-F'.** Filopodia-like structures containing Xin C (arrow) and disrupted architecture of the cortical actin cytoskeleton. **D''-F''.** Branched submembranous actin cytoskeleton exhibits continuous decoration with Xin C at sites of a prominent phalloidin signal. Scale bar 10  $\mu$ m.

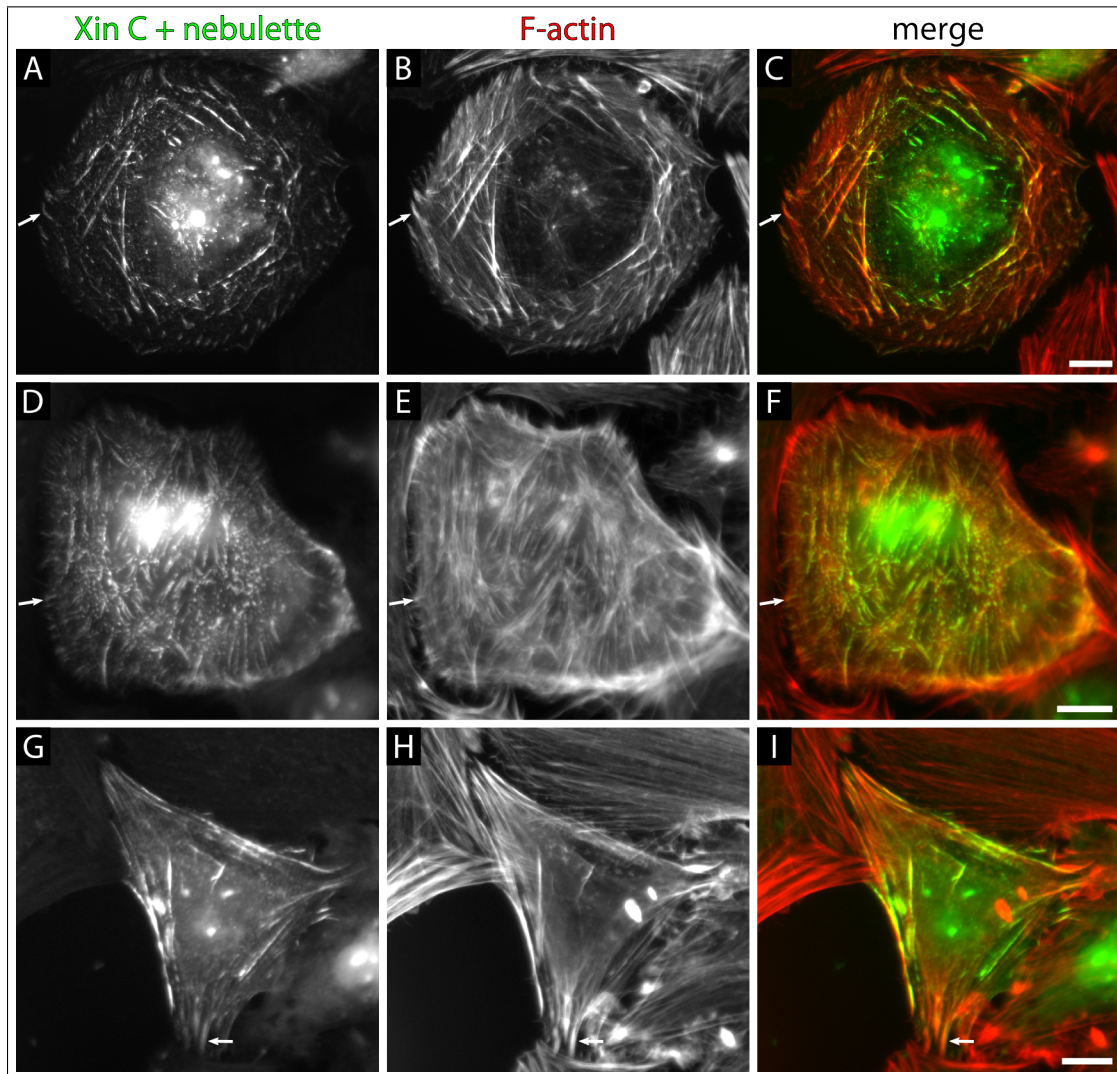


Figure 3.30: **Localization of the BiFC complex of nebullette and Xin C in A7r5 cells.** Epifluorescence images of A7r5 cells co-transfected with Xin C N-terminally tagged with a Venus fragment (aa 155-238) and nebullette fused to the C-terminus of a Venus fragment (aa 1-154). The cells were labeled with phalloidin. In merge images the BiFC complex of Xin C and nebullette and F-actin are tinted green and red, respectively. **A-C.** Large BiFC complexes are formed in the center of the cell which only occasionally contain F-actin. The cortical actin cytoskeleton reveals moderate alterations whereas no actin network can be detected in the center. Stress fibres strongly decorated with phalloidin exhibit a continuous association with the BiFC complex. Terminal end of actin filaments are also labeled (arrow). **D-F.** The Xin C-nebullette complex shows a punctate decoration of actin filaments which seem to be disordered. Both proteins also interact in microspike-like structures (arrow). **G-I.** The architecture of the actin cytoskeleton is affected by Xin C-nebullette complex formation in comparison to non-transfected cells. Terminal ends of actin filaments contain the BiFC complex (arrow). BiFC, bimolecular fluorescence complementation. Scale bar 10  $\mu\text{m}$ .

### 3.3.6.3 Localization of the Xin-Nebulette Interaction in Embryonic Mouse Cardiomyocytes

Nebulette is the only nebulin-repeat-containing protein, whose expression is restricted to heart tissue, where it is inserted into the Z-disc (Moncman und Wang, 1995). However, the newly identified binding partner Xin is not a constituent of the cardiac Z-disc in adult tissue but resides in the intercalated disc, which is described to be devoid of nebulette (Moncman und Wang, 1999). These observations favor an interaction during the development of cardiac muscle. Therefore embryonic mouse cardiomyocytes were isolated and electroporated with the fusion proteins utilized for establishing the BiFC assay (cf. sections 1.8.2, 2.10.6.2 and 3.3.6.2). Upon isolation embryonic cardiomyocytes reveal different stages of myofibril development thus offering a tool to investigate protein localizations at different developmental stages. As previously reported (Moncman und Wang, 1999), transfected nebulette is strongly targeted to mature Z-discs and Z-bodies in cells containing a high amount of myofibrils and is colocalized with titin Z-disc epitopes (fig. 3.31 A–C). Additionally, even in these cells of a later developmental phase, nebulette also decorated non-striated myofibrils (NSMF), where titin was not yet or only scarcely expressed in a dotted pattern (fig. 3.31 A–C, open arrowhead). A detailed analysis of the Z-disc architecture provided longitudinal structures connecting adjacent Z-discs, which were strongly decorated by nebulette but only occasionally contained titin (fig. 3.31 A'–C', arrowhead). These longitudinal connections could be predominantly detected at sites, where the Z-discs were not properly aligned laterally and their distance not adjusted yet (fig. 3.31 A'–C', open arrowhead) as well as the fusion to adjacent Z-bodies not been completed (fig. 3.31 A'–C', asterisk).

At the end of the myofibrillar apparatus, nebulette was a component of rope-like structures roughly perpendicular to the Z-disc they are connected to (fig. 3.31 D–E). These structures appeared to originate from the last fully developed Z-disc (fig. 3.31 D–E, arrowhead) and titin was either completely absent (open arrowhead) or only very scantily associated. Cardiomyocytes of an early developmental stage, i.e. they do not comprise mature myofibrils, displayed titin in a punctate pattern along developing myofibrils rather than ordered cross-striation (fig. 3.31 H). Nebulette targeted to these myofibrils but exhibited different localizations depending on the degree of myofibrillogenesis. NSMF's devoid of titin were continuously labeled by nebulette (fig. 3.31 G–I), especially at the end (arrow), which changed into a dotted pattern if titin was expressed. Furthermore, nebulette was also localized at submembranous regions not showing any titin expression (fig. 3.31



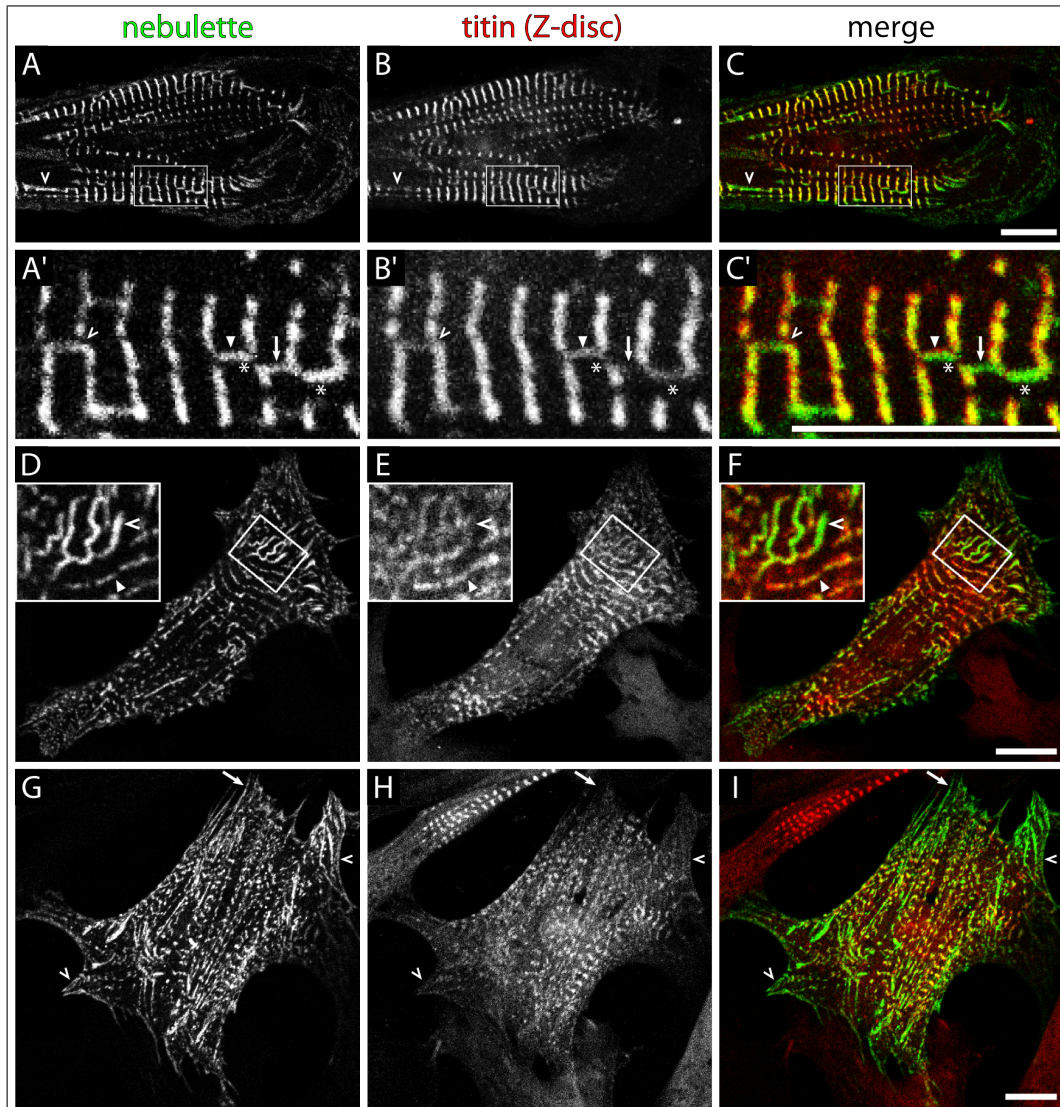
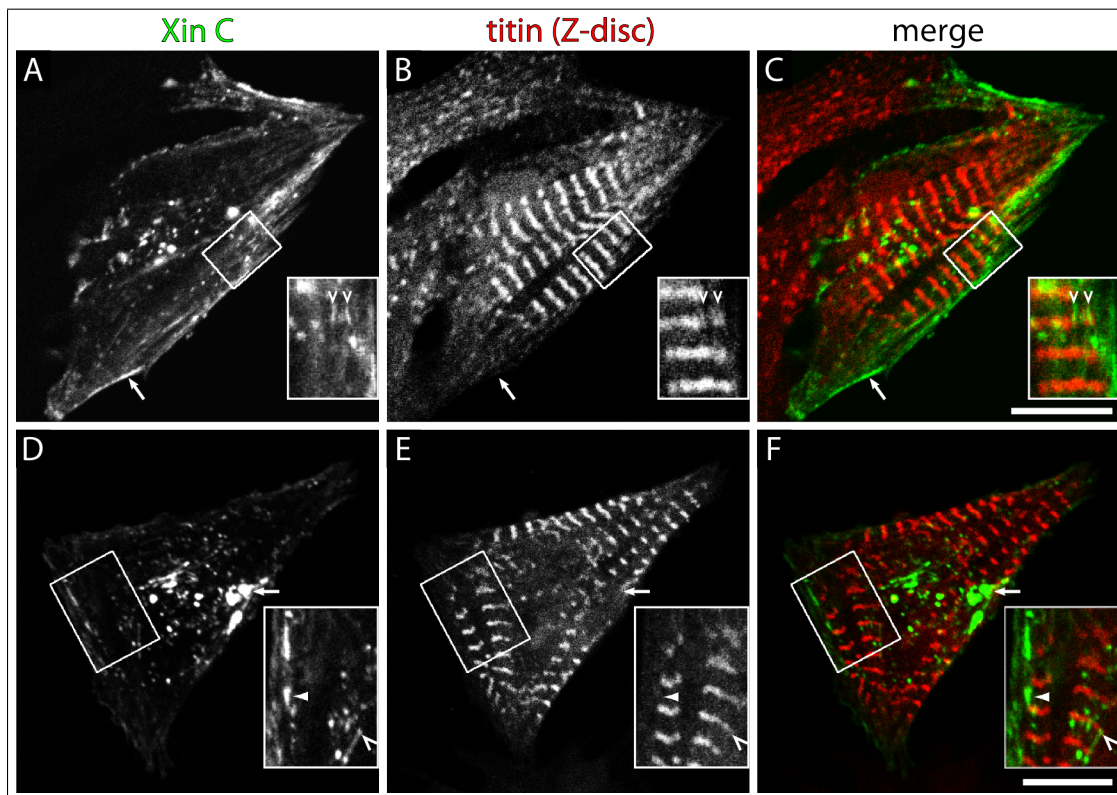


Figure 3.31: **Localization of nebullette in embryonic mouse Cardiomyocytes.** Confocal LSM images of embryonic mouse cardiomyocytes transfected with nebullette and labeled with an antibody against a titin Z-disc epitope. In merge images (C, C', F, I) nebullette and titin are tinted green and red, respectively. **A-C.** Cardiomyocyte containing well-developed myofibrils. Nebullette and titin colocalize at mature Z-discs and Z-bodies. NSMF without or emerging titin association are continuously decorated by nebullette (open arrowhead). **A'-C'.** Nebullette targets to longitudinally Z-disc connecting structures which can contain titin (arrowhead) or not (arrow). These structures can be identified at sites of incorrect lateral alignment of Z-discs (open arrowhead) or incomplete fusion of adjacent Z-bodies (asterisks). **D-F.** Nebullette is a component of rope-like structures lacking titin (open arrowhead) which seem to originate from the last Z-disc (arrowhead). **G-I.** Cardiomyocyte without fully developed Z-discs. Nebullette exhibits varying localization patterns depending on the degree of myofibril formation. It continuously decorates NSMF's lacking titin association (arrow) but exhibits a punctate pattern upon titin integration. At submembranous sites, nebullette does not reveal colocalization with titin (open arrowhead). NSMF, non-striated myofibril. Scale bar 10  $\mu\text{m}$ .





**Figure 3.32: Localization of Xin C in Embryonic Mouse Cardiomyocytes of late developmental stage.** Confocal LSM images of embryonic mouse cardiomyocytes containing prominent sarcomeres transfected with Xin C and labeled with an antibody against a titin Z-disc epitope. In merge images (C, F) Xin C and titin are tinted green and red, respectively. **A-C.** Xin C forms large aggregates in the cell center or smaller dots. Fusing Z-bodies are labeled at the edge (open arrowheads). Xin C targets to submembranous sites devoid of titin (arrow). **D-F.** Sites of Xin C accumulation are free from mature myofibrils (arrow). Within the contractile apparatus Xin C localizes between adjacent Z-discs (arrowhead) or decorates linear structures originating from the edges of Z-discs (open arrowhead). Scale bar 10  $\mu$ m.

G-I, open arrowheads). This transfection study revealed that nebullette can be associated to more structures than Z-disc or Z-bodies during development of cardiac muscle. It can target to NSMF and is a component of longitudinal Z-disc connecting structures at sites of incomplete Z-disc alignment, which only occasionally show titin colocalization. The decoration pattern of developing myofibrils changes from a continuous to a punctate one upon titin expression. This demonstrates that nebullette localization completely alters during cardiac myofibrillogenesis and supports the idea of previous reports that nebullette is important for myofibril organization (Moncman und Wang, 2002).

While nebullette is an integral part of the adult Z-disc of cardiac muscle, none of the three Xin isoforms has been detected in the Z-disc of healthy heart muscle. Nevertheless, transfection of Xin C into neonatal rat cardiomyocytes showed that Xin C can colocalize with  $\alpha$ -actinin in the Z-disc, whereas both other isoforms are excluded from this structure

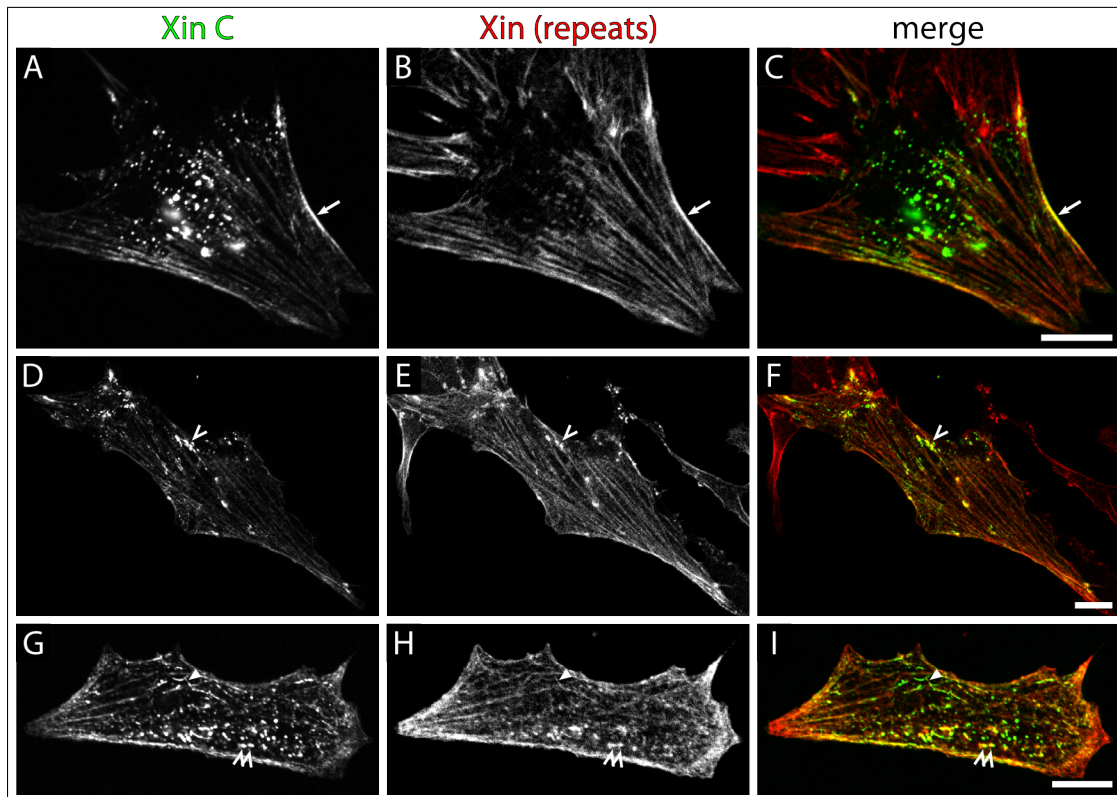


Figure 3.33: **Localization of Xin C in Embryonic Mouse Cardiomyocytes of early developmental stage.** Confocal LSM images of embryonic mouse cardiomyocytes lacking prominent sarcomeres transfected with Xin C and labeled with an antibody against Xin Repeats. In merge images (C, F, I) Xin C and Xin Repeats are tinted green and red, respectively. **A-C.** The early developmental stage is indicated by prominent NSMF's labeled with Xin-Repeats-containing isoforms. Xin C targets to these NSMF's but also exhibits typical aggregates in the cell center which rarely contain Xin-Repeat-containing isoforms. At submembranous sites, Xin C colocalizes with the other isoforms (arrow). **D-F.** Prominent NSMF decorated by all Xin isoforms and aggregates showing incorporation of Xin-Repeats-containing isoforms (open arrowhead). **G-I.** NSMF's cannot be detected and the cytoskeleton seems to be affected by the transfection. Xin C is associated with actin filaments continuously labeled with Xin-Repeats-containing isoforms (arrowhead). In some aggregates of Xin C, the other isoforms also accumulate. NSMF, non-striated myofibril. Scale bar 10  $\mu\text{m}$ .

(van der Ven *et al.*, 2006). A common feature of all Xin's is the targeting to NSMF while only Xin A and C are detected in ICD's upon transfection. Xin C also aggregates in the neonatal rat cardiomyocytes, which fits the observations in A7r5 cells (cf. section 3.3.6.2). Embryonic mouse cardiomyocytes transfected with Xin C always displayed large aggregates and dots in the cell center independent of the developmental stage of the myofibrils (fig. 3.32 and 3.33). The sites of larger aggregates were mostly devoid of sarcomeres (fig. 3.32 D–F, arrow) and generally a strong signal of Xin C was obtained, where no mature myofibril could be detected. Within the contractile apparatus, Xin C could label the edges of Z-disc or Z-bodies, which were about to fuse laterally (fig. 3.32 A–C, open arrowheads). Xin C also localized between 2 Z-discs and again rather to the lateral edges (fig. 3.32 D–F, arrowhead). A strong signal at the Z-disc was very rare, but there were structures originating from an intense dot at the Z-disc and ending in another intense dot, which was not part of the adjacent Z-disc (fig. 3.32 D–F, open arrowhead). In A7r5 cells Xin C targeted to submembranous regions which was also observed in embryonic mouse cardiomyocytes. At these sites, no titin could be detected (fig. 3.32 A–C, arrow) while Xin C colocalized with Xin-Repeats-containing isoforms (fig. 3.33 A–C, arrow).

Early stage cardiomyocytes exhibited many NSMF's depicted by the decoration with Xin-Repeat-containing isoforms (fig. 3.33 B, E and H). These isoforms were continuously associated with these immature myofibrils, the intensity increasing towards the end. Xin C colocalized with Xin A and B at these NSMF but the signal obtained was less prominent. While Xin A and B usually show neither aggregates nor smaller dots, Xin C was localized in a dot-like pattern in the cell center (fig. 3.33 A, D and G). However, some of these structures also contained either Xin A or B or both isoforms (fig. 3.33 D–I, open arrowheads). The actin cytoskeleton of A7r5 cells dramatically altered upon transfection of Xin C with stress fibres becoming reduced and the actin filaments more branched and arranged less linearly (fig. 3.29 D''–F''). To some extent, this effect could also be seen in embryonic mouse cardiomyocytes and these filaments were also decorated by Xin-Repeat-containing isoforms (fig. 3.33 G–I, arrowhead). Thus, Xin C exhibits a similar localization pattern as in A7r5 cells although the effect on the actin cytoskeleton is less prominent. Nevertheless, large aggregates of Xin C seem to interfere with the myofibrillar apparatus and occasionally alterations in the cytoskeleton can be detected. In early stage embryonic cardiomyocytes, Xin C colocalizes with the Xin-Repeats-containing isoforms at NSMF.

In adult heart tissue, nebullette and Xin are components of distinct structures of the Z-disc and the ICD, respectively. However, transfected Xin C was shown to colocalize with  $\alpha$ -actinin in the Z-discs of neonatal rat cardiomyocytes (van der Ven *et al.*, 2006).

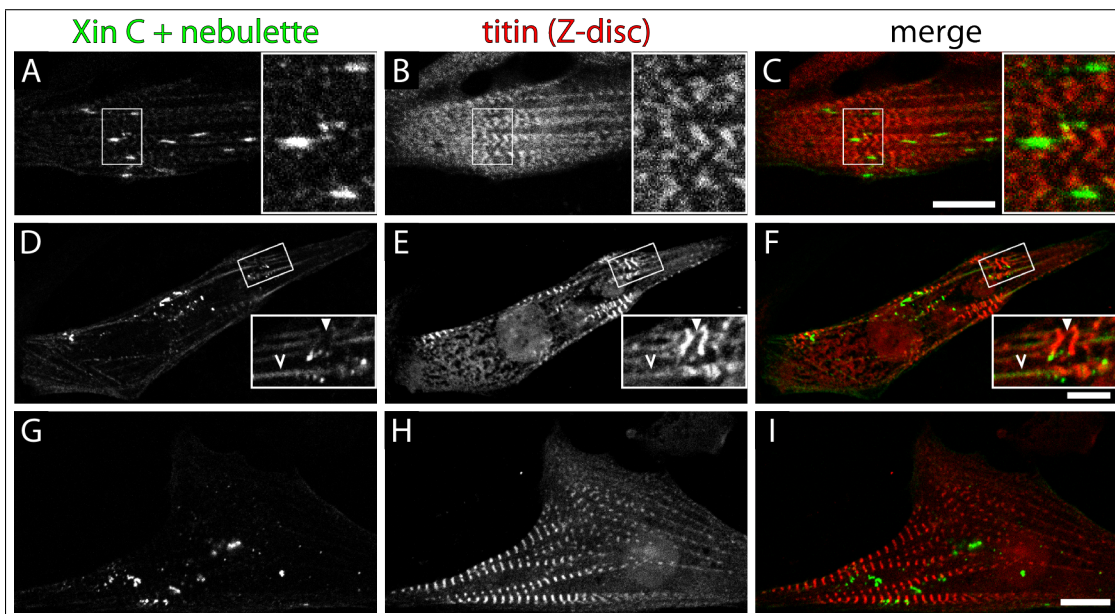


Figure 3.34: **Localization of the Xin C-nebulette complex in embryonic mouse cardiomyocytes of late developmental stage.** Confocal LSM images of embryonic mouse cardiomyocytes containing prominent sarcomeres co-transfected with Xin C and nebulette both tagged with non-fluorescent fragments of the Venus FP allowing for BiFC. Cells were labeled with an antibody against a titin Z-disc epitope. In merge images (C, F, I) the Xin C-nebulette BiFC complex and titin are tinted green and red, respectively. **A-C.** Prominent BiFC complex formation at longitudinal Z-disc connecting structures and a weak Z-disc targeting. **D-F.** Xin C and nebulette interact at NSMF's (open arrowhead) which is interrupted at sites of early Z-disc formation (arrowhead). A weak decoration of early Z-discs can be detected. **G-I.** Aggregates of Xin C-nebulette complex. BiFC, bimolecular fluorescence complementation. NSMF, non-striated myofibril. Scale bar 10  $\mu\text{m}$ .



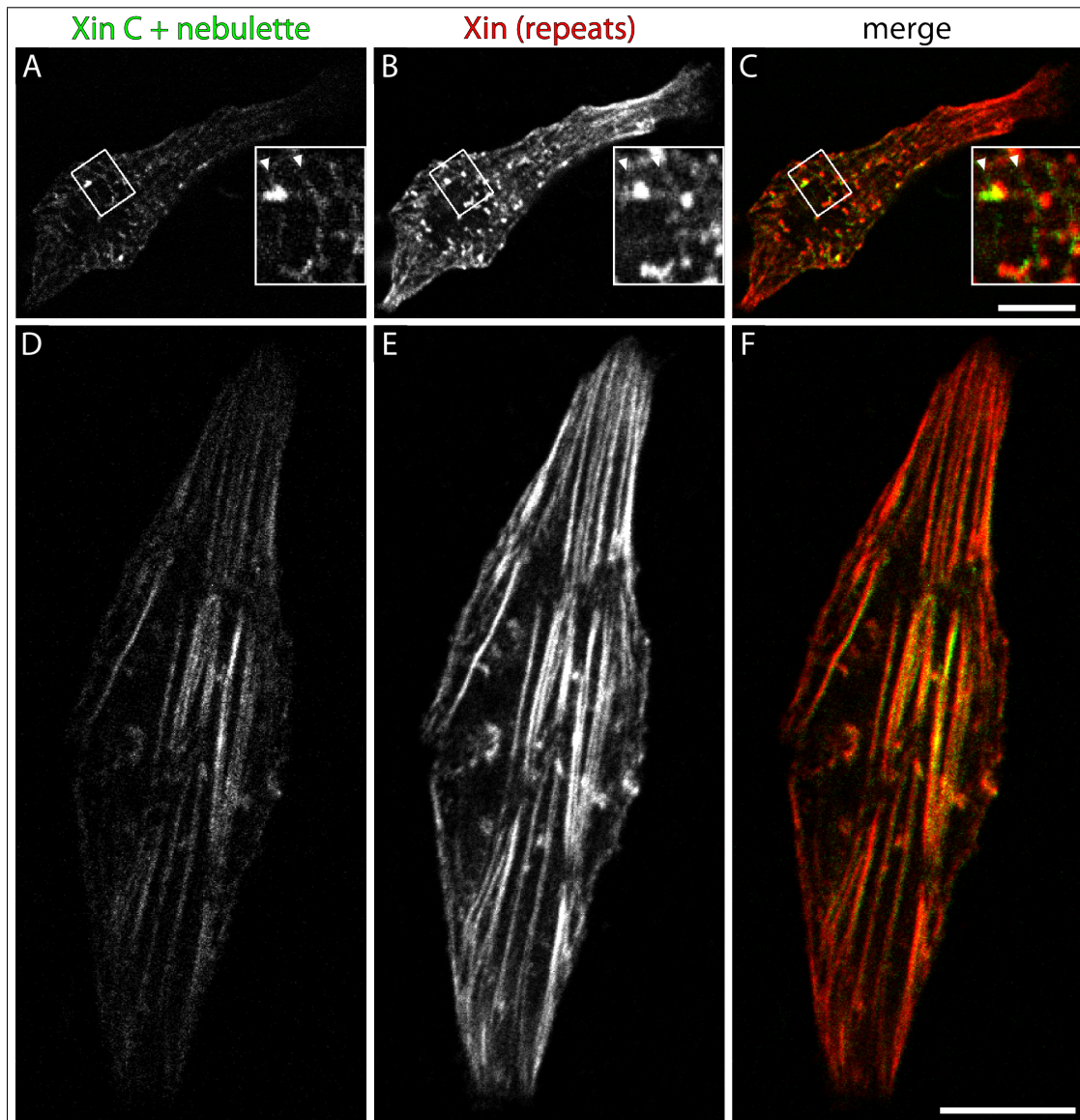


Figure 3.35: **Localization of the Xin C-nebulette complex in embryonic mouse cardiomyocytes.** Confocal LSM images of embryonic mouse cardiomyocytes co-transfected with Xin C and nebulette both tagged with non-fluorescent fragments of the Venus FP allowing for BiFC. Cells were labeled with an antibody against Xin Repeats. In merge images (C, F) the Xin C-nebulette BiFC complex and the Xin-Repeats-containing Xin isoforms are tinted green and red, respectively. **A-C.** In embryonic cardiomyocytes already containing Z-discs the Xin C-nebulette complex weakly targets to Z-discs (arrowheads) however Xin Repeats-containing isoforms do not clearly localize there but exhibit a punctate distribution. **D-F.** Early embryonic cardiomyocytes harbour prominent NSMF's which are decorated by Xin-Repeats-containing Xin isoforms and the Xin C-nebulette complex. BiFC, bimolecular fluorescence complementation. NSMF, non-striated myofibril. Scale bar 10  $\mu$ m.

The complex of Xin C and nebulin provided a BiFC signal not only in A7r5 cells but also highly specific in embryonic cardiomyocytes. The BiFC signal was formed very weakly at Z-discs (fig. 3.34 A, D, G and 3.35 A) but more prominently in longitudinal Z-disc connecting structures resembling those also obtained with nebulin alone (fig. 3.34 A–C). Both proteins, Xin C and nebulin, could target to NSMF and they also formed BiFC complexes at these myofibrillar precursor structures (fig. 3.34 D–F, open arrowhead, and 3.35 D–F). NSMF's could span the whole cell in early stages of myofibrillar development and contained considerable amounts of Xin A and or B (fig. 3.35 E). Upon formation of early Z-discs, the continuous labeling of NSMF by the Xin C-nebulin BiFC complex was interrupted (fig. 3.34 D–F, arrowhead). The more myogenic maturation proceeded the more NSMF's associated with the BiFC complex were lost and the localization of the fluorescence complementation signal changed to weak Z-disc targeting (fig. 3.35 A–C, arrowheads). At this stage, the Xin-Repeats-containing isoforms were not clearly situated at the sarcomeric boundaries. In conclusion, the Xin C-nebulin complex is formed at early developmental stages of embryonic mouse cardiomyocytes at NSMF'S and its localization changes during myogenic development into a weak association with Z-discs. Furthermore, emerging Z-discs can be connected by longitudinal structures containing the complex of Xin C and nebulin. Considering the localization of both proteins in adult heart tissue, this clearly demonstrates that they interact at certain developmental stages. This interaction is presumably lost after finishing sarcomere development due to disappearance of Xin from the Z-disc.

### 3.4 Xin Contains Functional Heptad Repeats

The human Xin A sequence harbours a region between amino acids 1462-1490, which is identified as a putative coiled-coil by the **Simple Modular Architecture Research Tool** (SMART, Schultz *et al.* (1998)). Coiled-coils are formed by a bundle of two or more  $\alpha$ -helices that are wound into a superhelical structure therefore representing an interface for homo- or heteromultimerization. In contrast to undistorted  $\alpha$ -helices which have approximately 3.6 residues per turn, the number of residues per turn is reduced to 3.5 in coiled-coils resulting in a repetition of the side-chain positions after seven residues or two turns, respectively. This sequence of seven amino acids displaying a certain hydrophobicity pattern and residue composition is generally referred to as heptad repeat whose positions are labelled *a-g*. The side chains of the positions *a* and *d* point to the center of the coiled-coil and are occupied by hydrophobic residues conferring a structure fundamentally



resembling an amphipathic  $\alpha$ -helix. The likelihood of the formation of coiled-coils can be estimated by various prediction methods, like MultiCoil (Wolf *et al.*, 1997), Paircoil2 (McDonnell *et al.*, 2006), PCOILS (Gruber *et al.*, 2005) and Marcoil (Delorenzi und Speed, 2002). Apart from the Marcoil program, which calculates posterior probabilities from a hidden Markov model, all others are built on a similar concept of a position-specific scoring matrix derived from the characteristic residue distribution at each position of the heptad. The main difference is the bioinformatical data, which was used to train these programs. MultiCoil predicts not only generic coiled-coils but additionally differentiates between two- and threestranded coils (Gruber *et al.*, 2006).

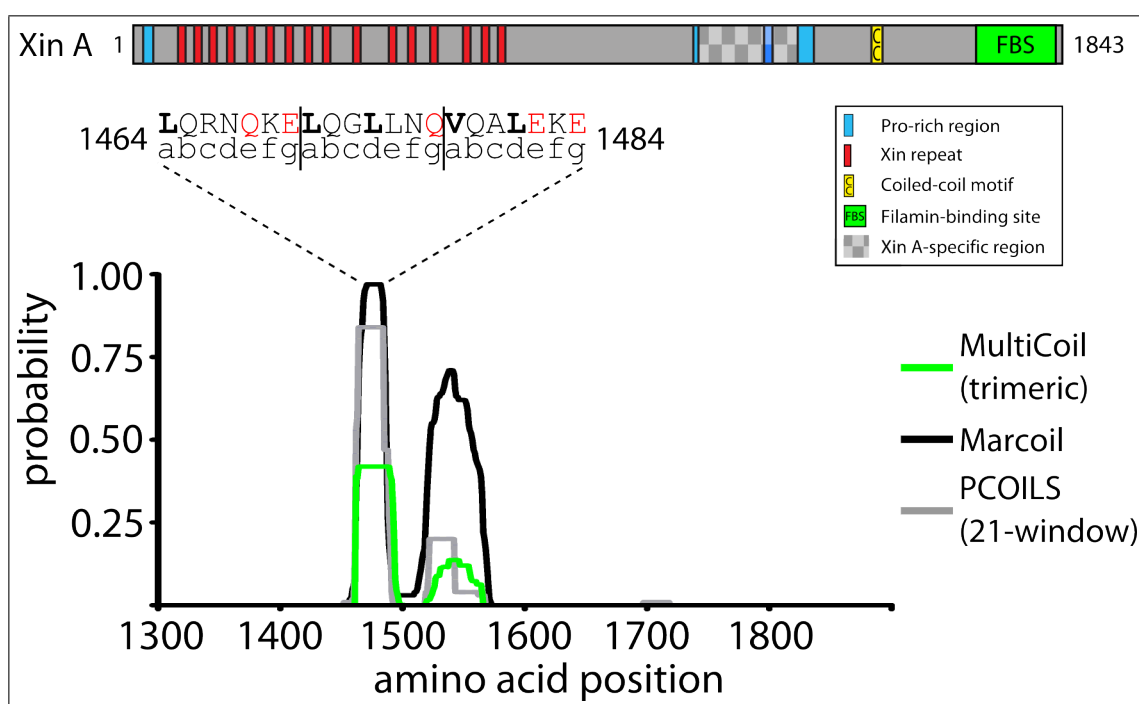


Figure 3.36: **Prediction of functional heptad motifs in human Xin.** A schematic overview of the domain organization of human Xin A is depicted at the top. Numbers correspond to amino acids. All three prediction methods MultiCoil (green), Marcoil (black) and PCOILS (grey) identify the highest probability of coiled-coil formation between amino acids 1464 and 1484. The respective sequence and the position within the heptad motif are illustrated above the graph. Hydrophobic residues at positions *a* or *d* and polar residues at positions *e* or *g* are shown as bold and red letters, respectively. For the MultiCoil algorithm, only probabilities of trimeric coils are depicted because dimeric coiled-coil formation does not provide high probability values. The PCOILS program was run using a window of 21 residues for prediction which offers the best compromise in detecting large and small coiled-coils.

In order to evaluate the probability of a coiled-coil in human Xin, all algorithms were applied to the human Xin A sequence. The PCOILS program identified three consecutive heptad repeats beginning with the amino acid leucine at position 1464 and closing with the lysine at position 1484 (fig. 3.36). These residues are only included in Xin isoforms A and

C but not in B. Depending on the parameters used the probability of coiled-coil formation ranged between 0,838 and 0,998. Marcoil uses a different approach than PCOILS but it basically yielded the same results. At a threshold of 90 % two consecutive heptad repeats could be identified between residues 1471 and 1484 (fig. 3.36). The preceding residues, which provided an equally high probability in PCOILS, also displayed significantly higher probabilities between 70 % and 90 % but this lay below the threshold. The MultiCoil algorithm did not provide any value above the default cutoff of 0.5 (fig. 3.36). Nevertheless, the program attributed probability values of around 0.4 to the amino acids 1464-1484, which was only slightly below and comparative analysis of coiled-coil prediction methods has already revealed that Multicoil systematically underpredicts coiled-coil segments (Gruber *et al.*, 2006). Interestingly, this probability could be almost completely traced back to trimeric coils. PairCoil2 does not report probabilities but documents scores. The cutoff is set to 0.025 and values below indicate a high likelihood. The residues 1462-1493 all exhibited a score below the cutoff (data not shown). In summary, the prediction methods clearly indicate that coiled-coil formation in the C-terminal part of Xin A between amino acids 1464 and 1484 is very likely. In addition, secondary structure analysis tools predict that this region most probably adopts an  $\alpha$ -helical conformation which fits the potential coiled-coil formation (data not shown).

To prove this hypothesis human Xin C which also contains these residues was tested for interaction with itself in a yeast two-hybrid assay. Here, Xin C showed a prominent homodimerization due to the high activation level of both reporter genes *HIS3* and *lacZ* (fig. 3.37). On the contrary, no association could be detected with human Xin B. These results clearly demonstrate that the heptad repeats predicted can form coiled-coils. However, it is still not clear how Xin C associates with itself, especially whether it forms homodimers or -multimers, since MultiCoil predicts a tendency to trimers (fig. 3.36). Therefore, chemical cross-linking of the purified Xin fragment Xin PR4+CC which contains the coiled-coil motif was performed (cf. section 2.9.3). Furthermore, a Xin fragment lacking the heptad repeats (Xin PR3+4) served as a negative control, whereas the actin-associated tetrameric protein VASP was included to show the general applicability of the assay for VASP is widely regarded to function as a tetramer formed by coiled-coils (Zimmermann *et al.*, 2002; Kühnel *et al.*, 2004).

This is reflected by the result of coiled-coil prediction using the algorithms mentioned above (fig. 3.38 A). All programs identified four heptad repeats located at the C-terminus in the EVH2 domain. The Marcoil and PCOILS methods provided high probability values above 0.95 for this region again demonstrating the reliability of these algorithms. The

MultiCoil method differentiates between dimeric and trimeric coils and surprisingly, only the probability of dimeric coils was above the threshold of 0.5. This result indicates that the prediction of coiled-coils forming motifs is trustworthy but determination of the exact stoichiometry is not possible. Immunodetection of purified VASP without addition of cross-linking reagent revealed that it can form SDS- and DTT-resistant dimers in solution to a minor degree indicated by the band between the 100 kDa and 130 kDa marker band which was approximately twice as high as the monomeric protein at 55 kDa (fig. 3.38 B). Immediately after the addition of a cross-linker an additional band migrating above 170 kDa occurred which very likely reflected tetrameric proteins and indicated oligomer formation in solution. Due to loading with cross-linker bands appeared more diffuse than the purified control protein, especially the highest bands. Furthermore, the highest band looked like a doublet which would display trimers and tetramers but the resolution of the gel was not sufficient to clearly separate these bands. Nevertheless, this result implies that VASP tetramers are formed in solution and the cross-linking assay is applicable to analyze oligomer formation.

Weak dimer formation of Xin PR4+CC in solution could be detected right at the beginning of the cross-linking reaction displayed by an emerging signal at 70 kDa (fig. 3.39 A). After 30 s, the dimer band had intensified and two faint bands migrating below 130 and 170 kDa, respectively, had occurred. These signals match quite well the calculated molecular weights of trimeric ( $\approx 105$  kDa) and tetrameric ( $\approx 140$  kDa) complexes estimated from the migration of the monomer ( $\approx 35$  kDa). In the course of the reaction the signal of the dimeric complex reached the highest intensity after 7 min whereas the formation of both the trimeric and the tetrameric complex increased until 15 min. Furthermore, the temporal occurrence and the course of the increase of signal intensity of the complexes depended on their stoichiometry, i.e., the amount of dimers increased faster than the one of trimers and tetramers. The Xin fragment Xin PR3+4 does not contain any heptad motifs predicted thus addition of cross-linker should not reveal any oligomer assembly. As expected, Xin PR3+4 did not form complexes with itself even after 15 min of incubation (fig. 3.39 B). These results clearly demonstrate that human Xin harbours functional heptad repeats which mediate the formation of oligomers.

### 3.4.1 Localization of Xin C Dimerization

Yeast two-hybrid studies and chemical cross-linking have shown that human Xin can homooligomerize presumably via heptad motifs located in the C-terminus which is only

included in isoforms A and C. Since Xin C exhibits selective targeting in A7r5 cells and has been approved in BiFC assays (cf. section 3.3.6.2), localization of Xin complexes was investigated with the BiFC approach in A7r5 cells using Xin C fused to non-fluorescent fragments of the Venus FP (cf. section 2.9.5).

All four combinations of fusion proteins were tested (fig. 2.1) and except from the co-transfection of Xin C expressed by the plasmids Venus1C and Venus2N3 they formed fluorescent complexes. The localization of the BiFC signal was not dependent on the combination used and hence all targeting patterns depicted were obtained with all combinations. In general, transfection of Xin C caused alterations in the actin cytoskeleton of A7r5 cells (fig. 3.29) which could also be detected in this BiFC assay. In most cases, transfected cells lacked prominent actin stress fibre bundles pervading the cell (fig. 3.40 A-C, asterisks) but displayed an unordered actin cytoskeleton. At low expression levels, Xin C complexes exhibited a punctate distribution throughout the cell and were only scarcely associated with actin-containing structures (fig. 3.40 A, D). The most prominent sites of Xin C dimerization or oligomerization were aggregates predominantly located in the center of the cell. Such an accumulation was occasionally accompanied by a simultaneous actin enrichment although Xin remained the major component of these aggregates (fig. 3.40 D-F, insert). Nevertheless, in areas containing large aggregates usually no actin filaments spanned the cell. Although Xin C lacks the actin-binding repeats, some actin filaments were continuously decorated (fig. 3.40 G-L, open arrowhead). The most prominent targeting of Xin C complexes could be seen at termini of actin filaments, however, not at very the tip (fig. 3.40 G-L, arrowhead). The amount of complexes associated with actin filaments at these sites could dramatically differ and upon Xin C enrichment the shape of the actin filaments changed into broader bundles due to actin accumulation (fig. 3.40 J-L). Xin C was also found in submembranous regions where it also formed complexes (fig. 3.40 J-l, arrow). In summary, the localization of Xin C BiFC complexes demonstrates that they are assembled at the same sites where Xin C alone is targeted to. Therefore, it can be speculated that Xin C usually acts as an oligomer *in vivo* or there exist monomeric and oligomeric protein populations with different functions.

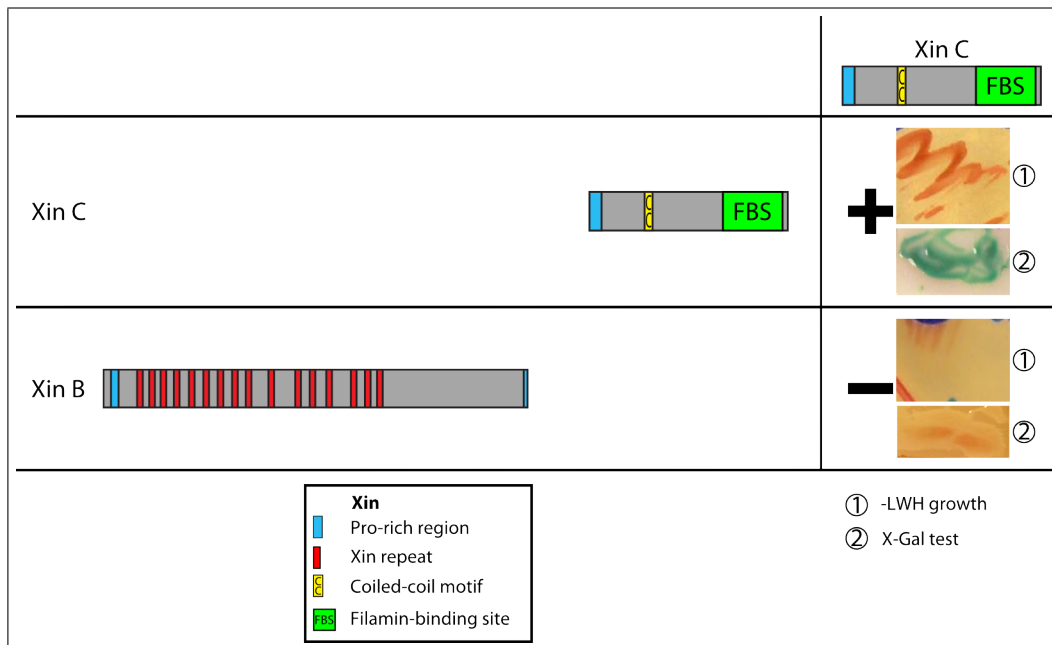


Figure 3.37: **Homodimerization of human Xin.** Results obtained in a yeast-two hybrid assay testing Xin C for homodimerization. Images marked as 1 depict growth on  $-LWH$  selective medium. Positive growth is indicated by newly formed deep red colonies. Activity of the  $\beta$ -galactosidase is displayed by blue-coloured colonies in images marked as 2. Xin C clearly homodimerizes but does not form dimers with Xin B.

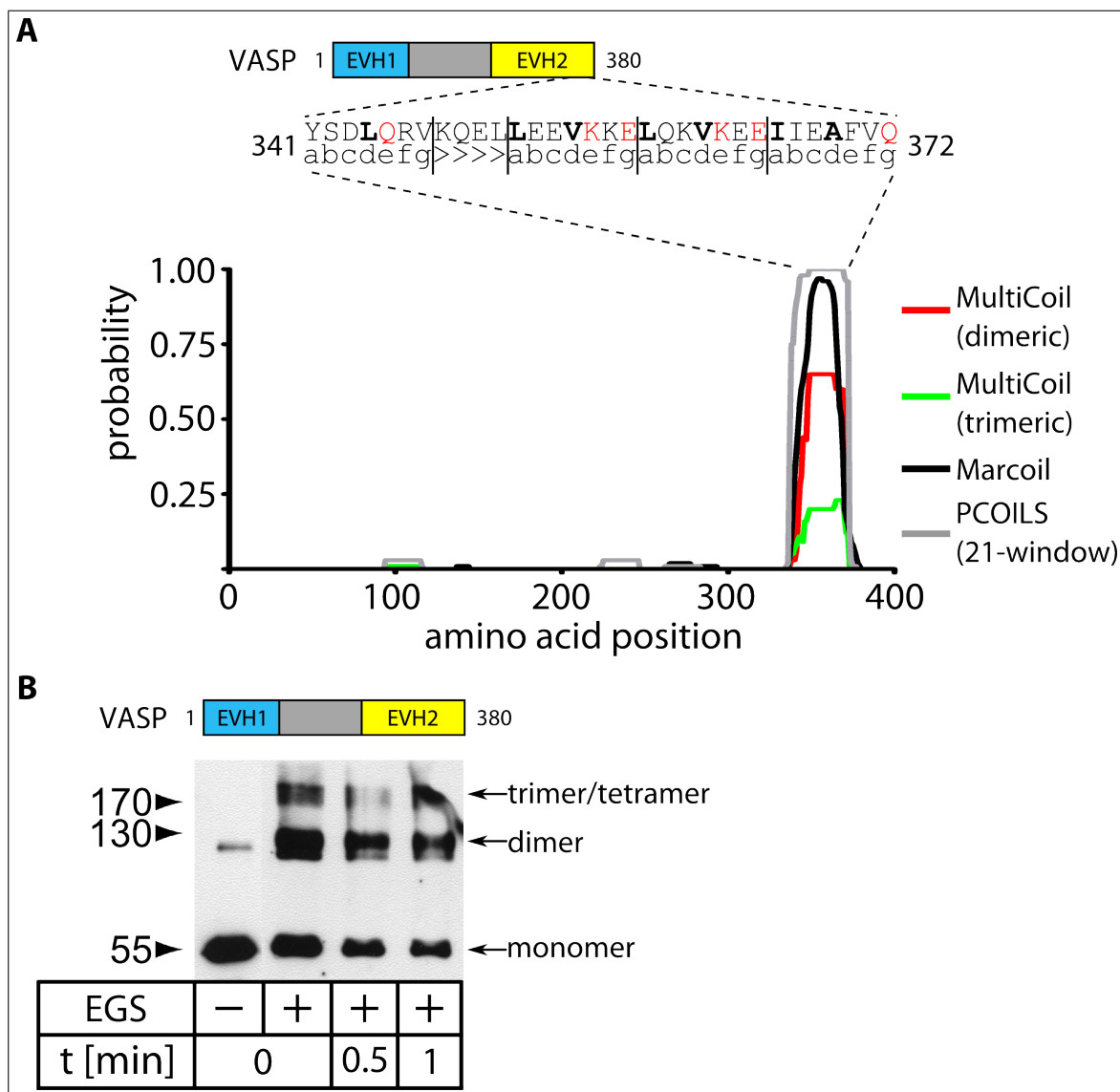


Figure 3.38: **Coiled-coil formation of human VASP.** **A.** Prediction of coiled-coil motifs in human VASP. A schematic overview of the domain organization of human VASP is depicted above the graph. Numbers correspond to amino acids. All three prediction methods MultiCoil (red/green), Marcoil (black) and PCOILS (grey) identify four heptad repeats between amino acids 341 and 372. The respective sequence and the position within the heptad motif are illustrated above the graph. Hydrophobic residues at positions *a* or *d* and polar residues at positions *e* or *g* are shown as bold and red letters, respectively. The MultiCoil algorithm provides highest probability of dimer formation (red). The PCOILS program was run using a window of 21 residues for prediction which offers the best compromise in detecting large and small coiled-coils. **B.** Chemical cross-linking of human VASP. Migration distances are shown in kDa. SDS- and DTT-resistant dimers can be identified in the purified protein. Addition of cross-linker (EGS) is indicated by a + below the respective lane and reveals a diffuse band migrating above 170 kDa which appears to be a doublet therefore displaying trimers and tetramers.



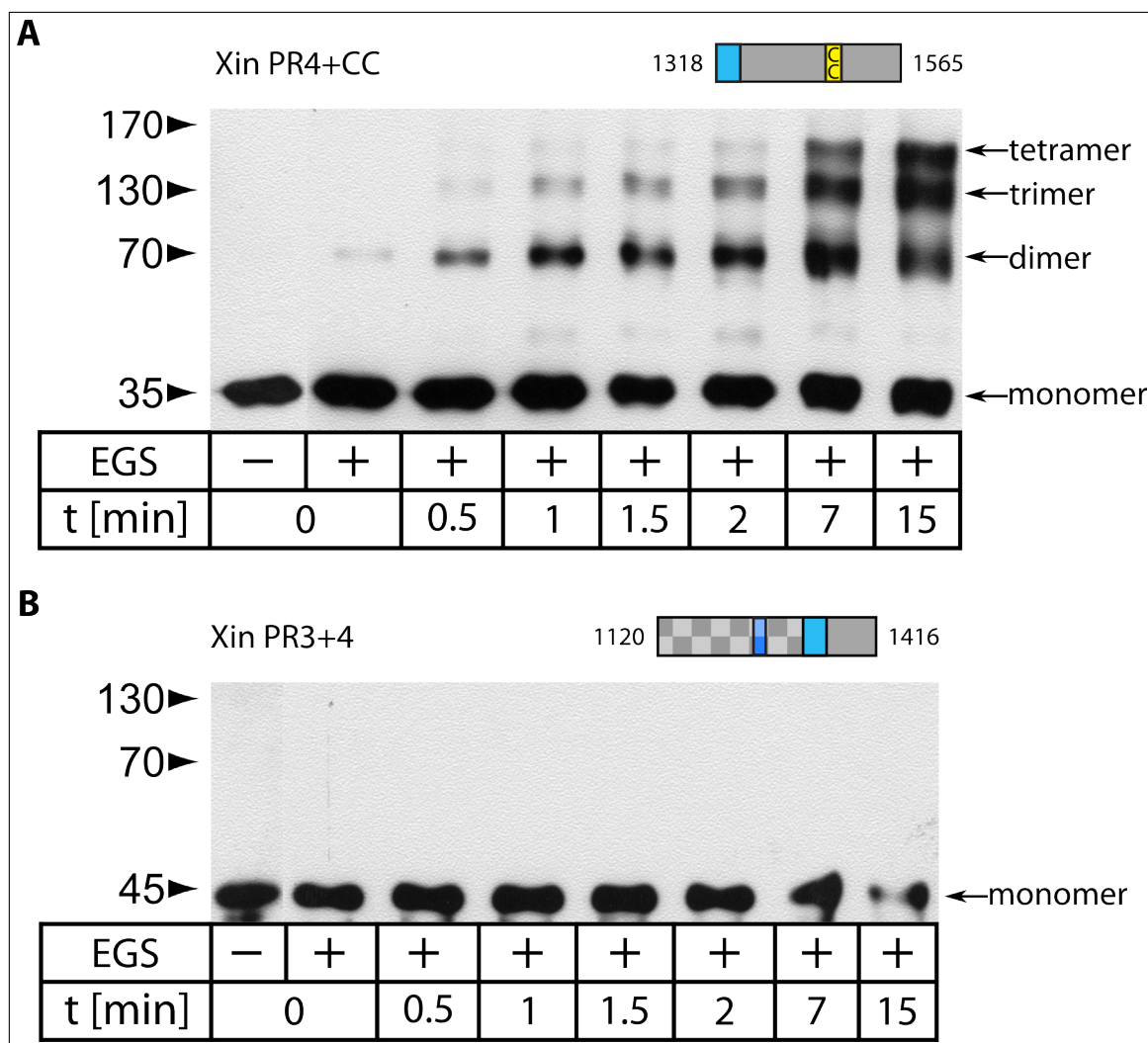


Figure 3.39: **Chemical cross-linking of human Xin.** Numbers at the schematic overview of the constructs refer to amino acid positions in human Xin A. Addition of cross-linking reagent (EGS) is indicated by a + below the respective lane. Migration distances are shown in kDa. **A.** Chemical cross-linking of Xin PR4+CC, a fragment containing the heptad repeats predicted. Purified protein does not show SDS- and DTT-resistant dimers but directly after the addition of EGS a faint dimer band can be detected. In the course of the reaction Xin PR4+CC forms trimeric and tetrameric complexes which increase until 15 min. **B.** Chemical cross-linking of Xin PR3+4. This fragment lacks heptad repeats and does not undergo homophilic interactions.

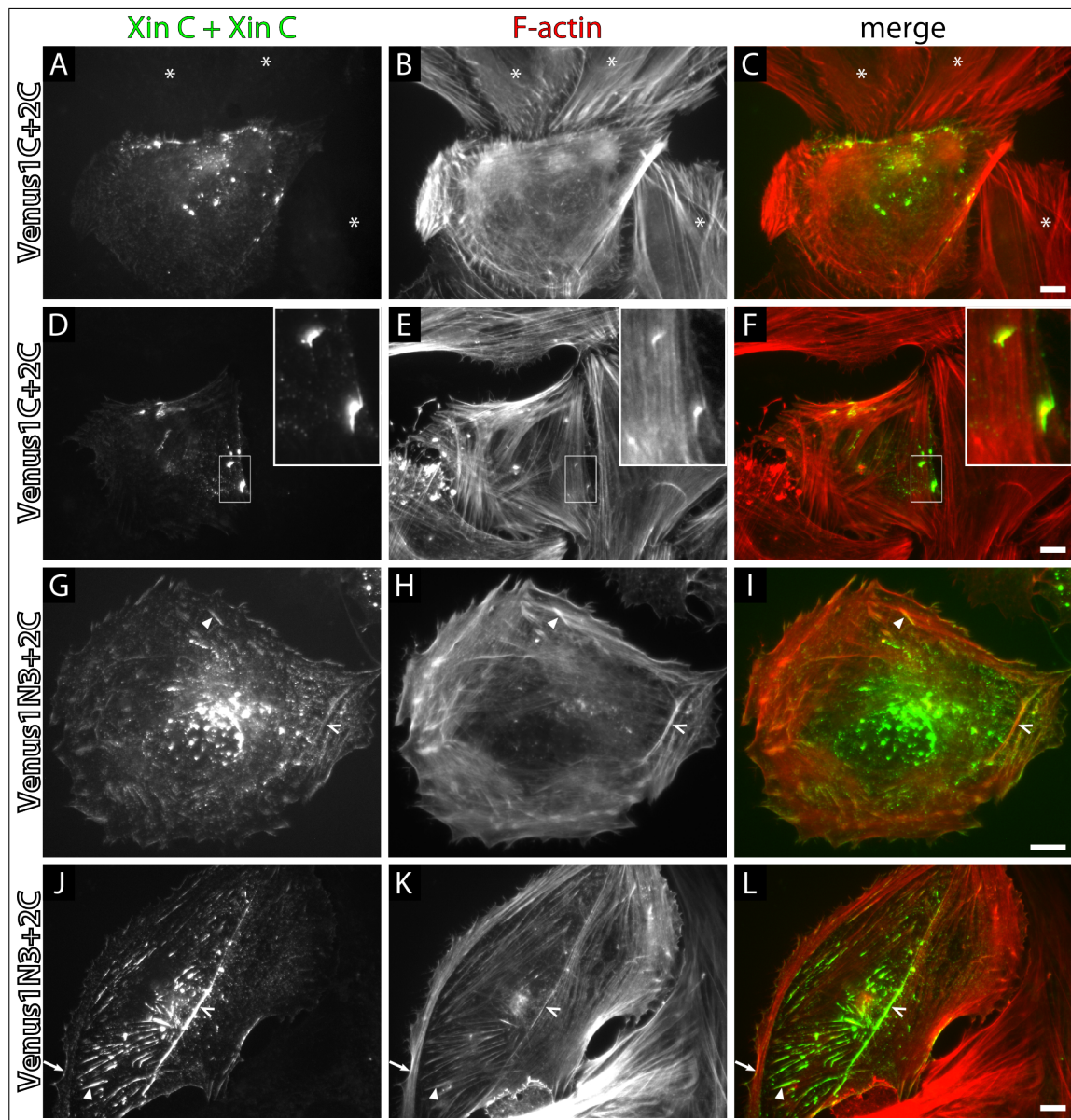


Figure 3.40: **Localization of Xin C dimers in A7r5 cells.** Epi-fluorescence images of A7r5 cells co-transfected with Xin C fused to Venus fragments enabling BiFC. The combination is depicted on the left side. The cells were labeled with phalloidin. In merge images (C, F, I, L) the BiFC complex of Xin C dimers and F-actin are tinted green and red, respectively. **A-C.** Transfection of Xin C alters the organization of the actin cytoskeleton in comparison to non-transfected cells (asterisks). Complexes are formed in large aggregates and small dot-like structures. **D-F.** Enrichment of Xin C complexes can cause further actin accumulation (insert). **G-I.** Some actin filaments are continuously decorated with Xin C dimers (open arrowhead) but Xin C mainly targets to terminal ends (arrowhead). **J-L.** Accumulation of Xin C complexes at terminal ends of actin filaments is accompanied by broadening of the filament (arrowhead). Interestingly, Xin C dimers are absent from the tip of actin filaments but can label actin filaments continuously (open arrowhead). Xin C complexes are also assembled at submembranous sites. BiFC, bimolecular fluorescence complementation. Scale bar 10  $\mu\text{m}$ .

### 3.4.2 Murine Xin Can Also Form Oligomers

Total loss of Xin in mice results in a very mild cardiac phenotype whereas mice only lacking Xin A and Xin B develop cardiac hypertrophy and suffer from disrupted ICD structure and myofilament disarray (Otten *et al.*, 2010; Gustafson-Wagner *et al.*, 2007) (cf. section 1.10). In order to investigate whether mouse Xin C (mXin C) also forms coiled-coils which could contribute to the phenotype of Xin AB-null mice, the mouse Xin sequence was analyzed with coiled-coil prediction methods since the sequence diversity between human and mouse Xin is increased in the C-terminal part. In general, all prediction methods detected less probability of coiled-coil formation than for human Xin (fig. 3.41 A). PCOILS provided the highest probability of 0.924 between amino acids 1510 and 1530 of mouse Xin A using the MTIDK matrix but this value dramatically decreased to 0.125 upon utilization of the iterative matrix and the PSI-BLAST. The Marcoil program identified seven consecutive potential heptad repeats at positions 1514-1555, however, only at a stringency level of 50 %. The probability obtained with MultiCoil only amounted to approximately 0.2 in the respective sequence segment, which is only half of the value of human Xin. Similar to human Xin, Multicoil predominantly predicted threestranded coiled-coils. Although the probability of coiled-coil formation in mouse Xin was significantly reduced in comparison to human Xin, chemical cross-linking of mouse Xin C was performed to elucidate species-specific differences of Xin. While purified mouse Xin C did not show any oligomer formation without cross-linking reagent and directly after its addition, two bands emerged migrating at 130 kDa and below the 250 kDa marker band, respectively, after 30 s of incubation (fig. 3.41 B). These bands very likely indicate dimeric and trimeric complexes since the Xin C monomer migrated slightly below 70 kDa resulting in an estimated molecular weight of  $\approx 140$  kDa and  $\approx 210$  kDa of the trimer and tetramer, respectively. Another band above 250 kDa occurred after 3 min of incubation, which was most clearly seen after 7 min and potentially reflected tetramer formation.

In summary, mouse Xin C forms oligomeric complexes *in vitro* although the probability is significantly lower than in human Xin. Thus, both human as well as mouse Xin isoforms A and C possess functional heptad repeats which mediate the formation of dimeric, trimeric or tetrameric complexes.

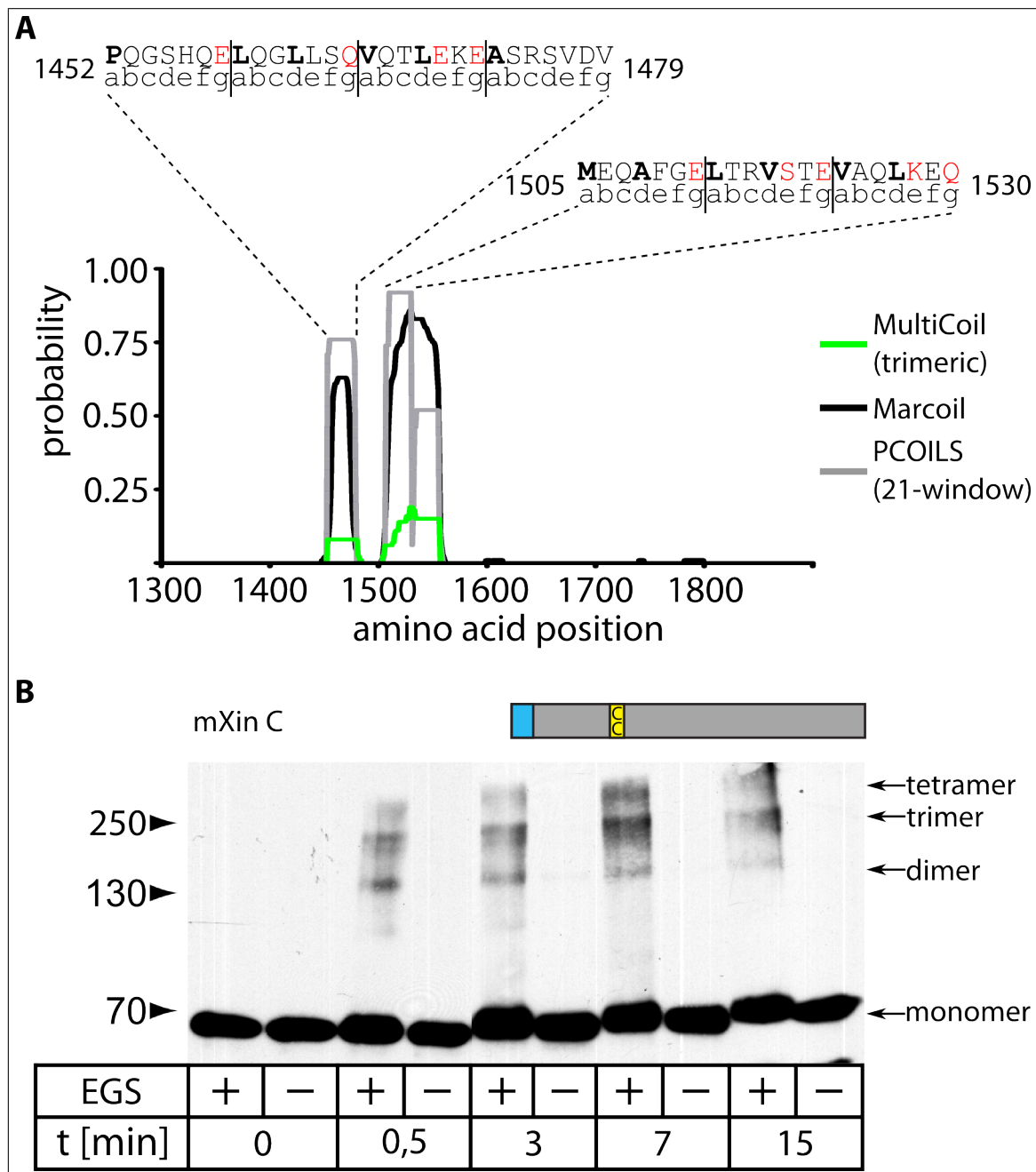


Figure 3.41: **Chemical cross-linking of murine Xin C.** **A.** Prediction of coiled-coil motifs in murine Xin C (mXin C). Numbers correspond to amino acid positions in murine Xin A. All three prediction methods MultiCoil (green), Marcoil (black) and PCOILS (grey) identify seven putative coiled-coil motifs between amino acids 1452 and 1530. The respective sequence and the position within the heptad motif are illustrated above the graph. Hydrophobic residues at positions *a* or *d* and polar residues at positions *e* or *g* are shown as bold and red letters, respectively. **B.** Chemical cross-linking of mXin C. Migration distances are shown in kDa. Addition of cross-linker (EGS) is indicated by a + below the respective lane and leads to the discovery of bands migrating around 130 kDa and below 250 kDa after 30 s which probably correspond to dimers and trimers, respectively. A potential tetrameric complex above 250 kDa can be identified after 3 min.

### 3.5 The Protein LIMCH1 is the First Xin A-Specific Binding Partner

Intraexonic splicing events in the single large coding exon of human Xin give rise to three different Xin isoforms. The largest isoform Xin A encoded by the complete exon comprises a unique region of 197 aa, which contains a small proline-rich region at its end (fig. 3.42 A). Identification of a Xin A-specific binding partner can provide more insight into the function of Xin proteins as it offers the possibility to allocate distinct functions to different isoforms. A Xin A fragment, containing the unique region and a proline-rich sequences also included in Xin C (Xin PR3+4) already used in the yeast two-hybrid screen, which identified the nebulin SH3 domain as a novel ligand (cf. section 3.3), provided four interacting clones of a cDNA named KIAA1102 in the same experiment (fig. 3.42 B).

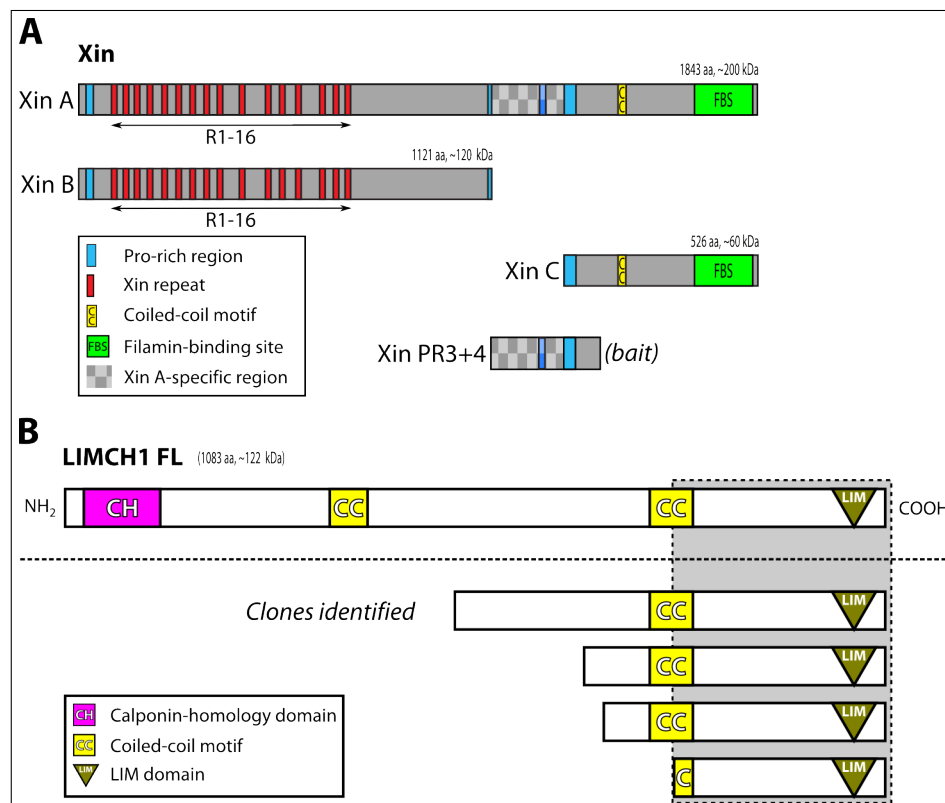


Figure 3.42: **LIMCH1 clones identified as Xin interaction partners in a yeast two-hybrid screen.** **A.** Schematic overview of the three human Xin isoforms. The fragment Xin PR3+4 was used as bait in a yeast two-hybrid screen of a human skeletal muscle cDNA library. **B.** Four clones encoding different portions of the C-terminus of a protein deriving from the human LIMCH1 gene. The hypothetical domain organization of the complete protein (LIMCH1 FL) is depicted above. The region included in all clones is indicated by a grey background.

These cDNA clones derive from a human gene designated as LIM and calponin ho-



mology domains 1 (LIMCH1) on chromosome 4. In human, three to five different splice variants are predicted (UCSC Genome Browser) and sequence analysis of the amino acids revealed that the largest variant presumably contains an N-terminal calponin homology (CH) domain and a C-terminal LIM domain. Additionally, the sequence comprises two regions of heptad motifs potentially mediating coiled-coil interactions. All clones identified harboured the C-terminal LIM domain and one half of the putative coiled-coil regions.

### 3.5.1 The LIM Domain of LIMCH1 Specifically Binds Xin A

The Xin A fragment, interacting with a C-terminal portion of LIMCH1 in a yeast two-hybrid assay, includes the Xin A-specific region and the proline-rich region also present in Xin C. To determine the binding region responsible in Xin, Xin C was also tested for binding to a C-terminal fragment of LIMCH1 comprising the second coiled-coil region and the Lim domain (LIMCH1 CC2) in a yeast two-hybrid assay (fig. 3.43).

While the original bait Xin PR3+4 and LIMCH1 CC2 activated the *HIS3* as well as the *lacZ* reporter gene as indicated by growth on –LWH minimal medium and a prominent blue colour in the X-Gal assay, respectively, Xin C and LIMCH1 CC2 could not induce the reporter gene products. This clearly demonstrates that LIMCH1 specifically interacts with the region unique to Xin A. The most prominent structural feature predicted in the fragment LIMCH1 CC2 is the C-terminal LIM domain. The term LIM derives from the first letters of the three proteins LIN-11, Isl1 and MEC-3, where this structural motif was first described. A LIM domain coordinates two zinc ions each with four conserved cysteine and or histidine residues. This establishes a tandem zinc finger structure, which is present in more than 100 sequences, and defines a versatile module for protein-protein interactions (Kadrmas und Beckerle, 2004). Although the zinc finger structure is common to all LIM domains, the variability in the non-conserved residues imparts individual binding properties so that the interaction partners share no obvious similarities in their binding interfaces and thus prediction of such an interaction is very limited (Kadrmas und Beckerle, 2004). Nevertheless, the hypothesis that the Xin–LIMCH1 interaction is mediated by the LIM domain was tested in another yeast two-hybrid assay using only the LIM domain as a prey (LIMCH1 LIM). This assay clearly identified the LIM domain as the responsible binding interface because yeasts co-transformed with Xin PR3+4 and LIMCH1 LIM activated both reporter genes, whereas Xin C and LIMCH1 LIM did not show any interaction (fig. 3.43). A LIMCH1 fragment lacking the LIM domain did also show no binding to Xin (data not shown), which confirms the LIM domain as the inter-




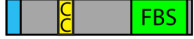
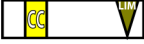
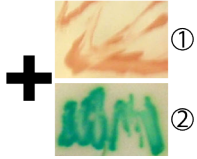
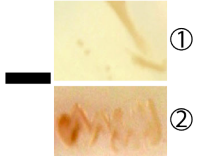

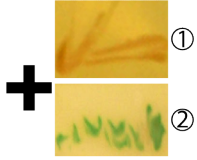
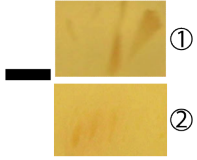
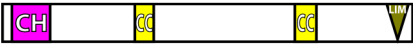
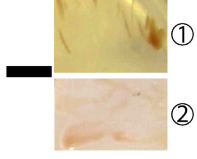

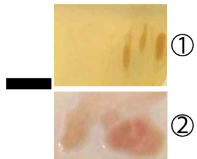

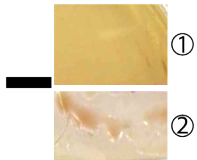
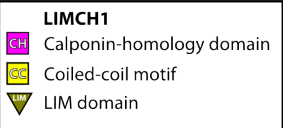
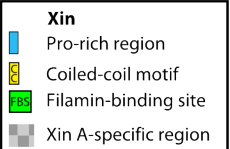
	Xin PR3+4 	Xin C 		
LIMCH1 CC2 	+ 	- 		
LIMCH1 LIM 	+ 	- 		
LIMCH1 FL 	- 	n.d.		
N-RAP LIM 	- 	n.d.		
MLP FL 	- 	n.d.		
<b>LIMCH1</b> 		<b>Xin</b> 		① -LWH growth ② X-Gal test

Figure 3.43: **The LIM domain of LIMCH1 specifically binds Xin A.** Results obtained in yeast two-hybrid experiments performed to map the exact binding region in Xin and LIMCH1. Images marked as 1 depict growth on –LWH selective medium. Positive growth is indicated by newly formed deep red colonies. Activity of the  $\beta$ -galactosidase is displayed by blue-coloured colonies in images marked as 2. In order to map the binding region in Xin, Xin PR3+4 and Xin C were used as a bait which only share a small sequence overlap of 99 aa. None of the LIMCH1 fragments tested interacts with Xin C. Therefore, the Xin-LIMCH1 interaction is Xin A-specific. The LIM domain alone (LIMCH1 LIM) binds to Xin PR3+4 which identifies the LIM domain as the binding interface to Xin. Surprisingly, the complete protein LIMCH1 FL does not show any interaction with Xin which is probably due to transformation problems and impaired growth of transformed colonies. The specificity of the LIM domain-mediated interaction is verified by the negative result of the tests with other LIM domain-containing proteins, MLP (MLP FL) and N-RAP (N-RAP LIM). MLP, muscle-LIM protein. NR-AP, nebulin-related-anchoring protein. n.d., not determined.

acting region. In order to prove the specificity of the interaction, LIM domains of other muscle-specific proteins, like nebulin-related-anchoring protein (N-RAP) and muscle-LIM protein (MLP), were analyzed. N-RAP belongs to the nebulin-repeat protein family because its N-terminal LIM domain is followed by 10–11 simple nebulin repeats and five nebulin-related super repeats. It is expressed in cross-striated muscle at the MTJ and ICD but is also present in myofibril precursor structures, there being involved in myofibril development. The N-RAP LIM domain has been already characterized as a specific binding partner of talin (Luo *et al.*, 1999). MLP (also called CRP3) is classified as a LIM-only protein since it consists of two consecutive LIM domains, which interact among others with  $\alpha$ -actinin and N-RAP (Arber *et al.*, 1994; Louis *et al.*, 1997; Ehler *et al.*, 2001). It is associated with the membrane of cross-striated muscle and mutations in the gene lead to various cardiomyopathies (Knöll *et al.*, 2002; Geier *et al.*, 2003). The LIM domains of both proteins were tested for binding to Xin PR3+4 in a yeast two-hybrid experiment but none revealed any interaction emphasizing the specificity of the LIMCH1 LIM domain (fig. 3.43). However, tests of the isoform with an N-terminal CH domain (LIMCH1 FL) provided puzzling results. This isoform was cloned in two steps since the length of 3252 bp seemed to impair cDNA amplification in a single assay. The LIMCH1 sequence contains a recognition site for the restriction endonuclease *SacII* at bp 1010, which was used to fuse a 5'- and 3'-end fragment in order to obtain a full-length cDNA. Therefore, the 3'-end fragment was amplified from the cDNA clone DKFZp451D112 purchased from imaGenes (Berlin) and the 5'-end sequence was obtained from cDNA of differentiating human skeletal muscle cells. Both fragments were combined and cloned into vectors utilized for yeast two-hybrid assays (cf. section 2.5.3). The transformation of yeasts with plasmids encoding the LIMCH1 FL cDNA was very inefficient requiring multiple attempts. Furthermore, the yeasts grew very slowly on the corresponding media. Thus, it is very likely that the negative result of the binding assay with Xin PR3+4 (fig. 3.43) was caused by the problems described.

In summary, these experiments clearly identify the human protein LIMCH1 as a specific binding partner of the largest human Xin isoform Xin A. This interaction is mediated by the C-terminal LIM domain of LIMCH1 and the recognition of Xin A is highly specific because no cross-reactivity with other selected LIM domains of muscle proteins can be observed.

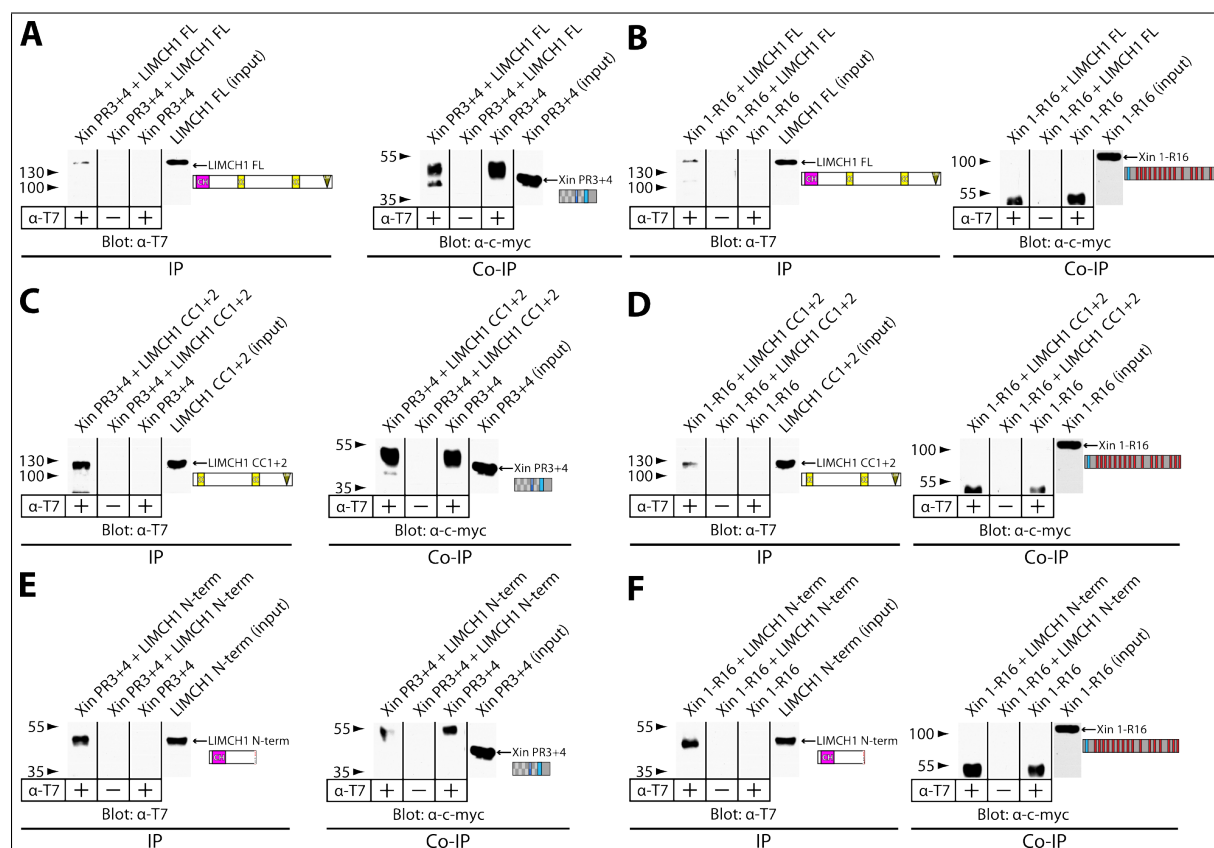


Figure 3.44: **Co-immunoprecipitation of human Xin and LIMCH1.** The protein composition of an assay is depicted above the particular lane. Fragments of LIMCH1 were precipitated with a monoclonal T7-tag antibody (tab. 2.8.2). Addition of antibody is indicated by a + below each lane. The antibody used for probing the membrane is noted at the bottom of the respective blot. The protein detected is marked by an arrow and a sketch below delineates the fragment. Blots probed with  $\alpha$ -T7 antibody show the successful immunoprecipitation (IP) of the respective LIMCH1 fragment whereas blots incubated with  $\alpha$ -c-myc antibody display the co-precipitated Xin fragment (Co-IP). Migration distances are shown in kDa. Bands migrating slightly below 55 kDa correspond to the heavy chains of the immunoglobulin. **A.** Co-immunoprecipitation of LIMCH1 FL and Xin PR3+4. **B.** No interaction of LIMCH1 FL and Xin 1-R16. **C.** Co-immunoprecipitation of LIMCH1 CC1+2 and Xin PR3+4. **D.** No interaction of LIMCH1 CC1+2 and Xin 1-R16. **E.** No interaction of LIMCH1 N-term and Xin PR3+4. **F.** No interaction of LIMCH1 N-term and Xin 1-R16. Interaction can only be detected if both Xin PR3+4 and the LIM domain of LIMCH1 are included in the assay.

### 3.5.2 Biochemical Verification of the Xin–LIMCH1 interaction

The yeast two-hybrid studies clearly provided the LIM domain of LIMCH1 as the binding interface of the interaction to Xin A. As the assay using LIMCH1 FL as a prey produced conflicting results, the interaction needed to be verified biochemically. For this purpose co-immunoprecipitations with bacterially expressed and purified proteins were performed (cf. sections 2.7.1 and 2.7.4.1). The two LIM domain-including fragments LIMCH1 FL and LIMCH1 CC1+2 were used to prove the interaction with the Xin fragment Xin PR3+4, which was initially utilized to identify the interaction (cf. section 3.5.1). An N-terminal construct of LIMCH1 (LIMCH1 N-term) lacking the coiled-coil regions and the LIM domain and a Xin fragment truncated after the repeats (Xin 1-R16) served as negative controls for LIMCH1 and Xin, respectively. The LIMCH1 proteins were precipitated and detected with the monoclonal T7-tag antibody since they were encoded by the pET23aT7 plasmid adding a N-terminal T7-tag to the protein (cf. section 2.5.1.2). All Xin fragments contained an N-terminal c-myc-tag utilized for detection as they were cloned into the pET23aMyc plasmid (cf. section 2.5.1.3). The co-immunoprecipitation was performed as described in section 2.9.2. The migration of the respective protein detected is indicated by an arrow (fig. 3.44 A–F). The blot probed with the anti-c-myc antibody (panel Co-IP) depicts the result of the co-precipitation and the precipitation is delineated by the blot probed with anti-T7 antibody (panel IP). The intense band below the 55 kDa marker band corresponded to the heavy chains of the T7 antibody used for the immunoprecipitation because of the strong reaction of the secondary antibody detecting the anti-c-myc antibody (tab. 2.7). The secondary antibody used against the T7 antibody did not exhibit such a strong reactivity with these heavy chains. The first lane of the blots depicting the IP (fig. 3.44 A–F) clearly shows that the precipitation of the LIMCH1 protein fragments has always worked due to the band at the corresponding molecular weight. Generally, the precipitation of LIMCH1 FL was less efficient than of the other fragments albeit doubtlessly detectable. In addition, neither unspecific binding to the magnetic beads nor to the antibody used for precipitation could be observed since no signals were obtained in lanes two and three of all blots. In contrast to the result in the yeast two-hybrid assay (cf. section 3.5.1), Xin PR3+4 was co-precipitated with LIMCH1 FL indicating the interaction of both proteins (fig. 3.44 A, blot Co-IP, lane 1). The interaction of Xin and LIMCH1 was also verified with the fragment LIMCH1 CC1+2, which co-precipitated Xin PR3+4 (fig. 3.44 C, blot Co-IP, lane 1). The C-terminally truncated LIMCH1 fragment LIMCH1 N-term was not capable of interacting with Xin PR3+4 (fig. 3.44 E, blot Co-IP, lane 1),

supporting the view of the LIM domain as the responsible binding region. Furthermore, none of the LIMCH1 fragments did interact with Xin 1-R16, which excludes other binding regions in Xin or unspecificity of the results obtained.

This biochemical assay corroborates the interaction of Xin and LIMCH1 for Xin PR3+4 specifically binds to fragments containing the LIM domain. Additionally, this experiment displays that the predicted complete isoform LIMCH FL including the LIM domain can also interact with Xin, which could not be shown in the yeast two-hybrid approach (cf. section 3.5.1).

### 3.5.3 Targeting of LIMCH1 Fragments in A7r5 Cells

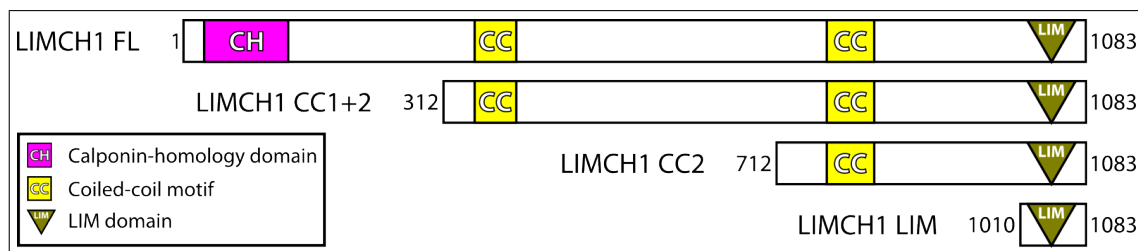


Figure 3.45: **Overview of LIMCH1 constructs used for transfection.** Numbers correspond to amino acid position according to LIMCH1 FL.

The LIM domain of human LIMCH1 is included at the C-terminus of the isoform LIMCH1 FL and has been identified as a novel ligand of human Xin A. In order to investigate the localization of this interaction in cells using the BiFC method (cf. section 3.5.4) LIMCH1 FL and differently truncated fragments were transfected into A7r5 cells in advance elucidating regions responsible for targeting (fig. 3.45). Apart from LIMCH1 FL, fragments were utilized lacking the predicted CH domain (LIMCH1 CC1+2), the CH domain and one putative coiled-coil motif (LIMCH1 CC2) and the LIM domain itself (LIMCH1 LIM). All constructs were transfected as fusion proteins with N- or C-terminal Venus FP. The site of FP fusion apparently did not affect their localization and, therefore, the presented results are typical of each construct transfected.

Transfection of LIMCH1 FL in A7r5 cells resulted in prominent targeting to stress fibres which were decorated in a dotted fashion (fig. 3.46 A-F). Interestingly, LIMCH1 FL was not incorporated into focal adhesions in contrast to Xin A (fig. 3.46 A-C, arrow). Association with submembranous regions (arrowhead) could also be detected although it was not as prominent as for Xin A (fig. 3.53 A). In polarized cells, decoration of actin stress fibres was most obvious in the center of the cell and decreased towards its



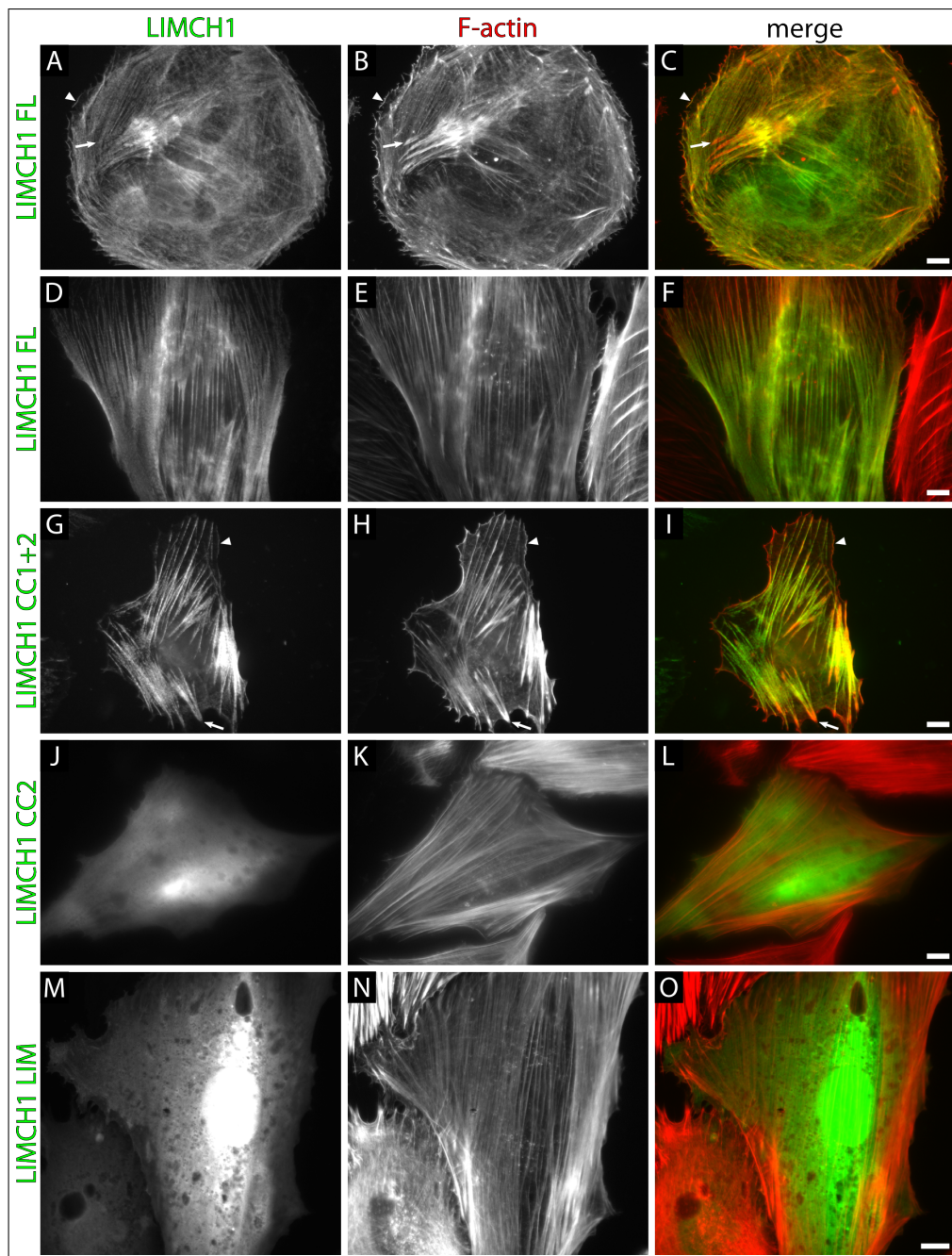


Figure 3.46: **Targeting of LIMCH1 fragments in A7r5 cells.** Epi-fluorescence images of A7r5 cells transfected with LIMCH1 fragments fused to the FP Venus. The respective construct is depicted left from the image series. The cells were labeled with phalloidin to visualize F-actin. In merge images (C, F, I, L, O) the transfected LIMCH1 and F-actin are tinted green and red, respectively. **A-C.** LIMCH1 FL decorates actin stress fibres in a dotted fashion and targets to submembranous regions (arrowhead) but not to focal adhesions (arrow). **D-E.** In polarized cells, the association of LIMCH1 FL and actin filaments is reduced in the periphery. **G-I.** LIMCH1 CC1+2 also targets to stress fibres and submembranous regions (arrowhead) and not to focal adhesions (arrow). **J-L.** Truncation of the CH domain and CC1 (LIMCH1 CC2) disrupts targeting. **M-O.** The LIM domain alone (LIMCH1 LIM) also shows diffuse cytoplasmic distribution. Scale bar 10  $\mu$ m.



periphery (fig. 3.46 D-F). Truncation of the N-terminal CH domain did not significantly alter the localization (fig. 3.46 G-I). LIMCH1 CC1+2 also associated with stress fibres in a punctate pattern and targeting to submembranous regions (arrowhead) could occasionally be discovered. Additionally, prominent labeling of focal adhesions was still missing (arrow). While absence of the CH domain did not affect localization, further N-terminal truncation disrupted targeting (fig. 3.46 J-O). Both LIMCH1 CC2 and LIMCH1 LIM exhibited diffuse distribution in the cytoplasm while the actin cytoskeleton remained unaffected. These results clearly demonstrate that LIMCH1 is an actin-associated protein which is not targeted to focal adhesions. Localization within the cells is mediated by regions located in the central part of the protein between both coiled-coil motifs.

### 3.5.4 Visualization of the Xin-LIMCH1 Interaction in A7r5 Cells Using BiFC

Transfection studies in A7r5 cells revealed that LIMCH1 FL targets to actin stress fibres in a punctate pattern. This localization is presumably mediated by the central part of the protein since C-terminal fragments exhibit a diffuse distribution and N-terminal truncation did not alter localization. A7r5 cells do not contain Xin so that these cells provide a good model system for analyzing functional combinations in order to visualize Xin interactions with the BiFC method. However, the existence of transcripts encoding the LIM domain of LIMCH1 has been proved in A7r5 cells although a confirmation on protein level was not successful yet (Merk, 2010). Therefore, it cannot be excluded that these cells effectively express LIMCH1 protein which could have influenced the assay. Nevertheless, the interaction of Xin A with the LIM domain of LIMCH1 was investigated with the BiFC method. In general, all possible combinations of BiFC vectors were tested for each construct used. An overview of the results and functional combinations is given in table 3.1.

All combinations of the same interacting proteins providing a BiFC signal always displayed identical localization patterns. Therefore, the images depicted represent the typical outcome of the respective combination.

The Xin fragment Xin PR3+4 contains the binding site of the LIM domain of LIMCH1 (cf. section 3.5.1). Transfection in A7r5 cells resulted in a diffuse distribution throughout the entire cell (cf. section 3.6 and fig. 3.55). Strikingly, co-transfection with LIMCH1 FL generated a BiFC signal and its localization resembled that of LIMCH1 FL (fig. 3.47 A-C). The BiFC complex targeted to actin stress fibres in a punctate pattern but was

Fragment	Vector	Xin PR3+4				Xin A			
		1C	2C	1N3	2N3	1C	2C	1N3	2N3
LIMCH1 FL	1C		+		-		-		-
	2C	+		+		+		-	
	1N3		+		-		-		-
	2N3	-		-		-		-	
LIMCH1 CC1+2	1C		+		+		-		-
	2C	+		+		+		+	
	1N3		+		+		-		-
	2N3	+		+		+		+	
LIMCH1 LIM	1C		+		-		-		-
	2C	+		+		+		-	
	1N3		+		+		-		-
	2N3	-		-		-		-	

Table 3.1: **Overview of BiFC vector combinations used for analyzing the Xin-LIMCH1 interaction.** Combinations exhibiting a BiFC signal are marked with '+'. Combinations giving no signal are labeled with '-'. Empty cells reflect incompatible combinations of Venus fragments.

explicitly reduced at termini of actin filaments and focal adhesions if not completely excluded (arrow). An identical distribution of a BiFC complex was obtained when co-transfecting Xin PR3+4 and LIMCH1 CC1+2 (fig. 3.47 D-F). In single transfection assays LIMCH1 CC1+2 showed the same localization pattern as LIMCH1 FL and the BiFC signal with Xin PR3+4 did not deviate from that. In contrast to enrichment of F-actin at focal adhesions, the BiFC complex appeared to be absent there (arrow) but decorated actin stress fibres in a punctate pattern. The LIM domain of LIMCH1 itself was not able to specifically target to distinct cellular structures (fig. 3.46 M-O). Surprisingly, LIMCH1 LIM and Xin PR3+4 formed a BiFC complex which did not show any allocatable localizations (fig. 3.47 G-I). That is even more unique because coincidental complex formation of non-interacting proteins which also exhibit a diffuse cytoplasmic distribution has never been observed. Furthermore, co-transfection of each of the constructs with a non-fluorescent Venus fragment enabling BiFC did not result in fluorescent complex formation although transfection of the Venus FP alone also provided a diffuse cytoplasmic targeting (data not shown).

Since Xin PR3+4 represents only a fragment of Xin A and therefore cannot reflect the *in vivo* situation, both complete proteins, Xin A and LIMCH1 FL, were co-transfected. Although Xin A prominently targeted to focal adhesions, BiFC complex formation could only be detected along actin stress fibres (fig. 3.48 A-C). Both proteins transfected alone decorated stress fibres in a discontinuous, punctate fashion. This pattern was also ob-

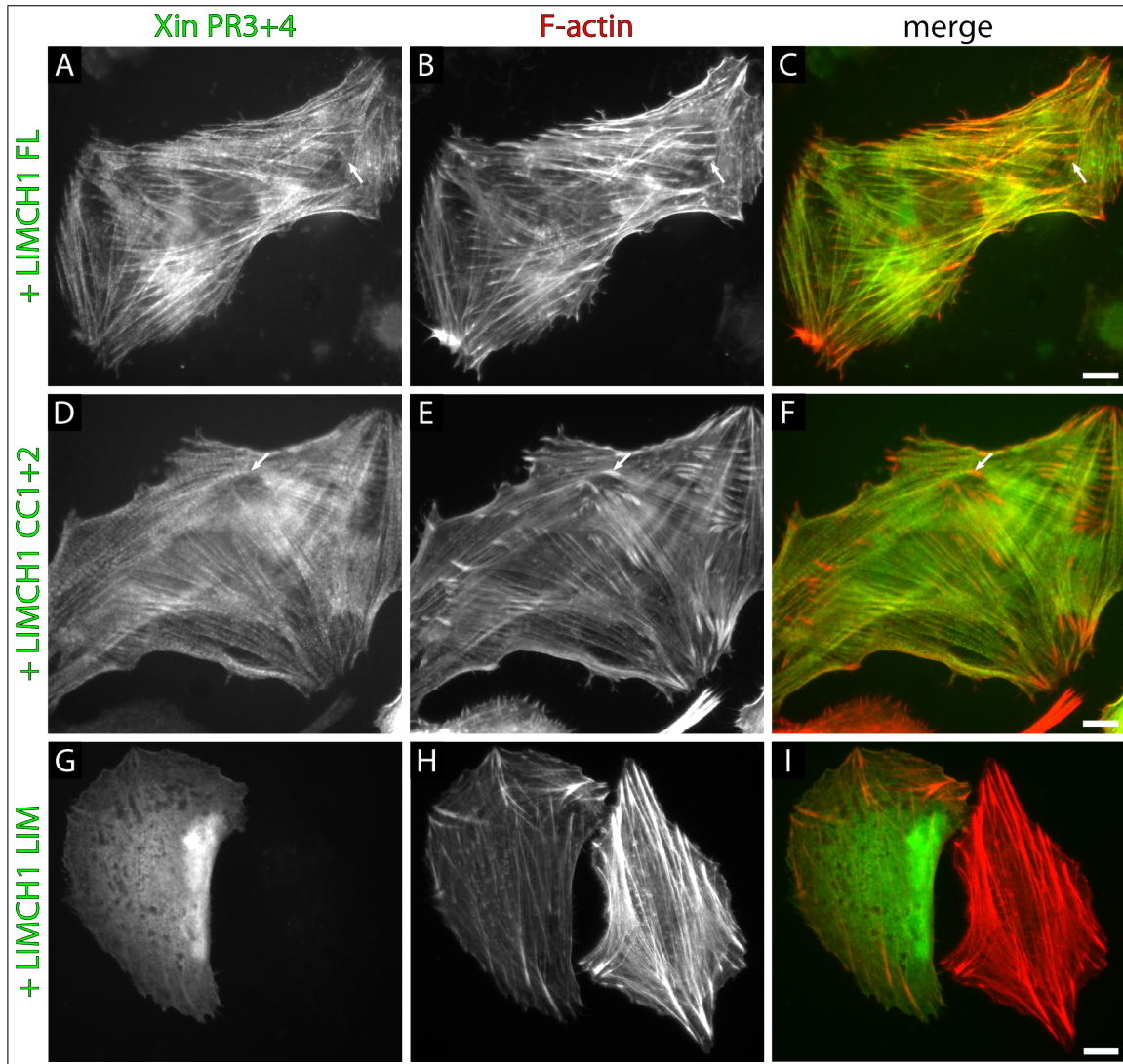


Figure 3.47: **BiFC complex formation of Xin PR3+4 and LIMCH1 fragments in A7r5 cells.** Epi-fluorescence images of A7r5 cells co-transfected with Xin PR3+4 and LIMCH1 fragments fused to non-fluorescent fragments of the FP Venus enabling BiFC. The respective LIMCH1 construct is depicted left from the image series. The cells were labeled with phalloidin to visualize F-actin. In merge images (C, F, I) the BiFC complex and F-actin are tinted green and red, respectively. **A-C.** LIMCH1 FL and Xin PR3+4 prominently interact at actin filaments but not at focal adhesions (arrow). The complex discontinuously decorates stress fibres. **D-E.** An identical localization pattern is obtained with LIMCH1 CC1+2, i.e. no focal adhesion targeting (arrow) and punctate association with actin filaments. **G-I.** LIMCH1 LIM and Xin PR3+4 form a BiFC complex but it does not show specific targeting. BiFC, bimolecular fluorescence complementation. Scale bar 10  $\mu\text{m}$ .

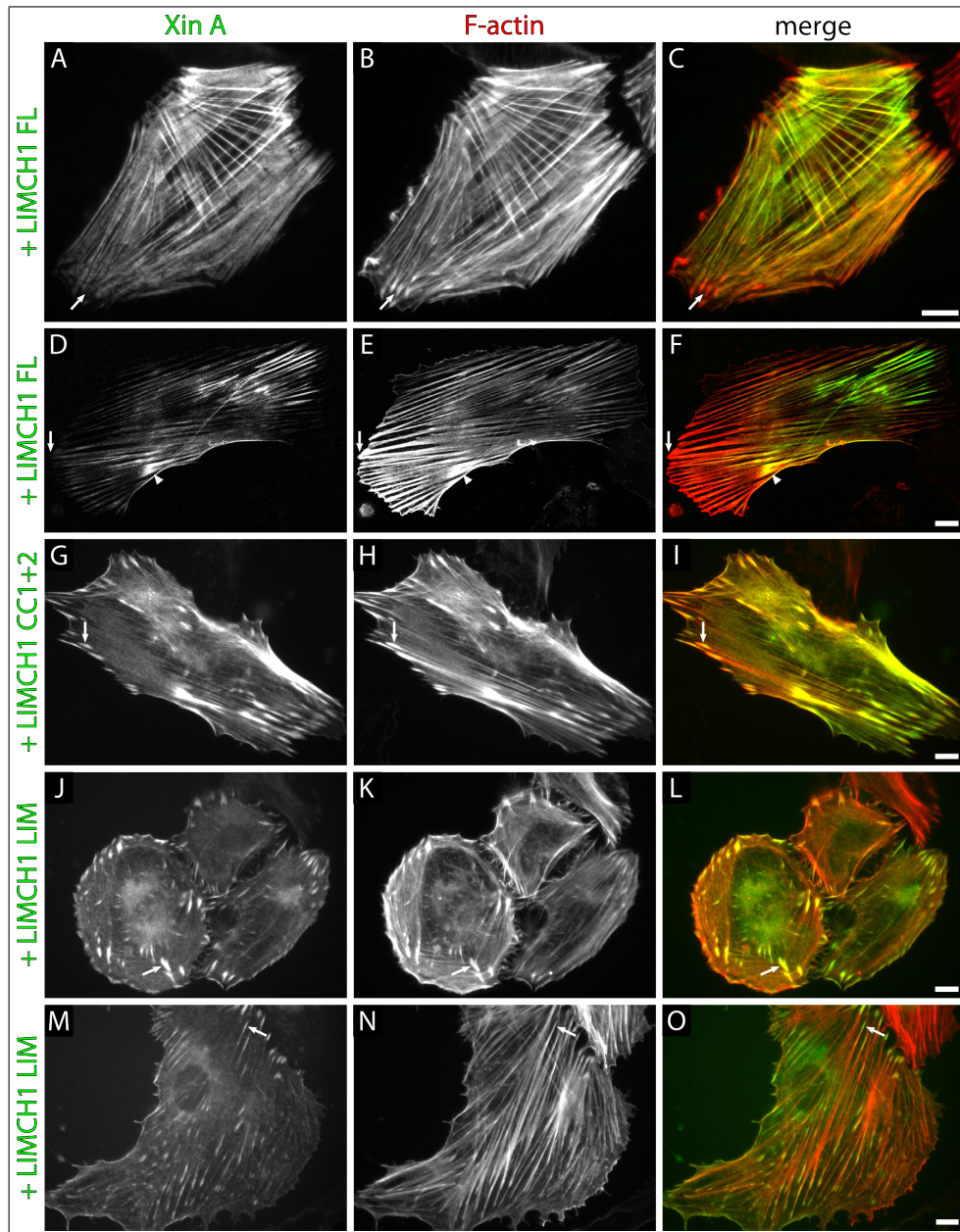


Figure 3.48: **BiFC complex formation of Xin A and LIMCH1 fragments in A7r5 cells.** Epifluorescence and confocal LSM images (D-F) of A7r5 cells co-transfected with Xin A and LIMCH1 fragments fused to non-fluorescent fragments of the FP Venus enabling BiFC. The respective LIMCH1 construct is depicted left from the image series. The cells were labeled with phalloidin to visualize F-actin. In merge images (C, F, I, L, O) the BiFC complex and F-actin are tinted green and red, respectively. **A-C.** LIMCH1 FL and Xin A form BiFC complexes at actin stress fibres but not at focal adhesions (arrow). **D-E.** Confocal LSM images confirm the absence of BiFC complexes at focal adhesions (arrow) and reveal that a high intense BiFC signal along stress fibres is accompanied by F-actin enrichment (arrowhead). **G-I.** Apart from punctate decoration of actin stress fibres, Xin A–LIMCH1 CC1+2 complexes are incorporated into focal adhesions (arrow). **J-O.** In a BiFC complex of Xin A and LIMCH1 LIM, targeting to stress fibres is reduced but the complex is still localized at focal adhesions (arrow) and terminal actin filaments. BiFC, bimolecular fluorescence complementation. Scale bar 10  $\mu\text{m}$ .



tained with the BiFC complex and confocal LSM images clearly demonstrated its absence from focal adhesions (fig. 3.48 D-F, arrow). The intensity of the BiFC signal was not evenly distributed along actin stress fibres. Some sites displayed a focal accumulation of the complex which was accompanied by an increased F-actin signal (arrowhead). N-terminal truncation of LIMCH1 resulted in an altered localization of the BiFC complex. Although LIMCH1 CC1+2 revealed the same targeting as LIMCH1 FL in single transfection assays (fig. 3.46 G-I), Xin A and LIMCH1 CC1+2 together decorated actin filaments in a punctate pattern and were additionally incorporated into focal adhesions which is completely different from Xin A–LIMCH1 FL complexes (fig. 3.48 G-I). If LIMCH1 lost its targeting ability due to removal of the important central region, the BiFC complex sorting again changed (fig. 3.48 J-O). Co-transfection of LIMCH1 LIM and Xin A resulted in prominent targeting to focal adhesions (arrow) but association with stress fibres was dramatically decreased. Decoration was mainly restricted to the ends of actin filaments although Xin A strongly binds F-actin along the entire filament (fig. 3.53 A). In summary, LIMCH1 FL and Xin A interact with each other upon co-transfection in A7r5 cells indicated by BiFC complex formation. This complex is excluded from focal adhesions and remains restricted to actin stress fibres. Truncation of Xin does not affect targeting of the BiFC complex because Xin PR3+4 exhibits the same localization patterns with LIMCH1 FL and LIMCH1 CC1+2. However, loss of the part responsible for targeting in LIMCH1 clearly alters sorting of the complex and then the distribution depends on the Xin fragment which is co-transfected. Xin A causes a BiFC signal at the termini of actin filaments and focal adhesions whereas complexes containing Xin PR3+4 reveal diffuse cytoplasmic distribution.

### 3.5.5 Expression of LIMCH1 in Cells and Tissues

LIMCH1 is the first ligand identified specifically binding to Xin A, thus opening up the opportunity to unravel different and overlapping functions of the three Xin isoforms. Therefore, further characterization of this gene and its products is necessary. Database (UCSC Genome Browser) analysis revealed that high levels of human LIMCH1 transcripts can be obtained in brain and lung, whereas low transcription levels are detected in liver, bone marrow and blood cells. The mRNA levels in human skeletal and cardiac muscle, the only tissues expressing its LIM domain interaction partner Xin A, did not show any peculiarities in any direction. However, transcriptional activity in murine cardiac and skeletal muscle was comparably high to brain and lung. In order to discover LIMCH1

protein in cells and tissues of different species, a commercially available polyclonal antibody (DKFZp686A01247, GeneTex, Inc.; tab. 2.8.2, LIMCH1 (GeneTex)) was tested on a recombinant human C-terminal fragment (LIMCH1 CC2) encompassing the immunogenic region, total protein extracts of human skeletal muscle cells of varying differentiation states, extracts of mouse tissue of lung, brain and heart as well as extracts of rat tissue of skeletal muscle, heart and lung.

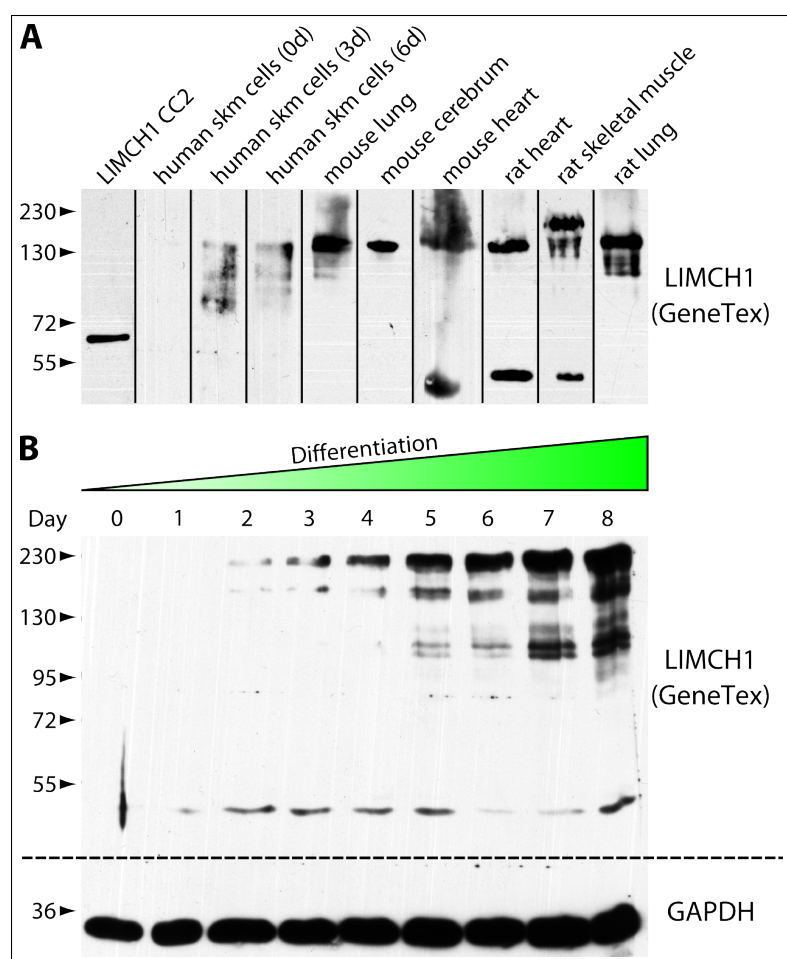


Figure 3.49: **Expression of LIMCH1 in cells and tissues.** The polyclonal antibody LIMCH1 (GeneTex) was tested on cell and tissue extracts and a recombinant fragment including the epitope (LIMCH1 CC2). Migration distances are shown in kDa. **A.** The antibody specifically decorates the recombinant protein fragment LIMCH1 CC2. Non-differentiated human skeletal muscle (skm) cells do not provide a signal but at differentiated stages a band migrating slightly above 130 kDa is detected. A signal at similar height can be identified in all tissues. An additional band below 55 kDa is identified in mouse and rat heart and rat skeletal muscle. In rat skeletal muscle the antibody decorates a band above the common signal at 130 kDa. **B.** Differentiation series of H-2K cells. GAPDH serves as a loading control. Two distinct bands are detected at day 2 which increase until day 8, one migrating above 130 kDa and the more prominent one below 230 kDa. Additionally, a smaller band below 55 kDa can be detected between day 1 and 8.

The tissue extracts were prepared as described in section 2.7.5 and the antibody signal was generated by enhanced chemoluminescence (cf. section 2.8.1.2). The LIMCH1 antibody detected the recombinant fragment LIMCH1 CC2 as a single band above the 55 kDa marker band (fig. 3.49 A). Although this protein fragment has a predicted molecular weight of  $\approx 44$  kDa, the detected band migrated significantly higher, but such a signal was also obtained with the respective tag antibody (data not shown). This demonstrates



that the LIMCH1 antibody recognizes the correct recombinant protein fragment. At the beginning of their differentiation, human skeletal muscle cells did not contain detectable amounts of LIMCH1 protein (fig. 3.49 A). Upon progression of differentiation, a faint band migrating slightly above 130 kDa occurred. Furthermore, additional weaker bands below this signal were obtained. The molecular weight of the isoform designated as LIMCH1 FL amounts to about 122 kDa, which almost fitted the height of the band detected. The increase of LIMCH1 expression albeit to a still low level pointed to a differentiation-dependent regulation in skeletal muscle cells. In mouse, the predicted molecular weight of the corresponding isoform is calculated to be approx. 120 kDa, which predicts a band in the same range as in human cells. The antibody detected a single band at 130 kDa in mouse lung, cerebrum and heart, which showed the same migration behaviour like in human skeletal muscle cells, demonstrating the antibody's cross-reactivity with the mouse orthologue. In addition, mouse heart tissue exhibited a second band migrating slightly below 55 kDa. Whether this represents an additional N-terminally truncated LIMCH 1 isoform is not clear but rat heart and skeletal muscle contained a similar band, which supports the probable existence of such an isoform. Moreover, all rat tissues confirmed the existence of a LIMCH 1 protein migrating around 130 kDa provided by mouse tissues and human skeletal muscle cells. Strikingly, in rat skeletal muscle a second more prominent band was detected slightly higher indicating the existence of another, larger isoform at least in skeletal muscle. The increase of LIMCH1 expression in human skeletal muscle cells and the putative existence of a larger isoform in skeletal muscle required an investigation of LIMCH1 expression during myofibrillogenesis of murine H-2K cells in order to verify these findings. Therefore, protein extracts of a differentiation series of H-2K cells from day 0 until day 8 were probed with the LIMCH1 antibody. The amount of protein was adjusted to the house-keeping protein glyceraldehyde 3-phosphate dehydrogenase (GAPDH). In the early phase of myogenic differentiation, no LIMCH1 protein was detected (fig. 3.49 B). The most prominent signal was obtained slightly below 230 kDa resembling the larger band decorated in rat skeletal muscle. The expression level of this protein gradually increased from day 2 to day 8 after initiation of differentiation. The same course of expression level was detected for a protein migrating above 130 kDa which probably corresponded to the most prominent signal obtained from tissue extracts (fig. 3.49 A). It also reached the highest level at the final stage of differentiation of H-2K cells but its expression level was lower than that of the upper band (fig. 3.49 B). Interestingly, a band migrating below 55 kDa, as identified in mouse and rat cross-striated muscle, was also present in H-2K cells during the entire differentiation process. At day 5, new bands

were detectable which migrated between 95 kDa and 130 kDa. Whether these bands reflected additional splice variants or proteolysis products remains to be determined because no mouse tissue revealed bands in the according range (fig. 3.49 A). However, differentiated human skeletal muscle cells provided bands in this molecular weight range albeit weakly and diffuse. In conclusion, the antibody detects a band matching the calculated molecular weight of the predicted largest isoform (LIMCH1 FL) in all cell and tissue extracts tested. Apart from that, a larger protein can be detected in rat skeletal muscle tissue and differentiating murine H-2K cells which also derive from skeletal muscle. This raises the possibility of another isoform fitting the specificity of this antibody. Furthermore, this isoform as well as LIMCH1 FL seem to be upregulated during myofibrillogenesis and remain a component of adult skeletal muscle. A significantly smaller putative isoform exists in cross-striated muscle tissue of rat and mouse. A protein of an adequate molecular weight is also expressed in differentiating H-2K cells which increases the probability of the existence of a smaller isoform presumably truncated at the N-terminus.

### 3.5.6 Identification of a New Murine LIMCH1 Splice Variant

Expression analysis of the LIMCH1 protein in rat skeletal muscle tissue and differentiating murine H-2K cells provided two bands migrating around 130 kDa and below 230 kDa, respectively (fig. 3.49). While the smaller band probably corresponds to the isoform LIMCH1 FL, the identity of the large protein remains elusive. Database analysis (UCSC Genome Browser) of rat or murine LIMCH1 transcripts could not explain the origin, however, the mRNA clone AL831962 identified in human skeletal muscle includes additional exon sequences which are inserted in front of the first coiled-coil motif (CC1) (fig. 3.50 A). This mRNA clone comprises 5364 bp containing an open reading frame (ORF) of 4404 bp which encodes a hypothetical protein of  $\approx$  165 kDa. The human LIMCH1 gene consists of 27 exons on chromosome 4 (fig. 3.50 B). The coding sequence of LIMCH1 FL starts in the middle of exon 1 and ends at the beginning of exon 27. This last exon is the largest one comprising 2885 bp but most of it presumably represents untranslated sequence. The alternative start codon of the mRNA clone AL831962 is located at the end of exon 6 within the same ORF as LIMCH1 FL thus representing amino acid 160 in LIMCH1 FL (fig. 3.50 A). The additional sequence is inserted between exons 8 and 9 and coded by 7 new exons. Due to the identification in skeletal muscle these exons are referred to as muscle exons 1-7. The coding sequence of this mRNA stops at the same stop codon described for LIMCH1 FL. Therefore, LIMCH1 FL and isoforms containing the muscle

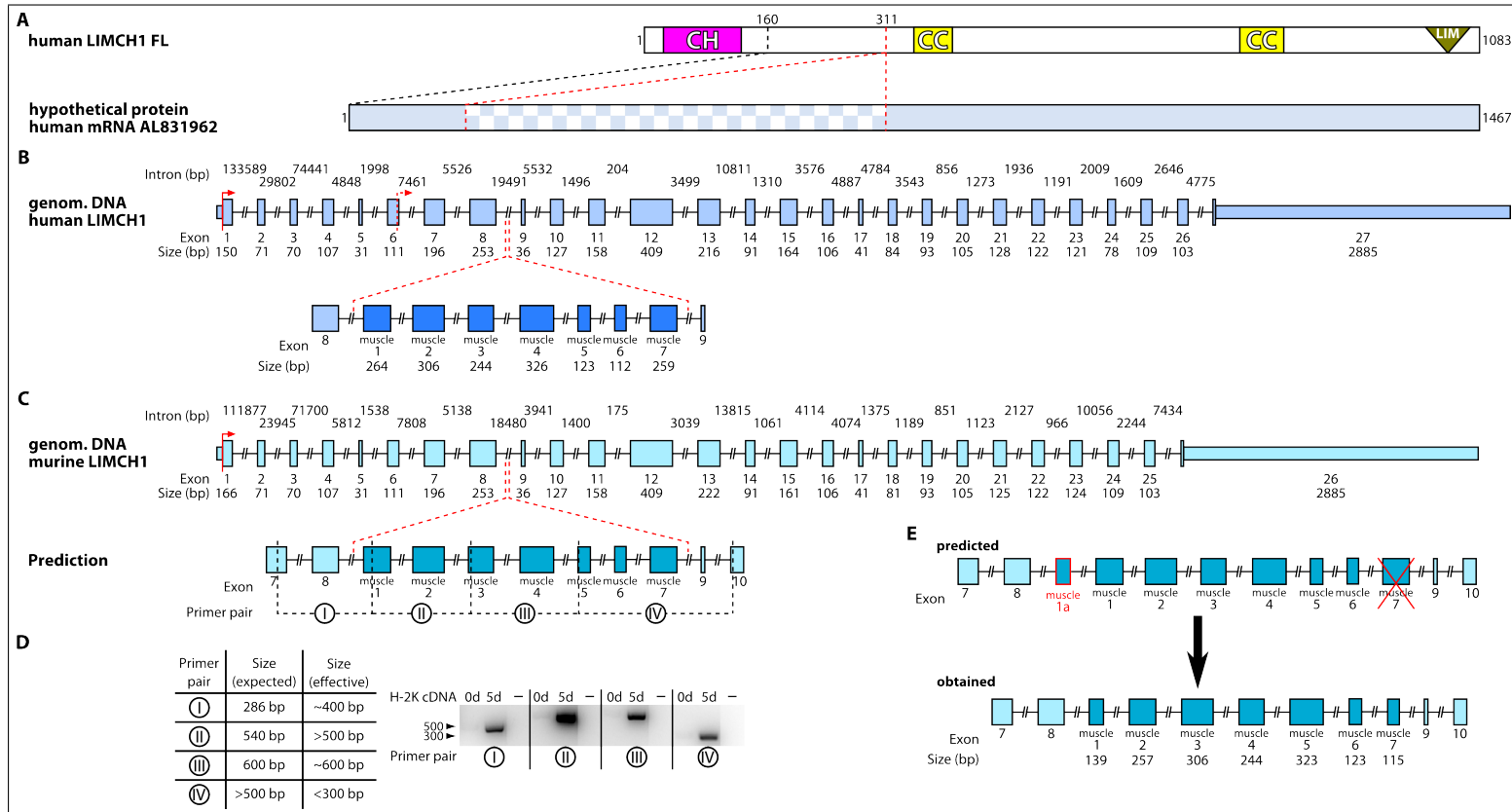


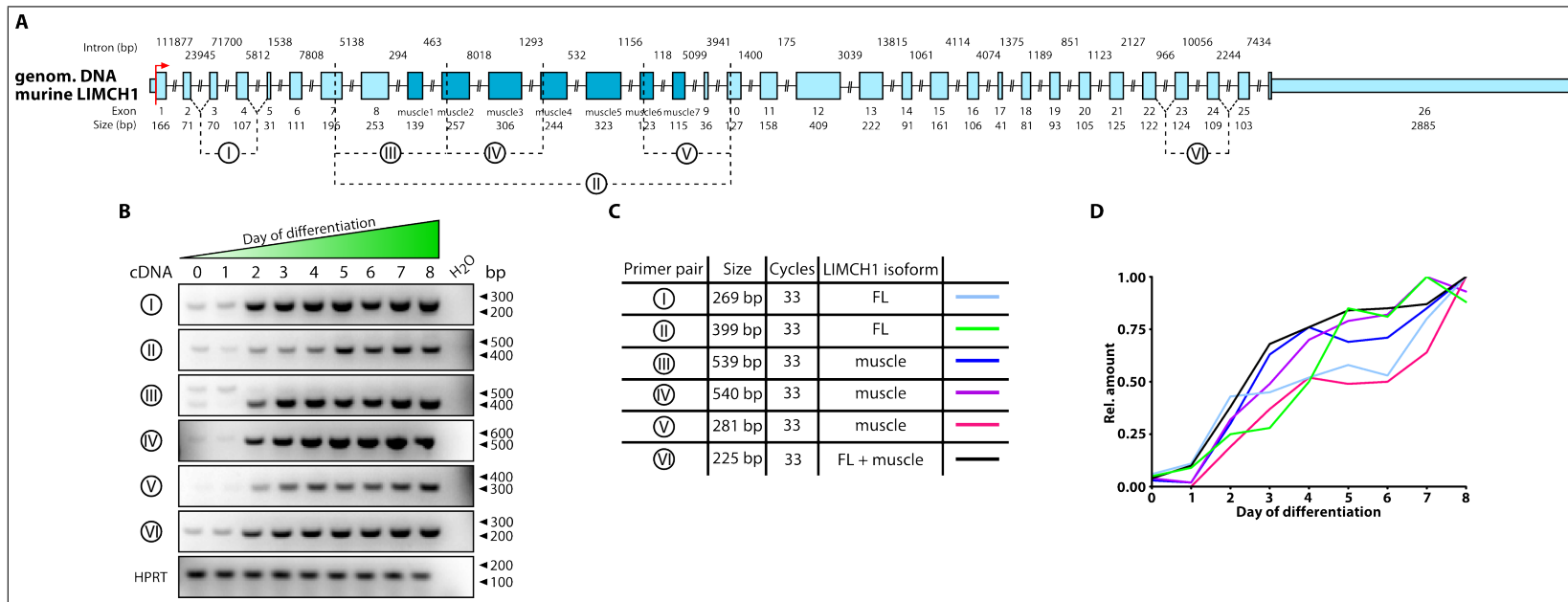
Figure 3.50: **Identification of novel exons in the murine LIMCH1 gene.** **A.** Schematic overview of the human isoform LIMCH1 FL and the hypothetical protein encoded by the mRNA clone AL831962 isolated from skeletal muscle. Numbers correspond to amino acid positions. The black dotted line marks the alternative start codon of the new protein. The sequence not included in LIMCH1 FL is indicated by a chequered filling. The red dotted line marks the site of insertion in LIMCH1 FL. **B.** Schematic overview of the genomic organization of human LIMCH1. The UTR's are indicated by narrow bars and the coding region is depicted by a broad bar. Transcription start of LIMCH1 FL and the new clone are marked by a red arrow and a red arrow with a dotted line, respectively. The localization of the new exons within the gene is displayed by red dotted lines. **C.** Schematic overview of the genomic organization of murine LIMCH1. The UTR's are indicated by narrow bars and the coding region is depicted by a broad bar. Transcription start of mLIMCH1 FL is marked by a red arrow. The localization predicted new exons in murine LIMCH1 is displayed by red dotted lines. Primers used for RT-PCR are numbered with Roman numerals and the respective amplicon is indicated by a dotted line. **D.** Tabular overview of the PCR primer pairs and the respective expected and effective product size. Lane numbering of the agarose gel corresponds to the day of differentiation at which the template RNA for cDNA synthesis was isolated. PCR reactions performed without cDNA template are depicted in lane '-'. **E.** Results of sequencing of PCR products and changes in the exon arrangement.

exons share an identical amino acid composition only interrupted by the insertion near the N-terminus after amino acid position 311 of LIMCH1 FL. In order to clarify whether such exons also exist in murine skeletal muscle and can account for the larger isoform, putative new exons were identified due to homologies to the human sequence (fig. 3.50 C). The murine LIMCH1 gene comprises only 26 exons on chromosome 5 with the gene structure being highly homologous to the human gene, since the start codon is also located in exon 1, exon size and arrangement are very similar and the last exon includes large non-coding sequence. The analysis revealed 7 potential additional exons between exon 8 and 9. Except for exon 7, the exon borders could be easily determined enabling primer design to prove their existence using RT-PCR (cf. section 2.6.1). Four primer pairs were selected covering the entire sequence including the new muscle exons between exon 8 and 10. RT-PCRs were performed on RNA of non-differentiated (0d) and contractile (5d) H-2K cells because protein expression analysis revealed potential differentiation-dependent regulation (fig. 3.50 D). While all primer combinations amplified high amounts of product with cDNA of contractile H-2K cells, no PCR product was obtained with non-differentiated cells. However, the amplicon of primer combinations I and IV did not match the expected size because product I migrated clearly above 300 bp (286 bp expected) and product IV is dramatically smaller ( $> 500$  bp expected vs.  $< 300$  bp obtained). Therefore, PCR products were subcloned and sequenced. This revealed that there were 7 exons between exons 8 and 9 but the arrangement differed from the prediction (fig. 3.50 E). The exon originally designated as muscle 1 was preceded by a 139 bp-comprising exon which explains the larger size of the amplicon I although it did not migrate above 500 bp which was expected from the effective size of 539 bp. Instead, the predicted exon muscle 7 did not exist and accordingly the PCR product IV only comprised the exons muscle 6, 9 and 10. In conclusion, a human mRNA clone from skeletal muscle contains additional exons resulting a hypothetical protein larger than the isoform LIMCH1 FL. The additional exons are located between exon 8 and 9 which can be also confirmed in mouse. Although both human and murine LIMCH1 contain 7 additional exons, their exon structure exhibits differences. Furthermore, splice variants containing the newly identified exons seem to be transcribed depending on the differentiation level, since they were not identified in non-differentiated H-2K cells. Therefore, it is very likely that addition of these new exons accounts for the larger protein identified in rat skeletal muscle and H-2K cells.

### 3.5.7 Transcription of Murine LIMCH1 During Myofibrillogenesis of H-2K<sup>b</sup>-tsA58 Myoblasts

The first prominent protein expression of murine LIMCH1 could be detected at day 2 of myofibrillogenesis of H-2K cells (fig. 3.49 B). An antibody against the C-terminus of LIMCH1 revealed 2 distinct proteins migrating at 130 kDa and below 230 kDa. The smaller protein fitted the calculated molecular weight of the mouse orthologue of the human isoform LIMCH1 FL (mLIMCH1 FL) and RT-PCR experiments pointed to newly identified exons providing a protein larger than LIMCH1 FL (mLIMCH1 muscle) (cf. section 3.5.6). In order to dissect the transcription of both isoforms during myofibrillogenesis, semiquantitative RT-PCR experiments were performed using RNA isolated from a differentiation series of H-2K cells as a template (cf. section 2.6.3). Primer combinations were selected amplifying transcripts of mLIMCH1 FL (I, II), mLIMCH1 muscle (III, IV, V) or both isoforms (VI) (fig. 3.51 A+C).

Surprisingly, all PCR reactions provided weak amplicons already before induction of differentiation although no protein could be detected at this stage which has not been obtained in earlier experiments (fig. 3.51 B and 3.49 B). The presence of transcripts could be either due to spontaneously differentiating cells which are however very rare or transcripts of LIMCH1 exist in proliferating myoblast albeit untranslated. The fact that transcription remained on the same low level after 1 day of differentiation shows that induction of differentiation was not directly affecting transcription level. A significant increase in mRNA level could be detected at day 2, the stage where the protein was identified for the first time, too (fig. 3.51 B+D). The increase continued until the end of differentiation when the highest transcription level was reached. Both isoforms showed an identical course of transcription which also matched the course of protein expression. However, primer pair III provided an additional PCR product above 500 bp which was decreased after day 1 and completely vanished at day 5 (fig. 3.51 B). Subsequent cloning and sequencing of the product failed leaving its identity still elusive. In summary, transcripts of mLIMCH1 FL and mLIMCH1 muscle can be already detected in proliferating myoblast but a significant increase occurs not before day 2. Afterwards, the transcription level of both isoforms is continuously raised until differentiation ends. These transcription data perfectly fit the course of protein expression. The identity of a putative novel alternative splice between exon 7 and muscle exon 2 has not yet been determined.



**Figure 3.51: Quantitation of the transcription level of murine LIMCH1 during myofibrillogenesis of H-2K cells.** **A.** Schematic overview of the genomic organization of murine LIMCH1. The UTR's are indicated by narrow bars and the coding region is depicted by a broad bar. Transcription start of mLIMCH1 FL is marked by a red arrow. Newly identified exons are tinted dark blue. Primers used for semiquantitative RT-PCR are numbered with Roman numerals and the respective amplicon is indicated by a dotted line. **B.** Results of the simplex RT-PCR's of the respective primer pairs. Lane numbering corresponds to the day of differentiation at which the template RNA for cDNA synthesis was isolated. PCR reactions performed without cDNA template are depicted in lane H<sub>2</sub>O. The mRNA of hypoxanthine phosphoribosyltransferase 1 (HPRT) serves as a reference. Migration distances of PCR products are shown in base pairs (bp). **C.** Tabular overview of the PCR primer pairs, expected product size, number of PCR cycles, detected isoform and the respective colours used in D. Changes in transcription level of murine LIMCH1 isoforms in relation to HPRT. The highest ratio between the LIMCH1 product and HPRT of each primer pair was set to 1.0.



### 3.5.8 LIMCH1 Contains Functional Heptad Repeats

Sequence analysis of the Xin A-specific interaction partner LIMCH1 revealed putative coiled-coil regions which can mediate multimerization. Both the isoform LIMCH1 FL and the newly identified splice variant in mouse mLIMCH1 muscle contain two cluster of consecutive heptad repeats. The N-terminal putative coiled-coil motif CC1 consists of seven heptads between amino acids 347 and 395, i.e., according to the positions in LIMCH1 FL (fig. 3.52 A). A second coiled-coil motif CC2 is located more C-terminally and comprises five potential heptads starting with amino acid 789. Estimation of the probability of coiled-coil formation using the prediction algorithms of MultiCoil, Marcoil and PCOILS (cf. section 3.4) showed that the probability is higher for CC2. While only the Marcoil program provided values high enough to assume coiled-coil formation of CC1, for CC2 all prediction methods calculated probabilities comparable to already proven functional heptad repeats (cf. section 3.4). Furthermore, the second coiled-coil motif provided a higher degree of conservation among species than CC1 which increases the probability being functional *in vivo*. Although the exact stoichiometry of a coiled-coil complex can hardly be predicted, it is worth mentioning that MultiCoil which distinguishes between dimer and trimer formation probability favored trimeric complexes for CC2 with a probability twice as high as for dimers. In general, the values of the MultiCoil prediction of trimers were comparable to those obtained with VASP (fig. 3.38 A). Therefore, an N-terminally truncated fragment of LIMCH1 comprising only the second coiled-coil motif and the complete C-terminus including the LIM domain (LIMCH1 CC2) was used in chemical cross-linking experiments to investigate multimer formation capacities (cf. section 2.9.3). LIMCH1 CC2 could form SDS- and DTT-resistant dimers *in vitro* as a faint band below 130 kDa could be detected without addition of cross-linker at the beginning of the experiment (cf. section 3.52 B). This mass roughly corresponds to doubling of the monomer migration width and therefore very likely represents dimeric complexes. The amount was slightly increasing during the course of reaction. Addition of cross-linker resulted in a significant increase in the amount of dimers and also revealed the formation of larger trimeric and tetrameric complexes already after 30 s of incubation. The number of dimeric and tetrameric complexes continuously grew during the whole experiment with trimers being less frequent in the end. Surprisingly, after 3 min of incubation also SDS- and DTT-resistant trimeric complexes could be identified albeit to a lower extend than dimers. The shift of the monomer band was due to loading with cross-linking reagent which always affects migration of the proteins. This experiment

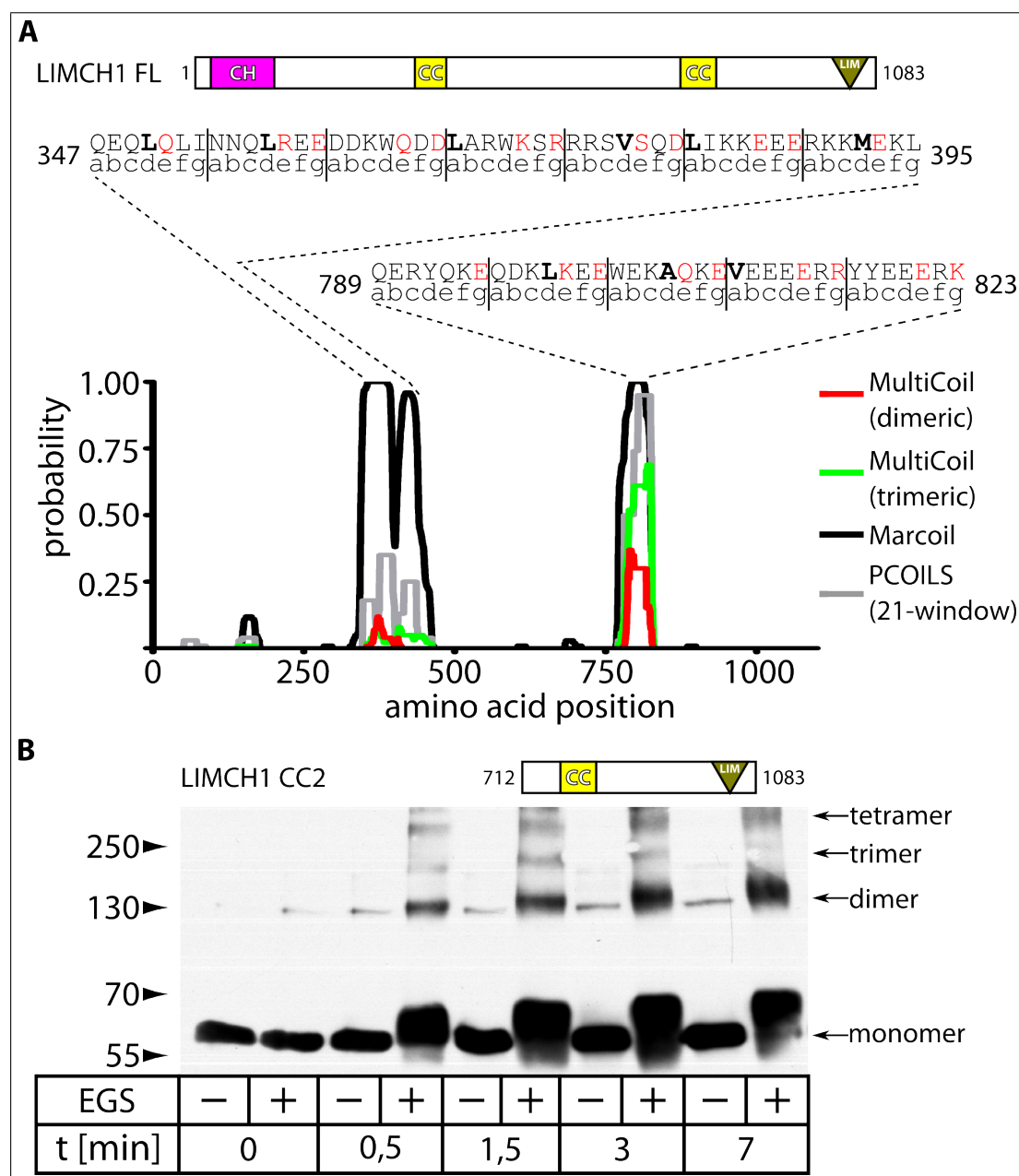


Figure 3.52: **Chemical cross-linking of human LIMCH1.** **A.** Prediction of coiled-coil motifs in human LIMCH1. A schematic overview about the putative domain organization of human LIMCH1 FL is depicted above the graph. Numbers correspond to amino acids. The Marcoil method (black) predicts two coiled-coil regions (CC1+CC2) whereas MultiCoil (red/green) and PCOILS (grey) only identify the second one. The respective sequences and the position within the heptad motif are illustrated above the graph. Hydrophobic residues at positions *a* or *d* and polar residues at positions *e* or *g* are shown as bold and red letters, respectively. The PCOILS program was run using a window of 21 residues for prediction which offers the best compromise in detecting large and small coiled-coils. **B.** Chemical cross-linking of human LIMCH1. Migration distances are shown in kDa. SDS- and DTT-resistant dimers and trimers can be identified in the purified protein. Addition of cross-linker (EGS) indicated by a + below the respective lane increases the amount of dimers and trimers and reveals the formation of tetramers.

clearly demonstrates that the C-terminus of LIMCH1 contains functional heptad repeats which can form multimeric complexes. These complexes can also be detected without cross-linking reagent indicating the formation of robust coiled-coils. The relevant composition of the coiled-coils *in vivo* remains unknown since the existence of dimers, trimers and tetramers can be seen *in vitro*. Furthermore, the existence of dimers and multimeric complexes resembles the results obtained with Xin since it can also assemble to multimeric complexes via coiled-coil motifs (cf. section 3.4).

### 3.6 The C-terminus of Xin B Targets to Focal Adhesions

Intraexonic splicing events in the single large coding exon of human Xin give rise to three different isoforms (fig. 1.8). The largest Xin isoform, Xin A, is encoded by the complete exon and contains the Xin-Repeats and the C-terminal filamin C-binding site (van der Ven *et al.*, 2006). In addition, Xin A includes a central region unique to this isoform, which harbours a binding site to the newly identified protein LIMCH1 (cf. section 3.5). The smaller isoforms consist of parts of Xin A, i.e. they are truncated either C-terminally (Xin B) or N-terminally (Xin C). In order to reveal the functional consequences of these truncations and to identify regions conveying certain properties to Xin, all isoforms and further truncated fragments were transfected in A7r5 cells and their localization studied. Targeting of the constructs used which is depicted in the following figures did not depend on the site of FP fusion, i.e. both N- and C-terminal fusion proteins exhibited the same localization pattern. The actin cytoskeleton was labeled with phalloidin and the actin-associated Ena/VASP-protein Mena was stained facilitating identification of cytoskeletal structures. Mena is also an *in vitro* binding partner of human Xin A and B and directly influences F-actin structure by antagonizing Arp2/3-dependent branching (van der Ven *et al.*, 2006; Krause *et al.*, 2003). It localizes to sites of dynamic action reorganization and cell contact structures, e.g. focal adhesions, which clearly helps to identify these structures.

Transfection of the smallest isoform Xin C resulted in a dramatic alteration of the organization of the actin cytoskeleton (fig. 3.29). This isoform lacks the F-actin-binding Xin-Repeats, nevertheless an association with actin filaments could occasionally be detected. Xin A and Xin B both targeted very prominently to actin stress fibres and the actin cytoskeleton did not seem to be altered because it displayed large stress fibre bundles

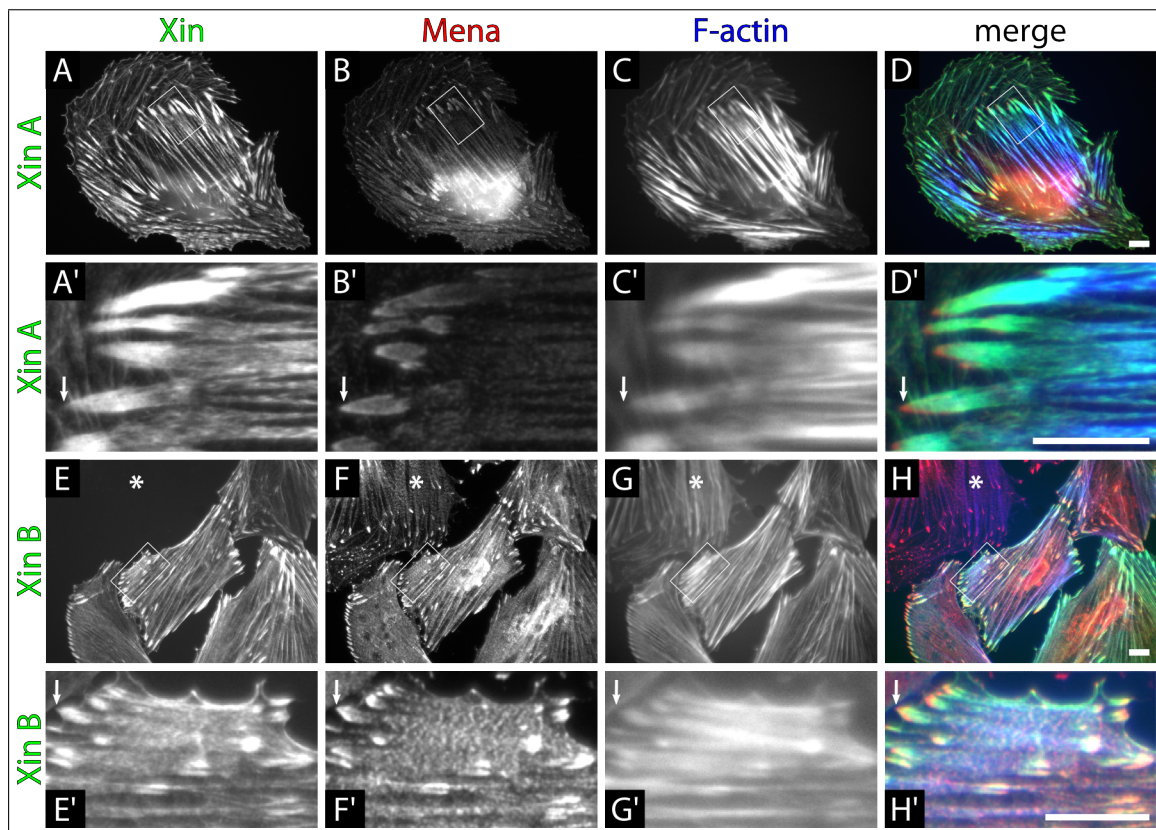


Figure 3.53: **Localization of Xin A and Xin B in A7r5 cells.** Epi-fluorescence images of A7r5 cells transfected with Xin A and B fused to the FP Venus. The cells were labeled with an antibody against Mena and phalloidin to visualize F-actin. In merge images (D, D', H, H') the transfected Xin is tinted green and Mena and F-actin are depicted in red and blue, respectively. **A-D.** Transfected Xin A targets to actin stress fibres in a punctate pattern and is highly enriched in focal adhesions. Mena is also associated with stress fibres in a dense-body-like fashion and accumulates in focal adhesion. **A'-D'.** Mena most prominently labels the tip of focal adhesions where Xin A and F-actin can only weakly be detected (arrow). Although both Xin A and Mena bind to actin in a punctate pattern, their binding site appears to be different. **E-H.** Transfection of Xin B does not lead to alterations in the actin cytoskeleton compared to non-transfected cells (asterisk). Xin B exhibits a targeting pattern identical to Xin A, i.e. focal adhesions and punctate association with stress fibres. **E'-H'.** The tips of focal adhesions contain remarkable amounts of Mena but Xin B and F-actin can hardly be identified there (arrow). Although Xin B and Mena do not continuously label stress fibres, they do not seem to occupy identical positions along the actin filament. Targeting to submembranous sites is common for both Xin isoforms, A and B (**A,E**). Scale bar 10  $\mu\text{m}$ .



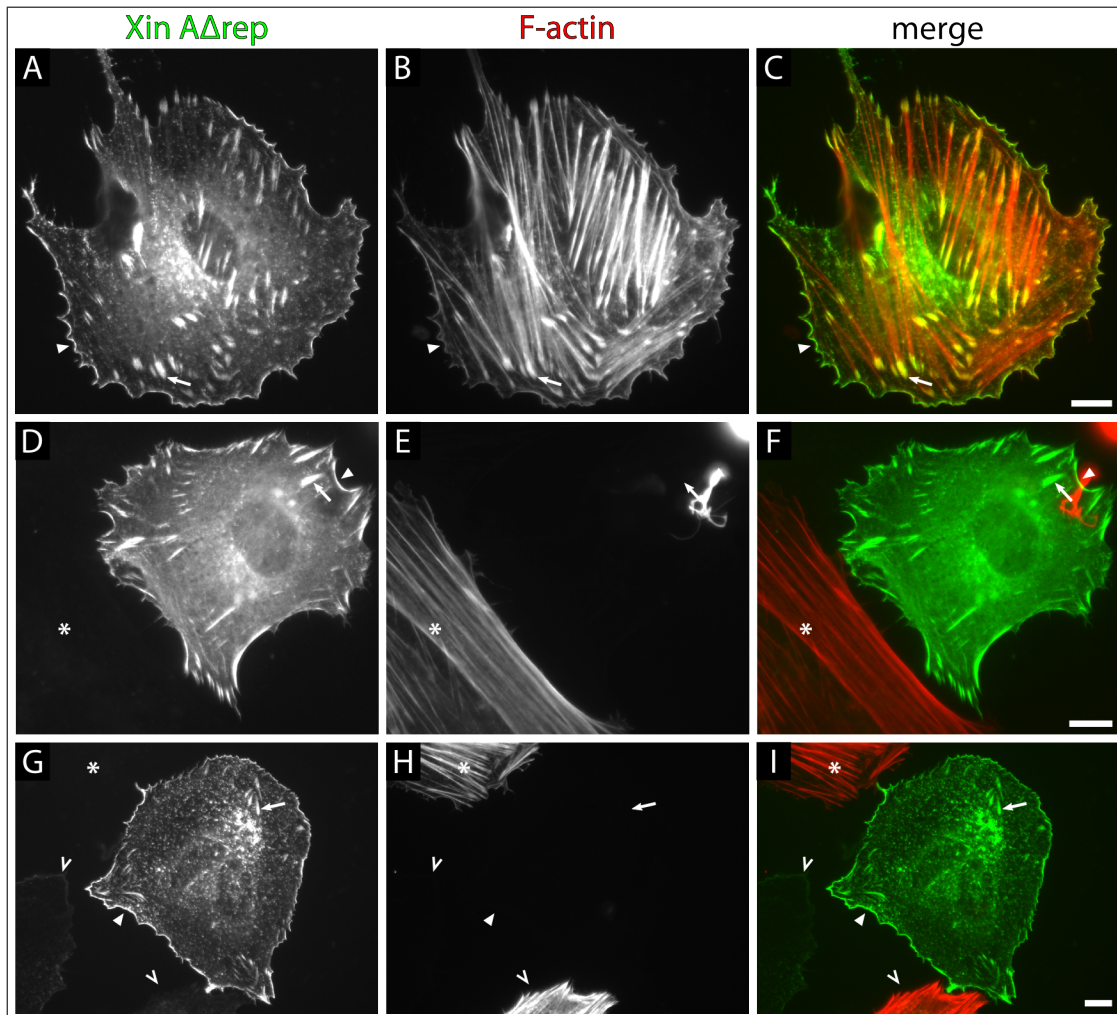


Figure 3.54: **Localization of Xin A $\Delta$ rep in A7r5 cells.** Epi-fluorescence images of A7r5 cells transfected with Xin A $\Delta$ rep, a N-terminally truncated fragment lacking the repeats fused to the FP Venus. The cells were labeled with phalloidin to visualize F-actin. In merge images (C, F, I) the transfected Xin and F-actin are tinted green and red, respectively. Non-transfected cells are marked with asterisks. **A-C.** Xin A $\Delta$ rep does not target to actin stress fibres but is still incorporated into focal adhesions (arrow). Submembranous localization (arrowhead) and a punctate cytoplasmic distribution is common to all Xin isoforms. **D-F.** In some cells, actin-labeling fails although non-transfected cells exhibit prominent F-actin staining and Xin A $\Delta$ rep provides its typical distribution at focal adhesions (arrow), submembranous regions (arrowhead) and in the cytoplasm. **G-I.** Reduced number and altered shape of focal adhesions (arrow) in a cell lacking F-actin labeling. Submembranous localization (arrowhead) and punctate cytoplasmic staining are preserved. Transfected cells expressing low levels of Xin A $\Delta$ rep can either lack actin labeling or not (open arrowhead). Scale bar 10  $\mu$ m.

and prominent focal adhesions typical of A7r5 cells (fig. 3.53 A-D, E-H, asterisk). Their binding mode also seemed to be quite similar, since both exhibited a punctate association with stress fibres although this was less prominent and different from Mena (fig. 3.53 A'-D', E'-H'). The most striking feature was the localization at focal adhesions, which was according to both repeat-containing isoforms but different from Xin C. While Xin A and B evenly labelled focal adhesions with the same intensity, Mena was highly enriched at their distal tips (fig. 3.53 A'-D', E'-H', arrow). At these sites of prominent Mena localization, no signal of phalloidin could be detected indicating the absence of polymerized actin at the tips of focal adhesions or inaccessibility of the phalloidin binding region. Furthermore, both Xin isoforms did not completely overlap with Mena either although their fluorescent signal was obtained closer to the tips than that of phalloidin. In addition to that, Xin A and B also targeted to submembranous regions which is comparable to Xin C (fig. 3.53 A-D, E-H and 3.29).

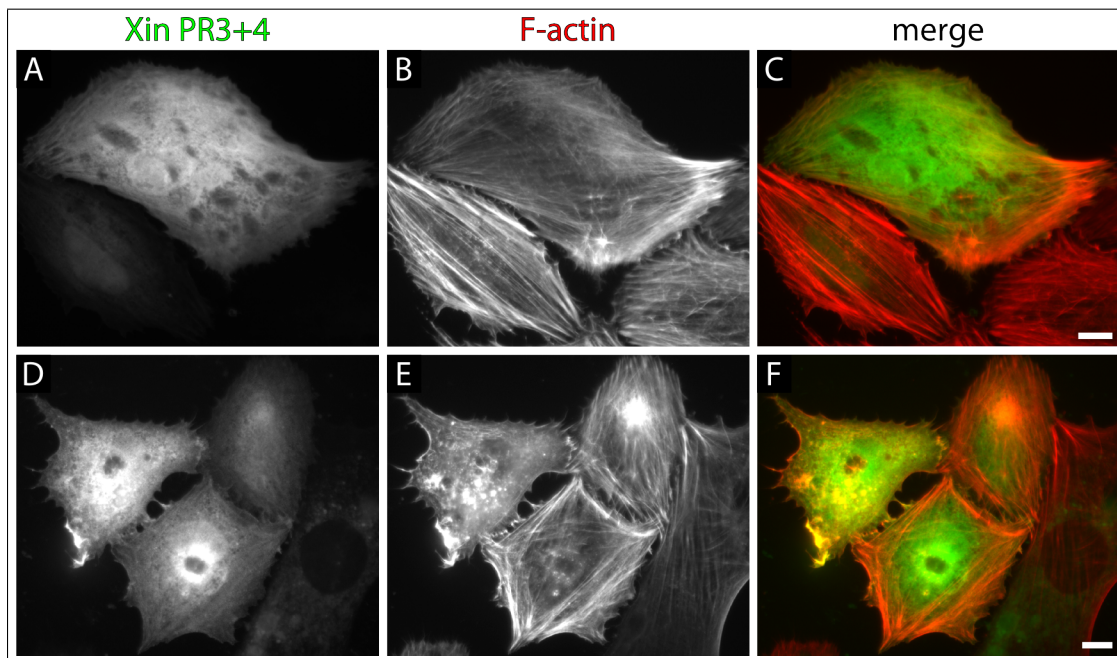


Figure 3.55: **Localization of Xin PR3+4 in A7r5 cells.** Epi-fluorescence images of A7r5 cells transfected with Xin PR3+4, a fragment only comprising the Xin A-specific region and proline-rich motifs of the Xin C N-terminus, fused to the FP Venus. The cells were labeled with phalloidin to visualize F-actin. In merge images (C, F) the transfected Xin and F-actin are tinted green and red, respectively. **A-C.** Xin PR3+4 exhibits diffuse distribution in the cytoplasm. Association with actin filaments can rarely be detected. The actin cytoskeleton is affected because prominent stress fibres and focal adhesions are reduced or eliminated. **D-F.** Different stages of disruption of the actin cytoskeleton. Cells highly expressing Xin PR3+4 do not contain stress fibres whereas they can be still identified in cells displaying lower expression. Scale bar 10  $\mu\text{m}$ .

Thus, Xin-Repeat-containing isoforms (A, B) predominantly target to actin stress



fibres and focal adhesions whereas the smallest isoform Xin C disrupts the actin cytoskeleton architecture causing the absence of prominent stress fibres and focal adhesions. Removal of repeats provided a novel variation of targeting (fig. 3.54). The fragment Xin A $\Delta$ rep did not associate with actin stress fibres but showed prominent incorporation into focal adhesions (fig. 3.54 A-C, arrow). Apart from that, a punctate distribution could be detected in the cytoplasm. A submembranous localization (arrowhead) which is common to all isoforms remained unaffected by the truncation. This reflected the predominant phenotype of cells transfected with Xin A $\Delta$ rep but intriguingly, some of the cells exhibited aberrations (fig. 3.54 D-F). In these cells the visualization of the actin cytoskeleton failed, although adjacent non-transfected cells were properly labeled (asterisk) and the localization pattern of Xin A $\Delta$ rep did not show any deviation since focal adhesion-like structures (arrow), submembranous targeting (arrowhead) and a punctate distribution in the cytoplasm occurred. Only the number of focal adhesions appeared to be slightly reduced but it remains to be determined if this is a significant effect. An effect on labeling of the actin cytoskeleton and associated structures was only observed in a fraction of transfected cells (fig. 3.54 G-I). Alterations could be identified analyzing number and shape of focal adhesions. In these cells focal adhesions generally lacked their typical arrowhead-like shape (arrow) and their number was reduced. However, punctate cytoplasmic localization and submembranous targeting (arrowhead) were preserved. If disruption of F-actin staining depended on the expression level of Xin A $\Delta$ rep, very low levels would be sufficient to cause this effect because cells expressing low amounts of Xin A $\Delta$ rep could either harbour an intact actin cytoskeleton or not (open arrowheads).

N-terminal truncation of Xin A therefore eliminates F-actin binding but retains targeting to focal adhesions. In order to uncover the region responsible for this localization, transfection of the fragment Xin PR3+4 was performed. This construct starts with the Xin A-specific region and lacks the C-terminal coiled-coil motifs and the FBS while still containing a proline-rich region localized at the N-terminus of Xin C. Surprisingly, this construct did not provide any specific targeting and remained diffusely distributed in the cytoplasm (fig. 3.55 A, D). The actin cytoskeleton seemed to be negatively affected by the transfection because stress fibres were reduced or exhibited an altered shape accompanied by a reduction of focal adhesions (fig. 3.55 B, E). In addition to the diffuse cytoplasmic distribution, an association with actin filaments could rarely be seen (fig. 3.55 A). In conclusion, these results clearly point to the C-terminus of Xin B as being responsible for targeting to focal adhesions. Furthermore, it can be stated that the Xin-Repeats are necessary for proper stress fibre decoration so that the association of Xin C with actin

must rely on a different mechanism. The Xin A-specific region and the proline-rich motifs at the N-terminus are not sufficient to target Xin to distinct structures within A7r5 cells so that specific localization of Xin C can be attributed to the C-terminus. Common to all Xin isoforms is the localization at submembranous sites which is preserved in Xin A $\Delta$ rep but lost in Xin PR3+4. Since there are no overlapping regions between Xin B and C the basis of this targeting remains unresolved.

## 3.7 Characterization of Human Xirp2

In human, the Xin-Repeat protein family comprises two members, Xin and Xirp2 (cf. section 1.10). The respective largest isoforms share a related domain layout starting at the N-terminus with a functional Ena/VASP-binding region followed by varying numbers of the characteristic repeats. Subsequently, clusters of proline-rich putative interaction motifs can be identified and both proteins harbour a different number of heptad repeats, which often convey coiled-coil interactions. In this work, novel ligands of Xin are described and the heptad motifs are shown to be functional (cf. sections 3.3, 3.5 and 3.4). In order to dissect distinct and overlapping properties of Xin and Xirp2, the function of putative interaction motifs in Xirp2 was analyzed.

### 3.7.1 Human Xirp2 is a Filamin C-Specific Binding Partner

The filamin family of actin-cross-linking proteins consists of three members, A, B and C, expressed by three independent genes. While filamin A is nearly ubiquitously expressed, filamin C is restricted to cross-striated musculature. All filamins display the same structure, an N-terminal actin-binding domain followed by 24 Ig-like domains, but filamin C possesses a unique insertion in Ig-domain 20 (fig. 1.3). The Xin-Repeat protein Xin represents the first specific binding partner for this insertion. The filamin binding site in Xin is located at the C-terminus within the amino acids 1741–1812 (Schröder, 2009). As Xin and Xirp2 share a similar domain layout, a C-terminal fragment of Xirp2 (Xirp2 FBS) comprising the amino acids 2982–3327 was tested for binding to fragments of human filamin C in a co-immunoprecipitation assay (cf. section 2.9.2).

Xirp2 FBS was expressed with an N-terminal c-myc-tag, which was utilized to precipitate the fragment with a specific antibody (tab. 2.8.2). The potential interacting fragments of filamin C encompassed the Ig domains 18–19 (FlnC d18-19), 18–21 (FlnC d18-21) and 20–21 (FlnC d20-21), respectively, and could be detected via a C-terminal EEF-

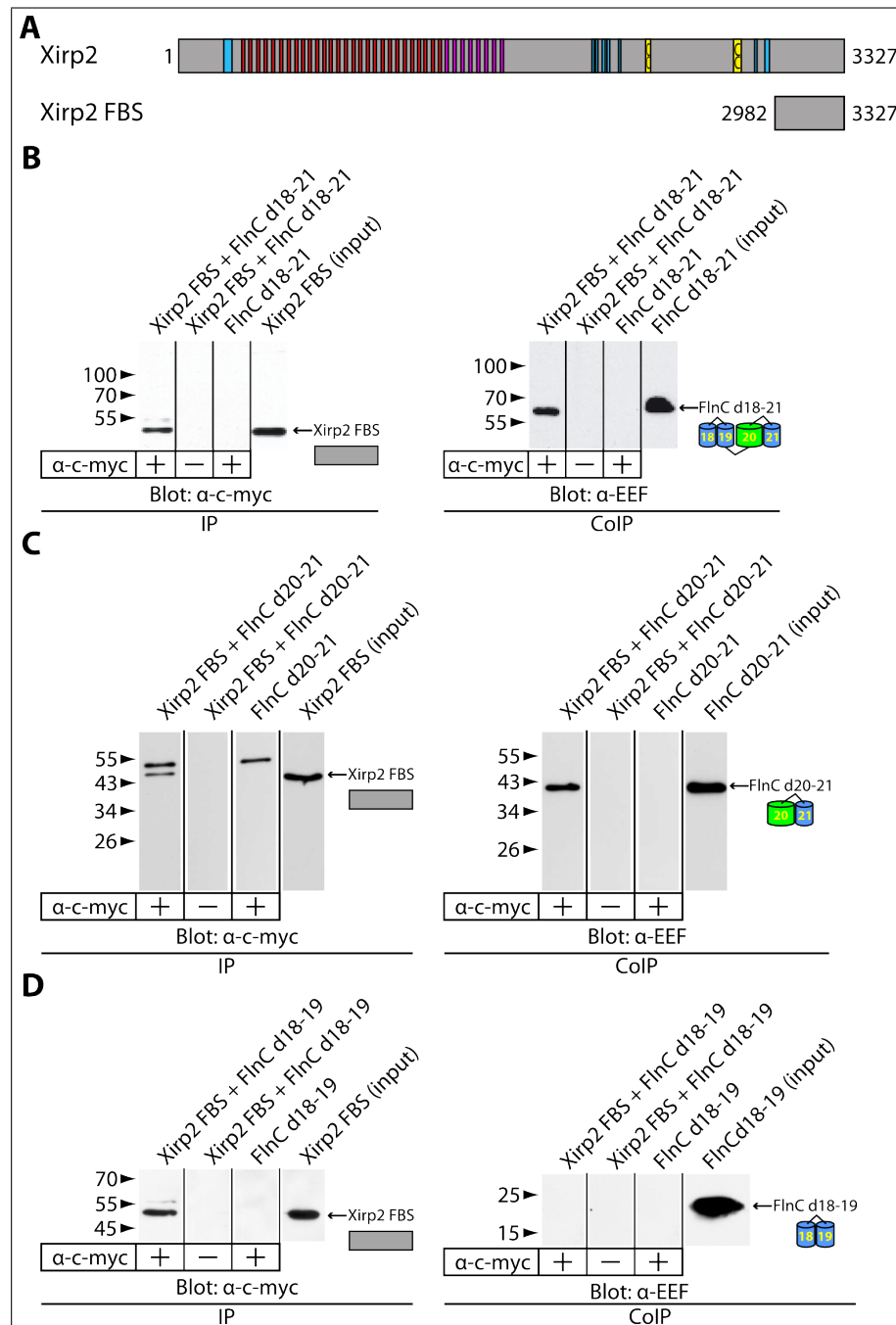


Figure 3.56: **Human Xirp2 interacts with the Ig-like domains 20 and 21 of filamin C. A.** Schematic overview of human Xirp2 and the fragment Xirp2 FBS used for co-immunoprecipitation. **B-D.** Co-immunoprecipitation of the c-myc-tagged fragment Xirp2 FBS and EEF-tagged fragments of filamin C. Xirp2 FBS was precipitated using a c-myc-specific antibody (tab. 2.8.2) shown on the IP panel. Co-precipitated EEF-tagged filamin C fragments were detected using an EEF-specific antibody (tab. 2.8.2) depicted on the CoIP panel. The migration distance of the respective molecular weight standard proteins is indicated by arrowheads and the molecular weight in kDa. Prominent signals at 55 kDa and above 26 kDa in the IP panel correspond to the heavy and light chains of the c-myc antibody, respectively. **B.** Filamin C d18-21 co-precipitates with Xirp2 FBS. **C.** Xirp2 FBS also interacts with filamin C d20-21. **D.** Filamin C d18-19 fails to bind to Xirp2 FBS which maps the binding site to the Ig-like domains 20 and 21.

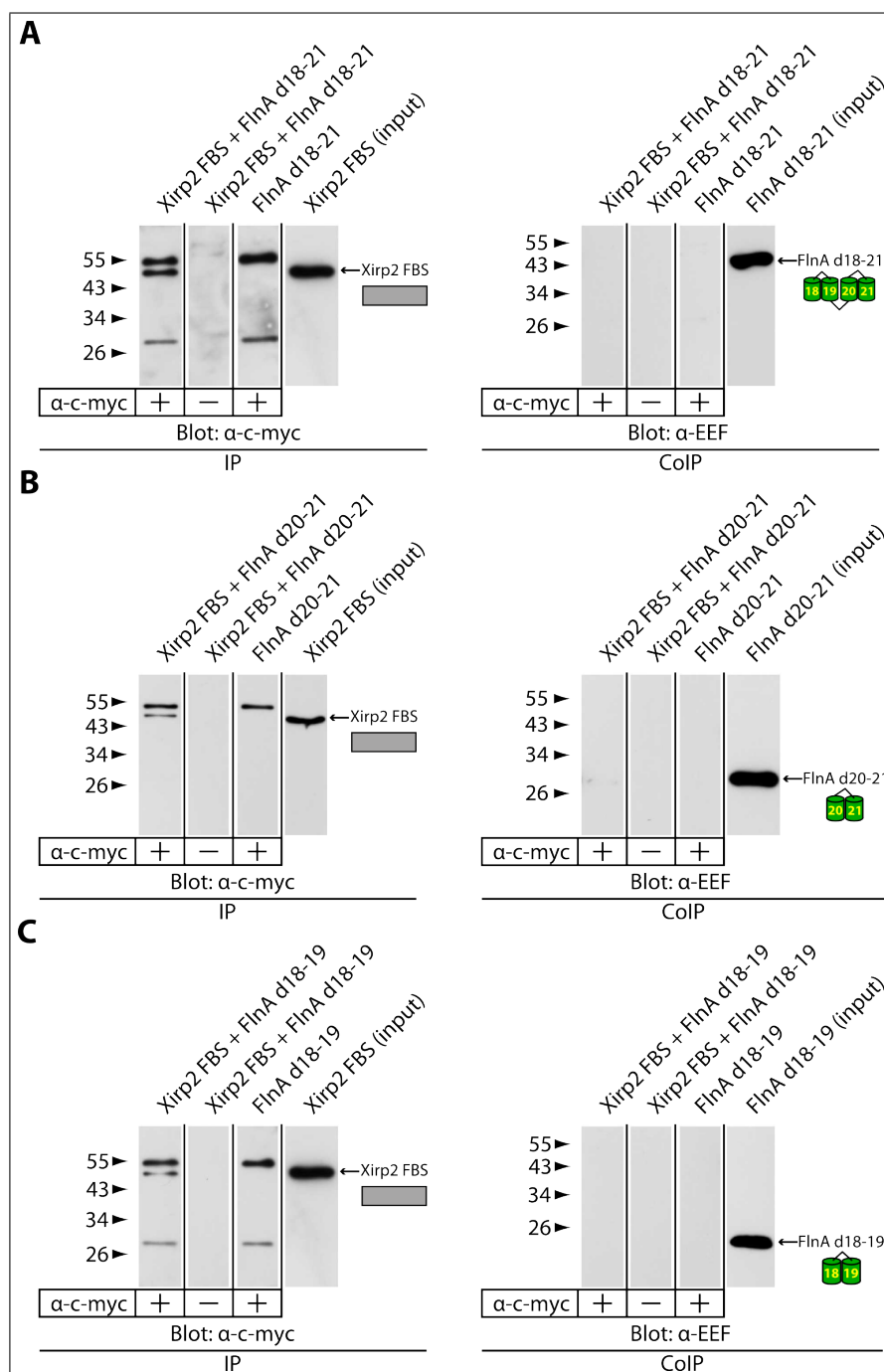


Figure 3.57: **Human Xirp2 does not interact with filamin A.** **A-C.** Co-immunoprecipitation of the c-myc-tagged fragment Xirp2 FBS and EEF-tagged fragments of filamin A. Xirp2 FBS was precipitated using a c-myc-specific antibody (tab. 2.8.2) shown on the IP panel. Co-precipitated EEF-tagged filamin C fragments were detected using an EEF-specific antibody (tab. 2.8.2) depicted on the CoIP panel. The migration distance of the respective molecular weight standard proteins is indicated by arrowheads and the molecular weight in kDa. Prominent signals at 55 kDa and above 26 kDa in the IP panel correspond to the heavy and light chains of the c-myc antibody, respectively. **A.** Xirp2 FBS shows no binding to filamin A d18-21. **B.** Filamin A d20-21 does not co-precipitate with Xirp2 FBS. **C.** Xirp2 FBS does not interact with filamin A d18-19. These results demonstrate that Xirp2 is not a binding partner of filamin A.

tag. This approach identified the Ig domains 20–21 of filamin C as a binding partner of Xirp2 FBS because only fragments comprising these domains (FlnC d18-21, FlnC d20-21) could be co-precipitated (fig. 3.56). FlnC d18-19 did not form a complex with Xirp2 FBS (fig. 3.56 C). The prominent protein bands detected with the c-myc antibody migrating at 55 kDa and slightly above 26 kDa reflected the heavy and light chains of the antibody used for precipitation, respectively. The binding interface in filamin C therefore matches the one responsible for the interaction to Xin, which raised the question whether Xirp2 is also a filamin C-specific binding partner or displays more promiscuity. Thus, various fragments of filamin A (FlnA d18-19, FlnA d18-21, FlnA d20-21) and B (FlnB d16-20, FlnB d19-21, FlnB d20-24) were also expressed as fusion proteins with an EEF-tag and analyzed in co-immunoprecipitation assays. None of the fragments used exhibited any binding activity (fig. 3.57 and 3.58). Although the precipitation efficiency of Xirp2 FBS was reduced in the binding studies with filamin B (fig. 3.58, IP panel), these amounts would be sufficient to effectively co-precipitate filamin C. Thus, if filamin B bound Xirp2 at all, it would only interact with a dramatically reduced affinity compared to filamin C which would raise the question of *in vivo* significance. Therefore, these results clearly demonstrate that Xirp2 similar to Xin is a filamin C-specific binding partner.

### 3.7.2 Human Xirp2 Binds to the SH3 Domain of Nebulin and Nebulette

Xin-Repeat proteins contain clusters of proline residues, which are located C-terminally of the repeats. A proline-rich peptide motif in Xin mediates the interaction to the SH3 domains of nebulin and nebulette, proteins predominantly expressed in skeletal and cardiac muscle, respectively (cf. section 3.3). Although this peptide motif cannot be found in Xirp2 (cf. section 4.3), there are many potential SH3 domain-binding sequences displaying an arrangement comparable to the essential residues in Xin.

Therefore, the binding properties of a Xirp2 fragment comprising the proline-rich cluster (Xirp2 PR2-6, fig. 3.59 A) were investigated in a yeast two-hybrid assay (cf. section 2.9.1) using N-terminally truncated fragments of nebulin (NEBm177) and nebulette (NET SH3+L) as a prey. Co-transformed yeasts were able to activate both the *HIS3* and *lacZ* reporter gene (fig. 3.59 B) showing that the interaction with nebulin and nebulette is a quality characteristic for the human Xin-Repeat protein family.

Co-immunoprecipitation studies with bacterially expressed and purified proteins confirmed this result, since Xirp2 PR2-6 was able to co-precipitate with both nebulin and

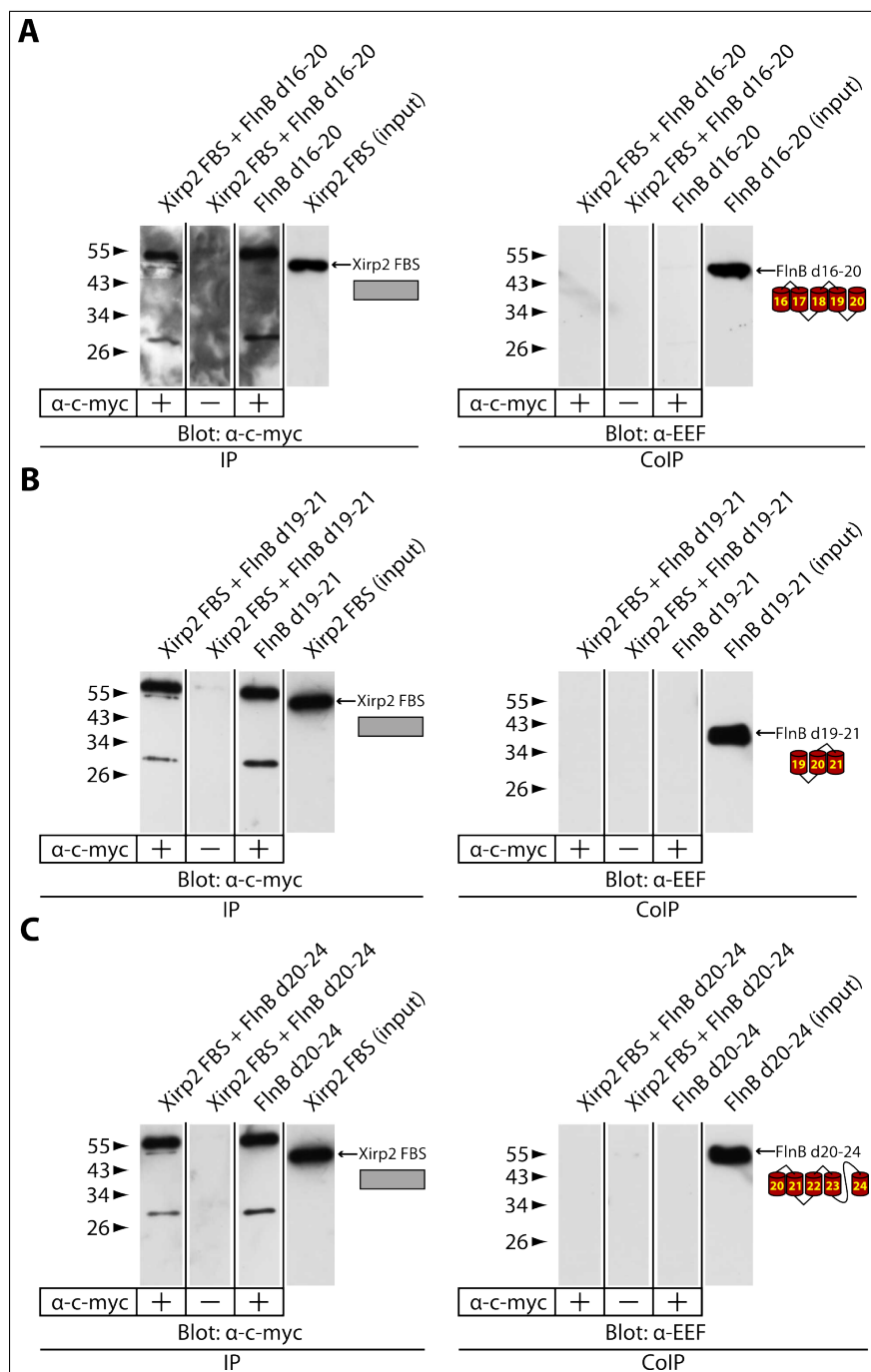


Figure 3.58: **Human Xirp2 does not interact with filamin B.** **A-C.** Co-immunoprecipitation of the c-myc-tagged fragment Xirp2 FBS and EEF-tagged fragments of filamin B. Xirp2 FBS was precipitated using a c-myc-specific antibody (tab. 2.8.2) shown on the IP panel. Co-precipitated EEF-tagged filamin C fragments were detected using an EEF-specific antibody (tab. 2.8.2) depicted on the CoIP panel. The migration distance of the respective molecular weight standard proteins is indicated by arrowheads and the molecular weight in kDa. Prominent signals at 55 kDa and above 26 kDa in the IP panel correspond to the heavy and light chains of the c-myc antibody, respectively. **A.** Xirp2 FBS shows no binding to filamin B d16-20. **B.** Filamin B d19-21 does not co-precipitate with Xirp2 FBS. **C.** Xirp2 FBS does not interact with filamin B d20-24. These results demonstrate that Xirp2 is not a binding partner of filamin B.



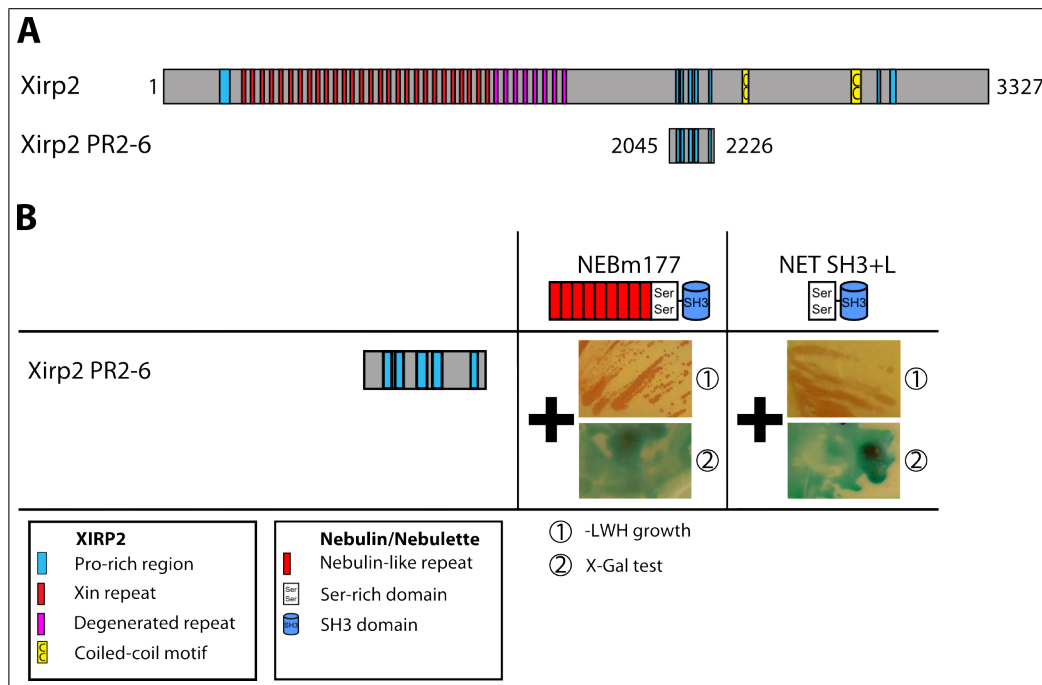


Figure 3.59: **Human Xirp2 interacts with nebulin and nebulette in a yeast two-hybrid assay.** **A.** Schematic overview of human Xirp2 and the proline-rich fragment Xirp2 PR2-6 used as bait **B.** Xirp2 PR2-6 interacts with both C-terminal fragments of nebulin and nebulette depicted by the growth on –LWH selection medium (1) and prominent activation of the  $\beta$ -galactosidase indicated by the blue colour of the colonies (2).

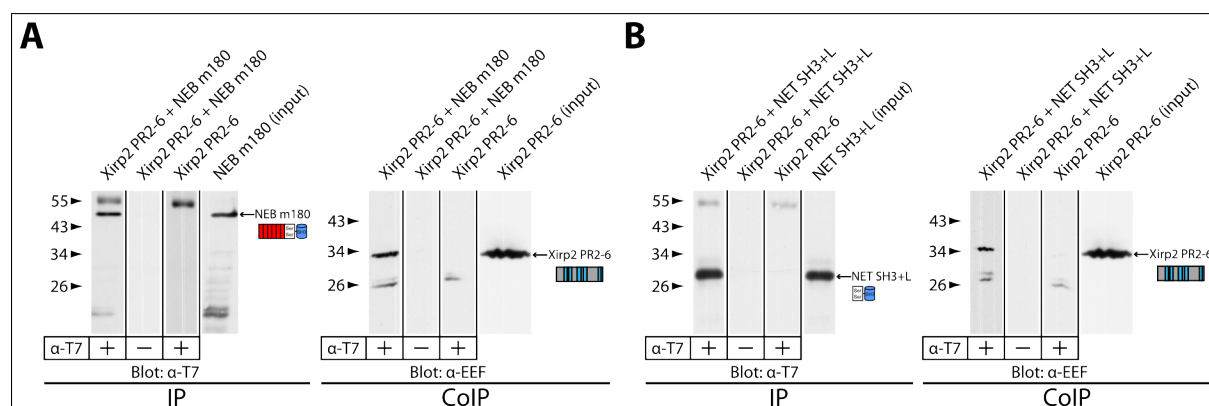


Figure 3.60: **Human Xirp2 co-precipitates with nebulin and nebulette.** **A+B.** Co-immunoprecipitation assays of T7-tagged fragments of nebulin (NEB m180) and nebulette (NET SH3+L) and the EEF-tagged fragment Xirp2 PR2-6. Nebulin and nebulette were precipitated using the T7 antibody (tab. 2.8.2) shown on the IP panel. Co-precipitated EEF-tagged Xirp2 PR2-6 was detected using the EEF antibody (tab. 2.8.2) depicted on the CoIP panel. The migration distance of the respective molecular weight standard proteins is indicated by arrowheads and the molecular weight in kDa. Prominent signals at 55 kDa and above 26 kDa correspond to the heavy and light chains of the T7 antibody, respectively. Xirp2 PR2-6 interacts with nebulin (A) and nebulette (B).

nebullette (fig. 3.60). In human Xin, the essential residues have been already analyzed identifying Xin as a class II ligand (cf. section 3.3.4). In order to compare the binding modes of Xin-Repeat proteins, the responsible peptide sequence was determined performing peptide scans (cf. section 2.9.4).

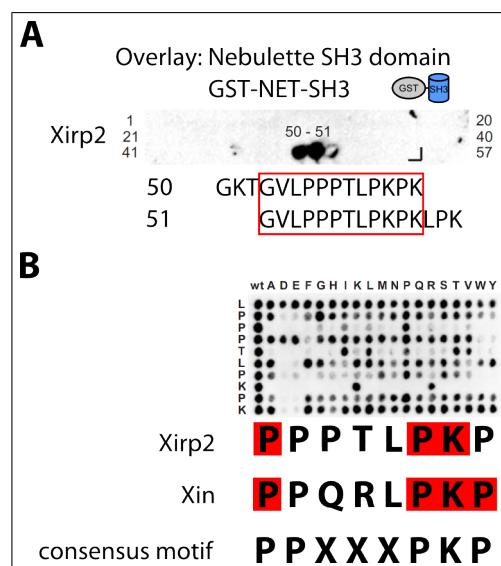


Figure 3.61: **Peptide scan for identification of the nebulin/nebulette SH3 domain binding sequence in Xirp2.** **A.** 15-mer peptides covering the complete sequence of the Xirp2 PR2-6 were coupled with a  $\beta$ -alanine spacer to a membrane. The sequence of consecutive peptides was shifted with three amino acids C-terminally. The membrane was probed with the nebulette SH3 domain N-terminally tagged with GST (GST-NET-SH3). The antibody against GST detected specific binding at spots 50 and 51, which determines the binding motif (red frame). **B.** In order to elucidate the essential residues and thus the binding mode the peptide sequence identified was mutated and the binding properties analyzed by overlaying GST-NET-SH3. All residues whose mutation severely affects the binding capacity are delineated at the bottom. Essential amino acids are highlighted by a red background. The essential lysine located C-terminally of indispensable prolines identifies Xirp2 as a class II ligand. Comparison with the motif in human Xin results in the consensus sequence depicted.

These experiments were carried out by Prisca Boisguerin (Department of Medical Immunology, Charité, Berlin, Germany) using a GST-tagged nebulette SH3 domain (GST-NET-SH3) to analyze the binding properties of the Xirp2 peptides spotted. A strong signal was obtained with the spots 50 and 51, which shared the overlapping sequence *GVLPPPTLPKPK* (fig. 3.61 A). This sequence harbours a typical SH3 domain-binding motif *PXXP* and a positively charged lysine residue located at the C-terminus of the consensus motif suggesting a class II type of binding. To verify this conclusion, mutational analysis of the identified peptide was performed (fig. 3.61 B). Interestingly, this experiment demonstrated that binding of Xin-Repeat proteins to the nebulette SH3 domain is mediated by a common consensus motif because the positions of indispensable residues were identical to Xin, since the initial proline and a pair of proline and lysine had to be

preserved otherwise binding was impaired. Furthermore, it substantiates the notion that Xirp2 also binds like a class II ligand due to the essential lysine situated C-terminally of the indispensable proline residues. A comparison of the binding motifs of Xin and Xirp2 (fig. 3.61 B) established the consensus sequence *PPXXXPKP* for binding of Xin-Repeat proteins to the SH3 domain of nebulin.

### 3.7.3 The Human Xirp2-Repeat Region and not the Xin-Repeat Region Interacts With $\alpha$ -Actinin

The most prominent feature of the Xin amino acid sequence are the multiple repetitive motifs, which define a novel F-actin-binding motif (Pacholsky *et al.*, 2004). A higher number of these repeats can also be found in an additional protein in human, which is therefore named Xin-Repeat protein 2 (Xirp2) resulting in the determination of the Xin-Repeat protein family (cf. section 1.10). Apart from the F-actin-binding function, additional interaction partners of these regions has already been identified. Murine Xin has been shown to bind  $\beta$ -catenin with a C-terminal portion of the repeat region (Choi *et al.*, 2007) and for murine Xirp2 (also called myomaxin and mXin $\beta$ ) two independent binding sites of  $\alpha$ -actinin (cf. section 1.5.5.1) within the repeat region have been described, one within the first nine repeats and the other within the degenerated motifs (Huang *et al.*, 2006). Despite the high homology between the repeat region of human and mouse Xirp2 (83 %) it cannot be excluded that this interaction is restricted to the murine orthologue, since the exact binding motif remains to be determined. Therefore, all 28 conserved repeats of human Xirp2 (Xirp2 rep) and the following degenerated motifs (Xirp2 degrep) were tested on binding to  $\alpha$ -actinin 2, the predominant isoform in skeletal muscle, in a yeast two-hybrid assay (cf. section 2.9.1).

While the transformation of Xirp2 degrep did not affect the growth rate of yeasts, Xirp2 rep clearly reduced it resulting in a considerably decreased number of colonies. Consequently, culturing of yeasts co-transformed with  $\alpha$ -actinin on –LWH selection medium did not provide prominent growth of colonies indicating no activation of the *HIS3* reporter gene (fig. 3.62). The co-transformation of yeasts already possessing the plasmid coding for Xirp2 degrep with the cDNA of  $\alpha$ -actinin did not reveal any disturbance of proliferation but similarly to Xirp2 rep, no proliferating colonies could be detected on –LWH selection medium. However, the yeasts co-transformed with Xirp2 rep and  $\alpha$ -actinin exhibited obvious activation of the *lacZ* reporter gene, which could not be seen with yeasts harbouring the degenerated repeats. These experiments demonstrate that in

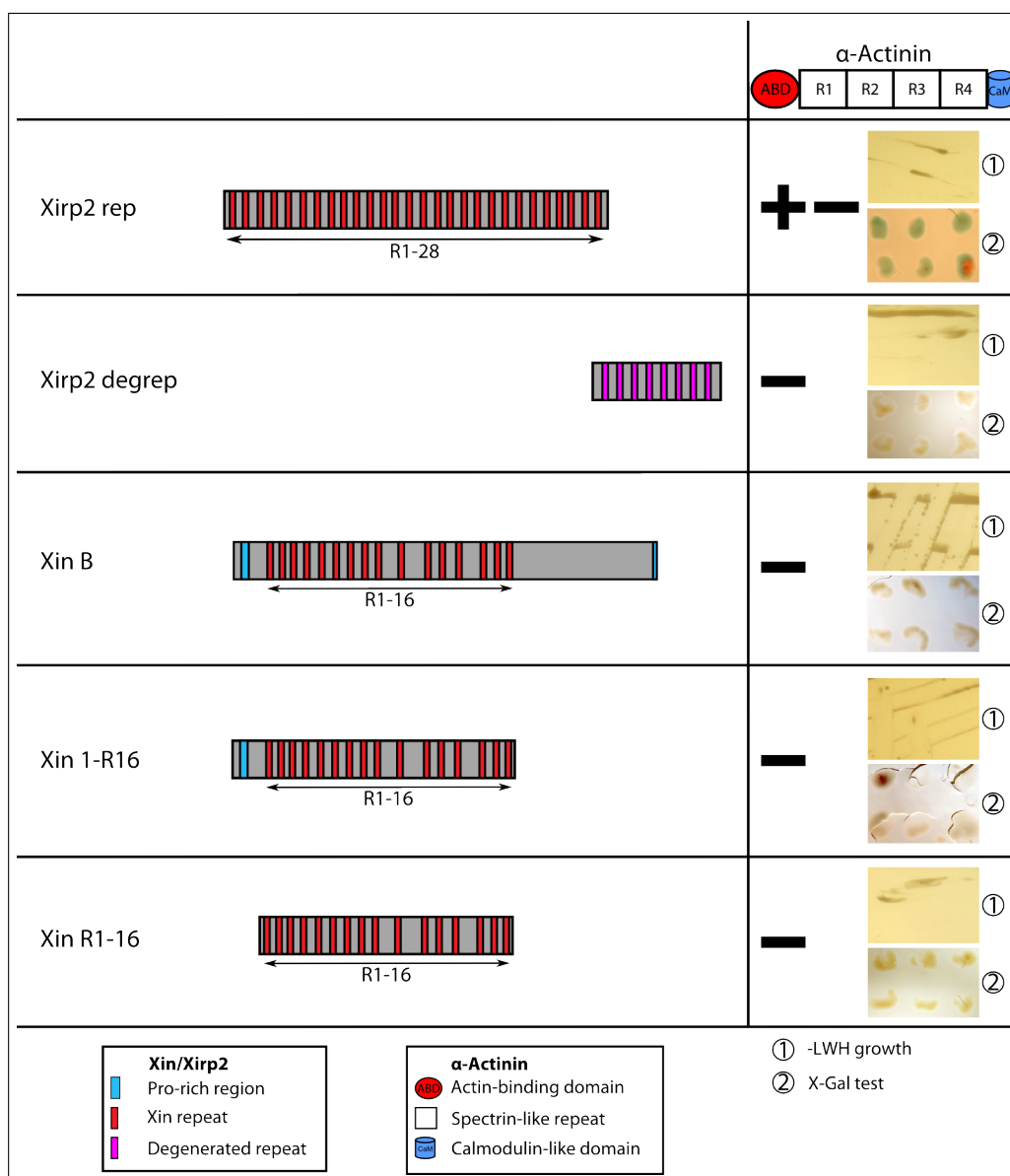


Figure 3.62: **Human Xirp2 and not Xin potentially interacts with α-actinin 2 in a yeast two-hybrid assay.** The conserved repeats in Xirp2 (Xirp2 rep) exhibit activation of the β-galactosidase (2) indicated by the blue colour but no prominent growth on –LWH selection medium (1) can be detected. Therefore binding of α-actinin to human Xirp2 cannot doubtlessly be shown. The degenerated repeats do not interact with α-actinin. The interaction is Xirp2-specific since no Xin fragment containing the repeats activates a reporter gene.

contrast to murine Xirp2, the human protein does not contain an  $\alpha$ -actinin binding site located within the degenerated repetitive motifs. The conserved repeats display ambiguous results because on the one hand no prominent activation of the *HIS3* reporter gene could be detected while on the other hand the  $\beta$ -galactosidase was clearly induced (fig. 3.62).

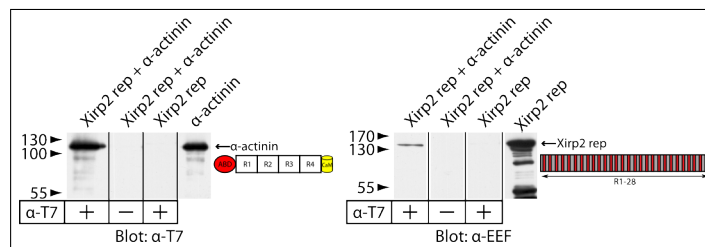


Figure 3.63: **Human Xirp2 co-precipitates with  $\alpha$ -actinin 2.**  $\alpha$ -Actinin 2 was precipitated with the T7-tag antibody (tab. 2.8.2) delineated on the IP panel. Co-precipitated Xirp2 rep was detected using the EEF-tag antibody (tab. 2.8.2) depicted on the CoIP panel. The CoIP panel clearly shows the interaction because of the band between 130 kDa and 170 kDa corresponding to Xirp2 rep. The migration distance of the respective molecular weight standard proteins is indicated by arrowheads and the molecular weight in kDa.

Therefore, biochemical verification via a CoIP assay of bacterially expressed and purified proteins was carried out.  $\alpha$ -actinin was expressed with an N-terminal T7-tag which was utilized for precipitation. The Xirp2 repeats were detected by an EEF-tag fused to the C-terminus. After incubation of both proteins and precipitation of  $\alpha$ -actinin with the T7-tag-specific antibody (tab. 2.8.2), the Xirp2 repeats clearly bound to  $\alpha$ -actinin shown by the prominent band slightly above 130 kDa on the CoIP blot probed with the EEF-tag-specific antibody (fig. 3.63). Furthermore, Xirp2 rep did not display any unspecific binding to assay components corroborating the conclusion that human Xirp2 interacts with  $\alpha$ -actinin via its conserved repeats. A further mapping of the  $\alpha$ -actinin binding site using truncated constructs of Xirp2 rep failed in yeast two-hybrid assays as well as in co-immunoprecipitations, so that the exact binding site still awaits its determination. In order to clarify whether this interaction is specific for Xirp2, various Xin fragments always including the complete repeat region were analyzed in a yeast two-hybrid assay concerning their binding properties to  $\alpha$ -actinin 2. Neither the repeats alone (Xin R1-16) and the repeats plus the complete N-terminus (Xin 1-R16) nor the entire isoform Xin B exhibited any activation of the *HIS3* or *lacZ* reporter gene (fig. 3.62). Thus, the human Xirp2 repeat region and not the Xin repeat region binds to  $\alpha$ -actinin 2.

### 3.7.4 Human Xirp2 Forms Dimers *In Vitro*

The human and mouse sequence of Xin contains functional heptad repeats in the isoforms A and C (cf. section 3.4). Sequence analysis of human Xirp2 also revealed potential coiled-coil segments in the C-terminal portion (amino acids 2322-2342 and 2778-2802) (fig. 3.64 A) which potentially mediate oligomerization (for further explanation of coiled-coils see section 3.4). Both regions were also predicted to form coiled-coils with a probability of more than 0.9 by PCOILS (fig. 3.64 B, cf. section 3.4, Gruber *et al.* 2005). The Marcoil method did not provide such high probabilities but calculates at least a probability around 80 % (Delorenzi und Speed, 2002). MultiCoil distinguishes between dimeric or trimeric coils and surprisingly it did not detect the amino acids 2322-2342 as a putative coiled-coil region whereas amino acids 2783-2806 were predicted to form dimers with a probability higher than 0.9 (Wolf *et al.*, 1997). In contrast to Xin, where MultiCoil favored trimeric coils, no trimeric coil probability was predicted for these residue. This region was also very likely regarded as coiled-coil according to the Paircoil2 algorithm since the score is less than the cutoff of 0.025 (McDonnell *et al.*, 2006). At least the amino acids 2778-2802 displayed high probabilities of coiled-coil formation independent of the prediction method. Thus, chemical cross-linking was utilized to verify coiled-coil formation (cf. section 2.9.3).

Due to size limitations for the recombinant expression in *E. coli*, an N-terminally truncated Xirp2 fragment comprising the amino acids 2220-2867 (Xirp2 CC) was used (fig. 3.64 A). The purified monomer migrated slightly above 70 kDa so that dimers were expected to run at 140 kDa (fig. 3.64 C). Even directly after the addition of cross-linkers a prominent band below 170 kDa could be detected. This probable dimer was observed throughout the complete reaction while no larger complexes could be found. This result corroborates the prediction of MultiCoil that Xirp2 does not tend to oligomer formation but to dimerization. Thus, human Xirp2 also contains functional heptad repeats and forms dimers but no higher oligomers *in vitro* which is completely different from Xin (cf. section 3.4). Both Xin-Repeat proteins are therefore capable of self-interaction via coiled-coils, however the resulting complexes most likely vary in their numeric composition.

### 3.7.5 Transcription of Murine Xirp2 During Myofibrillogenesis of H-2K<sup>b</sup>-tsA58 Cells

A common feature of the genomic organization of most Xin-Repeat protein encoding genes is the existence of a large coding exon (cf. sections 3.2.1, 1.10 and van der Ven



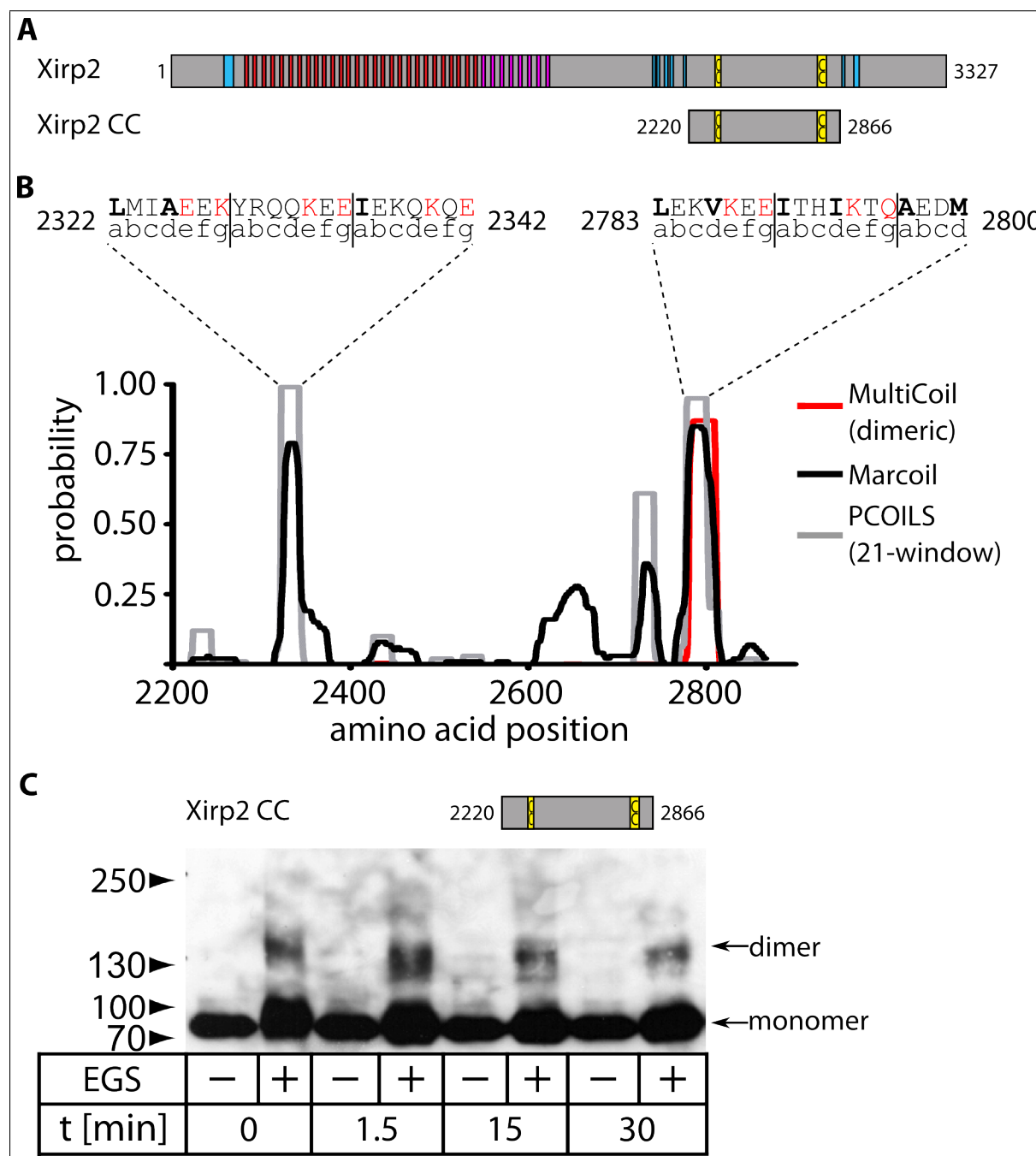


Figure 3.64: **Human Xirp2 forms dimers *in vitro*.** **A.** Schematic overview of Xirp2 and the fragment used for chemical cross-linking. **B.** Prediction of putative coiled-coil formation using different methods. The calculated probabilities are depicted in the diagram. Two regions are identified between amino acid position 2322 and 2342 as well as 2783 and 2800. The corresponding amino acid sequence and the position of every residue within the heptad repeat is designated as a-g. The positions a and d are usually occupied by hydrophobic residues indicated by bold characters. Polar residues at positions e and g stabilize the coiled-coil and are coloured red. **C.** Chemical cross-linking of Xirp2 CC. The migration distance of the respective molecular weight standard proteins is indicated by arrowheads and the molecular weight in kDa. Addition of cross-linker (EGS) is indicated by a + below the respective lane. Xirp2 CC forms dimers with a molecular weight above 130 kDa which can be detected directly from the beginning of the reaction.

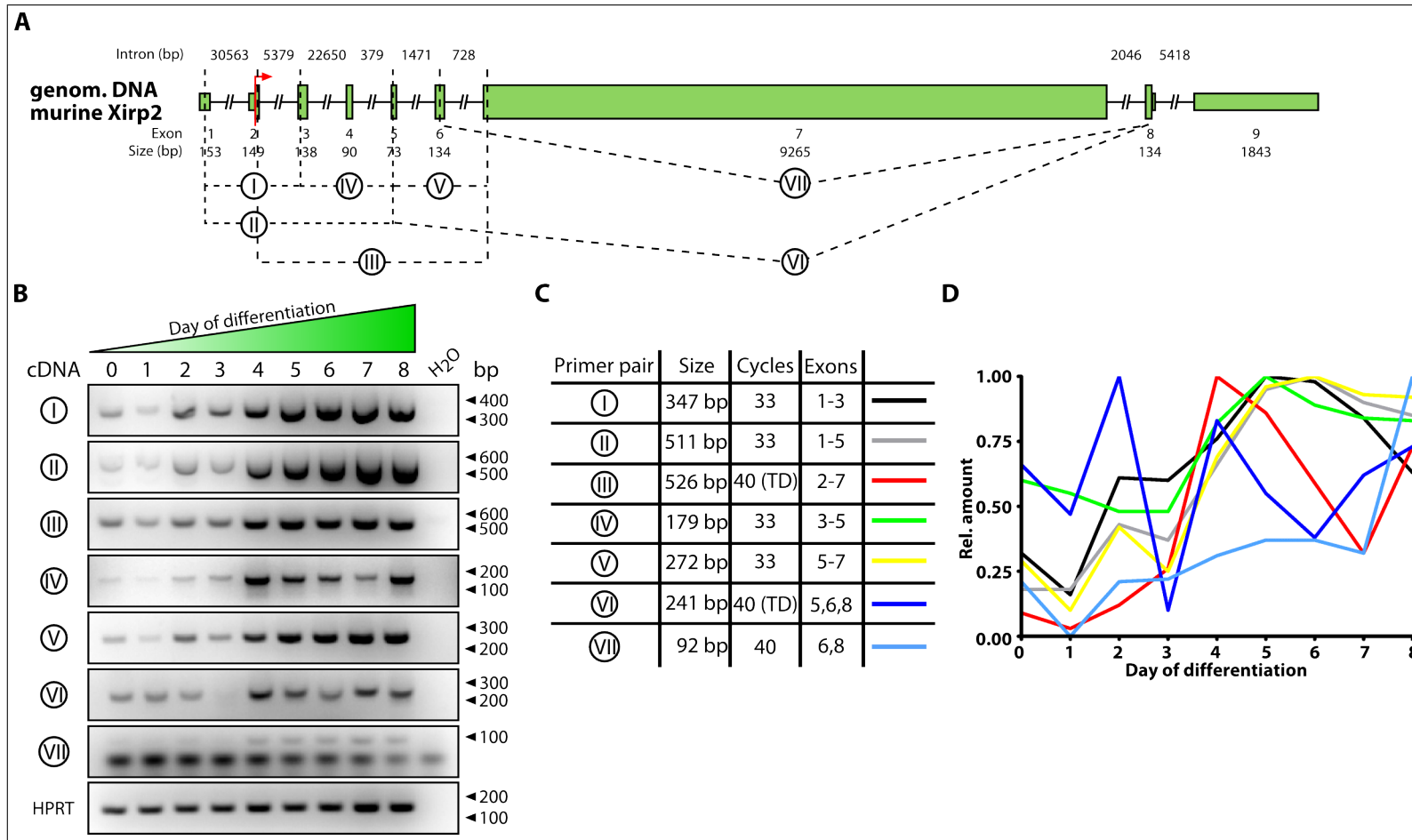


Figure 3.65: **Quantitation of the transcription level of murine Xirp2 during myofibrillogenesis of H-2K cells.** **A.** Schematic overview of the genomic organization of murine Xirp2. The UTR's are indicated by narrow bars and the coding region is depicted by a broad bar. Transcription start of murine Xirp2 is marked by a red arrow. Primers used for semiquantitative RT-PCR are numbered with Roman numerals and the respective amplicon is indicated by a dotted line. **B.** Results of RT-PCR's of the respective primer pairs. Lane numbering corresponds to the day of differentiation at which the template RNA for cDNA synthesis was isolated. PCR reactions performed without cDNA template are depicted in lane H<sub>2</sub>O. The mRNA of hypoxanthine phosphoribosyltransferase 1 (HPRT) serves as a reference. Migration distances of PCR products are shown in base pairs (bp). **C.** Tabular overview of the PCR primer pairs, expected product size, number of PCR cycles, detected exons and the respective colours used in D. Changes in transcription level of murine Xirp2 isoforms in relation to HPRT. The highest ratio between the Xirp2 product and HPRT of each primer pair was set to 1.0.

*et al.* 2006). The largest exon of murine Xirp2 is number 7 which accounts for more than 9000 bp and therefore harbours the majority of the 9852 bp comprising open reading frame (ORF) (fig. 3.65 A). The start codon is located in exon 2 and the coding sequence ends within exon 8. Recently, differentially spliced mRNAs of mouse Xirp2 were identified missing the first exon but displaying an alternative start codon upstream from exon 2. The most striking feature is the splicing out of the largest exon 7 resulting in a frame shift which moves the stop codon to exon 9. These clones were named xeplin and can be found in databases under this name or the accession numbers EMBL ABO69241.1, EMBL ABO69243.1, EMBL ABO69244.1. Analysis of the amino acid sequence revealed that the new protein probably contains a LIM domain encoded by nucleotides within exon 9. In order to investigate the course of transcription of Xirp2 during myofibrillogenesis semiquantitative RT-PCR experiments were carried out using RNA isolated from different stages of differentiating murine H-2K cells as a template (cf. section 2.6.3). Primer pairs were designed to detect transcription of isoforms with or without exon 7. Three independent differentiation series were analyzed and gave comparable results. Since it was only a semiquantitative approach, only one differentiation series is depicted as a representative. The amount of transcript was determined in relation to the yield of the PCR of hypoxanthine phosphoribosyl transferase (HPRT) performed at the same conditions. The maximum ratio was set to 1.0. All primer pairs already amplified PCR products before the induction of differentiation which has been also shown for Xin (fig. 3.65 B). Primer pairs I to III and V presumably exclusively indicate transcription of isoforms containing the large exon 7 because xeplin clones either do not comprise exon 1 or exon 7 (fig. 3.65 C). Although these primer pairs displayed a decreasing transcription level during the first day of differentiation, it can nevertheless be stated that all primer pairs exhibited a rather constant increase of transcription upon progression of differentiation (fig. 3.65 D). While primer pair III already amplified a maximum yield at day 4, primer pair I reached the maximum not until day 5 and primer pairs II and V at day 6. After their respective maximum the transcription level decreased again but remained significantly elevated at the final stage of differentiation of H-2K cells compared to the initial level. The PCR product of primer pair IV could be included in isoforms with or without exon 7 (fig. 3.65 A, C). The amount of mRNA was roughly constant during the first 3 days of differentiation but increased until day 5 (fig. 3.65 D). Then the transcription level underwent a modest decrease and remained constant until the final stage of H-2K cell differentiation. Interestingly, the course of transcription of mRNA species without exon 7 revealed some differences. While primer pair VI displayed large fluctuations around an

apparent average value, primer pair VII showed an increase until final differentiation of H-2K cells (fig. 3.65 D). In summary, all primer pairs reveal an increase of transcription during the first phases of differentiation of H-2K cells. Primer pairs amplifying parts of an mRNA containing the large exon 7 indicate maximum transcription between day 4 and 6, the stage of transition to contractility. The absolute amount of such mRNAs is significantly larger than that without exon 7. The latter provides inconsistent results because primer pair VI displays fluctuation whereas primer pair VII shows a constant increase until final differentiation. Thus, transcription of Xirp2 is clearly upregulated after the onset of differentiation but the exact course of transcription level still needs to be determined with quantitative PCR approaches.

### 3.7.6 Protein Expression of Murine Xirp2 During Myofibrillogenesis of H-2K<sup>b</sup>-tsA58 Cells

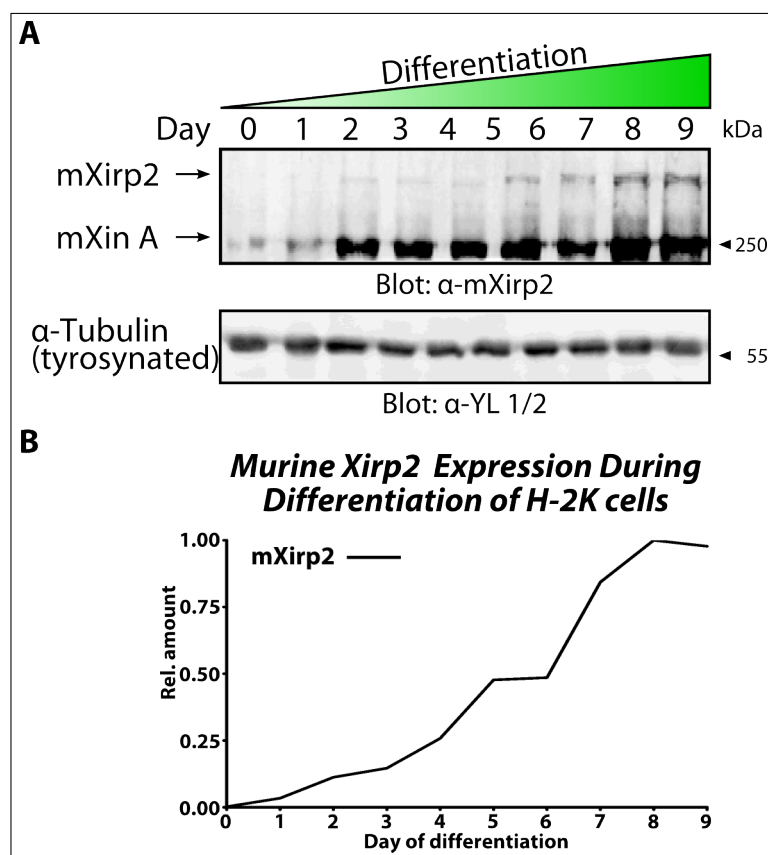


Figure 3.66: **Protein expression of murine Xirp2 during myofibrillogenesis of H-2K cells.** **A.** Blot of protein extracts of a differentiation series of H-2K cells. mXirp2 is decorated by the α-mXirp2 antibody and visualized using the Odyssey laser scanner system. The antibody exhibits extensive cross-reactivity with murine Xin A. Tyrosynated α-tubulin serves as a loading control. Migration distances are shown in kDa. The expression level of mXin A is higher than that of mXirp2. **B.** Quantitation of mXirp2 expression. The highest ratio of mXirp2 and α-tubulin expression is set to 1.0. mXirp2 does not seem to be expressed before induction of differentiation but is upregulated during differentiation and displays the highest expression at day 8.

Analysis of the transcription level of murine Xirp2 mRNA reveals an upregulation upon progression of H-2K cell differentiation (cf. section 3.7.5). In order to clarify whether this trend can be also detected on protein level, total protein extracts of differentiating H-

2K cells were tested for murine Xirp2 protein expression. The protein expression was quantified in relation to tyrosinated  $\alpha$ -tubulin using the infrared laser scanning system Odyssey and the highest ratio was set to 1.0. Since the antibodies used for localization of Xirp2 in human skeletal muscle tissue (cf. section 3.7.7) do not cross-react with the murine orthologue, the antibody  $\alpha$ -mXirp2 raised against the repeat region of murine Xirp2 was used (Huang *et al.*, 2006) (tab. 2.8.2). The calculated molecular weight of murine Xirp2 accounts for  $\approx$  400 kDa and the antibody decorated a band clearly above the 250 kDa marker band (fig. 3.66 A). However, more prominent bands around 250 kDa and 130 kDa (not shown) could also be detected. These bands correspond to mXin A and mXin B because this antibody cross-reacts with the repeats in Xin. Before induction of myogenic differentiation this antibody identified protein expression of mXin which has been already demonstrated with Xin-specific antibodies (cf. section 3.2.2) while no mXirp2 was found (fig. 3.66 A). After one day of differentiation a very faint band of mXirp2 could be detected and the amount constantly increased until the latest stages of differentiation (fig. 3.66 B). A comparison of the expression levels of mXin A and mXirp2 revealed that mXirp2 exhibited a significantly lower expression than mXin A. In conclusion, murine Xirp2 does not seem to be expressed before induction of differentiation although at this stage significant amounts of mRNA were detected (cf. section 3.7.5). After the onset of differentiation mXirp2 expression constantly increases and does not seem to be clearly reduced even in the latest stages of differentiation, which has been shown for the transcription level (cf. section 3.7.5). Furthermore, due to cross-reactivity of the  $\alpha$ -mXirp2 antibody with mXin A and B it could be consistently demonstrated that the expression level of mXin A is higher than that of mXirp2.

### 3.7.7 Human Xirp2 Localization in Adult Skeletal Muscle Tissue

The localization of murine Xirp2 in cross-striated muscle has been delineated before. In cardiac muscle, it seems to be a prominent component of the ICD and in skeletal muscle it can be detected in the Z-disc and in the periphery of myofibres (Wang *et al.*, 2010; Huang *et al.*, 2006). In order to unravel the position of human Xirp2 in skeletal muscle, three antibodies were raised against distinct portions of human Xirp2 (fig. 3.67).

An antibody against the N-terminus of Xirp2 was produced in rabbit and detects the first 311 amino acids. Another polyclonal antibody was raised against the central polyproline region harbouring the binding site for Ena/VASP proteins (Eulitz, 2005) and the

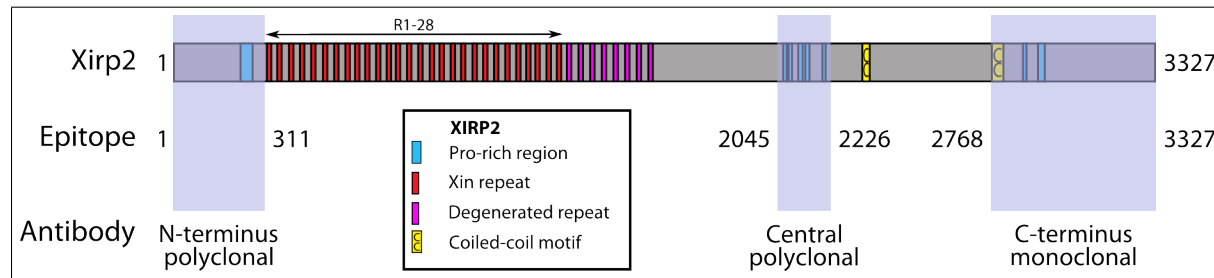


Figure 3.67: **Epitopes of human Xirp2 antibodies.** Schematic overview of human Xirp2. Three different antibodies were raised against distinct portions of human Xirp2. The numbering refers to the amino acids the epitope comprises. Two polyclonal antibodies were generated in rabbits against the N-terminus and the central proline-rich region. The monoclonal antibody recognizes the C-terminus of human Xirp2. The antibodies reveal no cross-reactivity to mouse Xirp2.

SH3 domain of nebulin and nebulette (amino acids 2045-2226, cf. section 3.7.2). The C-terminus can be detected with an antibody generated in mouse against the amino acids 2765-3327. All antibodies were tested for binding the respective bacterially expressed epitopes and they decorated one band significantly above 250 kDa in human skeletal muscle extracts (data not shown and P. van der Ven, personal communication). The antibody concentration was increased by using Centricon centrifugal filter units (Millipore) (cf. section 2.8.2.1). The secondary antibodies used were extensively tested for unspecific binding on human skeletal muscle sections originating from muscle biopsies (cf. sections 2.8.3 and 2.8.4). None of the antibodies revealed any background staining so that all signals obtained derived from the detection of the primary antibody. The localization of human Xirp2 was analyzed in relation to  $\alpha$ -actinin, which defines the center of the Z-disc (cf. section 1.5.5.1). Two different antibody combinations were used. In stainings with the polyclonal Xirp2 antibodies against the N-terminus and the central proline-rich region, the BM75.2 antibody (tab. 2.8.2) detecting all  $\alpha$ -actinin isoforms was chosen for the counterstaining. The monoclonal antibody against the C-terminus was combined with the a653 antibody, which only decorates sarcomeric  $\alpha$ -actinin.

The antibody against the N-terminus of Xirp2 did not provide a well-defined signal in healthy adult skeletal muscle (fig. 3.68 A). All over the section colocalization with  $\alpha$ -actinin was occasionally observed (fig. 3.68 A+B, arrowheads) but a prominent striated pattern was lacking. Most of the signal could not be allocated to a distinct sarcomeric structure, which was partly due to the likewise slightly diffuse signal obtained with the  $\alpha$ -actinin antibody resulting in a less defined cross-striation (fig. 3.68 B). Therefore, the localization of the N-terminus of human Xirp2 could not be doubtlessly determined although weak colocalizations with  $\alpha$ -actinin suggest Z-disc targeting particularly upon



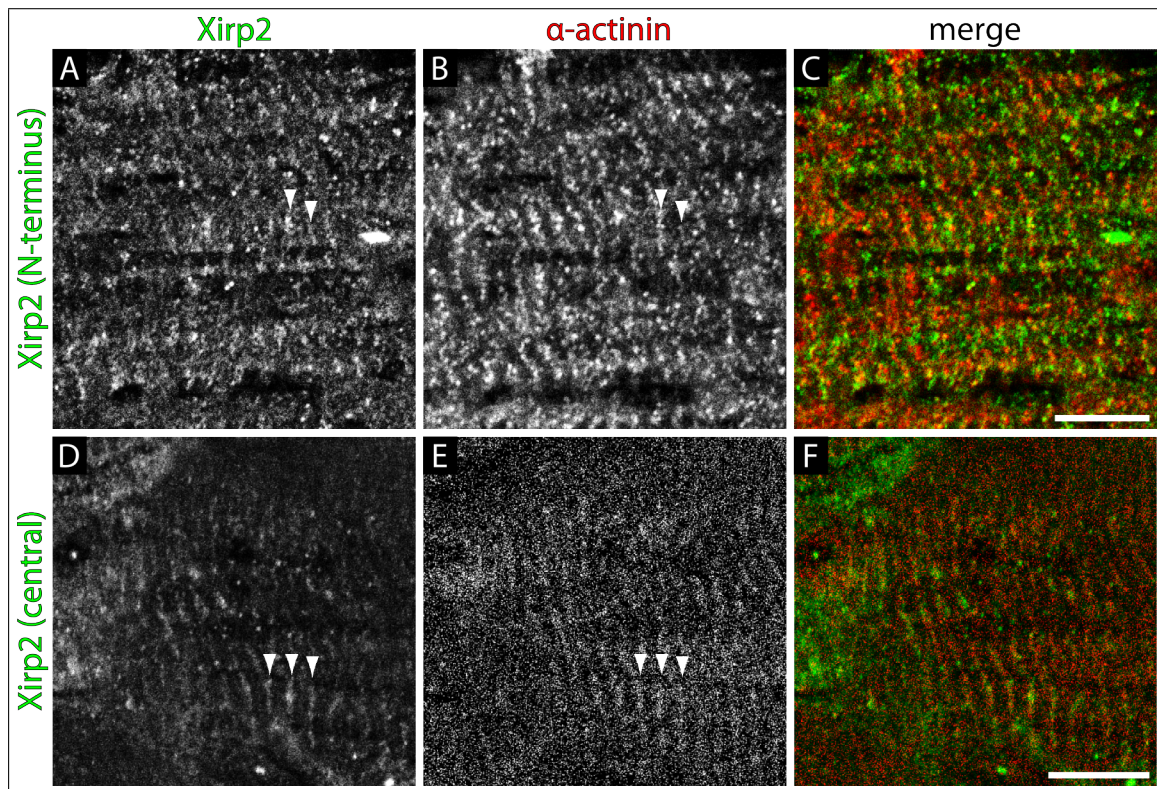


Figure 3.68: **Localization of the human Xirp2 N-terminus and central region in skeletal muscle.** Confocal LSM images of human skeletal muscle sections. The Xirp2 N-terminal antibody does not provide a well-defined signal (**A**) but reveals occasional colocalization with  $\alpha$ -actinin at the Z-disc (**A**, **B**, arrowheads). The antibody recognizing the central portion decorates the Z-disc more prominently (**D**) and colocalization with  $\alpha$ -actinin can be seen more clearly (**D**, **E**, arrowheads). In the merge images (**C**, **F**) Xirp2 and  $\alpha$ -actinin are tinted green and red, respectively. Scale bar 10  $\mu$ m.

consideration of the localization of the murine orthologue (cf. section 1.10). The principle functionality of the antibody was demonstrated in remodelling skeletal muscle, which raises the possibility that the epitope of the N-terminal antibody is masked in these samples (cf. section 3.8). In contrast to the Xirp2 N-terminus antibody, the Xirp2 central antibody revealed a clear albeit weak striated pattern (fig. 3.68 D, arrowheads). Although the  $\alpha$ -actinin signal was very weak (fig. 3.68 E), the striation could be attributed to the sarcomeric Z-disc further supporting the suggestion above.

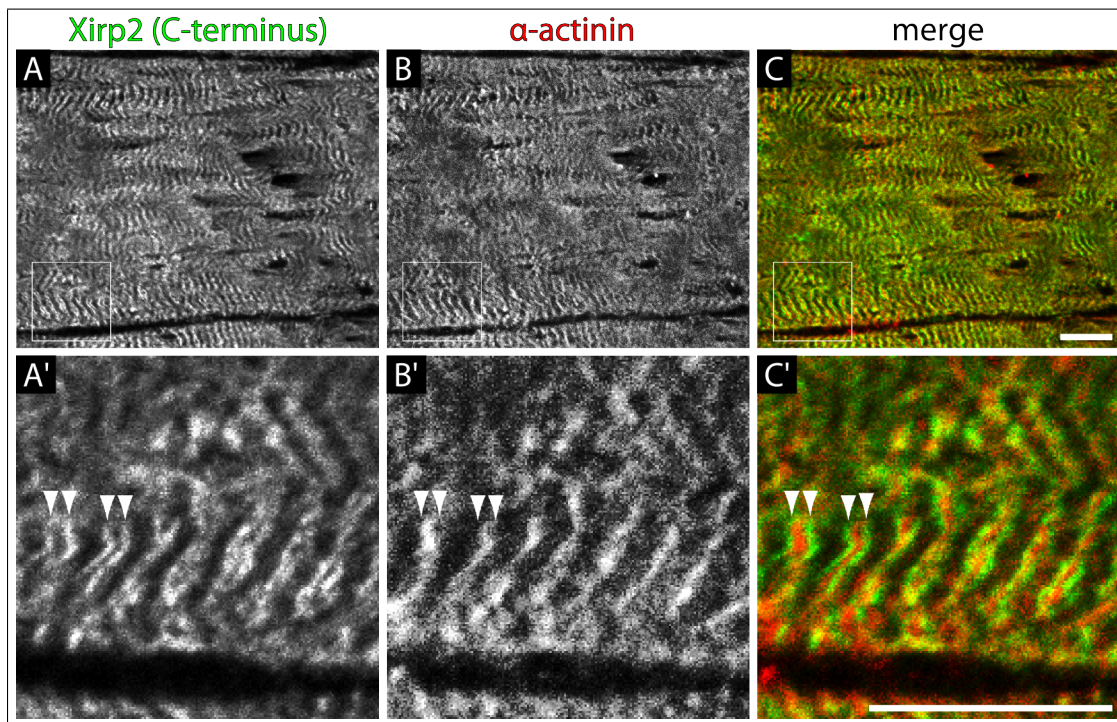


Figure 3.69: **The C-terminus of human Xirp2 flanks the Z-disc in skeletal muscle.** Confocal LSM images of human skeletal muscle sections. The monoclonal antibody raised against the C-terminus of Xirp2 exhibits prominent striation (A) which is located in the Z-disc region indicated by the  $\alpha$ -actinin signal (B). Magnification reveals that the C-terminal antibody decorates a doublet (A', arrowheads) flanking the center of the Z-disc (B', arrowheads). In the merge images (C, C') Xirp2 and  $\alpha$ -actinin are tinted green and red, respectively. Scale bar 10  $\mu$ m.

Stainings with the monoclonal antibody recognizing the Xirp2 C-terminus corroborated this notion and provided additional data about the orientation within the Z-disc. Skeletal muscle sections stained with the Xirp2 C-terminus antibody provided prominent cross-striation at the level of Z-discs (fig. 3.69 A-C) indicated by the  $\alpha$ -actinin signal obtained with the a653 antibody (tab. 2.8.2). Detailed analysis revealed that the antibody mostly decorated a double band flanking the  $\alpha$ -actinin signal (fig. 3.69 A'-C', arrowheads). The same result was obtained with a filamin antibody recognizing the N-terminus (RR90, tab. 2.8.2), which marked the center of the Z-disc (fig. 3.70 A-C). The signal of the



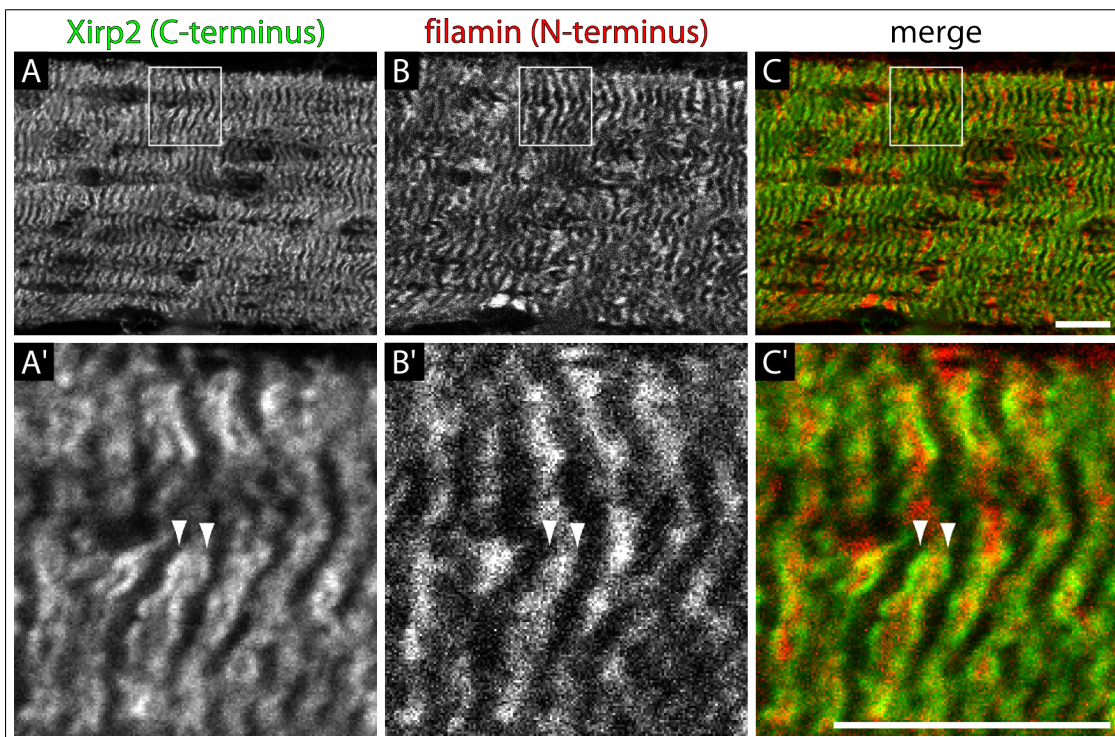


Figure 3.70: **The C-terminus of human Xirp2 flanks the position of the filamin N-terminus in the Z-disc of skeletal muscle.** Confocal LSM images of human skeletal muscle sections. The monoclonal antibody raised against the C-terminus of Xirp2 exhibits prominent striation (**A**) which is located in the Z-disc region indicated by the signal obtained with the N-terminal filamin antibody (**B**). Magnification reveals that the C-terminal antibody decorates a doublet (**A'**, arrowheads) flanking the position of the filamin N-terminus (**B'**, arrowheads). In the merge images (**C**, **C'**) Xirp2 and filamin are tinted green and red, respectively. Scale bar 10  $\mu$ m.

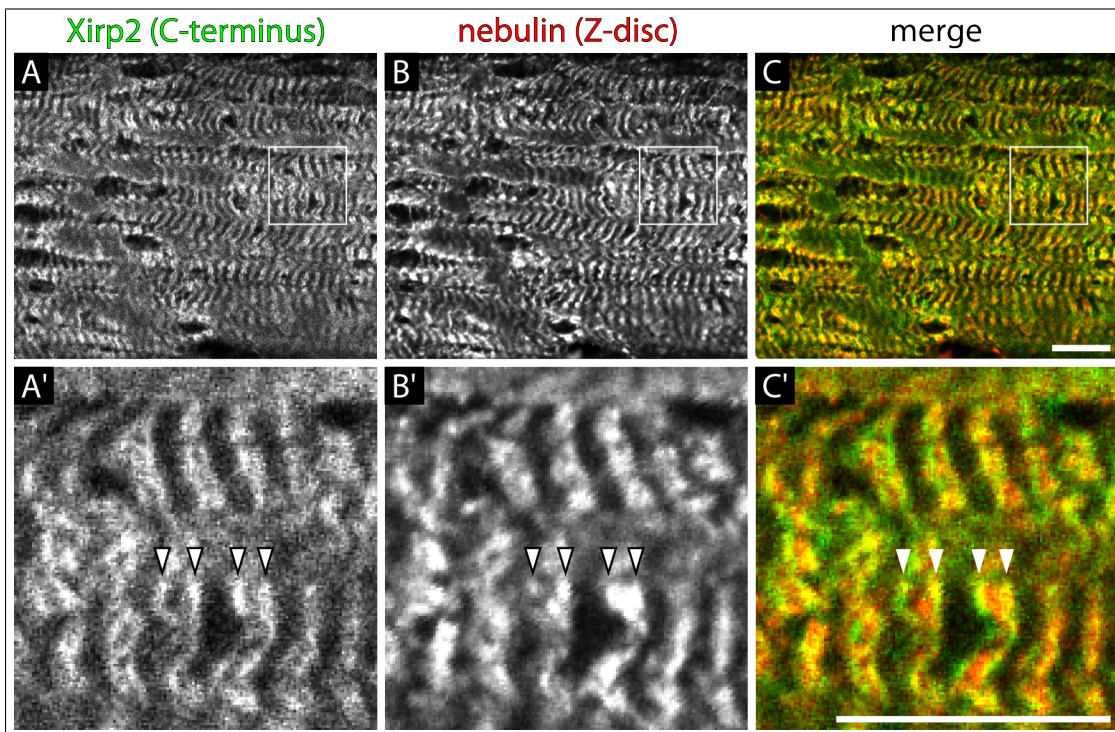


Figure 3.71: **The C-terminus of human Xirp2 partially overlaps with nebulin repeat modules 176-181 in the Z-disc of skeletal muscle.** Confocal LSM images of human skeletal muscle sections. The monoclonal antibody raised against the C-terminus of Xirp2 exhibits prominent striation (**A**) which is located in the Z-disc region indicated by the signal obtained with the nebulin Nbm176-181 antibody (**B**). The Z-disc decoration of this antibody is broader (**B'**) than that of  $\alpha$ -actinin (see fig. 3.69) and filamin N-terminus (see fig. 3.70). The doublet of the C-terminal Xirp2 antibody partially overlaps with the nebulin signal (**A'**, **B'**, arrowheads) but no decoration of the Z-disc center can be detected. In the merge images (**C**, **C'**) Xirp2 and nebulin are tinted green and red, respectively. Scale bar 10  $\mu$ m.

Xirp2 C-terminus antibody also enclosed the position of the filamin N-terminus further demonstrating the localization of the Xirp2 C-terminus in the periphery of the Z-disc (fig. 3.70 A'-C'). The nebulin antibody Nbm176-180 (tab. 2.8.2) was raised against the F-actin-binding repeat modules 176–180, which exhibited a somewhat broader Z-disc decoration than  $\alpha$ -actinin presumably due to the antiparallel overlap of nebulin molecules from adjacent sarcomeres (fig. 3.71 A-C and Pappas *et al.* (2008)). The C-terminus of Xirp2 partially overlapped with that signal at the edge but also extended the Z-disc decoration a bit (fig. 3.71 A'-C', arrowheads). These findings show that human Xirp2 is a Z-disc component of adult skeletal muscle. Even though the exact localization of the Xirp2 N-terminus has not been depicted doubtlessly, the fact that the central portion is centrally located within the Z-disc clearly demonstrates the Z-disc localization (fig. 3.69). Immunostainings with the Xirp2 C-terminus antibody provided further insight into the exact orientation of Xirp2. The signal appears as a doublet flanking the central core of the Z-disc marked by  $\alpha$ -actinin and the filamin N-terminus (fig. 3.69 and 3.70). Thus, the N-terminus and the central part of human Xirp2 are located within the center of the Z-disc while the C-terminus is exposed in its periphery.

### 3.8 Xin-Repeat Proteins During Skeletal Muscle Remodelling

Murine Xin expression starts at very early stages of embryonic development (cf. section 1.10). It can be detected in cells of the heart tube as early as E8.0 and in the first rostral somites at E10 (Sinn *et al.*, 2002). The apparent restriction to cross-striated muscle and its precursor structures implies an involvement in heart and skeletal muscle development. In this work, early upregulation upon induction of myogenic differentiation of H-2K cells has been proven for both murine Xin-Repeat proteins, Xin and Xirp2 (cf. sections 3.7.6 and 3.2.2). Furthermore, association of Xin C with NSMF's in embryonic cardiomyocytes shown in this work corroborates the assumption that Xin-Repeat proteins are involved in myofibrillar development (cf. section 3.3.6.3). In adult cross-striated muscle, the localization of Xin and Xirp2 significantly differs, since Xirp2 remains a component of the myofibrillar Z-disc (cf. section 3.7.7) whereas Xin is only located in the intercalated disc (ICD) or myotendinous junction (MTJ) (Beatham *et al.*, 2006; van der Ven *et al.*, 2006). Damage of the myofibrillar apparatus caused by diseases or unaccustomed exercise enforces repair and adaptation of the muscle in order to retain proper function

(cf. section 1.3). This process involves many growth factors, proteins and other yet unidentified elements and is among others characterized by local remodelling of the contractile apparatus including loss of myofibrillar registry and addition of new sarcomeres (cf. section 1.4). Such regions of remodelling can be also found in normal muscle albeit much less frequently (Yu und Thornell, 2002). The set of proteins taking part in these processes is still incomplete. Therefore, sections of a biopsy of human skeletal muscle exhibiting an inconspicuous phenotype were analyzed for localization of Xin-Repeat protein isoforms in relation to prominent constituents of the sarcomere using immunofluorescence microscopy. Since the antibodies raised against human Xin can detect the repeat regions of both Xin A and B and the antibody against the C-terminus of Xin A can identify Xin A and C, staining signals can indicate localization of two isoforms. Expression of Xin A and B in adult skeletal muscle has already been described in the MTJ whereas Xin C detection on the protein level has been only successful in specimens of pathologically altered heart muscle (Otten *et al.*, 2010). Therefore, a complete distinction of Xin isoforms with immunofluorescence microscopy is not possible.

### 3.8.1 Xin-Repeat Proteins and $\alpha$ -Actinin in Structures of Human Skeletal Muscle Remodelling

$\alpha$ -Actinin is the central component of the Z-disc of cross-striated muscle but in areas of remodelling  $\alpha$ -actinin is absent or exhibits misalignment of the transverse striations of Z-discs (Yu und Thornell, 2002; Yu *et al.*, 2004). It has been demonstrated that  $\alpha$ -actinin interacts with the repeat region of Xirp2 whereas Xin does not show any interaction (cf. section 3.7.3). Co-stainings of human skeletal muscle sections with antibodies against sarcomeric  $\alpha$ -actinin and the repeat region of human Xin detecting Xin A and B revealed that Xin is recruited to longitudinal strands spanning one or more neighbouring sarcomeres where  $\alpha$ -actinin is absent or diffusely distributed (fig. 3.72). These strands did not contain significant amounts of  $\alpha$ -actinin but it was displaced from its regular array of Z-discs at these sites implicating regions which were subjected to structural remodelling. Such areas of remodelling either appeared as large patches within a myofibre (fig. 3.72 A-C) or covered only small regions (D-F and D'-F') or occurred as single strands (G-I). Although Xin does not reside in fully developed sarcomeres, longitudinal strands were strongly decorated by Xin in remodelling regions implying a translocation to these sites.

Similar structures were observed with an antibody against the C-terminus of Xin A enabling detection of Xin A and Xin C. The antibody also labeled patches of longitudinal



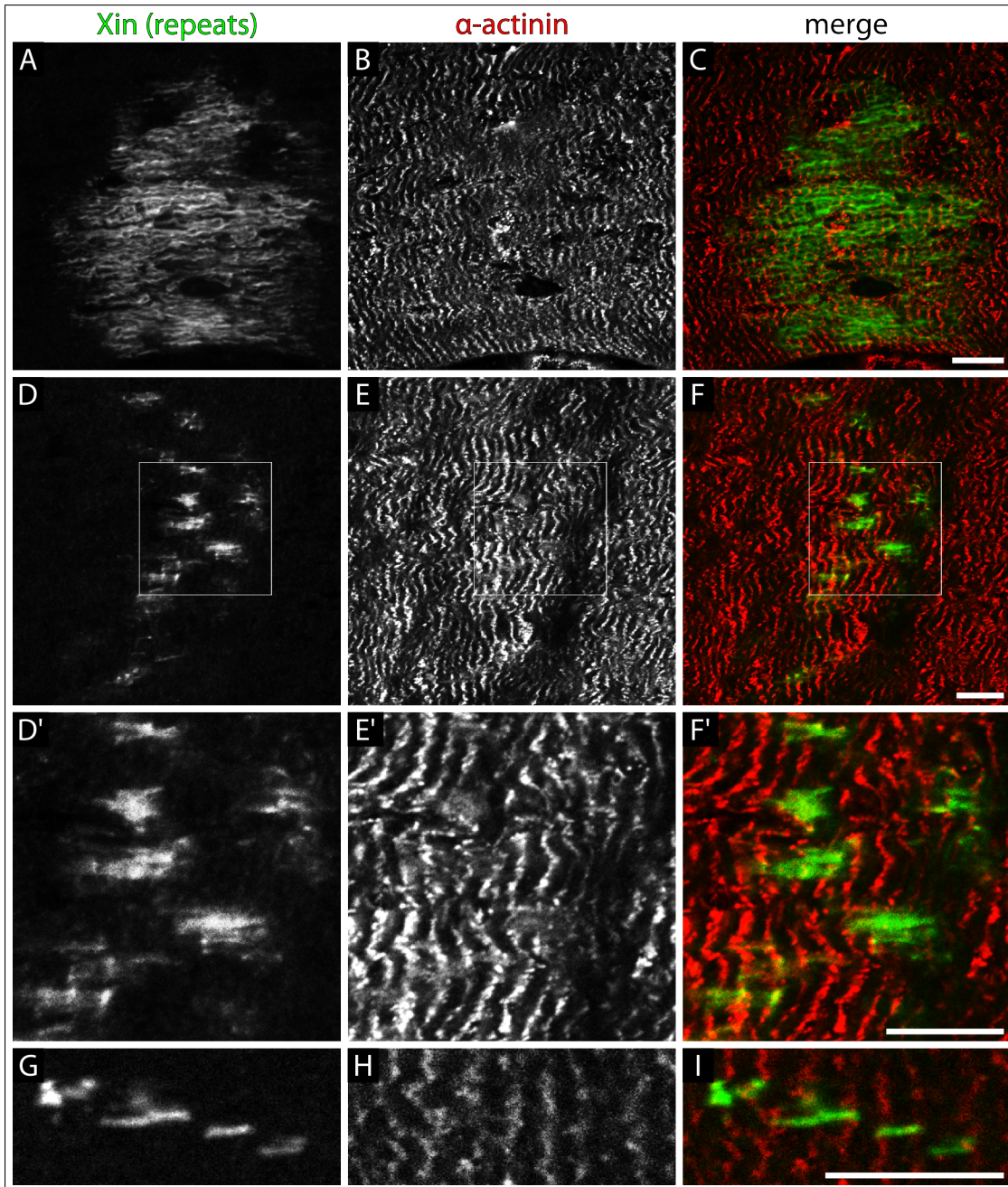


Figure 3.72: **Xin A/B and  $\alpha$ -actinin in areas of skeletal muscle remodelling.** Confocal LSM images of human skeletal muscle sections. The specimens were labeled with antibodies against the Xin repeat region (XR1B) and sarcomeric  $\alpha$ -actinin (a653). In merge images (C, F, F', I) Xin and  $\alpha$ -actinin are tinted green and red, respectively. **A-C.** Large patch of Xin-containing longitudinal strands connecting a varying number of successive sarcomeres. Localization of  $\alpha$ -actinin at the Z-disc is disturbed at these regions. **D-F.** Apart from large patches, smaller areas of longitudinal strands decorated by Xin are also observed. **D'-F'.** Magnification of the box in D-F. Regions of Xin-containing strands are characterized by a disruption of  $\alpha$ -actinin targeting at the Z-disc. **G-I.** Longitudinal strands can also occur as a single connection of two Z-discs. Scale bar 10  $\mu$ m.

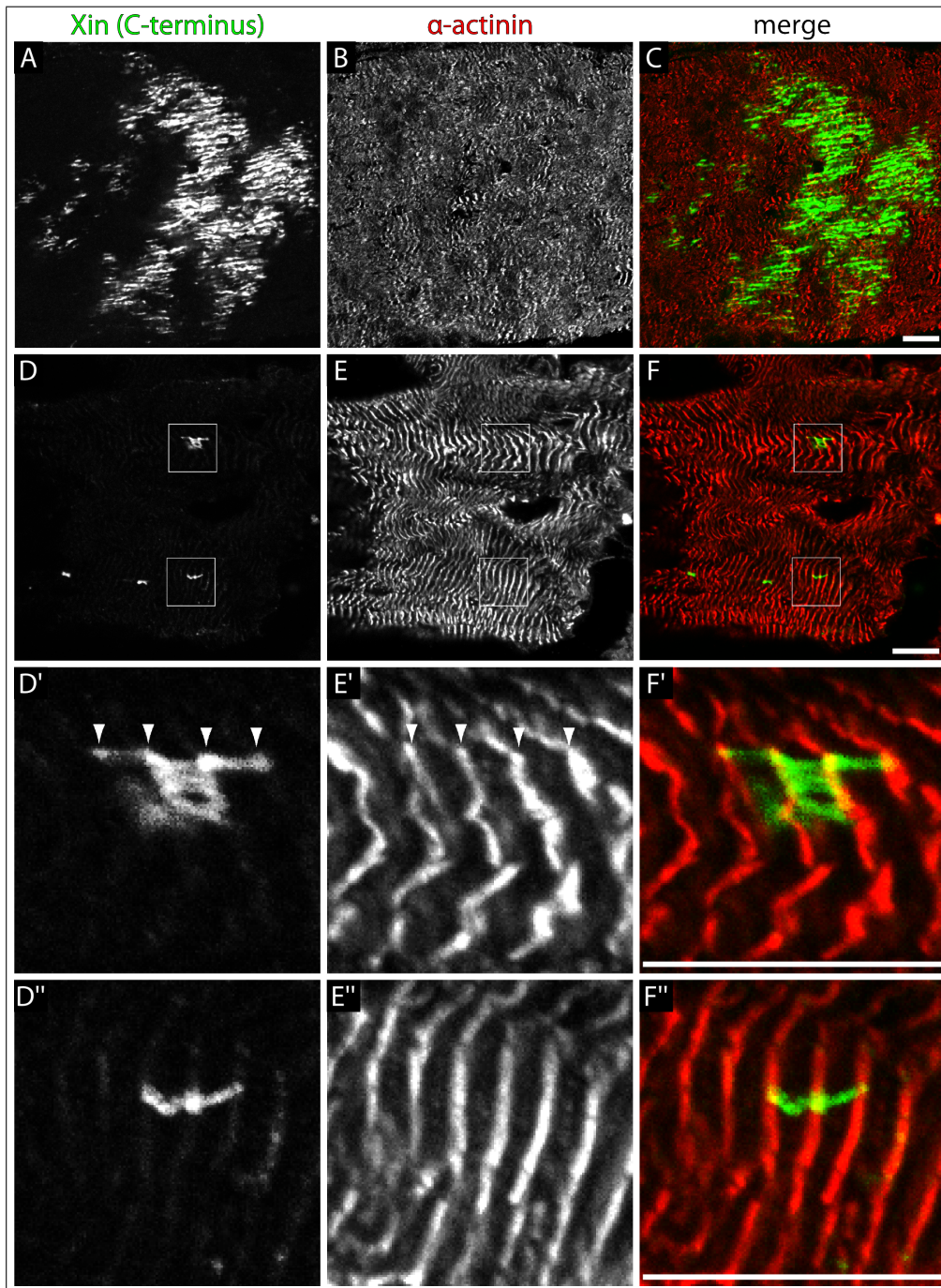


Figure 3.73: **Xin A/C and  $\alpha$ -actinin in areas of skeletal muscle remodelling.** Confocal LSM images of human skeletal muscle sections. The specimens were labeled with antibodies against the Xin A C-terminus (XC1) and sarcomeric  $\alpha$ -actinin (a653). In merge images (C, F, F', F'') Xin and  $\alpha$ -actinin are tinted green and red, respectively. **A-C.** Large patch of Xin-containing longitudinal strands connecting a varying number of successive sarcomeres which is accompanied by absence or diffuse distribution of  $\alpha$ -actinin. **D-F.** Sites displaying longitudinal strands labeled with Xin are also detected in regions which do not have visible alterations in Z-disc arrangement. **D'-F'.** Magnification of the upper box in D-F. This strand connects four Z-discs and the Xin signal intensifies at the level of the Z-discs (arrowheads).  $\alpha$ -Actinin prominently labels the Z-disc. **D''-F''.** Magnification of the lower box in D-F. Although no alteration in Z-disc structure can be detected three Z-discs are connected by a Xin-containing longitudinal strand. Low amounts of Xin are observed in the adjacent Z-discs. Scale bar 10  $\mu$ m.



strands connecting a varying number of successive sarcomeres (fig. 3.73 A-C). In these areas  $\alpha$ -actinin was not properly localized at Z-discs and was either absent or diffusely distributed. Apart from these patches, single longitudinal strands connecting adjacent sarcomeres which were strongly labeled by Xin were occasionally observed (fig. 3.73 D-F). Detailed analysis revealed that the Xin signal intensified at the level of Z-discs and the connective strands were less strongly decorated (fig. 3.73 D'-F', arrowheads). At these sites, Z-disc arrangement was not as dramatically disrupted as in the large patches but minor irregularities in the  $\alpha$ -actinin stain occurred. However, the incidence of Xin-containing longitudinal strands connecting Z-discs did not seem to depend on disruption of Z-disc architecture visible on light microscopic level because there were apparently normal Z-discs which were connected by such strands (fig. 3.73 D''-F''). Furthermore, low amounts of Xin could be detected in the surrounding Z-discs, a phenomenon which has already been described for cardiac tissue sections of patients suffering from dilated cardiomyopathy (DCM) (P. van der Ven, personal communication).

These results clearly point to human Xin as a protein involved in skeletal muscle remodelling. In order to elucidate whether this reflects a common feature of Xin-Repeat proteins cryo-sections of human skeletal muscle were labeled with the antibody against the C-terminus of human Xirp2 and against  $\alpha$ -actinin. Surprisingly, the typical Z-disc localization of Xirp2 was occasionally interrupted by longitudinal strands which exhibited very strong decoration (fig. 3.74 A-C). This was not necessarily expected because Xirp2 can interact with  $\alpha$ -actinin which however was not prominently recruited to these sites as demonstrated by co-stainings of Xin and  $\alpha$ -actinin. Nevertheless, these Xirp2-containing structures also connected a varying number of successive sarcomeres where  $\alpha$ -actinin localization was disordered (fig. 3.74 A'-C'). Such structures also occurred in regions where Z-discs displayed an overall regular arrangement (fig. 3.74 D-F). However, a closer look revealed that there is a misalignment of adjacent sarcomeres with the longitudinal strands appearing as laterally extended Z-discs (fig. 3.74 D'-F'). In summary, Xin-Repeat proteins are components of longitudinal strands in areas of skeletal muscle remodelling. Both Xin-Repeat proteins are associated with longitudinal strands in areas where  $\alpha$ -actinin staining reveals alterations or disruption of the regular Z-disc array. Interestingly, although Xirp2, a novel binding partner of  $\alpha$ -actinin, appears to be a prominent component of these structures,  $\alpha$ -actinin is only weakly associated, if at all. Thus, while Xin-Repeat proteins seem to play an important role in skeletal muscle remodelling,  $\alpha$ -actinin could be mainly actively involved in structural maintenance of the Z-disc but not its remodelling. Furthermore, these results make it tempting to speculate that the main

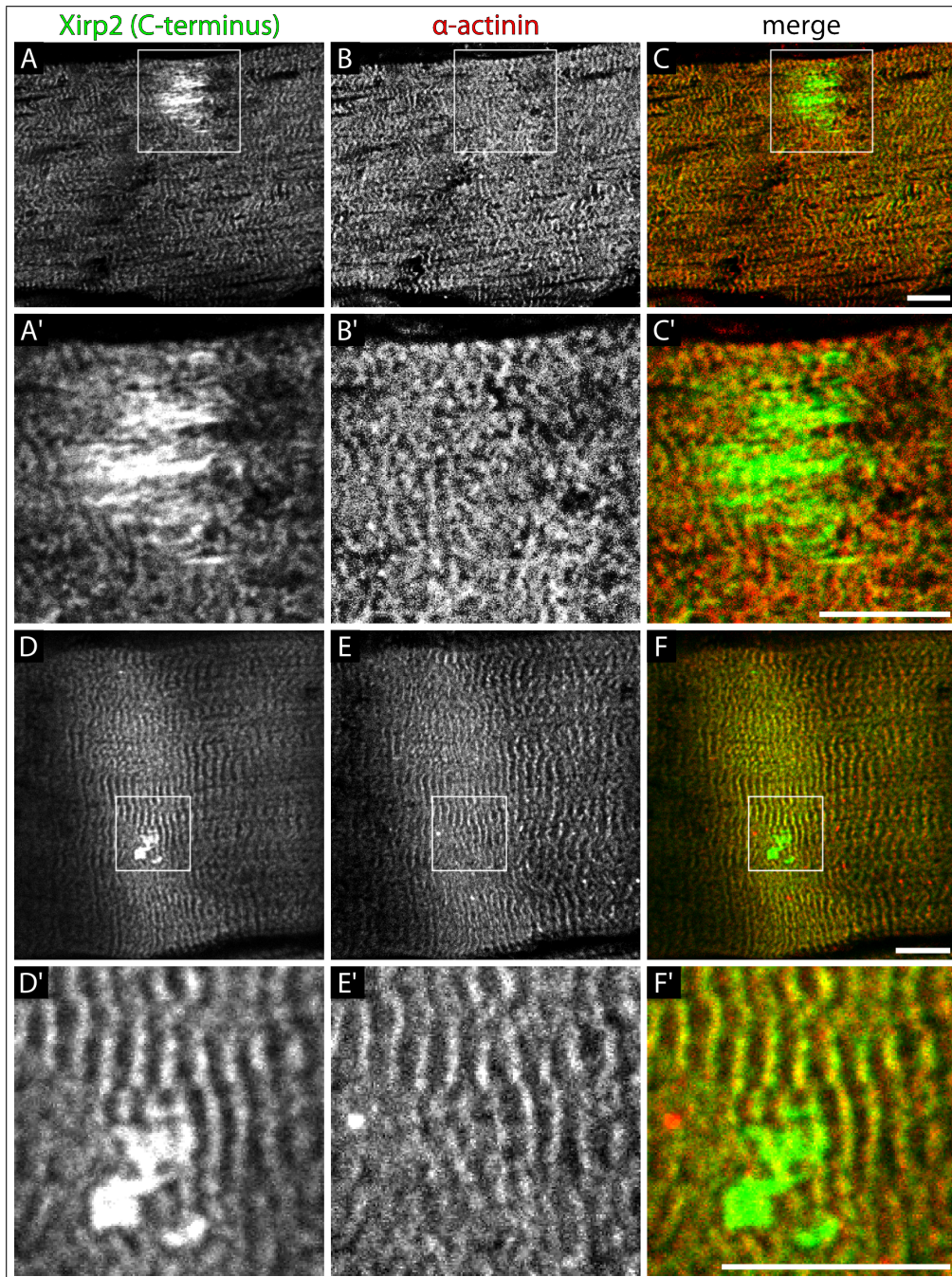


Figure 3.74: **Xirp2 and  $\alpha$ -actinin in areas of skeletal muscle remodelling.** Confocal LSM images of human skeletal muscle sections. The specimens were labeled with antibodies against the Xirp2 C-terminus and sarcomeric  $\alpha$ -actinin (a653). In merge images (C, C', F, F') Xirp2 and  $\alpha$ -actinin are tinted green and red, respectively. **A-C.** Patch of skeletal muscle remodelling containing longitudinal strands labeled with Xirp2 but not  $\alpha$ -actinin. **A'-C'.** Magnification of the box in A-C. The longitudinal strands detected with Xin connect a varying number of successive sarcomeres. There,  $\alpha$ -actinin localization is disrupted. **D-F.** Small regions of a more intense Xirp2 signal can be detected in areas generally exhibiting perfect alignment of Z-discs. **D'-F'.** Magnification of the box in D-F. The intense Xirp2 signal appears as broadened Z-discs rather than longitudinal strands.  $\alpha$ -Actinin localization reveals transverse misalignment of adjacent sarcomeres. Scale bar 10  $\mu$ m.

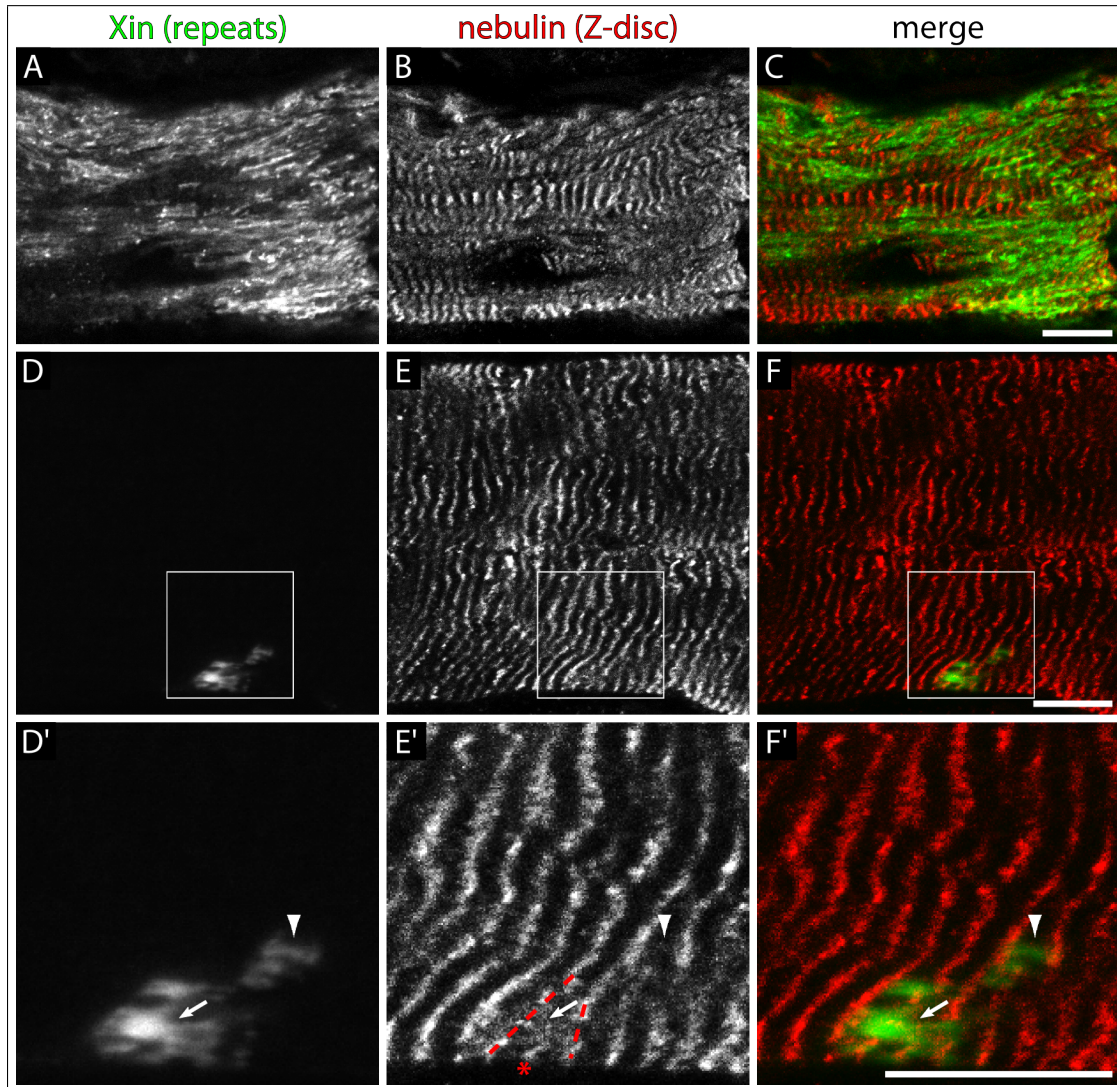
site of the interaction between Xirp2 and  $\alpha$ -actinin is not located at those remodelling structures but at the normal adult Z-disc.

### 3.8.2 Xin-Repeat Proteins and Nebulin in Structures of Human Skeletal Muscle Remodelling

Nebulin represents the fourth filament system in skeletal muscle cells and presumably conveys thin filament and more general sarcomere stability (cf. section 1.5.3). At the Z-disc level, it is connected to the intermediate filament system and costameres (cf. section 1.5.3). However, areas of muscle remodelling initially display absence of nebulin and a nebulin recruitment to the newly formed myofibrillar apparatus at later stages (Yu *et al.*, 2003). Co-stainings of Xin and nebulin in human skeletal support these findings. Large patches containing longitudinal strands strongly decorated by the Xin antibody directed against the repeats revealed that regular Z-disc arrangement of nebulin was lost (fig. 3.75 A-C). In these areas, nebulin did not seem to be completely absent but rather diffusely distributed. Such a localization pattern was also obtained in smaller regions of remodelling (fig. 3.75 D-F, D'-F', arrow). There, an area showing supernumerary sarcomeres, if the Z-disc is followed in transverse register across the myofibril, was covered by Xin-containing longitudinal strands and diffusely distributed nebulin (fig. 3.75 D'-F', asterisk, dotted line). Along single Xin-containing strands between neighbouring sarcomeres, nebulin appeared to be completely absent (fig. 3.75 D'-F', arrowhead).

Nebulin also showed alterations of Z-disc localization in areas of remodelling marked by the antibody against the C-terminus of Xin A. This antibody identified regions with large patches of longitudinal strands associated with Xin and single strands connecting adjacent sarcomeres (fig. 3.76). At sites of strong Xin labeling along these longitudinal structures the nebulin signal was completely diffuse and no Z-disc arrangement discernable (fig. 3.76 A'-C', arrow). The intensity of Xin decoration along these structures was not homogenous so that focal points with greater intensity could be distinguished (arrowheads). At sites of basic immature Z-disc arrangement as reflected by the nebulin localization, such focal points were situated at the Z-disc level and appeared rather not connected by longitudinal strands. A local intensification of the Xin signal at the level of Z-discs together with its reduction along the longitudinal strand was also shown in cryo-sections of human skeletal muscle co-stained with Xin and  $\alpha$ -actinin (fig. 3.73 D'-F'). This was most obvious in single strands located in areas of minor remodelling. Such areas were also detectable in samples labeled with the antibodies Xin C-terminus and nebulin Nbm176-181. There,





**Figure 3.75: Xin A/B and nebulin in areas of skeletal muscle remodelling.** Confocal LSM images of human skeletal muscle sections. The specimens were labeled with antibodies against the Xin repeat region (XR1B) and nebulin repeat modules near the Z-disc (Nbm176-181). In merge images (C, F, F') Xin and nebulin are tinted green and red, respectively. **A-C.** Large patch of Xin-containing longitudinal strands connecting a varying number of successive sarcomeres. Z-disc localization of nebulin is disturbed and more diffuse in these regions. **D-F.** Apart from large patches, smaller areas of longitudinal strands prominently decorated by Xin are also observed. **D'-F'.** Magnification of the box in D-F. Regions of Xin-containing strands are characterized by a disruption of nebulin targeting at the Z-disc in favor of a diffuse distribution (arrow). Here, supernumerary sarcomeres can be identified exhibiting a typical delta-shaped structure (dotted lines, asterisk). Longitudinal strands can also occur as a single connection of two Z-discs (arrowhead). Scale bar 10  $\mu\text{m}$ .



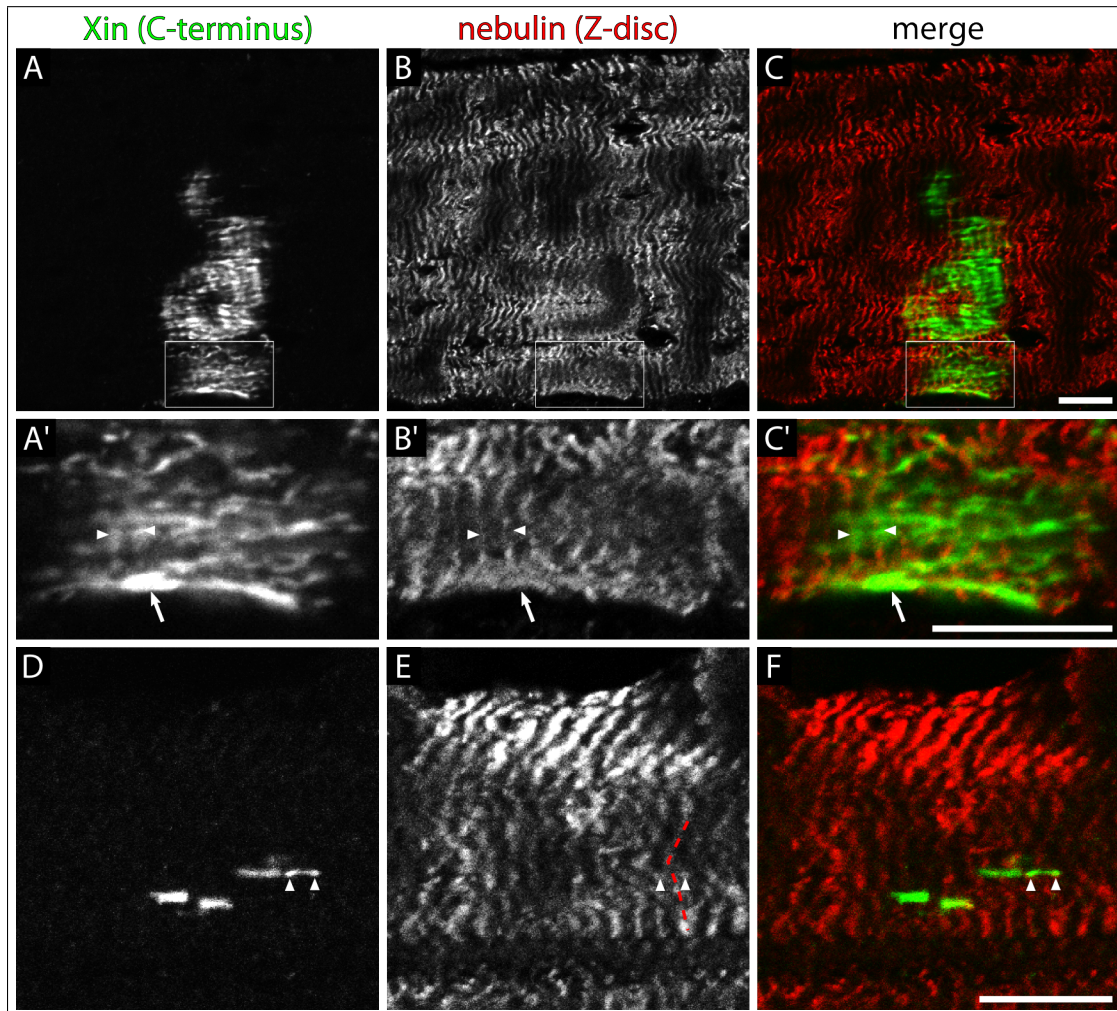


Figure 3.76: **Xin A/C and nebulin in areas of skeletal muscle remodelling.** Confocal LSM images of human skeletal muscle sections. The specimens were labeled with antibodies against the Xin A C-terminus (XC1) and nebulin repeat modules near the Z-disc (Nbm176-181). In merge images (C, C', F) Xin and nebulin are tinted green and red, respectively. **A-C.** Large patch of Xin-containing longitudinal strands connecting a varying number of successive sarcomeres. Z-disc localization of nebulin is disturbed and more diffuse in these regions. **A'-C'.** Magnification of the box in A-C. Strong Xin labeling is accompanied by diffuse nebulin distribution (arrow). Xin can also appear as intense points at the level of rudimentary Z-discs (arrowheads). **D-F.** Apart from large patches single Xin-containing strands can be detected. One strand exhibits a more intense signal at each end and interrupts the regular Z-disc array although it originates in nebulin-containing dense bodies (arrowheads). Scale bar 10  $\mu$ m.

Xin-containing single strands were located between adjacent sarcomeres (fig. 3.76 D-F). Although the array of Z-discs was quite well established, minor remodelling processes could be identified. One longitudinal strand displayed more intense signals at each end and at first sight it did not seem to connect adjacent sarcomeres (arrowheads). However, this strand originated in nebulin-containing dots presumably representing Z-bodies or Z-disc-related precursor structures. Therefore, this arrangement potentially depicts insertion of an additional sarcomere because the regular alignment of the neighbouring Z-disc was interrupted (dotted line).

These longitudinal strands in remodelling skeletal muscle have been shown to be a structure which is generally associated with the whole Xin-Repeat protein family for labeling with an antibody raised against the C-terminus of Xirp2 has revealed comparable structures (cf. section 3.8.1). This antibody clearly identifies Xirp2 as a Z-disc protein whereas antibodies against the N-terminus and the central proline-rich region did not provide such a clear signal (cf. section 3.7.7). However, in areas of skeletal muscle remodelling both antibodies displayed very strong labeling of the characteristic longitudinal strands (fig. 3.77 and 3.78). The high signal intensity obscured any putative signal at the Z-disc as the signal in normal adult skeletal muscle is very weak. Co-stainings with an antibody against nebulin detecting an epitope 220 nm away from the Z-disc (Nb2, tab. 2.8.2) revealed nebulin localization being altered into a diffuse distribution in areas of these longitudinal strands (figs. 3.77, 3.78, arrow). Similar to Xin, single strands could be identified which connected adjacent sarcomeres at sites of minor remodelling with showing no prominent colocalization with nebulin (fig. 3.78 arrowhead).

In summary, these stainings confirm the character of the longitudinal strands which are associated with both human Xin-Repeat proteins as comparable to those identified in DOMS muscle (cf. section 1.4) which harbours areas of remodelling defined by longitudinal actin- and or desmin-containing filamentous structures. These strands do not contain  $\alpha$ -actinin or nebulin as it also applies to the strands observed in the present specimen. On the contrary, nebulin exhibits a diffuse staining pattern which is reinforced upon intensification of Xin-Repeat protein association. These data suggest that longitudinal strands in remodelling skeletal muscle does not represent the main site of Xin-Repeat protein-nebulin interaction due to large deviations in expression level and localization pattern in such areas. Furthermore, detailed analysis reveals that such longitudinal strands can definitely connect adjacent sarcomeres because they originate and end in the neighbouring Z-disc.



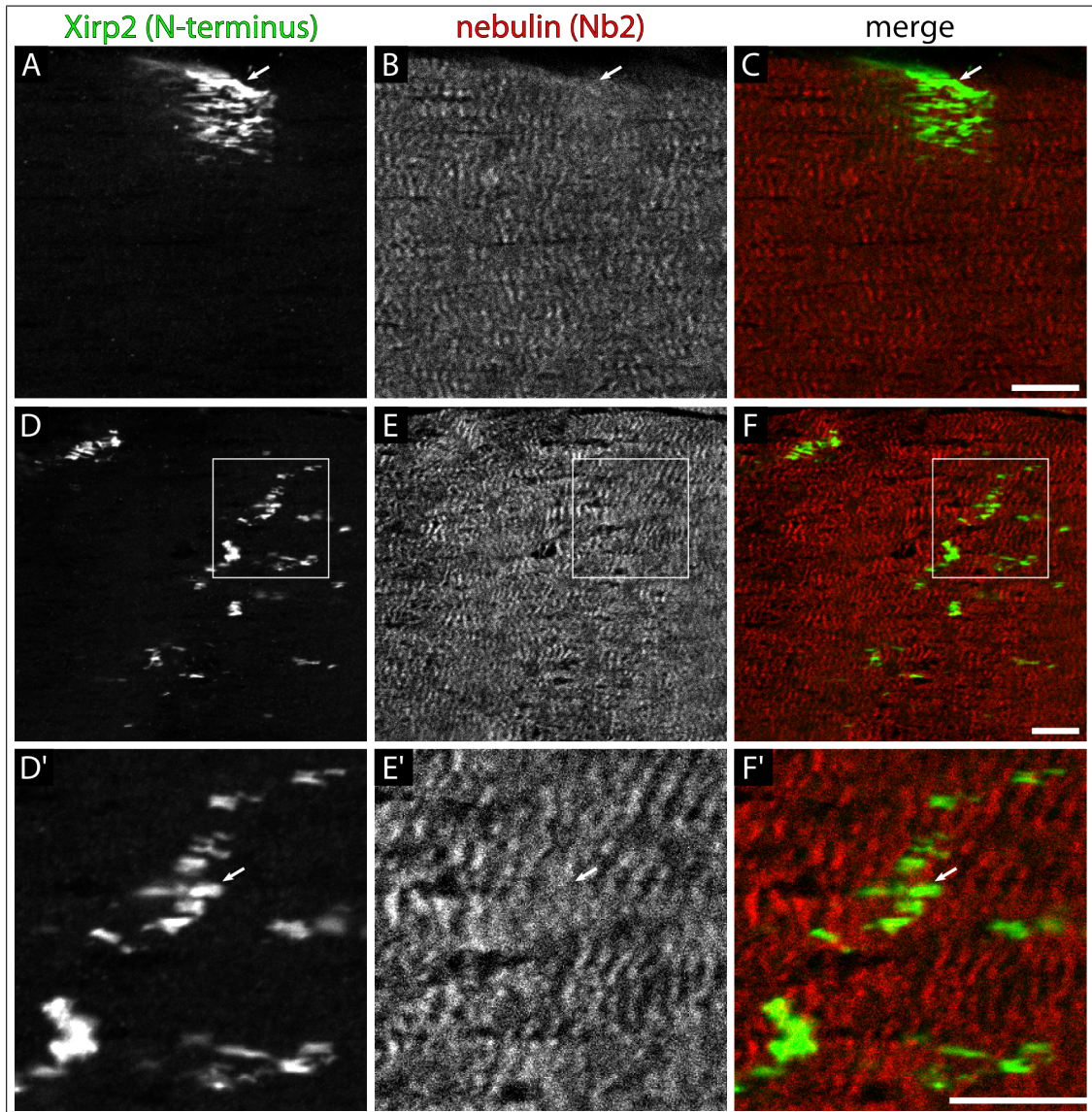


Figure 3.77: **Xirp2 (N-terminus) and nebulin in areas of skeletal muscle remodelling.** Confocal LSM images of human skeletal muscle sections. The specimens were labeled with antibodies against the Xirp2 N-terminus and a nebulin epitope 220 nm away from the Z-disc (Nb2). In merge images (C, F, F') Xirp2 and nebulin are tinted green and red, respectively. **A-C.** Large patch of Xirp2-containing longitudinal strands connecting a varying number of successive sarcomeres. The striated pattern of nebulin is disturbed and more diffuse in these regions (arrow). **D-F.** The N-terminus of Xirp2 can be also identified at single longitudinal strands. **D'-F'.** Magnification of the box in D-F. Although less pronounced, even in these smaller Xirp2-containing remodelling structures nebulin localization is diffuse (arrow). Scale bar 10  $\mu\text{m}$ .

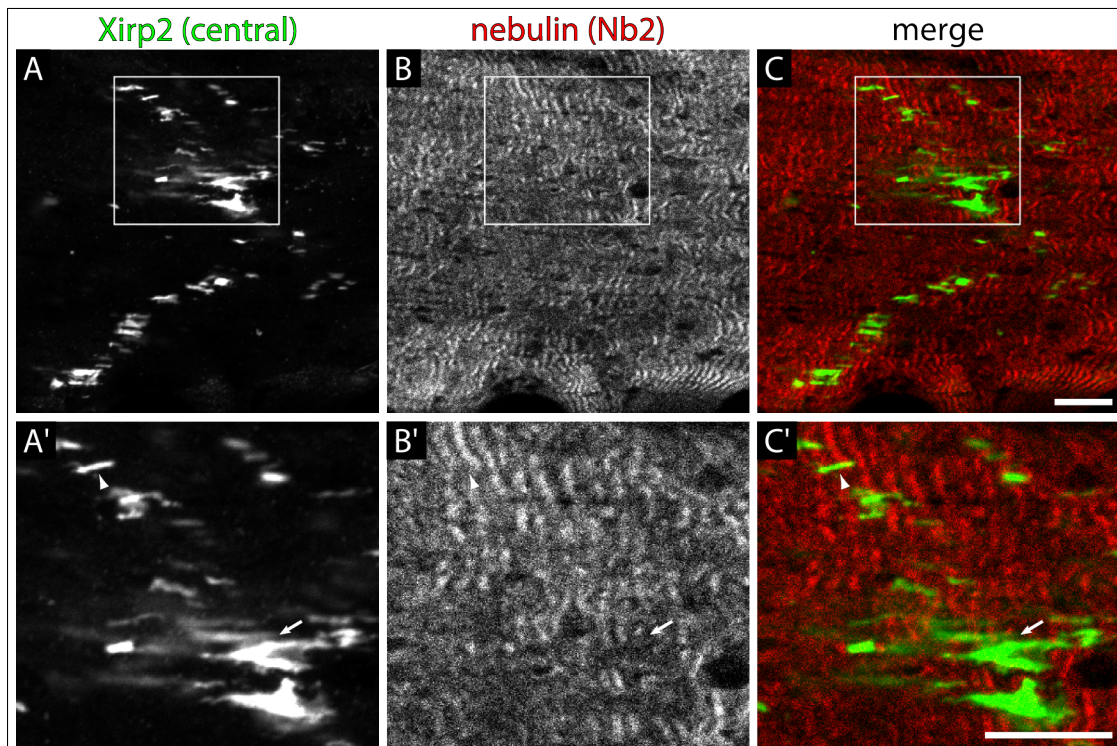


Figure 3.78: **Xirp2 (central) and nebulin in areas of skeletal muscle remodelling.** Confocal LSM images of human skeletal muscle sections. The specimens were labeled with antibodies against the central proline-rich region of Xirp2 and a nebulin epitope 220 nm away from the Z-disc (Nb2). In merge images (C, C') Xirp2 and nebulin are tinted green and red, respectively. **A-C.** A large patch of longitudinal strands labeled with Xirp2 is accompanied by disturbance of the sarcomere array. Single strands are also widely distributed. **A'-C'.** Magnification of the box in A-C. The larger the cluster of Xirp2-containing strands the more disruption of nebulin striation is detected (arrow). Single longitudinal strands containing Xirp2 span the distance of a sarcomere connecting the adjacent Z-discs (arrowhead). Scale bar 10  $\mu$ m.

### 3.8.3 Xin-Repeat Proteins and Filamin C in Structures of Human Skeletal Muscle Remodelling

Xin-Repeat proteins are the first binding partners identified exclusively interacting with the muscle-specific filamin isoform C (cf. section 3.7.1 and van der Ven *et al.* 2006). The interaction to both human Xin-Repeat proteins, Xin and Xirp2, is mediated by the Ig-like domain 20 of filamin C which harbours a unique insertion of 81 amino acids (cf. section 1.5.5.2). The binding site in Xin and Xirp2 has been mapped to a C-terminal portion which excludes the Xin isoform B from binding. Filamin as well as Xin-Repeat proteins have been identified to display an altered localization in certain myofibrillar myopathies assigning them to a group of “sensitive” proteins concerning disease conditions (Claeys *et al.*, 2009). The findings that Xin-Repeat proteins seem to be involved in myofibrillar remodelling processes raise the question whether, in contrast to other binding partners of Xin-Repeat proteins such as nebulin or  $\alpha$ -actinin, filamin C is also associated with specific structures in areas of skeletal muscle remodelling as demonstrated above for Xin-Repeat proteins (cf. sections 3.8.2 and 3.8.1). Therefore, sections of the same human skeletal muscle specimen already utilized for previous stainings were labeled with antibodies against Xin and the C-terminus of filamin C and the C-terminus of Xirp2 and the N-terminus of filamin, respectively.

These sections again revealed areas of Xin-Repeat protein-containing longitudinal strands which reflect muscle remodelling (fig. 3.79, 3.80 and 3.81). Such structures could cover either large patches where they spanned more than one successive sarcomere (A-C) or only a single sarcomere (D-F). The intensity of the respective Xin-Repeat protein appeared to be strongly increased as compared to normal Z-disc stain of Xirp2 (fig. 3.81) and, of course, compared to the general absence of Xin in the contractile apparatus (fig. 3.79 and 3.80). Strikingly, filamin C was associated with these longitudinal strands, too (fig. 3.79, 3.80 and 3.81). Although colocalization was not 100 %, the signal of both Xin and Xirp2 and filamin C greatly overlapped. Since filamin C is a component of the sarcomeric Z-disc, alterations in filamin C localization indicate disruption of the regular Z-disc array of normal skeletal muscle. Apart from the conspicuous arrangement of Xin-Repeat proteins in such areas, disturbance of filamin C position was another prominent indicator that these longitudinal structures reflected muscle cell remodelling. Additionally, these strands revealed another potential trend. As already detected for Xirp2, the amount of associated filamin C seemed to be clearly elevated at the longitudinal strands in comparison to the expression level in Z-discs although this can also be caused by improved



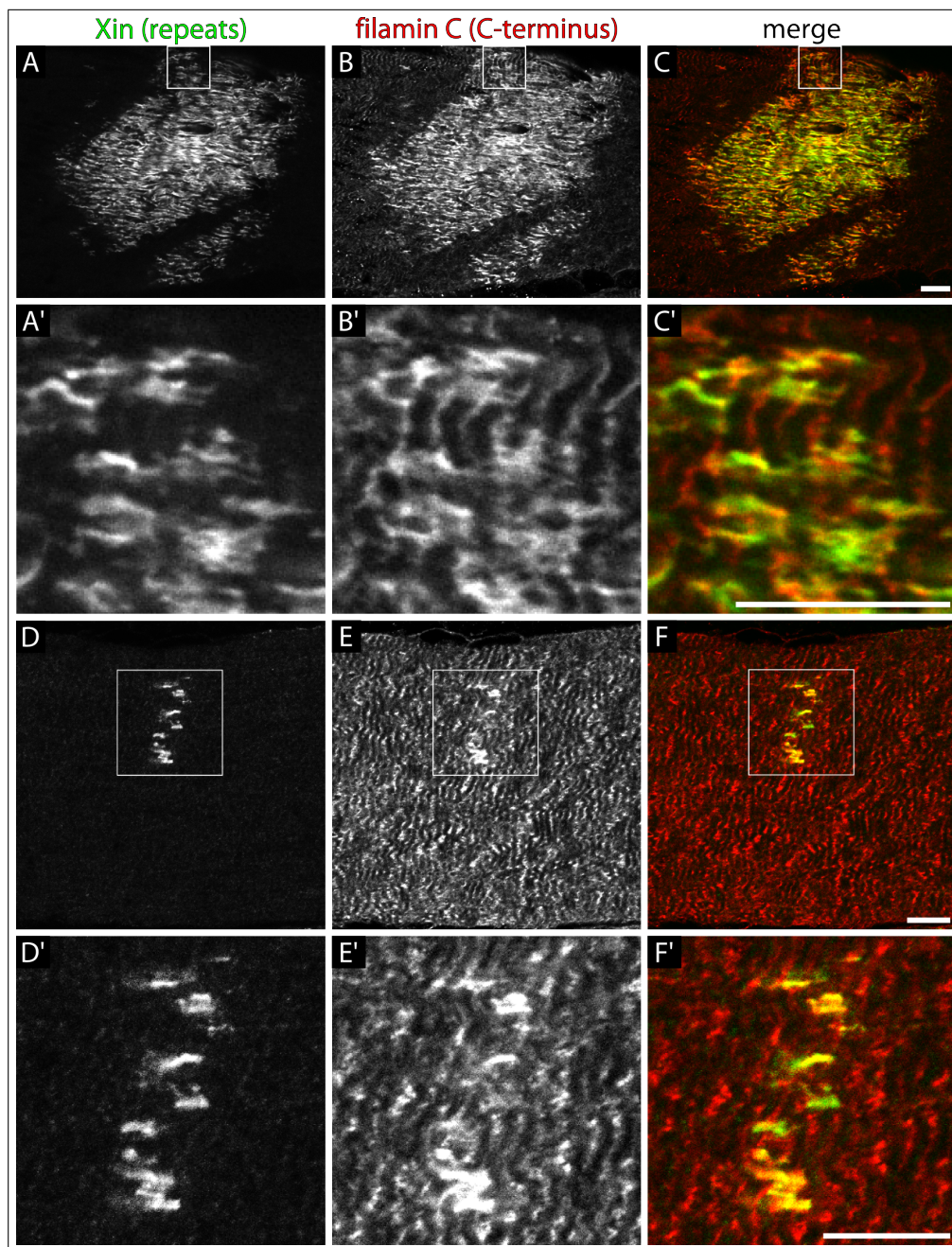


Figure 3.79: **Xin A/B and filamin C in areas of skeletal muscle remodelling.** Confocal LSM images of human skeletal muscle sections. The specimens were labeled with antibodies against the Xin repeat region (XR1B) and the C-terminus of filamin C. In merge images (C, C', F, F') Xin and filamin C are tinted green and red, respectively. **A-C.** Large patch of Xin-containing longitudinal strands connecting a varying number of successive sarcomeres. Filamin C exhibits Z-disc labeling and a strong association with longitudinal strands. **A'-C'.** Magnification of the box in A-C. Filamin C reveals alterations in Z-disc arrangement and colocalization with Xin only in longitudinal structures. **D-F.** The Xin signal also identifies small areas of remodelling. **D'-F'.** Magnification of the box in D-F. Even in single longitudinal strands, Xin and filamin C colocalize and the filamin C labeling seems to be increased. Scale bar 10  $\mu\text{m}$ .



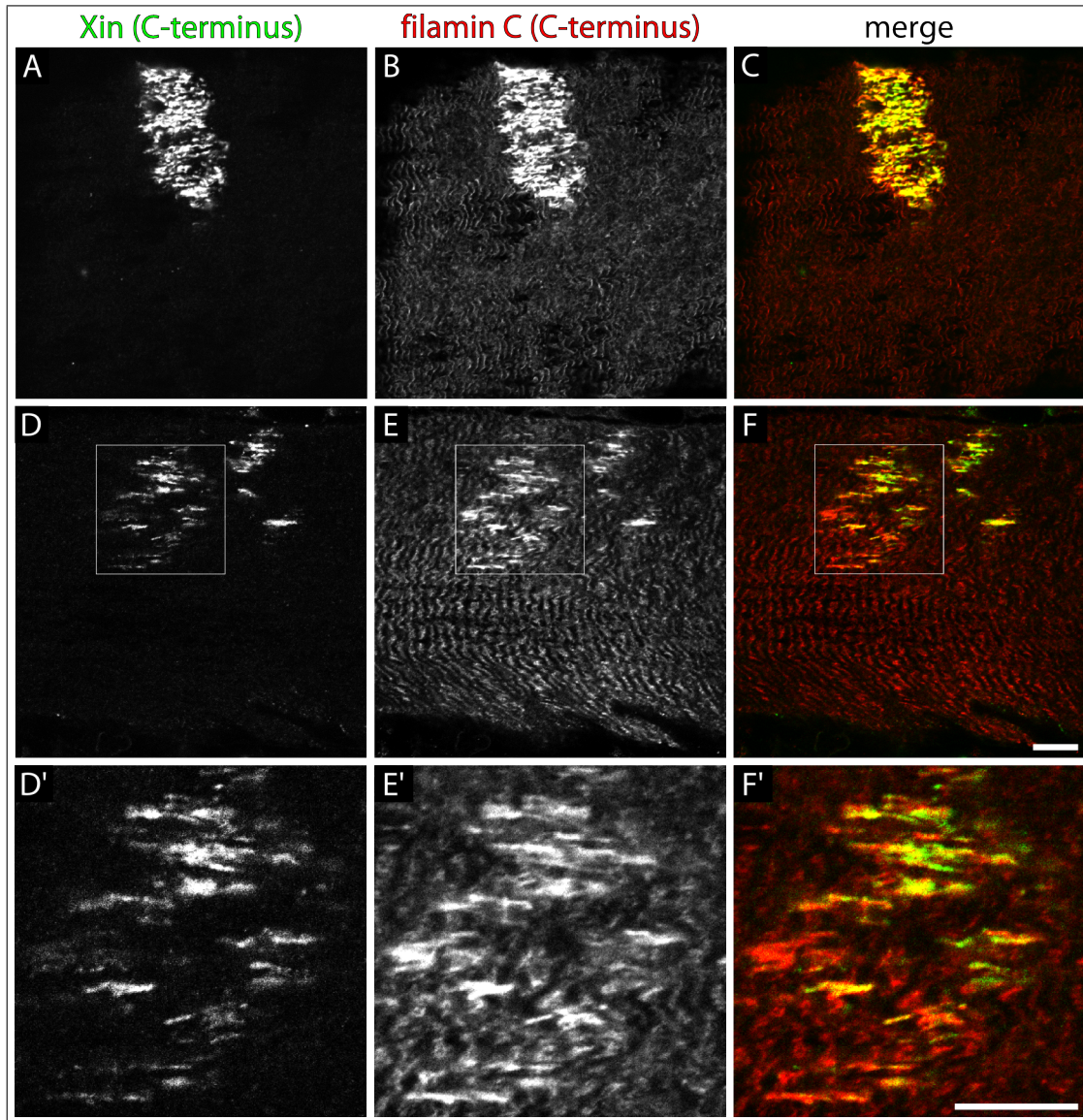


Figure 3.80: **Xin A/C and filamin C in areas of skeletal muscle remodelling.** Confocal LSM images of human skeletal muscle sections. The specimens were labeled with antibodies against the Xin A C-terminus (XC1) and the C-terminus of filamin C. In merge images (C, F, F') Xin and filamin C are tinted green and red, respectively. **A-C.** Large patch of Xin-containing longitudinal strands connecting a varying number of successive sarcomeres. Only in areas of Xin staining, filamin C displays longitudinal strands instead of the regular Z-disc array. **D-F.** Filamin C also colocalizes with Xin in single longitudinal strands. **D'-F'.** Magnification of the box in D-F. The structures are not equally labeled with Xin and filamin C. Some contain more filamin C than Xin and vice versa. Scale bar 10  $\mu\text{m}$ .

accessibility of the respective epitopes.

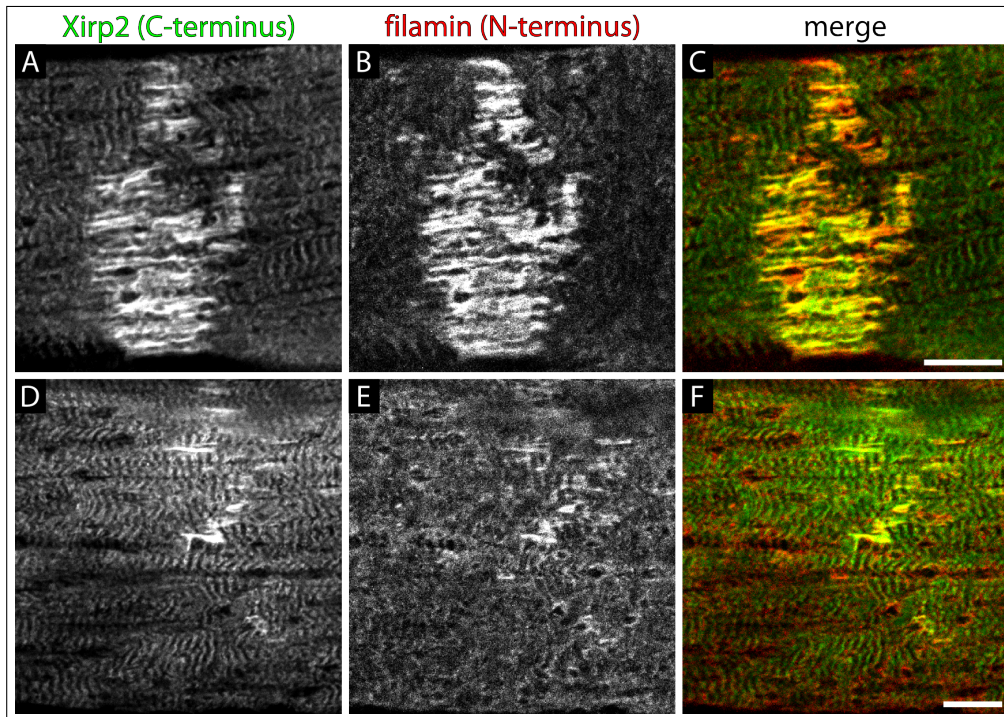


Figure 3.81: **Xirp2 and filamin in areas of skeletal muscle remodelling.** Confocal LSM images of human skeletal muscle sections. The specimens were labeled with antibodies against the Xirp2 C-terminus and the N-terminus of filamin isoforms (RR90). In merge images (C, F) Xirp2 and filamin are tinted green and red, respectively. **A-C.** Xirp2 and filamin colocalize in large patches of longitudinal strands spanning multiple successive sarcomeres and at the Z-disc although the filamin signal is weak in normal areas. The association of filamin with remodelling is greatly increased. **D-F.** Single longitudinal strands also contain both Xirp2 and filamin. Scale bar 10  $\mu$ m.

In conclusion, these results demonstrate that filamin C is a new interaction partner of Xin-Repeat proteins associated with structures of muscle cell remodelling. While  $\alpha$ -actinin and nebulin exhibit only a diffuse distribution or a complete absence, filamin C targeting to longitudinal strands is apparently increased. These findings also fit the observation in this work that both Xin-Repeat proteins can interact with filamin C (cf. section 3.7.1). The wide colocalization of filamin C and Xin-Repeat proteins in areas of skeletal muscle remodelling turn these longitudinal strands into promising candidates for the site of interaction of filamin C and Xin-Repeat proteins.

# Chapter 4

## Discussion

### 4.1 Myofibrillogenesis of Murine H-2K<sup>b</sup>-tsA58 Cells

Formation of multinucleated myofibres and mature sarcomeres is a multistep process involving fusion of precursor cells (myoblasts) to myotubes and concomitant assembly of the contractile apparatus (cf. section 1.2.2.4). This assembly starts directly upon induction of the myogenic program and is indicated by the expression of muscle-specific proteins which begin to form precursor structures of the Z-disc, the sarcomere boundary. The assembly of precursors is potentially initiated at sites of integrin adhesions and these precursors already contain multiple proteins which will be later major components of the mature Z-disc, like  $\alpha$ -actinin, titin. Actin filaments of opposing polarity originating in these precursor structures incorporate nonmuscle myosin II which is then replaced with muscle myosin II upon further maturation of the myofibril. These precursor structures fuse and align to form the regular striated array which reach the final developmental stage through contraction.

Dissection of this process requires model systems which have to meet certain demands. The most basic requirement is the myogenic differentiation under laboratory conditions which should ideally reach the final stage of an adult muscle. Additionally, the onset of differentiation needs to be controlled reliably and the process has to produce results of constant quality without exceeding reasonable experimental costs. Concerning the final differentiation stage and the control of the process investigation of whole organisms such as zebrafish (*Danio rerio*), fruit fly (*Drosophila melanogaster*) or nematode (*Caenorhabditis elegans*) offers the opportunity to observe *in vivo* all stages of development with appropriate effort and constant quality and to easily manipulate organisms (Sparrow *et al.*,



2008). However, despite some similarities, muscle development of fish or invertebrates is different from that of mammalia so that studying this process requires alternatives (Ochi und Westerfield, 2007; Ciglar und Furlong, 2009; Moerman und Williams, 2006). Unfortunately, the standard animal model for mammalian research, the mouse, is more complicated to handle and to manipulate with embryonic development being more difficult to analyze due to impeded accessibility of the mouse embryo *in utero*. Therefore, model cell systems have been established to follow myogenic differentiation *in vitro* based on myogenic cell lines like C2C12 or satellite cells isolated from muscle biopsy material (Blau *et al.*, 1983; van der Ven *et al.*, 1992). Both systems have been providing a tool to analyze myofibrillogenesis in cell culture for many years although there are some disadvantages. For a high percentage of differentiated cells, one has to use early passages of C2C12 cells because they lose their differentiation capacity significantly upon culturing and there is no other mechanism to control the onset of differentiation than changing the medium. Primary human skeletal muscle cells also exhibit ageing symptoms accompanied by the inability to reach final differentiation stages and differentiation is also only induced by the change of culture medium. Furthermore, early passages of C2C12 cells are difficult to obtain and establishing of new satellite cells is very laborious. Thus, improving the quality of *in vitro* myogenic development is rather problematic. On the contrary, myoblasts isolated from leg muscles of H-2K<sup>b</sup>-tsA58 transgenic mice allow for conditional immortalization and concomitant retention of their differentiation capacity (Morgan *et al.*, 1994). This is achieved by constitutive expression of a thermolabile large tumor antigen under the control of the major histocompatibility complex of the H-2K<sup>b</sup> class I promotor which can be induced to high levels by interferon (Jat *et al.*, 1991). This genetic modification enables controlling the myogenic program via two mechanisms, increase of culturing temperature and exposure to interferon. Such a dual control helps synchronizing the cells which eventually increases the percentage of fully differentiated cells. It has already been demonstrated that H-2K cells can form multinucleated myotubes in culture however a detailed description of myofibrillogenesis is still missing. In this work, differentiation of H-2K cells was analyzed studying the localization of  $\alpha$ -actinin and titin, major components of the Z-disc, myomesin, a constituent of the M-band, and F-actin which builds up the core thin filament system. According to morphological observations differentiation of H-2K cells was subdivided into 3 phases, early, intermediate and late (cf. section 3.1). These phases are characterized by elongation of cells and first small myotubes (early), interconnection of multinucleated myotubes (intermediate) and formation of a dense meshwork of contractile myotubes (late). On protein level, sarcomeric

proteins like  $\alpha$ -actinin, filamin C, muscle myosin heavy chain II and myomesin constantly increased until the final stage of H-2K cells which is reached around day 9 of differentiation (cf. section 3.1.2). The level of nonmuscle myosin heavy chain decreased until the final stage but did not vanish completely. A cell culture dish contains always a mixture of cells at different developmental stages, so that only general trends can be observed by analyzing total protein extracts. Although H-2K cells gain contractility at day 5 of differentiation, not all cells reach late stages as indicated by the presence of nonmuscle myosin even in the latest stage. Nevertheless, immunofluorescence stainings demonstrated that H-2K cells provide a reliable tool to investigate myofibrillogenesis. In early stages, Z-disc precursor structures decorating actin filaments in a punctate pattern could be detected and it was apparent that the M-band protein myomesin was expressed significantly later thus confirming the results of the protein expression analysis (cf. section 3.1.1.1). A distinction of the differentiation stage according to the spacing of Z-disc precursor structures as it has been postulated by *in situ* analysis of avian heart (Du *et al.*, 2008) was not possible since these precursors occasionally exhibited mature spacing even in early stages. Additionally, the steps of myofibrillogenesis proposed by the premyofibril model (Sanger *et al.*, 2005) could not clearly be identified but this can be due to differences of myofibrillogenesis in cell culture and *in vivo* (cf. sections 3.1.1.1, 3.1.1.2 and 3.1.1.3). In order to reveal differences between H-2K differentiation and model conceptions, further analysis of other markers such as integrins, vinculin, talin, ZASP or muscle myosin heavy chain II are required. Nevertheless, these cells exhibited nice cross-striations which were further adjusted upon contraction. Although properly aligned myofibrils pervaded the myotubes, detailed analysis revealed slight irregularities where the number of Z-discs to be fused needed to be adjusted (cf. section 3.1.1.3). Since threedimensional anchorage is missing, it remains to be determined how costameres, if at all, are formed or not. In general, H-2K cells are suitable to study myofibrillogenesis until the formation of contractile sarcomeres but further characterization is needed to integrate findings obtained with these cells into other established model systems and *in vivo* analysis.

## 4.2 Xin-Repeat Proteins During *In Vitro* Myofibrillogenesis of Murine H-2K<sup>b</sup>-tsA58 Cells

### 4.2.1 Transcription and Expression of Xin Isoforms

Expression of mammalian Xin is restricted to cross-striated muscle tissue and identification in early stages of muscle development renders it a potentially important protein in muscle development. This is corroborated by the observation that blocking of its expression in chicken results in heart malformation (Wang *et al.*, 1999). In this work, differentiation of murine H-2K cells is presented as a cellular model system for examination of myofibrillogenesis (cf. section 3.1). Xin function during myofibrillogenesis was analyzed by comparing the localization of Xin in relation to key players of sarcomere structure in H-2K cells. Two antibodies were available to identify murine Xin (tab. 2.8.2). One had been raised against the repeat region and was therefore able to detect the two repeat-containing isoforms mXin A and B. The other antibody was directed against the isoform mXin C whose sequence is also completely included in the largest isoform Xin A. Hence, this antibody can decorate mXin A and C. Thus, both antibodies always identify two isoforms if both are expressed without any means to distinguish them. In order to obtain information about the expression of all isoforms, total protein extracts of a differentiation series of H-2K cells were analyzed with both antibodies (cf. section 3.2.2). This revealed that both Xin repeat-containing isoforms are expressed already before induction of differentiation with the expression rather constantly increasing until day 8 of differentiation followed by a decrease at the final day 9 (fig. 3.12 A). It is difficult to determine whether Xin is really expressed before the onset of myogenic differentiation or whether spontaneously differentiating cells are responsible for that result. As indicated by co-stainings with  $\alpha$ -actinin and other myogenic marker proteins (see below), immunofluorescence labeling could not provide evidence for Xin A/B in proliferating myoblasts. Nevertheless, it is possible that the expression level in proliferating myoblasts is below the limit of detection while in total extracts the accumulation of cells leads to its discovery in western blot experiments. Some H-2K cells spontaneously start to differentiate and perhaps this is the reason for detection of Xin in these extracts although it is a rare event. The quite constant increase after induction of differentiation demonstrates that Xin A/B function is already needed during early stages of myofibrillogenesis and confirms data obtained with C2C12 cells (Sinn *et al.*, 2002). Reduction of protein expression at the final stage of differentiation was observed which is compatible with the fact that Xin A/B is not a sarcomeric



protein. But further data is required to verify when exactly expression decreases in order to get insight into the processes depending on Xin A/B. Expression of mXin C could not be doubtlessly detected in extracts of differentiating H-2K cells so that a potential function during myofibrillogenesis remains elusive (further discussion cf. section 4.2.2).

All Xin isoforms were not only detected on protein level before induction of differentiation but also on mRNA level (cf. section 3.2.1). However, comparing the increase of mRNA and protein level during differentiation revealed that the initial amount of mRNAs is significantly higher than the amount of expressed proteins. Thus, it is unlikely that such a high amount of mRNAs can be completely attributed to spontaneously differentiating cells. This implies that untranslated mRNA of Xin isoforms does already exist before induction of differentiation perhaps in order to accelerate the differentiation process however *in situ* hybridization will be needed for confirmation. The following course of the transcription level also deviates from the course of protein expression level. While the protein content rather constantly increased during differentiation followed by a reduction at the final stage, the mRNA level exhibited stronger fluctuation (fig. 3.11). Furthermore the results depended on the method used, i.e. simplex-PCR reactions provided results divergent from duplex-PCR reactions, which demonstrates that semiquantitative approaches are not an adequate method to analyze minor quantitative changes and are therefore limited to the discovery of prominent differences and trends. Nevertheless, some general observations are consistent. Transcription of all Xin isoforms is elevated during differentiation and reaches the maximum presumably before the first myotubes gain contractility but the exact stage needs to be determined individually for each isoform using quantitative real-time RT-PCR. In the late phases of differentiation transcription is clearly reduced which is also reflected by the decrease of protein expression at the final stage and would be consistent with the observation that Xin is not a constituent of the mature sarcomere. Xin seems to be involved in developmental processes during myofibrillogenesis but is not required for maintenance of sarcomere structure.

In contrast to Xin, Xirp2 is a constituent of the sarcomeric Z-disc which implies maintenance of protein expression in late stages of differentiation (cf. section 3.7.7). This assumption was confirmed since mXirp2 exhibited the highest expression level at the latest stages (cf. section 3.7.6). Upon induction of differentiation, mXirp2 protein expression could be observed at day 2 which indicates delayed expression in comparison to Xin. Later, the protein level constantly increased reaching its maximum at day 8 and did not considerably decrease at day 9 which is different from Xin. This course of protein expression was also basically reflected by transcription of mXirp2 (cf. section 3.7.5). The transcription

level of an isoform lacking the large coding exon 7 revealed some inconsistencies. The two primer pairs indicating the splicing out of the large exon displayed a deviating course since one exhibited large fluctuations whereas the other yielded increasing amounts upon progression of differentiation. However, the efficiency and absolute amount of PCR product was very low which is also indicated by the high amount of unbound primers and a larger number of cycles (fig. 3.65 B, C). Therefore, the transcription level and presumably also the expression level of this isoform is lower than that of mXirp2 and only specific antibodies could dissect the function of this isoform. Binding studies with the putative LIM domain encoded due to the frame shift could also help to gain further knowledge. Furthermore, the fact that some of the xepilin named mRNA species (variant 3 and 4, EMBL ABO69243.1, EMBL ABO69244.1) were identified in testis and not cross-striated muscle tissue demands careful investigation of Xirp2 isoform transcription and expression because these findings could imply that mXirp2 is only the muscle-specific isoform of the gene and other isoforms are expressed in other tissues and adopt different functions. The generation of a mXirp2-null mouse resulted in a misorganized myocardium and postnatal growth defects while no phenotypes affecting other tissues were mentioned (Wang *et al.*, 2010). Taking into account that the *LacZ-Neo<sup>r</sup>*-cassette was inserted in the intron region between exon 6 and 7 it is possible that such mice still express the potential other isoform thereby protecting other tissues from impact. Another strategy targeting exons 4–6 provided a mouse exhibiting greatly reduced amounts of mXirp2 protein lacking sequence encoded by these exons (McCalmon *et al.*, 2010). This mouse also displayed a cardiac phenotype characterized by global dysregulation of cardiac gene expression. Since these mice demonstrate that splicing events are possible which were not anticipated yet, it is also necessary to evaluate the isoform expression and their influence in both genetically modified mice.

#### 4.2.2 Localization of Xin Isoforms

As delineated in section 4.2.1, the antibodies available to detect murine Xin in principle always labeled two isoforms since they were raised against portions either included in Xin A and B or Xin A and C. Analysis of transcription and protein expression revealed that mXin A and B are the predominant isoforms during differentiation of H-2K cells while mXin C is expressed significantly weaker, if at all. There was no detectable difference between the labeling pattern of both antibodies in confocal microscopy in differentiating H-2K cells (cf. section 3.2.3.5). This could either reflect that mXin A and B colocalize

almost completely and mXin C is not expressed which would be in a way consistent with the results of protein expression and transcription (cf. section 4.2.1) or that mXin C colocalizes also with mXin A. Since Xin C cannot be detected in normal healthy human cross-striated muscle but seems to be upregulated in hypertrophic hearts (Otten *et al.*, 2010), it is likely to speculate that Xin C is regulated differently from the other isoforms. Interestingly, mice lacking Xin A and B but not Xin C are not able to compensate that loss and exhibit cardiac hypertrophy, disruption of ICD and myofilament disarray (Gustafson-Wagner *et al.*, 2007). Such a severe phenotype cannot be observed in mice lacking all Xin isoforms which indicates facilitated compensation of the loss and demonstrates the need for a tightly regulated balance between the expression of Xin isoforms (Otten *et al.*, 2010). In order to gain further insight into the interplay of Xin isoforms, generation of a Xin A-specific antibody is required and would also provide a means to dissect Xin C function.

Localization studies of mXin A/B and  $\alpha$ -actinin showed that Xin is expressed later than  $\alpha$ -actinin but still in a very early stage (cf. section 3.2.3.1). This was in a way surprising as Xin is early expressed during embryogenesis and directly upregulated in satellite cells upon damage indicating a function at early stages of development (Sinn *et al.*, 2002; Hawke *et al.*, 2007). Upon expression of Xin both proteins colocalize at some actin filaments in a continuous pattern (fig. 3.13). However, Xin is nearly absent from actin filaments which exhibit a dense body-like association with  $\alpha$ -actinin already in early stages of differentiation. Such dense bodies could be precursor structures of the Z-disc if they are also associated with other sarcomeric components like titin or filamin C (Sparrow und Schöck, 2009). A dense body-like pattern along actin filaments of Xin in early stages of H-2K differentiation has never been observed. Therefore, Xin is apparently not a component of Z-disc precursors in early stages but labels actin filaments presumably designated to develop into myofibrils before Z-disc precursor structures are formed. This is further corroborated by co-stainings with filamin C (cf. section 3.2.3.2). Directly after induction of differentiation Xin and filamin C colocalized at peripheral, cellular presumably actin-based extensions in a continuous pattern and at some actin filaments in the cell body. The latter is lost upon progression of differentiation whereas peripheral cellular extensions are still decorated by Xin and filamin C in multinucleated myotubes. When filamin C localization changed into Z-disc arrangement, continuous Xin labeling was restricted to NSMFs. In general, continuous decoration of Xin along actin filaments changed already into a mainly punctate pattern in the intermediate phase. This signal cannot be attributed to a defined sarcomeric precursor structure and it appears to be randomly distributed

(cf. section 3.2.3). Xin labeling therefore provides a means to indicate the differentiation status of a cell and revealed that a differentiating cell can contain areas of different stages. The change of Xin localization does not depend on the replacement of nonmuscle by muscle myosin, i.e. the transformation of premyofibrils into nascent myofibrils, because the punctate distribution was already displayed before nonmuscle myosin had vanished (cf. section 3.2.3.3). Thus, earlier events in myofibrillogenesis must trigger altered localization of Xin (cf. section 4.3.1).

Xin has been implicated in cellular junction formation via its interaction with  $\beta$ -catenin (Choi *et al.*, 2007). This could not be observed here in differentiating H-2K cells (cf. section 3.2.3.4). While  $\beta$ -catenin was enriched at junctional sites, Xin did not colocalize there. Although submembranous targeting of Xin was often detected in H-2K cells as well as in transfected cells (cf. section 3.3.6.2), there was no prominent overlap with the  $\beta$ -catenin signal in H-2K cells. Furthermore, *in vitro* binding studies of  $\beta$ -catenin and human Xin A and B failed to confirm the interaction. Therefore, the significance of this interaction remains being discussed and further investigations are needed for confirmation.

### 4.3 Xin-Repeat Proteins Are Novel Ligands of the SH3 Domain of Nebulin and Nebulette

Actin filaments represent one key component of the cytoskeleton spanning eukaryotic cells with related filaments also having been identified in prokaryotes (Carballido-López, 2006). The morphology of the actin cytoskeleton is tightly regulated by a plethora of actin binding proteins (Dominguez, 2009; Wang und Coluccio, 2010; Rohn und Baum, 2010). In muscle sarcomeres actin filaments adopt a unique threedimensional arrangement with the conformity of their length being tightly regulated (Clark *et al.*, 2002; Burgoyne *et al.*, 2008). In cooperation with associated proteins such as tropomyosin and the troponin complex, actin filaments form the thin filament system of cross-striated muscle (cf. section 1.5.1). Although the exact mechanism of sarcomere assembly is still elusive, many proteins have been demonstrated to be involved in thin filament assembly and sarcomere development (Clark *et al.*, 2002; Sanger *et al.*, 2005; Sparrow und Schöck, 2009). Two capping proteins are considered to maintain thin filament length at the barbed and the pointed end. At the sarcomeric Z-disc, the barbed end capping protein CapZ prevents thin filaments from uncontrolled filament elongation and disassembly while at the pointed end demarcating the end of thin and thick filament overlap the capping protein tropo-

modulin takes over an analogue function (Clark *et al.*, 2002). The giant protein nebulin has been identified to interact with both capping proteins therefore rendering this protein to be an ideal candidate for thin filament length regulation (McElhinny *et al.*, 2001; Pappas *et al.*, 2008). However, recent studies suggest a more general stabilization of actin filaments by nebulin which comprises filaments of varying lengths and a positive effect on cross-bridge-cycling efficiency (Pappas *et al.*, 2010; Chandra *et al.*, 2009). However, such a ruler function could only be valid for skeletal muscle since the expression level of nebulin in cardiac muscle is remarkably lower (Kazmierski *et al.*, 2003). In cardiac muscle the related protein nebulin is expressed which displays a similar domain layout but lacks the super repeats containing instead only 22 copies of single repeats (cf. section 1.5.4). These repeat modules are regarded as actin binding units thus nebulin does not encompass a sufficient number of repeats to convey a ruler function. Nevertheless, the presence of nebulin seems to have an impact on thin filament length since in skeletal muscle filament length is constant in a rather narrow range whereas length variation in cardiac muscle is significantly higher (Robinson und Winegrad, 1977; Burgoyne *et al.*, 2008). The contribution of nebulin's low abundance in cardiac muscle to this phenotype is not yet clear but it has been demonstrated that disturbance of nebulin function affects thin filament length in skeletal as well as in cardiac muscle (Bang *et al.*, 2006; McElhinny *et al.*, 2005). Identification of the prominent regulator of actin assembly N-WASP as a novel interaction partner of the SH3 domain of nebulin in the Z-disc of skeletal muscle directly links nebulin to the control of thin filament dynamics in the sarcomere (Takano *et al.*, 2010). This is even more intriguing as all other binding partners of the SH3 domain identified or suggested, like  $\alpha$ -actinin, myopalladin and titin, are mainly considered as structural links. Thus, nebulin function probably goes beyond providing structural framework of sarcomere architecture. In this work, Xin-Repeat proteins were described as novel binding partners of the SH3 domain of nebulin and nebulin. Multiple clones comprising the C-terminus of nebulin interacted with the Xin fragment Xin PR3+4 in a yeast two-hybrid screen of a skeletal muscle cDNA library (cf. section 3.3). Mapping of the binding region in Xin revealed that a proline-rich region located in the C-terminal part of Xin A which is also included in the small isoform Xin C mediates the interaction to nebulin (cf. section 3.3.1). The smallest clone of nebulin identified consisted of the complete SH3 domain and only half of the adjacent serine-rich linker sequence which strongly pointed to the SH3 domain as the interacting domain. Since the SH3 domain of nebulin and the related cardiac protein nebulin is conserved to nearly 90 % whereas conservation of the linker region amounts to only 36 %, Xin was also tested on binding to nebulin

and this demonstrated that interaction is possible with both related SH3 domains (cf. section 3.3.2). Mammals have two genes encoding Xin-Repeat proteins, Xin and Xirp2 (cf. section 1.10). Both share a similar domain layout and an overlapping set of binding partners has already been described (cf. section 4.6) which led to the investigation of the binding capacity for Xirp2 to the SH3 domain of nebulin and nebulette. Interestingly, a proline-rich part situated identically in Xirp2 as the binding region in Xin was also able to interact with nebulin and nebulette (cf. section 3.7.2). Although both proteins contain several potential SH3 domain binding sequences within the respective binding region, a similar motif could not be identified. Therefore, the precise binding motif in Xin and Xirp2 was revealed with the help of spotted overlapping 15-mer peptides comprising the complete sequence of the binding region of Xin and Xirp2, respectively (cf. section 2.9.4). The purified nebulette SH3 domain-GST fusion protein specifically bound to the peptides *SHPPQRLPKPLP* (Xin) and *GVLPPPTLPKPK* (Xirp2) (cf. sections 3.3.4 and 3.7.2). Surprisingly, only the Xirp2 peptide harboured a classical *PXXP* motif which defines the minimal binding motif of SH3 domains. In order to dissect essential residues, substitution analysis was performed. Strikingly, this demonstrated that both motifs share the common consensus sequence *PPXXXPKP*. SH3 ligands can be categorized into class I and II peptides according to the position of a positively charged residue (Politou *et al.*, 2002). This residue interacts with the RT-loop of the SH3 domain and confers directionality to the interaction. Peptides binding with their N-terminus to the RT-loop are designated as class I motifs and accordingly peptides interacting with their C-terminus are class II motifs. Ligand preferences of the nebulin SH3 domain have already been determined and revealed selective interaction of class II peptides (Politou *et al.*, 2002). The consensus motif of Xin-Repeat proteins belongs to class II, for the positively charged essential lysine residue is located at the C-terminus of the peptide implying that both Xin-Repeat proteins contain a peptide motif which fits the requirements of the nebulin SH3 domain. Due to the high degree of conservation of the SH3 domain between nebulin and nebulette mentioned above, it can be concluded that the binding mode of the nebulette SH3 domain is comparable. This is supported by the findings that Xin-Repeat proteins bind the SH3 domain of nebulette in a nanomolar range rendering Xin-Repeat proteins as high affinity ligands of nebulette and very likely nebulin (Florian Sauer, personal communication). Such a high affinity is unique to Xin-Repeat proteins since other ligands such as  $\alpha$ -actinin, myopalladin and titin exhibit only micromolar affinity (Moncman und Wang, 1999; Ma und Wang, 2002). This strongly suggests an important role *in vivo* although *in vivo* binding data of endogenous proteins is missing as the high insolubility and the giant size of



both Xin-Repeat proteins and nebulin impairs co-immunoprecipitation assays in skeletal muscle and the lack of an available antibody against nebulin impedes such experiments in cardiac muscle.

### 4.3.1 The Site of Interaction of Xin-Repeat Proteins with Nebulin/Nebulette Interaction

Xin-Repeat proteins differ in their localization in adult skeletal muscle. While Xirp2 is a prominent component of the sarcomeric Z-disc, Xin can be only found in the MTJ. Both proteins are able to interact with nebulin and its cardiac relative nebulin which also reside in the Z-disc in adult muscle. Since no antibody against mXirp2 suitable for immunofluorescence analysis was at disposal, such studies could only be performed with mXin. As Xin is not a Z-disc component the question arises where and when can Xin and nebulin interact? It is obvious to assume that this can take place during myogenic differentiation, for both proteins are already described to be involved in myofibrillogenesis. Therefore, differentiating H-2K cells were analyzed on the localization of mXin and a nebulin Z-disc epitope (cf. section 3.3.5). The Xin antibody detects the Xin repeats and therefore the isoforms A and B (further discussion cf. section 4.2.2). These experiments revealed that Xin presumably precedes nebulin expression (fig. 3.23). While Xin was enriched at peripheral cellular extensions, nebulin expression started in the perinuclear space which has been already described for sarcomeric proteins (Abe *et al.*, 2004). Xin and nebulin exhibited only a partial overlap along actin filaments. Interestingly, Xin always labeled the filament portion pointing towards the periphery whereas nebulin was associated with the filament part close to the nucleus. Since Xin association with actin filaments was progressively lost upon nebulin decoration and Xin enriched at submembranous sites which were almost devoid of nebulin (fig. 3.24), the partial colocalization at non-striated myofibrils (NSMF) can be regarded as the main site of Xin-nebulin interaction implying a transient interaction during myofibrillogenesis. The different association of actin filaments with either Xin or nebulin suggests that there is a difference between those filaments. Perhaps this reflects binding of different protein sets to actin which influence actin filament structure or incorporation of muscle actin isoforms. Such an effect on F-actin conformation has already been described for a variety of proteins. One major protein associated with muscle thin filaments and nonmuscle actin filaments in general is tropomyosin (Wang und Coluccio, 2010). Xin has been demonstrated to compete for F-actin binding with pigstomach tropomyosin (Pacholsky *et al.*, 2004). During myofibril-

logenesis several tropomyosin isoforms are expressed and it would be interesting to learn whether actin filaments labeled with Xin are associated with a different tropomyosin isoform than actin filaments labeled with nebulin. Recently, it has been shown that thin filaments adopt a flat conformation (Oda *et al.*, 2009) but it is obvious to speculate that this represents only one of multiple possible conformations of F-actin since there is a gigantic number of actin binding proteins presumably capable of slightly altering F-actin structure. Therefore, it is appealing to propose that the partial overlap of Xin and nebulin could mark the site where the transition to a different set of associated proteins and/or a change in conformation takes place. This is further supported by the appearance of the filament systems in the SEM (fig. 3.23 and 3.24). At sites exclusively labeled with Xin, the filaments exhibited a smaller diameter than at sites of nebulin expression and a more branched network, whereas large bundles could be detected in the area of nebulin binding. The finding that nebulin and Xin almost exclude each other from actin filaments except the few sites of overlap can be due to occupying identical binding sites on actin (Cherepanova *et al.*, 2006). Co-existence then again reflects transition from one to the other binding partner.

Co-stainings with nebulin also revealed another prominent structure which associated with Xin. Late stage H-2K myotubes contain large areas of perfectly aligned Z-discs but there are still minor irregularities in the arrangement, e.g. the number of adjacent Z-disc which are about to fuse needs to be adjusted or alternatively, fusion of Z-bodies has not finished yet (fig. 3.25). At these sites, prominent labeling of Xin could be detected along longitudinal strands connecting adjacent immature Z-discs. Although nebulin is also present at these strands, decoration is faint and appeared to be diffuse. These structures are reminiscent of longitudinal strands observed in areas of remodelling in human skeletal muscle which are also strongly associated with Xin (cf. sections 3.8 and 4.4). Therefore it seems likely that these longitudinal strands are analogous to those in human skeletal muscle and that Xin is involved in the final maturation process of sarcomeres which would also explain that Xin protein is still significantly expressed at these stages (cf. section 4.2.1).

In order to directly address the question where Xin and nebulin/nebulette interaction takes place, BiFC experiments were performed in embryonic cardiomyocytes. In such an assay, a fluorescence signal is generated when two non-fluorescent fragments of a fluorescent protein (FP) come into close proximity and form a functional FP (cf. section 2.9.5). This can be achieved through fusion of these fragments to proteins which interact and therefore enable the BiFC signal. Thus, a signal is not a direct proof of interaction of the

fusion proteins since close proximity is sufficient for fluorescence complex formation which increases the probability of false positives. In order to reduce that careful testing of vector combinations and experimental conditions is essential. This was carried out intensively in advance of any experiment. In principal, it is possible that non-fluorescent fragments which are not fused to another protein can accidentally form fluorescent complexes in the cytoplasm upon transfection. However, no such unspecific complex formation could be detected. Additionally, the combination of a fusion protein and a non-fused compatible non-fluorescent fragment did provide the same results. Nevertheless, transfection of protein fragments which are not able to interact but target to nearly identical sites can form BiFC complexes in *in vitro* cell systems. Therefore, experiments performed in cells usually not containing the interacting proteins can provide false positives and every result needs to be verified by transfection into cells reflecting their *in vivo* environment. In order to meet these requirements, BiFC studies of the interaction between Xin C and nebullette were performed in embryonic cardiomyocytes apart from A7r5 cells (cf. sections 3.3.6.2 and 3.3.6.3). Single transfections of both proteins revealed that each targets to NSMFs in cardiomyocytes of the early stage (fig. 3.31 and 3.33). In cardiomyocytes already containing Z-discs, nebullette strongly decorated Z-discs whereas Xin C was absent which is contradictory to transfections in neonatal rat cardiomyocytes where Xin C was the only isoform targeting to Z-discs (fig. 3.32, van der Ven *et al.* 2006). However, both exhibited association with longitudinal strands between adjacent Z-disc. Interestingly, BiFC complexes were specifically formed at structures where both proteins were also detected in single transfection. Early cardiomyocytes which were completely pervaded by NSMFs displayed an interaction of Xin C and nebullette exactly at NSMFs (fig. 3.35). If the myofibrillar apparatus had further matured and Z-disc staining exhibited a striated pattern, BiFC complex formation was restricted to longitudinal strands connecting immature Z-discs (fig. 3.34). Admittedly, very weak staining could be obtained at the Z-disc. This could either reflect that these Z-discs were not fully developed as a very weak Xin Z-disc signal was also seldomly observed in H-2K cells of a late stage of differentiation or alternatively, unspecific complexes had formed. However, the site of the BiFC signal seems not to be formed randomly. Although this experiment was only performed using Xin C, it is tempting to speculate that Xin A also interacts with nebullette at NSMFs and these longitudinal strands between adjacent Z-disc, for Xin A also targets to NSMFs in rat cardiomyocytes and is detected in H-2K cells at NSMFs, albeit partially colocalizing, and longitudinal structures resembling those obtained with Xin C. Of course, this does not reflect an *in vivo* situation since both interaction partners are overexpressed and upon

complex formation the interaction is stabilized to become eventually irreversible so that accumulation of complexes can occur and the potential transient character of this interaction is lost (cf. section 3.3.6.1). Nevertheless, the fact that complexes are being formed at these sites demonstrates that these can be sites of Xin–nebulin/nebulette interaction. Thus, the BiFC results support the conclusions drawn from the H-2K cell analysis and finally render Xin a protein directly linked to myofibrillogenesis by the interaction to nebulin-repeat proteins.

Xirp2 prominently targets to the Z-disc in adult human skeletal muscle cells and this has been also shown for its murine orthologue (Huang *et al.*, 2006). Stainings with antibodies against different epitopes of Xirp2 suggest a certain orientation of Xirp2 within the Z-disc (cf. section 4.7). Simultaneous staining of nebulin Z-disc epitopes and an antibody against the C-terminus of Xirp2 revealed a partial overlap of the signals at the borders of the Xirp2 doublet band which encompasses the central core of the Z-disc (cf. section 3.7.7). Since an antibody against the nebulin binding region in Xirp2 does not display a doublet but a single Z-disc signal, it can be concluded that this Xirp2 region and the nebulin SH3 domain interact within the Z-disc. In contrast to Xin and nebulin, Xirp2 and nebulin colocalize also in adult muscle. It is therefore tempting to assume that the Xirp2-nebulin interaction has a more persistent character.

### 4.3.2 Evolutionary Conservation of the Nebulin/Nebulette Binding Motifs in Xin-Repeat Proteins

The emergence of Xin coincides with the genesis of heart chamber presumably after divergence of vertebrates and cephalochordates (Grosskurth *et al.*, 2008). Except from lamprey and chicken all other Xin-Repeat protein-containing species possesses multiple genes encoding Xin-Repeat proteins. Analysis of the conservation of binding motifs can provide new insights into the relevance of an interaction and can reveal differences between species which helps to allocate function.

Both human Xin-Repeat proteins bind the SH3 domain of nebulin and nebulette with the consensus motif *PPXXXPKP* (cf. section 3.7.2). The essential residues are the initial proline, the proline in front of the lysine residue and the lysine residue itself (fig. 4.1 B). Xin requires an additional proline C-terminal to the lysine. Replacement of these residues most likely disrupts the interaction as demonstrated by substitutional analysis (cf. sections 3.3.4 and 3.7.2). Xin was identified in the yeast two-hybrid screen as a binding partner and Xirp2 was only tested because of similarities in the domain layout which

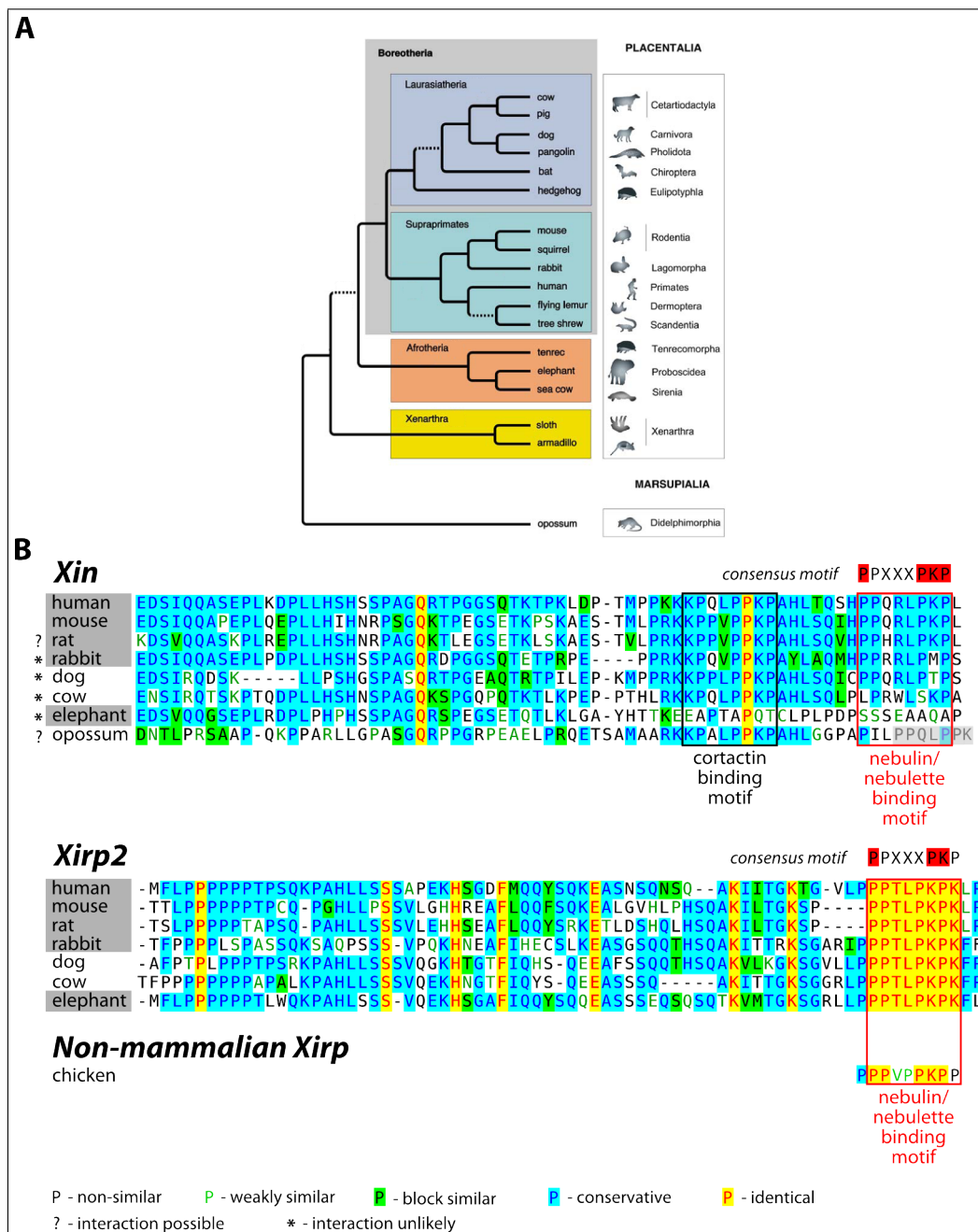


Figure 4.1: Alignment of the nebulin/nebulette interaction motif in Xin-Repeat proteins of different species. **A.** Evolutionary tree of placental mammals modified from Kriegs *et al.* (2006). **B.** Alignment of the nebulin/nebulette binding motif in Xin and Xirp2. Sequences were obtained from UCSC Genome Browser. Essential residues of the consensus motif are marked with a red background. The potential binding motif in the opossum sequence is highlighted with a light grey background.

also surfaced Xirp2 as a binding partner. Analyzing the conservation of the Xin motif in placental mammals reveals unexpected results (fig. 4.1 A). While in mouse the motif is 100 % identical, rat shows a divergence as the glutamine at position 3 is replaced by a histidine (fig. 4.1 B). According to the substitutional analysis this would presumably not abolish the interaction but reduce its affinity. A related difference at this position (Q >> R) can be also found in rabbit. However, the highly important lysine residue is replaced by a methionine which very likely impairs the interaction. Thus, even within the tree of Supraprimates (Euarchontoglires) of placental mammals this interaction does not seem to be conserved. The same is true for the tree of Laurasiatheria because in dog the essential lysine is replaced by a threonine which impairs binding and in cow conversion of an important proline and two other residues also disrupts nebulin/nebulette binding. Elephant completely deviates from other placental mammals since there is no apparent motif. Interestingly, the opossum belonging to the class of Marsupialia contains a motif suitable for mediating the interaction with nebulin/nebulette. While the nebulin/nebulette binding motif is not highly conserved among placental mammals, the predicted cortactin motif seems to be more preserved except for elephants, because only conservative replacements can be detected (Eulitz, 2005). However, whether cortactin is an *in vivo* binding partner remains to be determined. In contrast to Xin, the Xirp2 motif is 100 % conserved among placental mammals (fig. 4.1 B). Even in chicken a slightly modified motif can be identified which is presumably able to bind the nebulin/nebulette SH3 domain since the replacements do not affect the binding affinity according to the substitution experiment. A functional nebulin binding site has been also described for zebrafish Xirp1. Therefore, the interaction with nebulin/nebulette seems to be an ancient feature of Xin-Repeat proteins and at least preserved in one protein. The finding that most Xin proteins in placental mammals are probably not able to interact with nebulin/nebulette is puzzling. Since it is very likely that even in the supraprimate tree not all species can bind nebulin/nebulette, one can assume that human and mouse Xin have regained this feature and perhaps this reflects differences in myofibrillogenesis among species. However, data from other species concerning nebulin/nebulette binding activity is needed to interpret this result.



## 4.4 Xin-Repeat Proteins and Skeletal Muscle Remodelling

Delayed onset muscle soreness (DOMS) is a result of high force eccentric contraction of unaccustomed skeletal muscle (Yu *et al.*, 2003). This is usually accompanied by pain and stiffness. The processes responsible for that phenotype are still being controversially discussed but recent results point rather to muscle remodelling than to muscle damage and inflammation (Yu *et al.*, 2002; Yu und Thornell, 2002; Yu *et al.*, 2003, 2004). This conclusion is based on findings obtained with high resolution immunohistochemistry of eccentric contracted human skeletal muscle. These experiments revealed areas within the muscle which have lost the characteristic striated pattern when labeling characteristic Z-disc proteins like  $\alpha$ -actinin or titin Z-disc epitopes. Instead, longitudinal strands have been observed containing F-actin and myotilin which span these regions and connect intact Z-discs (Yu *et al.*, 2003; Carlsson *et al.*, 2007). The intermediate filament protein desmin also pervades such area (Yu und Thornell, 2002). Such structures can also be detected at single Z-discs which then appear as broadened Z-disc without  $\alpha$ -actinin, titin or nebulin. It has been suggested that these areas reflect insertion of new sarcomeres as an adaptation to the increased force. In this work, cryo-sections of human skeletal muscle were analyzed with antibodies against different portions of Xin and Xirp2 (cf. section 3.8). The specimen derived from a muscle biopsy of the M. vastus lateralis of a 23-year old man did not reveal any abnormalities. While Xin was absent from the normal sarcomere as expected, areas exhibiting strong Xin labeling were occasionally observed. Both antibodies against the N- and the C-terminus of Xin A displayed a similar staining pattern. Xin-containing structures longitudinally connected one or more successive sarcomeres and the ordered striated pattern of the Z-discs was often disrupted in these areas indicated by a lack or diffuse staining of  $\alpha$ -actinin and nebulin (cf. sections 3.8.1 and 3.8.2). These longitudinal strands could appear as a large patch of multiple strands within the muscle fibre or as single strands. Such single strands could also connect apparently normal sarcomeres, i.e. sarcomeres with unobvious  $\alpha$ -actinin labeling (fig. 3.73). Then, Xin staining was intensified at the Z-disc level while the labeling of the connecting strands was reduced. Since most of the sites of Xin labeling in the myofibril exhibited disruption of Z-disc structure as indicated by a loss of typical  $\alpha$ -actinin and nebulin arrangement, it is obvious to suggest that these areas reflect sites of muscle remodelling. Furthermore, it could be demonstrated that Xin is targeted to regions displaying a typical delta-shape of areas

with supernumerary sarcomeres, i.e. the number of sarcomeres in transverse register does not match (fig. 3.75). Remodelling upon eccentric contraction leads to the insertion of additional sarcomeres indicated by such delta-shaped arrangements which support the notion that the structures identified reflect remodelling (Yu *et al.*, 2003). Interestingly, it has already been shown that Xin is upregulated in muscle after eccentric contraction (Barash *et al.*, 2004) which clearly points to an involvement of Xin in subsequent processes and corroborates the conclusion that these Xin-containing structures display remodelling. Although eccentric exercised muscle does not reveal prominent damage or inflammation, it is very likely to assume that the addition of new sarcomeres during remodelling is based on mechanisms fundamentally related to muscle development and regeneration since there is a significant overlap of proteins involved as e.g. Xin. Muscle satellite cells directly start expressing Xin upon muscle damage and the expression persists during regeneration (Hawke *et al.*, 2007). Thus, Xin is an important player in developmental and remodelling processes in cross-striated muscle. Strikingly, the interaction partner filamin C could also be identified as a component of such longitudinal strands in areas of skeletal muscle remodelling (cf. section 3.8.3). Both proteins colocalized at longitudinal strands but not at Z-discs independent of the developmental stage of the Z-disc. Similar to Xin, filamin C is also upregulated upon damage and early expressed during skeletal muscle development which supports the view that these processes recapitulate related mechanisms (Goetsch *et al.*, 2005; van der Ven *et al.*, 2000a). As Xin is absent from Z-discs, these longitudinal strands during muscle remodelling represent promising candidates for the site of the Xin-filamin C interaction. Nebulin does not seem to be involved in the formation of these strands since no decoration could be observed. Xin can interact with nebulin as demonstrated in this work (cf. section 3.3) and it is proposed that this interaction is transient during myofibrillogenesis (cf. section 4.3.1). Exactly where and when Xin and nebulin interact during remodelling processes requires high resolution analysis but it can be speculated that it takes place at the transition zone where the actin filaments building these strands transform into thin filaments at the level of newly formed Z-discs perhaps upon association with specific thin filament proteins. However, nothing much is known about the composition of these strands in comparison to thin filaments apart from the described association with myotilin and perhaps obscurin (Carlsson *et al.*, 2007, 2008).

Xin and Xirp2 share an overlapping set of binding partners and presumably related function. Decoration of longitudinal structures between one or more successive sarcomeres in areas of skeletal muscle remodelling seems to be a common feature of Xin-Repeat

proteins. All Xirp2 antibodies labeled structures similar to those obtained with Xin antibodies (cf. section 3.8). Intriguingly, the antibodies Xirp2 N-terminus and central exhibited also strong signals at these strands although they scarcely labeled normal Z-discs (fig. 3.77 and 3.78). This points to the notion that their epitopes are buried within the dense protein meshwork of the Z-disc but are easily accessible along these strands. The areas of such a Xirp2 staining pattern could also appear as large patches or single strands where normal striation of  $\alpha$ -actinin and nebulin is disrupted as has been described for Xin (cf. sections 3.8.1 and 3.8.2). In contrast to Xin, Xirp2 can interact with both nebulin and  $\alpha$ -actinin (cf. sections 3.7.3 and 3.7.2), but the interaction to F-actin or filamin C at these strands seems to be more dominant. It is attractive to speculate that Xirp2 provides the structural framework for the incorporation of  $\alpha$ -actinin and nebulin into the newly formed Z-disc which is the site of their interaction (cf. section 4.7).

Myofibrillar myopathies are characterized by the dislocation of certain Z-disc proteins resulting in alteration of myofibril structure and aggregate formation (Claeys *et al.*, 2009). The subset of proteins found in these aggregates comprises Xirp2, filamin C and myotilin, all proteins involved in remodelling or regeneration. Interestingly, although Xin is not a sarcomeric component, it can be also identified in aggregates of such specimens. Other prominent Z-disc proteins like  $\alpha$ -actinin or the podin-family of proteins are not affected so that Z-disc proteins were subdivided into being stress-responsive or not. Interestingly, FRAP experiments displayed clear differences between the exchange rate of different Z-disc proteins. While  $\alpha$ -actinin revealed a rather slow exchange rate, myotilin was much faster (Wang *et al.*, 2005). Filamin C transfected into rat cardiomyocytes recovers within seconds which is surprisingly fast (Yvonne Hahn, personal communication). Perhaps proteins can be classified according to their fast exchange rate as stress-responsive. It would be very interesting to know about the exchange rate of Xirp2 since it is a very large protein ( $\approx 400$  kDa) but exhibits a stress-responsive phenotype. In addition, highly dynamic proteins are presumably also candidates for remodelling processes.

But how are such processes regulated and accordingly Xin and Xirp2? Upon muscle damage satellite cells are activated and myogenic transcription factors induce the expression of muscle-specific proteins. Xin has already been shown to be transactivated by known myogenic transcription factors such as MEF2, MyoD or Myf-5 (Hawke *et al.*, 2007). Additionally, Xin seems to be a downstream target of a BMP (bone morphogenetic protein)–Nkx2.5–MEF2C pathway (Wang *et al.*, 1999). Some findings suggest that Xin could be a target of the PI3-kinase/AKT pathway through its interaction with LIMCH1 and/or nebulin (Cizkova *et al.*, 2010; Takano *et al.*, 2010). Since Xirp2 can also interact

with nebulin this link could be valid for Xirp2, too. The regulation of the nebulin-N-WASP complex depends on IGF-1 (insulin-like growth factor 1) and the loss of Xirp2 in mice results in a downregulation of the IGF-1 receptor which proposes an involvement of Xirp2 in this signalling cascade (Wang *et al.*, 2010). The promotor of Xirp2 contains MEF2A-responsive elements which are regulated by angiotensin II (McCalmon *et al.*, 2010). This seems to modulate hypertrophic responses of the heart. However, nothing is known about posttranslational modifications or proteins directly regulating Xin and Xirp2 function so that the physiological role of these findings and speculations remains to be determined.

## 4.5 LIMCH1 – The First Xin A-Specific Binding Partner

The Xin gene in human and mouse gives rise to three different isoforms A, B and C which result from intraexonic splicing of the large coding exon (van der Ven *et al.*, 2006). While the whole sequence of Xin B and C is included in the largest isoform Xin A which comprises a unique sequence without any predicted domains but with a proline-rich cluster. A discrimination of the function of the three isoforms could therefore be achieved by analyzing the properties of this unique region. In this work, the first interaction partner of this Xin A-specific sequence was identified in a yeast two-hybrid screen of a skeletal muscle cDNA library (cf. section 3.5). Multiple clones were obtained comprising varying lengths of the C-terminus of a protein encoded by the gene LIMCH1 on chromosome 4. As indicated by the gene name, the corresponding protein presumably harbours an N-terminal single CH domain and a C-terminal LIM domain (fig. 3.42). Further yeast two-hybrid studies identified the LIM domain as the responsible binding interface and demonstrated the binding specificity of this domain since LIM domains of other muscle proteins like N-RAP and MLP did not interact (cf. section 3.5.1). This is even more striking as LIM domains can exhibit extensive promiscuity in *in vitro* binding assays (K. Gehmlich, D.O. Fürst, personal communication) but neither in yeast two-hybrid experiments nor in co-immunoprecipitations unspecific binding activity was observed (cf. sections 3.5.1 and 3.5.2. LIM domains are present in various proteins functioning as a versatile binding interface identified originally in three eponymous proteins LIN-11, Isl1 and MEC-3 (Kadrmaz und Beckerle, 2004). The conserved structure comprises a tandem zinc finger which is established by two motifs of four conserved cysteine or histidine residues each co-

ordinating one zinc ion. Although the structure is conserved, exposed residues mediating the interaction reveal high variability rendering this domain a versatile binding module (Kadrmaz und Beckerle, 2004). Analysis of the exact binding mode and identification of the involved residues of the Xin-LIMCH1 interaction could not be performed but would provide further insight how specificity is accomplished.

#### 4.5.1 Expression of LIMCH1 Isoforms in Cells and Tissues

In order to get more information about the physiological relevance of LIMCH1 and its interaction, the LIMCH1 gene and encoded proteins were analyzed. Database queries revealed that in contrast to Xin human LIMCH1 transcription is not restricted to cross-striated muscle tissue and high mRNA levels are detected in brain and lung whereas transcription is reduced in blood cells, liver and bone marrow (UCSC Genome Browser). Since both proteins can only interact in cardiac or skeletal muscle, expression of LIMCH1 protein was studied at different stages of differentiating human skeletal muscle cells and in mouse and rat tissue of lung, heart and skeletal muscle using a commercially available antibody raised against the C-terminus of the predicted full-length protein (LIMCH1 FL) (cf. section 3.5.5). This is exactly the region also included in the LIMCH1 clones identified in the yeast two-hybrid screen (fig. 3.42). The estimated molecular mass of LIMCH1 FL accounts for  $\approx 122$  kDa in human (NM 014988) and rat (NM 001191678) and  $\approx 120$  kDa in mouse (NM 001001980). The antibody detected polypeptides in all cell and tissue extracts except from non-differentiated human skeletal muscle cells which migrated at  $\approx 130$  kDa (fig. 3.49 A). The specificity of these signals was underlined by the detection of a recombinantly expressed LIMCH1 fragment comprising the immunogenic region (LIMCH1 CC2) demonstrating that the bands in cells and tissues do really reflect LIMCH1 FL. These results show that LIMCH1 is expressed in muscle cells of human, mouse and rat and an interaction *in vivo* with Xin is possible. Expression of Xin in mouse can be detected in the heart tube and the first rostral somites as early as E8.0 and E10, respectively (Sinn *et al.*, 2002). Nothing is known about LIMCH1 protein expression during embryonic development but transcription of LIMCH1 mRNA is detected in presomitic mesoderm at E9.5, which among others contributes to the muscle precursor cell pool, whereas somites appear not to contain prominent amounts of LIMCH1 transcripts (Sewell *et al.*, 2009) so that the site and developmental stage of Xin-LIMCH1 interaction remains elusive. Nevertheless, it cannot be excluded that Xin is expressed in presomitic mesoderm cells. However, the absence of LIMCH1 in non-differentiated human skeletal muscle cells and the emergence

in differentiated cells points to an upregulation during myofibrillogenesis. This was confirmed analyzing a differentiation series of H-2K cells where expression was detectable at day 2 constantly increasing until the final stage of differentiation (fig. 3.49 B). A related course was also observed with LIMCH1 transcripts which showed prominent increase at day 2 of differentiation (cf. section 3.5.7). Transcripts were already detectable before induction of differentiation which could be either due to untranslated mRNA since no protein was found in proliferating myoblast or due to spontaneously differentiating cells which were occasionally observed. The latter would also explain why no protein could be detected in cell lysates. Hence, interaction of Xin A and LIMCH1 could also play a role during myofibrillogenesis apart from early embryonic development. Interestingly, the antibody stainings of tissue and cell extracts provided more bands than that at 130 kDa. Rat skeletal muscle extracts exhibited an additional signal significantly above 130 kDa which could also be observed in differentiating H-2K cells, where it was actually the most prominent band (cf. section 3.5.5). Therefore, it was very likely that this signal reflected a novel isoform and in fact, one mRNA clone (AL831962) identified in human skeletal muscle was obtained from databases which potentially encodes a larger LIMCH1 protein (cf. section 3.5.6). Although the start codon of this clone is presumably located in exon 6 causing the absence of the N-terminal CH1 domain, 7 additional exons situated between exon 8 and 9 of LIMCH1 FL generate a protein of a calculated molecular mass of  $\approx 165$  kDa (fig. 3.50 A+B) (Friedberg, 2009). The existence of mRNA species comprising these novel exons could be also verified for the murine orthologue in RNA isolated from differentiated H-2K cells (fig. 3.50 D). While the number of newly identified exons is the same in mLIMCH1, the arrangement deviates from the human layout (fig. 3.50 E). Nevertheless, the resulting murine protein has also a higher molecular weight than mLIMCH1 FL. As these exons were identified in an mRNA clone isolated from human skeletal muscle tissue and larger proteins were detected in rat skeletal muscle and H-2K cells, they are designated as muscle exons. Strikingly, in protein extracts of differentiated human skeletal muscle cells no such large protein could be identified although the mRNA clone derived from human skeletal muscle (fig. 3.49 A). Whether this indicates a different regulation of protein expression in human and mouse or reflects an anomaly of the cultured human cells remains unclear and further analysis of human skeletal muscle tissue is needed. Such experiments could also clarify the exact composition of the LIMCH1 muscle isoform, for only the existence of a splice variant containing the muscle exons has been shown while the complete sequence is still a prediction and has to be verified. Apart from the band above 130 kDa, blot analysis of tissue extracts revealed additional bands below



the LIMCH1 FL isoform at 130 kDa which could be also detected in H-2K cell extracts (fig. 3.49 A). At the moment, there is no evidence whether these are additional isoforms although existence of other isoforms than LIMCH1 FL and LIMCH1 muscle has been already predicted (Friedberg 2009, UCSC Genome Browser).

#### 4.5.2 Oligomer Formation of LIMCH1

Both proteins LIMCH1 FL and LIMCH1 muscle comprise the LIM domain and are therefore in principle capable of interacting with Xin. Thus, it is necessary to dissect functional parts of LIMCH1 in order to determine the differences between both isoforms and the functional consequences upon binding the respective isoform. Both isoforms contain putative coiled-coil motifs, one located in the N-terminal part (CC1), the other more C-terminally (CC2), which can impart the ability of homodimerization or oligomerization (cf. section 3.5.8). Since most of the common prediction methods favored the C-terminal coiled-coil motif CC2 to be functional, an N-terminally truncated fragment of LIMCH1 (LIMCH1 CC2) was tested on multivalent complex formation with chemical cross-linking although it cannot be excluded that the N-terminal coiled-coil motif CC1 is also functional (fig. 3.52 A). This experiment uncovered that LIMCH1 CC2 can form SDS- and DTT-resistant dimers and trimers and addition of cross-linker revealed an increase of dimeric and trimeric as well as existence of tetrameric complexes (fig. 3.52 B). Although oligomers were clearly detected, the efficiency of complex formation is decreased in comparison to other dimeric proteins like filamin where the proportion of monomeric protein in cross-linking assays was shown to be greatly reduced (Himmel *et al.*, 2003; Löwe *et al.*, 2007). On the one hand this could reflect that the majority of LIMCH1 is in a monomeric state within the cell with multivalent complexes being formed occasionally. On the other hand such complex formation must be tightly regulated and this was not taken into account in the *in vitro* experiment. It might be possible that multimerization is dramatically influenced by posttranslational modification or splicing events even outside the coiled-coil motifs (Barbash *et al.*, 2011; Ma *et al.*, 2010; Araya *et al.*, 2002). Thus, LIMCH1 can be regarded as a protein which can adopt multimeric states but determination of the ratio and regulation of these states requires future work. As both isoforms contain the functional coiled-coil motif the possibility of heteromeric complex formation arises and it would be important to know whether Xin and LIMCH1 can also interact with each other in multimeric state since Xin is also able to form multimers.

### 4.5.3 Dissection of Functional Domains in LIMCH1

One eponymous structural feature presumably missing in muscle LIMCH1 is the N-terminal CH domain (fig. 3.50 A). A tandem of CH domains can be found in actin binding proteins such as  $\alpha$ -actinin and filamin where it is considered to be an actin binding domain (Gimona *et al.*, 2002). However, single CH domains have already been shown to completely impart different functions, e.g. binding to microtubules or adaptor proteins (Sjöblom *et al.*, 2008). In order to get more insight into the functional domains of LIMCH1, differentially truncated fragments of LIMCH1 FL were transfected into A7r5 cells (fig. 3.45). LIMCH1 FL was associated with actin filaments in a punctate pattern and submembranous regions but did not prominently target to focal adhesion (cf. section 3.5.3). Truncation of the N-terminal CH domain (LIMCH1 CC1+2) did not result in an obvious alteration of targeting. Interestingly, removal of the N-terminal coiled-coil motif CC1 and the central part of LIMCH1 (LIMCH1 CC2) completely disrupted targeting and caused a diffuse cytoplasmic distribution which was also observed with the LIM domain alone (LIMCH1 LIM). This indicates that the CH domain is obviously not necessary for the association with actin filaments since LIMCH1 CC1+2 could be identified there in the same pattern. As truncation of CC1 and the central part impairs targeting, it is obvious to allocate targeting function to that region since the LIM domain is not able to specifically localize alone. As transcripts of rat LIMCH1 FL could be detected in A7r5 cells although verification on protein level failed (Merk, 2010), it is possible that targeting could be conveyed by N-terminal regions, e.g. the CH domain, provided that the N-terminal coiled-coil region is functional and the transfected LIMCH1 CC1+2 fragment forms multimers with endogenous LIMCH1 via CC1 and not CC2. This implies the exciting possibility that the single CH domain can act like actin binding tandem domains upon coiled-coil formation. However, the protein level of endogenous LIMCH1 appears to be too low to target transfected LIMCH1 and the probability that the CC1 motif is functional is low. Hence, it is most likely that LIMCH1 localizes to actin filaments due to specific interactions within the central 400 aa between aa 312 and 712 either directly or indirectly.

### 4.5.4 The Site of Xin–LIMCH1 Interaction

The most remarkable difference of transfected LIMCH1 FL and Xin A concerning localization in A7r5 cells is the absence of LIMCH1 from focal adhesions (cf. section 3.5.3). While Xin is highly enriched there although not directly at the tips as co-stainings with Mena

revealed (cf. section 3.6), LIMCH1 did not exhibit prominent labeling of focal adhesions. Interestingly, co-transfection of Xin A and LIMCH1 FL resulted in BiFC complexes along actin filaments but not at focal adhesions which was confirmed by confocal microscopy (cf. section 3.5.4). This demonstrates that Xin A is not able to recruit LIMCH1 into focal adhesions. The restriction of the Xin-LIMCH1 complex to actin filaments seems to be lost if the LIMCH1 fragment is N-terminally truncated because LIMCH1 CC1+2 generates a BiFC signal at actin filaments and at focal adhesions. It is tempting to speculate that the exclusion of LIMCH1 from focal adhesions depends on the CH domain. This is further corroborated by the finding that Xin A can also form BiFC complexes at focal adhesions with the LIM domain alone, a fragment which usually does not target specifically (cf. section 3.5.4). Surprisingly, BiFC complexes along actin filaments were greatly reduced upon co-transfection of Xin A and LIMCH1 LIM although they provided a prominent signal at focal adhesions. Since Xin A can target LIMCH1 CC1+2 to actin filaments and focal adhesions, it was expected that the association with actin filaments remains unaffected by further truncation of LIMCH1, especially because Xin A alone prominently decorates actin filaments (cf. section 3.6). This points to the direction that Xin A is not responsible for localization of LIMCH1 but vice versa. This notion could also explain the findings that a specific BiFC signal could be obtained if both LIMCH1 FL and LIMCH1 CC1+2 were co-transfected with the Xin fragment Xin PR3+4 which was only diffusely distributed in single transfection assay (cf. sections 3.5.4 and 3.6). The BiFC complexes specifically decorated actin filaments in a punctate fashion but not focal adhesions. This suggests that LIMCH1 is able to target a Xin fragment which cannot target itself. Unspecific BiFC complex formation in the cytoplasm was never observed in any combination of proteins if a fragment was neither capable to interact with the second protein nor specifically localize within the cell (personal observation). Thus, the BiFC complex generated by Xin PR3+4 and LIMCH1 LIM very likely reflects a specific interaction although diffusely distributed in the cytoplasm. Assuming that LIMCH1 is responsible for targeting of Xin A, this would explain why this complex did not target because LIMCH1 LIM lacks the potential targeting sequence in the central part. In this case, the line of argument would also work assigning targeting function to Xin but this would not easily explain its exclusion from focal adhesions. Admittedly, BiFC data need to be carefully interpreted as delineated in section 4.3.1 but the selectivity of complex formation is striking. Nevertheless, the experiment in A7r5 cells does not display the *in vivo* situation since Xin expression is restricted to cross-striated muscle, and direct experimental evidence is needed for these conclusions, but it gives a first clue how distinct

sorting of Xin isoforms mediated by unique binding partners can be achieved. It would be interesting to find out whether and how LIMCH1 accomplishes distinctive targeting of Xin A. As these experiments revealed that an N-terminal region is presumably responsible, the identification of the novel LIMCH1 muscle isoform offers the exciting possibility that LIMCH1 isoforms direct Xin A to different cellular sites because the sequence of the newly identified exons of LIMCH1 muscle are inserted N-terminally from the first coiled-coil motif.

#### 4.5.5 The Potential Role of the Xin–LIMCH1 Interaction

What is the physiological significance of the Xin-LIMCH1 interaction? It is not clear where and when Xin and LIMCH1 interact but gene expression studies in breast tumors exhibiting aberrant PI3-kinase/AKT signalling detected a prominent upregulation of LIMCH1 gene expression (Cizkova *et al.*, 2010). The PI3-kinase/AKT pathway in muscle is involved in muscle hypertrophy and can prevent from apoptosis (Kandarian und Jackman, 2006; Zhang *et al.*, 2010; Glass, 2005). Although direct evidence is still missing, the interaction with LIMCH1 could render Xin A a downstream target of the PI3-kinase/AKT signalling pathway. Besides the interaction with nebulin which is an effector of PI3-kinase/AKT signalling through its interaction with N-WASP (Takano *et al.*, 2010), this is a potential second link of Xin to this pathway which increases the probability of physiological relevance of this speculation.

### 4.6 Xin and Xirp2 – Overlapping and Distinct Function

The eponymous feature of the Xin-Repeat protein family is a repetitive amino acid sequence which defines a novel F-actin binding motif (Pacholsky *et al.*, 2004). This has led to the discovery of multiple genes in different species encoding proteins harbouring this motif. The number of genes can vary between three in zebrafish and only one in chicken (cf. section 1.10). As demonstrated for the two human genes encoding Xin and Xirp2 by van der Ven *et al.* 2006 and in this work, splicing events can generate isoforms lacking the repeats (cf. section 3.7.5). Nevertheless, Xin-repeat-containing isoforms generally represent the most prominent ones (cf. sections 3.2.1, 3.2.2, 3.7.5 and 3.7.6).

The proteins display a similar domain layout starting with a proline-rich region at the N-terminus (fig. 4.2). This comprises a motif capable of interacting with Ena/VASP

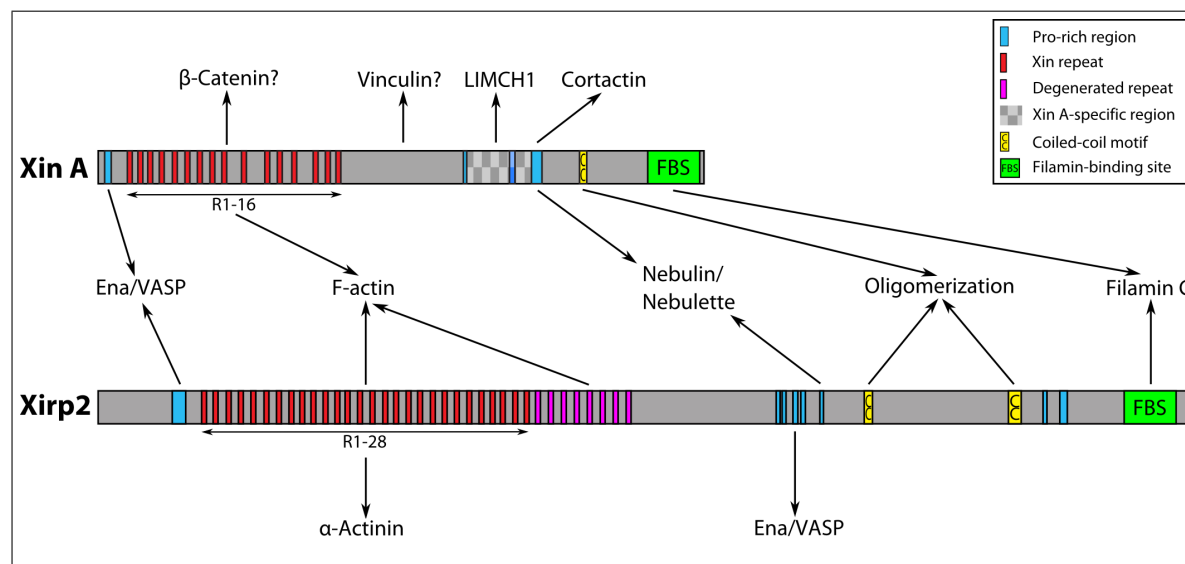


Figure 4.2: **Proteins interacting with Xin and Xirp2.** Schematic overview of the domain layout of human Xin and Xirp2. Proteins interacting with both Xin-Repeat proteins are depicted in between. The origin of the arrows indicate the respective binding region in Xin and Xirp2, respectively.  $\beta$ -Catenin and Vinculin are marked with a '?' because their interaction is only described for the murine orthologue.

proteins in both human family members, Xin and Xirp2 (Eulitz, 2005; van der Ven *et al.*, 2006). Although the respective binding motif in Xin has been described to be only conserved in placental mammals (Grosskurth *et al.*, 2008), such potential Ena/VASP-binding sequences can be also identified in chicken, clawed frog and zebrafish, the latter has already been shown to be functional (Steinhagen, 2009). Admittedly, the interaction data comprises only *in vitro* binding assays. Thus, it is necessary to determine whether Ena/VASP proteins represent the *in vivo* binding partners or whether other proteins containing an EVH1 type I domain occupy this interaction motif. Despite the physiological relevance of the Ena/VASP interaction is still elusive, it is obvious to conclude that these motifs have a function *in vivo*. Xin-Repeat proteins differ in the number of repeats they contain (fig. 4.2). Apart from the F-actin binding function (Pacholsky *et al.*, 2004) the discovery of other proteins interacting with that region expanded the view of Xin repeat function. In murine Xirp2,  $\alpha$ -actinin was described as the first protein binding to the repeats except from F-actin. Huang *et al.* identified two independent binding sites, one within the first 9 repeats and the other within the degenerated repeats. In this work,  $\alpha$ -actinin binding to human Xirp2 could be confirmed but it was impossible to determine the exact number and position of the binding site (cf. section 3.7.3). However, the idea of two or more  $\alpha$ -actinin binding sites within the repeats is very attractive concerning potential implications for Z-disc architecture (cf. section 4.7). Strikingly, the repeat region of human

Xin was not able to bind to  $\alpha$ -actinin highlighting the interaction as a distinct feature of Xirp2 (cf. section 3.7.3). In contrast to that, the armadillo repeat protein  $\beta$ -catenin has been identified as a binding partner of the murine Xin repeat region (Choi *et al.*, 2007). Therefore, Xin has been implied into cellular junction formation in the heart and skeletal muscle (Choi *et al.*, 2007; Sinn *et al.*, 2002). The potential binding region of  $\beta$ -catenin is conserved among all Xin isoforms but a proof of this interaction using human proteins has been failed until now (data not shown). During myofibrillogenesis of H-2K cells, no prominent colocalization of Xin and  $\beta$ -catenin could be observed at cell-cell contact sites (cf. section 3.2.3.4). The function of this interaction remains controversial and it would be interesting to know whether binding to  $\beta$ -catenin reflects a specific quality of the repeats in Xin which would indicate functional diversification of Xin-Repeat proteins. The human Xin region located C-terminally from the repeats and included in Xin A and B was shown to be responsible for targeting to focal adhesions (cf. section 3.6). Interestingly, vinculin has been described to be a potential interaction partner of mouse Xin with the binding region being located in the same region (Choi *et al.*, 2007). Vinculin is a major component of focal adhesions and links integrins to the actin cytoskeleton (cf. section 1.9.3). In muscle, vinculin and its relative meta-vinculin can be found in adhesion structures like costameres or the ICD. Assuming that integrin adhesion structures form early precursors of myofilament attachment points during development, this interaction could link Xin to these structures. Intriguingly, vinculin can also interact with Ena/VASP proteins (Hüttelmaier *et al.*, 1998). Since vinculin nucleates actin polymerization and VASP can act as a processive actin polymerase (Wen *et al.*, 2009; Hansen und Mullins, 2010), such a ternary complex could be involved in actin filament generation and regulation during early stages of development. Furthermore, the complex could take over a function related to the nebulin–N-WASP complex but at a different developmental stage (Takano *et al.*, 2010). In that regard, it is interesting that both human proteins are able to interact with the SH3 domains of nebulin and nebulette (cf. section 3.3). While the respective proline-rich motif in Xirp2 responsible for binding to nebulin/nebulette is highly conserved in placental mammals (cf. section 4.3.2) and has been demonstrated to be functional in zebrafish (Steinhagen, 2009), the conservation of a functional motif in Xin is apparently limited to human, mouse and rat (cf. section 4.3.2). The significance of this discovery is still speculative but it could indicate slight differences in the myogenic differentiation process between human and other distantly related placental mammals. Nevertheless, it seems likely that binding to nebulin/nebulette can be regarded as an ancient feature of Xin-Repeat proteins due to the high conservation of the motif in Xirp2.



Adjacent to the proline-rich region, human Xin-Repeat protein sequence contains potential coiled-coil regions (fig. 4.2). Cross-linking assays confirmed the ability of multimer formation *in vitro* for both human Xin and Xirp2 (cf. sections 3.4 and 3.7.4). Although the predicted probability of coiled-coil formation in murine Xin was reduced, chemical cross-linking revealed that multimer formation is possible (cf. section 3.4.2). Sequence analysis of other species points to coiled-coil formation as a general feature of Xin-Repeat proteins. Despite less conservation and probability values of the motifs in Xin, coiled-coil motifs can be identified even in distantly related species like the clawed frog and chicken using prediction methods described in section 3.4.2. The efficiency of multimer formation *in vitro* is reduced in comparison to other prominent dimeric proteins like filamin (Himmel *et al.*, 2003; Löwe *et al.*, 2007). Surprisingly, the tetrameric protein VASP did also not display a high tetramerization rate in cross-linking assays (fig. 3.38). Therefore, the multimer formation rate of Xin-Repeat proteins is comparable to other proteins like VASP and does imply an *in vivo* relevance, especially because potential motifs are identified in a high number of Xin-Repeat proteins of different distantly related species like the clawed frog and chicken. Although the probability is higher in Xirp2 orthologues, this does not exclude that oligomerization is also a general quality of Xin. However, the exact stoichiometry is still unknown but especially the experiments with Xin fragments suggest more than dimer formation (cf. sections 3.4). The potential of such a complex formation emphasizes the putative role as multiadaptor proteins functioning as a molecular scaffold for protein association. BiFC analysis of Xin C complexes imply that complexes are also formed at sites where Xin C targets to upon single transfection in A7r5 cells. Perhaps, oligomer formation can explain why overexpression of Xin C has a quite severe impact on the structure of the actin cytoskeleton (cf. sections 3.3.6.2 and 3.4.1), for Xin C does not have an actin-binding site but contains interaction sites for other actin-associated proteins like cortactin (fig. 4.2) and could relocalize these proteins from actin thereby disrupting F-actin architecture. A related effect can be also observed in mice which cannot express Xin A and B but retain Xin C expression. These animals develop a severe disruption of myofibrillar structure whereas complete loss of Xin causes only a mild phenotype (Gustafson-Wagner *et al.*, 2007; Otten *et al.*, 2010). At the C-terminus, Xin harbours a binding site for the Ig domain 20 of the muscle-specific filamin isoform C (fig. 4.2 and van der Ven *et al.* 2006). Binding assays in this work showed that this feature is also common to Xirp2 (cf. section 3.7.1). This interaction further renders Xin-Repeat proteins important players in myofibrillogenesis since the switch from filamin A to filamin C expression upon induction of myogenic differentiation is a key event (van der

Ven *et al.*, 2000a) in myofibrillogenesis. Furthermore, it potentially links Xin-Repeat proteins to the membrane either via integrins or the sarcoglycan complex (Pentikäinen und Yläanne, 2009; Thompson *et al.*, 2000) which could in part explain the submembranous targeting observed during differentiation of H-2K cells (cf. section 3.2.3).

In summary, most of the binding partners described can interact with both Xin-Repeat proteins. The identification of novel specific binding partners such as  $\alpha$ -actinin,  $\beta$ -catenin and LIMCH1 (cf. section 4.5) will help to further reveal the exact function of Xin and Xirp2. While  $\alpha$ -actinin adds a prominent structural role to Xirp2 (cf. section 4.7), the potential  $\beta$ -catenin interaction with Xin points to a role in cell-cell contact formation and or Wnt-signalling which is an important regulator of embryonic development (cf. section 1.9.1.1). Characterization of LIMCH1 function will provide additional insight into Xin A function. Thus, searching for novel interaction partners can be a suitable means to get a first hint to Xin-Repeat protein function.

## 4.7 Xirp2 Orientation and Interactions Within the Sarcomeric Z-disc - Implications for Z-disc Structure

The sarcomeric Z-disc is a dense meshwork of myriad proteins conveying structural and or signalling functions which renders this structure a key element of sarcomere integrity (Pyle und Solaro, 2004; Frank *et al.*, 2006; Luther, 2009). Therefore, it is not surprising that Z-disc structure and composition adapt to the needs of different muscle types. This is most clearly reflected in morphological differences observed in electron micrographs of longitudinal muscle sections. In general, the Z-disc width increases from fast to slow twitch muscle and ultrastructural analysis of Z-disc structure has revealed zigzag links between opposing terminal ends of actin filaments from two adjoining sarcomeres (Rowe, 1973). The number of these Z-links has been shown to correlate with Z-disc width and until now Z-discs have been observed containing 2, 3, 4 and 6 layers of Z-links (Luther, 2009). The major actin filament cross-linker in the Z-disc is sarcomeric  $\alpha$ -actinin which mainly builds these Z-links although contributions of other Z-disc proteins belonging to the plethora of  $\alpha$ -actinin interaction partners cannot be excluded. The amount of Z-links therefore correlates with the amount of  $\alpha$ -actinin links, i.e. the more Z-links the more  $\alpha$ -actinin, but it does not specify the exact number because one zigzag layer corresponds

to two  $\alpha$ -actinin layers (Luther, 2009). In this work, human Xirp2 could be identified as a binding partner of  $\alpha$ -actinin which has already been shown for murine Xirp2 (cf. section 3.7.3, Huang *et al.* 2006). The binding site of  $\alpha$ -actinin in human Xirp2 could be allocated to the repeat region similar to the murine orthologue (cf. section 3.7.3, Huang *et al.* 2006). Interestingly, this interaction turned out to be specific for Xirp2 since the Xin repeats were not able to bind  $\alpha$ -actinin (cf. section 3.7.3). While Huang *et al.* (2006) postulated two independent binding sites of  $\alpha$ -actinin within the repeats of murine Xirp2, the exact number and localization of the binding site of  $\alpha$ -actinin in human Xirp2 could not be defined exactly despite multiple attempts (cf. section 3.7.3). Both proteins are components of the Z-disc (fig. 3.68 and 3.69) hence it is very likely to assume that the interaction takes place there. Furthermore, the related Xin protein is not permanently localized at the Z-disc (van der Ven *et al.*, 2006) and its repeats lack the ability to bind  $\alpha$ -actinin which could suggest that this interaction is necessary to stably anchor Xirp2 in the Z-disc. Admittedly, there are more candidates to take over this function like filamin C or nebulin/nebulette (cf. sections 3.7.1 and 3.7.2) and it is undoubted that Xirp2 can interact with multiple binding partners simultaneously but all of these proteins are interaction partners of both Xin and Xirp2 (cf. section 3.3, van der Ven *et al.* 2006). Thus, it is more probable that the unique feature of permanent Z-disc localization is conveyed by a unique binding partner which is only  $\alpha$ -actinin until now.

Immunofluorescence studies of human skeletal muscle specimens using human Xirp2-specific antibodies raised against three different portions of Xirp2 pointed to a defined orientation within the Z-disc. An antibody labeling the N-terminus of human Xirp2 did not show a prominent localization at the Z-disc in healthy adult muscle (fig. 3.68 A-C). However, in areas of muscle remodelling this antibody like the other Xirp2 antibodies provided a strong signal at longitudinal strands connecting one or more Z-discs (fig. 3.77) which demonstrates that this antibody is also suitable for immunofluorescence stainings. The fact that the epitope is not strongly recognized in normal skeletal muscle could be due to impaired accessibility since the Z-disc is an extremely dense protein meshwork especially in its center. This view is supported by the strong decoration of remodelling structures where the dense protein meshwork is not yet established and therefore epitopes are presumably more exposed (cf. section 3.8). A related result was obtained with an antibody detecting the central proline-rich region of Xirp2 (fig. 3.67). This region was shown to bind the nebulin/nebulette SH3 domain (cf. section 3.7.2) thus it is obvious to conclude that this part of human Xirp2 is embedded within the Z-disc center since both nebulin/nebulette and Xirp2 are permanent components of the sarcomeric Z-discs

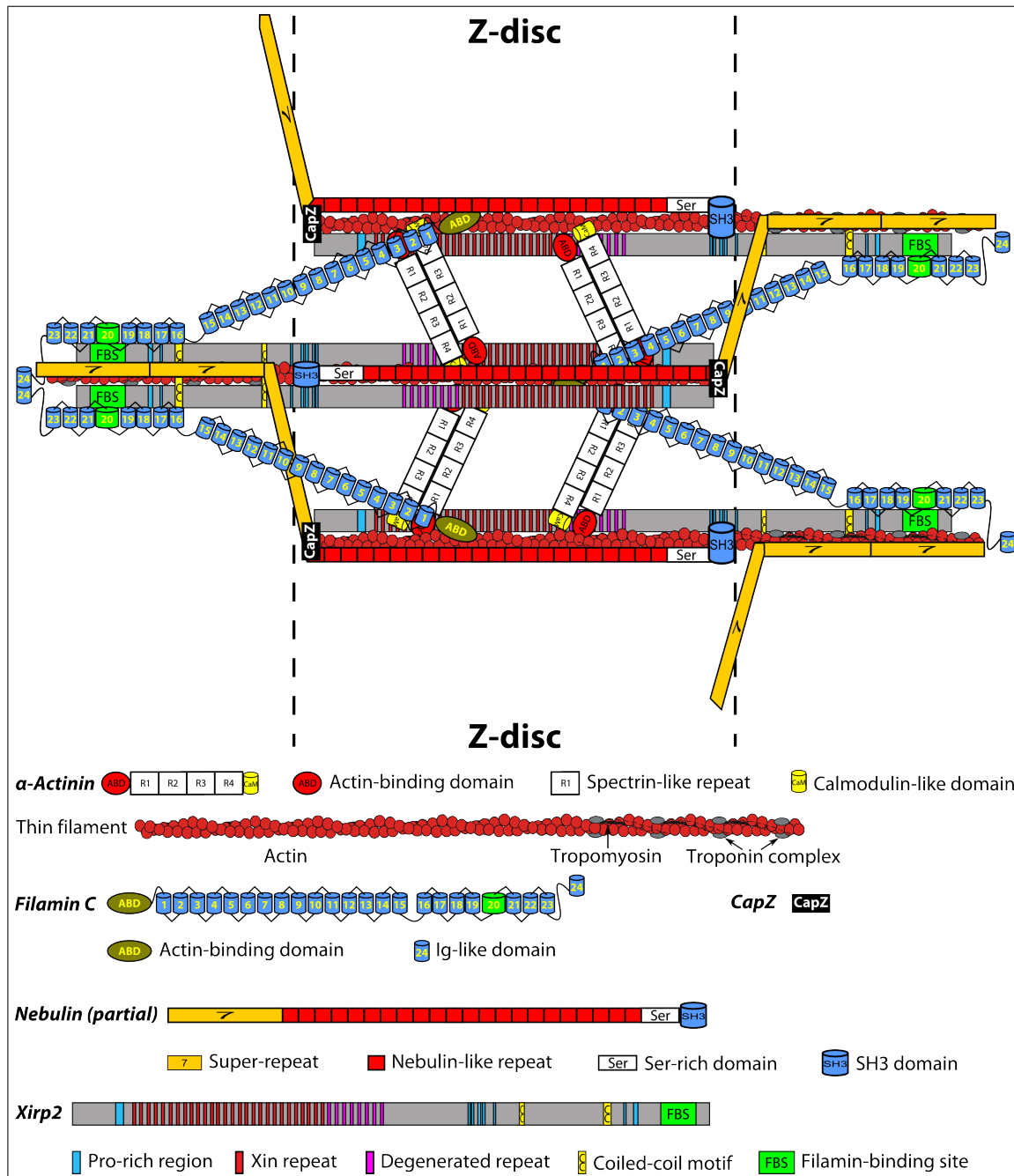


Figure 4.3: **Model of Z-disc architecture.** Schematic overview of a potential Xirp2 arrangement at the sarcomeric Z-disc. This model does not consider threedimensional constraints and for clarity reasons only selected proteins are depicted. The orientation of nebulin is adopted from Pappas *et al.* (2008). The following interactions are considered: Xirp2- $\alpha$ -actinin, Xirp2-filamin C, Xirp2-nebulin, Xirp2-F-actin, Xirp2-Xirp2,  $\alpha$ -actinin-F-actin, filamin C-F-actin, filamin C-filamin C, nebulin-F-actin, nebulin-CapZ. Any other overlap does not reflect an interaction.

(Millevoi *et al.*, 1998; Moncman und Wang, 1999). Although this antibody gave signals at the level of Z-discs, it was again surprising that the intensity was rather weak since the antibody against the repeat region of the murine orthologue strongly decorates the Z-disc (fig. 3.68 D-F). As depicted for the antibody against the N-terminus, the labeling intensity dramatically increased in areas of remodelling at longitudinal strands (fig. 3.78). Hence, the antibody against the central proline-rich region gave also similar results and this could again be a matter of epitope accessibility. This notion is additionally corroborated by taking into account the results of stainings using the antibody raised against the C-terminus (fig. 3.67). Strikingly, this antibody provided prominent Z-disc decoration but detailed analysis revealed that the signal appeared as a doublet flanking the center of the Z-disc. This was most obvious upon counterstaining  $\alpha$ -actinin which is generally regarded as the central Z-disc marker (fig. 3.69). Similar results were obtained with co-stainings using antibodies against Z-disc epitopes of nebulin (fig. 3.71) and the N-terminus of filamin C (fig. 3.70). In co-stainings with  $\alpha$ -actinin, both signals did not seem to overlap whereas nebulin (Z-disc epitope) and filamin (N-terminus) revealed partial colocalization with Xirp2 at the edges of the double band. Apart from this double bands, there were also Z-discs appearing as a singlet. Nevertheless, the antibody against the C-terminus of Xirp2 mostly decorated a double band and the occurrence of single banded Z-discs could be attributed to variable three-dimensional orientations of the Z-discs in the sectioning plane of the specimen and therefore causing varying appearances. Additionally, it cannot be excluded that the resolution of immunofluorescence microscopy will not be sufficient to display the double band if the angle of the section deviates too much from the myofibril axis. Due to the different appearance of the Z-disc signals obtained with the Xirp2 antibodies, it is tempting to propose a certain orientation of the Xirp2 protein within the Z-disc (fig. 4.3). While the N-terminus and the central portion seem to be located closer to the Z-disc center, the C-terminus is pointing towards the M-band and farthest from the Z-disc center. Such an orientation would fit the localization of relevant interaction partners and their identified binding region. Xirp2 possesses one or more  $\alpha$ -actinin binding sites within the repeats and this region is very likely located in the Z-disc center as  $\alpha$ -actinin. The adjacent proline-rich region binds to the SH3 domain of nebulin/nebulette which presumably adjoins the layers of  $\alpha$ -actinin cross-links according to a recent model proposed by Pappas *et al.* (2008). This would also conform to the orientation concluded for Xirp2, because the nebulin binding region is situated at a greater distance from the Z-disc center. The C-terminus has been shown to interact with the C-terminally located Ig domain 20 of filamin C (cf. section 3.7.1). Interestingly, localization studies of filamin

in differentiating H-2K cells using an antibody raised against the C-terminus also revealed a potential double band flanking the Z-disc center (cf. section 3.2.3.2) which cannot be detected with an antibody labeling the N-terminus (cf. sections 3.7.7 and 3.8.3). Although this double band did not have such sharp edges as observed with Xirp2 and appeared more like a broad band, the maximum distance from the Z-disc center of  $\approx 650$  nm has a dimension comparable to the Xirp2 doublet (cf. section 3.2.3.2). Due to the heterogeneity of the cryo-section a proper quantitative analysis was not performed but the Xirp2 doublet was mostly separated by 600-700 nm apart from rare maximum distances around 850 nm. Despite the lack of ultrastructural data and because these observations were made in samples from a different type and species, i.e. mouse vs. human and cell culture vs. muscle biopsy, it is tempting to speculate that filamin C is anchored on thin filaments with its N-terminal actin binding domain in the Z-disc center and the C-terminus is pointing towards the M-band which would position the filamin C-terminus near the Xirp2 C-terminus harbouring the filamin binding site. Although this model is attractive since it facilitates to explain Z-disc architecture, immunofluorescence microscopy studies are not sufficient and further ultrastructural prove is needed. These could also determine whether Xirp2 does overlap or not with its repeat region in the Z-disc center as it is in the model depicted here. Another question is important to be answered. Since the number of  $\alpha$ -actinin cross-links vary among different muscle types (Luther, 2009), it is necessary to determine the exact number of  $\alpha$ -actinin binding sites in human Xirp2. It is tempting to speculate that the number could be variable due to splicing events and perhaps correlates with the muscle type. This would require intraexonic splicing of the large coding exon 7 which encodes the repeat region. Interestingly, such events are described for human Xin and result in three different isoforms (van der Ven *et al.*, 2006). Proof of the existence of such splice variants would underline the structural importance of Xirp2 for the sarcomere.



# Bibliography

- Abe, T., Takano, K., Suzuki, A., Shimada, Y., Inagaki, M., Sato, N., Obinata, T., and Endo, T. (2004). Myocyte differentiation generates nuclear invaginations traversed by myofibrils associating with sarcomeric protein mRNAs. *J Cell Sci*, **117**(Pt 26), 6523–6534.
- Agarkova, I. and Perriard, J.-C. (2005). The m-band: an elastic web that crosslinks thick filaments in the center of the sarcomere. *Trends Cell Biol*, **15**(9), 477–485.
- Agarkova, I., Schoenauer, R., Ehler, E., Carlsson, L., Carlsson, E., Thornell, L.-E., and Perriard, J.-C. (2004). The molecular composition of the sarcomeric m-band correlates with muscle fiber type. *Eur J Cell Biol*, **83**(5), 193–204.
- Anastasi, G., Cutroneo, G., Gaeta, R., Mauro, D. D., Arco, A., Consolo, A., Santoro, G., Trimarchi, F., and Favaloro, A. (2009). Dystrophin-glycoprotein complex and vinculin-talin-integrin system in human adult cardiac muscle. *Int J Mol Med*, **23**(2), 149–159.
- Araya, E., Berthier, C., Kim, E., Yeung, T., Wang, X., and Helfman, D. M. (2002). Regulation of coiled-coil assembly in tropomyosins. *J Struct Biol*, **137**(1-2), 176–183.
- Arber, S., Halder, G., and Caroni, P. (1994). Muscle lim protein, a novel essential regulator of myogenesis, promotes myogenic differentiation. *Cell*, **79**(2), 221–231.
- Askari, J. A., Tynan, C. J., Webb, S. E. D., Martin-Fernandez, M. L., Ballestrem, C., and Humphries, M. J. (2010). Focal adhesions are sites of integrin extension. *J Cell Biol*, **188**(6), 891–903.
- Au, Y., Atkinson, R. A., Guerrini, R., Kelly, G., Joseph, C., Martin, S. R., Muskett, F. W., Pallavicini, A., Faulkner, G., and Pastore, A. (2004). Solution structure of zasp pdz domain; implications for sarcomere ultrastructure and enigma family redundancy. *Structure*, **12**(4), 611–622.

- Bajanca, F. and Thorsteinsdóttir, S. (2002). Integrin expression patterns during early limb muscle development in the mouse. *Mech Dev*, **119 Suppl 1**, S131–S134.
- Bajanca, F., Luz, M., Raymond, K., Martins, G. G., Sonnenberg, A., Tajbakhsh, S., Buckingham, M., and Thorsteinsdóttir, S. (2006). Integrin  $\alpha 6\beta 1$ -laminin interactions regulate early myotome formation in the mouse embryo. *Development*, **133**(9), 1635–1644.
- Bang, M. L., Mudry, R. E., McElhinny, A. S., Trombitás, K., Geach, A. J., Yamasaki, R., Sorimachi, H., Granzier, H., Gregorio, C. C., and Labeit, S. (2001). Myopalladin, a novel 145-kilodalton sarcomeric protein with multiple roles in z-disc and i-band protein assemblies. *J Cell Biol*, **153**(2), 413–427.
- Bang, M.-L., Gregorio, C., and Labeit, S. (2002). Molecular dissection of the interaction of desmin with the c-terminal region of nebulin. *J Struct Biol*, **137**(1-2), 119–127.
- Bang, M.-L., Li, X., Littlefield, R., Bremner, S., Thor, A., Knowlton, K. U., Lieber, R. L., and Chen, J. (2006). Nebulin-deficient mice exhibit shorter thin filament lengths and reduced contractile function in skeletal muscle. *J Cell Biol*, **173**(6), 905–916.
- Bang, M.-L., Caremani, M., Brunello, E., Littlefield, R., Lieber, R. L., Chen, J., Lombardi, V., and Linari, M. (2009). Nebulin plays a direct role in promoting strong actin-myosin interactions. *FASEB J*, **23**(12), 4117–4125.
- Barash, I. A., Mathew, L., Ryan, A. F., Chen, J., and Lieber, R. L. (2004). Rapid muscle-specific gene expression changes after a single bout of eccentric contractions in the mouse. *Am J Physiol Cell Physiol*, **286**(2), C355–C364.
- Barbash, O., Lee, E. K., and Diehl, J. A. (2011). Phosphorylation-dependent regulation of scf(fbx4) dimerization and activity involves a novel component, 14-3-3. *Oncogene*.
- Beatham, J., Gehmlich, K., van der Ven, P. F. M., Sarparanta, J., Williams, D., Underhill, P., Geier, C., Fürst, D. O., Udd, B., and Blanco, G. (2006). Constitutive upregulations of titin-based signalling proteins in ky deficient muscles. *Neuromuscul Disord*, **16**(7), 437–445.
- Beckmann, J. S. and Spencer, M. (2008). Calpain 3, the gatekeeper of proper sarcomere assembly, turnover and maintenance. *Neuromuscul Disord*, **18**(12), 913–921.

- Behrens, J., von Kries, J. P., Kühl, M., Bruhn, L., Wedlich, D., Grosschedl, R., and Birchmeier, W. (1996). Functional interaction of beta-catenin with the transcription factor lef-1. *Nature*, **382**(6592), 638–642.
- Belkin, A. M., Zhidkova, N. I., Balzac, F., Altruda, F., Tomatis, D., Maier, A., Tarone, G., Koteliansky, V. E., and Burridge, K. (1996). Beta 1d integrin displaces the beta 1a isoform in striated muscles: localization at junctional structures and signaling potential in nonmuscle cells. *J Cell Biol*, **132**(1-2), 211–226.
- Benjamin, J. M., Kwiatkowski, A. V., Yang, C., Korobova, F., Pokutta, S., Svitkina, T., Weis, W. I., and Nelson, W. J. (2010). Alpha-catenin regulates actin dynamics independently of cadherin-mediated cell-cell adhesion. *J Cell Biol*, **189**(2), 339–352.
- Biressi, S., Molinaro, M., and Cossu, G. (2007a). Cellular heterogeneity during vertebrate skeletal muscle development. *Dev Biol*, **308**(2), 281–293.
- Biressi, S., Tagliafico, E., Lamorte, G., Monteverde, S., Tenedini, E., Roncaglia, E., Ferrari, S., Ferrari, S., Angelis, M. G. C.-D., Tajbakhsh, S., and Cossu, G. (2007b). Intrinsic phenotypic diversity of embryonic and fetal myoblasts is revealed by genome-wide gene expression analysis on purified cells. *Dev Biol*, **304**(2), 633–651.
- Blau, H. M., Chiu, C. P., and Webster, C. (1983). Cytoplasmic activation of human nuclear genes in stable heterocaryons. *Cell*, **32**(4), 1171–1180.
- Boisguerin, P., Leben, R., Ay, B., Radziwill, G., Moelling, K., Dong, L., and Volkmer-Engert, R. (2004). An improved method for the synthesis of cellulose membrane-bound peptides with free c termini is useful for pdz domain binding studies. *Chem Biol*, **11**(4), 449–459.
- Bonzo, J. R., Norris, A. A., Esham, M., and Moncman, C. L. (2008). The nebulin repeat domain is necessary for proper maintenance of tropomyosin with the cardiac sarcomere. *Exp Cell Res*, **314**(19), 3519–3530.
- Borello, U., Berarducci, B., Murphy, P., Bajard, L., Buffa, V., Piccolo, S., Buckingham, M., and Cossu, G. (2006). The wnt/beta-catenin pathway regulates gli-mediated myf5 expression during somitogenesis. *Development*, **133**(18), 3723–3732.
- Borg, T. K. and Caulfield, J. B. (1980). Morphology of connective tissue in skeletal muscle. *Tissue Cell*, **12**(1), 197–207.

- Borrmann, C. M., Grund, C., Kuhn, C., Hofmann, I., Pieperhoff, S., and Franke, W. W. (2006). The area composita of adhering junctions connecting heart muscle cells of vertebrates. ii. colocalizations of desmosomal and fascia adhaerens molecules in the intercalated disk. *Eur J Cell Biol*, **85**(6), 469–485.
- Bradford, M. M. (1976). A rapid and sensitive method for the quantitation of microgram quantities of protein utilizing the principle of protein-dye binding. *Anal Biochem*, **72**, 248–254.
- Broek, R. W. T., Grefte, S., and den Hoff, J. W. V. (2010). Regulatory factors and cell populations involved in skeletal muscle regeneration. *J Cell Physiol*, **224**(1), 7–16.
- Bruneau, B. G. (2002). Transcriptional regulation of vertebrate cardiac morphogenesis. *Circ Res*, **90**(5), 509–519.
- Buck, D., Hudson, B. D., Ottenheijm, C. A. C., Labeit, S., and Granzier, H. (2010). Differential splicing of the large sarcomeric protein nebulin during skeletal muscle development. *J Struct Biol*, **170**(2), 325–333.
- Buckingham, M. (2006). Myogenic progenitor cells and skeletal myogenesis in vertebrates. *Curr Opin Genet Dev*, **16**(5), 525–532.
- Buckingham, M., Bajard, L., Chang, T., Daubas, P., Hadchouel, J., Meilhac, S., Montarras, D., Rocancourt, D., and Relaix, F. (2003). The formation of skeletal muscle: from somite to limb. *J Anat*, **202**(1), 59–68.
- Burgoyne, T., Muhamad, F., and Luther, P. K. (2008). Visualization of cardiac muscle thin filaments and measurement of their lengths by electron tomography. *Cardiovasc Res*, **77**(4), 707–712.
- Burkin, D. J. and Kaufman, S. J. (1999). The alpha7beta1 integrin in muscle development and disease. *Cell Tissue Res*, **296**(1), 183–190.
- Cachaço, A. S., Pereira, C. S., Pardal, R. G., Bajanca, F., and Thorsteinsdóttir, S. (2005). Integrin repertoire on myogenic cells changes during the course of primary myogenesis in the mouse. *Dev Dyn*, **232**(4), 1069–1078.
- Carballido-López, R. (2006). The bacterial actin-like cytoskeleton. *Microbiol Mol Biol Rev*, **70**(4), 888–909.

- Carlsson, L., Li, Z., Paulin, D., and Thornell, L. E. (1999). Nestin is expressed during development and in myotendinous and neuromuscular junctions in wild type and desmin knock-out mice. *Exp Cell Res*, **251**(1), 213–223.
- Carlsson, L., Yu, J.-G., Moza, M., Carpén, O., and Thornell, L.-E. (2007). Myotilin: a prominent marker of myofibrillar remodelling. *Neuromuscul Disord*, **17**(1), 61–68.
- Carlsson, L., Yu, J.-G., and Thornell, L.-E. (2008). New aspects of obscurin in human striated muscles. *Histochem Cell Biol*, **130**(1), 91–103.
- Castillo, A., Nowak, R., Littlefield, K. P., Fowler, V. M., and Littlefield, R. S. (2009). A nebulin ruler does not dictate thin filament lengths. *Biophys J*, **96**(5), 1856–1865.
- Chandra, M., Mamidi, R., Ford, S., Hidalgo, C., Witt, C., Ottenheijm, C., Labeit, S., and Granzier, H. (2009). Nebulin alters cross-bridge cycling kinetics and increases thin filament activation: a novel mechanism for increasing tension and reducing tension cost. *J Biol Chem*, **284**(45), 30889–30896.
- Chargé, S. B. P. and Rudnicki, M. A. (2004). Cellular and molecular regulation of muscle regeneration. *Physiol Rev*, **84**(1), 209–238.
- Charrasse, S., Causeret, M., Comunale, F., Bonet-Kerrache, A., and Gauthier-Rouvière, C. (2003). Rho gtpases and cadherin-based cell adhesion in skeletal muscle development. *J Muscle Res Cell Motil*, **24**(4-6), 309–313.
- Chen, A. E., Ginty, D. D., and Fan, C.-M. (2005). Protein kinase a signalling via creb controls myogenesis induced by wnt proteins. *Nature*, **433**(7023), 317–322.
- Chereau, D., Boczkowska, M., Skwarek-Maruszczyńska, A., Fujiwara, I., Hayes, D. B., Rebowski, G., Lappalainen, P., Pollard, T. D., and Dominguez, R. (2008). Leiomodin is an actin filament nucleator in muscle cells. *Science*, **320**(5873), 239–243.
- Cherepanova, O., Orlova, A., Galkin, V. E., van der Ven, P. F. M., Fürst, D. O., Jin, J.-P., and Egelman, E. H. (2006). Xin-repeats and nebulin-like repeats bind to f-actin in a similar manner. *J Mol Biol*, **356**(3), 714–723.
- Choi, H.-J., Gross, J. C., Pokutta, S., and Weis, W. I. (2009). Interactions of plakoglobin and beta-catenin with desmosomal cadherins: basis of selective exclusion of alpha- and beta-catenin from desmosomes. *J Biol Chem*, **284**(46), 31776–31788.

- Choi, S., Gustafson-Wagner, E. A., Wang, Q., Harlan, S. M., Sinn, H. W., Lin, J. L.-C., and Lin, J. J.-C. (2007). The intercalated disk protein, mxinalpha, is capable of interacting with beta-catenin and bundling actin filaments [corrected]. *J Biol Chem*, **282**(49), 36024–36036.
- Ciglar, L. and Furlong, E. E. M. (2009). Conservation and divergence in developmental networks: a view from drosophila myogenesis. *Curr Opin Cell Biol*, **21**(6), 754–760.
- Cizkova, M., Cizeron-Clairac, G., Vacher, S., Susini, A., Andrieu, C., Lidereau, R., and Bièche, I. (2010). Gene expression profiling reveals new aspects of pik3ca mutation in eralalpha-positive breast cancer: major implication of the wnt signaling pathway. *PLoS One*, **5**(12), e15647.
- Claeys, K. G., van der Ven, P. F. M., Behin, A., Stojkovic, T., Eymard, B., Dubourg, O., Laforêt, P., Faulkner, G., Richard, P., Vicart, P., Romero, N. B., Stoltenburg, G., Udd, B., Fardeau, M., Voit, T., and Fürst, D. O. (2009). Differential involvement of sarcomeric proteins in myofibrillar myopathies: a morphological and immunohistochemical study. *Acta Neuropathol*, **117**(3), 293–307.
- Clark, K. A., McElhinny, A. S., Beckerle, M. C., and Gregorio, C. C. (2002). Striated muscle cytoarchitecture: an intricate web of form and function. *Annu Rev Cell Dev Biol*, **18**, 637–706.
- Coates, J. C. (2003). Armadillo repeat proteins: beyond the animal kingdom. *Trends Cell Biol*, **13**(9), 463–471.
- Conti, F. J., Felder, A., Monkley, S., Schwander, M., Wood, M. R., Lieber, R., Critchley, D., and Müller, U. (2008). Progressive myopathy and defects in the maintenance of myotendinous junctions in mice that lack talin 1 in skeletal muscle. *Development*, **135**(11), 2043–2053.
- Conti, F. J., Monkley, S. J., Wood, M. R., Critchley, D. R., and Müller, U. (2009). Talin 1 and 2 are required for myoblast fusion, sarcomere assembly and the maintenance of myotendinous junctions. *Development*, **136**(21), 3597–3606.
- Craig, S. W. and Pardo, J. V. (1983). Gamma actin, spectrin, and intermediate filament proteins colocalize with vinculin at costameres, myofibril-to-sarcolemma attachment sites. *Cell Motil*, **3**(5-6), 449–462.



- Critchley, D. R. and Gingras, A. R. (2008). Talin at a glance. *J Cell Sci*, **121**(Pt 9), 1345–1347.
- Dalkilic, I., Schienda, J., Thompson, T. G., and Kunkel, L. M. (2006). Loss of filaminC (fnc) results in severe defects in myogenesis and myotube structure. *Mol Cell Biol*, **26**(17), 6522–6534.
- de Melker, A. A. and Sonnenberg, A. (1999). Integrins: alternative splicing as a mechanism to regulate ligand binding and integrin signaling events. *Bioessays*, **21**(6), 499–509.
- Debrand, E., Jai, Y. E., Spence, L., Bate, N., Praekelt, U., Pritchard, C. A., Monkley, S. J., and Critchley, D. R. (2009). Talin 2 is a large and complex gene encoding multiple transcripts and protein isoforms. *FEBS J*, **276**(6), 1610–1628.
- Delorenzi, M. and Speed, T. (2002). An hmm model for coiled-coil domains and a comparison with pssm-based predictions. *Bioinformatics*, **18**(4), 617–625.
- Demonbreun, A. R., Lapidos, K. A., Heretis, K., Levin, S., Dale, R., Pytel, P., Svensson, E. C., and McNally, E. M. (2010). Myoferlin regulation by nfat in muscle injury, regeneration and repair. *J Cell Sci*, **123**(Pt 14), 2413–2422.
- Deshmukh, L., Tyukhtenko, S., Liu, J., Fox, J. E. B., Qin, J., and Vinogradova, O. (2007). Structural insight into the interaction between platelet integrin  $\alpha$ IIb $\beta$ 3 and cytoskeletal protein skelemin. *J Biol Chem*, **282**(44), 32349–32356.
- Dominguez, R. (2009). Actin filament nucleation and elongation factors—structure–function relationships. *Crit Rev Biochem Mol Biol*, **44**(6), 351–366.
- Du, A., Sanger, J. M., and Sanger, J. W. (2008). Cardiac myofibrillogenesis inside intact embryonic hearts. *Dev Biol*, **318**(2), 236–246.
- Ehler, E., Horowitz, R., Zuppinger, C., Price, R. L., Perriard, E., Leu, M., Caroni, P., Sussman, M., Eppenberger, H. M., and Perriard, J. C. (2001). Alterations at the intercalated disk associated with the absence of muscle lim protein. *J Cell Biol*, **153**(4), 763–772.
- Epstein, J. A., Shapiro, D. N., Cheng, J., Lam, P. Y., and Maas, R. L. (1996). Pax3 modulates expression of the c-met receptor during limb muscle development. *Proc Natl Acad Sci U S A*, **93**(9), 4213–4218.

- Ervasti, J. M. (2003). Costameres: the achilles' heel of herculean muscle. *J Biol Chem*, **278**(16), 13591–13594.
- Ervasti, J. M. (2007). Dystrophin, its interactions with other proteins, and implications for muscular dystrophy. *Biochim Biophys Acta*, **1772**(2), 108–117.
- Esham, M., Bryan, K., Milnes, J., Holmes, W. B., and Moncman, C. L. (2007). Expression of nebulin during early cardiac development. *Cell Motil Cytoskeleton*, **64**(4), 258–273.
- Eulitz, S. (2005). *Charakterisierung der Interaktionen von Xin-Repeat Proteinen mit Aktinzytoskelett-assoziierten Proteinen*. Master's thesis, Institut für Biochemie und Biologie, Abteilung Zellbiologie, Universität Potsdam.
- Ford-Speelman, D. L., Roche, J. A., Bowman, A. L., and Bloch, R. J. (2009). The rho-guanine nucleotide exchange factor domain of obscurin activates rhoa signaling in skeletal muscle. *Mol Biol Cell*, **20**(17), 3905–3917.
- Frank, D., Kuhn, C., Katus, H. A., and Frey, N. (2006). The sarcomeric z-disc: a nodal point in signalling and disease. *J Mol Med*, **84**(6), 446–468.
- Frank, R. (1992). Spot-synthesis: an easy technique for the positionally addressable, parallel chemical synthesis on a membrane support. *Tetrahedron*, **48**(42), 9217 – 9232.
- Franke, W. W., Borrmann, C. M., Grund, C., and Pieperhoff, S. (2006). The area composita of adhering junctions connecting heart muscle cells of vertebrates. i. molecular definition in intercalated disks of cardiomyocytes by immunoelectron microscopy of desmosomal proteins. *Eur J Cell Biol*, **85**(2), 69–82.
- Friedberg, F. (2009). Alternative splicing for members of human mosaic domain super-families. i. the ch and lim domains containing group of proteins. *Mol Biol Rep*, **36**(5), 1059–1081.
- Fürst, D. O., Osborn, M., Nave, R., and Weber, K. (1988). The organization of titin filaments in the half-sarcomere revealed by monoclonal antibodies in immunoelectron microscopy: a map of ten nonrepetitive epitopes starting at the z line extends close to the m line. *J Cell Biol*, **106**(5), 1563–1572.
- Fujita, H., Nedachi, T., and Kanzaki, M. (2007). Accelerated de novo sarcomere assembly by electric pulse stimulation in c2c12 myotubes. *Exp Cell Res*, **313**(9), 1853–1865.

- Fukuzawa, A., Lange, S., Holt, M., Vihola, A., Carmignac, V., Ferreiro, A., Udd, B., and Gautel, M. (2008). Interactions with titin and myomesin target obscurin and obscurin-like 1 to the m-band: implications for hereditary myopathies. *J Cell Sci*, **121**(Pt 11), 1841–1851.
- G. Rabut, J. E. (2005). *Live cell imaging: a laboratory manual*. John Inglis.
- Gareus, R. (2001). *Profilin II : novel functions in membrane trafficking*. Ph.D. thesis, Universität Heidelberg, Fakultät für Biologie.
- Geeves, M. A., Fedorov, R., and Manstein, D. J. (2005). Molecular mechanism of actomyosin-based motility. *Cell Mol Life Sci*, **62**(13), 1462–1477.
- Gehmlich, K., Pinotsis, N., Hayess, K., van der Ven, P. F. M., Milting, H., Banayoso, A. E., Körfer, R., Wilmanns, M., Ehler, E., and Fürst, D. O. (2007). Paxillin and ponsin interact in nascent costameres of muscle cells. *J Mol Biol*, **369**(3), 665–682.
- Gehmlich, K., Hayess, K., Legler, C., Haebel, S., der Ven, P. F. M. V., Ehler, E., and Fürst, D. O. (2010). Ponsin interacts with nck adapter proteins: implications for a role in cytoskeletal remodelling during differentiation of skeletal muscle cells. *Eur J Cell Biol*, **89**(5), 351–364.
- Geier, C., Perrot, A., Ozcelik, C., Binner, P., Counsell, D., Hoffmann, K., Pilz, B., Martiniak, Y., Gehmlich, K., van der Ven, P. F. M., Fürst, D. O., Vornwald, A., von Hodenberg, E., Nürnberg, P., Scheffold, T., Dietz, R., and Osterziel, K. J. (2003). Mutations in the human muscle lim protein gene in families with hypertrophic cardiomyopathy. *Circulation*, **107**(10), 1390–1395.
- Geiger, B., Bershadsky, A., Pankov, R., and Yamada, K. M. (2001). Transmembrane crosstalk between the extracellular matrix–cytoskeleton crosstalk. *Nat Rev Mol Cell Biol*, **2**(11), 793–805.
- Gimona, M., Djinovic-Carugo, K., Kranewitter, W. J., and Winder, S. J. (2002). Functional plasticity of ch domains. *FEBS Lett*, **513**(1), 98–106.
- Glass, D. J. (2005). Skeletal muscle hypertrophy and atrophy signaling pathways. *Int J Biochem Cell Biol*, **37**(10), 1974–1984.

- Goetsch, S. C., Martin, C. M., Embree, L. J., and Garry, D. J. (2005). Myogenic progenitor cells express filamin c in developing and regenerating skeletal muscle. *Stem Cells Dev*, **14**(2), 181–187.
- Goichberg, P., Shtutman, M., Ben-Ze'ev, A., and Geiger, B. (2001). Recruitment of beta-catenin to cadherin-mediated intercellular adhesions is involved in myogenic induction. *J Cell Sci*, **114**(Pt 7), 1309–1319.
- Gontier, Y., Taivainen, A., Fontao, L., Sonnenberg, A., van der Flier, A., Carpen, O., Faulkner, G., and Borradori, L. (2005). The z-disc proteins myotilin and fatz-1 interact with each other and are connected to the sarcolemma via muscle-specific filamins. *J Cell Sci*, **118**(Pt 16), 3739–3749.
- Grosskurth, S. E., Bhattacharya, D., Wang, Q., and Lin, J. J.-C. (2008). Emergence of xin demarcates a key innovation in heart evolution. *PLoS One*, **3**(8), e2857.
- Gruber, M., Söding, J., and Lupas, A. N. (2005). Repper–repeats and their periodicities in fibrous proteins. *Nucleic Acids Res*, **33**(Web Server issue), W239–W243.
- Gruber, M., Söding, J., and Lupas, A. N. (2006). Comparative analysis of coiled-coil prediction methods. *J Struct Biol*, **155**(2), 140–145.
- Gullberg, D., Velling, T., Lohikangas, L., and Tiger, C. F. (1998). Integrins during muscle development and in muscular dystrophies. *Front Biosci*, **3**, D1039–D1050.
- Gustafson-Wagner, E. A., Sinn, H. W., Chen, Y.-L., Wang, D.-Z., Reiter, R. S., Lin, J. L.-C., Yang, B., Williamson, R. A., Chen, J., Lin, C.-I., and Lin, J. J.-C. (2007). Loss of mxinalpha, an intercalated disk protein, results in cardiac hypertrophy and cardiomyopathy with conduction defects. *Am J Physiol Heart Circ Physiol*, **293**(5), H2680–H2692.
- Hansen, S. D. and Mullins, R. D. (2010). Vasp is a processive actin polymerase that requires monomeric actin for barbed end association. *J Cell Biol*, **191**(3), 571–584.
- Hawke, T. J. and Garry, D. J. (2001). Myogenic satellite cells: physiology to molecular biology. *J Appl Physiol*, **91**(2), 534–551.
- Hawke, T. J., Atkinson, D. J., Kanatous, S. B., der Ven, P. F. M. V., Goetsch, S. C., and Garry, D. J. (2007). Xin, an actin binding protein, is expressed within muscle satellite

- cells and newly regenerated skeletal muscle fibers. *Am J Physiol Cell Physiol*, **293**(5), C1636–C1644.
- Heikkinen, O. K., Ruskamo, S., Konarev, P. V., Svergun, D. I., Iivanainen, T., Heikkinen, S. M., Permi, P., Koskela, H., Kilpeläinen, I., and Yläanne, J. (2009). Atomic structures of two novel immunoglobulin-like domain pairs in the actin cross-linking protein filamin. *J Biol Chem*, **284**(37), 25450–25458.
- Himmel, M., Ven, P. F. M. V. D., Stöcklein, W., and Fürst, D. O. (2003). The limits of promiscuity: isoform-specific dimerization of filamins. *Biochemistry*, **42**(2), 430–439.
- Hirschy, A., Schatzmann, F., Ehler, E., and Perriard, J.-C. (2006). Establishment of cardiac cytoarchitecture in the developing mouse heart. *Dev Biol*, **289**(2), 430–441.
- Hollnagel, A., Grund, C., Franke, W. W., and Arnold, H.-H. (2002). The cell adhesion molecule m-cadherin is not essential for muscle development and regeneration. *Mol Cell Biol*, **22**(13), 4760–4770.
- Holmes, W. B. and Moncman, C. L. (2008). Nebulette interacts with filamin c. *Cell Motil Cytoskeleton*, **65**(2), 130–142.
- Hotulainen, P. and Lappalainen, P. (2006). Stress fibers are generated by two distinct actin assembly mechanisms in motile cells. *J Cell Biol*, **173**(3), 383–394.
- Hüttelmaier, S., Mayboroda, O., Harbeck, B., Jarchau, T., Jockusch, B. M., and Rüdiger, M. (1998). The interaction of the cell-contact proteins vasp and vinculin is regulated by phosphatidylinositol-4,5-bisphosphate. *Curr Biol*, **8**(9), 479–488.
- Hu, C.-D. and Kerppola, T. K. (2003). Simultaneous visualization of multiple protein interactions in living cells using multicolor fluorescence complementation analysis. *Nat Biotechnol*, **21**(5), 539–545.
- Huang, H.-T., Brand, O. M., Mathew, M., Ignatiou, C., Ewen, E. P., McCalmon, S. A., and Naya, F. J. (2006). Myomaxin is a novel transcriptional target of mef2a that encodes a xin-related alpha-actinin-interacting protein. *J Biol Chem*, **281**(51), 39370–39379.
- Hughes, A. L. (2001). Evolution of the integrin alpha and beta protein families. *J Mol Evol*, **52**(1), 63–72.
- Humphries, J. D., Byron, A., and Humphries, M. J. (2006). Integrin ligands at a glance. *J Cell Sci*, **119**(Pt 19), 3901–3903.

- Humphries, J. D., Wang, P., Streuli, C., Geiger, B., Humphries, M. J., and Ballestrem, C. (2007). Vinculin controls focal adhesion formation by direct interactions with talin and actin. *J Cell Biol*, **179**(5), 1043–1057.
- Hutcheson, D. A., Zhao, J., Merrell, A., Haldar, M., and Kardon, G. (2009). Embryonic and fetal limb myogenic cells are derived from developmentally distinct progenitors and have different requirements for beta-catenin. *Genes Dev*, **23**(8), 997–1013.
- Hynes, R. O. (2002). Integrins: bidirectional, allosteric signaling machines. *Cell*, **110**(6), 673–687.
- Ikeya, M. and Takada, S. (1998). Wnt signaling from the dorsal neural tube is required for the formation of the medial dermomyotome. *Development*, **125**(24), 4969–4976.
- Inoue, H., Nojima, H., and Okayama, H. (1990). High efficiency transformation of *escherichia coli* with plasmids. *Gene*, **96**(1), 23–28.
- Ithychanda, S. S., Das, M., Ma, Y.-Q., Ding, K., Wang, X., Gupta, S., Wu, C., Plow, E. F., and Qin, J. (2009). Migfilin, a molecular switch in regulation of integrin activation. *J Biol Chem*, **284**(7), 4713–4722.
- Jani, K. and Schöck, F. (2007). Zasp is required for the assembly of functional integrin adhesion sites. *J Cell Biol*, **179**(7), 1583–1597.
- Jat, P. S., Noble, M. D., Ataliotis, P., Tanaka, Y., Yannoutsos, N., Larsen, L., and Kioussis, D. (1991). Direct derivation of conditionally immortal cell lines from an h-2kb-tsa58 transgenic mouse. *Proc Natl Acad Sci U S A*, **88**(12), 5096–5100.
- Jin, J. P. and Wang, K. (1991). Cloning, expression, and protein interaction of human nebulin fragments composed of varying numbers of sequence modules. *J Biol Chem*, **266**(31), 21215–21223.
- Jockusch, B. M. and Isenberg, G. (1981). Interaction of alpha-actinin and vinculin with actin: opposite effects on filament network formation. *Proc Natl Acad Sci U S A*, **78**(5), 3005–3009.
- Jones, D. A., Newham, D. J., Round, J. M., and Tolfree, S. E. (1986). Experimental human muscle damage: morphological changes in relation to other indices of damage. *J Physiol*, **375**, 435–448.



- Kadrmaz, J. L. and Beckerle, M. C. (2004). The lim domain: from the cytoskeleton to the nucleus. *Nat Rev Mol Cell Biol*, **5**(11), 920–931.
- Kandarian, S. C. and Jackman, R. W. (2006). Intracellular signaling during skeletal muscle atrophy. *Muscle Nerve*, **33**(2), 155–165.
- Kassar-Duchossoy, L., Gayraud-Morel, B., Gomès, D., Rocancourt, D., Buckingham, M., Shinin, V., and Tajbakhsh, S. (2004). Mrf4 determines skeletal muscle identity in myf5:myod double-mutant mice. *Nature*, **431**(7007), 466–471.
- Kazmierski, S. T., Antin, P. B., Witt, C. C., Huebner, N., McElhinny, A. S., Labeit, S., and Gregorio, C. C. (2003). The complete mouse nebulin gene sequence and the identification of cardiac nebulin. *J Mol Biol*, **328**(4), 835–846.
- Kerppola, T. K. (2006). Visualization of molecular interactions by fluorescence complementation. *Nat Rev Mol Cell Biol*, **7**(6), 449–456.
- Kerppola, T. K. (2008). Bimolecular fluorescence complementation (bifc) analysis as a probe of protein interactions in living cells. *Annu Rev Biophys*, **37**, 465–487.
- Kühnel, K., Jarchau, T., Wolf, E., Schlichting, I., Walter, U., Wittinghofer, A., and Strelkov, S. V. (2004). The vasp tetramerization domain is a right-handed coiled coil based on a 15-residue repeat. *Proc Natl Acad Sci U S A*, **101**(49), 17027–17032.
- Kimes, B. W. and Brandt, B. L. (1976). Characterization of two putative smooth muscle cell lines from rat thoracic aorta. *Exp Cell Res*, **98**(2), 349–366.
- Knöll, R., Hoshijima, M., Hoffman, H. M., Person, V., Lorenzen-Schmidt, I., Bang, M.-L., Hayashi, T., Shiga, N., Yasukawa, H., Schaper, W., McKenna, W., Yokoyama, M., Schork, N. J., Omens, J. H., McCulloch, A. D., Kimura, A., Gregorio, C. C., Poller, W., Schaper, J., Schultheiss, H. P., and Chien, K. R. (2002). The cardiac mechanical stretch sensor machinery involves a z disc complex that is defective in a subset of human dilated cardiomyopathy. *Cell*, **111**(7), 943–955.
- Kollias, H. D. and McDermott, J. C. (2008). Transforming growth factor-beta and myostatin signaling in skeletal muscle. *J Appl Physiol*, **104**(3), 579–587.
- Koslov, E. R., Maupin, P., Pradhan, D., Morrow, J. S., and Rimm, D. L. (1997). Alpha-catenin can form asymmetric homodimeric complexes and/or heterodimeric complexes with beta-catenin. *J Biol Chem*, **272**(43), 27301–27306.

- Kovanen, V. (2002). Intramuscular extracellular matrix: complex environment of muscle cells. *Exerc Sport Sci Rev*, **30**(1), 20–25.
- Kramerova, I., Kudryashova, E., Wu, B., and Spencer, M. J. (2006). Regulation of the m-cadherin-beta-catenin complex by calpain 3 during terminal stages of myogenic differentiation. *Mol Cell Biol*, **26**(22), 8437–8447.
- Krause, M., Dent, E. W., Bear, J. E., Loureiro, J. J., and Gertler, F. B. (2003). Ena/vasp proteins: regulators of the actin cytoskeleton and cell migration. *Annu Rev Cell Dev Biol*, **19**, 541–564.
- Krauss, R. S., Cole, F., Gaio, U., Takaesu, G., Zhang, W., and Kang, J.-S. (2005). Close encounters: regulation of vertebrate skeletal myogenesis by cell-cell contact. *J Cell Sci*, **118**(Pt 11), 2355–2362.
- Kriegs, J. O., Churakov, G., Kiefmann, M., Jordan, U., Brosius, J., and Schmitz, J. (2006). Retroposed elements as archives for the evolutionary history of placental mammals. *PLoS Biol*, **4**(4), e91.
- Kuang, S., Chargé, S. B., Seale, P., Huh, M., and Rudnicki, M. A. (2006). Distinct roles for pax7 and pax3 in adult regenerative myogenesis. *J Cell Biol*, **172**(1), 103–113.
- Kucharczak, J., Charrasse, S., Comunale, F., Zappulla, J., Robert, B., Teulon-Navarro, I., Pèlerin, A., and Gauthier-Rouvière, C. (2008). R-cadherin expression inhibits myogenesis and induces myoblast transformation via rac1 gtpase. *Cancer Res*, **68**(16), 6559–6568.
- Labeit, S. and Kolmerer, B. (1995). The complete primary structure of human nebulin and its correlation to muscle structure. *J Mol Biol*, **248**(2), 308–315.
- Lad, Y., Kiema, T., Jiang, P., Pentikäinen, O. T., Coles, C. H., Campbell, I. D., Calderwood, D. A., and Yläanne, J. (2007). Structure of three tandem filamin domains reveals auto-inhibition of ligand binding. *EMBO J*, **26**(17), 3993–4004.
- Laemmli, U. K. (1970). Cleavage of structural proteins during the assembly of the head of bacteriophage t4. *Nature*, **227**(5259), 680–685.
- Lange, S., Ouyang, K., Meyer, G., Cui, L., Cheng, H., Lieber, R. L., and Chen, J. (2009). Obscurin determines the architecture of the longitudinal sarcoplasmic reticulum. *J Cell Sci*, **122**(Pt 15), 2640–2650.

- Lee, M.-A., Joo, Y. M., Lee, Y. M., Kim, H. S., Kim, J.-H., Choi, J.-K., Ahn, S.-J., Min, B.-I., and Kim, C.-R. (2008). Archvillin anchors in the z-line of skeletal muscle via the nebulin c-terminus. *Biochem Biophys Res Commun*, **374**(2), 320–324.
- Licha, K., Bhargava, S., Rheinländer, C., Becker, A., Schneider-Mergener, J., and Volkmer-Engert, R. (2000). Highly parallel nano-synthesis of cleavable peptide-dye conjugates on cellulose membranes. *Tetrahedron Letters*, **41**(11), 1711 – 1715.
- Linker, C., Lesbros, C., Gros, J., Burrus, L. W., Rawls, A., and Marcelle, C. (2005). beta-catenin-dependent wnt signalling controls the epithelial organisation of somites through the activation of paraxis. *Development*, **132**(17), 3895–3905.
- Linnemann, A., van der Ven, P. F. M., Vakeel, P., Albinus, B., Simonis, D., Bendas, G., Schenk, J. A., Micheel, B., Kley, R. A., and Fürst, D. O. (2010). The sarcomeric z-disc component myopodin is a multiadapter protein that interacts with filamin and alpha-actinin. *Eur J Cell Biol*, **89**(9), 681–692.
- Louis, H. A., Pino, J. D., Schmeichel, K. L., Pomiès, P., and Beckerle, M. C. (1997). Comparison of three members of the cysteine-rich protein family reveals functional conservation and divergent patterns of gene expression. *J Biol Chem*, **272**(43), 27484–27491.
- Lu, M. and Krauss, R. S. (2010). N-cadherin ligation, but not sonic hedgehog binding, initiates cdo-dependent p38alpha/beta mapk signaling in skeletal myoblasts. *Proc Natl Acad Sci U S A*, **107**(9), 4212–4217.
- Luo, G., Herrera, A. H., and Horowitz, R. (1999). Molecular interactions of n-rap, a nebulin-related protein of striated muscle myotendon junctions and intercalated disks. *Biochemistry*, **38**(19), 6135–6143.
- Luther, P. K. (2009). The vertebrate muscle z-disc: sarcomere anchor for structure and signalling. *J Muscle Res Cell Motil*, **30**(5-6), 171–185.
- Löwe, T., Kley, R. A., van der Ven, P. F. M., Himmel, M., Huebner, A., Vorgerd, M., and Fürst, D. O. (2007). The pathomechanism of filaminopathy: altered biochemical properties explain the cellular phenotype of a protein aggregation myopathy. *Hum Mol Genet*, **16**(11), 1351–1358.

- Ma, K. and Wang, K. (2002). Interaction of nebulin sh3 domain with titin pevk and myopalladin: implications for the signaling and assembly role of titin and nebulin. *FEBS Lett*, **532**(3), 273–278.
- Ma, L., song Gao, J., Guan, Y., Shi, X., Zhang, H., Ayrapetov, M. K., Zhang, Z., Xu, L., Hyun, Y.-M., Kim, M., Zhuang, S., and Chin, Y. E. (2010). Acetylation modulates prolactin receptor dimerization. *Proc Natl Acad Sci U S A*, **107**(45), 19314–19319.
- MacDonald, B. T., Tamai, K., and He, X. (2009). Wnt/beta-catenin signaling: components, mechanisms, and diseases. *Dev Cell*, **17**(1), 9–26.
- Marone, M., Mozzetti, S., Ritis, D. D., Pierelli, L., and Scambia, G. (2001). Semiquantitative rt-pcr analysis to assess the expression levels of multiple transcripts from the same sample. *Biol Proced Online*, **3**, 19–25.
- Mayer, U., Saher, G., Fässler, R., Bornemann, A., Echtermeyer, F., von der Mark, H., Miosge, N., Pöschl, E., and von der Mark, K. (1997). Absence of integrin alpha 7 causes a novel form of muscular dystrophy. *Nat Genet*, **17**(3), 318–323.
- McCalmon, S. A., Desjardins, D. M., Ahmad, S., Davidoff, K. S., Snyder, C. M., Sato, K., Ohashi, K., Kielbasa, O. M., Mathew, M., Ewen, E. P., Walsh, K., Gavras, H., and Naya, F. J. (2010). Modulation of angiotensin ii-mediated cardiac remodeling by the mef2a target gene xirp2. *Circ Res*, **106**(5), 952–960.
- McDonald, K. A., Lakonishok, M., and Horwitz, A. F. (1995). Alpha v and alpha 3 integrin subunits are associated with myofibrils during myofibrillogenesis. *J Cell Sci*, **108** ( Pt 7 ), 2573–2581.
- McDonnell, A. V., Jiang, T., Keating, A. E., and Berger, B. (2006). Paircoil2: improved prediction of coiled coils from sequence. *Bioinformatics*, **22**(3), 356–358.
- McElhinny, A. S., Kolmerer, B., Fowler, V. M., Labeit, S., and Gregorio, C. C. (2001). The n-terminal end of nebulin interacts with tropomodulin at the pointed ends of the thin filaments. *J Biol Chem*, **276**(1), 583–592.
- McElhinny, A. S., Kazmierski, S. T., Labeit, S., and Gregorio, C. C. (2003). Nebulin: the nebulous, multifunctional giant of striated muscle. *Trends Cardiovasc Med*, **13**(5), 195–201.

- McElhinny, A. S., Schwach, C., Valichnac, M., Mount-Patrick, S., and Gregorio, C. C. (2005). Nebulin regulates the assembly and lengths of the thin filaments in striated muscle. *J Cell Biol*, **170**(6), 947–957.
- Merk, N. (2010). *Charakterisierung Xin-Isoform spezifischer Interaktionen*. Master's thesis, Rheinische Friedrich-Wilhelms-Universität Bonn.
- Michael McKinley, V. O. (2009). *Human Anatomy*. McGraw-Hill, second edition edition.
- Millevoi, S., Trombitas, K., Kolmerer, B., Kostin, S., Schaper, J., Pelin, K., Granzier, H., and Labeit, S. (1998). Characterization of nebulin and emerging concepts of their roles for vertebrate z-discs. *J Mol Biol*, **282**(1), 111–123.
- Miroux, B. and Walker, J. E. (1996). Over-production of proteins in escherichia coli: mutant hosts that allow synthesis of some membrane proteins and globular proteins at high levels. *J Mol Biol*, **260**(3), 289–298.
- Männer, J. (2009). The anatomy of cardiac looping: a step towards the understanding of the morphogenesis of several forms of congenital cardiac malformations. *Clin Anat*, **22**(1), 21–35.
- Moerman, D. G. and Williams, B. D. (2006). Sarcomere assembly in *c. elegans* muscle. *WormBook*, pages 1–16.
- Moncman, C. L. and Wang, K. (1995). Nebulette: a 107 kd nebulin-like protein in cardiac muscle. *Cell Motil Cytoskeleton*, **32**(3), 205–225.
- Moncman, C. L. and Wang, K. (1999). Functional dissection of nebulin-like repeats and z-line targeting of sh3 and linker domains. *Cell Motil Cytoskeleton*, **44**(1), 1–22.
- Moncman, C. L. and Wang, K. (2002). Targeted disruption of nebulin protein expression alters cardiac myofibril assembly and function. *Exp Cell Res*, **273**(2), 204–218.
- Morgan, J. E., Beauchamp, J. R., Pagel, C. N., Peckham, M., Ataliotis, P., Jat, P. S., Noble, M. D., Farmer, K., and Partridge, T. A. (1994). Myogenic cell lines derived from transgenic mice carrying a thermolabile t antigen: a model system for the derivation of tissue-specific and mutation-specific cell lines. *Dev Biol*, **162**(2), 486–498.

- Nagai, T., Ibata, K., Park, E. S., Kubota, M., Mikoshiba, K., and Miyawaki, A. (2002). A variant of yellow fluorescent protein with fast and efficient maturation for cell-biological applications. *Nat Biotechnol*, **20**(1), 87–90.
- Nave, R., Fürst, D. O., and Weber, K. (1990). Interaction of alpha-actinin and nebulin in vitro. support for the existence of a fourth filament system in skeletal muscle. *FEBS Lett*, **269**(1), 163–166.
- Nawrotzki, R., Willem, M., Miosge, N., Brinkmeier, H., and Mayer, U. (2003). Defective integrin switch and matrix composition at alpha 7-deficient myotendinous junctions precede the onset of muscular dystrophy in mice. *Hum Mol Genet*, **12**(5), 483–495.
- Nollet, F., Kools, P., and van Roy, F. (2000). Phylogenetic analysis of the cadherin superfamily allows identification of six major subfamilies besides several solitary members. *J Mol Biol*, **299**(3), 551–572.
- Ochi, H. and Westerfield, M. (2007). Signaling networks that regulate muscle development: lessons from zebrafish. *Dev Growth Differ*, **49**(1), 1–11.
- Oda, T., Iwasa, M., Aihara, T., Maéda, Y., and Narita, A. (2009). The nature of the globular- to fibrous-actin transition. *Nature*, **457**(7228), 441–445.
- Ogut, O., Hossain, M. M., and Jin, J.-P. (2003). Interactions between nebulin-like motifs and thin filament regulatory proteins. *J Biol Chem*, **278**(5), 3089–3097.
- Oh, S. W., Pope, R. K., Smith, K. P., Crowley, J. L., Nebl, T., Lawrence, J. B., and Luna, E. J. (2003). Archvillin, a muscle-specific isoform of supervillin, is an early expressed component of the costameric membrane skeleton. *J Cell Sci*, **116**(Pt 11), 2261–2275.
- Olson, E. N. and Williams, R. S. (2000). Remodeling muscles with calcineurin. *Bioessays*, **22**(6), 510–519.
- Otten, J., van der Ven, P. F. M., Vakeel, P., Eulitz, S., Kirfel, G., Brandau, O., Boesl, M., Schrickel, J. W., Linhart, M., Hayess, K., Naya, F. J., Milting, H., Meyer, R., and Fürst, D. O. (2010). Complete loss of murine xin results in a mild cardiac phenotype with altered distribution of intercalated discs. *Cardiovasc Res*, **85**(4), 739–750.
- Oustanina, S., Hause, G., and Braun, T. (2004). Pax7 directs postnatal renewal and propagation of myogenic satellite cells but not their specification. *EMBO J*, **23**(16), 3430–3439.



- Oxford, E. M., Musa, H., Maass, K., Coombs, W., Taffet, S. M., and Delmar, M. (2007). Connexin43 remodeling caused by inhibition of plakophilin-2 expression in cardiac cells. *Circ Res*, **101**(7), 703–711.
- Pacholsky, D., Vakeel, P., Himmel, M., Löwe, T., Stradal, T., Rottner, K., Fürst, D. O., and van der Ven, P. F. M. (2004). Xin repeats define a novel actin-binding motif. *J Cell Sci*, **117**(Pt 22), 5257–5268.
- Pappas, C. T., Bhattacharya, N., Cooper, J. A., and Gregorio, C. C. (2008). Nebulin interacts with capz and regulates thin filament architecture within the z-disc. *Mol Biol Cell*, **19**(5), 1837–1847.
- Pappas, C. T., Krieg, P. A., and Gregorio, C. C. (2010). Nebulin regulates actin filament lengths by a stabilization mechanism. *J Cell Biol*, **189**(5), 859–870.
- Pardo, J. V., Siliciano, J. D., and Craig, S. W. (1983). A vinculin-containing cortical lattice in skeletal muscle: transverse lattice elements (costameres) mark sites of attachment between myofibrils and sarcolemma. *Proc Natl Acad Sci U S A*, **80**(4), 1008–1012.
- Passerieux, E., Rossignol, R., Chopard, A., Carnino, A., Marini, J. F., Letellier, T., and Delage, J. P. (2006). Structural organization of the perimysium in bovine skeletal muscle: Junctional plates and associated intracellular subdomains. *J Struct Biol*, **154**(2), 206–216.
- Passerieux, E., Rossignol, R., Letellier, T., and Delage, J. P. (2007). Physical continuity of the perimysium from myofibers to tendons: involvement in lateral force transmission in skeletal muscle. *J Struct Biol*, **159**(1), 19–28.
- Pentikäinen, U. and Ylännä, J. (2009). The regulation mechanism for the auto-inhibition of binding of human filamin a to integrin. *J Mol Biol*, **393**(3), 644–657.
- Pernigo, S., Fukuzawa, A., Bertz, M., Holt, M., Rief, M., Steiner, R. A., and Gautel, M. (2010). Structural insight into m-band assembly and mechanics from the titin-obscurin-like-1 complex. *Proc Natl Acad Sci U S A*, **107**(7), 2908–2913.
- Pieperhoff, S. and Franke, W. W. (2007). The area composita of adhering junctions connecting heart muscle cells of vertebrates - iv: coalescence and amalgamation of desmosomal and adhaerens junction components - late processes in mammalian heart development. *Eur J Cell Biol*, **86**(7), 377–391.

- Pieperhoff, S., Schumacher, H., and Franke, W. W. (2008). The area composita of adhering junctions connecting heart muscle cells of vertebrates. v. the importance of plakophilin-2 demonstrated by small interference rna-mediated knockdown in cultured rat cardiomyocytes. *Eur J Cell Biol*, **87**(7), 399–411.
- Politou, A. S., Millevoi, S., Gautel, M., Kolmerer, B., and Pastore, A. (1998). Sh3 in muscles: solution structure of the sh3 domain from nebulin. *J Mol Biol*, **276**(1), 189–202.
- Politou, A. S., Spadaccini, R., Joseph, C., Brannetti, B., Guerrini, R., Helmer-Citterich, M., Salvadori, S., Temussi, P. A., and Pastore, A. (2002). The sh3 domain of nebulin binds selectively to type ii peptides: theoretical prediction and experimental validation. *J Mol Biol*, **316**(2), 305–315.
- Pollard, T. D. (2007). Regulation of actin filament assembly by arp2/3 complex and formins. *Annu Rev Biophys Biomol Struct*, **36**, 451–477.
- Purslow, P. P. (2002). The structure and functional significance of variations in the connective tissue within muscle. *Comp Biochem Physiol A Mol Integr Physiol*, **133**(4), 947–966.
- Pyle, W. G. and Solaro, R. J. (2004). At the crossroads of myocardial signaling: the role of z-discs in intracellular signaling and cardiac function. *Circ Res*, **94**(3), 296–305.
- Rüdiger, M., Korneeva, N., Schwienbacher, C., Weiss, E. E., and Jockusch, B. M. (1998). Differential actin organization by vinculin isoforms: implications for cell type-specific microfilament anchorage. *FEBS Lett*, **431**(1), 49–54.
- Relaix, F., Rocancourt, D., Mansouri, A., and Buckingham, M. (2004). Divergent functions of murine pax3 and pax7 in limb muscle development. *Genes Dev*, **18**(9), 1088–1105.
- Relaix, F., Montarras, D., Zaffran, S., Gayraud-Morel, B., Rocancourt, D., Tajbakhsh, S., Mansouri, A., Cumano, A., and Buckingham, M. (2006). Pax3 and pax7 have distinct and overlapping functions in adult muscle progenitor cells. *J Cell Biol*, **172**(1), 91–102.
- Reynolds, J. G., McCalmon, S. A., Tomczyk, T., and Naya, F. J. (2007). Identification and mapping of protein kinase a binding sites in the costameric protein myospryn. *Biochim Biophys Acta*, **1773**(6), 891–902.

- Riazi, A. M., Takeuchi, J. K., Hornberger, L. K., Zaidi, S. H., Amini, F., Coles, J., Bruneau, B. G., and Arsdell, G. S. V. (2009). Nkx2-5 regulates the expression of beta-catenin and gata4 in ventricular myocytes. *PLoS One*, **4**(5), e5698.
- Rimm, D. L., Koslov, E. R., Kebriaei, P., Cianci, C. D., and Morrow, J. S. (1995). Alpha 1(e)-catenin is an actin-binding and -bundling protein mediating the attachment of f-actin to the membrane adhesion complex. *Proc Natl Acad Sci U S A*, **92**(19), 8813–8817.
- Robinson, T. F. and Winegrad, S. (1977). Variation of thin filament length in heart muscles. *Nature*, **267**(5606), 74–75.
- Rohn, J. L. and Baum, B. (2010). Actin and cellular architecture at a glance. *J Cell Sci*, **123**(Pt 2), 155–158.
- Rooney, J. E., Welser, J. V., Dechert, M. A., Flintoff-Dye, N. L., Kaufman, S. J., and Burkin, D. J. (2006). Severe muscular dystrophy in mice that lack dystrophin and alpha7 integrin. *J Cell Sci*, **119**(Pt 11), 2185–2195.
- Ross, R. S. (2002). The extracellular connections: the role of integrins in myocardial remodeling. *J Card Fail*, **8**(6 Suppl), S326–S331.
- Round, J. M., Jones, D. A., and Cambridge, G. (1987). Cellular infiltrates in human skeletal muscle: exercise induced damage as a model for inflammatory muscle disease? *J Neurol Sci*, **82**(1-3), 1–11.
- Rowe, R. W. (1973). The ultrastructure of z disks from white, intermediate, and red fibers of mammalian striated muscles. *J Cell Biol*, **57**(2), 261–277.
- Saiki, R. K., Gelfand, D. H., Stoffel, S., Scharf, S. J., Higuchi, R., Horn, G. T., Mullis, K. B., and Erlich, H. A. (1988). Primer-directed enzymatic amplification of dna with a thermostable dna polymerase. *Science*, **239**(4839), 487–491.
- Samarel, A. M. (2005). Costameres, focal adhesions, and cardiomyocyte mechanotransduction. *Am J Physiol Heart Circ Physiol*, **289**(6), H2291–H2301.
- Sanger, J. M., Mittal, B., Pochapin, M. B., and Sanger, J. W. (1986). Myofibrillogenesis in living cells microinjected with fluorescently labeled alpha-actinin. *J Cell Biol*, **102**(6), 2053–2066.

- Sanger, J. W., Kang, S., Siebrands, C. C., Freeman, N., Du, A., Wang, J., Stout, A. L., and Sanger, J. M. (2005). How to build a myofibril. *J Muscle Res Cell Motil*, **26**(6-8), 343–354.
- Sato, T., Rocancourt, D., Marques, L., Thorsteinsdóttir, S., and Buckingham, M. (2010). A pax3/dmrt2/myf5 regulatory cascade functions at the onset of myogenesis. *PLoS Genet*, **6**(4), e1000897.
- Schoenauer, R., Lange, S., Hirschy, A., Ehler, E., Perriard, J.-C., and Agarkova, I. (2008). Myomesin 3, a novel structural component of the m-band in striated muscle. *J Mol Biol*, **376**(2), 338–351.
- Schröder, E. (2009). *Charakterisierung der Interaktionen zwischen Xin-Repeat Proteinen und deren Liganden in Mensch und Zebrafisch*. Master's thesis, Rheinische Friedrich-Wilhelms-Universität Bonn.
- Schultz, J., Milpetz, F., Bork, P., and Ponting, C. P. (1998). Smart, a simple modular architecture research tool: identification of signaling domains. *Proc Natl Acad Sci U S A*, **95**(11), 5857–5864.
- Schwander, M., Leu, M., Stumm, M., Dorchies, O. M., Ruegg, U. T., Schittny, J., and Müller, U. (2003). Beta1 integrins regulate myoblast fusion and sarcomere assembly. *Dev Cell*, **4**(5), 673–685.
- Sellers, J. R. (2000). Myosins: a diverse superfamily. *Biochim Biophys Acta*, **1496**(1), 3–22.
- Senetar, M. A. and McCann, R. O. (2005). Gene duplication and functional divergence during evolution of the cytoskeletal linker protein talin. *Gene*, **362**, 141–152.
- Senetar, M. A., Moncman, C. L., and McCann, R. O. (2007). Talin2 is induced during striated muscle differentiation and is targeted to stable adhesion complexes in mature muscle. *Cell Motil Cytoskeleton*, **64**(3), 157–173.
- Severs, N. J., Bruce, A. F., Dupont, E., and Rothery, S. (2008). Remodelling of gap junctions and connexin expression in diseased myocardium. *Cardiovasc Res*, **80**(1), 9–19.

- Sewell, W., Sparrow, D. B., Smith, A. J., Gonzalez, D. M., Rappaport, E. F., Dunwoodie, S. L., and Kusumi, K. (2009). Cyclical expression of the notch/wnt regulator nrarp requires modulation by dll3 in somitogenesis. *Dev Biol*, **329**(2), 400–409.
- Shai, S.-Y., Harpf, A. E., Babbitt, C. J., Jordan, M. C., Fishbein, M. C., Chen, J., Omura, M., Leil, T. A., Becker, K. D., Jiang, M., Smith, D. J., Cherry, S. R., Loftus, J. C., and Ross, R. S. (2002). Cardiac myocyte-specific excision of the beta1 integrin gene results in myocardial fibrosis and cardiac failure. *Circ Res*, **90**(4), 458–464.
- Sharp, W. W., Simpson, D. G., Borg, T. K., Samarel, A. M., and Terracio, L. (1997). Mechanical forces regulate focal adhesion and costamere assembly in cardiac myocytes. *Am J Physiol*, **273**(2 Pt 2), H546–H556.
- Shattil, S. J., Kim, C., and Ginsberg, M. H. (2010). The final steps of integrin activation: the end game. *Nat Rev Mol Cell Biol*, **11**(4), 288–300.
- Shatunov, A., Olivé, M., Odgerel, Z., Stadelmann-Nessler, C., Irlbacher, K., van Landeghem, F., Bayarsaikhan, M., Lee, H.-S., Goudeau, B., Chinnery, P. F., Straub, V., Hilton-Jones, D., Damian, M. S., Kaminska, A., Vicart, P., Bushby, K., Dalakas, M. C., Sambuughin, N., Ferrer, I., Goebel, H. H., and Goldfarb, L. G. (2009). In-frame deletion in the seventh immunoglobulin-like repeat of filamin c in a family with myofibrillar myopathy. *Eur J Hum Genet*, **17**(5), 656–663.
- Sinn, H. W., Balsamo, J., Lilien, J., and Lin, J. J.-C. (2002). Localization of the novel xin protein to the adherens junction complex in cardiac and skeletal muscle during development. *Dev Dyn*, **225**(1), 1–13.
- Sjöblom, B., Ylänne, J., and Djinovic-Carugo, K. (2008). Novel structural insights into f-actin-binding and novel functions of calponin homology domains. *Curr Opin Struct Biol*, **18**(6), 702–708.
- Snyder, M., Huang, X.-Y., and Zhang, J. J. (2010). Stat3 directly controls the expression of tbx5, nkx2.5, and gata4 and is essential for cardiomyocyte differentiation of p19cl6 cells. *J Biol Chem*.
- Sparks, A. B., Rider, J. E., Hoffman, N. G., Fowlkes, D. M., Quillam, L. A., and Kay, B. K. (1996). Distinct ligand preferences of src homology 3 domains from src, yes, abl, cortactin, p53bp2, plcgamma, crk, and grb2. *Proc Natl Acad Sci U S A*, **93**(4), 1540–1544.

- Sparrow, J., Hughes, S. M., and Segalat, L. (2008). Other model organisms for sarcomeric muscle diseases. *Adv Exp Med Biol*, **642**, 192–206.
- Sparrow, J. C. and Schöck, F. (2009). The initial steps of myofibril assembly: integrins pave the way. *Nat Rev Mol Cell Biol*, **10**(4), 293–298.
- Steinhagen, A. (2009). *Charakterisierung von Xin-Repeat Proteinen und ihren Interaktionspartnern im Zebrafisch*. Master's thesis, Rheinische-Friedrich-Wilhelms Universität Bonn.
- Takano, K., Watanabe-Takano, H., Suetsugu, S., Kurita, S., Tsujita, K., Kimura, S., Karatsu, T., Takenawa, T., and Endo, T. (2010). Nebulin and n-wasp cooperate to cause igf-1-induced sarcomeric actin filament formation. *Science*, **330**(6010), 1536–1540.
- Taniguchi, K., Takeya, R., Suetsugu, S., Kan-O, M., Narusawa, M., Shiose, A., Tominaga, R., and Sumimoto, H. (2009). Mammalian formin fhod3 regulates actin assembly and sarcomere organization in striated muscles. *J Biol Chem*, **284**(43), 29873–29881.
- Thompson, T. G., Chan, Y. M., Hack, A. A., Brosius, M., Rajala, M., Lidov, H. G., McNally, E. M., Watkins, S., and Kunkel, L. M. (2000). Filamin 2 (fln2): A muscle-specific sarcoglycan interacting protein. *J Cell Biol*, **148**(1), 115–126.
- Thornell, L. E., Holmbom, B., Eriksson, A., Reiz, S., Marklund, S., and Näslund, U. (1992). Enzyme and immunohistochemical assessment of myocardial damage after ischaemia and reperfusion in a closed-chest pig model. *Histochemistry*, **98**(6), 341–353.
- Tokuyasu, K. T. (1989). Immunocytochemical studies of cardiac myofibrillogenesis in early chick embryos. iii. generation of fasciae adherentes and costameres. *J Cell Biol*, **108**(1), 43–53.
- Tonino, P., Pappas, C. T., Hudson, B. D., Labeit, S., Gregorio, C. C., and Granzier, H. (2010). Reduced myofibrillar connectivity and increased z-disk width in nebulin-deficient skeletal muscle. *J Cell Sci*, **123**(Pt 3), 384–391.
- Trotter, J. A. (2002). Structure-function considerations of muscle-tendon junctions. *Comp Biochem Physiol A Mol Integr Physiol*, **133**(4), 1127–1133.
- van der Ven, P. F., Schaart, G., Jap, P. H., Sengers, R. C., Stadhouders, A. M., and Ramaekers, F. C. (1992). Differentiation of human skeletal muscle cells in culture:



- maturation as indicated by titin and desmin striation. *Cell Tissue Res*, **270**(1), 189–198.
- van der Ven, P. F., Obermann, W. M., Lemke, B., Gautel, M., Weber, K., and Fürst, D. O. (2000a). Characterization of muscle filamin isoforms suggests a possible role of gamma-filamin/abp-1 in sarcomeric z-disc formation. *Cell Motil Cytoskeleton*, **45**(2), 149–162.
- van der Ven, P. F., Wiesner, S., Salmikangas, P., Auerbach, D., Himmel, M., Kempa, S., Hayess, K., Pacholsky, D., Taivainen, A., Schröder, R., Carpén, O., and Fürst, D. O. (2000b). Indications for a novel muscular dystrophy pathway. gamma-filamin, the muscle-specific filamin isoform, interacts with myotilin. *J Cell Biol*, **151**(2), 235–248.
- van der Ven, P. F. M., Ehler, E., Vakeel, P., Eulitz, S., Schenk, J. A., Milting, H., Micheel, B., and Fürst, D. O. (2006). Unusual splicing events result in distinct xin isoforms that associate differentially with filamin c and mena/vasp. *Exp Cell Res*, **312**(11), 2154–2167.
- Venuti, J. M., Morris, J. H., Vivian, J. L., Olson, E. N., and Klein, W. H. (1995). Myogenin is required for late but not early aspects of myogenesis during mouse development. *J Cell Biol*, **128**(4), 563–576.
- Vinkemeier, U., Obermann, W., Weber, K., and Fürst, D. O. (1993). The globular head domain of titin extends into the center of the sarcomeric m band. cDNA cloning, epitope mapping and immunoelectron microscopy of two titin-associated proteins. *J Cell Sci*, **106** ( Pt 1), 319–330.
- Vorgerd, M., van der Ven, P. F. M., Bruchertseifer, V., Löwe, T., Kley, R. A., Schröder, R., Lochmüller, H., Himmel, M., Koehler, K., Fürst, D. O., and Huebner, A. (2005). A mutation in the dimerization domain of filamin c causes a novel type of autosomal dominant myofibrillar myopathy. *Am J Hum Genet*, **77**(2), 297–304.
- Wagers, A. J. and Conboy, I. M. (2005). Cellular and molecular signatures of muscle regeneration: current concepts and controversies in adult myogenesis. *Cell*, **122**(5), 659–667.
- Wang, C.-L. A. and Coluccio, L. M. (2010). New insights into the regulation of the actin cytoskeleton by tropomyosin. *Int Rev Cell Mol Biol*, **281**, 91–128.

- Wang, D. Z., Hu, X., Lin, J. L., Kitten, G. T., Solursh, M., and Lin, J. J. (1996). Differential displaying of mRNAs from the atrioventricular region of developing chicken hearts at stages 15 and 21. *Front Biosci*, **1**, a1–15.
- Wang, D. Z., Reiter, R. S., Lin, J. L., Wang, Q., Williams, H. S., Krob, S. L., Schultheiss, T. M., Evans, S., and Lin, J. J. (1999). Requirement of a novel gene, *xin*, in cardiac morphogenesis. *Development*, **126**(6), 1281–1294.
- Wang, J., Shaner, N., Mittal, B., Zhou, Q., Chen, J., Sanger, J. M., and Sanger, J. W. (2005). Dynamics of z-band based proteins in developing skeletal muscle cells. *Cell Motil Cytoskeleton*, **61**(1), 34–48.
- Wang, Q., Lin, J. L.-C., Reinking, B. E., Feng, H.-Z., Chan, F.-C., Lin, C.-I., Jin, J.-P., Gustafson-Wagner, E. A., Scholz, T. D., Yang, B., and Lin, J. J.-C. (2010). Essential roles of an intercalated disc protein, *mxinbeta*, in postnatal heart growth and survival. *Circ Res*, **106**(9), 1468–1478.
- Wehland, J., Henkart, M., Klausner, R., and Sandoval, I. V. (1983). Role of microtubules in the distribution of the golgi apparatus: effect of taxol and microinjected anti-alpha-tubulin antibodies. *Proc Natl Acad Sci U S A*, **80**(14), 4286–4290.
- Weiss, E. E., Kroemker, M., Rüdiger, A. H., Jockusch, B. M., and Rüdiger, M. (1998). Vinculin is part of the cadherin-catenin junctional complex: complex formation between alpha-catenin and vinculin. *J Cell Biol*, **141**(3), 755–764.
- Welser, J. V., Rooney, J. E., Cohen, N. C., Gurple, P. B., Singer, C. A., Evans, R. A., Haines, B. A., and Burkin, D. J. (2009). Myotendinous junction defects and reduced force transmission in mice that lack alpha7 integrin and utrophin. *Am J Pathol*, **175**(4), 1545–1554.
- Wen, K.-K., Rubenstein, P. A., and DeMali, K. A. (2009). Vinculin nucleates actin polymerization and modifies actin filament structure. *J Biol Chem*, **284**(44), 30463–30473.
- Winder, S. J. and Ayscough, K. R. (2005). Actin-binding proteins. *J Cell Sci*, **118**(Pt 4), 651–654.
- Witt, C. C., Burkart, C., Labeit, D., McNabb, M., Wu, Y., Granzier, H., and Labeit, S. (2006). Nebulin regulates thin filament length, contractility, and z-disk structure in vivo. *EMBO J*, **25**(16), 3843–3855.

- Witt, S., Zieseniss, A., Fock, U., Jockusch, B. M., and Illenberger, S. (2004). Comparative biochemical analysis suggests that vinculin and metavinculin cooperate in muscular adhesion sites. *J Biol Chem*, **279**(30), 31533–31543.
- Wolf, E., Kim, P. S., and Berger, B. (1997). Multicoil: a program for predicting two- and three-stranded coiled coils. *Protein Sci*, **6**(6), 1179–1189.
- Yamada, S., Pokutta, S., Drees, F., Weis, W. I., and Nelson, W. J. (2005). Deconstructing the cadherin-catenin-actin complex. *Cell*, **123**(5), 889–901.
- Yu, J.-G. and Russell, B. (2005). Cardiomyocyte remodeling and sarcomere addition after uniaxial static strain in vitro. *J Histochem Cytochem*, **53**(7), 839–844.
- Yu, J.-G. and Thornell, L.-E. (2002). Desmin and actin alterations in human muscles affected by delayed onset muscle soreness: a high resolution immunocytochemical study. *Histochem Cell Biol*, **118**(2), 171–179.
- Yu, J.-G., Malm, C., and Thornell, L.-E. (2002). Eccentric contractions leading to doms do not cause loss of desmin nor fibre necrosis in human muscle. *Histochem Cell Biol*, **118**(1), 29–34.
- Yu, J.-G., Fürst, D. O., and Thornell, L.-E. (2003). The mode of myofibril remodelling in human skeletal muscle affected by doms induced by eccentric contractions. *Histochem Cell Biol*, **119**(5), 383–393.
- Yu, J.-G., Carlsson, L., and Thornell, L.-E. (2004). Evidence for myofibril remodeling as opposed to myofibril damage in human muscles with doms: an ultrastructural and immunoelectron microscopic study. *Histochem Cell Biol*, **121**(3), 219–227.
- Zaffran, S. and Frasch, M. (2002). Early signals in cardiac development. *Circ Res*, **91**(6), 457–469.
- Zammit, P. S. (2008). All muscle satellite cells are equal, but are some more equal than others? *J Cell Sci*, **121**(Pt 18), 2975–2982.
- Zemljic-Harpf, A. E., Miller, J. C., Henderson, S. A., Wright, A. T., Manso, A. M., Elsherif, L., Dalton, N. D., Thor, A. K., Perkins, G. A., McCulloch, A. D., and Ross, R. S. (2007). Cardiac-myocyte-specific excision of the vinculin gene disrupts cellular junctions, causing sudden death or dilated cardiomyopathy. *Mol Cell Biol*, **27**(21), 7522–7537.

- Zhang, Y., Li, H., Lian, Z., and Li, N. (2010). Myofibroblasts protect myoblasts from intrinsic apoptosis associated with differentiation via b1 integrin-pi3k/akt pathway. *Dev Growth Differ*, **52**(8), 725–733.
- Zhou, A.-X., Hartwig, J. H., and Akyürek, L. M. (2010). Filamins in cell signaling, transcription and organ development. *Trends Cell Biol*, **20**(2), 113–123.
- Ziegler, W. H., Liddington, R. C., and Critchley, D. R. (2006). The structure and regulation of vinculin. *Trends Cell Biol*, **16**(9), 453–460.
- Zimmermann, J., Labudde, D., Jarchau, T., Walter, U., Oschkinat, H., and Ball, L. J. (2002). Relaxation, equilibrium oligomerization, and molecular symmetry of the vasp (336-380) evh2 tetramer. *Biochemistry*, **41**(37), 11143–11151.

# Appendix A

## Abbreviations

ABD	actin-binding domain
ADH	alcohol dehydrogenase
APC	adenomatous polyposis coli tumor suppressor protein
bp	base pairs
BP	bandpass
BSA	bovine serum albumin
C	celsius
CaM	calmodulin
CCD	charge-coupled device
cDNA	complementary DNA
cfu	colony forming units
CH	calponin homology
CMYA	cardiomyopathy-associated
CO <sub>2</sub>	carbon dioxide
ddH <sub>2</sub> O	double distilled water
DGC	dystrophin-glycoprotein complex
DMEM	Dulbecco's modified Eagle medium
DMSO	dimethyl sulfoxide
DNA	deoxyribonucleic acid
DOB-medium	dropout base medium
dpi	dots per inch
E	day of embryonic development
EC	extracellular cadherin (domain)

---

ECL	enhanced chemiluminescence
ECM	extracellular matrix
<i>E. coli</i>	<i>Escherichia coli</i>
EGFP	enhanced green fluorescent protein
EDTA	ethylenediaminetetraacetic acid
EGS	ethylene glycol bis[sulfosuccinimidylsuccinate]
EVH	ena/VASP homology
FCS	fetal calf serum
fig.	figure
Fn	fibronectin type
FP	fluorescent protein
FRAP	fluorescence recovery after photobleaching
FT	beam splitter filter transmission from ... nm
GAPDH	glyceraldehyde 3-phosphate dehydrogenase
h	hour
H-2K	H-2K <sup>B</sup> -tsA58
HA	human influenza hemagglutinin
HE	high efficiency
HEK293	human embryonic kidney cells 293
i.e.	that is ( <i>id est</i> , latin)
ICD	intercalated disc
IFN- $\gamma$	interferon- $\gamma$
Ig	immunoglobulin
IMCT	intramuscular connective tissue
IMDM	Iscove's modified Dulbecco's medium
IPTG	isopropyl- $\beta$ -D-thiogalactoside
kDa	kilodalton
l	litre
LiAc	lithium acetate
MPa	mega pascal
MRF	myogenic regulatory factor family
MS	molecular sieve
MTJ	myotendinous junction
NEAA	nonessential amino acids



---

NGS	normal goat serum
NHS	N-hydroxysuccinimide
NJ	neuromuscular junction
NPG	N-propyl gallate
N-RAP	nebulin-related-anchoring protein
NSMF	non-striated myobril
PAGE	polyacrylamide gel electrophoresis
PBS	phosphate buffered saline
PCR	polymerase chain reaction
PEG	polyethylene glycol
PIPES	piperazine-N,N'-bis(2-ethane-sulfonic acid)
PJP	Perimysial Junctional Plate
RNA	ribonucleic acid
RGB	red, green, blue
rpm	rounds per minutes
RT	room temperature
RT-PCR	reverse transcriptase PCR
SDS	sodium dodecyl sulfate
SEM	scanning electron microscope
SH3	src homology 3
skm	skeletal muscle
SV40	simian virus 40
TAg	tumor antigen
TBST	Tris buffered saline plus triton
Tris	Tris-(hydroxymethyl)-aminomethan
U	Units
VASP	vasodilator-stimulated phosphoprotein
X-Gal	5-bromo-4-chloro-3-indolyl- $\beta$ -D-galactopyranoside
YFP	yellow fluorescent protein

# Appendix B

## Sequences of Primers

Name	Sequence	Fragment
moXinC 1f	TTT <i>ACGCGT</i> ATGCTTCCAAGAAAGAAACCC	mXin C
moXinC 1f	TTT <i>GTCGAC</i> ATGCTTCCAAGAAAGAAACCC	mXin C
moXin endrev	TTT <i>GTCGAC</i> CTGGGCAGCCGGGTGGAAGTT	mXin C
moXin endrev	TTT <i>GCGGCCGC</i> CTGGGCAGCCGGGTGGAAGTT	mXin C (pGEX-6P-3)
Xin 132f	TTT <i>ACGCGT</i> ATGGCCGACACCCAGACACAG	Xin A+B, 1-R16
Xin 247f	TTT <i>ACGCGT</i> TCTGAGGAACCCACCGAGGG	Xin R1-R16
Xin 2269f	TTT <i>ACGCGT</i> AGCCCCTCAGGCAACAGGATG	Xin A $\Delta$ rep
Xin 2378r	TTT <i>GTCGAC</i> GTTGCCCCCTTGGATGCTCTC	Xin 1-R16, R1-R16
Xin 3490f	TTT <i>ACGCGT</i> GTCAGTAGGGAAGAGCAAGC	Xin PR3+4
Xin 3953f	TTT <i>ACGCGT</i> ATGCCCCCAAAGAAGAAGCCG	Xin C, PR4, PR4+CC
Xin 4380r	TTT <i>GTCGAC</i> TGTAGCCTGATTCTTGGTGG	Xin PR3+4, PR4
Xin endrev	TTT <i>GTCGAC</i> CTGGGCAGCTGGCTGGGAGTAG	Xin A+C, A $\Delta$ rep
Xinsplev	TTT <i>GTCGAC</i> CCAGCAGCTTTCTGGGGGCTGCTGGGATC	Xin B
Xin SSMSS rev	TTT <i>GTCGAC</i> CTGGAGGCTAGACATGGAGC	Xin PR4+CC

Table B.1: Primers used for cloning of Xin fragments. Recognition sites of restriction endonucleases are depicted in *italic*.

Name	Sequence	Fragment
hXIRP2 3136f	TTT <i>ACGCGT</i> ATGGAAAGGTCCTTGAATCC	Xirp2 PR2-6
hXIRP2 3944f	TTT <i>ACGCGT</i> AATGAAACTAGAGTAGAAAAG	Xirp2 degrep
hXIRP2 6678r	TTT <i>GTCGAC</i> GGTTGCCAGTTCAACTTTGGG	Xirp2 PR2-6
hXIRP2 9981r	TTT <i>GTCGAC</i> TGAAAATTCTGCTTGTCTGCC	Xirp2 FBS
hXIRP2 CCfw	TTT <i>ACGCGT</i> CCCAAAGTTGAACTGGCAACC	Xirp2 CC
hXIRP2 CCendr	TTT <i>GTCGAC</i> ATGATGAGCTGCTACTTG	Xirp2 CC
hXR2 degrep rev	TTT <i>GTCGAC</i> TGACTTGAGTGTGGCTAG	Xirp2 degrep
huxlp 7764f	TTT <i>ACGCGT</i> CCCGTTCCAATTGTAGAGAAG	Xirp2 FBS
huxlp repf	TTT <i>ACGCGT</i> TTCAGCAGATGTGCAACAAGCC	Xirp2 rep
huxlp repr	TTT <i>GTCGAC</i> GGTTTCTTTAATGCTGTTGCC	Xirp2 rep

Table B.2: Primers used for cloning of Xirp2 fragments. Recognition sites of restriction endonucleases are depicted in *italic*.

Name	Sequence	Fragment
hu NEBm180 f	TTT <i>ACGCGT</i> GAGAACCTGGGGAAAGCAAC	NEB m180
nebsh3stop	TTT <i>GTCGAC</i> CCTAAATAGCTTCAACGTAGTT	NEB m180
huNET1f	TTT <i>ACGCGT</i> ATGAGGGTCCCTGTATTTGAG	NET FL
hu NET L f	TTT <i>ACGCGT</i> ATCTTCGACCTTGATCCC	NET SH3+L
huNETSH3f	TTT <i>ACGCGT</i> GCCATGTACGATTACAGTGCC	NET SH3
netsh3stop	TTT <i>GTCGAC</i> TTAATTAACAAACTCAATGTA	NET FL, SH3+L, SH3

Table B.3: Primers used for cloning of nebulin and nebulette fragments. The primers were designed according to the cDNA sequences with the accession numbers NM 004543 and NM 006393 of nebulin and nebulette, respectively. Recognition sites of restriction endonucleases are depicted in *italic*.

Name	Sequence	Fragment
hu KIAA1102 DKFZ fw	TTT <i>ACGCGT</i> ATGAGATACGGTCCGAGAAC	LIMCH1 CC1+2
hu KIAA1102 fusion rev	TTT <i>GTCGAC</i> TTGTCGTCCTCTTCCCTCAGCTGG	LIMCH1 FL, N-term
KIAA1102 1f	TTT <i>ACGCGT</i> ATGGCTTGTCCCGCTCTCGG	LIMCH1 FL, N-term
KIAA1102 F5 fw	TTT <i>ACGCGT</i> AAGAAGCTGTGCTCTTCCTGT	LIMCH1 LIM
KIAA1102endr	TTT <i>GTCGAC</i> CAATGTTGTAGGCTGCCCGG	LIMCH1 FL, CC1+2, CC2, LIM
KIAA XS26 fw	TTT <i>ACGCGT</i> AAGGTGGTAAAGCCAAAATCTCCA	LIMCH1 CC2

Table B.4: Primers used for cloning of LIMCH1 fragments. Recognition sites of restriction endonucleases are depicted in *italic*.

Name	Sequence
moXinC 328r	GGGGTTTCTTTCTTGGGAAGC
moXinEx1 95f	GGCTAGACACCCAAAAGCAC
moXinEx2b RT1f	CCACTCCTGCCACTGGGGTTACTCA
moXinEx2b-c fw	CATCCCCAGAAAGGTCAGTG
moXinEx2c RTr	ACTCTGACCTTGGTCTGCCTGGGGT
moXinEx2d RT1r	TTGGGTGGTCAGGATCTT
Xin RT 1r	CCAGCGCATACACTGAACATC

Table B.5: Sequences of primers used for RT-PCR of murine Xin.

Name	Sequence
moXIRP2 Ex1 RTf	ACTGGGAAATTTGCTGTGTG
moXIRP2 Ex5 RTf	CTTGAAAAGCACACTGAGGAAAC
moXIRP2 Ex6 RTf	CTTCCTCCGCTCTGATAAAG
moXIRP2 Ex7 RTr	GCCTGGTTGAAGTATAAGAA
moXIRP2 Ex8 RTr	CCATTGGATAAACTGTCTTT
XIRP2 RT 1f	GCAGCTTCTCGGCTAATGTCA
XIRP2 RT 1r	AGGCGTTGCAGGTTGAAGTC
XIRP2 RT 2r	TGTTTCCTCAGTGTGCTTTTCAA

Table B.6: Sequences of primers used for RT-PCR of murine Xirp2.

Name	Sequence
mKIAA1102 RT CHf	GAAGTGGATCGAGCAAGTCA
mKIAA1102 RT CHr1	CGAGGTTCTTGACAGTGACC
mKIAA1102 RT LIMf	AGGCGGAAGTCTATAAGCGG
mKIAA1102 RT LIMr	GGCACTTCTGGATCGCATGT
mLIMCH1 Ex7 fw	TCCTTTGACAGCCTGGAT
mLIMCH1 Ex10 rev	ACACCGCATGTCAAACAT
mLIMCH1 muscleEx1 fw	CTGAAGATGACCCGAGCA
mLIMCH1 muscleEx1 rev	TGCTCGGGTCATCTTCAG
mLIMCH1 muscleEx3 rev	ACATCTTCTCGCTGACCC
mLIMCH1 muscleEx5 fw	CACAGATGGTCGTCTCAA

Table B.7: Sequences of primers used for RT-PCR of murine LIMCH1.

# Appendix C

## Vector Maps

**pET23aEEF**

Length: 3.6 kb

Origin: Novagen (pET23a)

- T7 Promotor
- His6-tag
- EEF-tag
- F1 Origin
- ampicillin resistance

```

                T7 Promotor
                ───────────────────►
BglIII
AGATCTCGATCCCGCGAAATTAATACGACTCACTATAGGGAGACCACAACGGTTTCCC

XbaI                      rbs                      NdeI  MluI      SalI
TCTAGAAATAATTTTGTTTAACTTTAAGAAGGAGATATAACATATGACGCGTTTTGTTCGAC

        His6-Tag      Immuno-Tag      XhoI
CACCACCACCACCACCACGAGGAGTTCTGACTCGAGCACCACCACCACCACCACTGAGAT
        H H H H H H  E E F Stop
CCGGCTGCTAACAAAGCCCGAAAGGAAGCTGAGTTGGCTGCTGCCACCGCTGAGCAATAA

                T7-Terminator
CTAGCATAACCCCTTGGGGCCTCTAAACGGGTCTTGAGGGGT
    
```

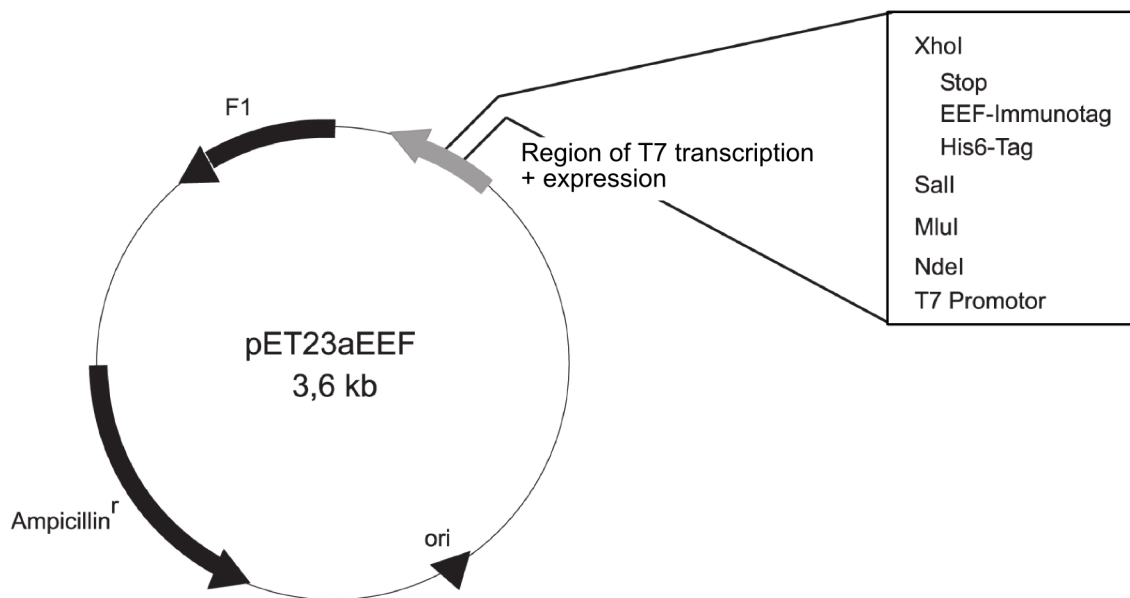


Figure C.1: Vector map pET23aEEF



### pET23aMyc

Length: 3.6 kb

Origin: Novagen (pET23a)

T7 Promotor

His6-tag

c-myc-tag

F1 Origin

ampicillin resistance

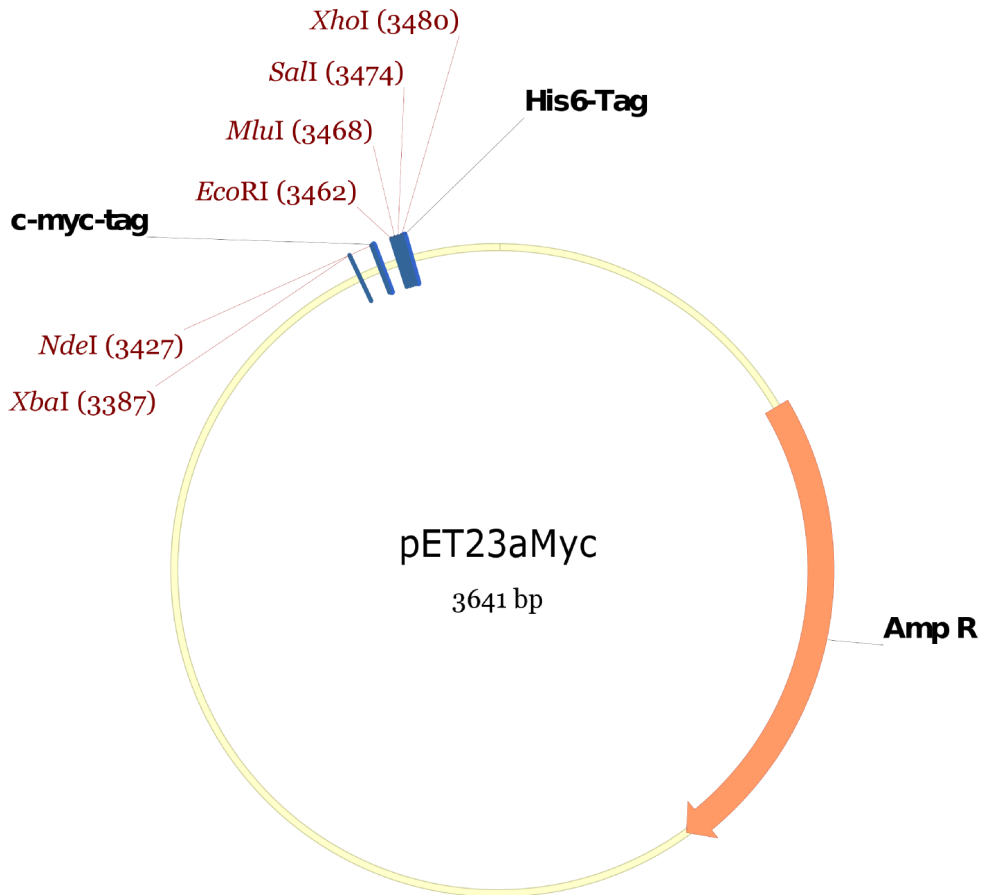
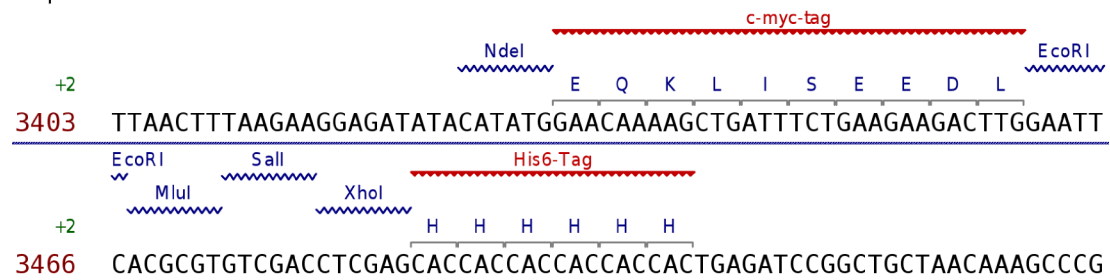


Figure C.2: Vector map pET23aMyc

**pET23aT7**

Length: 3.6 kb

Origin: Novagen (pET23a)

T7 Promotor

His6-tag

T7-tag

F1 Origin

ampicillin resistance

```

          T7 Promotor
          ────────────────────────────────────▶
BgIII
AGATCTCGATCCCGCGAAATTAATACGACTCACTATAGGGAGACCACAACGGTTTCCC

XbaI                                     rbs           NdeI  NheI
TCTAGAAATAATTTTGTTTAACTTTAAGAAGGAGATATACATATGGCTAGCATGACT
                                M   A   S   M   T
                                ┌───────────┐
                                │   Insert   │
                                └───────────┘
      T7-Immuntag          BamHI MluI          SalI
GGTGGACAGCAAATGGGTCGCGGATCCACGCGT          GTCGAC
GG  GG  QQ  MM  GR  GS  TR          VD

XhoI          His6-Tag
CTCGAGCACCACCACCACCACCTGAGATCCGGCTGCTAACAAAGCCCGAAAGGAAG
LEHHHHHH Stop

                                           T7-Terminator
CTGAGTTGGCTGCTGCCACCGCTGAGCAATAACTAGCATAACCCCTTGGGGCCTCTAA
ACGGGTCTTGAGGGGT
    
```

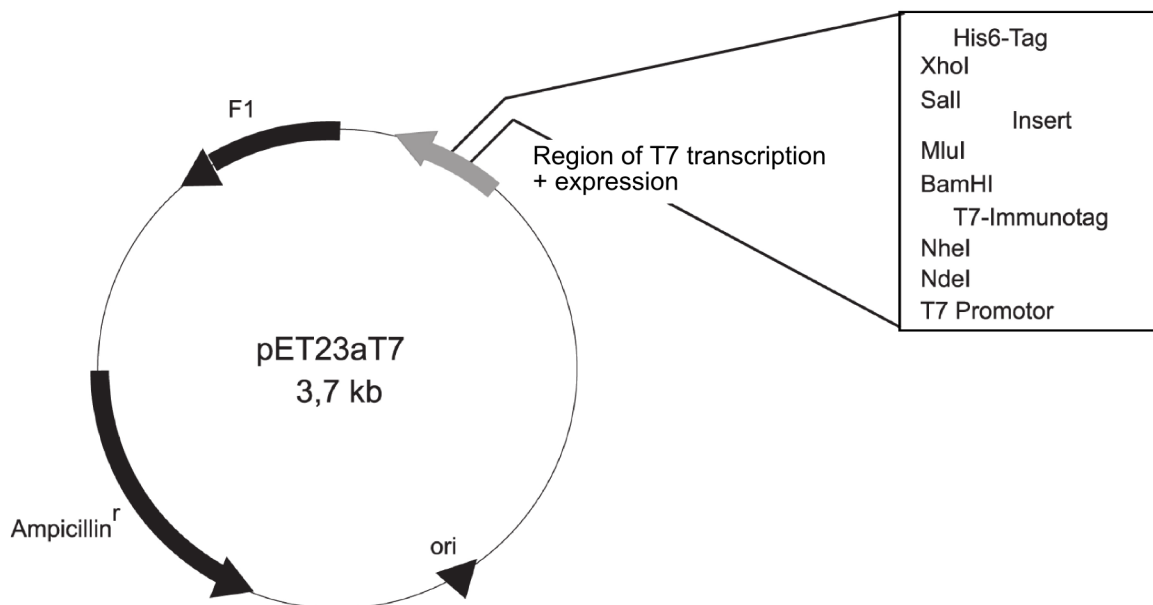


Figure C.3: Vector map pET23aT7

### pET28a

Length: 5.4 kb  
Origin: Novagen

T7 Promotor  
His6-tag (N-terminal)  
T7-tag  
F1 Origin  
kanamycin resistance

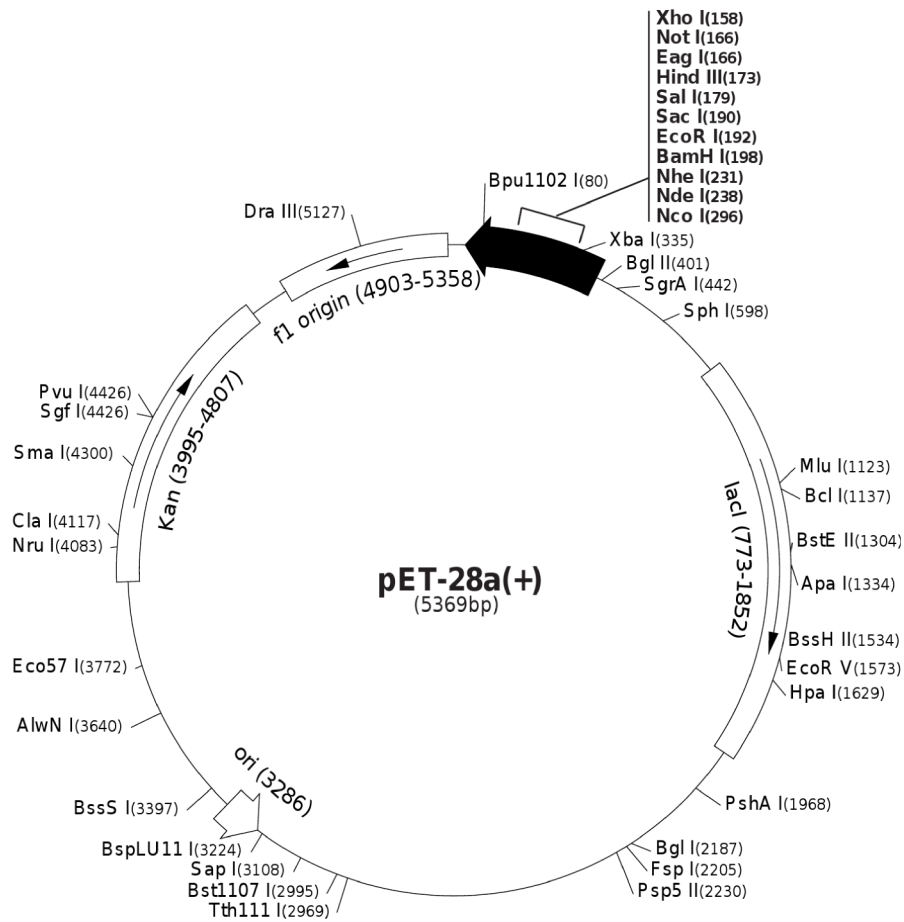
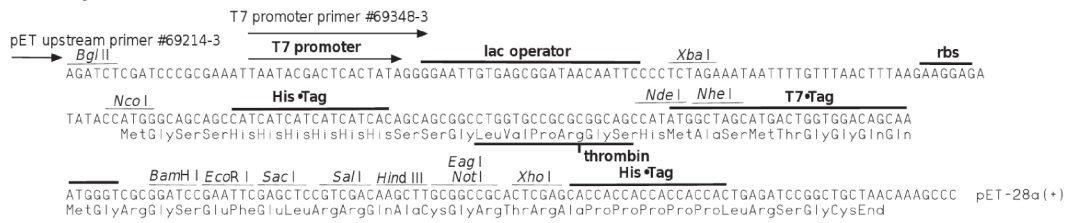


Figure C.4: Vector map pET28a

### pLexPd

Length: 6 kb

Origin: Clontech

TRP1 (tryptophane synthesis in yeast)

P<sub>ADH1</sub> (ADH Promotor)

T<sub>ADH1</sub> (ADH Terminator)

lexA DNA-binding domain

ColE1 Origin

kanamycin resistance

```

CCA AAA AAA GAA TTC ACG CGT CCA TGG TCT AGA GTC GAC TAA TTC GAC
GGT TTT TTT CTT AAG TGC GCA GGT ACC AGA TCT CAG CTG ATT AAG CTG
- - LexA BD EcoRI MluI NcoI XbaI SalI Stop
    
```

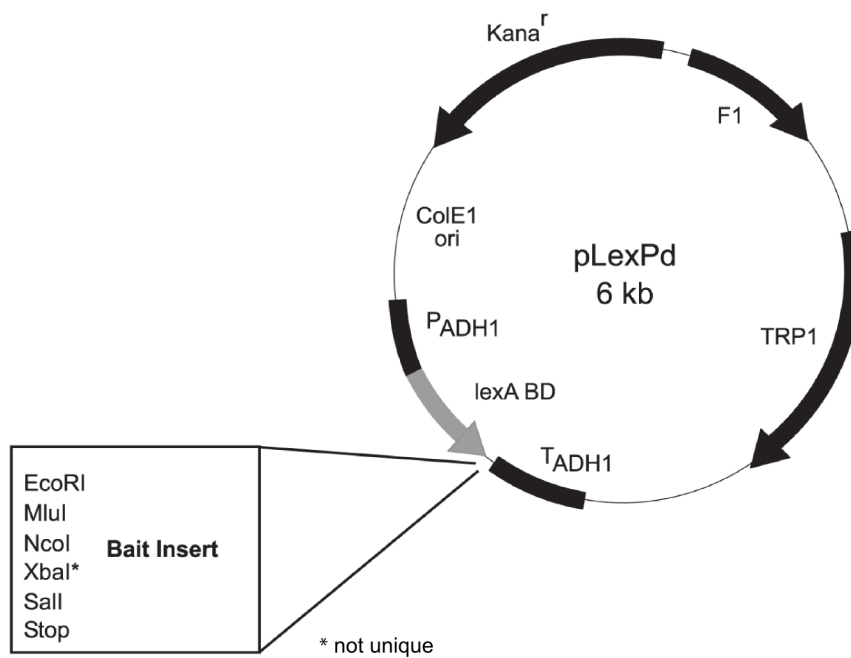


Figure C.5: Vector map pLexPD

**pACT2**

Length: 8.1 kb

Origin: Clontech

LEU2 (leucine synthesis in yeast)

P<sub>ADH1</sub> (ADH Promotor)

T<sub>ADH1</sub> (ADH Terminator)

HA-tag

GAL4 activation domain

ColE1 Origin

ampicillin resistance

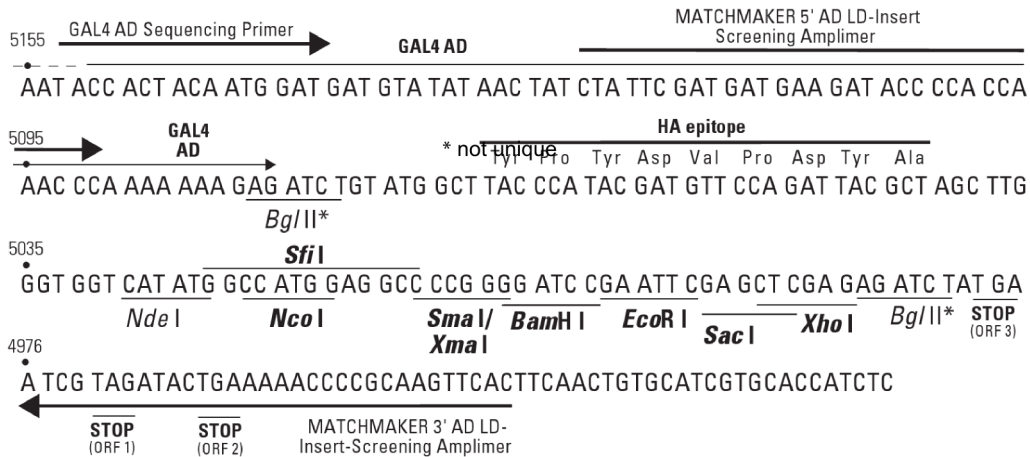
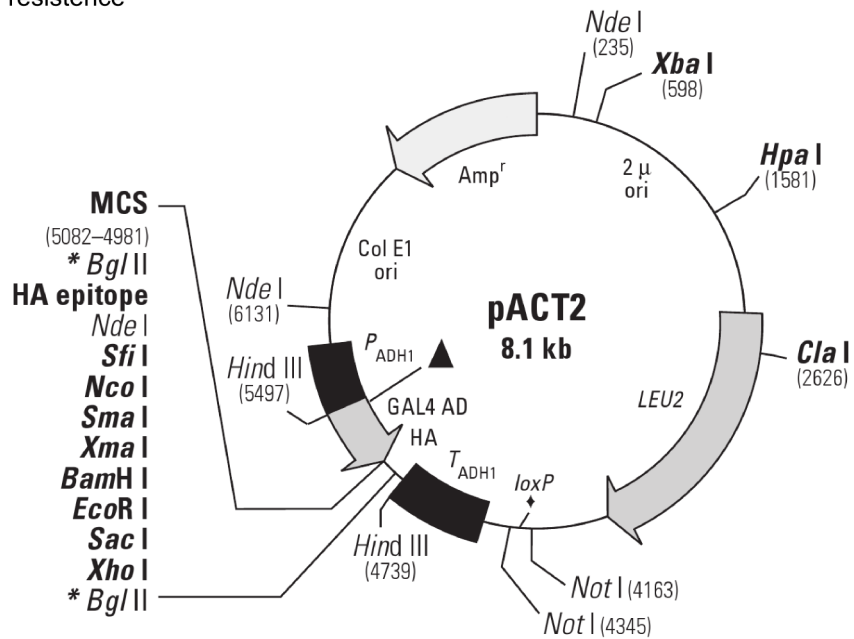


Figure C.6: Vector map pACT2

### Venus NT

Length: 4.7 kb

Origin: Clontech (pECFP-C1)

Cytomegalovirus immediate early gene enhancer/promotor

Venus

kanamycin resistance

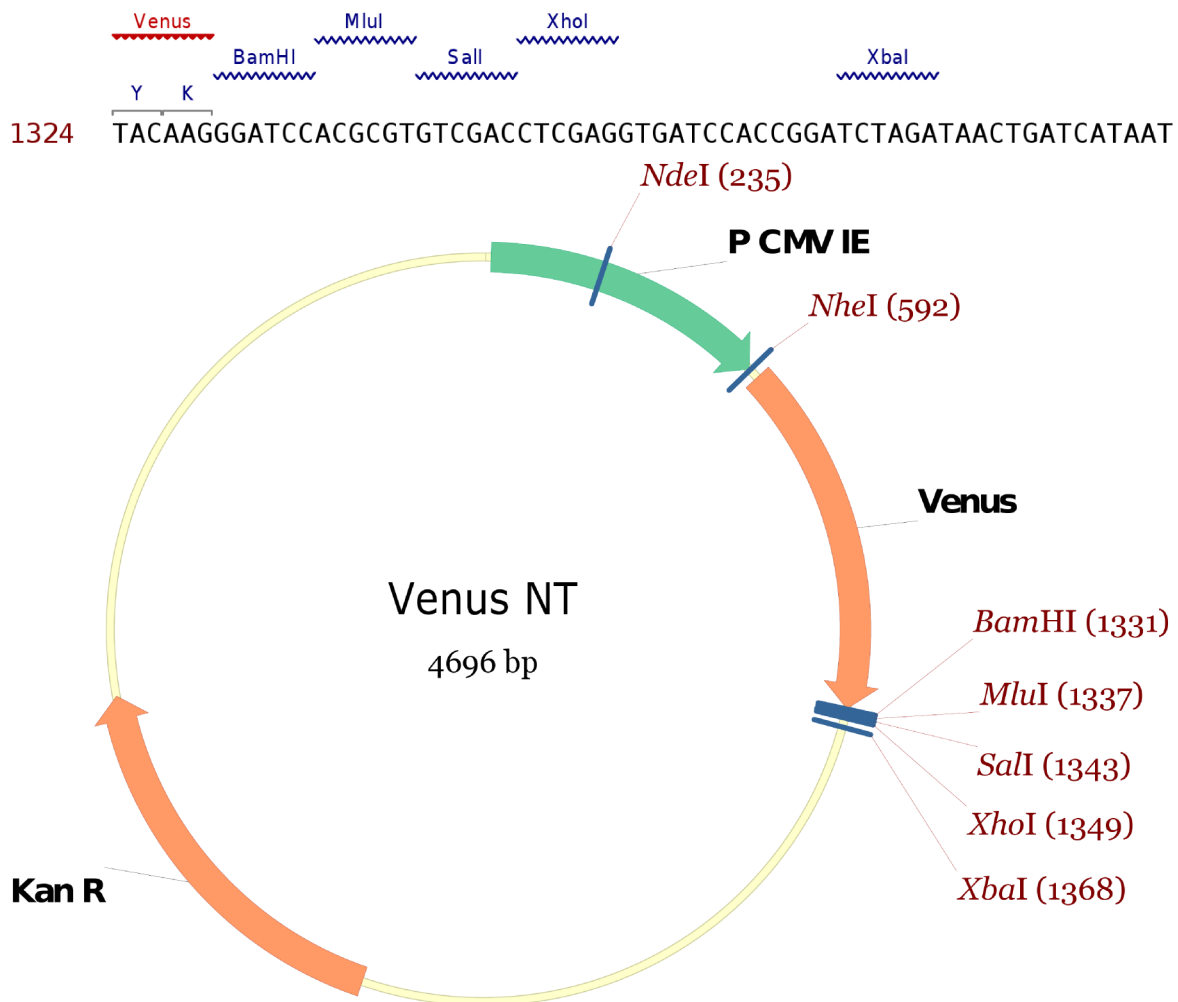


Figure C.7: Vector map Venus NT



### Venus CT

Length: 4.7 kb

Origin: Clontech (pECFP-N1)

Cytomegalovirus immediate early gene enhancer/promotor

Venus

kanamycin resistance

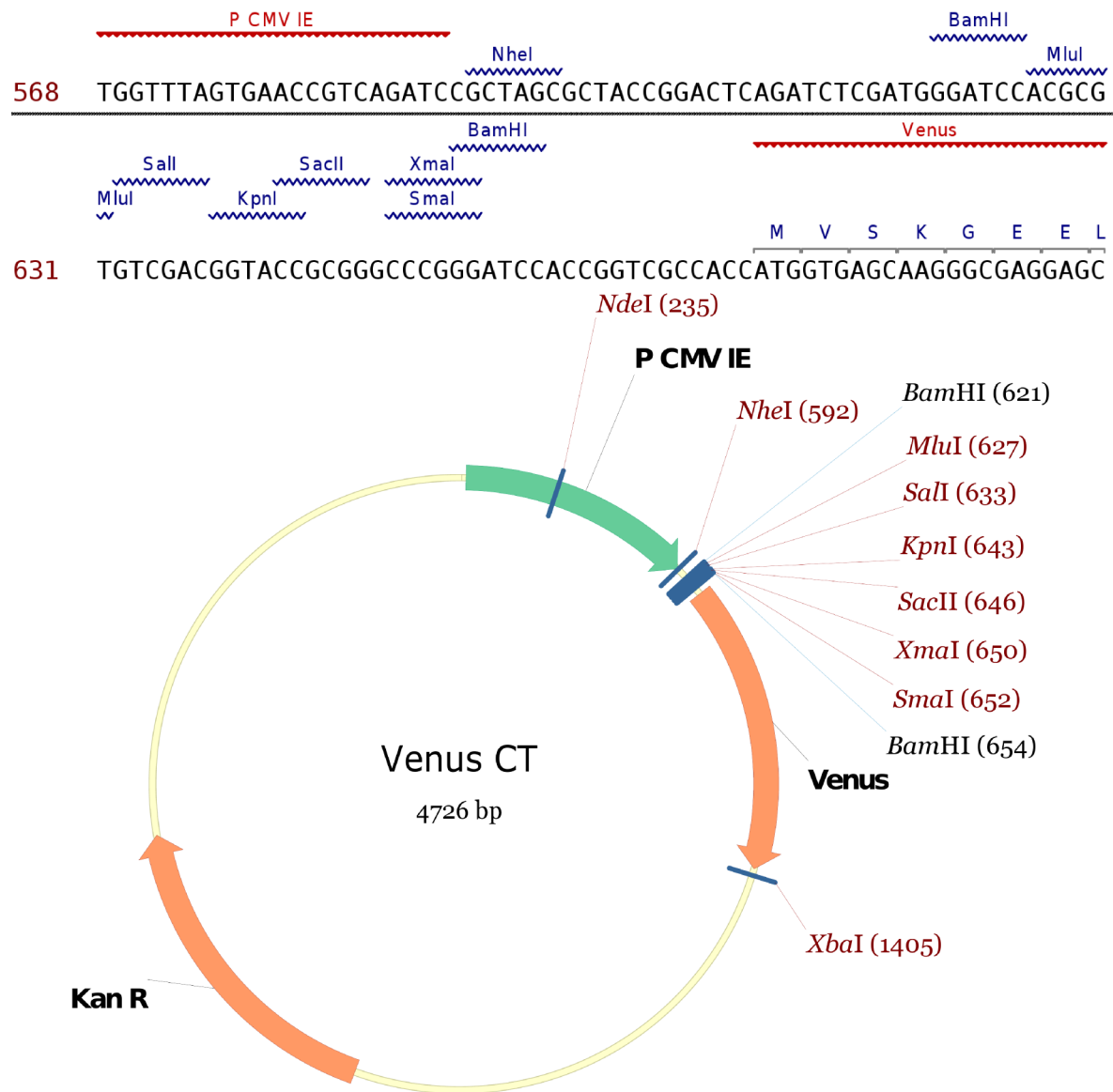


Figure C.8: Vector map Venus CT

### Venus1-C

Length: 4.7 kb

Origin: Clontech (pECFP-C1)

Cytomegalovirus immediate early gene enhancer/promotor

Flag-tag

Venus1 (aa 1-154)

kanamycin resistance

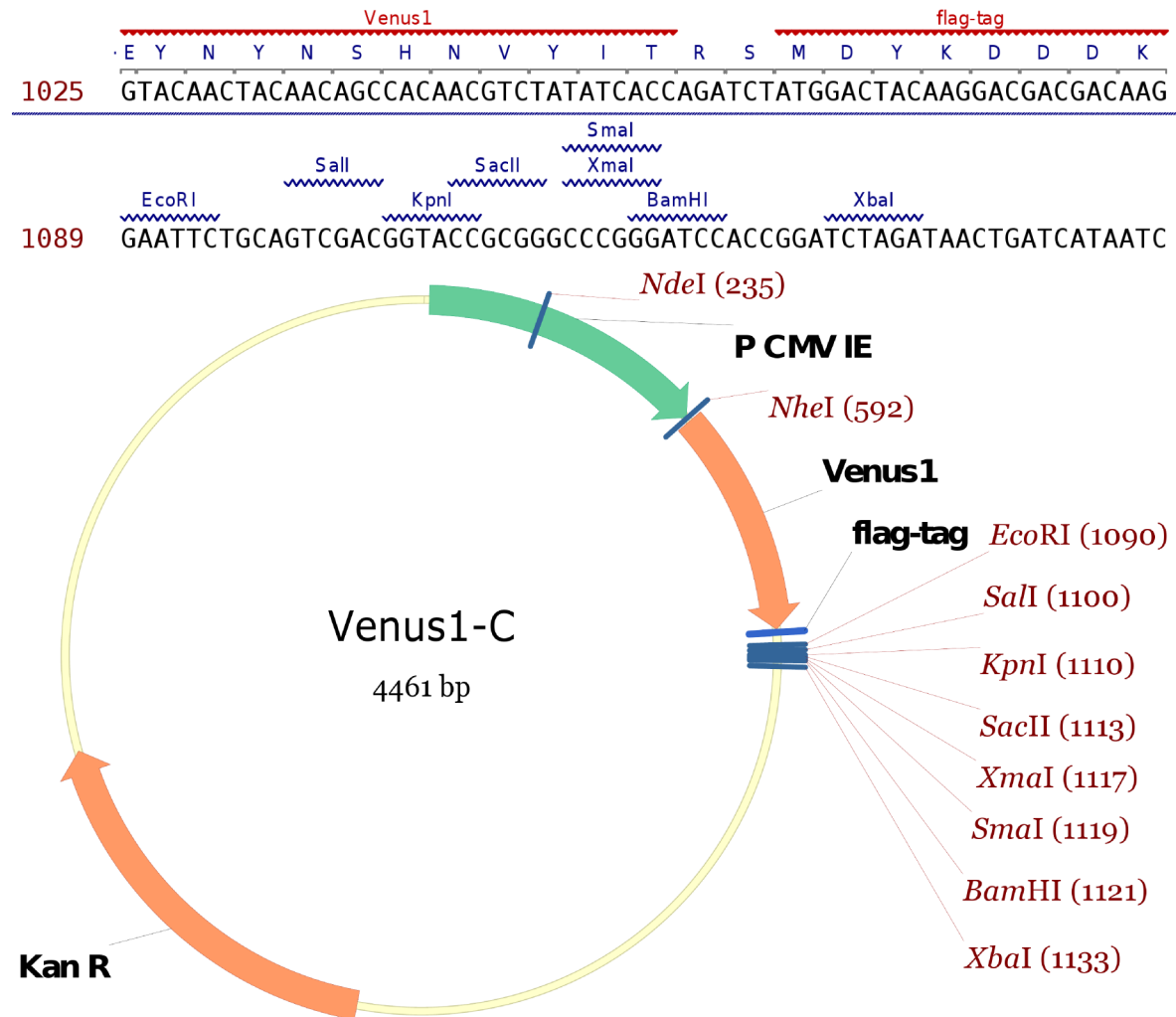


Figure C.9: Vector map Venus1-C

### Venus2-C

Length: 4.3 kb

Origin: Clontech (pECFP-C1)

Cytomegalovirus immediate early gene enhancer/promotor

HA-tag

Venus2 (aa 155-238)

kanamycin resistance

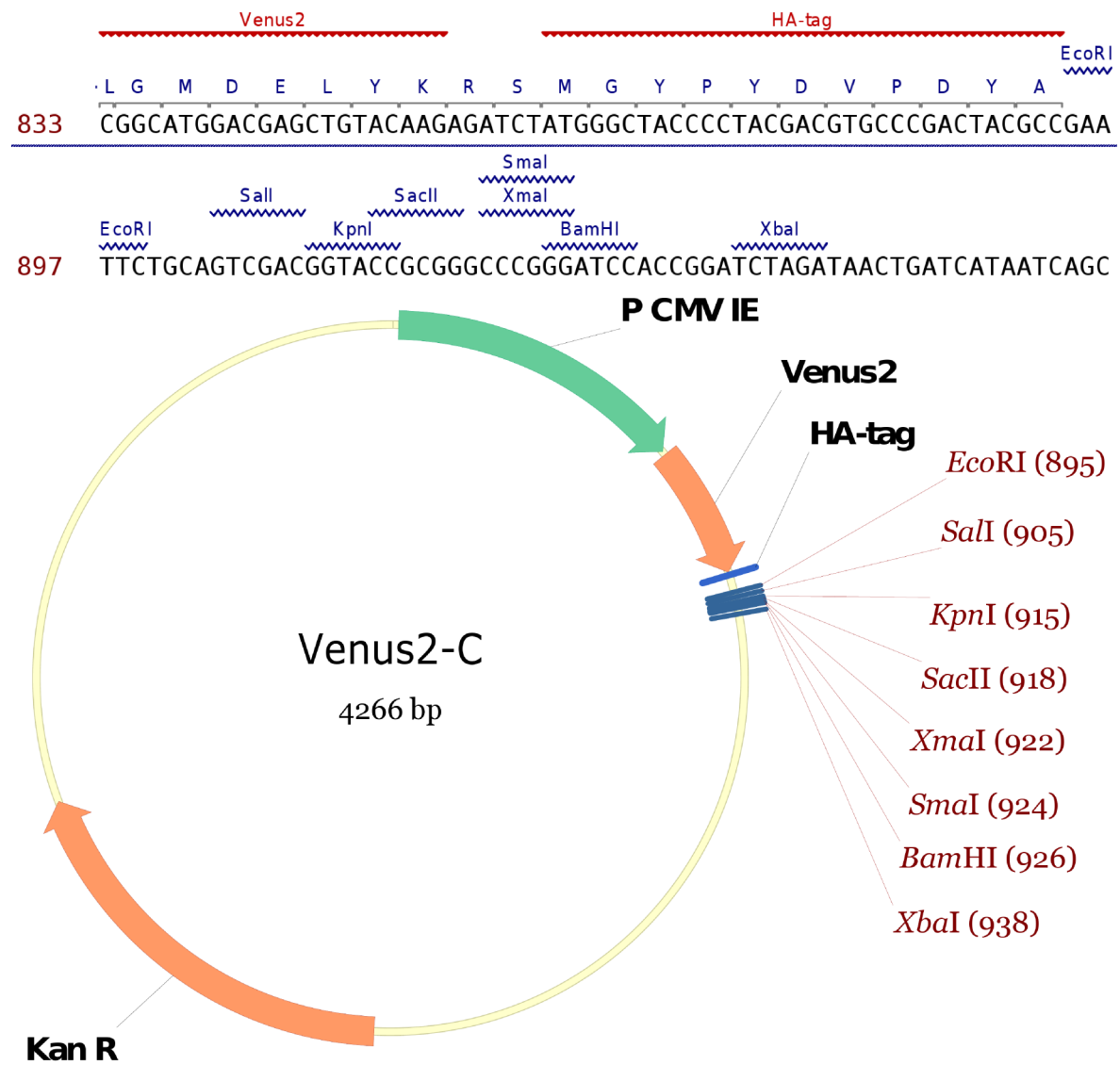


Figure C.10: Vector map Venus2-C

### Venus1-N3

Length: 4.5 kb

Origin: Clontech (pECFP-C1/pEGFP-N3)

Cytomegalovirus immediate early gene enhancer/promotor

Flag-tag

Venus1 (aa 1-154)

kanamycin resistance

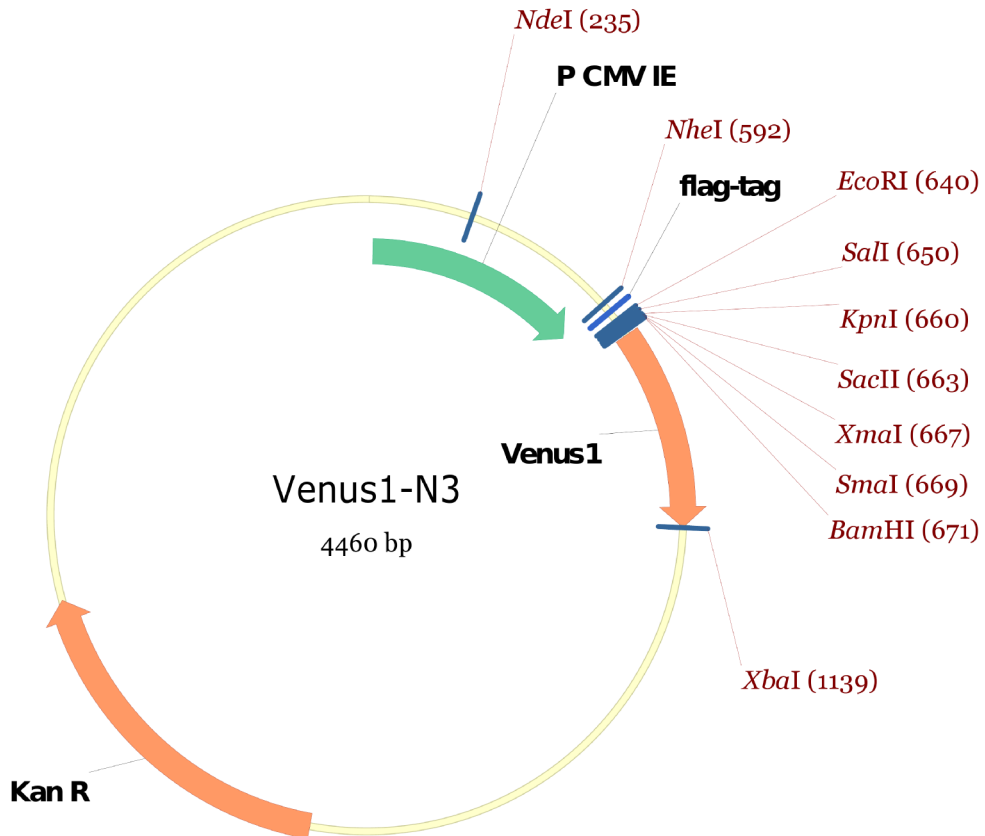
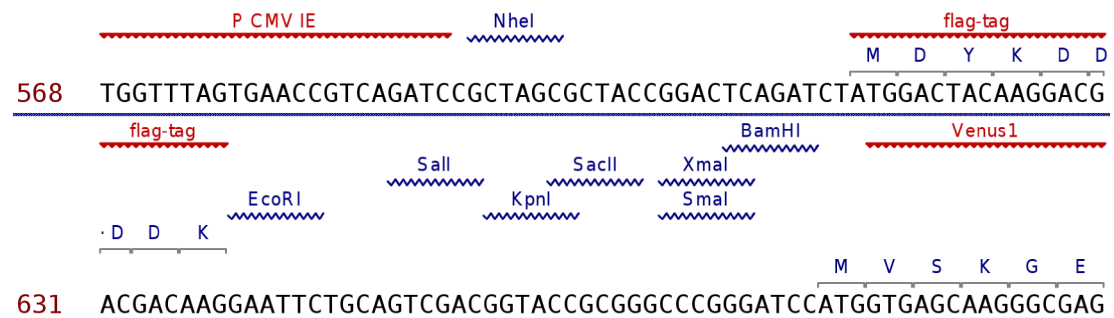


Figure C.11: Vector map Venus1-N3

### Venus2-N3

Length: 4.3 kb

Origin: Clontech (pECFP-N1/pEGFP-N3)

Cytomegalovirus immediate early gene enhancer/promotor

HA-tag

Venus2 (aa 155-238)

kanamycin resistance

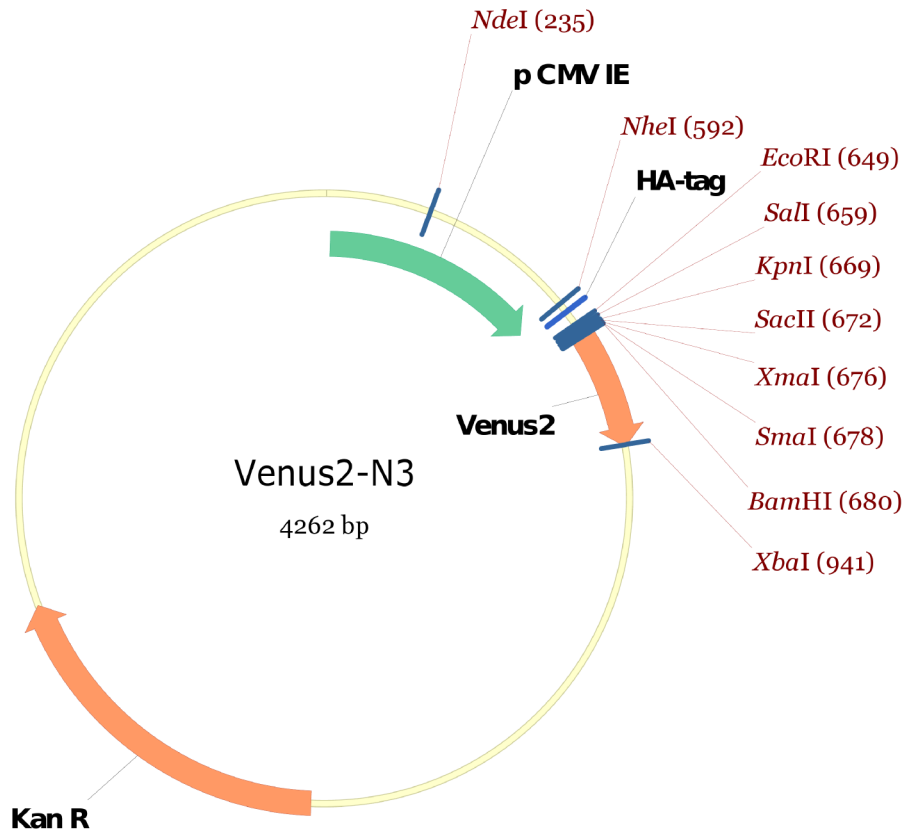
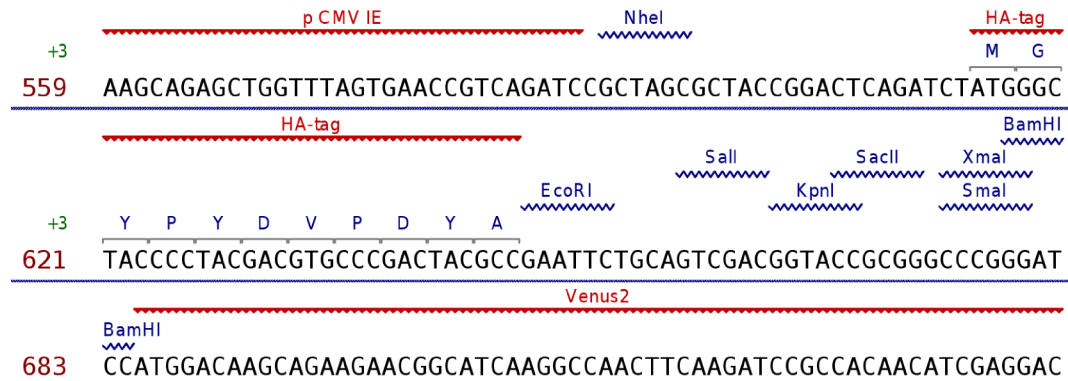


Figure C.12: Vector map Venus2-N3

# Appendix D

## Human Xin cDNA Sequence



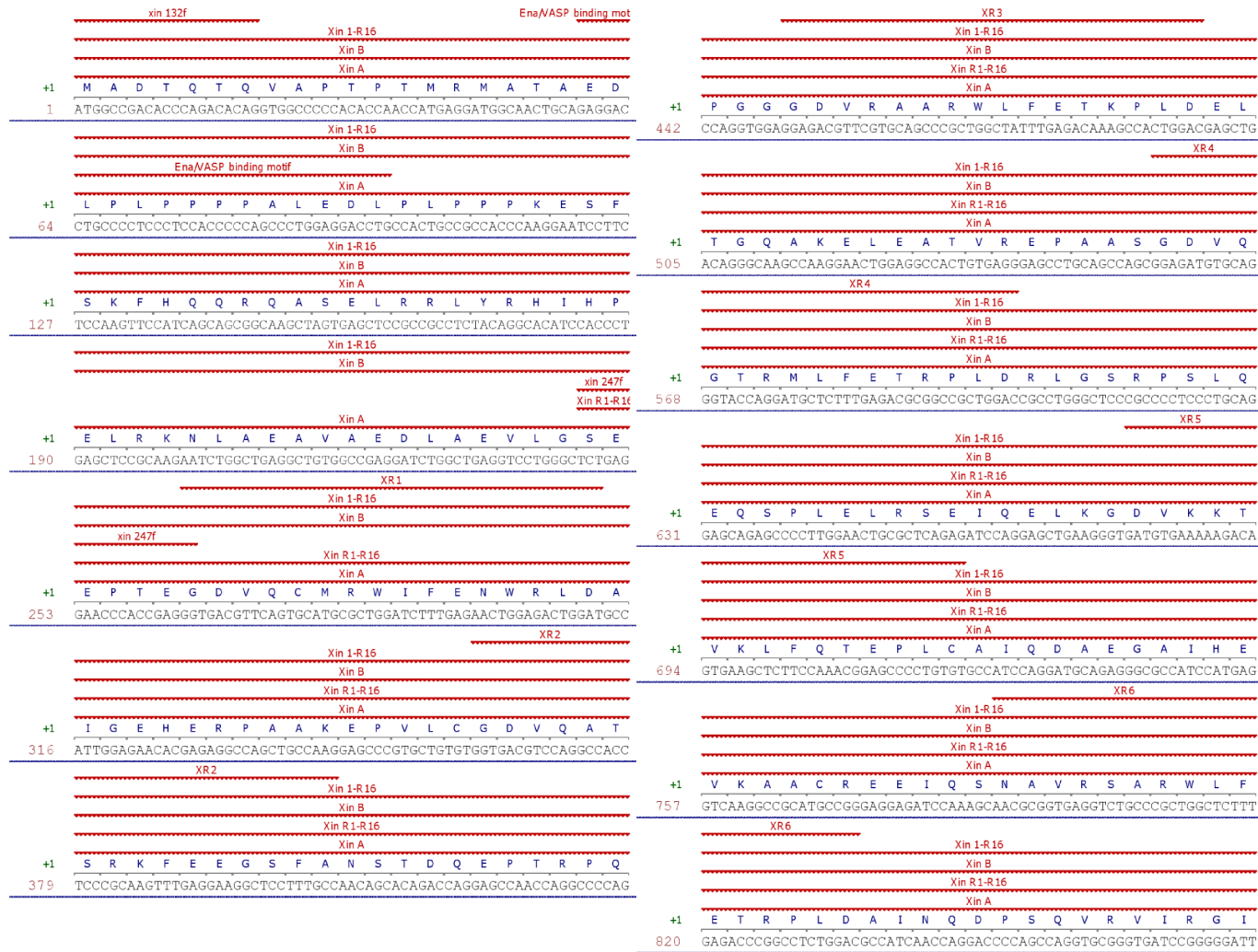


Figure D.1: Human Xin cDNA

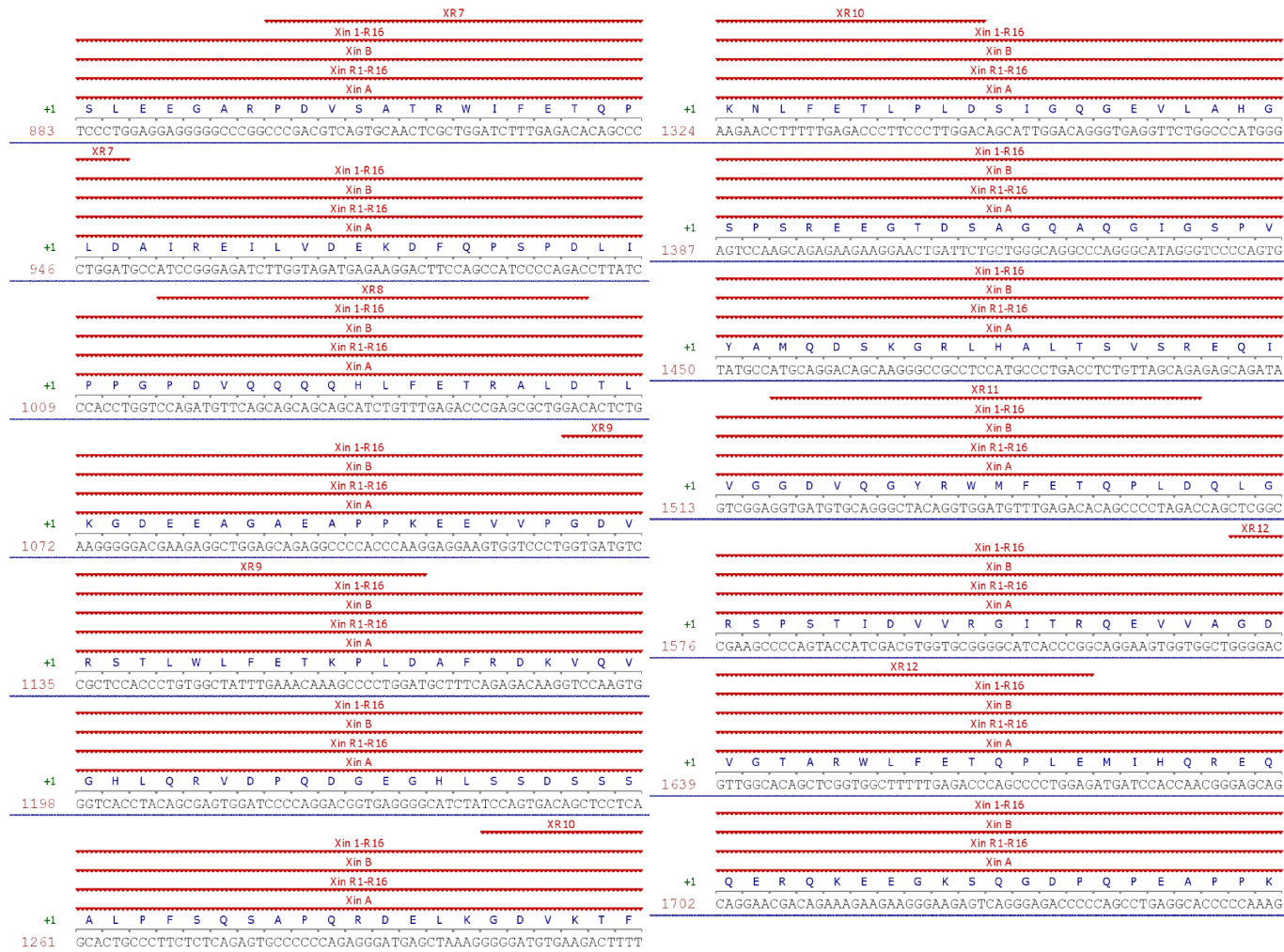


Figure D.2: Human Xin cDNA - continuation

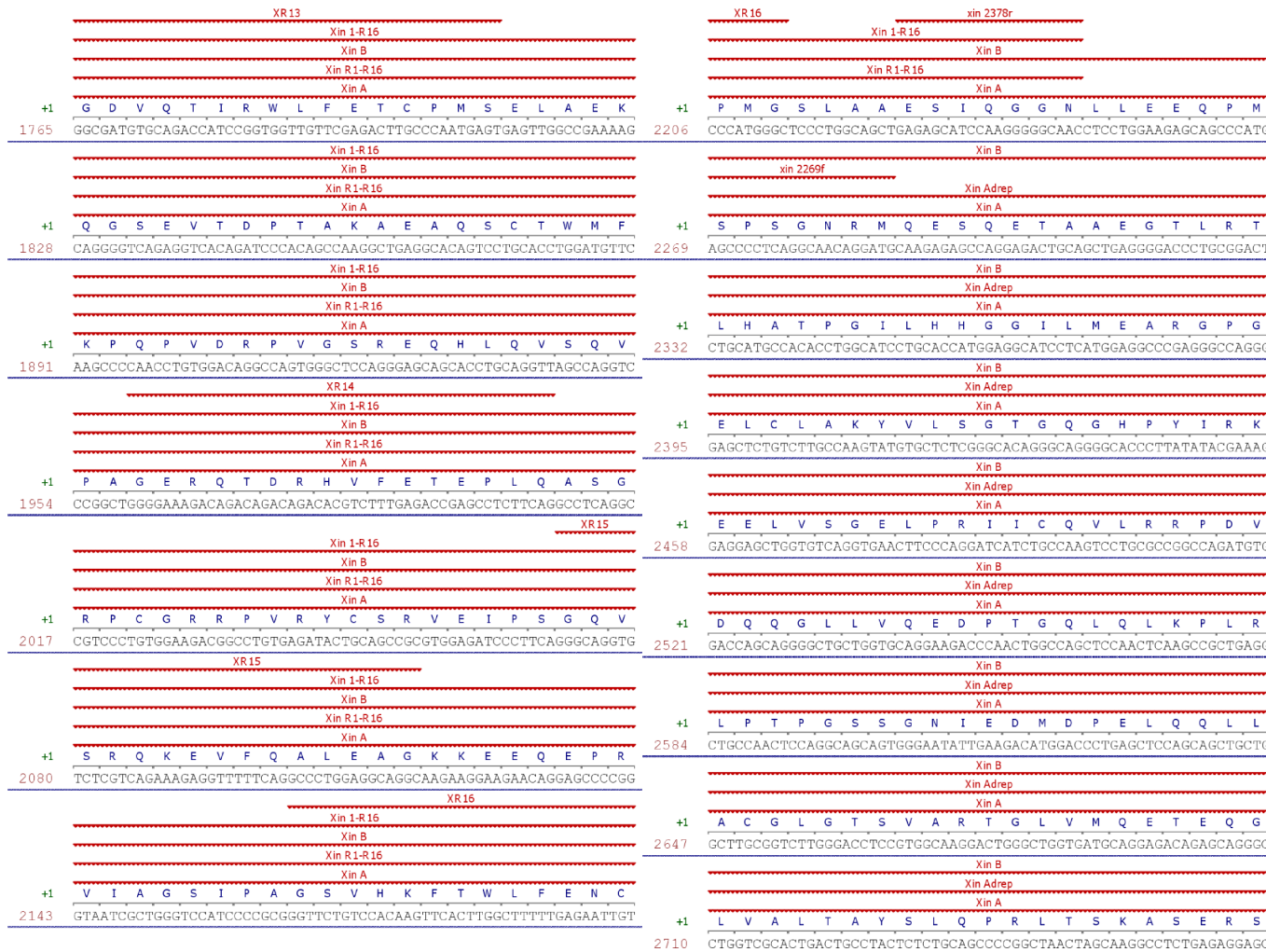


Figure D.3: Human Xin cDNA - continuation

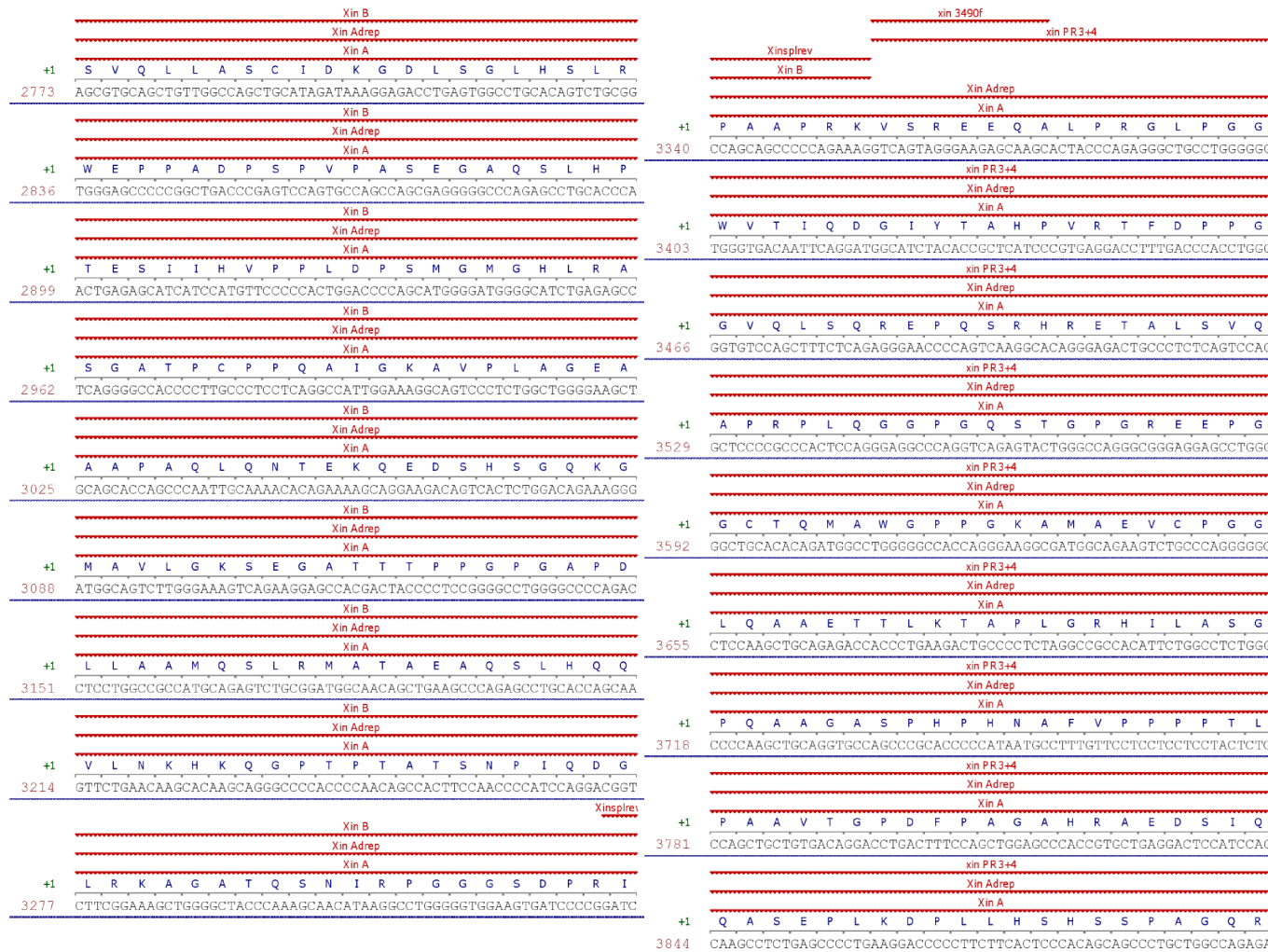


Figure D.4: Human Xin cDNA - continuation

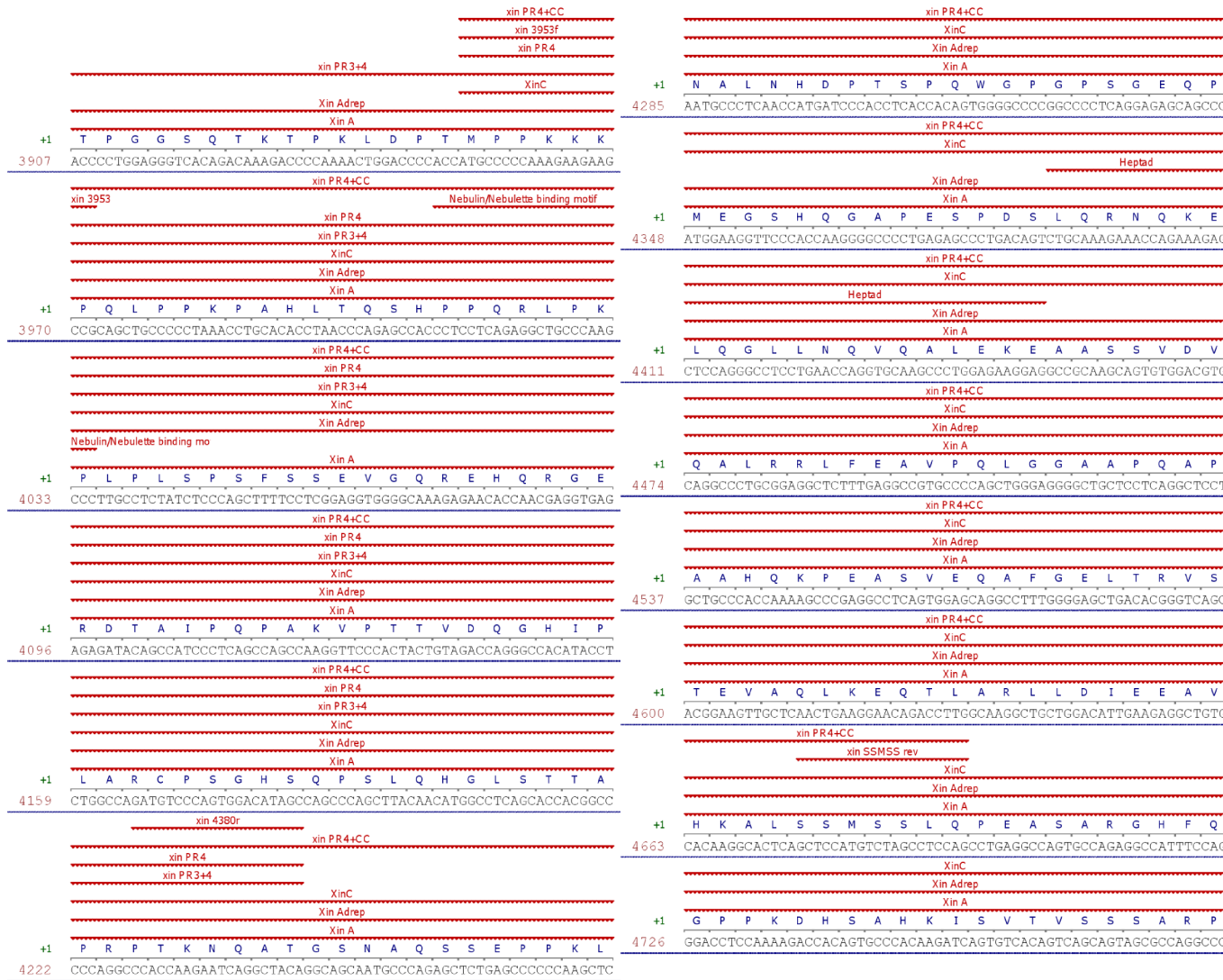


Figure D.5: Human Xin cDNA - continuation



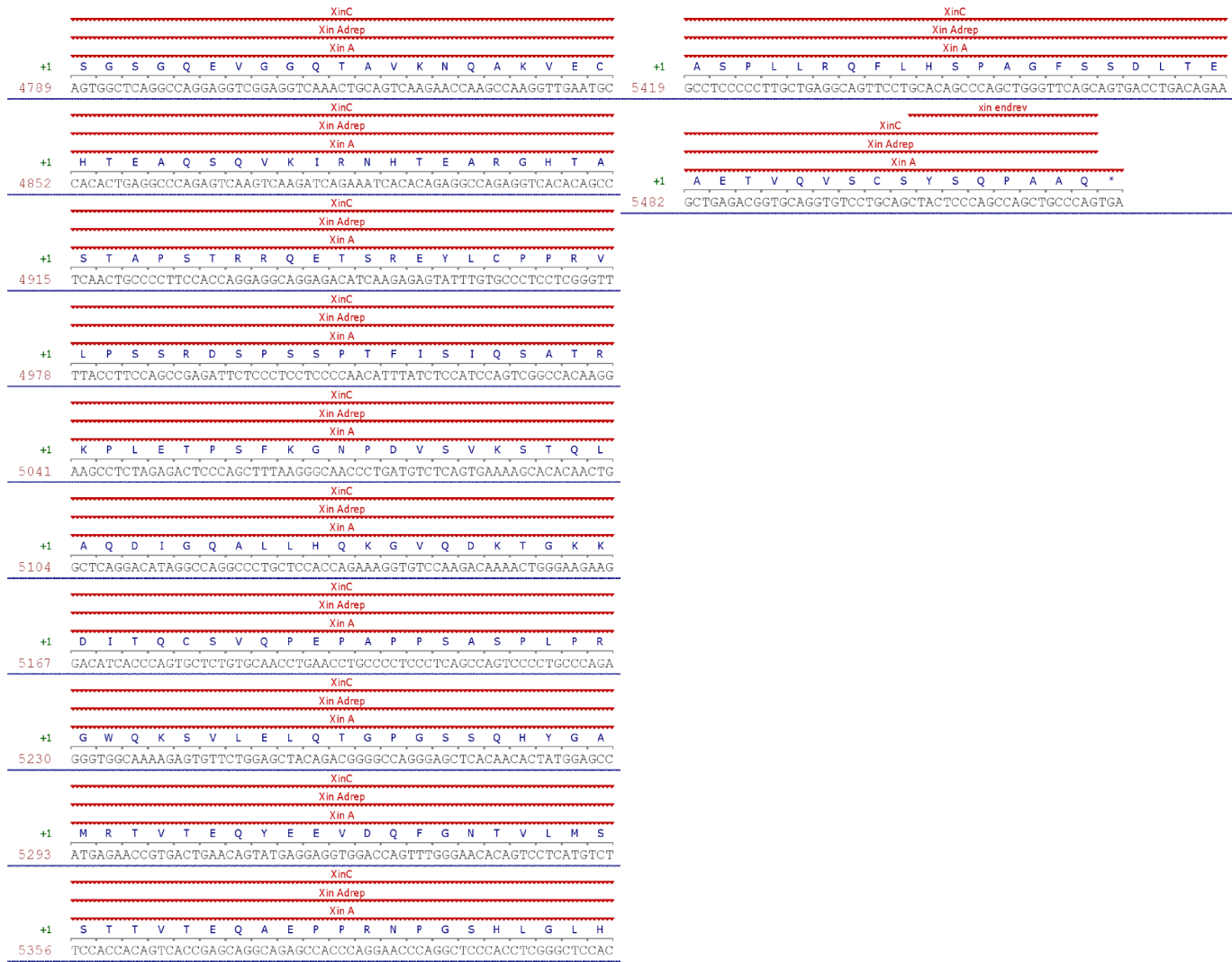


Figure D.6: Human Xin cDNA - continuation



# Appendix E

## Murine Xin cDNA Sequence

	mXin A		mXin A
+1	M A D A Q M Q V A P T P T I Q M R T E E D	+1	P P G P D V Q H Q R H L F E T C S L D T L
1	ATGGCTGATGCCAGATGCAGGTAGCTCTACACCAACCATCCAATGAGGACAGAAGAGGAC	1009	CCTCCTGGCCCAGATGTTACGATCAGCGACATCTGTTTGAACCTGTTCCTGGACACTCTG
	mXin A		mXin A
+1	L S L P H P S A P E G L P P P P P K E T F	+1	K G E R E T E A E V P P K E E V I P G D V
64	CTGTCCCTCCCTCATCCCTCAGCCCCAGAGGCTTCCGCCACCACCCCCCAAGAAACCTTC	1072	AAGGGTGAAGAGAAACAGAGGCAGAGGTGCCACCCCAAGGAGGAGGTGATTCCTGGCGATGTC
	mXin A		mXin A
+1	S K F Q Q Q R Q A S E L R R L Y K H I H P	+1	R S T L W L F E T K P L D A F R D Q V Q V
127	TCCAAGTTCAGCAGCAGCGCAAGCCAGTGAAGTCCGGCGTCTCTACAAACACATCCACCT	1135	GGCTCTACACTCTGGCTATTTGAACAAAACCCCTGGATGCTTCAGAGACCAGGTCCAAGTG
	mXin A		mXin A
+1	E L R K N L E E A V A E D L A E V L G S E	+1	G H L Q R V G H Q E G E G L V T E C L P S
190	GAGCTTCGGAAGAACCTCGAGGAGGCTGTGGCTGAGGACCTGGCCGGAGTCTCGGTTCCGGAG	1198	GGTCACCTGCAACGGGTGGGTACCAGGAGGGTGGGGGCTTGTGACAGAGTGTCTACCCAGT
	Xin RT 1r		mXin A
	mXin A		mXin A
+1	E P T E G D V Q C M R W I F E N W R L D A	+1	N G T S V L P L S Q G V P Q N D G L K G D
253	GAGCCCACTGAGGGCGATGTTCAAGTATGCTTGGATCTTTGAACTGGCGGTAGATGCC	1261	AATGGTACTTCGGTGTGGCTCTGTCTCAGGGTGTCCCCCAGAATGATGGTTGAAAGGGAT
	mXin A		mXin A
+1	I G D H E R P A A R E P V S G G N V Q A T	+1	V K T F K N L F E T L P L D S I G Q G E P
316	ATTGGCGATCACGAGAGGCCGGCTGCCAGGGAACCTGTGTCAAGTGGCAACGTCAGGCCACC	1324	GTGAAAACCTCAAGAATCTTTTGAAGCCCTCCCTTAGACAGCATTTGGCAGGGTGAACCT
	mXin A		mXin A
+1	S R K F E E G S F T N S S D Q E P E G L R	+1	S A Y G N I N R G Q N T D S A E Q S Q G S
379	TCTCGAAAGTTTGAGGAAGGCTCCTTTACCAACAGCTCAGATCAGGAGCCGGAGGACTCCGG	1387	TCAGCCTATGGAAACATAAACAGAGCACAAAACACTGATTCGCCGAGCAGTCCCAGGGTCT
	mXin A		mXin A
+1	P S G G D V Q A A R Q M F E T K P L D A L	+1	D A P V Y A M Q D S R G Q L H A L T S V S
442	CCATCAGGGGTGATGTCCAAGCTGCCAGACAGATGTTTGAACCAAGCCACTGGATGCGCTG	1450	GACGCCCGGTATATGCTATGCAGGACAGCAGGGGACAGCTTCATGCCCTGACTTCGTGACG
	mXin A		mXin A
+1	R G Q E E A T Q T T M R E P A A T G D V Q	+1	R E Q V V G G D V Q G Y K W M F E T Q P L
505	AGAGGCCAGGAGGGAACACAGACAACCATGAGGGAACCTGCAGCCACTGGAGATGTACAG	1513	AGAGAGCAGGTAGTTGGAGGTGATGTTACAGGCTACAAGTGGATGTTTGAACACAGCCCTG
	mXin A		mXin A
+1	G T R K L F E T R P L D R L G S R P S I Q	+1	D T L G R S P S T I D V V R G I T R Q E V
568	GGAAACAGAAAGCTCTTTGAGACTAGGCCCTGGACCGACTGGGGTCCCGCCCTCTATCCAG	1576	GACACGCTGGTGAAGCCCCAGTACCATCGATGTGGTACGAGGTATCACTCGCAGGAAGTG
	mXin A		mXin A
+1	E Q S P L E L R S E I Q E L K G D V K K T	+1	V A G D V G T T R W L F E T Q P L E M I H
631	GAGCAGAGTCTTTAGAGCTGCCTCAGAGATTCAGGAGTGAAGGGCGATGTGAAGAAGACG	1639	GTGGCTGGGGATGTCGGCACCACTCGGTGGCTCTTTGAGACGCAGCCATTGGAGATGATCCAC
	mXin A		mXin A
+1	V K L F Q T E P L C A I Q D A E G T I H E	+1	Q Q E Q Q K P E E E E G K G P G G P P P E
694	GTGAAGCTGTTTTCAGACGGAACCTCTATGCGCCATCCAGGATGCCAGGGCACCATCCACGAA	1702	CAACAAGAGCAACAGAAACAGAGGAGGAAGGGGAAGGGTCCAGGAGGCCCCCTGAG
	mXin A		mXin A
+1	V K A A C R E E I Q S N A V R S A R W L F	+1	L P K K G D V Q T I R W L F E T Y P M S E
757	GTCAAGGCTGCCGTGCGGAGGAGATTCAAAGCAATGCAGTGAAGTCTGCTCGCTGGCTCTT	1765	CTCCCCAAAAGGGTGTATGACAGACTATCCGTTGGCTGTTTGAACCTACCCTATGAGCGAG
	mXin A		mXin A
+1	E T R P L D A F N Q D P S Q V R V I R G I	+1	L A E K R E S E V T D P V S K A E T Q S C
820	GAGACCGACTCTGGATGCTTCAACAGGACCCAGCCAGGTGCGGGTATTGCGGGATC	1828	TTGGCAGAGAAGCGAAGTCTGAGGTACAGACCCCTGAGCAAGCTGAGACACAGTCTCTGC
	mXin A		mXin A
+1	S L E E G A L P D V S A T R W I F E T Q P	+1	T W M F G P Q S L N P A E G S G E Q H L Q
883	TCCCTTGAGGAGGGACCTGCGGATGTCAGTCAACTCGTTGATCTTTGAGACGACGCT	1891	ACCTGGATGTTGGGCCCCAATCTCTGAACCCAGCAGAAGGCTCTGGGGAGCCACCTGCAA
	mXin A		mXin A
+1	L D A I R E I E V D E K D F Q P S P D L I	+1	T S Q V P A G D R Q T D R H V F E T E S L
946	TTGGATGCCATTCTGAGATCGAGGTGGACGAGAAGGACTTCCAGCCATCTCCGGATCTCATC	1954	ACCAGCCAGGTTCGGCTGGAGACAGGCAGACAGACAGACATGTCTTTGAGACTGAATCTCTG

Figure E.1: Murine Xin cDNA

	mXin A		mXin A
+1	P A S N Q S S G R K P V R Y C S R V E I P	+1	L P N G K P V A Q A P L Q E A R K K T D I
2017	CCAGCCTCAAACCAATCCAGTGGGAGAAAGCCGTGAAGGTACGACGCGGGTGGAGATTCCCT	3025	CTTCCAAATGGGAAACCTGTAGCCCAAGCTCCATTGCAGGAAGCAAGGAAAGAAACGGATATC
	mXin A		mXin A
+1	S G Q V S R Q K E V F Q A L E A G K K E V	+1	S H A G Q K G K A A S G R P E G T I A S P
2080	TCCGGCCAGGTATCTCGGCAGAAAGAGTTTCCAGGCCCTGGAGCCGGGCAAGAAGGAGGTC	3088	AGCCATGCTGGGCAGAAAGGGAAGGCAGCCTCAGGAAGACCAGAAGGAACATTGCTTCCCCT
	mXin A		mXin A
+1	P E T T I N L G S I P T G S V H K F T W L	+1	L G S G A P D L Q E A M Q N L R L A T A E
2143	CCGGAGACCACAATCAACCTGGGGTCCATCCCCACAGGCTCTGTGCATAAATTCACCTGGGTC	3151	CTAGGGTCTGGGGTCCAGATCTCCAGGAAGCCATGCAGAATCTGCGTTGGCAACCGCTGAG
	mXin A		mXin A
+1	F E N C P M G S L A A E S I R G D N L Q E	+1	A Q S L H Q Q V L S R H P Q G S D P V A T
2206	TTTGAANAACGTCCCATGGGCTCCCTGGCAGCTGAGAGCATCAGAGGGGACAACCTCCAGGAA	3214	GCCCAAGGCTGCACCAAGCAGGTCTTGAGCAGGCATCCACAGGGCTCTGACCTGTAGCCACC
	mXin A		moXinEx2b RT1f
+1	E Q P K G S A G H G T P E R Q E T A A E R	+1	S M P V Q D V L Q A S T P A T G V T Q G S
2269	GAACAGCAAAAAGGCTCTGCAGGCCATGGGACACCCAGAGAGGACAGAGCAGCCGAGAGA	3277	TCCATGCCTGTCCAAGATGTTCTGCAAGCATCCACTCCCTGCCACTGGGGTACTCAAGGCAGC
	mXin A		moXinEx2b-c fw
+1	T L R R T L H A T P G I L H H G G I L M E A	+1	I R P V A G S E A R I P A F P R K V S G D
2332	ACCCTTCGGACTTTGCATGCCACCCCGGCACTCTGCACCATGGAGGCACTCCATGGAGGCC	3340	ATCAGGCTGTGGCTGGAAGTGAAGCCAGGATCCAGCATTCCTCCAGAAAGGTCAGTGGGGAC
	mXin A		mXin A
+1	R G P G E L C L A K Y V L P S P G Q G R P	+1	N K A V P R G L P R G W V T I Q D G I Y A
2395	CGAGGGCCAGGGGAGCTCTGTCTTGCAGATGTGCTCCCAAGCCAGGGCAGGGCCGCCCC	3403	AACAAAGCAGTCCCCAGAGGGCTGCCAGGGGGTGGGTGACCATACAGGATGGCATCTACGCT
	mXin A		mXin A
+1	Y I R K E E L V C G E L P R I V R Q V L R	+1	A H P V R T S D P H G A I Q P S E K E P H
2458	TACATACGGAAGGAGGAGCTGGTGTGTGGTGAAGCTCCAGGATCGTCCGTCAGTGTCTCGCC	3466	GCTCACCTGTGAGAACCCTCTGACCCACATGGGGTATCCAGCCTCTGAAAAGAGCCCCAT
	mXin A		moXinEx2c RT1r
+1	R T D V D Q Q G L L V Q E D T A G Q L Q L	+1	L R H S P P Q A D Q G Q S P R P G Y R E P
2521	CGGACAGAGTGGACAGCAGGGACTGTGGTTCAAGGAGACACAGCTGGGCAGCTCCAGCTC	3529	CTGAGGCACAGCCCAAGGAGCAGCAAGGTCAGAGTCCAGGCCGGGGTATCGTGAAGCCT
	mXin A		mXin A
+1	H P L T L P G P G D P G N I E D M D P E L	+1	G G H T Q R A W E P L G K V M P Q I S L E
2584	CACCCACTCACGCTGCCAGGGCCTGGTGAATATTGAAGACATGGACCTGAGCTC	3592	GGGGTCATACAAAGGGCTTGGGAACCTCTGGGAAAGTGTGCCCAATCTCGCTTGAG
	mXin A		mXin A
+1	Q Q L L A C G L G V S V S K T G L V M Q E	+1	C L R A A A D T S L K T A P L T H H T L T S
2647	CAGCAGCTGCTGGCCTGTGGCTGGGAGTCTCTGTGTCAAAGACGGGGCTGGTGAATGCAAGAG	3655	TGCTCCGGGCAGCAGACACCTCCCTGAAGACTGCCCTCTAACTCACCAGCCCTGACATCT
	mXin A		mXin A
+1	T G Q G L V A L T A Y A S L Q P Q L T S R A	+1	K P A G A S L H S H N A S V P P P P T L P
2710	ACAGGACAGGGCCTAGTGGCACTGACTGCCTACTCCCTCCAGCCCCAGCTTACCAGCAGGGCC	3718	AAACCAGCAGGTGCCAGCCTGCACCTCCCAATAGCCTCTGTTCCTCCCCTCTACTCTCCCA
	mXin A		moXinEx2d RT1r
+1	P E R S S V Q L L A S C I D K G D L H S L	+1	A A V T E D P D H P T Q G H H Q E D S I Q
2773	CCTGAAAGAAGCAGTGTGCAGCTGTGGCCAGCTGCATAGACAAAGGAGACCTGCACAGCCTT	3781	GCTGCTGTGACAGAAGATCTGACCACCACTCAAGGCCACCAGGAGGACTCCATCCAG
	mXin A		mXin A
+1	H S L R W E P P T D P S S G P A T E E S Q	+1	Q A P E P L Q E P L L H I H N R P S G Q K
2836	CACAGTTTGCAGTGGGAGCCGCAACAGACCCAAAGTTCTGGACCTGCTACTGAGGAGTCCAG	3844	CAGGCCCGGAGCCCTGCAGGAACCCCTTCTTCATATTCAACAACAGACCTTCTGGCCAGAAA
	mXin A		
+1	R V P Q T E S I I H V T P L D S T M E M G		
2899	AGGGTCCCCAAACTGAGAGCATCATACATGTTACCCCAATTAGACTCCACCATGGAGATGGGG		
	mXin A		
+1	Q L R I S G S T P C P P P S R A A G K V V		
2962	CAGCTGAGAAATCCAGGATCCACACCCCTGCCACCTCCATCTCGGGCAGCTGGAAAAGTGGTC		

Figure E.2: Murine Xin cDNA - continuation

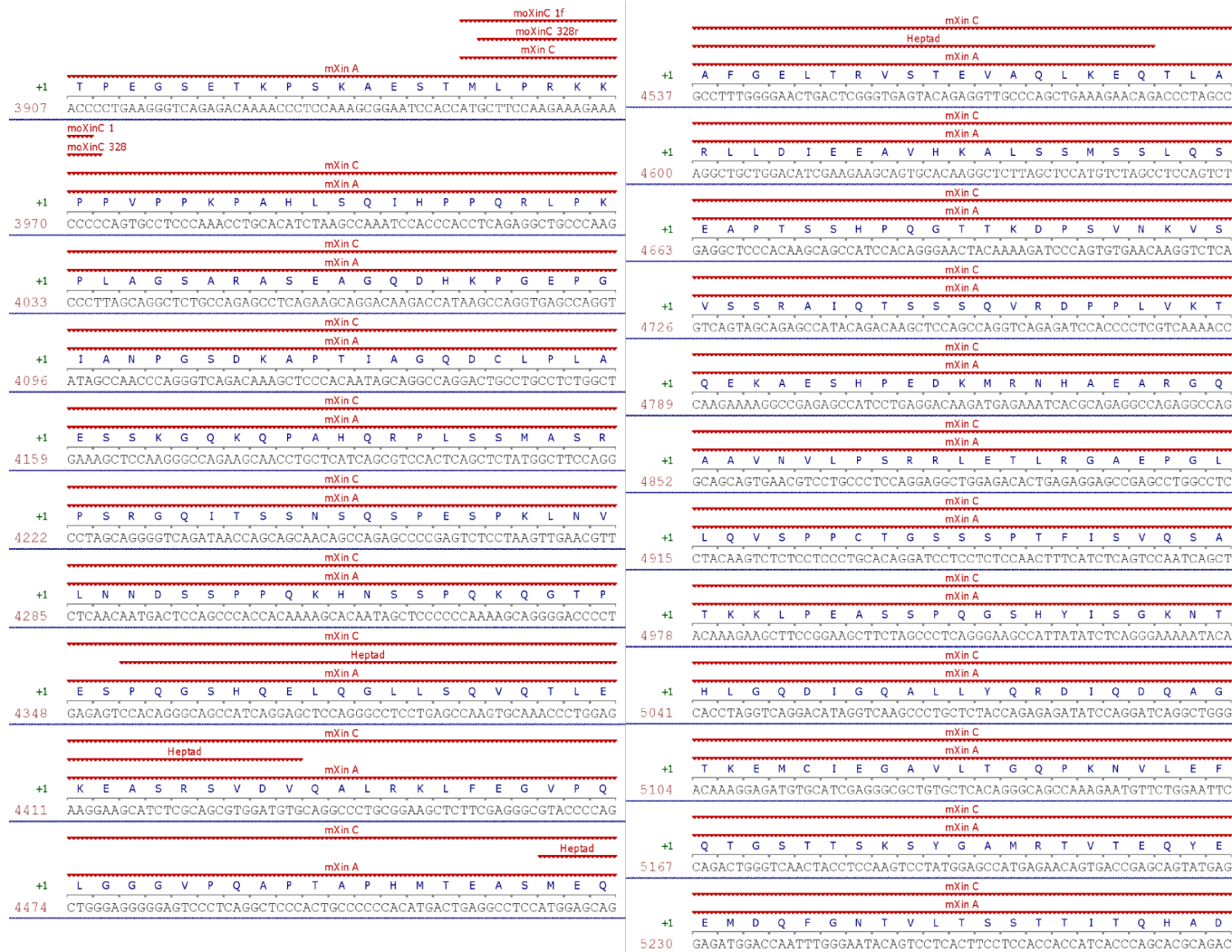


Figure E.3: Murine Xin cDNA - continuation

```

                                     mXin C
                                     mXin A
+1  P L T D P R P Q L C L H T S P M L R Q L L
5293 CCACTGACGGACCCCAGACCCCAGCTCTGCCTGCACACTTCTCCCATGCTAAGGCAGTIACTC
                                     mXin C
                                     mXin A
+1  H S P S R L N S D L A E A E I T W T P C N
5356 CACAGCCCCCTCCAGGCTCAACAGTGACCTGGCAGAAGCTGAGATAACATGGACTCCCTGTAAC
                                     moXin endrev
                                     mXin C
                                     mXin A
+1  N F H P A A Q
5419 AACTTCCACCCGGCTGCCAG

```

Figure E.4: Murine Xin cDNA - continuation

## Appendix F

### Human Xirp2 cDNA Sequence



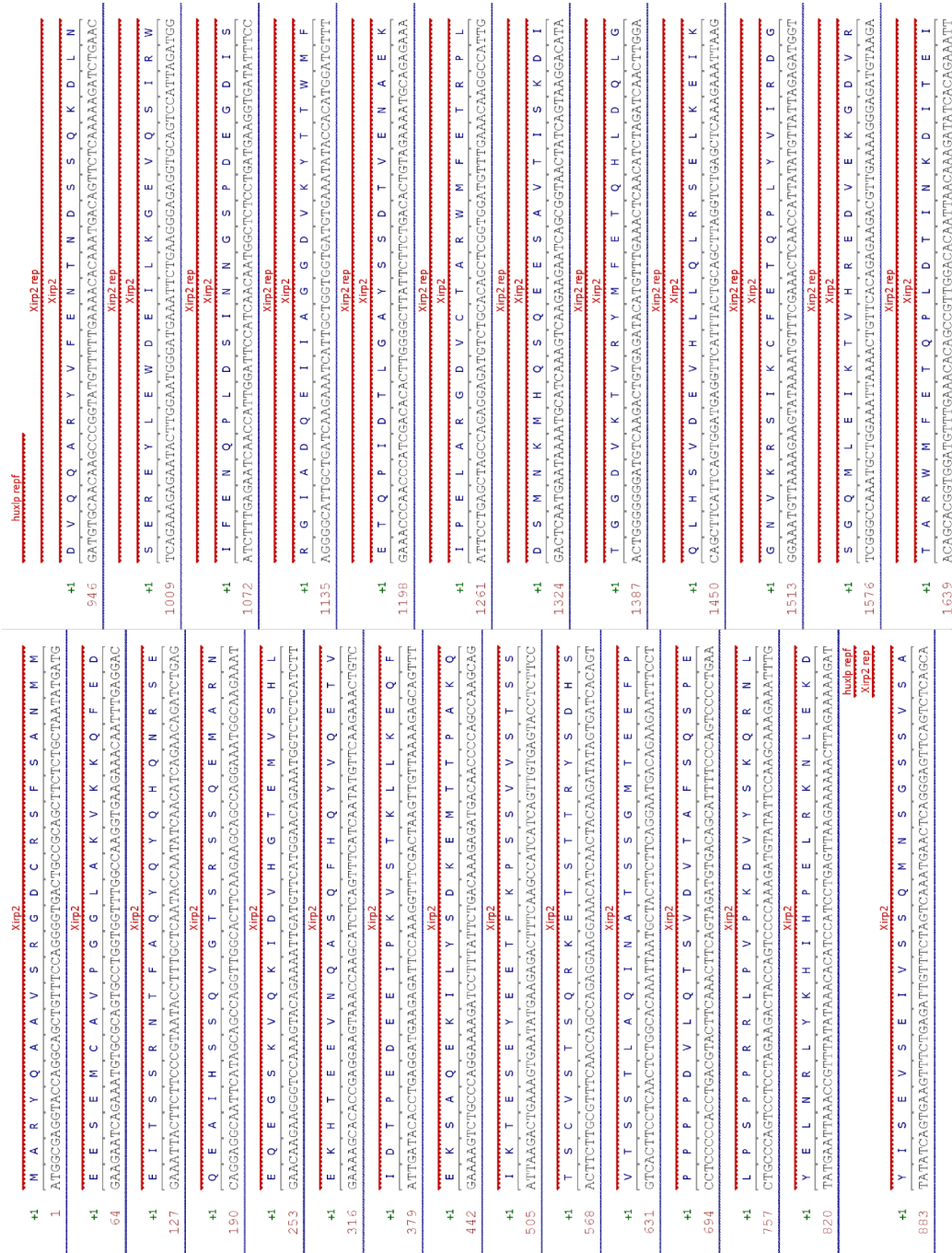


Figure F.1: Human Xirp2 cDNA

	Xirp2 rep Xirp2		Xirp2 rep Xirp2
+1	K V V R G I S M E E N V K G G V S K A K W	+1	I S A Q E I Q T G N V K S A K W L F E T Q
1702	AAAGTTGTCGAGGAATATCCATGGAAGAAAATGTCAAAAGGTGGGGTGAAGTAAAGCAAGTGG	2458	ATATCTGCTCAAGAAAATACAGACTGGAAATGTGAAAATCTGCCAAAATGGTTTGTTTGAAACCCAA
	Xirp2 rep Xirp2		Xirp2 rep Xirp2
+1	L F E T Q P L E K I K E S E E V I I E K E	+1	P L D S I K Y F S D V E E T E S K T E Q T
1765	TTATTTGAAACCCAAACCCTTTGGAGAAAATCAAGAGATCCAGAGGTCATCAATTGAAAAGGAA	2521	CCCTTGATTCAAATTAATAATTTTGTAGTGTGTGGAGAAACAGAAAAGTAAAACTGGAACAAACT
	Xirp2 rep Xirp2		Xirp2 rep Xirp2
+1	K I I G T D V S R K C W M F E T Q P L D I	+1	R D I V K G D V K K T C K W L F E T L P M E
1828	AAAATAATAGTACAGATGCTCCAGAAAGTGTGGATGTTTGAACCCAGCCATTAGACATT	2584	AGAGATATTTAAAGGGGATGTCAAACCTCTAAAATGGCTTTTGGACCCCTGCCAATGGAG
	Xirp2 rep Xirp2		Xirp2 rep Xirp2
+1	L K E V P D A D S L Q R E E I I G G D V Q	+1	S L Y E K V S L M T S S E E I H K G D V K
1891	CTAAAAGAGTTCCTGATGCAATTCCTCAACGTTGAGGAGATPAAAGTGGTGTGATGACAA	2647	TCCTTTATGAAAAGTTCTGTTAATGACCGAGTGAAGAAAATTCATAGGGAGATGTCAAA
	Xirp2 rep Xirp2		Xirp2 rep Xirp2
+1	T T K H L F E T L P I E A L K D S P D I G	+1	T C T W L F E T Q P L D T I K D D S E T A
1954	ACTACTAAGCATCTATTTGAAACACTTCCAAATTTGAAGCATTAAGAAGACAGTCCCTGATATAGGA	2710	ACTTGTACTTGGCTCTTGAACACTCAGCCACTTGATACCATAAAAAGATGACTGTGAAACAGCA
	Xirp2 rep Xirp2		Xirp2 rep Xirp2
+1	K L Q K I T A S E E E K G D V R H Q K W I	+1	V K L Q T V K Q E E I Q G G D V R T A C F
2017	AAGCTTCAAAAATCACTGCCTGTGAAGAAGAAAAGGGATGTTAGGCATCAAAAATGGATT	2773	GTCAAAITGCCAAACTGTAAAACAGAGGAGATCCCAAGGTGGGGATGTCGTACAGCATGTTTT
	Xirp2 rep Xirp2		Xirp2 rep Xirp2
+1	F E T Q P L E D I R K D K K E Y T R T V K	+1	L F E T E N L D S I Q G E E V K E I K P V
2080	TTTGAACCCACCTCGAAGCATTAGAAAAGATAAAAGGATACACAGCAACAGTGA	2836	CTTTTGGACAGAAAATTTGGACAGATACAGGAGAGAGTGAAGAAATCAAGCCCTTT
	Xirp2 rep Xirp2		Xirp2 rep Xirp2
+1	L E E V D R G D V K N Y T H I F E S N N L	+1	E M D I Q A G D V S S M R Y K F E N Q S L
2143	CTTGAAGAAGTTGACAGAGGAGATGTGAAGAAATACACACATATCTTTGAAATCAAAACAATTA	2899	GAAATGGATATACAAGCTGGAGATGTTTCCAGCATGAGGTAATAATTTGAAAATCAGTCCCTTA
	Xirp2 rep Xirp2		Xirp2 rep Xirp2
+1	I K F D A S H K I E V E G V T R G A V E L	+1	D S I S S S E E V L K K I K T L K T E D
2206	ATTAATTTGATGCATCAATAAAAATAGAGGTGGAAAGGATTAACAAGAGGCTGTAGAGTTA	2962	GATTCATAAGTTCATGTCAGAGGAAAGTTTGGAAAAGATCAAAAACCTTAAAAACTGAAGAT
	Xirp2 rep Xirp2		Xirp2 rep Xirp2
+1	N K S L F E T T P L Y A I Q D P L G K Y H	+1	I Q K G N V L N C R W L F E N Q P I D K I
2269	AAATAATCTCTTCGAGACACACCCTGTATGCCATTCAGAATCCCCCTTGGAAAATATCAT	3025	ATTCAGAAAGGCAATGTTTAAAATTTGATGGTGGCTTTTGGAAAACCAACCAATTTGATAAGATA
	Xirp2 rep Xirp2		Xirp2 rep Xirp2
+1	Q V K T V Q Q E E I V R G D V R S C R W L	+1	K E S Q E G D E C V K T V T D I Q G G D V
2332	CAAGTAAAGCATCCAGCAAGAAATCGTAAAGGATGATGTAAGAGCTGTAGGTGGCTT	3088	AAAGAAACCAAGAGGTGAATGATGTTAAGACGGTACAGACATCAAGAGTGGGATGTA
	Xirp2 rep Xirp2		Xirp2 rep Xirp2
+1	F E T R P I D Q F D E S I H K F Q I I R G	+1	R K G C F I F E T F S L D E I K E E S D Y
2395	TTTGAACAGGCCCAATGACCAAGTTTGATCAAAAGCAATTCATAAAATTCAAAATATATAGGA	3151	AGAAAAGGGTGGCTTTATTTTGGACACTTTTCTTTAGATGATTAAGAAAAGAAATCTGACTAT

Figure F.2: Human Xirp2 cDNA - continuation







	Xirp2		Xirp2 CC
	Nebulin/Nebulette binding motif		Xirp2
	Xirp2 PR2-6		Xirp2
+1	S Q A K I I T G K T G V L P P P T L P K F	+1	A A K R L H H V L A A S E D K D K M K K E
6553	TCTCAGGCTAAAAATCATAACAGGAAAAACCGGTGTGTGGCACCTCCACATTTGCCCAAACCC	7246	GCTGCCAAGAGGCTCCACCATGTTTATAGCAGCTTCAGAAAGACAAAAGATAAGATGAAAAAGGAA
	Xirp2 PR2-6		Xirp2 CC
	hXirp2 CCfw		Xirp2
	Xirp2		Xirp2
	Xirp2 CC		Xirp2
	hXIRP2 6678r		Xirp2 CC
+1	K L P K H I K D N K N D F S P K V E L A T	+1	V L Q S S R D I M Q S K S A C E I K Q S H
6616	AAACTTCCAAGCATATAAAAAGATAATAAGAACGATTTTCCCCCAAAGTTGAACTGGCAACC	7309	GTTTTACAAAGCTCAAGGGACATATGCAATCCAAAATCAGCTTGCGAATAAACAAAGTCAC
	Xirp2 CC		Xirp2 CC
	Xirp2		Xirp2
+1	S L S D M E C K I T T S K D Q K K V M V M	+1	Q E C S T Q Q T Q Q K K Y L E Q L H L P Q
6679	TCCCTGTCAGATGGAATGTAAAATTACTACCTCAAAGGATCAGAAAAAGTAATGGTGATG	7372	CAAGAATGTAGTACCCACAAACACAACAGAGAAGTATTTGGAGCAGTTGCACTTGCCCCAA
	Xirp2 CC		Xirp2 CC
	Xirp2		Xirp2
+1	T S S E H T E T K Q N V I S K S L D E R K	+1	S K P I S P N F K V K T I K L P T L D H T
6742	ACCAGCAGTGAACACACGGAGACAAAGCAGAACGTTATTAGTAAGAGTCTTGATGAAAGAAAA	7435	AGCAAACCAATTTCCCAAATTTCAAAGTTAAAACCATCAAACCTCCAACTTAGATCATACA
	Xirp2 CC		Xirp2 CC
	Xirp2		Xirp2
+1	Q L S I D S A N C L S H T V P G T S A P R	+1	L N E T D H S Y E S H K Q Q S E I D V Q T
6805	CAATTATCTATTGACTCTGCAAACTGTCTCTCACACACAGTTCAGGAACTTCAGCACCCAGG	7498	TTAAATGAAACAGACCACAGCTATGAAAGTCATAAACAGCAATCTGAGATTGATGTTCAAACC
	Xirp2 CC		Xirp2 CC
	Xirp2		Xirp2
+1	K K Q I A P L I K S H S F P E S S G Q Q N	+1	F T K K Q Y L K T K K T E A S T E C S H K
6868	AAAAACAGATTGGCGCTTATAAAAATCTCATTCATTTCCAGAGAGTTCAGGACAACAAAAT	7561	TTTACCAAAAAACAATATCTGAAAACCAAGAAAACCTGAAGCAAGCACTGAATGTAGTCATAAG
	Xirp2		Xirp2 CC
	Xirp2 CC		Xirp2
	Heptad		Xirp2
+1	P K P Y M R K F K T P L M I A E E K Y R Q	+1	Q S L A E R H Y Q L P K K E K R V T V Q L
6931	CCAAAACCTTATATGAGAAAAATTAAGACACCTTTAATGATTGCTGAAGAAAAATATAGACAA	7624	CAATCTCTGGCTGAAAACATATCAGTTACCTAAGAAGGAGAAAAGAGTGACAGTACAATTG
	Xirp2		Xirp2 CC
	Xirp2 CC		Xirp2
	Heptad		Xirp2
+1	Q K E E I E K Q K Q E S S Y Y N I V K T Q	+1	P T E S I Q K N Q E D K L K M V P R K Q R
6994	CAAAAAGAAGAAATGAAAACAGAAACAGGAGAGTCTTAC TACAACATGTTAAAAC TCAA	7687	CCTACAGAATCCATACAGAAGAACCAGGAAGATAAGCTCAAGATGGTTCCCGGAAAGCAAGA
	Xirp2 CC		Xirp2 CC
	Xirp2		Xirp2
+1	S Q N Q H I T E V E K E M P L Q K T N E E	+1	E F S G S D R G K L F G S E E K N Q G P S
7057	AGCCAAAATCAACACATAACAGAGGTGAAAAGGAAATGCCATTACAAAAACCAATGAGGAG	7750	GAATTTAGCGGATCTGACAGAGGGAAACTTCCAGGAAGTGAAGAAAAAATCAGGGACCATCA
	Xirp2 CC		Xirp2 CC
	Xirp2		Xirp2
+1	V S L S G I D S E C T V V Q P S P G S Q S	+1	M I G R K E E R L I T E R K H E H L K N K
7120	GTTTCCCTATCTGGAATTGATTCAAGATGCATGTGGTTCAACCCAGCCAGGCTCAAAAT	7813	ATGATTGGTCGAAAAGAAGAGAGATTAACTAAGTAAAAGAAAACACGAACATCTGAAGATAAA
	Xirp2 CC		Xirp2 CC
	Xirp2		Xirp2
+1	N A R I L G V C S D N Q L S T T S P E T V	+1	S A P K V V K Q K V I D A H L D S Q T Q N
7183	AATGCTCGGATACTAGGAGTGTGTTCTGATAACCAACTCCACAACATCGCCAGAAAACAGTC	7876	TCAGCACCAAAAGGTCGTAAGCAAAAAGTTATCGATGCACATCTTGATTACAGACTCAGAAT
	Xirp2 CC		Xirp2 CC
	Xirp2		Xirp2
+1	N A R I L G V C S D N Q L S T T S P E T V	+1	F Q Q T Q I Q T A E S K A E H K K L P Q P
7183	AATGCTCGGATACTAGGAGTGTGTTCTGATAACCAACTCCACAACATCGCCAGAAAACAGTC	7939	TTTCAGCAAAACAAAATACAGACCCTGAAAGTAAAGCTGAACATAAAAAATTGCCCAAGCCA

Figure F.5: Human Xirp2 cDNA - continuation

		Xirp2 CC			Xirp2
		Xirp2			Xirp2
+1		Y N S L Q E E K C L E V K G I Q E K Q V F		+1	S Q S P K K D S Y V E P P P R R P M S Q K
8002		TATAATAGTCTGCAGGAAGAAAAATGTCGGAAGTCAAGGGCATAACAAGAAACAAGTCTTC		8758	TCTCAGTCCCCTAAAAAGGACAGTTATGTTGAACCCCAACAAGAGGCCATGTCGCAAAAA
		Xirp2 CC			Xirp2
		Xirp2			Xirp2
+1		S N T K D S K Q E I T Q N K S F F S S V K		+1	S E I H R A N T S P S P P R S R S E Q L V
8065		TCTAACTACTAAAGATTCAAAGCAAGAGATTACACAGAACAAATCTTTCTTTCCCTCTGTGAAA		8821	TCTGAAATTCACAGAGCAACACTTCCCCTTCTCCACCCAGGAGTGCCTCTGAACAACCTTGT
		Xirp2 CC			Xirp2
		Xirp2			Xirp2 FBS
+1		E S Q R D D G K G A L N I V E F L R K R E		+1	R L K D T T A K L S K G A I P C P A A T P
8128		GAATCCCAGCGGGATGATGGAAAAGTGCCTTAAATATAGTGAATCTTGAGAAAACGTGAA		8884	AGACTCAAAGACACCCTGCAAAGTTATCCAAAGGGGCCATCCCATGTCCAGCAGCAACCCCG
		Xirp2 CC			Xirp2
		Xirp2			hu xlp 7764f
+1		E L Q Q I L S R V K Q F E A E P N K S G L		+1	V P I V E K R S E I I M S P A T L R R Q I
8191		GAACTGCAACAGATTTTGTGAGAGTGAACAGTTGAAGCAGAGCCAAATAAAAGTGGCCCT		8947	GTTCCAATTTGATAGAGAAGGTTGAAATCATCATGTCTCCTGCAACACTTCGTCTGCAAAAT
		Xirp2 CC			Xirp2 FBS
		Xirp2			Xirp2
+1		K T F Q T L L N T I P G W L I S E D K R E		+1	K I E T R G R D S P P T I T I P V N I N H
8254		AAAACATTCAGACACTATAAATACTATCCAGGATGGCTGATAAGTGAAGATAAGAGAGAA		9010	AAGATAGAAACTCGTGGTAGGGACTTCCACCTACAATACAATACCAGTAAATATAAATCAT
		Xirp2			Xirp2 FBS
		Xirp2 CC			Xirp2
+1		Y A V H I A M E N N L E K V K E E I T H I		+1	A A S G S F R G S V D A Q E E I R K V E K
8317		TATGCGTTACACTGCCATGGAGAATAATTAGAAAAAGTAAAAAGAAATAACACATATT		9073	GCTGTAGTGGTTCCTCAGAGGATCTGTGGACGCTCAAGAGGAAATCAGGAAAGTGGAGAAG
		Xirp2			Xirp2 FBS
		Xirp2			Xirp2
+1		K T Q A E D M L V S Y E N I I Q T A M M S		+1	R A T Y V H K D G L N S T D H M V P D T E
8380		AAAACCTAAGCGGAAGATATGCTTGTGTCCTATGAAAATATAATTCAGACAGCCATGATGTC		9136	AGAGCTACTTATGTTCAATAAGATGGACTAAATCCACTGATCACATGGTCCCCGACTGAA
		Xirp2 CC			Xirp2 FBS
		Xirp2			Xirp2
+1		S K T G K P G N K P T S L D E T S S K V S		+1	S Y D A V E I I R K V A V P P R L S E H T
8443		TCCAAAACAGGAAAACCGGAAATAAACCCACTAGTCTTTGATGAAACATCATCCAAGTATCT		9199	AGTTATGATGCAGTTGAAATCATCCGCAAGTTGCAGTGCCCTCTCGCCTGTGACAGCACACA
		Xirp2 CC			Xirp2 FBS
		Xirp2			Xirp2
+1		N V H V S N N K N S E Q K E N K I A K E K		+1	Q R Y E A A N R T V Q M A E N F V N D P E
8506		AATGTTATGTCAGCAATAATAAAAATAGTGAACAGAAAGAAAATAAAAATGCCAAAGAGAAA		9262	CAGAGATATGAAGCGGCCAACCGAAGTTCCAAATGGCTGAAAATTCGTGAATGACCCGTGAA
		Xirp2 CC			Xirp2 FBS
		hXirp2 CCendr			Xirp2
+1		T V Q H Q V A A H H E A T V R S H V K T H		+1	N E I N R W F R E F E H G P V S E A K S N
8569		ACAGTACAGCACCAGTAGCAGCTCATCATGAAGCAACTGTTTCGTAGTACAGTGAACCCCAT		9325	AATGAAATAAACAGATGGTTCAGGGAATTTAGCATGGCCAGTTTCTGAAGCAAAGTCAAAT
		Xirp2			Xirp2 FBS
		Xirp2			Xirp2
+1		Q E I K L D D S N I P P P S L K T R P P S		+1	R R V Y A K G E T N H N I Q Q E S R T F C
8632		CAGGAAATTAACCTTGATAGCAACATTCCTCCTCCCTCTTTAAAAACACGCCACCCGTCAC		9388	AGAAGAGTTTATGCAAAGGGGAGAAACAAACCATAACATACAACAAGAAAGTCGTACATTTTGT
		Xirp2			Xirp2 FBS
		Xirp2			Xirp2
+1		P T F I T I E S T A R R T E N P T K N E L		+1	K E E F G L T S L G N T S F T D F S C K H
8695		CCAACCTTTATCACAATAGAAATCTACTGCCGACGAAACAGAAAACCCCTACTAAGAACGAGCTT		9451	AAGGAGGAATTTGATTAACATCTTTAGGAACACAGATTTTACAGACTTTTCTGCAAAACAT

Figure F.6: Human Xirp2 cDNA - continuation



```

Xirp2 FBS
Xirp2
+1 P R E L R E K I P V K Q P R I C S E T R S
9514 CCTAGAGAACTGCGAGAAAAGATTCCTGTTAAGCAGCCAGGATCTGCTCTGAAACAGGTCCT

Xirp2 FBS
Xirp2
+1 L S E H F S G M D A F E S Q I V E S K M K
9577 CTAAGTGAACATTTCTCAGGCATGGATGCATTTGAGAGTCAAATTTGTTGAGTCGAAGATGAAA

Xirp2 FBS
Xirp2
+1 T S S S H S S E A G K S G C D F K H A P P
9640 ACCTCTTCATCACATAGCTCAGAAGCTGGCAAATCTGGCTGTGACTTCAAGCATGCCCCACCA

Xirp2 FBS
Xirp2
+1 T Y E D V I A G H I L D I S D S P K E V R
9703 ACCTATGAGGATGTCATTGCTGGACATATTTAGATATCTCTGATTCACCTAAAGAAGTAAGA

Xirp2 FBS
Xirp2
+1 K N F Q K T W Q E S G R V F K G L G Y A T
9766 AAAAATTTCAAAGACGTGGCAAGAGAGTGAAGAGTTTTAAAGGCTGGGATATGCAACC

Xirp2 FBS
Xirp2
+1 A D A S A T E M R T T F Q E E S A F I S E
9829 GCAGATGCTTCTGCAACTGAGATGAGAACCACCTTCCAAGAGGAATCTGCATTTATAAGTGAA

Xirp2 FBS
Xirp2
+1 A A A P R Q G N M Y T L S K D S L S N G V
9892 GCTGCTGCTCCAAGACAAGGAAAATGTATACTTTGTCAAAGACAGTTTATCCAATGGAGTG

Xirp2
Xirp2 FBS
hXIRP2 9981r
+1 P S G R Q A E F S *
9955 CCTAGTGGCAGACAAGCAGAATTTTCATAA

```

Figure F.7: Human Xirp2 cDNA - continuation

## Appendix G

### Murine *Xirp2* cDNA Sequence

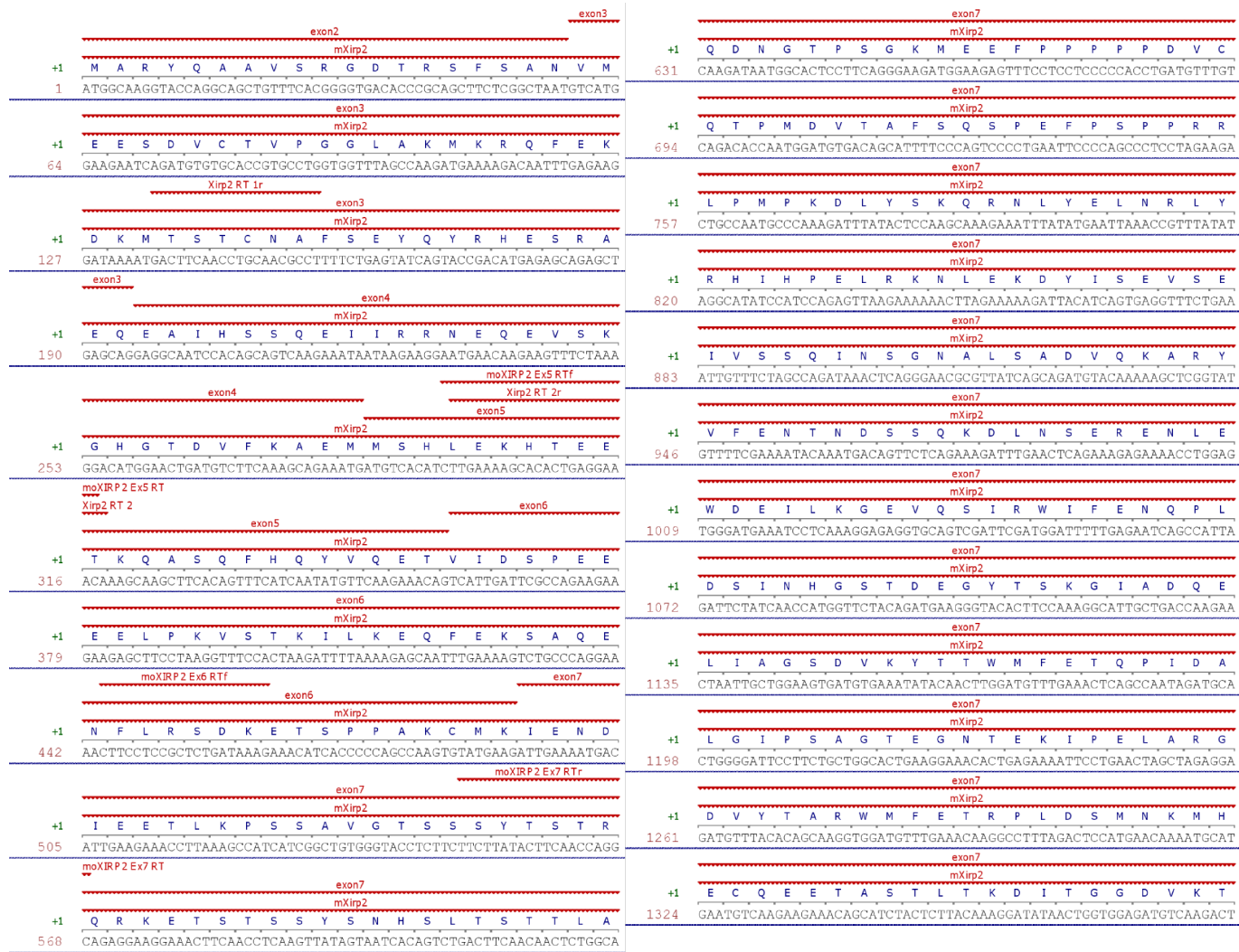


Figure G.1: Murine Xirp2 cDNA

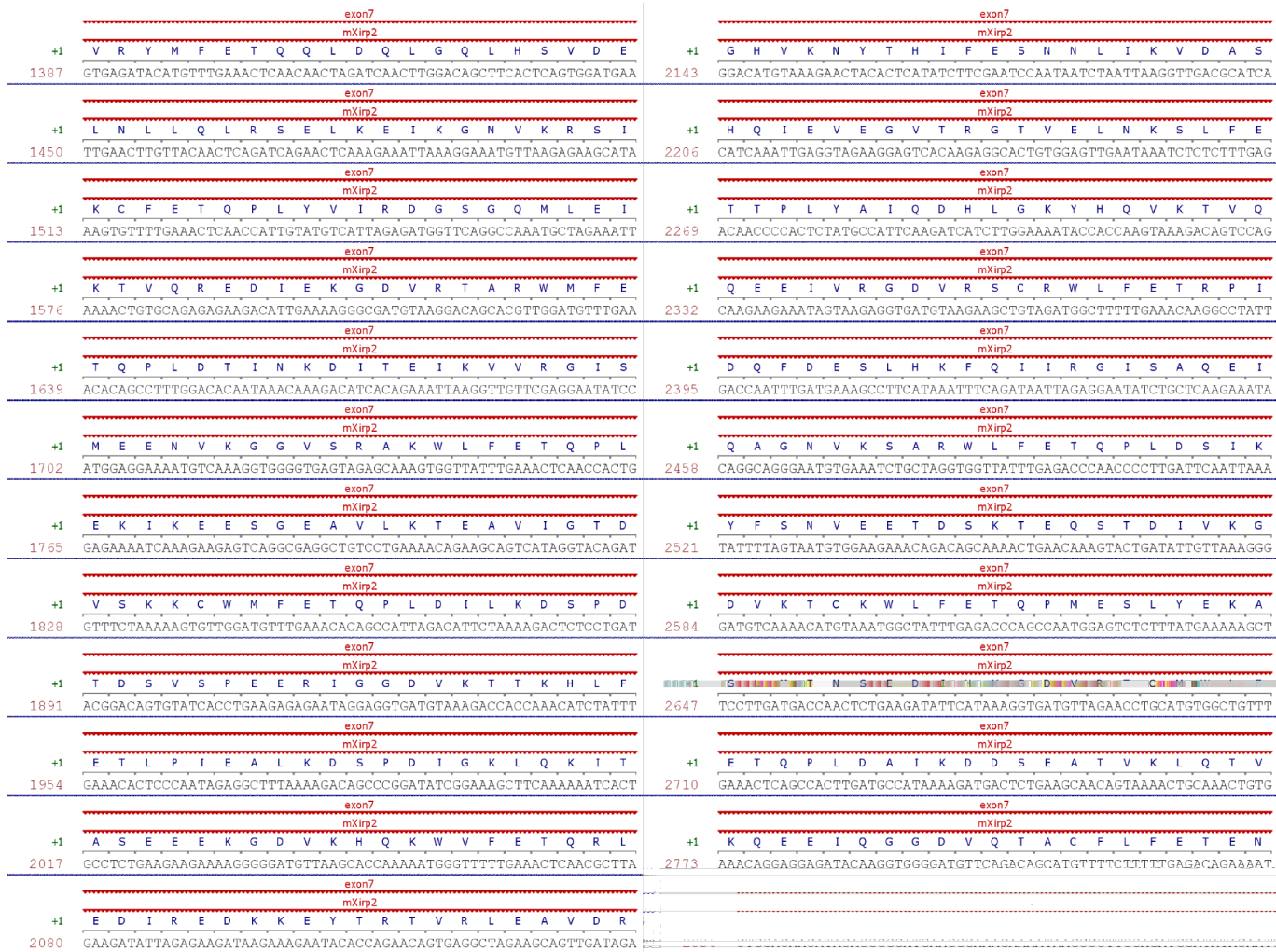


Figure G.2: Murine Xirp2 cDNA - continuation

<p style="text-align: center;">exon7 mXirp2</p> <p>+1 2899 G D V S G M K F K F E N Q S L D S I N C S GGGGATGCTCTGGCATGAAGTTTAAGTTTGAAAATCAGTCCTTAGACTCTATAAAATTCGAGT</p>	<p style="text-align: center;">exon7 mXirp2</p> <p>+1 3655 G N V K T S T W L F E T H R I D E L G E E GGCAATGTTAAGACTTCTACTTGGCTCTTTGAAACTCAGAGAATAGATGAGTTGGGAGAAAG</p>
<p style="text-align: center;">exon7 mXirp2</p> <p>+1 2962 S E N V L S K I K T L K A E D I Q K G N V TCAGAGAATGTTCTAAGTAAGATCAAACGCTAAAAGCCGAAGACATTCAGAAAGGCAATGTT</p>	<p style="text-align: center;">exon7 mXirp2</p> <p>+1 3718 S R Y E N I K T V T Q E D V Q K G D V K Q TCCAGATATGAAAATATCAAGACAGTCACCCAGGAAGCGTGCGAGAAAGGTGATGTGAAGCAA</p>
<p style="text-align: center;">exon7 mXirp2</p> <p>+1 3025 L K C R W L F E N Q P I D M I K E S Q E C CTAAAATGCAGGTGGCTATTTGAAAACCAACCTATTGATATGATAAAAGAAAGTCAAGAATGT</p>	<p style="text-align: center;">exon7 mXirp2</p> <p>+1 3781 A V W L F E N Q T L D S I N E L D E N D T GCAGTGTGGCTTTTTGAAAACCAAGACTTTGGATTCATTAAATGAACCTTGAATAAGATGATACC</p>
<p style="text-align: center;">exon7 mXirp2</p> <p>+1 3088 D G L V K T V T D V Q G G D V R K G C F I GATGGATTGGTTAAACAGTGACAGACCTACAAGGTGGAGATGTAAGAAAGGGATGCTTCATT</p>	<p style="text-align: center;">exon7 mXirp2</p> <p>+1 3844 K M T K E E I P P S D V K T T T W L F E T AAAATGACAAGGAAGAAATTCCTCCGTCGGATGTCAAGACAACACAGTGGCTCTTTGAAACA</p>
<p style="text-align: center;">exon7 mXirp2</p> <p>+1 3151 F E T F S L D E I K D E S D G I S M R E T TTTGAGACATTTCTTTAGATGAGATTAAGATGAATCCGATGGCATCAGCATGAGAGAAACA</p>	<p style="text-align: center;">exon7 mXirp2</p> <p>+1 3907 T P I H E F N K T R V E K E E I I G K S I ACACCTATTCAGAAATTAACAAAACAGTAGAGAGGAAGAAATTAATTTGGTAAAAGTATT</p>
<p style="text-align: center;">exon7 mXirp2</p> <p>+1 3214 N L G E I I K G D V K S Y K M L F E T Q P AATCTCGGGGAAATAAAAAGGTGATGTGAAAAGCTACAAAATGCTTTTTGAAAACACAACCA</p>	<p style="text-align: center;">exon7 mXirp2</p> <p>+1 3970 K E T L E D L Y S Q R V V E A P G I I I E AAAGAAACCTGGAAAGCCTCTACTCTCAAAGAGTTGTTGAAGCTCCCGGAATTATCATTGAA</p>
<p style="text-align: center;">exon7 mXirp2</p> <p>+1 3277 L Y A I Q D H E G F Y H E V T T V K K E E CTCTATGCAATTCAGACCATGAAGGGTTTATCATGAAGTGACAACAGTTAAAAGAAAGAA</p>	<p style="text-align: center;">exon7 mXirp2</p> <p>+1 4033 A D E V G D V R H A K Y K L M N Q T T P E GCTGATGAAGTTGGAGATGTCAGAAATGGCCAAATACAAGCTCATGAACCAACAACCTCCTGAG</p>
<p style="text-align: center;">exon7 mXirp2</p> <p>+1 3340 T I H G D V R G T R W L F E T K P L D S I ACAATACATGGAGATGTACGAGGAACAAGGTGGCTCTTTGAAACAAAACCATTAGACTCAATT</p>	<p style="text-align: center;">exon7 mXirp2</p> <p>+1 4096 I Q K E E V I R A D L G N I M M N L L S Q ATCCAGAAGGAAGTATTCAGGGCTGATCTCGGAACATCATGATGAACCTGCTTTCCCAA</p>
<p style="text-align: center;">exon7 mXirp2</p> <p>+1 3403 H E S E D V Y V I K S V T Q E D I Q K G D CACGAATCAGAAGATGTATACGTTATTAATCCGTCACCCAGGAAGACATTCAGAAAGGGGAT</p>	<p style="text-align: center;">exon7 mXirp2</p> <p>+1 4159 R D C T K K E I F V S E E E K G N V N F T AGAGACTGCACAAAAGAAAGAGATATTTGTCAGTGAAGAGGAGAAAGGAAACGTCATTTTACT</p>
<p style="text-align: center;">exon7 mXirp2</p> <p>+1 3466 V S S V R Y R F E T Q P L D M I S D K S H GTGAGTTCTGTGAGATACAGGTTTGAAACTCAACCACTGGATATGATTTTCAGACAAAATCCCAT</p>	<p style="text-align: center;">exon7 mXirp2</p> <p>+1 4222 K T Q L L N R S M E F H A E K E E I V R G AAAACCAATTATTAACAGATCGATGGAAATTCATGCTGAAAAGGAAGAGATAGTGAGAGGG</p>
<p style="text-align: center;">exon7 mXirp2</p> <p>+1 3529 N I V P T V D Y I Q G G N V Q M N K Q L F AATATTGTCGCCACTGTGACTATATTCAAGGAGCAATGTGCAGATGAATAACAATATATT</p>	<p style="text-align: center;">exon7 mXirp2</p> <p>+1 4285 D V K Q A I Q K L F S E E R R A K K G I L GATGTAACAAGCAATCCAAAAGCTGTTCTCAGAGGAAAGGCGTGCAAGAAAGGCATATTA</p>
<p style="text-align: center;">exon7 mXirp2</p> <p>+1 3592 E S E G G N K K N Y V R T V S V N E I Q K GAGTCTGAAGGTGTTACAAGAAGAACTATGTAAGAACGTAAGTGTCAATGAAATACAAAAG</p>	<p style="text-align: center;">exon7 mXirp2</p> <p>+1 4348 I Q E D E K G D I N M T I Y C L L H E N A ATTCAAGAAGTGAAGGAGATATTAACATGACTATCTATTCTCTTCATGAAAATGCT</p>

Figure G.3: Murine Xirp2 cDNA - continuation

4411	<p>exon7 mXirp2</p> <p>+1 G D K T E R E D I L G G D V R R T I H N L</p> <p>GGTGACAAGACTGAGAGAGAAGACATACTGGGAGGTGATGTGAGGCGCACCATTCATAATCTG</p>	5167	<p>exon7 mXirp2</p> <p>+1 G M L G F S E R P K I G I H P A A V Q R D</p> <p>GGGATGCTAGGATTTTCAGAAAGGCCAAAATATGGGATCCATCCAGCAGCTGTCCAGAGAGAC</p>
4474	<p>exon7 mXirp2</p> <p>+1 L S S A S N G K I S E R T K I D A S E R G</p> <p>TTATCTTCTGCATCAAAATGGTAAGATATCCGAAAGGACAAAAATCGATGCTTCGGAGAGGGGA</p>	5230	<p>exon7 mXirp2</p> <p>+1 K K S L L Q P V P G P F E P A I K Q Q A G</p> <p>AAAAAAGTCTTCTTCAACCAAGTCCAGGACCATTTGAACCAAGCAATCAAGCAGCAAGCAGGA</p>
4537	<p>exon7 mXirp2</p> <p>+1 N V Q F F T T C I E T G A L D Y L K Q L Q</p> <p>AATGTTCAAGTCTTCACAACATGCATCGAACTGGAGCTTTGGATTACCTCAAGCAACTCCAA</p>	5293	<p>exon7 mXirp2</p> <p>+1 P G T L D E T T Q K P C L R S L I E E R T</p> <p>CCAGGCACCTTGTATGAACTACACAGAAACCCCTGCCTTCGGTCTTTAATAGAAGAAAGAACT</p>
4600	<p>exon7 mXirp2</p> <p>+1 T G S N E S T L T A S K Q E G E E E I I G</p> <p>ACAGGGTCAAAATGAAAGCACACTCACAGCTAGCAAGCAGGAAGGAGAGAAAGAAATAATTGGT</p>	5356	<p>exon7 mXirp2</p> <p>+1 E A N L P K A P K G T V K I V I D R E Q N</p> <p>GAAGCTAATCTTCCCAAAGCCCTTAAGGGCACGTAAAGATTGTCAATTGATCGTGAACAAAAC</p>
4663	<p>exon7 mXirp2</p> <p>+1 G D V E G T K F L L K K R Q S S F E R T V</p> <p>GGTGATGTTGAGGGAACAAAATTCCTACTGAAGAAAAGCAGCTTCCTTTGAACGACTACTGTT</p>	5419	<p>exon7 mXirp2</p> <p>+1 N D A L E K S L R K M S N S E H R A M K N</p> <p>AATGATGCTCTTGAGAAAAGCCCTTGA AAAATGTCTAATTCAGAGCATAGAGCTATGAAAAAT</p>
4726	<p>exon7 mXirp2</p> <p>+1 S E T D I I P G D V R H T V K V F M T E P</p> <p>AGTGAGACTGACATCATCCAGGCGATGTGCGTCAACAGTTAAAGTCTTCATGACAGAGCCCT</p>	5482	<p>exon7 mXirp2</p> <p>+1 V L D M S D R M G I W T E S K E Y L C S D</p> <p>GTCTTAGACATGAGTGACAGAATGGGTATCTGGACTGAGAGCAAAAGAAATATCTGTGTAGTGAT</p>
4789	<p>exon7 mXirp2</p> <p>+1 Q S S S Y K T V K D E I I K G D L K S T L</p> <p>CAGAGTTCATCTTATAAGACAGTGAAGACGAGATTATAAAAGGTGATTTGAAATCAACCTTG</p>	5545	<p>exon7 mXirp2</p> <p>+1 D H M S K H L S A T M S I K E S L K S K E</p> <p>GACCATATGAGCAAACACTTAAAGTCCACCATGTCAATTAAGGAAAGTCTAAAATCCAAGGAA</p>
4852	<p>exon7 mXirp2</p> <p>+1 N S L N Q A M N Q K T V A K A E E I V K D</p> <p>AATTCTCAACAGGCCATGAATCAGAAAACAGTGGCTAAAGCAGAAGAAATGTTGAAAGAT</p>	5608	<p>exon7 mXirp2</p> <p>+1 S E N M R E A K D D V I S S T Q S V D K T</p> <p>TCAGAGAACATGAGAGAAGCAAAGGATGATGTCATTAGCTCCACCCAGCTGTGGATAAAAA</p>
4915	<p>exon7 mXirp2</p> <p>+1 D R L A I L K S L K E S G D R Q K E P K Q</p> <p>GACAGGCTGGCCATCTCAAGTCACTTAAGGAGTCAGGGGACAGAGAGAAAGAACCCAAACAA</p>	5671	<p>exon7 mXirp2</p> <p>+1 F R K Q Q T Q T C E L G N D Q K S R F Q D</p> <p>TTTAGAAAGCAACAGACTCAAACCTGTGAGCTAGGCAATGATCAGAAGTCTCGGTTCCAGGAT</p>
4978	<p>exon7 mXirp2</p> <p>+1 S G G M S R D I G Q A I E C L E R A T N T</p> <p>TCTGGTGGCATGTCTAGAGATATCGGGCAAGCTATTGAGTGCCTCGAGAGGGCTACAATACA</p>	5734	<p>exon7 mXirp2</p> <p>+1 S Y G K N Q K N I Q N I E I T R D F Q K Q</p> <p>TCCTATGGGAAGAAATCAAAAAATTCAAAAACATTTGATCACAAGGGACTTTCAGAAGCAA</p>
5041	<p>exon7 mXirp2</p> <p>+1 R T E I L K K E L I L D D L K T S L R S L</p> <p>AGGACTGAAATCTTGAAAAAGAGCTGATATTAGATGATCTTAAACATCACTAAGGCTCTTG</p>	5797	<p>exon7 mXirp2</p> <p>+1 A L L S Q E K Q Y S N K E M K K N E A S L</p> <p>GCCTTGCTCAGTCAGGAAAAGCAGTATCTTAATAAAGAGATGAAAGAAAAATGAGGCGAGCCTT</p>
5104	<p>exon7 mXirp2</p> <p>+1 K E E Q C G F K E V D K Q G I V K D V L P</p> <p>AAAGAAGAACAGTGTGGTTTCAAAGAGTTGATAAACAGGGAATAGTCAAAGATGTACTACCT</p>	5860	<p>exon7 mXirp2</p> <p>+1 Q P L P V G K E V H S V P G V T V S G K N</p> <p>CAACCTTTGCCGTGGGTAAGGAGGTACACAGTGTACCAGGAGTGACAGTCTCTGGAAAAAC</p>

Figure G.4: Murine Xirp2 cDNA - continuation



<p style="text-align: center;">exon7 mXirp2</p> <p>+1 5923</p> <p style="text-align: center;">exon7 mXirp2</p> <p>+1 5986</p> <p style="text-align: center;">exon7 mXirp2</p> <p>+1 6049</p> <p style="text-align: center;">exon7 mXirp2</p> <p>+1 6112</p> <p style="text-align: center;">exon7 mXirp2</p> <p>+1 6175</p> <p style="text-align: center;">exon7 mXirp2</p> <p>+1 6238</p> <p style="text-align: center;">exon7 mXirp2</p> <p>+1 6301</p> <p style="text-align: center;">exon7 mXirp2</p> <p>+1 6364</p> <p style="text-align: center;">exon7 mXirp2</p> <p>+1 6427</p> <p style="text-align: center;">exon7 mXirp2</p> <p>+1 6490</p> <p style="text-align: center;">exon7 mXirp2</p> <p>+1 6553</p> <p style="text-align: center;">exon7 mXirp2</p> <p>+1 6616</p>	<p style="text-align: center;">exon7 mXirp2</p> <p>+1 6679</p> <p style="text-align: center;">exon7 mXirp2</p> <p>+1 6742</p> <p style="text-align: center;">exon7 mXirp2</p> <p>+1 6805</p> <p style="text-align: center;">exon7 mXirp2</p> <p>+1 6868</p> <p style="text-align: center;">exon7 mXirp2</p> <p>+1 6931</p> <p style="text-align: center;">exon7 mXirp2</p> <p>+1 6994</p> <p style="text-align: center;">exon7 mXirp2</p> <p>+1 7057</p> <p style="text-align: center;">exon7 mXirp2</p> <p>+1 7120</p> <p style="text-align: center;">exon7 mXirp2</p> <p>+1 7183</p> <p style="text-align: center;">exon7 mXirp2</p> <p>+1 7246</p> <p style="text-align: center;">exon7 mXirp2</p> <p>+1 7309</p> <p style="text-align: center;">exon7 mXirp2</p> <p>+1 7372</p>
---	---

Figure G.5: Murine Xirp2 cDNA - continuation

	exon7 mXirp2		exon7 mXirp2
+1	D I Q T S T E Q T D K E I K K T Q A S I Q	+1	E K R E Y G V R V A M E N N F E K V K E E
7435	GACATTCAAACCACTACTGAACAAACAGATAAGGAAATCAAGAAAACCCAGGCCAAGCATACAG	8191	GAGAAAAGAGAATATGGAGTTCGTGTGCCATGGAGAATAATTCGAAAAAGTCAAAGAAGAA
	exon7 mXirp2		exon7 mXirp2
+1	C D D D K P S V P E K Y F Q L P K T E K R V	+1	I T H I K T Q A E E M L L L Q C E H V I Q T
7498	TGTGATGATAAGCCATCTGTGCCTGAAAAATATTTTCAGTTACCTAAAACAGAGAAACGGGTG	8254	ATAACACATATTAACCTCAAGCCGAGGAGATGCTTTCAGTGTGAACATGTAATTCAGACA
	exon7 mXirp2		exon7 mXirp2
+1	T I Q M P K E Y A E K S H K S K L Q T V P	+1	A M M A S Q T G K Q R D K P T N L N E M P
7561	ACCATACAAATGCCCAAAGAATATGCAGAGAAAAGTCATAAAAGTAAAGTCCAGACAGTTCC	8317	GCCATGATGGCTTCCCAAACAGGAAAGCAGAGAGATAAACCTACCAACCTTAATGAAATGCCA
	exon7 mXirp2		exon7 mXirp2
+1	K K Q G I F G E F D R G N V L G R E G K N	+1	L N V S N V N L S S S K C T E Q K E S K T
7624	AAGAAGCAAGGAATATTTGGGGAGTTTCACAGAGGGAATGTCCCTGGGGAGGGAAGAAAAAAT	8380	CTGAATGTGTCTAATGTAACTCAGCTCGAGTAAATGCACCGAACAGAAAAGTAAAACT
	exon7 mXirp2		exon7 mXirp2
+1	Q D S S V S C S K E D R L I D E R K Q E H	+1	V E E K L T H R Q V T T H P E A A T R N P
7687	CAGGACTCCTCCGTGACTGTTCAAAAGAAGACAGACTAATAGATGAAAGAAGCAGAACAT	8443	GTAGAAGAAAATTAACACACCACAGTAACAACCTCATCTGAGCAGCAACCCGTAACTCT
	exon7 mXirp2		exon7 mXirp2
+1	L Q N Q R V P R S V Q Q K V I N E R L D S	+1	V K P Y Q E A K G E D G K M A P P S L K T
7750	CTGCAGAACCAAGGGTACCAAGGTCAGTCCAACAAAAGGTTATCAATGAACGCCTGGACTCA	8506	GTTAAACCATACCAGGAGGCTAAGGGGAAGACGGTAAAGATGGCTCCTCCCTCTTTGAAAAC
	exon7 mXirp2		exon7 mXirp2
+1	Q M Q N F Q Q T E I Q T S R S T I E C E E	+1	R P P S P T F I T I E S T A R R A E T S T
7813	CAGATGCAGAAATTTTCAGCAGACAGAAATACAAACTTCTAGAAGTACAATTGAGTGTGAAGAA	8569	CGCCCTCCATCAACCACTTTTATTACAATAGAGTCCACTGCCCGTAGAGCAGAAACCTCCACG
	exon7 mXirp2		exon7 mXirp2
+1	F S Q S Y N A T Q E K T C L K D K G K Q Q	+1	K S E L S Q S P K N N R C I E P P P R R P
7876	TTCTCCAGTCTTACAATGTCTACGCAAGAGAAAACATGCCTTAAAGACAAGGGCAACACAG	8632	AAGAGTGAGCTTCTCAGTCCCTAAAAATAACCGTTGTATTGAACCTCCACCCGAGACCC
	exon7 mXirp2		exon7 mXirp2
+1	G Q V T S N T E E S K Q E L R Q N Q S A F	+1	V E H A S G L P R S R T P P S P P R S R S
7939	GGACAGGTCACCTCTAACACTGAAGAGTCAAGCAAGAGCTAAGACAGAACCAATCTGCATTT	8695	GTGGAACATGCATCTGGACTTCCAGATCAAGAACACCACCTTCCCAACCAAGGAGTCTTCA
	exon7 mXirp2		exon7 mXirp2
+1	S S V K D S Q H D D G K C T I N I L E F L	+1	E Q L V R L K D T T A R L A K G T I P C S
8002	TCCTCTGTGAAAGATTTCCAGCAGATGATGGAAAATGTACCATAAATATATTGGAATTCCTTG	8758	GAACAATTGTGAGACTCAAAGACACCACGGCCAGGCTAGCCAAAGGCACCATCCCTTGTTC
	exon7 mXirp2		exon7 mXirp2
+1	R K R E E L Q Q I L S R V K Q F E A E S S	+1	P G T P V P I V E K R S E V V M S P A T L
8065	CGAAAACGTGAAGACTACAGCAGATTTGCTCAGGGTAAAACAGTTTGAAGCAGAGTCAAGT	8821	CCAGGAACCCAGTCCAATTGTAGAGAAGAGATCTGAGGTTGTCATGCTCCAGCCACACTC
	exon7 mXirp2		exon7 mXirp2
+1	K S G L K T F Q I L L N I V P V W L I S E	+1	R R Q I K I E S R G G D S P P T I T I P V
8128	AAAAGTGGCTTAAAACGTTTCAGATACTGTAAATATGTCCCGGTATGGCTGATAAGTGG	8884	CGCAGACAAATCAAGATAGAAGTCTGGTGGGGACTCACCCACCACATCAATACCTGTG

Figure G.6: Murine Xirp2 cDNA - continuation

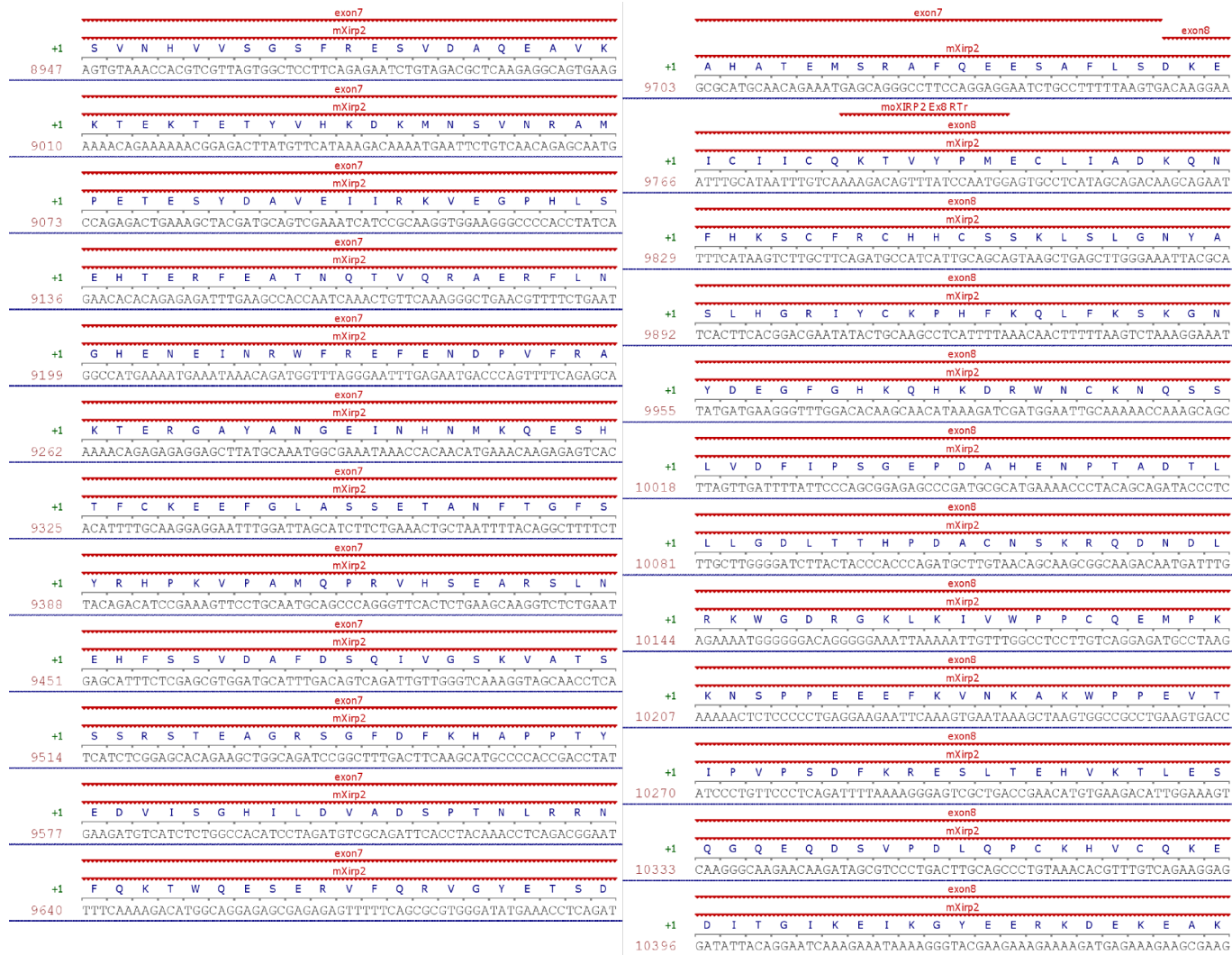


Figure G.7: Murine Xirp2 cDNA - continuation



Figure G.8: Murine Xirp2 cDNA - continuation

## Appendix H

### Human LIMCH1 cDNA Sequence

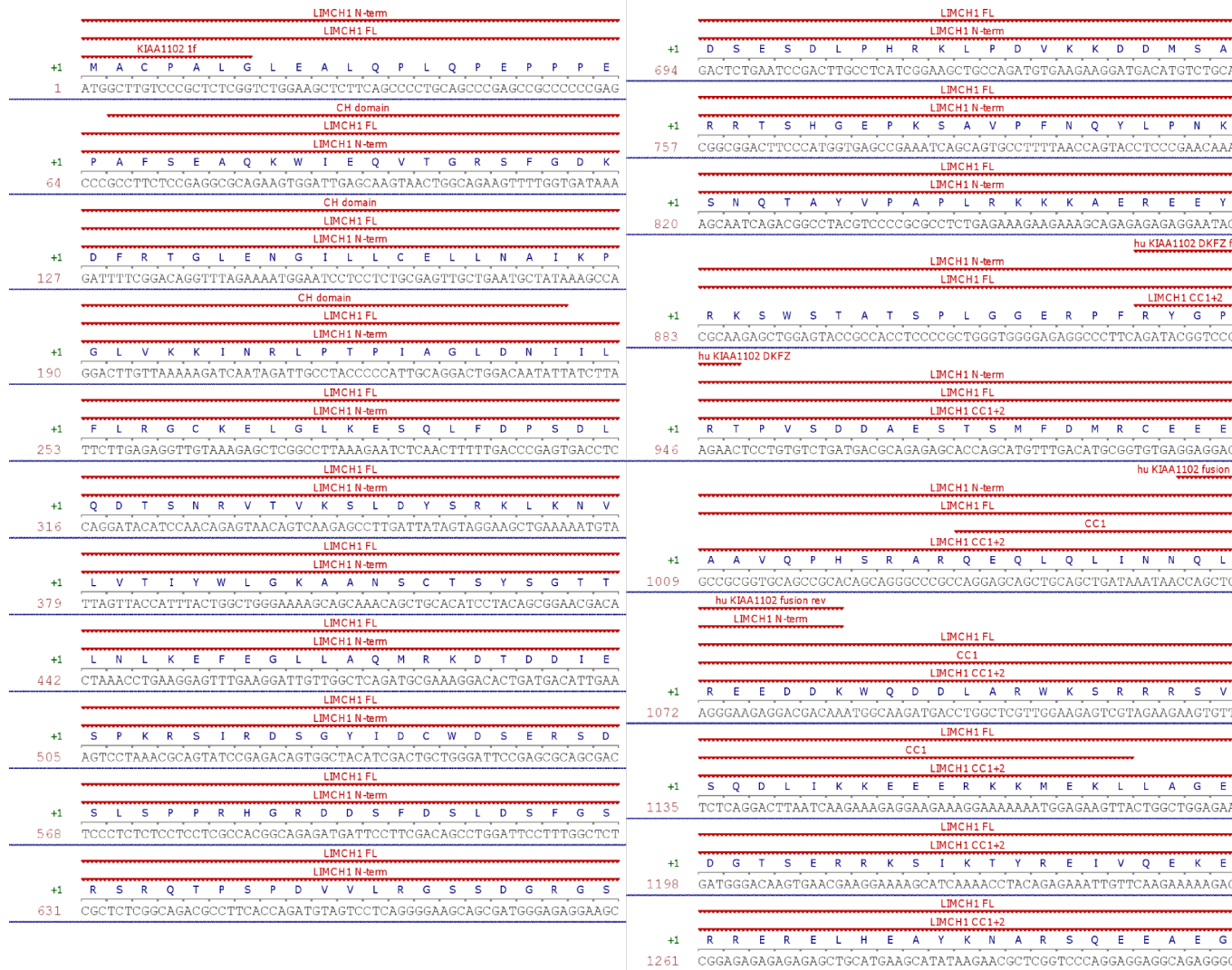


Figure H.1: Human LIMCH1 cDNA



	LMCH1 FL		LMCH1 CC1+2		LMCH1 CC2
+1	I L Q Q Y I E R F T I S E A V L E R L E M				
1324	ATCCTTCAACAGTACATTGAGAGGTTCCACATCAGTGAGGCTGTTCTCGAAGCCTTGGAGATG				
	LMCH1 FL		LMCH1 CC1+2		LMCH1 CC2
+1	P K I L E R S H S T E P N L S S F L N D P				
1387	CCAAAAATTCGGAAGAACCCATTCAACAGAGCCAAATTTATCCTCCCTCTGAATGACCCP				
	LMCH1 FL		LMCH1 CC1+2		LMCH1 CC2
+1	N P M K Y L R Q Q S L P P P K F T A T V E				
1450	AATCCCATGAAATACCTGCGGCAACAGTCAC'TGCC'TCCACCCAAATTCAC'TGCCACTGTTGAA				
	LMCH1 FL		LMCH1 CC1+2		LMCH1 CC2
+1	T T I A R A S V L D T S M S A G S G S P S				
1513	ACCACCATTGCTCGTGCAGTGTCTGGATACCAGCATGTCAGGAGGCAGTGGGTCTCCAAAGC				
	LMCH1 FL		LMCH1 CC1+2		LMCH1 CC2
+1	K T V T P K A V P M L T P K P Y S Q P K N				
1576	AAAAC'TGCTACTCCCAAAGCAGTGCCTATGCTGACACCCAAAGCCTTACTCCAGCCCAAAAAAT				
	LMCH1 FL		LMCH1 CC1+2		LMCH1 CC2
+1	S Q D V L K T F K V D G K V S V N G E T V				
1639	TCTCAAGATGTTCTGAAGACCTTTAAGGTAGACGGGAAAGTCAGTGTGAATGGAGAGACGGTT				
	LMCH1 FL		LMCH1 CC1+2		LMCH1 CC2
+1	H R E E E K E R E C P T V A P A H S L T K				
1702	CATAGAGAGGAGAGAAGGAAAGAGAGTGTCCACGGTGGCACTGCCACTCCTTAACCAAA				
	LMCH1 FL		LMCH1 CC1+2		LMCH1 CC2
+1	S Q M F E G V A R V H G S P L E L K Q D N				
1765	TCCCAGATGTTTGAAGGTGTGGCCAGAGTGCACGGGTCTCCACTGGAGCTGAAACAAGACAAC				
	LMCH1 FL		LMCH1 CC1+2		LMCH1 CC2
+1	G S I E I N I K K P N S V P Q E L A A T T				
1828	GGTAGCATCGAGATCAACATAAAGCAAACTCTGTCCCAAGAGCTCGCAGCAACCCT				
	LMCH1 FL		LMCH1 CC1+2		LMCH1 CC2
+1	E K T E P N S Q E D K N D G G K S R K G N				
1891	GAGAAAACCGAACCGAATAGTCAAGAGGACAAGAATGATGGTGGAAAAACAAGAAAAGGGAAT				
	LMCH1 FL		LMCH1 CC1+2		LMCH1 CC2
+1	I E L A S S E P Q H F T T T V T R C S P T				
1954	ATAGAACTTGCCTCATCAGAACCACAGCATTTTACAACAACGTGTACTCGATGCAGCCCGACC				
	LMCH1 FL		LMCH1 CC1+2		LMCH1 CC2
+1	V A F V E F P S S P Q L K N D V S E E K D				
2017	GTGGCCTTTGTGAATTTCCCTCCAGCCCCAGCTGAAGAATGATGTGTCGGAAGAAAAGAC				
	LMCH1 CC1+2		LMCH1 CC2		LMCH1 CC2
+1	Q K K P E N E M S G K V E L V L S Q K V V				
2080	CAGAAGAAACCAGAAAAATGAAATGAGTGGAAAGGTGGAGTTGGTGTGTACAAAAAGGTGGTA				
	LMCH1 FL		LMCH1 CC1+2		LMCH1 CC2
+1	K P K S P E P E A T L T F P F L D K M P E				
2143	AAGCCAAAATCTCCAGAACCAGCAACGCTGACATTTCCATTTCTGGACAAAATGCCTGAA				
	LMCH1 FL		LMCH1 CC1+2		LMCH1 CC2
+1	A N Q L H L P N L N S Q V D S P S S E K S				
2206	GCCAAACCACTACATTTGCCAAATCTCAATTTCAAGTGGATTCTCCAAGCAGTGAGAAGTCA				
	LMCH1 FL		LMCH1 CC1+2		LMCH1 CC2
+1	P V M T P Q F K F W A W D P E E E R R R Q				
2269	CCTGTTATGACACCTCAGTTTAAAGTTC'TGGGCATGGGACCCAGAAGAGGAGCGCAGGCACAG				
	LMCH1 FL		LMCH1 CC1+2		LMCH1 CC2
+1	E K W Q Q E Q E R L L Q E R Y Q K E Q D K				
2332	GAAAAATGGCAACAGGAACAGGAACGTTTCTCCAGGAGAGATACCAGAAGGAGCAGGACAAG				
	LMCH1 FL		LMCH1 CC1+2		LMCH1 CC2
+1	L K E E W E K A Q K E V E E E E R R Y Y E				
2395	CTGAAAGAAGAGTGGGAAAAGGCCAAAAGGAGGTGGAAAGAGGAAGAACGCAGATACTATGAG				
	LMCH1 FL		LMCH1 CC1+2		LMCH1 CC2
+1	E E R K I I E D T V V P F T V S S S S A D				
2458	GAGGAGCGTAAGATAATTGAAGACACTGTGGTTCCATTTACTGTTTCTCAAGTTCGCGTGAC				
	LMCH1 FL		LMCH1 CC1+2		LMCH1 CC2
+1	Q L S T S S S M T E G S G T M N K I D L G				
2521	CAGTGTCTACCTTCTCCATGACTGAAGGCAGTGGGACAAATGAATAAGATAGACCTGGGA				
	LMCH1 FL		LMCH1 CC1+2		LMCH1 CC2
+1	N C Q D E K Q D R R W K K S F Q G D D S D				
2584	AACTGTCAAGATGAAAAACAAGACAGAAGATGGAAAGAAATCAATTCAGGGAGATGACAGTGAC				

Figure H.2: Human LIMCH1 cDNA - continuation

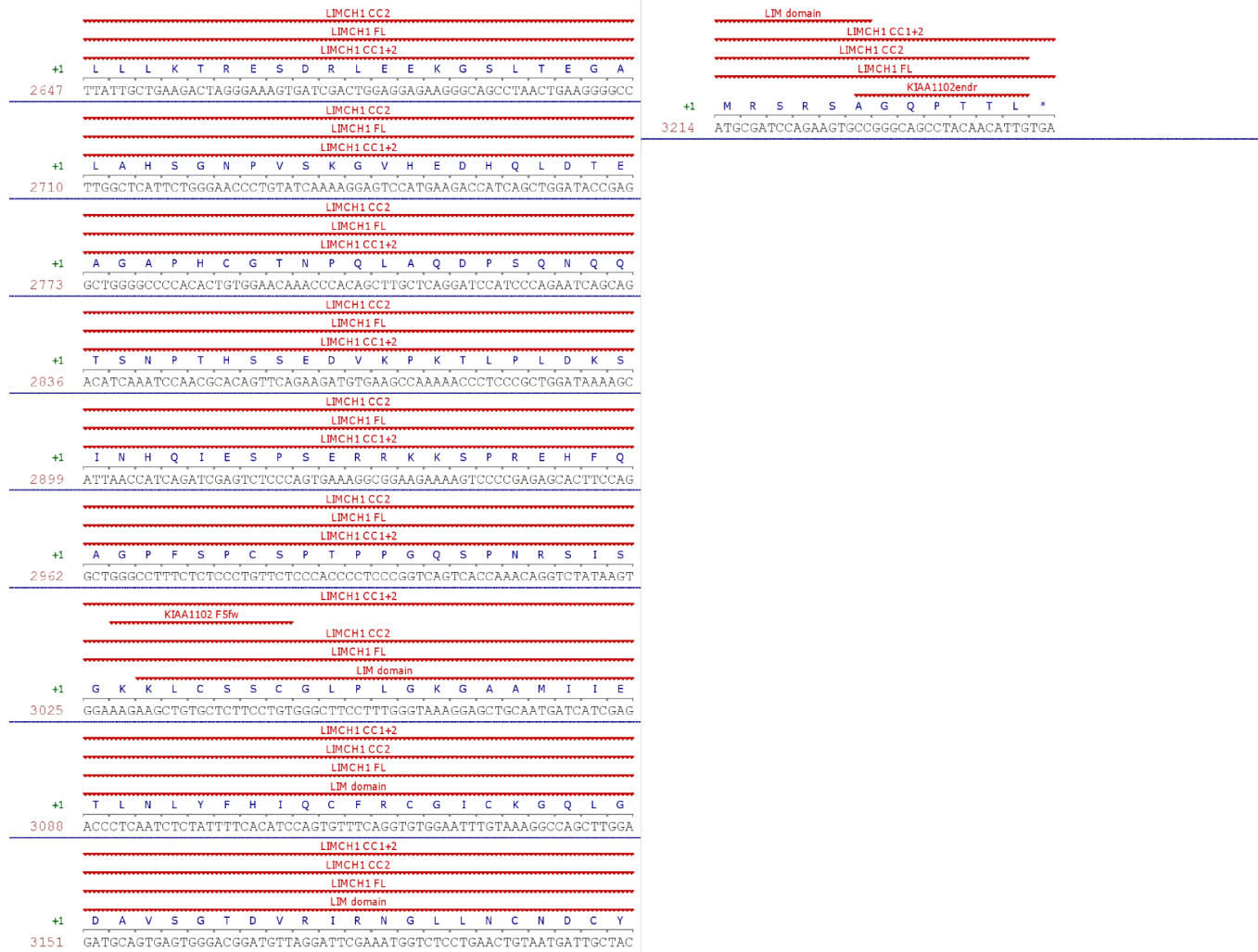


Figure H.3: Human LIMCH1 cDNA - continuation

# Appendix I

## Murine LIMCH1 cDNA Sequence

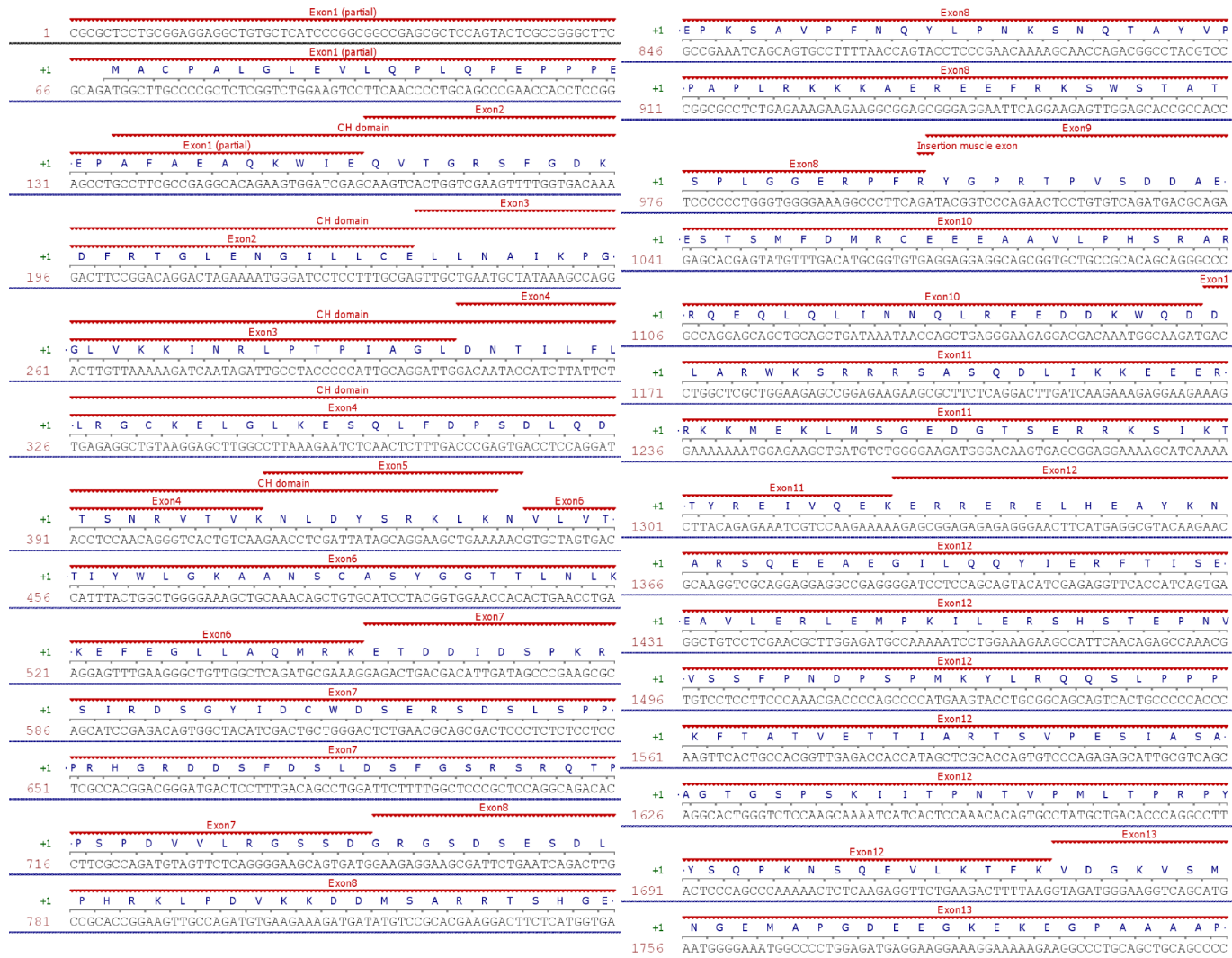


Figure I.1: Murine LIMCH1 cDNA

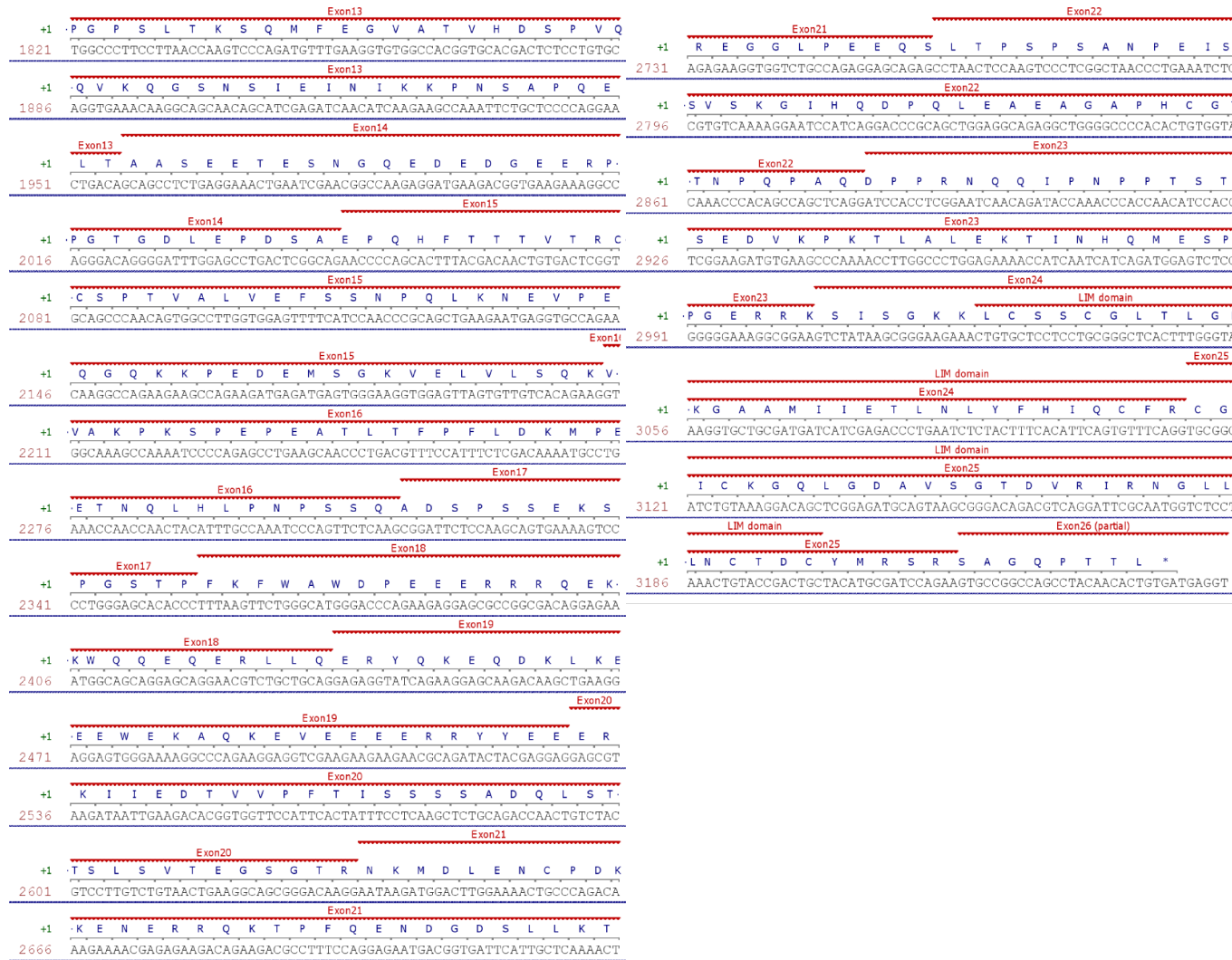


Figure I.2: Murine LIMCH1 cDNA - continuation



Figure I.3: Murine LIMCH1 cDNA of the insertion identified in skeletal muscle